ICRF ANTENNA COUPLING AND WAVE PROPAGATION IN A TOKAMAK PLASMA

Thesis by

Glenn Joel Greene

In Partial Fulfillment of the Requirements

for the Degree of

Doctor of Philosophy

California Institute of Technology

Pasadena, California

1984

(Submitted February 9, 1984)

This thesis is dedicated

to the memory of my mother, Sylvia,

and to my father, Franklin

ACKNOWLEDGEMENTS

I would like to thank my thesis advisor, Dr. Roy Gould, for his guidance during the course of this work, and for the benefit of his clear insight into many aspects of physics.

I enjoyed discussions with Eric Fredrickson, Larry Sverdrup, and Dr. Mark Hedemann on a variety of topics, including, occasionally, plasma physics. I am indebted to Dr. Mark Dolson for a clear introduction to digital signal processing, as well as for providing company during many late evenings on the second floor of Steele laboratories.

The facilities and staff of C.E.S. (Central Engineering Services) proved invaluable during the experimental phase of this work. In particular, I extend my sincere thanks to Louis Johnson, Asst. Manager of C.E.S., for services which went far beyond his official duties. On many occasions when an experiment was halted for lack of a part (particularly before a long holiday), Louis somehow found a way to have it produced. I have also benefited from his tutorials on materials technology and production technique. I am indebted to Norman Keidel, Manager of C.E.S., for his help on many projects, and to staff members Michael Gerfen, Marty Gould, Ralph Ortega, and Ricardo Paniagua for their skillfull work. I thank Herb Adams for demonstrating that function can indeed still have form.

I would also like to thank Frank Cosso for his elegant work on the power and diagnostic systems of the tokamak, on the data acquisition system, and on the laboratory computers. His expertise in electronics was a valuable asset to the laboratory.

To all of my friends from the Keck House Colony, particularly Dr.'s Mark Dolson, Neil Gehrels, Jack Kaye, Ken McCue, Andy Pesthy, Satwindar Sadhal, Betty Vermeire, Vatché Vorpérian, and Ellen Williams, my appreciation for contributing to an enjoyable community. I am also grateful to Mrs. Marilyn Chandler for her generous hospitality during my stay in her home.

I genuinely enjoyed my interactions with Dr. James Hudspeth, who catalyzed my interest in neurobiology and provided many stimulating discussions. I extend my appreciation as well to Edith Huang, who was proficient in eliminating many problems associated with the typesetting program on which this thesis was produced.

Organizations which provided support for this research include the Westinghouse Corporation, the Earle C. Anthony Foundation, Rockwell International Corporation, and the U.S. Department of Energy.

I am grateful to my family and relatives for their continued support and encouragement during my stay at Caltech.

Finally, I thank Wendy All for apprehending me thirteen years ago at the San Diego Science Fair. Her return to my life has made these last difficult years more enjoyable. I am also grateful to her for the many excellent illustrations which enhance this thesis.

G. J. G.

ABSTRACT

A variety of experiments are reported pertaining to the excitation, propagation, and damping of waves in the ion cyclotron range of frequencies (ICRF) in the Caltech Research Tokamak.

Complex impedance studies on five different RF antennas addressed the nature of the anomalous density-dependent background loading observed previously in several laboratories. A model was proposed which successfully explained many of the observed impedance characteristics solely in terms of particle collection and rectification through the plasma sheath surrounding the antenna electrode. Peaks were observed on the input resistance of the shielded antennas and were coincident with toroidal eigenmode production; their magnitude was explained by a simple coupling theory.

The toroidal eigenmodes were studied in detail with magnetic field probes. The mode dispersion curves in density-frequency space were mapped out and the results compared with various theoretical models. A surprising result was that all of the antennas, both magnetic and electric in nature, coupled to the eigenmodes with comparable efficiency with respect to the antenna excitation current. Wave damping was investigated and found to be considerably higher than predicted by a variety of physical mechanisms. A numerical model of the wave equations permitting an arbitrary radial density profile was developed, and a possible mechanism for enhanced cyclotron damping due to density perturbations was proposed. Toroidal modes were identified using phase measurements between pairs of magnetic probes; they were found to have $m = 1$ poloidal character and low integral toroidal mode numbers, in accordance with theoretical predictions.

A new approach to the study of ICRF wave propagation was investigated: wave-packets were launched and their propagation was followed around the tokamak using magnetic probes. This technique avoided the dominant effect of the eigenmode resonances because it observed propagation on a time scale short compared to the formation time for the modes. The transit time of the packets around the machine yielded the toroidal group velocity, and the results of the experiments were compared with several theoretical models. The inclusion of a vacuum layer at the plasma edge was useful in explaining some of the observations.

Finally, a plasma-compatible Rogowski current probe was developed and used to observe, for the first time, RF particle current in a tokamak plasma. The diagnostic permitted investigation of the spatial form of the RF current driven in the edge plasma by the electric field antennas. The results dramatically showed that the current from these antennas flows largely along the toroidal field lines. This highly localized current distribution suggests a mechanism for the good coupling to the eigenmode fields observed with these antennas.

TABLE OF CONTENTS

CHAPTER I

Introduction

Controlled thermonuclear fusion promises to provide a virtually unlimited source of energy, provided the enormous technical challenges can be overcome. Among the current schemes to achieve a demonstration of scientific feasibility, the tokamak approach has been the most promising.

In order to achieve the desired goal of a net energy yield from a controlled fusion reaction, the plasma must be both confined for a sufficient period of time and heated to a sufficient temperature. In the tokamak configuration of magnetic confinement, the poloidal field which provides the rotational transform is generated by driving a large current toroidally around the machine. Besides providing one component of the necessary confinement field, this current provides initial heating of the plasma through collisional losses.

The conductivity of a high-temperature plasma increases as the temperature rises, and the efficiency of this ohmic-heating consequently decreases. The maximum permissible toroidal current is limited by the onset of MHD instabilities, and it has long been recognized that some form of supplemental heating will be necessary to achieve ignition temperatures [Artsimovich, 1972]. Neutral-beam heating (injection of high-energy neutralized particle beams across the toroidal field lines) has been used successfully [Hawryluk, 1981; Fonck, 1983], and it is projected that it will be sufficient to reach breakeven in the TFTR tokamak at Princeton within a few years. Nevertheless, it is possible that neutral-beam heating will not be easily or economically scalable to reac-

tor regimes [Furth, 1983], and alternate plasma heating schemes are being actively pursued.

One of the most promising supplemental heating mechanisms involves the use of electromagnetic waves near the ion cyclotron frequency. To first order, the plasma particles execute helical orbits about the magnetic field lines, precessing at their respective cyclotron frequencies. If a circularly polarized electric field with the appropriate phase and frequency could be somehow imposed in the plasma volume, the particles would be accelerated by the wave field and would gain energy. This approach is particularly attractive since energy can be deposited directly in the ion population. The plasma, however, is a complex, anisotropic media, and one cannot in general impose a prescribed field. Rather, a wave is launched from some point on the plasma boundary, and it propagates into the plasma, being damped as it travels. Careful consideration of the properties of the waves being excited is necessary to insure that energy is deposited in the desired region. Note that because the toroidal magnetic field falls off as $1/R$, where R is the major radius, resonant cyclotron effects take place on a cylindrical surface of constant major radius where the cyclotron frequency (which is now a function of major radius) becomes equal to the excitation frequency.

In the ion-cyclotron range of frequencies (ICRF), cold plasma theory predicts that, in a hydrogenic plasma, two waves can propagate: the so-called fast and slow waves (see Chapter 2). The slow wave, also called the ion cyclotron wave, has a resonance (wavenumber $\rightarrow \infty$) at the ion cyclotron frequency and does not propagate immediately above it. For propagation below the ion cyclotron frequency and along the static magnetic field direction, however, the electric field of the slow wave is completely left-hand circularly polarized, i.e., polarized in the same sense as the ion precession. The earliest attempts to use ICRF waves to heat a plasma utilized the slow wave in a stellerator device [Stix

and Palladino, 1960]. The waves were launched in a region where the excitation frequency (ω) was less than the cyclotron frequency (ω_{ci}). The slow wave was excited and propagated into a magnetic "beach" region where the confinement field decreased until $\omega > \omega_{ci}$; wave energy was absorbed by the plasma at the resonant ($\omega = \omega_{ci}$) layer. In a tokamak geometry, however, the static magnetic field gradient is in the radial direction, and calculations suggest that the slow wave does not propagate to the plasma core but is rather absorbed in the outer plasma region [Klima, 1975; Colestock, 1983].

The other propagating wave is called the fast or magnetosonic wave; at higher frequencies it becomes the whistler or electron cyclotron wave. This wave does not have a resonance at $\omega = \omega_{ci}$ and easily propagates throughout the plasma. At the fundamental cyclotron frequency, however, the electric field of the fast wave is completely right-hand circularly polarized with respect to the static magnetic field; hence no fundamental cyclotron absorption might be expected. Inclusion of warm-plasma effects predicts a small left-hand component of the wave electric field at $\omega = \omega_{ci}$; the absorption, however, is calculated to be very small (for a hydrogenic plasma). Nevertheless, a variety of other damping mechanisms exist by which the plasma particles can absorb energy from the fast wave (see section 2.3), and the use of ICRF fast waves to heat tokamak plasmas has been successful in some laboratories.

Introduction of a second ion species results in new resonances (e.g., the ion-ion hybrid resonance) and further wave damping mechanisms. For instance, when a small concentration of a light ion is added to a plasma consisting of heavier ions, the wave propagation and field structure is still dominated by the majority species. Thus a fast wave can propagate which has a substantial left-hand circularly polarized electric field component at the fundamental resonance of the lighter minority species. Minority heating and ion-ion hybrid heating have been studied on several tokamaks [Adam et al., 1974;

Takahashi et al., 1977; Josea et al., 1979]. The Caltech Research Tokamak, however, has only been operated using pure hydrogen, so there are no minority ions with fundamental resonant frequencies above that of the protons. Wave damping due to high harmonic cyclotron absorption by relatively cold, heavy impurity ions is probably negligible.

Including thermal effects in the wave propagation theory shows the possibility of a mode conversion process in which energy from the fast wave is converted, via a gradient in some plasma parameter, to an electrostatic thermal wave (e.g., an ion Bernstein wave) which may be heavily damped. A detailed analysis of some of these effects is given by Colestock [1982]; these effects are not considered in this thesis.

Heating of a tokamak plasma at the second harmonic of the cyclotron frequency ($2\omega_{ci}$) has also been effective in several tokamaks. This mechanism is attractive because it allows heating at a higher frequency which, in a reactor configuration, could allow the use of waveguide coupling to the plasma. Initial results from the T.F.R. tokamak [Adam, 1974] showed significantly higher wave damping than was predicted theoretically. This was later found to be due to the presence of a small proton impurity in a predominantly deuterium plasma; ion-ion hybrid effects substantially enhanced the damping. More recent experiments on the PLT tokamak used a hydrogen plasma to avoid ion-ion hybrid effects and still succeeded in coupling $\sim$3 MW of power to the plasma, producing an effective plasma temperature of $\sim$4.8 keV [Hwang et al., 1983].

Efforts to heat plasmas using ICRF fast waves have, however, been unsuccessful in some tokamaks. Experiments at power levels of 100 kW on the Alcator A high density tokamak at M.I.T. showed evidence of antenna loading and wave generation but no evidence of bulk heating; the destination of the power dissipated by the antenna was unclear [Gaudreau, 1981]. Efforts on the Microtor tokamak at U.C.L.A. also failed to demonstrate plasma bulk heating.

Heating experiments on the larger Macrotor tokamak showed a dramatic and deleterious decrease in particle confinement time [Taylor et al., 1981]. The reasons for these diverse results are not currently understood.

In some regimes, such as that in which the Caltech Research Tokamak operates, the wave damping per tokamak circumference is small, so waves can propagate around the machine many times and interfere with each other, forming cavity resonances. In other regimes (for instance, when an ion-ion hybrid resonance layer is present), wave damping can be sufficiently large that eigenmodes are not seen.

Fast wave cavity resonances, or toroidal eigenmodes as they are often called, were first observed in a tokamak plasma in the TM-1-Vch and TO-1 tokamaks at the Kurchatov Institute in Moscow [Ivanov et al., 1971; Vdovin et al., 1971] and have been studied in a number of other tokamaks (see Chapter 7). Eigenmodes are potentially useful from a plasma heating point of view for two reasons. First, the resonant buildup of the electric field at the antenna causes an increase in the loading resistance of the antenna. Since the antenna loading due to excitation and damping of waves in the plasma is often small ($\lesssim 1\ \Omega$), an increase in antenna loading can increase the efficiency of power transfer to the plasma. Second, the eigenmodes are global modes, so energy can be deposited uniformly around the tokamak rather than in a localized region near the antenna.

One problem associated with the use of fast wave eigenmodes for heating a reactor-sized plasma involves mode separation. As is shown in Chapter 2, for a fixed plasma density and magnetic field, there exist an infinite set of modes at discrete frequencies. The modes have a finite width due to wave damping, and the number or density of modes per unit frequency interval increases as the size of the tokamak and its density increases [Stix, 1975]. For fusion reactor parameters and excitation frequencies near the ion cyclotron frequency, there

is expected to be a virtual continuum of overlapping modes. Unfortunately, as Stix points out [1983], simultaneous excitation of multiple modes is undesirable as it leads to very strong fields in the local vicinity of the antenna which may cause substantial and deleterious plasma edge heating. There has recently, however, been renewed interest in utilizing the advantages of eigenmode heating for future reactor-grade plasmas [Stix, 1983]. Mode separation can be retained by lowering the excitation frequency. Because the fast wave has no resonance at the fundamental cyclotron frequency (ω_{ci}), the excitation frequency ω can be lower than ω_{ci}. Although cyclotron absorption would no longer be present, it is speculated that other damping mechanisms could still lead to efficient wave absorption and plasma heating.

It was the point of this thesis to study various features of fast wave propagation, damping, and antenna-plasma coupling in a tokamak plasma, with an emphasis on the physics of the processes rather than on bulk heating. Small tokamaks such as the Caltech Research Tokamak provide a unique opportunity to make use of probes in the outer plasma; larger machines cannot tolerate such experiments due to the much higher plasma temperatures involved.

Motivation for some of this work came from unexplained observations in several other laboratories. One effect was the so-called "anomalous ICRF antenna loading" which was seen with certain antennas in some tokamaks; this was a density-dependent background resistive loading which was apparently unconnected with wave propagation and was not predicted theoretically. Simple theory predicts a series of peaks on the input antenna resistance coincident with excitation of toroidal eigenmodes in the plasma volume.

This anomalous antenna loading (sometimes called parasitic loading) was seen in the TO-4 tokamak at the Kurchatov Institute [Buzankin et al., 1976]. There, the fast wave was excited in the frequency range $\omega_{ci} < \omega < 3\omega_{ci}$ with a loop antenna at the plasma edge which was uninsulated but protected with

side diaphragms. The background loading depended greatly on the particular discharge characteristics and did not exhibit any peaks associated with eigenmode generation. The authors speculated that the loading was due to heating and/or expulsion of plasma entering the gap between the loop and the protective diaphragm.

The Erasmus tokamak at the Ecole Royale Militaire in Brussels was also was used for studies of ICRF antenna loading. One antenna investigated consisted of a full loop which completely encircled the plasma column. The antenna was simply a formed rod of copper encased in a glass tube and placed in the shadow of a limiter. With this antenna, a large background loading was observed ($1-10\ \Omega$) which did not vary during the eigenmode resonances which were observed elsewhere in the plasma with magnetic probes. The loading was explained as arising from the excitation of some form of electrostatic waves in the plasma periphery [Bhatnagar et al., 1978a]. It was noted that with a smaller electrostatically shielded side loop antenna, the background loading was greatly reduced and peaks on the loading due to eigenmodes were observed.

Parasitic or anomalous ICRF antenna loading was also observed in both the Microtor and Macrotor tokamaks at U.C.L.A. [Taylor and Morales, 1978]. The loading was reported to increase with plasma density and excitation frequency and was observed with a wide variety of antennas, both shielded and unshielded (leading the authors to refer to the phenomenon as "universal plasma loading"). In Microtor, the parasitic loading swamped out resonant loading due to eigenmodes under all plasma conditions; in Macrotor, the eigenmode loading could be seen, but only at low density when the parasitic loading was small.

The first observations of fast wave eigenmodes on the Caltech Research Tokamak were reported by Hwang [1978a, 1979], who also investigated the

complex antenna impedance. Using a small two-turn glass-covered loop antenna, only resonant peaks on the antenna loading resistance were found, as expected from theory. No evidence of background anomalous loading was found.

Identification of the origin of the anomalous ICRF antenna loading is of some importance, since energy deposited in that impedance is probably not being deposited in the plasma bulk and is thus wasted. The above observations led this author to an extensive impedance study with a series of antennas specifically designed to enhance the anomalous loading. On the basis of that study, a model is proposed which accounts for many of the observed antenna impedance features solely in terms of particle collection through the plasma sheath surrounding the antenna.

Another surprising observation in early ICRF experiments was that the observed wave damping in the tokamak was much too great to be explained in terms of classical damping mechanisms (i.e., cyclotron, Landau, TTMP, collisional, and resistive). This result was observed both in pure hydrogen plasmas such as are used in the Caltech tokamak [T.F.R. Group, 1977; Bhatnagar et al., 1978a], and in two-ion mixtures [Takahashi, 1977]. The results for the two-ion case have been reasonably well accounted for in terms of mode conversion at the ion-ion hybrid layer, but the anomalously high damping observed in a pure hydrogen plasma remains unexplained. These observations led to a series of investigations of wave propagation and damping in the Caltech machine. In addition to measurements of the eigenmode fields using magnetic probes, a new approach involving the propagation of wave-packets was utilized to study the waves unencumbered by the toroidal resonance effects.

Unexpected results obtained with simple electric field antennas led to the design of a new diagnostic - a high frequency Rogowski current probe which was compatible with the tokamak edge plasma. This allowed direct observation

for the first time of RF plasma particle current. The current probe was used to investigate the spatial distribution of current in the tokamak plasma driven by an electric field antenna.

Thesis Outline

This thesis begins in Chapter 2 with a review of cold-plasma wave theory appropriate to the conditions encountered in the Caltech Research Tokamak. The torus is modeled as a cylinder with periodic boundary conditions, and the fast-wave toroidal eigenmodes which result are discussed. A review of some classical wave damping mechanisms (fundamental cyclotron, second-harmonic cyclotron, electron Landau and transit-time magnetic pumping, collisional, and resistive wall) is presented, and expected cavity Qs for various eigenmodes are calculated. A previously overlooked wave damping mechanism due to dielectric losses in the toroidal insulating gap is similarly evaluated for the eigenmodes of interest.

The wave model is then extended to allow an arbitrary radial density profile (within some mild constraints). Quadratic density profiles are considered, and the resulting effects on the eigenmode dispersion curves and on the wave fields are discussed. Radially-oscillating density profiles are investigated to simulate coherent plasma density fluctuations, and a dramatic effect on the left-hand circularly polarized component of the wave magnetic field is discovered. It is speculated that this effect could lead to enhanced cyclotron wave damping.

A description of the Caltech Research Tokamak is presented in Chapter 3, including some features of its design and construction.[1] Operation of the tokamak and its associated diagnostics and data acquisition system is dis-

1. Some material in Chapter 3 has been previously reported [Greene and Hedemann, 1978].

cussed, and data from typical tokamak shots are shown. A section is also included detailing the construction and operation of the new charge-exchange diagnostic which provided an ion temperature measurement for the first time on the Caltech tokamak.

Chapter 4 provides a detailed description of the RF systems and components which were constructed for these experiments, including the high power (100 kW) RF amplifier, directional coupler, impedance-matching network, and amplitude and phase detectors. Phase detectors were required both for antenna impedance measurements and for investigations of the mode structure of the wave magnetic fields in the tokamak. Because the antenna reactance was typically much larger than its resistance, the phase between the antenna voltage and current was nearly 90° and changed very little during the plasma shot. The impedance measurements thus required a phase detector which could respond to changes of a fraction of a degree. The wave measurements, on the other hand, required a detector with a range of 360° which was insensitive to the large amplitude variations (up to ~35 db) occurring at the eigenmode resonances. The design of a novel and simple phase detector which satisfied the above requirements is presented.

Chapter 5 describes the five RF antennas which were used in these investigations: the bare loop, insulated loop, Faraday-shielded loop, bare plate, and "T" antennas.[2] The antennas were designed to be easily interchangable and could be removed from the tokamak through an airlock chamber. The construction of the magnetic field probes and the Langmuir probes is also discussed. Magnetic field measurements near the loop antennas, made in a laboratory test stand, are presented and some effects of the Faraday shield are noted. Finally, the design and construction of a plasma-compatible Rogowski

2. Some material in Chapters 4 and 5 has been previously presented [Greene and Gould, 1981].

RF current monitor is described, along with a novel mounting fixture which allowed investigation of the spatial dependence of the RF current in the edge plasma near a small electric field antenna.

Impedance measurements on the five RF antennas are presented in detail in Chapter 6. The impedance was investigated as a function of the excitation frequency, the toroidal magnetic field, the plasma density, the antenna radial position, and the antenna current level.[3] Langmuir probe studies are also discussed here. The shielded antennas display loading resistance peaks corresponding to the excitation of eigenmodes, while the uninsulated antennas all show the large anomalous density-dependent background loading. A simple theoretical model is described, based on particle collection by the antenna and making use of the Langmuir probe measurements, which successfully explains many of the observed features of the background loading.

Wave experiments are discussed in Chapter 7. Magnetic field probes are used to observe the eigenmode wave fields, and the locations of the resonances in frequency-density space are mapped out and compared to theoretical predictions. Eigenmode excitation efficiencies are examined and seen to be comparable for all of the antennas. Investigations of the wave field mode structure using pairs of magnetic probes are presented and found to be in accordance with theoretical expectations. Further experiments measured the eigenmode radial magnetic field profiles and the eigenmode resonance Qs and wave damping lengths.

The wave-packet experiments are then described and the observed variation of the packet velocity with plasma and RF parameters is displayed. A wave propagation model which includes a vacuum layer at the plasma edge is applied to the theoretical calculation of the group velocity, and comparison

3. Some results presented in Chapters 6 and 7 have been previously reported [Greene and Gould, 1983].

with the experimental results yields surprisingly good agreement.

Finally, results from the measurements with the RF Rogowski current monitor are presented. The spatial distribution of the RF plasma current driven by a small electric field antenna is investigated and found to be highly localized along the toroidal field direction. This result suggests a mechanism for the good coupling to the eigenmodes observed with the electric field antennas.

Chapter 8 concludes the thesis with a brief summary of the major experimental results.

Two appendices are included which are not directly related to the rest of this work. Appendix A presents observations of efficient power coupling between two identical ICRF antennas in the Caltech tokamak,[4] an experiment which ties in well with a simple circuit model of the eigenmode resonances. Appendix B discusses the effect of a transient RF pulse on surface heating in a conducting cylinder, a subject which may be important for the design of future very high power RF systems.

4. This paper has been previously presented [Greene and Gould, 1979].

CHAPTER 2

Wave Theory

This chapter begins with a review of cold plasma theory appropriate to study the propagation of waves near the ion cyclotron frequency. The tokamak is then modeled as a cylinder with periodic boundary conditions, and solutions for the normal modes of the system are found for parameters appropriate to the Caltech Research Tokamak. Retaining the electron mass terms reveals the form of the small E_z component of the waves. The approximation $m_e \to 0$ is then considered and the solutions are compared with the previous results. A variety of wave damping mechanisms are reviewed and the resulting cavity Qs are calculated for appropriate parameters and modes; the dependence of Q on $k_{\|}$ is noted. A numerical solution of Maxwell's equations is then developed for the cold plasma model which allows an arbitrary radial density profile to be included. Several profiles are considered, including quadratic and oscillatory functions, and the effect of the profiles on the eigenmode dispersion curves and on the wave fields is investigated. The left-hand circularly polarized component of the electric field is found to be very sensitive to radial density perturbations, and the possibility of enhanced cyclotron damping arising from this source is discussed. Finally, previous work on the effects of the poloidal magnetic field and of toroidal geometry are briefly reviewed.

2.1 Review of Cold Plasma Wave Theory

2.1.1 Cold Plasma Dielectric Tensor

The well-known cold plasma effective dielectric tensor can be derived from the two-fluid momentum conservation equation together with Maxwell's equations. Neglecting pressure and collision terms, the equations can be written as [Krall and Trivelpiece, 1973]:

$$n_\alpha m_\alpha \left(\frac{\partial}{\partial t} + \mathbf{V}_\alpha \cdot \nabla \right) \mathbf{V}_\alpha = n_\alpha q_\alpha \left(\mathbf{E} + \frac{1}{c} \mathbf{V}_\alpha \times \mathbf{B} \right) \tag{2.1a}$$

$$\nabla \times \mathbf{B} = \frac{4\pi}{c} \sum_\alpha n_\alpha q_\alpha \mathbf{V}_\alpha + \frac{1}{c} \frac{\partial \mathbf{E}}{\partial t} \tag{2.1b}$$

$$\nabla \times \mathbf{E} = -\frac{1}{c} \frac{\partial \mathbf{B}}{\partial t} \ , \tag{2.1c}$$

where α refers to a species of charged particle (electrons or ions), n_α, m_α, and q_α are the particle density, mass, and charge, respectively, and $\mathbf{V}_\alpha$ is the fluid velocity of species α. $\mathbf{B}$ and $\mathbf{E}$ are the magnetic induction and electric field, respectively, and c is the velocity of light. Assuming a steady state background magnetic field, $\mathbf{B}_0$, and linearizing the momentum equation for small perturbations with harmonic time dependence ($e^{-i\omega t}$) yields

$$-i\omega n_\alpha m_\alpha \tilde{\mathbf{V}}_\alpha = n_\alpha q_\alpha \left(\tilde{\mathbf{E}} + \frac{1}{c} \tilde{\mathbf{V}}_\alpha \times \mathbf{B}_0 \right) , \tag{2.2}$$

where the tilde indicates a perturbed variable. The above equation can be solved for the mobility tensor, $\overleftrightarrow{\mu}_\alpha$, defined by $\tilde{\mathbf{V}}_\alpha = \overleftrightarrow{\mu}_\alpha \cdot \tilde{\mathbf{E}}$. The result, in Cartesian (x, y, z) or cylindrical (ρ, θ, z) coordinates, is

$$\overleftrightarrow{\mu}_\alpha = \begin{bmatrix} \dfrac{i q_\alpha}{m_\alpha \omega F_\alpha} & \dfrac{\omega_{c\alpha} q_\alpha}{m_\alpha \omega^2 F_\alpha} & 0 \\ \dfrac{\omega_{c\alpha} q_\alpha}{m_\alpha \omega^2 F_\alpha} & \dfrac{i q_\alpha}{\omega m_\alpha F_\alpha} & 0 \\ 0 & 0 & \dfrac{i q_\alpha}{\omega m_\alpha} \end{bmatrix} \tag{2.3}$$

where $\omega_{c\alpha} = \frac{q_\alpha B_0}{m_\alpha c}$ and $|\omega_{c\alpha}|$ is the cyclotron frequency for charge species α and $F_\alpha = 1 - \frac{\omega_{c\alpha}^2}{\omega^2}$. The particle current in the plasma is $\tilde{\mathbf{J}} = \sum_\alpha n_\alpha q_\alpha \tilde{\mathbf{V}}_\alpha$ and is related to the electric field in the plasma through $\tilde{\mathbf{J}} = \overleftrightarrow{\sigma} \cdot \tilde{\mathbf{E}}$, where

$$\overleftrightarrow{\sigma} = \sum_\alpha n_\alpha q_\alpha \overleftrightarrow{\mu}_\alpha \ . \tag{2.4}$$

Note that since the conductivity tensor is anti-Hermitian, energy absorption is not described in this model [Ichimaru, 1973]. Equation 2.1b can be written as

$$\nabla \times \tilde{\mathbf{B}} = \left(\frac{4\pi}{c} \overleftrightarrow{\sigma} - \frac{i\omega}{c} \overleftrightarrow{I} \right) \cdot \tilde{\mathbf{E}}$$

$$= -\frac{i\omega}{c} \left(\overleftrightarrow{I} - \frac{4\pi}{i\omega} \overleftrightarrow{\sigma} \right) \cdot \tilde{\mathbf{E}} \ , \tag{2.5}$$

where $\overleftrightarrow{I}$ is the unit dyad. The effects of the particle current $\tilde{\mathbf{J}}$ can thus be included in an effective dielectric tensor $\overleftrightarrow{\varepsilon} = \overleftrightarrow{I} - \frac{4\pi}{i\omega} \overleftrightarrow{\sigma}$. The cold plasma dielectric tensor, $\overleftrightarrow{\varepsilon}$, is found from equations 2.3 and 2.4; in cartesian (or cylindrical) coordinates, the result is

$$\overleftrightarrow{\varepsilon} = \begin{bmatrix} \varepsilon_\perp & -i\varepsilon_\times & 0 \\ i\varepsilon_\times & \varepsilon_\perp & 0 \\ 0 & 0 & \varepsilon_\parallel \end{bmatrix} \tag{2.6}$$

where

$$\varepsilon_\perp = 1 - \sum_\alpha \frac{\omega_{p\alpha}^2}{\omega^2 - \omega_{c\alpha}^2}$$

$$\varepsilon_\parallel = 1 - \sum_\alpha \frac{\omega_{p\alpha}^2}{\omega^2}$$

$$\varepsilon_\times = \sum_\alpha \frac{\omega_{p\alpha}^2}{\omega^2 - \omega_{c\alpha}^2} \frac{\omega_{c\alpha}}{\omega}$$

and $\omega_{p\alpha} = \left(4\pi n_\alpha \frac{q_\alpha^2}{m_\alpha} \right)^{\frac{1}{2}}$ is the plasma frequency for species α.

For a hydrogenic plasma such as is used in the Caltech tokamak, the general forms of $\varepsilon_\perp$, $\varepsilon_\times$, and $\varepsilon_\parallel$, as functions of frequency, are shown in Figure 2-1. $\varepsilon_\parallel$ has a pole at $\omega=0$ and a zero at the plasma frequency $\omega=\omega_p\equiv\left(\omega_{pe}^2+\omega_{pi}^2\right)^{\frac{1}{2}}$. $\varepsilon_\perp$ has poles at the electron and ion cyclotron frequencies, and the solutions for its two zeroes at $\omega=\omega_{lh}, \omega_{uh}$ are called the lower and upper hybrid frequencies. $\varepsilon_\times$ has poles also at the cyclotron frequencies and has zeroes at $\omega=0,\infty$. For the Caltech tokamak, the ion cyclotron frequency is small compared to the other characteristic frequencies (except at the plasma-wall boundary) which are ordered approximately as

$$\omega_{ci}^2 \ll \omega_{lh}^2 \lesssim \omega_{pi}^2 \ll \omega_{ce}^2 \lesssim \omega_{pe}^2 < \omega_{uh}^2 \,. \tag{2.7}$$

2.1.2 Plane Waves

Maxwell's equations can now be written in the form

$$\nabla\times\mathbf{B} = -\frac{i\omega}{c}\overleftrightarrow{\varepsilon}\cdot\mathbf{E} \tag{2.8a}$$

$$\nabla\times\mathbf{E} = \frac{i\omega}{c}\mathbf{B} \tag{2.8b}$$

where the subscripts indicating perturbed quantities have been dropped. The wave equations for the fields are then

$$\nabla\times(\nabla\times\mathbf{E}) + \frac{\omega^2}{c^2}\overleftrightarrow{\varepsilon}\cdot\mathbf{E} = 0 \tag{2.9a}$$

$$\nabla\times(\nabla\times\mathbf{B}) + \frac{\omega^2}{c^2}\overleftrightarrow{\varepsilon}\cdot\mathbf{B} = 0 \,. \tag{2.9b}$$

Considering infinite boundary plane wave solutions of the form $e^{i\mathbf{k}\cdot\mathbf{x}-i\omega t}$, where $\mathbf{k}$ is the wavevector, the equation for $\mathbf{E}$ becomes

$$\mathbf{n}\times(\mathbf{n}\times\mathbf{E}) + \overleftrightarrow{\varepsilon}\cdot\mathbf{E} = 0 \,, \tag{2.10}$$

where $\mathbf{n}=\frac{c}{\omega}\mathbf{k}$ and $n=|\mathbf{n}|$ is called the refractive index. The magnitude of

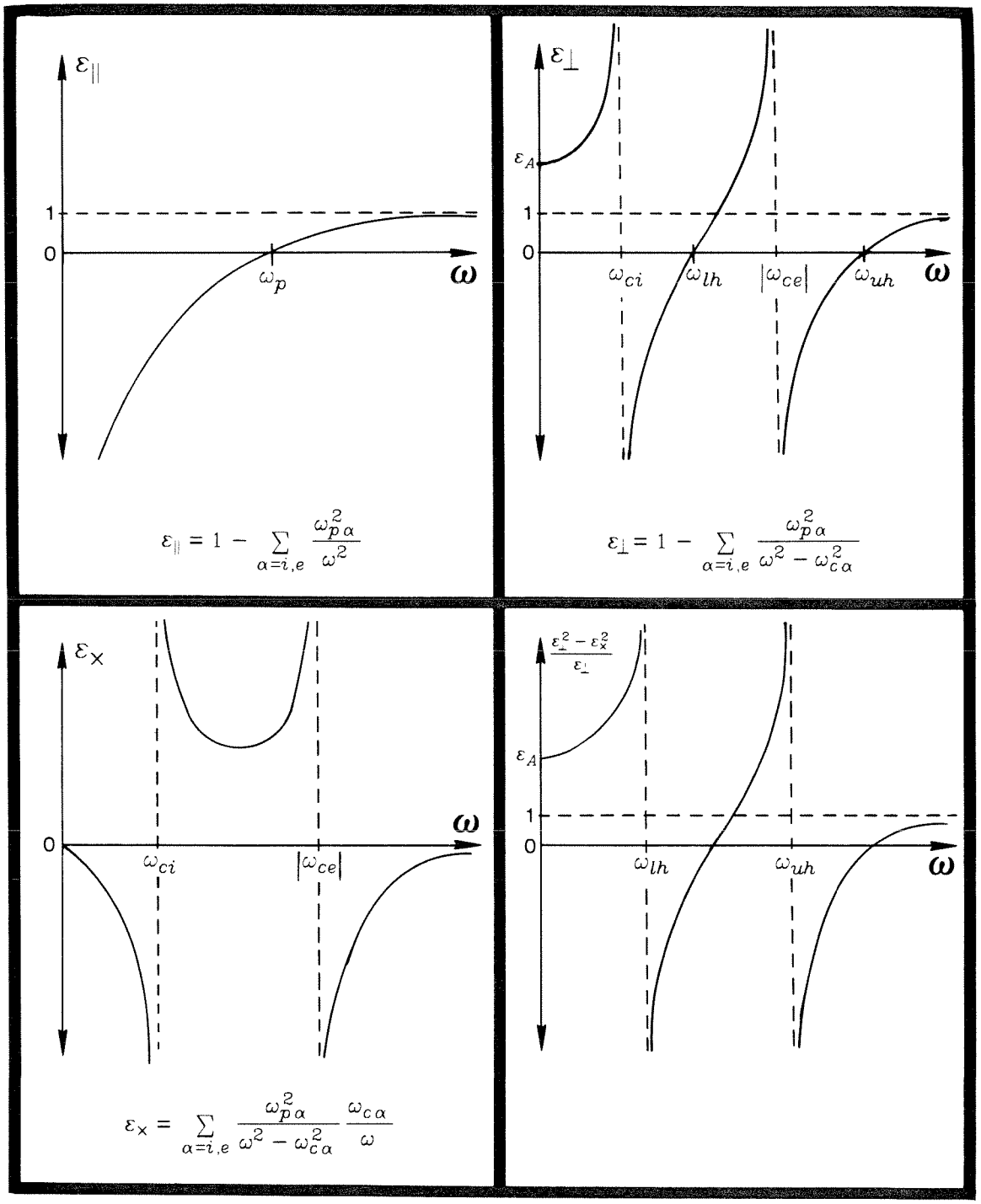

FIG. 2-1. Plots of the elements of the cold plasma dielectric tensor, $\varepsilon_\parallel$, $\varepsilon_\perp$, $\varepsilon_\times$, and of $(\varepsilon_\perp^2 - \varepsilon_\times^2)/\varepsilon_\perp$ as functions of frequency, for a hydrogenic plasma. Summations are over electrons and ions. $\omega_{c\alpha}$ and $\omega_{p\alpha}$ are the cyclotron and plasma frequencies for species α; ω_{lh} and ω_{uh} are the lower and upper hybrid frequencies; $\varepsilon_A = 1 + 4\pi n m_i c^2 / B_0^2$. Plots are not to scale.

the phase velocity of the wave is then $v_{ph} = \frac{\omega}{k} = \frac{c}{n}$ and the direction is normal to surfaces of constant phase, i.e., in the direction of $\mathbf{k}$. Taking the steady state background magnetic field to be $\mathbf{B}_0 = B_0 \hat{\mathbf{z}}$, where $\hat{\mathbf{z}}$ is a unit vector in the $z-$direction, and taking $\mathbf{n}$ to lie in the $x-z$ plane and θ to be the angle between $\mathbf{n}$ and $\mathbf{B}_0$, the wave equation becomes

$$\begin{bmatrix} \varepsilon_\perp - n^2\cos^2\theta & -i\varepsilon_\times & n^2\sin\theta\cos\theta \\ i\varepsilon_\times & \varepsilon_\perp - n^2 & 0 \\ n^2\sin\theta\cos\theta & 0 & \varepsilon_\parallel - n^2\sin^2\theta \end{bmatrix} \begin{bmatrix} E_x \\ E_y \\ E_z \end{bmatrix} = 0 \qquad (2.11)$$

For $E_x = E_y = 0$, the only non-trivial solutions are $\theta = 0$ or π, $\varepsilon_\parallel = 0$ (i.e., $\omega^2 = \omega_{pe}^2 + \omega_{pi}^2 \equiv \omega_p^2$, the plasma oscillation) and $\theta = \frac{\pi}{2}$ or $\frac{3\pi}{2}$, $n^2 = \varepsilon_\parallel$ (i.e., $\omega^2 = \omega_p^2 + k^2c^2$, the ordinary transverse electromagnetic wave).

For E_x or E_y not equal to zero, the determinant of the matrix in equation 2.11 must be set equal to zero, resulting in the well known unbounded cold plasma dispersion relation:

$$n^2 = \frac{B \pm \left(B^2 - 4AC\right)^{\frac{1}{2}}}{2A}, \qquad (2.12)$$

where

$$A = \varepsilon_\parallel \cos^2\theta + \varepsilon_\perp \sin^2\theta$$

$$B = (1 + \cos^2\theta)\,\varepsilon_\parallel \varepsilon_\perp + (\varepsilon_\perp^2 + \varepsilon_\times^2)\sin^2\theta$$

$$C = \varepsilon_\parallel (\varepsilon_\perp^2 - \varepsilon_\times^2)\,.$$

Equation 2.12 gives n as a function of the plasma parameters (i.e., plasma density, static magnetic field, and ω) and of the angle of propagation, θ. The dispersion relation may be rearranged to yield θ as a function of the plasma parameters and of n:

$$\tan^2\theta = -\varepsilon_\parallel \frac{(n^2 - R)(n^2 - L)}{(\varepsilon_\perp n^2 - RL)(n^2 - \varepsilon_\parallel)}, \qquad (2.13)$$

where $R = \varepsilon_\perp + \varepsilon_x$ and $L = \varepsilon_\perp - \varepsilon_x$ [Boyd and Sanderson, 1969].

In general, equation 2.12 admits two distinct solutions, although one or both may be evanescent ($n^2 < 0$) for a particular set of plasma parameters and angle of propagation θ. For propagation in the direction of the principal axes ($\theta = 0, \frac{\pi}{2}$), the dispersion relation may be greatly simplified. For propagation *along* the static magnetic field ($\theta = 0$), and for $\omega \ll |\omega_{ce}|, \omega_{pe}$, the dispersion relation may be written in the form

$$\frac{\omega}{k} = v_{ph} = v_A \left(1 \pm \frac{\omega}{\omega_{ci}}\right)^{\frac{1}{2}}, \tag{2.14}$$

where $v_A = B_0 / (4\pi n_0 m_i)^{\frac{1}{2}}$ is the Alfvén velocity. From equation 2.11, the polarization of the two waves can be found:

$$\frac{E_y}{E_x} = \frac{\varepsilon_\perp - n^2}{i\,\varepsilon_x} = \pm i \ , \tag{2.15}$$

so the waves are circularly polarized, the electric field vector rotating in the same sense or in the opposite sense as the direction of ion precession (this will be called left-hand and right-hand circular polarization, respectively, by convention). The wave associated with the "+" sign in equation 2.12, the right-hand circularly polarized wave, is variously called the fast or compressional Alfvén wave; at higher frequencies, it is termed the whistler or electron cyclotron wave. The wave associated with the "-" sign is left-hand circularly polarized and is called the ion cyclotron wave, or the slow or torsional Alfvén wave. (Note that its phase velocity, at a given frequency, is *slower* than that of the compressional wave). It is also apparent that the slow wave does not propagate immediately above ω_{ci}, since k is imaginary there.

For propagation *across* the static magnetic field ($\theta = \frac{\pi}{2}$), the dispersion relation reduces to

$$\frac{\omega}{k} = v_{ph} = v_A \left[1 - \frac{\omega^2}{|\omega_{ce}|\,\omega_{ci}}\right]^{\frac{1}{2}} = v_A \,, \tag{2.16}$$

for the "+" sign in equation 2.12; the other solution is evanescent ($n^2 < 0$). The propagating wave is found to be elliptically polarized in the $x-y$ plane:

$$\frac{E_y}{E_x} = -i\,\frac{\varepsilon_\times}{\varepsilon_\perp} = i\,\frac{\omega}{\omega_{ci}} \,. \tag{2.17}$$

Note that at the fundamental ion cyclotron frequency (ω_{ci}), the wave associated with the "+" sign (the fast wave) is right-hand circularly polarized for *all* directions of propagation.

2.1.3 Phase and Group Velocity Surfaces

The phase velocity surface (sometimes called the wave-normal surface) may be defined by a polar plot of v_{ph} as a function of θ, for fixed plasma parameters and fixed ω. ("Surface" here refers to the surface of revolution which would be generated by rotation of the plot of $v_{ph}(\theta)$ about the $z-$axis. The three-dimensional surface is rarely plotted.) The CMA diagram (after Clemmow, Mullaly, and Allis [Stix, 1962]) provides a useful classification of cold plasma waves based on the topology of the phase velocity surface as the plasma parameters are varied. Figure 2-2 is a CMA diagram for a two component (hydrogenic) plasma and shows parameter space (i.e., density−magnetic field space) divided into 13 regions with distinct phase velocity surfaces. In regions where both waves propagate, one phase velocity surface is always (except for some possible singular points) contained within the other. The wave corresponding to the outer surface is called the fast wave; the other one, the slow wave.

For waves of interest in these experiments, $\frac{\omega}{\omega_{ci}} \approx 1-3$ and $\omega \ll \omega_{ce}, \omega_{lh}, \omega_p$. These waves then occur in region 10 on the CMA diagram. For

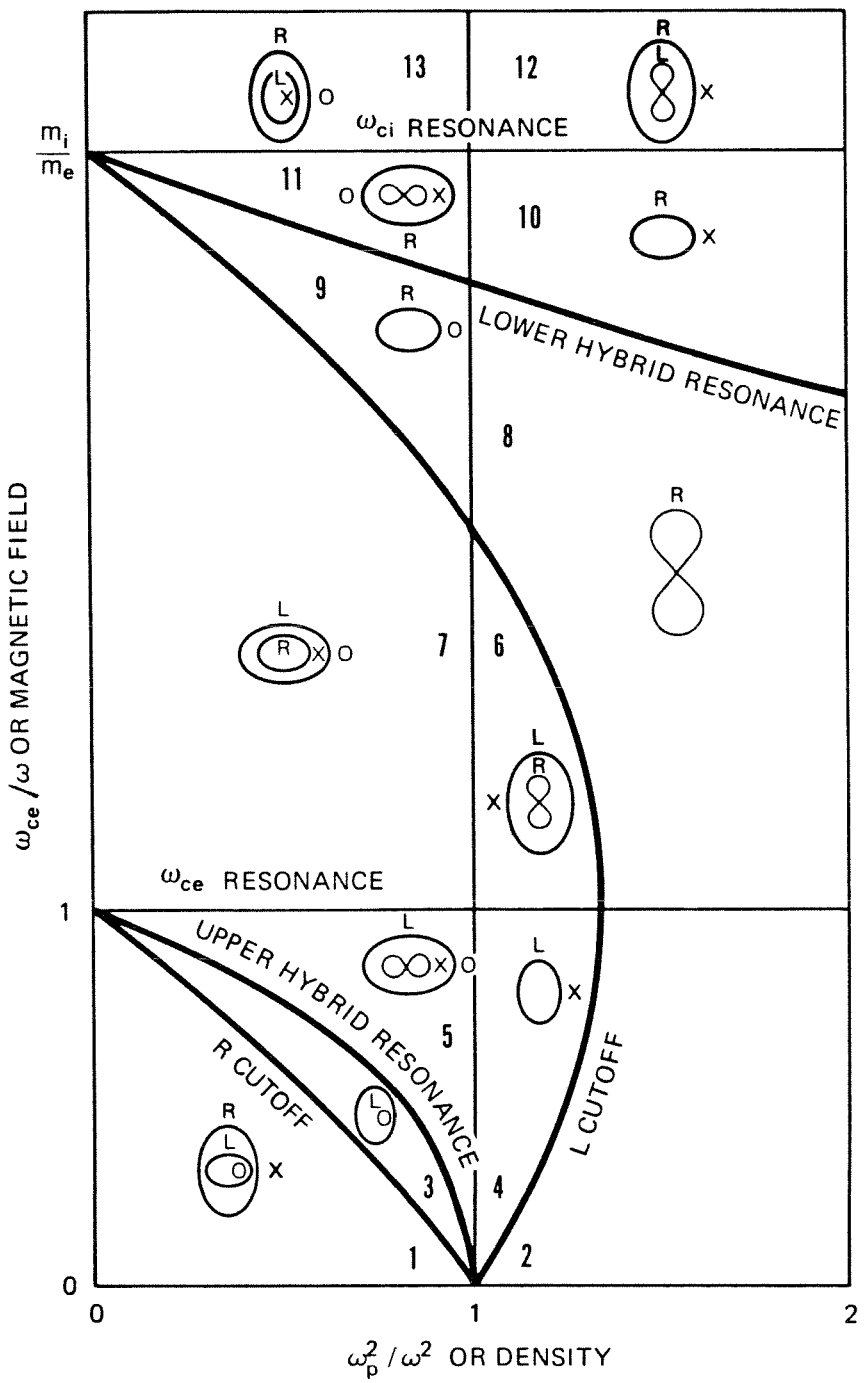

FIG. 2-2. The CMA diagram for a hydrogenic plasma, showing the topology of the phase-normal surfaces as functions of the plasma density and the static magnetic field (after Chen [1974]). The experiments described in this thesis were confined to region 10.

$\omega < \omega_{ci}$ (region 12), both the fast and slow waves propagate (although the slow wave does not propagate for all angles θ). As ω increases and crosses the ion cyclotron resonance (at ω_{ci}), the slow wave becomes evanescent (for all θ) while the fast wave is largely unaffected by the transition. Hence the mode in region 10 is also called the fast wave.

The vector phase velocity is $\mathbf{v}_{ph} = \frac{\omega}{k^2}\mathbf{k}$. The velocity of a local disturbance or wave packet, however, is the group velocity $\mathbf{v}_g = \frac{\partial \omega}{\partial \mathbf{k}}$ (provided the dispersion and spread of wavenumbers are not too great) and is, in general, not in the same direction as the phase velocity. The group velocity can be written as

$$\mathbf{v}_g = \frac{\partial \omega}{\partial k}\hat{\mathbf{k}} + \frac{1}{k}\frac{\partial \omega}{\partial \theta}\hat{\boldsymbol{\theta}}, \tag{2.18}$$

where $\hat{\mathbf{k}} = \frac{\mathbf{k}}{k}$ and $\hat{\boldsymbol{\theta}} = \hat{\mathbf{k}} \times (\hat{\mathbf{k}} \times \hat{\mathbf{z}})$ is a unit vector in the θ-direction. Hence $\mathbf{v}_g$ and $\mathbf{v}_{ph}$ will lie in the same direction only when $\frac{\partial \omega}{\partial \theta} = 0$. From the symmetry of the dispersion relation, this occurs at least at $\theta = 0, \frac{\pi}{2}$.

A group velocity surface may be defined, in similar fashion to the phase velocity surface, as a polar plot of v_g versus θ_g, where θ_g is the angle between $\mathbf{v}_g$ and the static magnetic field $B_0\hat{\mathbf{z}}$. From equation 2.18,

$$v_g = |\mathbf{v}_g| = \left[\left(\frac{\partial \omega}{\partial k}\right)^2 + \frac{1}{k^2}\left(\frac{\partial \omega}{\partial \theta}\right)^2\right]^{\frac{1}{2}}, \tag{2.19a}$$

and

$$\theta_g = \tan^{-1}\left(\frac{\frac{\partial \omega}{\partial \theta}}{k\frac{\partial \omega}{\partial k}}\right). \tag{2.19b}$$

Plots of the phase and group velocity surfaces are shown in Figure 2-3 for several different frequencies; the Alfvén velocity (v_A) is also shown for comparison. It should be noted that, in general, $\theta_{ph} \neq \theta_g$, except along the princi-

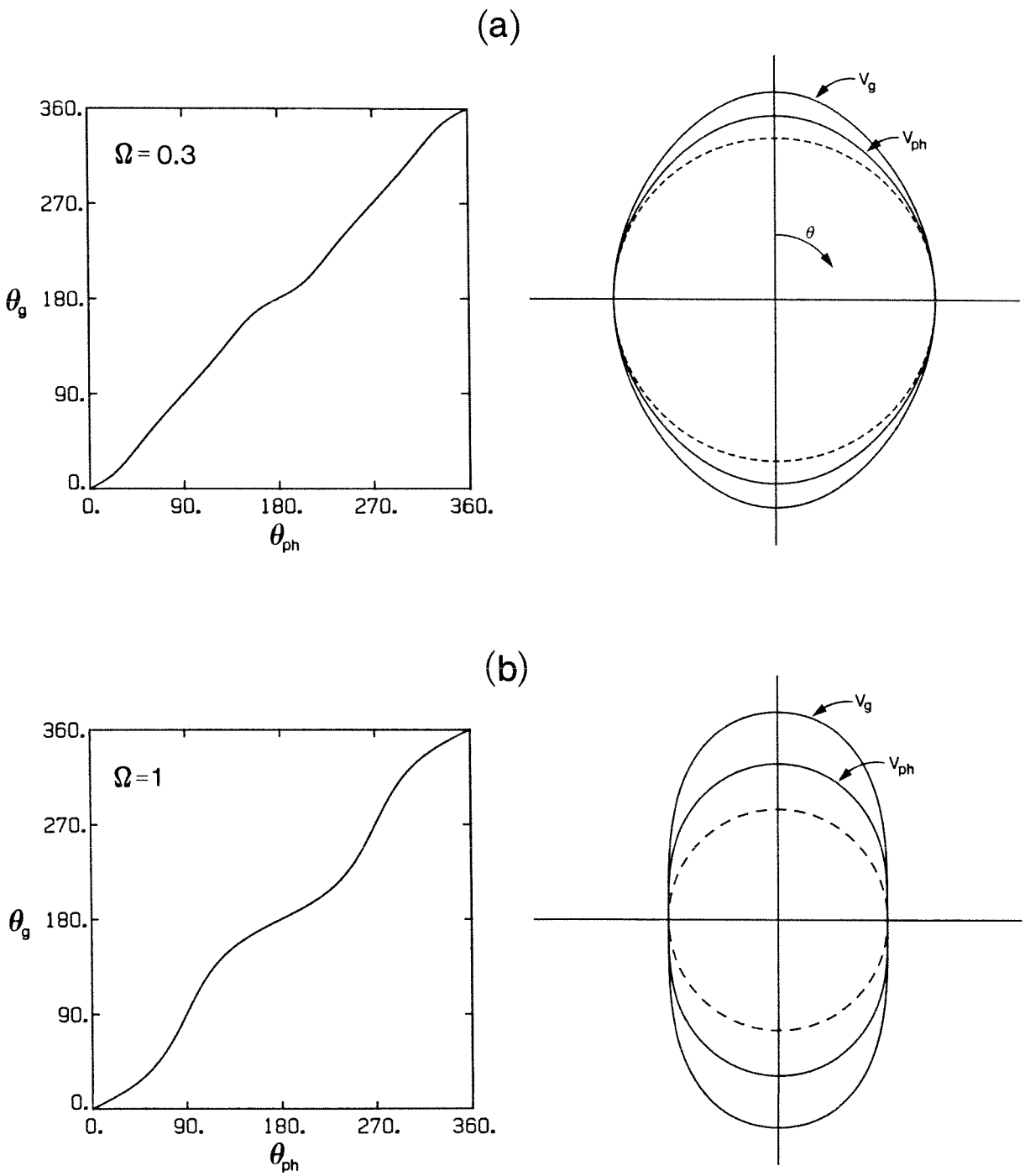

FIG. 2-3. Polar plots of $v_g(\theta_g)$ and $v_{ph}(\theta_{ph})$ (right column) and plots of θ_g vs. θ_{ph} (left column) for different frequencies. Units for the plots of θ_g and θ_{ph} are degrees. The plasma density is $n = 10^{13}$ cm^{-3}; the static magnetic field is $B_0 = 4.0$ kG. The dashed circle in each polar plot represents the Alfvén velocity $v_A = 2.8 \times 10^8$ cm/sec. a) $\Omega \equiv \omega/\omega_{ci} = 0.3$ b) $\Omega = 1.0$

(c)

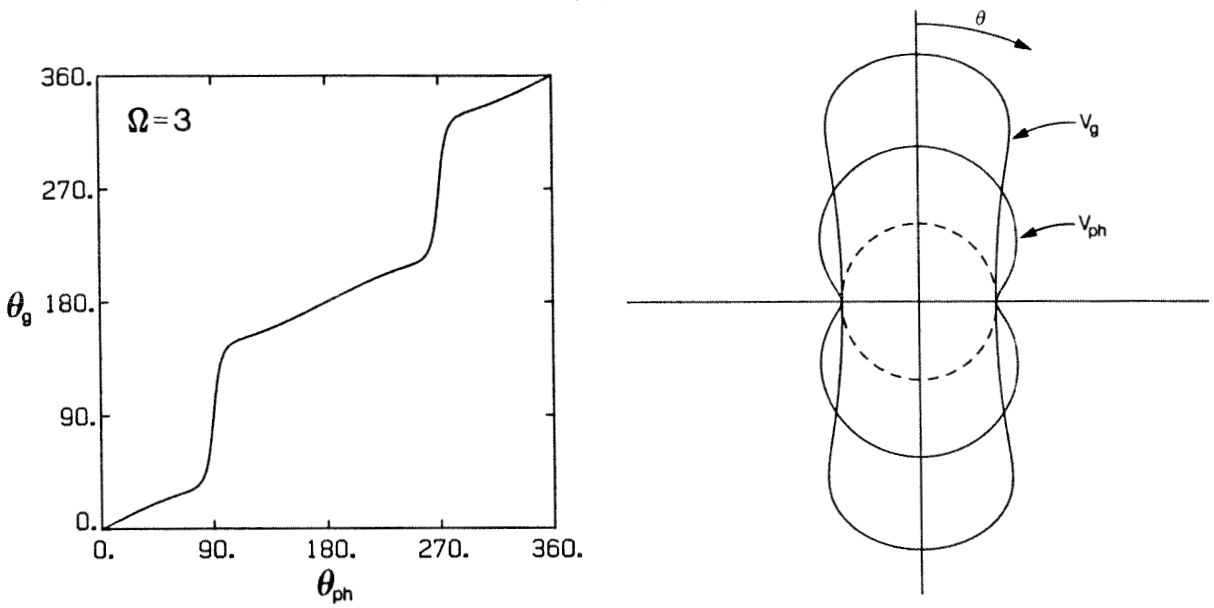

(d)

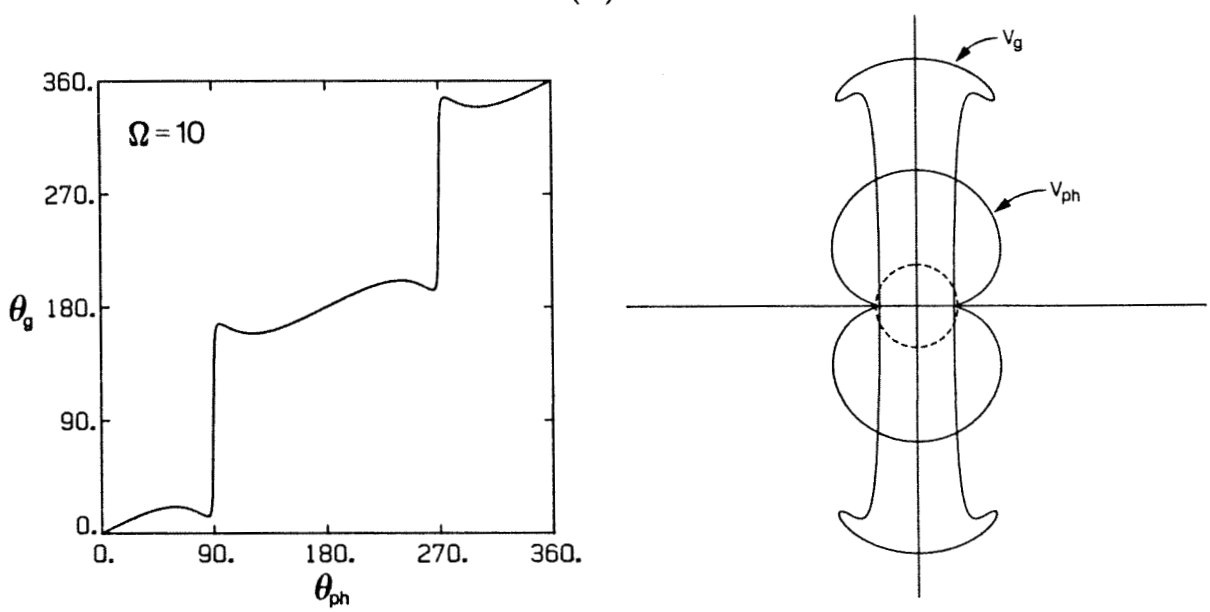

FIG. 2-3, continued. c) $\Omega = 3.0$ d) $\Omega = 10.0$

pal axes. At low frequencies (near ω_{ci}), the two surfaces do not differ greatly. The phase and group velocities become equal at $\theta_{ph} = \theta_g = \frac{\pi}{2}, \frac{3\pi}{2}$, while at $\theta_{ph} = \theta_g = 0, \pi$, the group velocity exceeds the phase velocity by a factor of approximately $2\left(\frac{\omega}{\omega_{ci}} + 1\right)\left(\frac{\omega}{\omega_{ci}} + 2\right)^{-1}$. At high frequencies ($\gg \omega_{ci}$), the group velocity becomes substantially larger than the phase velocity for θ_g near 0 or π, and the group velocity surface may become multi-valued.

2.1.4 Wave Energy

The energy associated with a wave propagating through a lossless plasma has three components: the magnetic field energy, the electric field energy, and the particle kinetic energy. The energy density associated with the magnetic field, averaged over the wave period, is just

$$W_B = \frac{\tilde{\mathbf{B}}^* \cdot \tilde{\mathbf{B}}}{16\pi}, \tag{2.20}$$

where "*" indicates the complex conjugate, while that associated with the vacuum electric field is

$$W_E = \frac{\tilde{\mathbf{E}}^* \cdot \tilde{\mathbf{E}}}{16\pi}. \tag{2.21}$$

Since the effects of the particle motion are being included in the effective dielectric tensor, the energy density associated with the particle motions may be expressed in terms of this tensor. Brillouin [1960] considers a process in which the wave is built up slowly from $\mathbf{E}=0$ to $\mathbf{E}=\tilde{\mathbf{E}}e^{-i\omega t}$ and integrates the incremental energy $\delta W = \frac{\mathbf{E}^* \cdot \delta \mathbf{D}}{4\pi}$, where $\mathbf{D} = \overleftrightarrow{\varepsilon}(\omega) \cdot \tilde{\mathbf{E}}$. The result, valid provided the medium is lossless and $\frac{\partial \overleftrightarrow{\varepsilon}}{\partial \omega}$ is not too great, is

$$W_{KE} = \frac{1}{16\pi} \tilde{\mathbf{E}}^* \cdot \left[\frac{\partial(\omega \overleftrightarrow{\varepsilon})}{\partial \omega} - \overleftrightarrow{I}\right] \cdot \tilde{\mathbf{E}}. \tag{2.22}$$

The ratios of the electric field energy to the magnetic field energy, and of the particle kinetic energy to the magnetic field energy, are plotted as functions of the angle of propagation (θ_{ph}) in Figures 2-4a and 2-4b, for parameters appropriate to the experiments on the Caltech tokamak. The ratio of electric to magnetic field energies is peaked for propagation perpendicular to the static magnetic field (Figure 2-4a), and this directional asymmetry as well as the magnitude of the ratio increases as ω increases. Even at $\omega = 6\,\omega_{ci}$, however, the peak of the ratio reaches only 3.1×10^{-3}; hence the vacuum electric field energy is a negligible fraction of the total wave energy. Although not shown in this plot, the ratio of electric to magnetic field energies increases linearly with density in the range of parameters being considered ($n = 10^{12} - 10^{14}$ cm^{-3}).

The ratio of particle kinetic energy to magnetic field energy (Figure 2-4b) is larger, reaching a peak of ~ 5 for propagation across the static magnetic field. The directional asymmetry also increases as the frequency increases, but the magnitude of the ratio decreases. For propagation nearly perpendicular to the static field, the ratio of energies depends little on frequency; also, the ratio is nearly independent of density.

Using the form of the dielectric tensor $\overleftrightarrow{\varepsilon}$, the expression 2.22 for the particle energy can be separated into terms arising from electron and ion motion. The ratio of the electron to ion kinetic energy associated with the wave is plotted in Figure 2-4c as a function of θ_{ph} for several frequencies. The electron energy exceeds the ion energy by a moderate factor ($4 - 16$) and the ratio is peaked for propagation along the static magnetic field. As the frequency decreases, the ion portion of the kinetic energy becomes more important (although for frequencies below ω_{ci}, the ion component *decreases* as the frequency decreases). The values of the ratio are also nearly independent of density over the range $10^{12} - 10^{14}$ cm^{-3}.

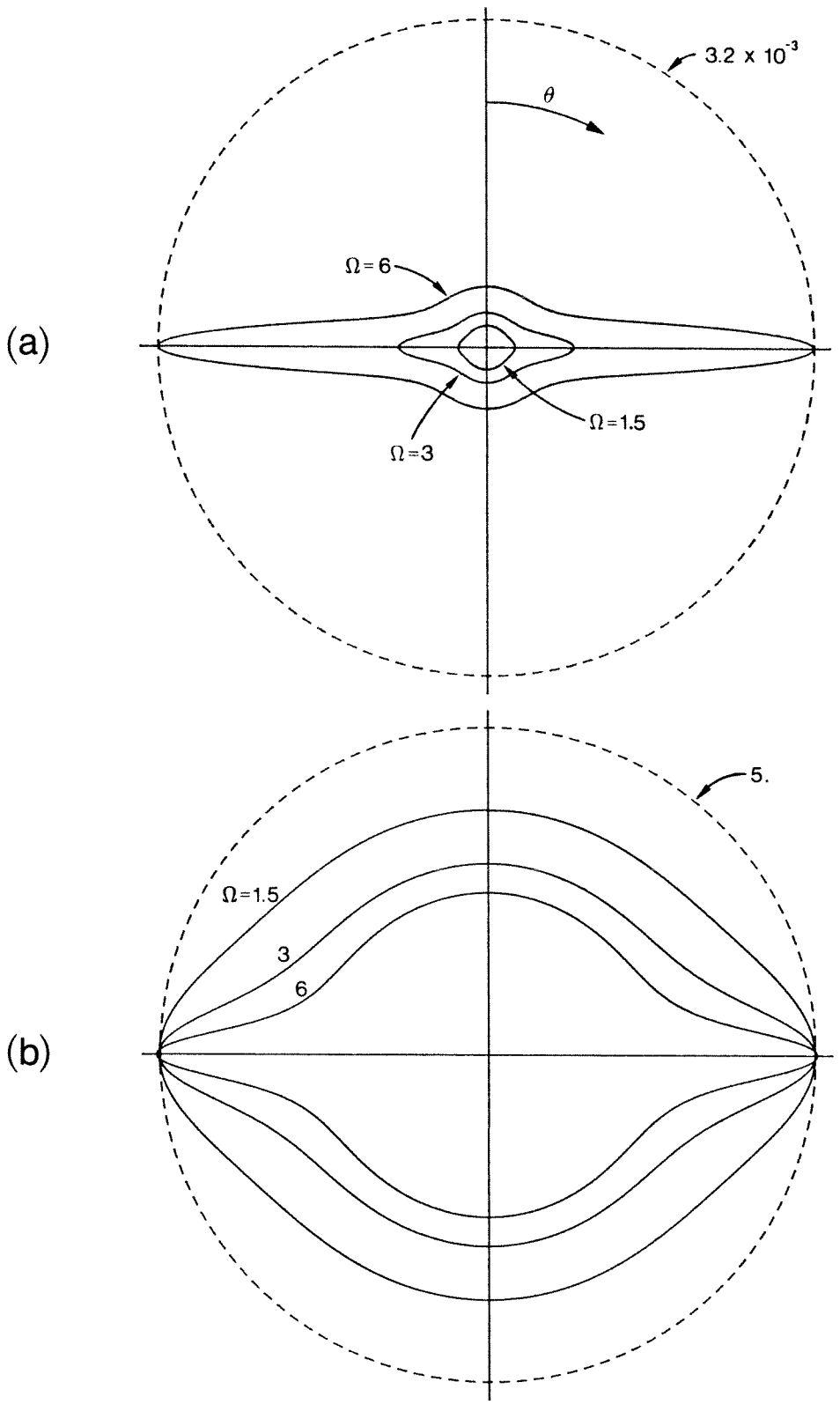

FIG. 2-4. Polar plots of the ratio of the vacuum electric field energy to the magnetic field energy (a), and the ratio of the particle kinetic energy to the magnetic field energy (b), for a plane wave, as a function of the angle of propagation (θ) with respect to the static magnetic field. In each case, the curves are shown for three frequencies: $\Omega \equiv \omega/\omega_{ci} = 1.5, 3.0, 6.0$. The plasma density is $n = 10^{13}$ cm^{-3} and the static magnetic field is $B_0 = 4$ kG. The dashed circles are drawn at the radius corresponding to the maximum ratio of the energies for each plot; that maximum is 3.2×10^{-3} for the figure in a), 5.0 for the figure in b).

(c)

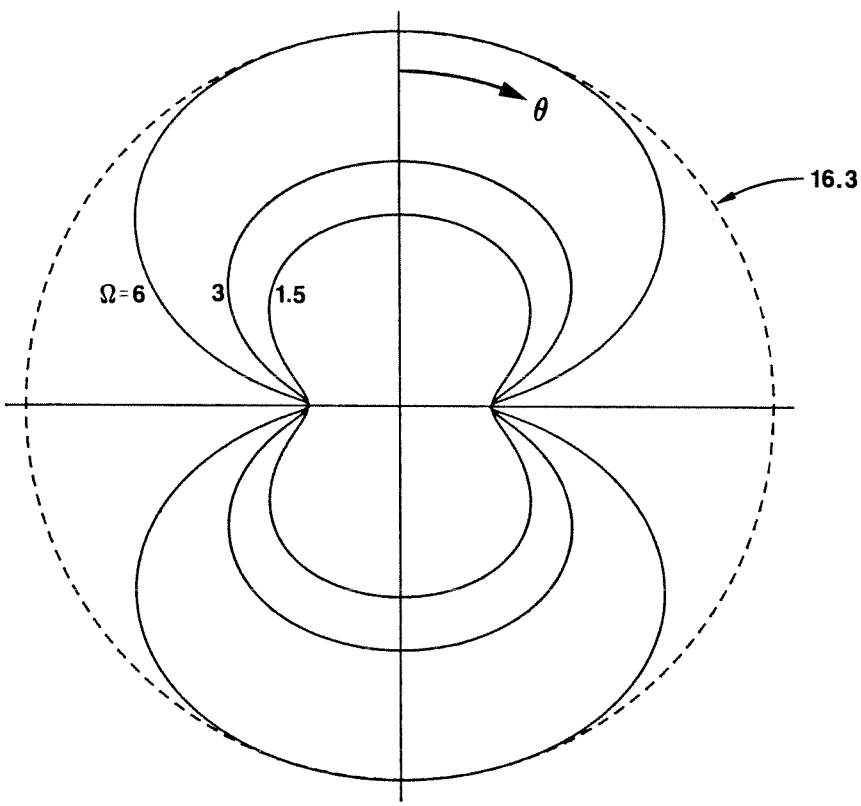

FIG. 2-4, continued. c) Ratio of electron to ion kinetic energy associated with a plasma wave, as a function of angle of propagation (θ) with respect to the static magnetic field. The curves are shown for three frequencies: Ω = 1.5, 3.0, 6.0. The plasma density is $n = 10^{13}$ cm^{-3} and the static magnetic field is $B_0 = 4.0$ kG. The dashed circle is drawn at a radius corresponding to the maximum ratio ($\sim$16.3) for the $\Omega = 6.0$ curve.

Hence, over the range of parameters appropriate to the Caltech tokamak, the energy associated with the fast wave is largely shared between the magnetic field and the particle motions; the vacuum electric field energy is very small. This, then, is why traditional approaches to the coupling of energy to the fast wave generally employ magnetic field antennas.

2.2 Toroidal Eigenmodes

2.2.1 Introduction

The torus which forms the tokamak wall can be regarded as a resonant cavity which may support a variety of electromagnetic modes. In the absence of plasma, there are no propagating modes because the lowest resonant frequency of the vacuum-filled torus is well above the frequencies of interest here. This follows because the free-space wavelengths involved are much larger than the dimensions of the tokamak. With the addition of plasma, however, the wavelengths may become much smaller (since the elements of the effective plasma dielectric tensor can be very large), and, if the damping of the waves is sufficiently small, cavity modes may then exist.

Analysis of the resonant frequencies of the plasma-filled torus is complicated by the toroidal geometry and by the anisotropic nature of the plasma dielectric tensor. Several simplifying assumptions are made to make the problem tractable. The toroidal geometry is replaced with a cylinder (Figure 2-5); the length of the cylinder (L) is taken to be the "unfolded" length of the tokamak ($2\pi R$) and the radius of the cylinder (ρ_0) is equal to the minor radius of the tokamak. The closed nature of the torus is taken into account by imposing periodic boundary conditions: all field components (Φ) must satisfy

$$\Phi(z) = \Phi(z + NL), \qquad N = 0, \pm 1, \pm 2, \cdots \tag{2.23}$$

The external magnetic field $\mathbf{B}_0$ is assumed to be constant and parallel to the

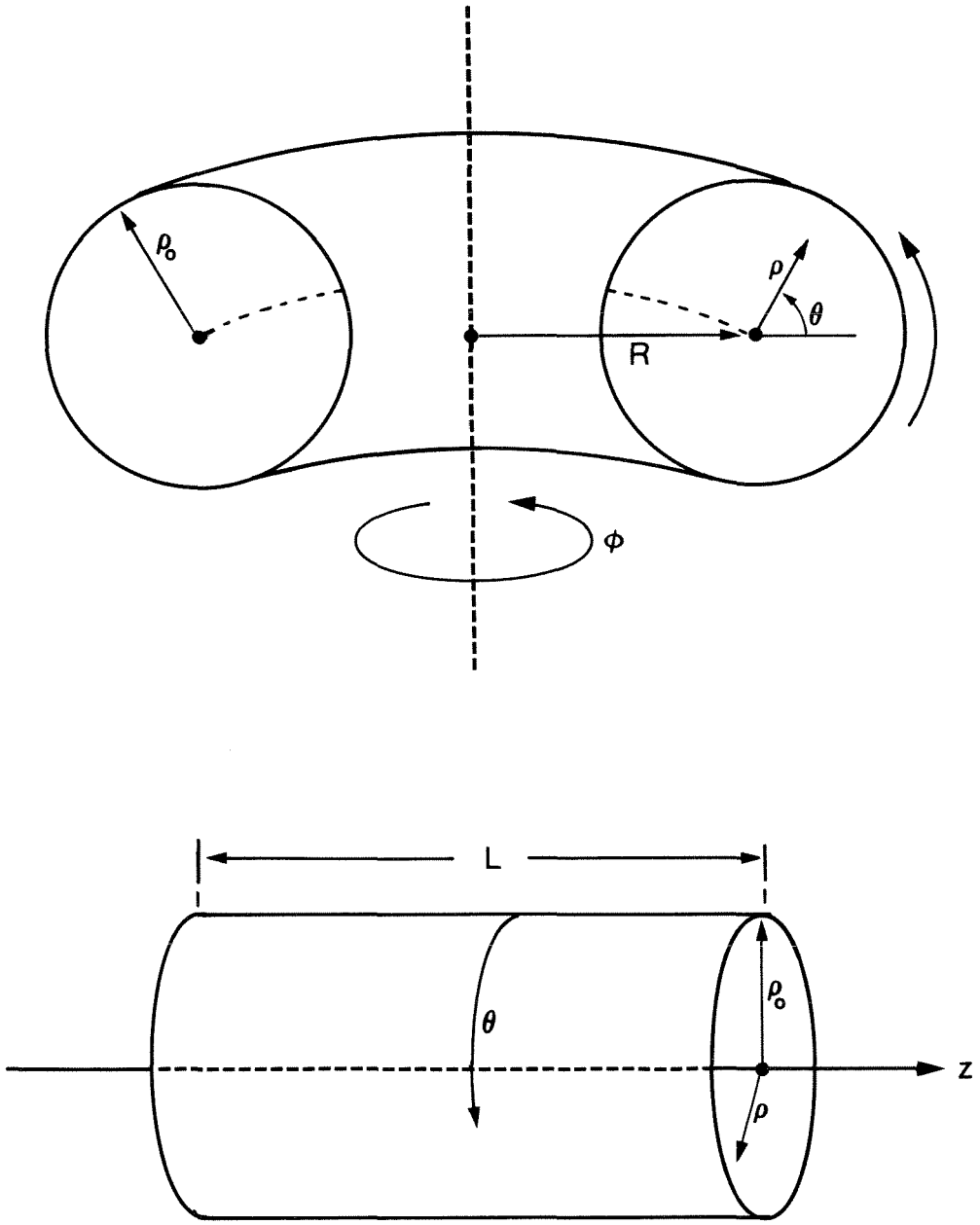

FIG. 2-5. Geometry of the periodic cylinder model of the tokamak. The radius of the cylinder (ρ_0) is equal to the minor radius of the torus, while the length of the cylinder (L) is equal to the major circumference of the torus ($2\pi R$). Periodic boundary conditions are imposed at the ends of the cylinder to simulate the closed nature of the torus.

cylinder axis. Thus the $1/R$ variation of the actual toroidal magnetic field in the tokamak is neglected in this model as well as the effect of the poloidal magnetic field generated by the plasma current.

The case of a homogeneous plasma completely filling a conducting cylinder is considered first. The wave equation and the general relations between field components are derived, following the approach of Allis [1963]. Boundary conditions are then applied to the solutions of the wave equation, yielding an eigenvalue equation which determines the frequencies of the fundamental modes of the system. The equation is solved numerically for parameters appropriate to the Caltech tokamak, and the radial dependence of the wave fields associated with these eigenfrequencies is obtained.

The approximation $m_e \to 0$ (which requires $E_z \to 0$) is then considered and the effects on the wave fields and on the normal mode dispersion relation is noted.

2.2.2 Wave Equations

It is useful in the following discussion to introduce a separation of the wave fields into components parallel and perpendicular to the external static magnetic field $\mathbf{B}_0 = B_0 \hat{\mathbf{z}}$. The subscript "$\perp$" refers to a component perpendicular to $\mathbf{B}_0$, while subscripts "$\parallel$" or "z" refer to components parallel to $\mathbf{B}_0$. Then a vector field $\mathbf{A}$ can be written as $\mathbf{A} = \mathbf{A}_\perp + A_z \hat{\mathbf{z}}$, where $A_z = \mathbf{A} \cdot \hat{\mathbf{z}}$ and $\mathbf{A}_\perp = (\hat{\mathbf{z}} \times \mathbf{A}) \times \hat{\mathbf{z}}$. We look for solutions where all field quantities vary in the $\hat{\mathbf{z}}$ direction as $e^{ik_\parallel z}$, where $k_\parallel$ is called the parallel (or toroidal) wavenumber. The gradient operation can then be written as $\nabla = \nabla_\perp + ik_\parallel \hat{\mathbf{z}}$; the divergence as $\nabla \cdot \mathbf{A} = \nabla_\perp \cdot \mathbf{A}_\perp + ik_\parallel A_z$; the Laplacian as $\nabla^2 \mathbf{A} = \nabla_\perp^2 \mathbf{A} - k_\parallel^2 \mathbf{A}$; and the curl as $\nabla \times \mathbf{A} = \nabla_\perp \times \mathbf{A} + ik_\parallel \hat{\mathbf{z}} \times \mathbf{A}$. Some useful relations are easily derived:

$$\nabla_\perp \times \mathbf{A} = \left[\left(\nabla \times \mathbf{A} \right) \cdot \hat{\mathbf{z}} \right] \hat{\mathbf{z}} \tag{2.24}$$

and

$$\hat{\mathbf{z}}\times\left(\nabla\times\mathbf{A}\right) = \nabla_{\perp}(A_z) - i\,k_{\parallel}\mathbf{A}_{\perp}\,. \tag{2.25}$$

Maxwell's equations may then be written as

$$\nabla\times\mathbf{E} = -\frac{1}{c}\frac{\partial\mathbf{B}}{\partial t} = i\,k_0\mathbf{B} \tag{2.26a}$$

$$\nabla\times\mathbf{B} = \frac{1}{c}\frac{\partial}{\partial t}(\overleftrightarrow{\varepsilon}\cdot\mathbf{E}) = -i\,k_0\overleftrightarrow{\varepsilon}\cdot\mathbf{E}\,, \tag{2.26b}$$

where $k_0 = \frac{\omega}{c}$ is the free-space wavenumber and an $e^{-i\omega t}$ time dependence has been assumed. Taking the curl of equation 2.26a yields a wave equation for the electric field:

$$\nabla^2\mathbf{E} - \nabla(\nabla\cdot\mathbf{E}) + k_0^2\overleftrightarrow{\varepsilon}\cdot\mathbf{E} = 0\,. \tag{2.27}$$

It will be shown subsequently that a knowledge of E_z and B_z is sufficient to completely determine all components of the wave fields, hence we consider the z-component of equation 2.27:

$$\nabla_{\perp}^2 E_z - k_{\parallel}^2 - i\,k_{\parallel}\left[\nabla_{\perp}\cdot\mathbf{E}_{\perp} + i\,k_{\parallel}E_z\right] + k_0^2\,\varepsilon_{\parallel}E_z = 0\,. \tag{2.28}$$

Since there are no external charges in this system (those comprising the plasma having already been taken into account by the effective dielectric tensor), the Poisson equation is just:

$$\nabla\cdot\mathbf{D} = \nabla\cdot\left[\overleftrightarrow{\varepsilon}\cdot\mathbf{E}\right] = 0\,. \tag{2.29}$$

Using the form of the cold-plasma dielectric tensor discussed previously,

$$\overleftrightarrow{\varepsilon}\cdot\mathbf{E} = \varepsilon_{\perp}\mathbf{E}_{\perp} + i\,\varepsilon_{\times}\hat{\mathbf{z}}\times\mathbf{E}_{\perp} + \varepsilon_{\parallel}E_z\,\hat{\mathbf{z}}\,. \tag{2.30}$$

Expanding Poisson's equation, we have:

$$\nabla_{\perp}\cdot\mathbf{E}_{\perp} = -\frac{1}{\varepsilon_{\times}}\left[i\,k_{\parallel}\varepsilon_{\parallel}E_z + \varepsilon_{\times}k_0B_z\right]\,. \tag{2.31}$$

Substituting equation 2.31 into equation 2.28 yields the wave equation for E_z:

$$\nabla_\perp^2 E_z + \left[k_0^2\,\varepsilon_\parallel - k_\parallel^2\,\frac{\varepsilon_\parallel}{\varepsilon_\perp}\right] E_z = -k_\parallel k_0\,\frac{\varepsilon_x}{\varepsilon_\perp} B_z\ . \tag{2.32}$$

The wave equation for B is obtained by taking the curl of equation 2.26b:

$$\nabla_\perp^2 \mathbf{B} = i\,k_0 \nabla \times \left(\overleftrightarrow{\boldsymbol{\varepsilon}} \cdot \mathbf{E}\right)\ . \tag{2.33}$$

The $z-$component of the above is, using equations 2.24 and 2.30,

$$\nabla_\perp^2 B_z - k_\parallel^2\,B_z = i\,k_0 \nabla_\perp \times \left(\varepsilon_\perp \mathbf{E}_\perp + i\,\varepsilon_x \hat{\mathbf{z}} \times \mathbf{E}_\perp\right) \tag{2.34}$$

Since $\nabla_\perp \times \mathbf{E}_\perp = i\,k_0 B_z$ and $\nabla_\perp \times (\hat{\mathbf{z}} \times \mathbf{E}_\perp) = \hat{\mathbf{z}}(\nabla_\perp \cdot \mathbf{E}_\perp)$, the above equation can be recast, using equation 2.31 , as

$$\nabla_\perp^2 B_z + \left[k_0^2 \left(\frac{\varepsilon_\perp^2 - \varepsilon_x^2}{\varepsilon_\perp}\right) - k_\parallel^2\right] B_z = i\,k_\parallel k_0\,\frac{\varepsilon_x \varepsilon_\parallel}{\varepsilon_\perp} E_z \tag{2.35}$$

Equations 2.32 and 2.35 are a pair of coupled second-order differential equations for the field components E_z and B_z. These equations can be solved for E_z or B_z, resulting in a single fourth-order equation satisfied by both E_z and B_z. Introducing new constants a, b, f, and g, the wave equations can be written as

$$\nabla_\perp^2 E_z + a\,E_z = i\,b\,B_z \tag{2.36a}$$

$$\nabla_\perp^2 B_z + f\,B_z = -i\,g\,E_z \tag{2.36b}$$

where

$$a = k_0^2\,\varepsilon_\parallel - k_\parallel^2\,\frac{\varepsilon_\parallel}{\varepsilon_\perp} \qquad f = k_0^2 \left(\frac{\varepsilon_\perp^2 - \varepsilon_x^2}{\varepsilon_\perp}\right) - k_\parallel^2$$

$$b = -k_\parallel k_0\,\frac{\varepsilon_x}{\varepsilon_\perp} \qquad g = -k_\parallel k_0\,\frac{\varepsilon_x \varepsilon_\parallel}{\varepsilon_\perp}\ .$$

Solving for E_z or B_z then yields

$$\nabla_\perp^2 \begin{bmatrix} E_z \\ B_z \end{bmatrix} + (a + f)\nabla_\perp^2 \begin{bmatrix} E_z \\ B_z \end{bmatrix} + (af - bg)\begin{bmatrix} E_z \\ B_z \end{bmatrix} = 0 . \tag{2.37}$$

Since a homogeneous plasma is being considered at this point, the coefficients a, b, f, and g are not functions of position, and the equation can be rewritten in biquadratic form:

$$\left(\nabla_\perp^2 + p_1^2\right)\left(\nabla_\perp^2 + p_2^2\right)\begin{bmatrix} E_z \\ B_z \end{bmatrix} = 0 . \tag{2.38}$$

Expanding equation 2.38 and comparing with equation 2.37 yields an equation for p_1 and p_2 in terms of a, b, f, and g:

$$\left(p_{1,2}\right)^2 = \frac{a + f}{2} \pm \frac{1}{2}\left[(a + f)^2 - 4(af - bg)\right]^{\frac{1}{2}} . \tag{2.39}$$

where p_1 is associated with the "+" sign and p_2 is associated with the "-" sign. The four linearly independent solutions which are associated with equation 2.37 are then given by the two pairs of solutions of the second-order equation:

$$\left(\nabla_\perp^2 + p_i^2\right)\begin{bmatrix} E_z \\ B_z \end{bmatrix} = 0 \tag{2.40}$$

for $p_i = p_1$ or p_2.

To proceed further with the solution of the wave equation requires specification of the transverse geometry. The periodic cylinder model is used and equation 2.40 becomes, in cylindrical coordinates,

$$\frac{1}{\rho}\frac{\partial}{\partial \rho}\left(\rho \frac{\partial \psi}{\partial \rho}\right) + \frac{1}{\rho^2}\frac{\partial^2 \psi}{\partial \theta^2} + p_i^2 \psi = 0 , \tag{2.41}$$

where $\psi = E_z$ or B_z. Separation of variables, $\psi(\rho, \theta) = R(\rho)\varphi(\theta)$, yields

$$\frac{\rho}{R}\frac{\partial}{\partial \rho}\left(\rho \frac{\partial R}{\partial \rho}\right) + \rho^2 p_i^2 = -\frac{1}{\varphi}\frac{\partial^2 \varphi}{\partial \theta^2} = m^2 , \tag{2.42}$$

where m is a constant called the poloidal mode number. Solutions of the

above are simply $\varphi(\theta) = e^{im\theta}$ and $R(\rho) = J_m(p_i\rho)$, $Y_m(p_i\rho)$, where J_m and Y_m are the Bessel functions of order m. Physically, the solutions must be periodic functions of θ with period 2π, and m must therefore be an integer. Solutions for E_z and B_z which are finite as $\rho \to 0$ can then be written explicitly:

$$E_z(\rho, \theta, z) = \alpha J_m(p_1\rho)\, e^{i(m\theta + k_\parallel z)} + \beta J_m(p_2\rho)\, e^{i(m\theta + k_\parallel z)} \tag{2.43a}$$

$$i B_z(\rho, \theta, z) = \frac{a - p_1^2}{b} \alpha J_m(p_1\rho)\, e^{i(m\theta + k_\parallel z)} + \frac{a - p_2^2}{b} \beta J_m(p_2\rho)\, e^{i(m\theta + k_\parallel z)}, \tag{2.43b}$$

where $m = 0, \pm 1, \pm 2...$, α and β are arbitrary constants, and equations 2.36 have been used.

The above results are not valid, however, when $k_\parallel = 0$, for then b and g vanish and equations 2.36 are uncoupled. In that case the solutions are given by

$$E_z(\rho, \theta, z) = \gamma J_m(\sqrt{a}\,\rho) e^{im\theta} \tag{2.44a}$$

$$B_z(\rho, \theta, z) = \delta J_m(\sqrt{f}\,\rho) e^{im\theta}, \tag{2.44b}$$

where γ and δ are arbitrary constants.

2.2.3 Relations Between Field Components

As mentioned earlier, all field components can be derived from E_z and B_z and their spatial derivatives. The explicit relations between the field components are derived from Maxwell's equations together with the form of the cold plasma dielectric tensor. Taking the cross-product of $\hat{\mathbf{z}}$ with equation 2.26a and using equation 2.25 yields

$$i k_0 \hat{\mathbf{z}} \times \mathbf{B}_\perp = \hat{\mathbf{z}} \times (\nabla \times \mathbf{E}) = \nabla_\perp E_z - i k_\parallel \mathbf{E}_\perp. \tag{2.45}$$

The cross-product of $\hat{\mathbf{z}}$ with equation 2.26b is given by

$$\hat{\mathbf{z}} \times (\nabla \times \mathbf{B}) = -i k_0 \hat{\mathbf{z}} \times (\overleftrightarrow{\boldsymbol{\varepsilon}} \cdot \mathbf{E}) \tag{2.46}$$

or

$$\nabla_\perp(B_z) - i\,k_\parallel \mathbf{B}_\perp = -i\,k_0\,\varepsilon_\perp \hat{\mathbf{z}}\times\mathbf{E}_\perp - k_0\,\varepsilon_\times \mathbf{E}_\perp, \tag{2.47}$$

where equations 2.25 and 2.30 have been used. Now the cross-product of $\hat{\mathbf{z}}$ with equation 2.45 is

$$\hat{\mathbf{z}}\times(\nabla_\perp E_z) = i\,k_\parallel \hat{\mathbf{z}}\times\mathbf{E}_\perp - i\,k_0\,\mathbf{B}_\perp, \tag{2.48}$$

while the cross-product of $\hat{\mathbf{z}}$ with equation 2.47 is

$$\hat{\mathbf{z}}\times(\nabla_\perp B_z) = i\,k_\parallel \hat{\mathbf{z}}\times\mathbf{B}_\perp + i\,k_0\,\varepsilon_\perp\mathbf{E}_\perp - k_0\,\varepsilon_\times \hat{\mathbf{z}}\times\mathbf{E}_\perp. \tag{2.49}$$

Equations 2.45, 2.47, 2.48, and 2.49 can now be combined into a matrix expression relating $\nabla_\perp E_z$ and $\nabla_\perp B_z$ to E_z and B_z and their respective cross-products with $\hat{\mathbf{z}}$:

$$\begin{bmatrix} \nabla_\perp E_z \\ \nabla_\perp B_z \\ \hat{\mathbf{z}}\times\nabla_\perp E_z \\ \hat{\mathbf{z}}\times\nabla_\perp B_z \end{bmatrix} = \begin{bmatrix} ik_\parallel & 0 & 0 & ik_0 \\ -k_0\varepsilon_\times & ik_\parallel & -ik_0\varepsilon_\perp & 0 \\ 0 & -ik_0 & ik_\parallel & 0 \\ ik_0\varepsilon_\perp & 0 & -k_0\varepsilon_\times & ik_\parallel \end{bmatrix} \begin{bmatrix} \mathbf{E}_\perp \\ \mathbf{B}_\perp \\ \hat{\mathbf{z}}\times\mathbf{E}_\perp \\ \hat{\mathbf{z}}\times\mathbf{B}_\perp \end{bmatrix} \tag{2.50}$$

What is actually desired, however, is the relation between the transverse components $\mathbf{E}_\perp$, $\mathbf{B}_\perp$ and the gradients of E_z, B_z. The above matrix must therefore be inverted. The algebra is straightforward [Allis et al., 1963], yielding

$$\begin{bmatrix} \mathbf{E}_\perp \\ \mathbf{B}_\perp \\ \hat{\mathbf{z}}\times\mathbf{E}_\perp \\ \hat{\mathbf{z}}\times\mathbf{B}_\perp \end{bmatrix} = \begin{bmatrix} iG_1 & G_2 & G_3 & iG_4 \\ G_5 & iG_1 & iG_6 & G_3 \\ -G_3 & -iG_4 & iG_1 & G_2 \\ -iG_6 & -G_3 & G_5 & iG_1 \end{bmatrix} \begin{bmatrix} \nabla_\perp E_z \\ \nabla_\perp B_z \\ \hat{\mathbf{z}}\times\nabla_\perp E_z \\ \hat{\mathbf{z}}\times\nabla_\perp B_z \end{bmatrix} \tag{2.51}$$

where

$$G_1 = \frac{k_0^2 k_\parallel \varepsilon_\perp - k_\parallel^3}{\Delta} \qquad G_4 = \frac{k_0 k_\parallel^2 - k_0^3 \varepsilon_\perp}{\Delta}$$

$$G_2 = \frac{k_0^3 \varepsilon_x}{\Delta} \qquad G_5 = -\frac{k_0 k_\parallel^2 \varepsilon_x}{\Delta}$$

$$G_3 = \frac{k_0^2 k_\parallel \varepsilon_x}{\Delta} \qquad G_6 = \frac{k_0^3 (\varepsilon_\perp^2 - \varepsilon_x^2) - k_0 k_\parallel^2 \varepsilon_\perp}{\Delta}$$

and $\Delta = k_\parallel^4 - 2k_0^2 k_\parallel^2 \varepsilon_\perp + k_0^4 (\varepsilon_\perp^2 - \varepsilon_x^2)$, and the inverse exists provided $\Delta \neq 0$.

For cylindrical geometry, it is convenient to derive explicitly the relations between E_ρ, E_θ, B_ρ, B_θ, and E_z, B_z. For azimuthal variation $e^{im\theta}$, the transverse gradient is $\nabla_\perp = \hat{\rho}\frac{\partial}{\partial\rho} + \hat{\theta}\frac{im}{\rho}$. Writing out the $\hat{\rho}$ and $\hat{\theta}$ components of the first two terms in equation 2.51 yields the desired result, which can also be expressed in matrix form:

$$\begin{bmatrix} E_\theta \\ E_\rho \\ B_\theta \\ B_\rho \end{bmatrix} = \begin{bmatrix} -\frac{m}{\rho}G_1 & G_3 & \frac{im}{\rho}G_2 & iG_4 \\ -\frac{im}{\rho}G_3 & iG_1 & \frac{m}{\rho}G_4 & G_2 \\ \frac{im}{\rho}G_5 & iG_6 & -\frac{m}{\rho}G_1 & G_3 \\ \frac{m}{\rho}G_6 & G_5 & -\frac{im}{\rho}G_3 & iG_1 \end{bmatrix} \begin{bmatrix} E_z \\ \frac{\partial E_z}{\partial\rho} \\ B_z \\ \frac{\partial B_z}{\partial\rho} \end{bmatrix} \qquad (2.52)$$

2.2.4 Boundary Conditions

Thus far we have determined acceptable solutions to Maxwell's equations for a periodic-cylinder geometry filled with a homogeneous plasma magnetized in the $\hat{z}$ direction. Appropriate boundary conditions must be applied which will restrict the set of allowable solutions.

The tokamak wall is made of stainless steel much thicker than the skin depth at the frequencies of interest ($>\omega_{ci}$), and it is continuous except for small access ports and a toroidal insulating gap. The effect of the gap is

ignored in this discussion and the boundary for the model is taken to be a perfectly conducting cylinder at radius ρ_0. The tangential components of the electric field (E_z and E_θ) and the normal component of the magnetic field (B_ρ) must therefore vanish at $\rho = \rho_0$.

Periodicity in the azimuthal ($\hat{\theta}$) direction has already been taken into account by restricting m to be an integer. Periodicity in the $\hat{z}$ direction requires that $k_\parallel = \frac{N}{R}$, where $N = 0, 1, 2, \ldots$ will be termed the toroidal mode number, and R is the major radius of the tokamak.

Case 1: $N \neq 0$

Imposing the boundary condition $E_z(\rho_0) = 0$ on equation 2.43a yields

$$\alpha J_m(p_1\rho_0) + \beta J_m(p_2\rho_0) = 0 , \tag{2.53}$$

where $N \neq 0$. The $\hat{z}$ components of the fields are then determined to within an arbitrary constant α:

$$E_z = \alpha \left[J_m(p_1\rho) - \frac{J_m(p_1\rho_0)}{J_m(p_2\rho_0)} J_m(p_2\rho) \right] e^{i(m\theta + \frac{N}{R}z)} \tag{2.54a}$$

$$B_z = -i\alpha \left[\left[\frac{a - p_1^2}{b} \right] J_m(p_1\rho) - \left[\frac{a - p_2^2}{b} \right] \frac{J_m(p_1\rho_0)}{J_m(p_2\rho_0)} J_m(p_2\rho) \right] e^{i(m\theta + \frac{N}{R}z)} \tag{2.54b}$$

Using equation 2.52, the boundary condition $E_\theta(\rho_0) = 0$ can be written as

$$G_3 \left. \frac{\partial E_z}{\partial \rho} \right|_{\rho=\rho_0} + \frac{im}{\rho_0} G_2 B_z(\rho_0) + i\, G_4 \left. \frac{\partial B_z}{\partial \rho} \right|_{\rho=\rho_0} = 0 . \tag{2.55}$$

Using equation 2.54a to evaluate the derivatives yields, after some algebra and using equation 2.53,

$$\frac{m}{\rho_0}(G_2 + G_4)\left[\frac{p_2^2 - p_1^2}{b}\right] J_m(p_1\rho_0) - p_1\left[G_3 + G_4\left[\frac{a - p_1^2}{b}\right]\right] J_{m+1}(p_1\rho_0)$$

$$+ p_2\left[G_3 + G_4\left[\frac{a - p_2^2}{b}\right]\right] \frac{J_{m+1}(p_2\rho_0)\, J_m(p_1\rho_0)}{J_m(p_2\rho_0)} = 0 \quad . \tag{2.56}$$

For fixed toroidal and poloidal mode numbers N and m, and fixed plasma density and static magnetic field, the left-hand side of equation 2.56 is a function only of frequency. The roots of the function therefore determine distinct frequencies for which the given mode satisfies the boundary condition. These eigenfrequencies correspond to different radial propagation constants p_1 and p_2, and each solution is labeled a different "radial mode", l. By convention, that solution corresponding to the lowest frequency (if there is one) is called the first radial mode ($l = 1$), and so on. Alternatively, for fixed frequency (typical of actual experiments), the left-hand side of equation 2.56 is a function of density, and its roots give the distinct densities at which the modes occur.

Case 2: $N = 0$

When $N = 0$ (corresponding to a mode with no toroidal variation), the solutions for the fields are given by equations 2.44. Application of the boundary condition on E_z results in two possibilities: either $\gamma = 0$ or $\sqrt{a}\,\rho_0 = \xi_{mn}$, where ξ_{mn} is the n^{th} zero of the Bessel function of order m. However, $a < 0$ for $\omega < \omega_p$ and since the zeroes of the Bessel function J_m are all real [Abramowitz and Stegun, 1972], it follows that $\gamma = 0$. This implies that E_z is zero everywhere and so the only allowable solution in this case is a TE (transverse electric) mode.

The boundary condition on E_θ is, from equation 2.52,

$$\frac{m}{\rho} G_2 B_z(\rho_0) + G_4 \left.\frac{\partial B_z}{\partial \rho}\right|_{\rho=\rho_0} = 0 \quad . \tag{2.58}$$

Using equation 2.44b and the definitions of G_1 and G_2, this becomes

$$\frac{m}{\rho}(\varepsilon_\times - \varepsilon_\perp) J_m\left[\sqrt{f_0}\,\rho_0\right] + \sqrt{f_0}\,\varepsilon_\perp J_{m+1}\left[\sqrt{f_0}\,\rho_0\right] = 0\,, \tag{2.59}$$

where $f_0 = k_0^2\left[\frac{\varepsilon_\perp^2 - \varepsilon_\times^2}{\varepsilon_\perp}\right]$ and $f_0 > 0$ for $\omega < \omega_{lh}$. For fixed m, ω, and B_0, then, this equation determines the allowable plasma densities for each mode. The fields in this case are just

$$E_z = 0 \tag{2.60a}$$

$$B_z = \alpha J_m\left[\sqrt{f_0}\,\rho\right] e^{im\theta}\,, \tag{2.60b}$$

where α is an arbitrary constant.

2.2.5 Numerical Results

It is useful to investigate the form of p_1 and p_2 for parameters appropriate to the Caltech tokamak. p_1^2 is plotted in Figure 2-6a, for a density of $10^{13}\,\mathrm{cm}^{-3}$, as a function of frequency for various parallel wavenumbers ($k_\parallel = N/R$); p_1^2 as a function of frequency is plotted for $N = 1$ and different densities in Figure 2-6b. Similar plots are shown in Figures 2-7a and 2-7b for p_2^2. It is clear that for parameters appropriate to the experiments performed ($\Omega \equiv \frac{\omega}{\omega_{ci}} \approx 1-3$; $n \approx 10^{12} - 10^{13}\ \mathrm{cm}^{-3}$), p_1^2 is less than zero and p_2^2 is greater than zero. Hence p_1 is imaginary while p_2 is real. The Bessel functions $J_m(p_1\rho)$ then become $(i)^m I_m(|p_1|\rho)$. From Figure 2-6a, $|p_1|\rho_0 > 90$ for $n = 10^{13}\ \mathrm{cm}^{-3}$ and $\Omega > 1$. Since, for large ξ, $I_m(\xi) \sim \frac{e^\xi}{\sqrt{2\pi\xi}}$, it follows that the contributions from the I_m functions will be important only near the wall (i.e., near $\rho = \rho_0$).

Equations 2.56 and 2.59 were solved numerically to find the locations of the eigenmodes in density–frequency space. All of the modes occurring in the

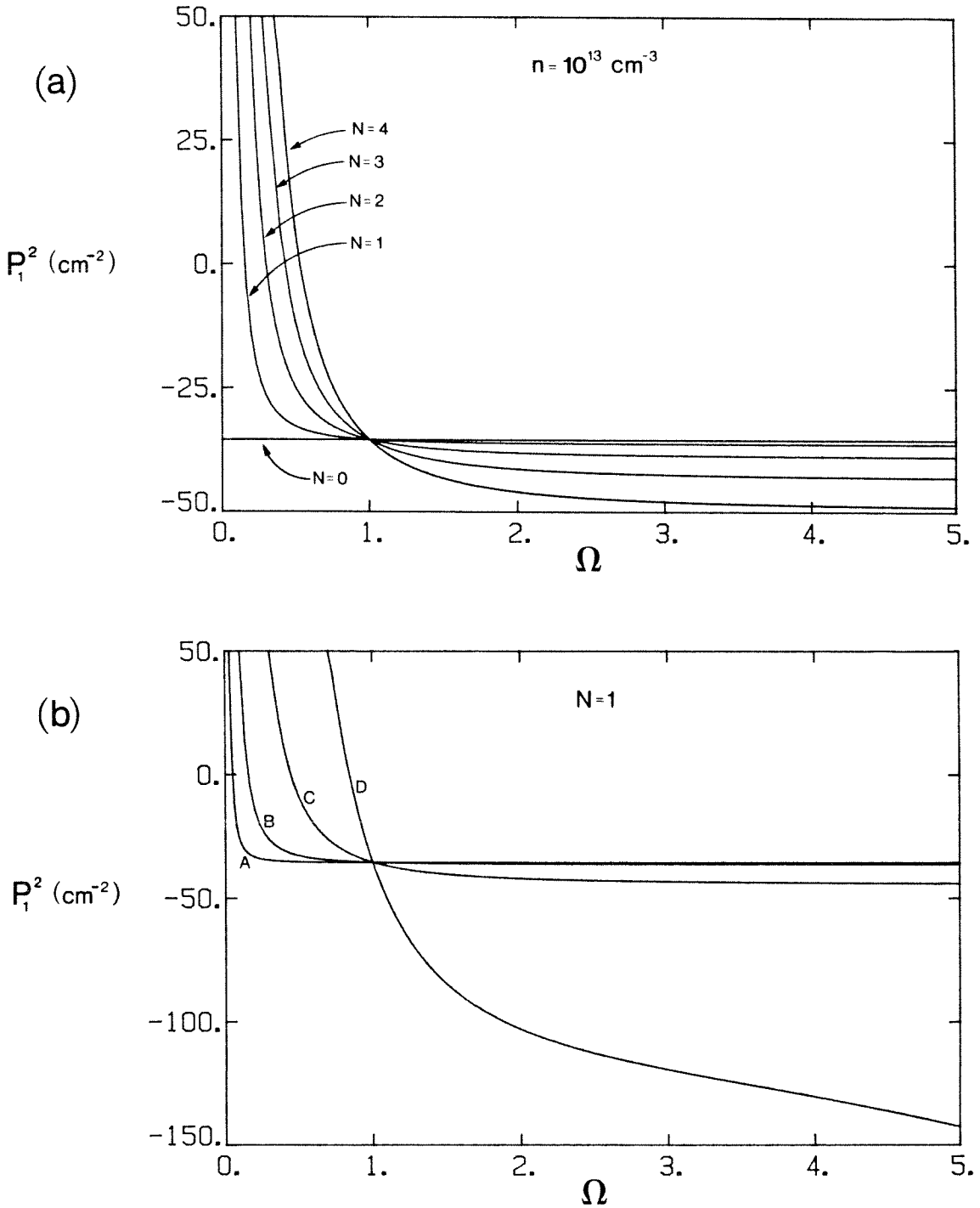

FIG. 2-6. a) Plots of P_1^2 as a function of Ω for different values of the toroidal mode number $N = k_{\parallel} R_0$. The plasma density is $n = 10^{13}$ cm^{-3}; the static magnetic field is $B_0 = 4$ kG. b) Plots of P_1^2 as a function of Ω for different densities n and fixed toroidal mode number $N = 1$. Curve A: $n = 10^{14}$ cm^{-3}, vertical scale $\times$ 10. Curve B: $n = 10^{13}$ cm^{-3}, vertical scale $\times$ 1. Curve C: $n = 10^{12}$ cm^{-3}, vertical scale $\times$ 10^{-1}. Curve D: $n = 10^{11}$ cm^{-3}, vertical scale $\times$ 10^{-2}.

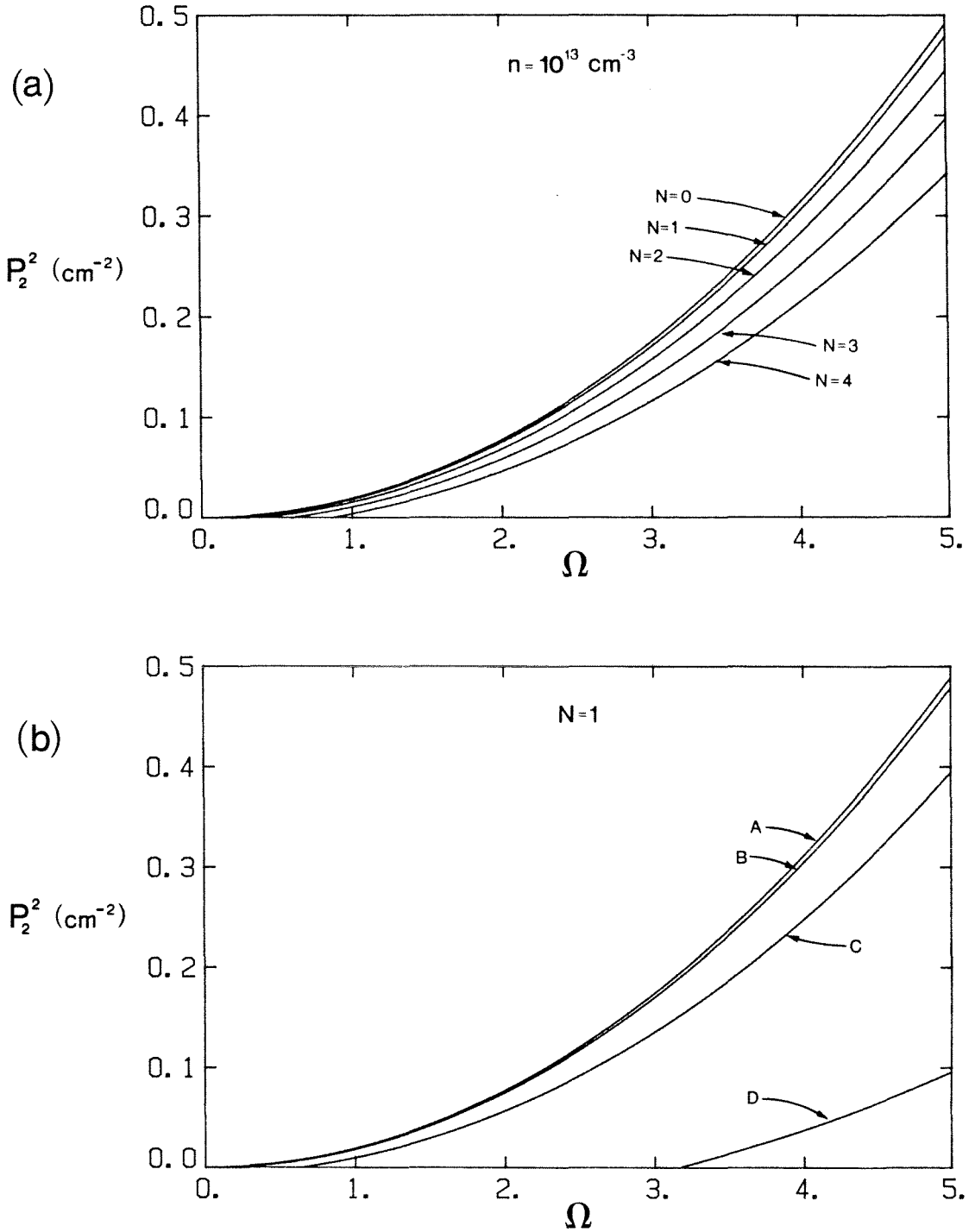

FIG. 2-7. a) Plots of P_2^2 as a function of Ω for different values of the toroidal mode number $N = k_{\|} R_0$. The plasma density is $n = 10^{13}$ cm^{-3}; the static magnetic field is $B_0 = 4$ kG. b) Plots of P_2^2 as a function of Ω for different densities n and fixed toroidal mode number $N = 1$. Curve A: $n = 10^{14}$ cm^{-3}, vertical scale $\times$ 10. Curve B: $n = 10^{13}$ cm^{-3}, vertical scale $\times$ 1. Curve C: $n = 10^{12}$ cm^{-3}, vertical scale $\times 10^{-1}$. Curve D: $n = 10^{11}$ cm^{-3}, vertical scale $\times 10^{-2}$.

region bounded by $0.5 \leq \Omega \leq 3.0$ and $0 < n \leq 1.5 \times 10^{13}$ cm^{-3} are shown in Figure 2-8; more than 75 modes are present. The modes become very dense as either Ω or n are increased.

The modes are conveniently categorized by their poloidal (m), toroidal (N) and radial (l) mode numbers. Plus and minus N modes are degenerate, yielding the same solutions in equation 2.56 (this follows from the symmetry of the geometry). Plus and minus m modes, however, are not degenerate and yield different solutions. This arises physically from the anisotropy introduced by the static magnetic field: wave field patterns rotating in the direction of electron precession see a different environment from those rotating in the opposite sense. This means that the eigenfunctions of θ are necessarily complex; $\sin(m\theta)$ and $\cos(m\theta)$ functions will not satisfy the equations.

Figure 2-9a shows the solutions to the eigenvalue equation for the $m = 1$ modes; the solid lines are $l = 1$ modes while the dotted lines, occurring at higher frequencies and densities, are the $l = 2$ modes. There are no higher radial modes present within the region plotted. As the toroidal mode number increases, the frequencies and densities at which the modes occur also increase; furthermore, there are no modes which occur below the $N = 0$ mode (the mode "cutoff"), as below this mode the parallel wavenumber becomes complex. Solutions for $m = 0$ and $m = 2$ modes are shown in Figures 2-9b and 2-9c, respectively. Cutoff curves are shown in Figure 2-9d for all of the $l = 1$ modes occurring within the region; the $m = 1$ cutoff mode is the first mode encountered as either the frequency or the density is increased.

In an actual experiment, the frequency of the exciter is fixed while the density is increased from $\sim 10^{12}$ cm^{-3} to $\sim 10^{13}$ cm^{-3} through gas puffing. We then expect to see a succession of peaks in the amplitude of the wave fields in the tokamak as the density sweeps through successive eigenmode resonances. For frequencies $\Omega \lesssim 2$, for instance, the first five modes encountered as the

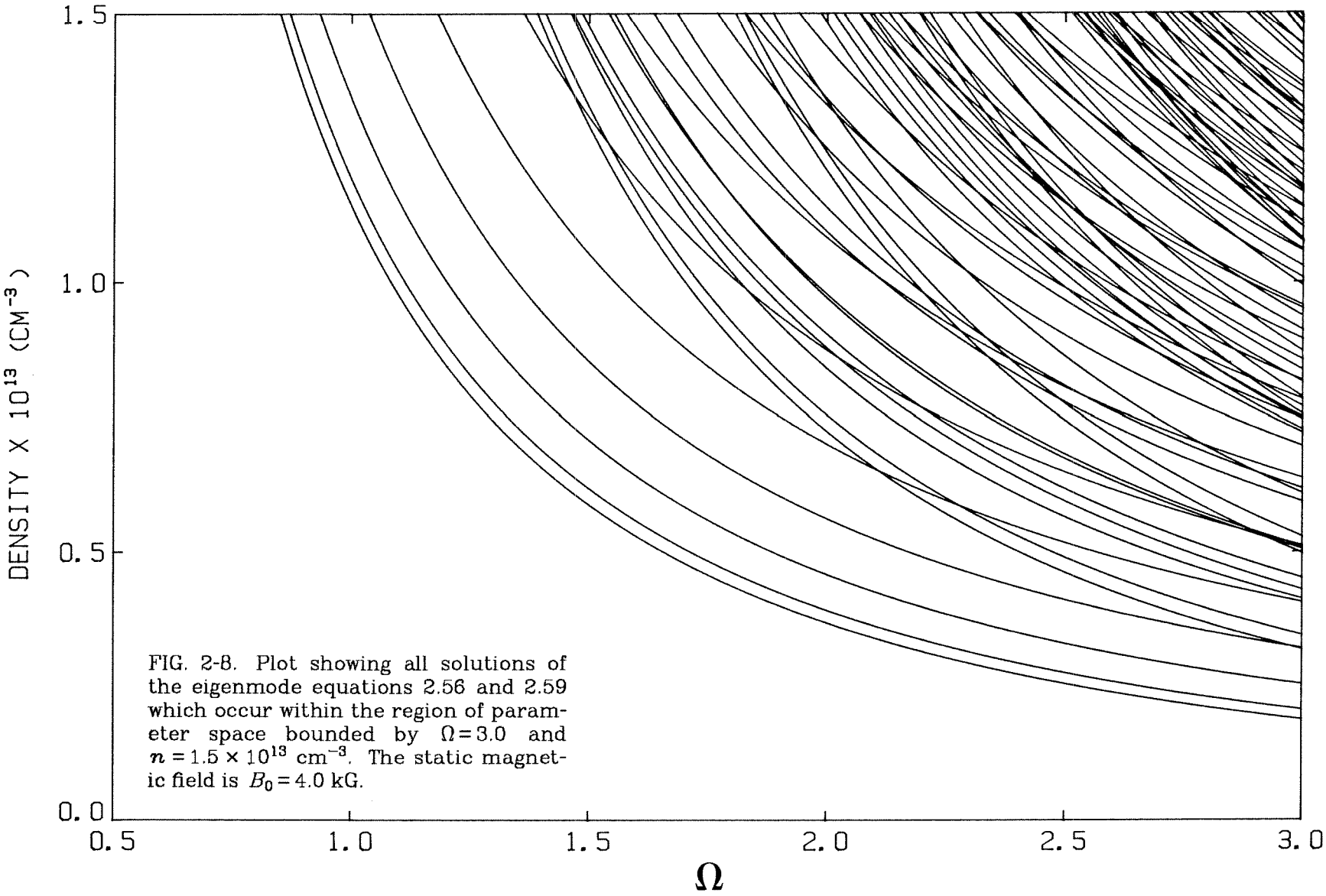

FIG. 2-8. Plot showing all solutions of the eigenmode equations 2.56 and 2.59 which occur within the region of parameter space bounded by $\Omega = 3.0$ and $n = 1.5 \times 10^{13}$ cm^{-3}. The static magnetic field is $B_0 = 4.0$ kG.

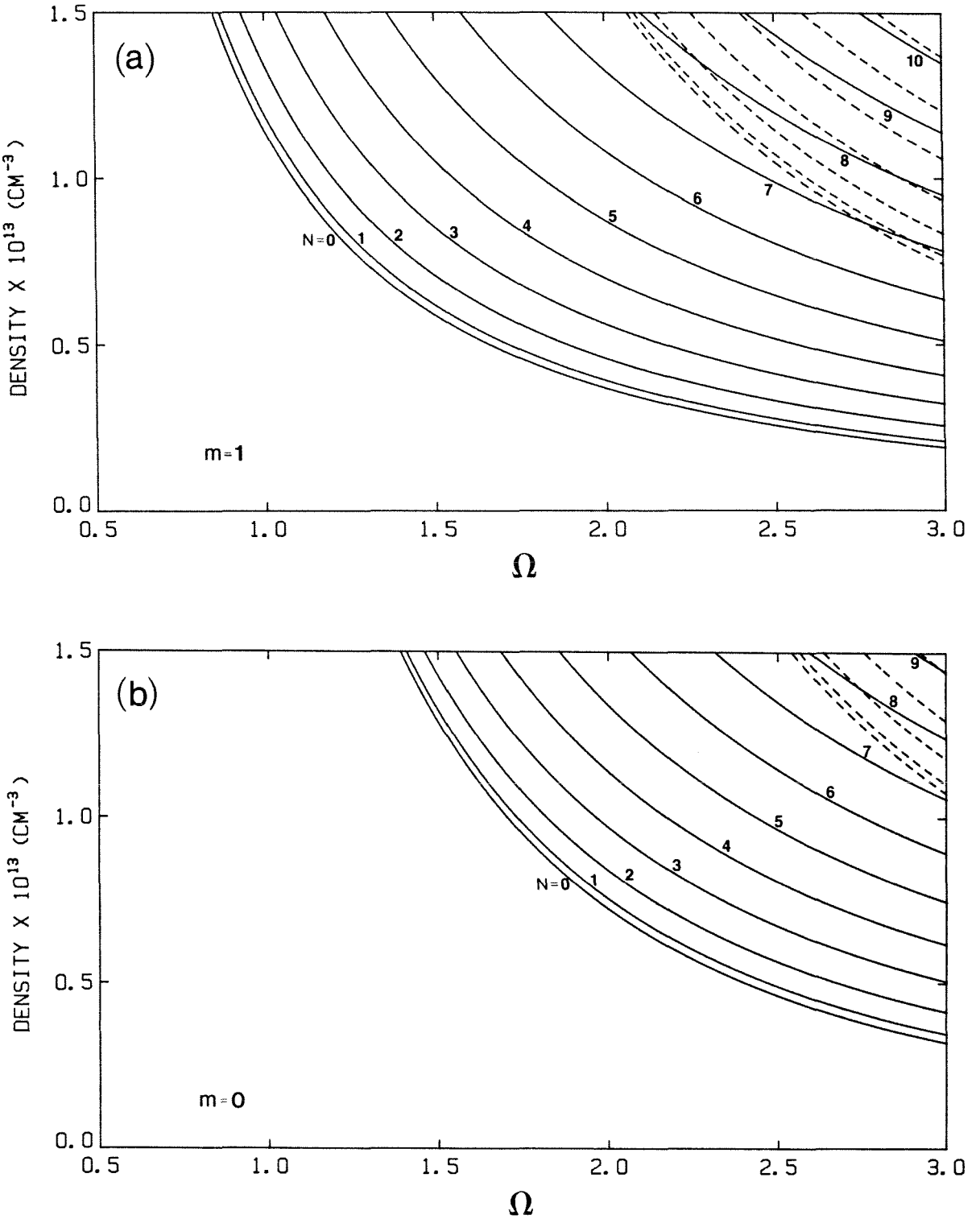

FIG. 2-9. Eigenmode curves for various modes. Solid lines are the first radial mode solutions ($l=1$) and are labeled by their toroidal mode number (N); dashed lines are the second radial modes ($l=2$). The static magnetic field is $B_0=4.0$ kG. a) Eigenmode curves for $m=1$ poloidal modes. b) Eigenmode curves for $m=0$ poloidal modes.

Note that throughout this thesis, the suffix " $\times 10^L$ " on an axis label means that the numbers labeling that axis are to be multiplied by 10^L.

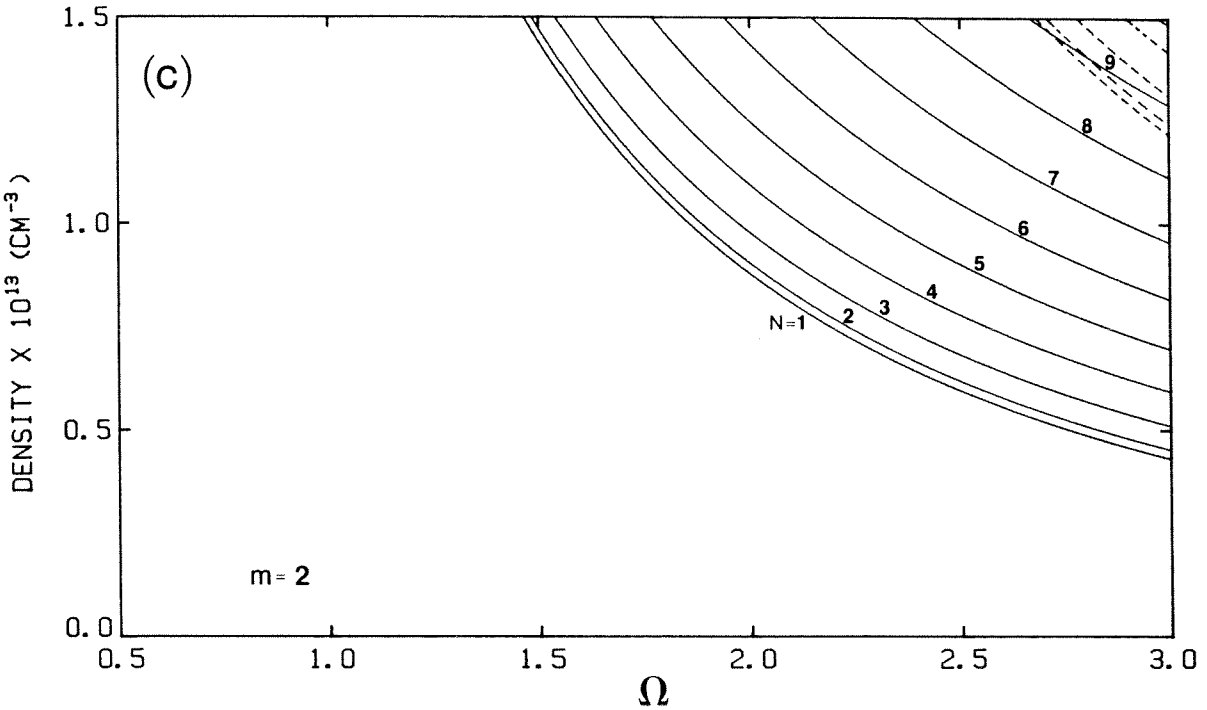

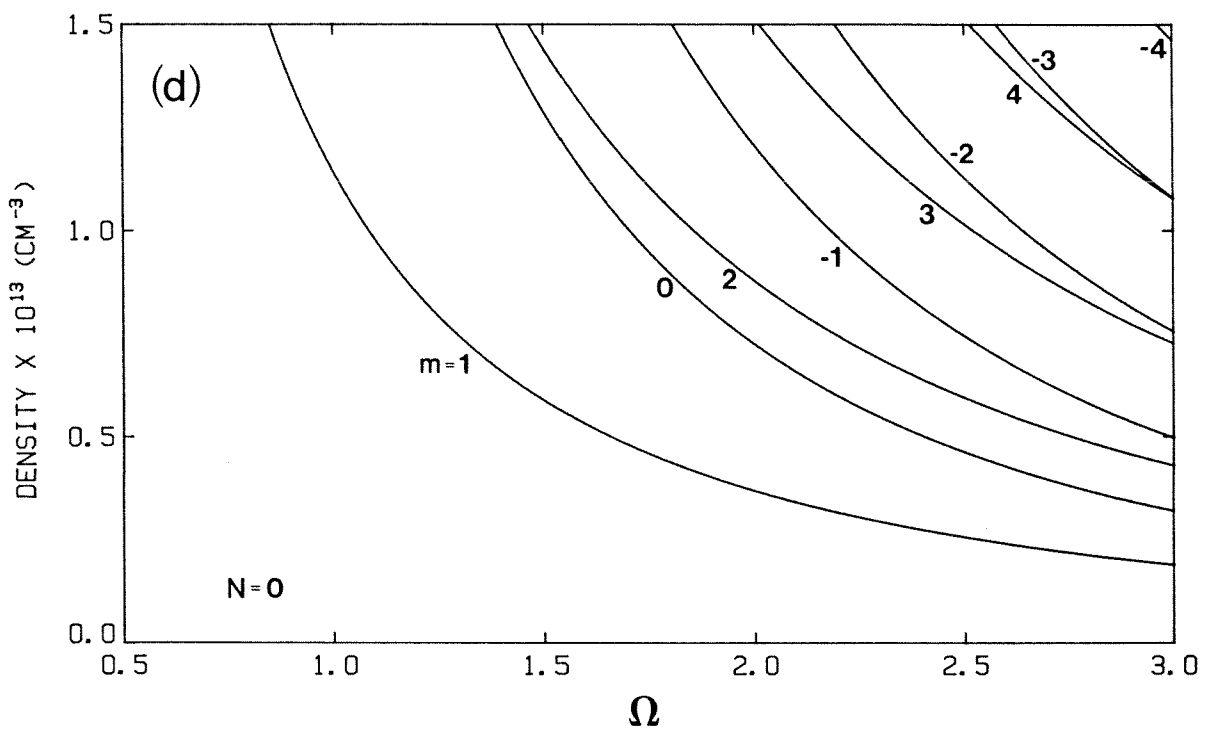

FIG. 2-9, continued. c) Eigenmode curves for $m = 2$ poloidal modes. d) Eigenmode cutoff curves ($N = 0$) for the first radial mode and for various poloidal mode numbers.

density is ramped up are all $l = 1$, $m = 1$ modes; the toroidal mode numbers are $N = 0$, 1, 2, 3, and 4.

The wave fields may be found from equations 2.43, 2.44, and 2.52 once the frequency and density have been chosen to satisfy the eigenvalue equation for a particular mode. Note that if E_z is taken to be real (by choosing α appropriately), then E_θ and B_ρ are also purely real, while E_ρ, B_z and B_θ are purely imaginary (i.e., out of phase by $\pi/2$ radians with respect to the real field components).

Another quantity of interest is the particle current $\mathbf{J}$ associated with the wave. Although the effects of the particle current have been lumped into the effective dielectric tensor, it is the particle motions that are fundamentally responsible for wave propagation. The particle current is given by $\mathbf{J} = \overleftrightarrow{\sigma} \cdot \mathbf{E}$, and the components can be written explicitly as

$$J_\rho = \frac{\omega}{4\pi}\left[i\left(1 - \varepsilon_\perp\right) E_\rho + \varepsilon_\times E_\theta\right] \tag{2.61a}$$

$$i\, J_\theta = -\frac{\omega}{4\pi}\left[i\,\varepsilon_\times E_\rho + \left(1 - \varepsilon_\perp\right) E_\theta\right] \tag{2.61b}$$

$$i\, J_z = -\frac{\omega}{4\pi}\left(1 - \varepsilon_\parallel\right) E_z \ . \tag{2.61c}$$

The radial distributions of the components of the electric field, the magnetic field, and the particle current are shown in Figure 2-10 for the $l = 1$, $m = 1$, $N = 0$, 1, 4 modes and the $l = 1$, $m = 0$, $N = 0$, 1, 4 modes. The plots are normalized so that the peak magnetic field is one gauss; the units for the plots of the electric field are volts/cm, while the current density is plotted in units of amperes/cm^2.

In all cases, B_z is the largest component of the magnetic field near the wall; for $N = 0$ modes, B_z is the only non-zero component. As the toroidal mode number increases, the ρ and z components of the magnetic field

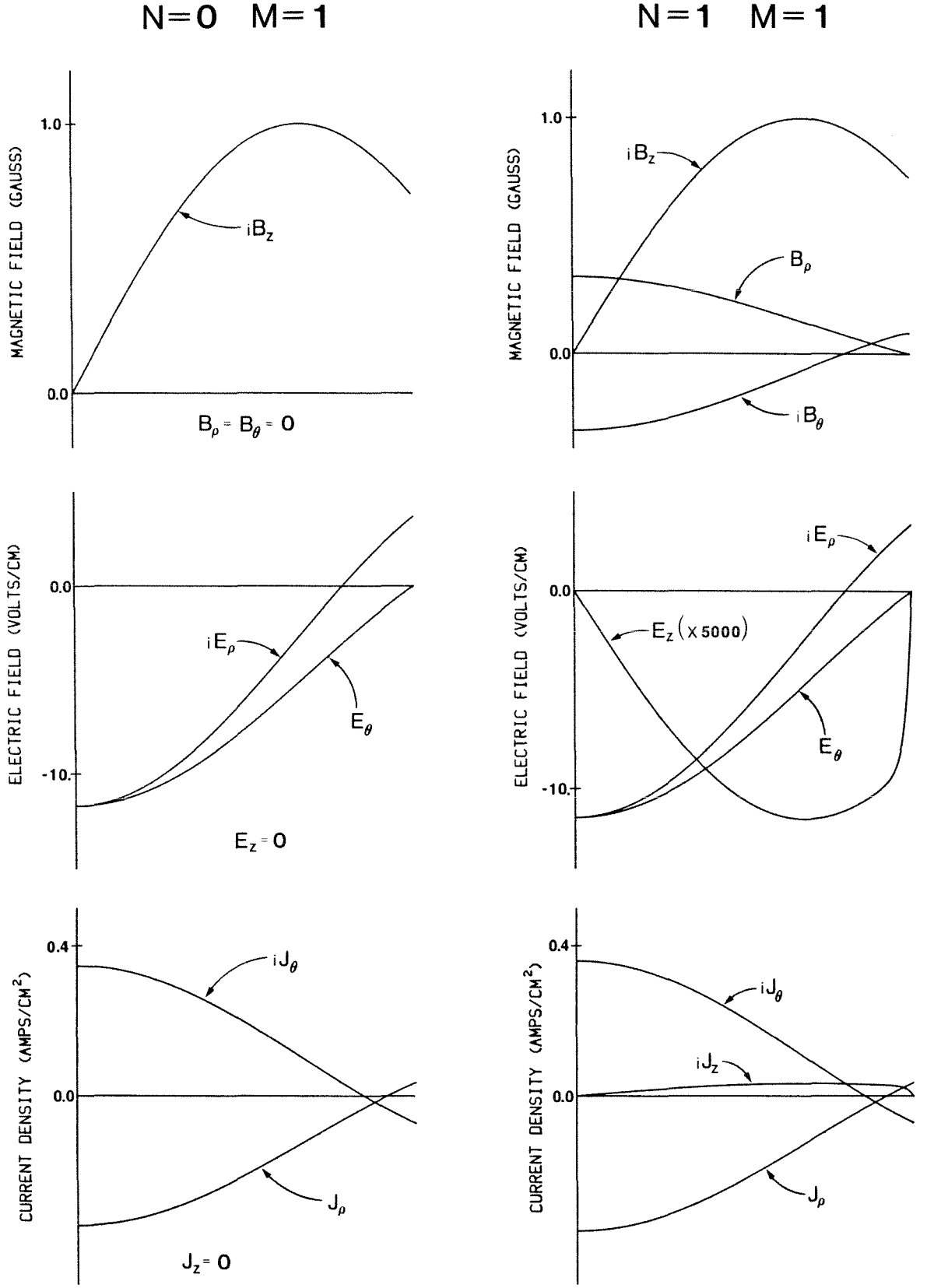

FIG. 2-10. Radial distributions of the components of the wave magnetic field (top), electric field (middle) and particle current density (bottom) for the $N=0$, $m=1$, $l=1$ mode (left-hand column) and the $N=1$, $m=1$, $l=1$ mode (right-hand column). The horizontal axis in each plot is the radius ρ; the limits are 0 (left-hand end) and ρ_0 (right-hand end). Also $\Omega=2.0$ and $B_0=4.0$ kG.

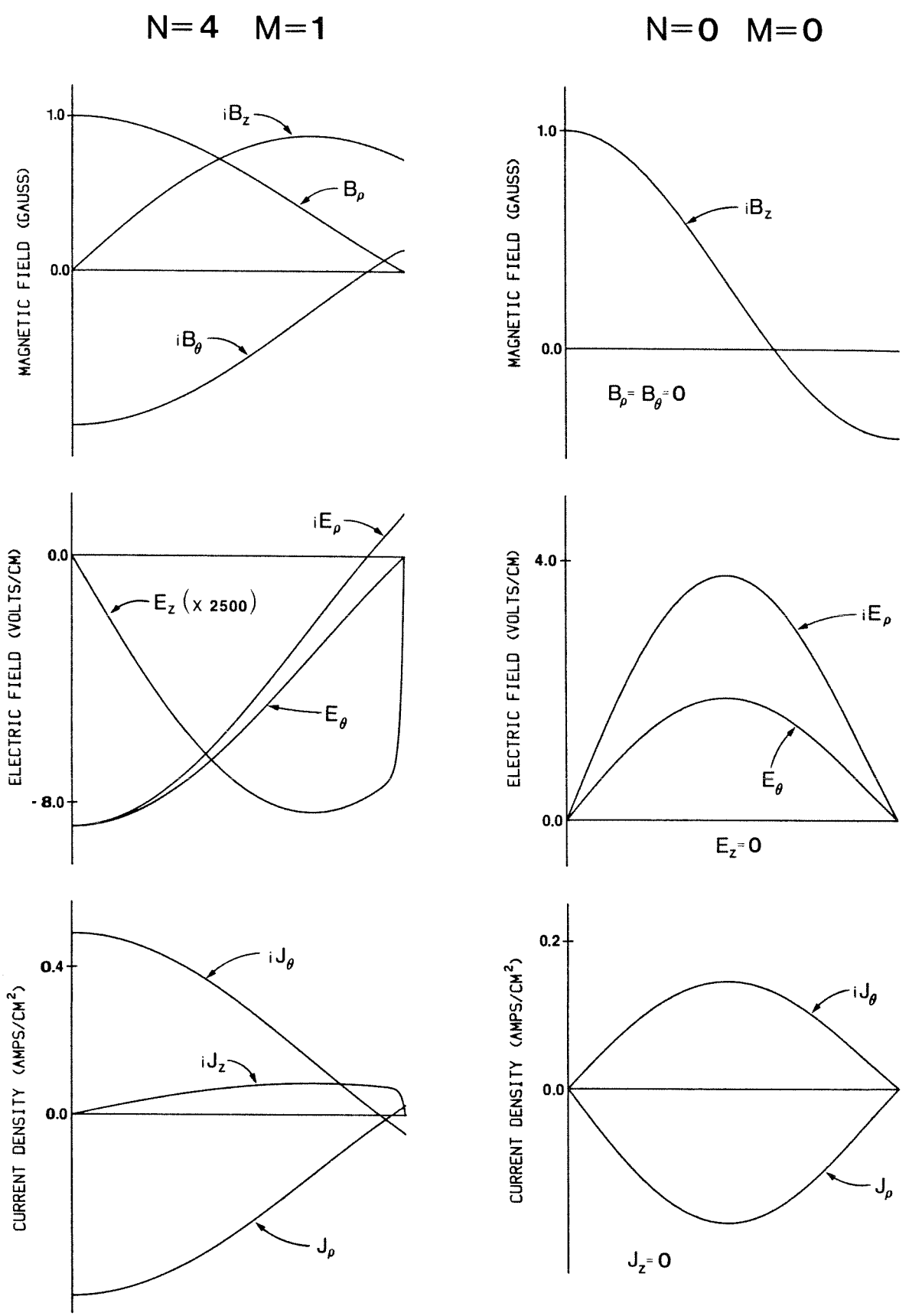

FIG. 2-10, continued. Radial distributions of the wave magnetic field, electric field, and particle current density for the $N=4$, $m=1$, $l=1$ mode (left-hand column) and the $N=0$, $m=0$, $l=1$ mode (right-hand column).

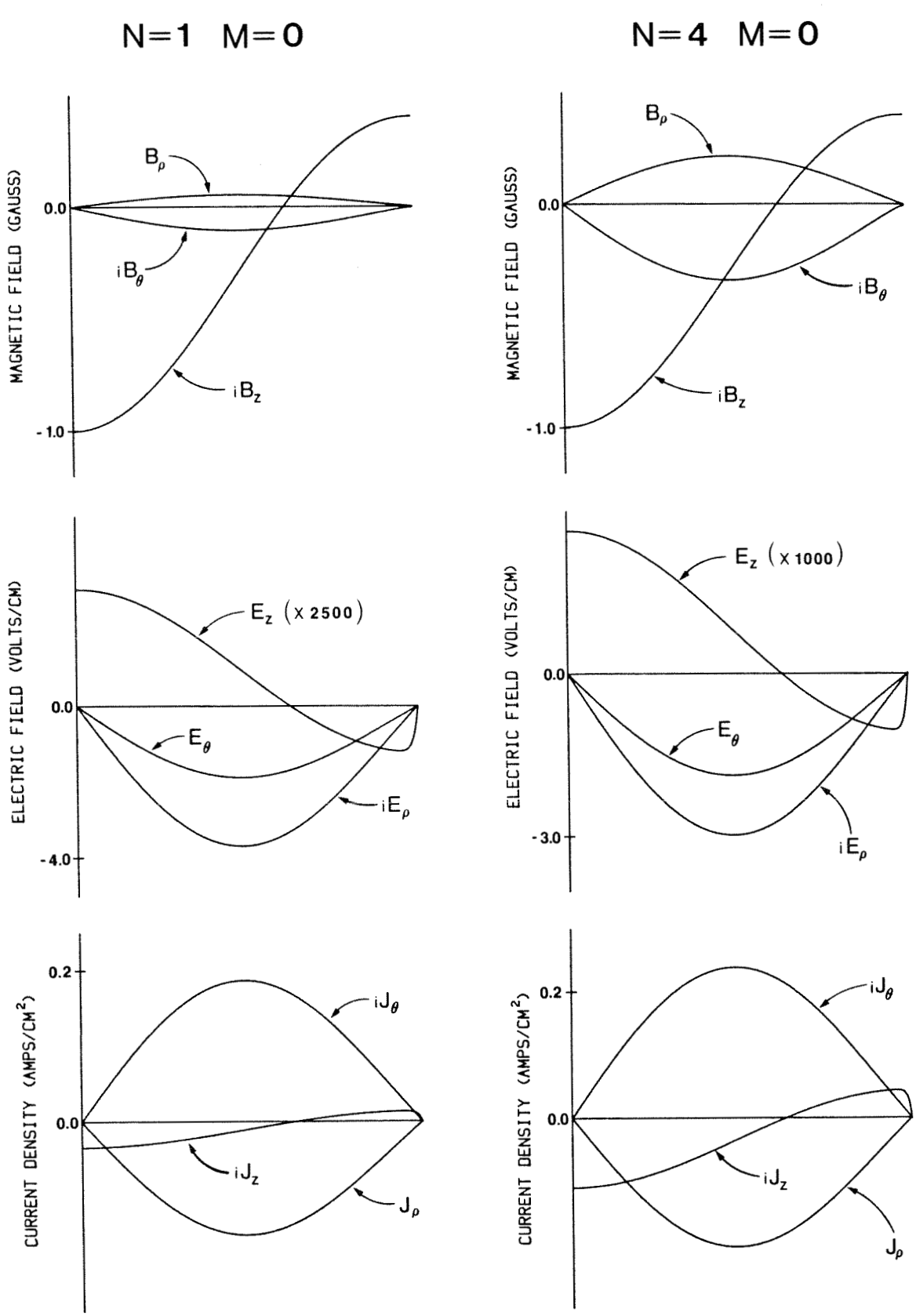

FIG. 2-10, continued. Radial distributions of the wave magnetic field, electric field, and particle current density for the $N=1$, $m=0$, $l=1$ mode (left-hand column) and the $N=4$, $m=0$, $l=1$ mode (right-hand column).

become relatively larger. For the $m=1$ modes, $B_z \to 0$ as $\rho \to 0$, while the magnitudes of B_ρ and B_θ become equal at $\rho=0$. For $m=0$ modes, B_z is finite at $\rho=0$ while B_ρ and B_θ vanish there. As is necessary to satisfy the boundary conditions, B_ρ always vanishes at the wall ($\rho=\rho_0$).

The magnitudes of E_ρ and E_θ also become equal at $\rho=0$; they vanish there for $m=0$ modes and are finite for $m\neq 0$ modes. For $N\neq 0$, E_z is non-zero although, as is evident from the plots, its amplitude is very small. The magnitude of E_z changes very abruptly near the wall; this is the due to the influence of the $I_m(|p_1|\rho)$ function. E_z and E_θ vanish at the wall, while E_ρ and E_θ vanish at $\rho=0$ for $m\neq 0$.

Although the magnitude of E_z is several thousand times smaller than the other components, the magnitude of J_z is comparable to the other components because the parallel conductivity is large. The relative size of J_z increases as the toroidal wavenumber N increases, and in some regions J_z may be the largest component of the current.

2.2.6 Zero Electron Mass Approximation

An approximation often found in the literature dealing with fast wave propagation is to set E_z equal to zero. In this section, the approximation is seen to follow from ignoring the electron mass in the wave equations.

In the limit $m_e \to 0$, the elements of the cold plasma dielectric tensor become

$$\begin{aligned}
\varepsilon_\parallel &\to -\frac{4\pi n_0 e^2}{m_e \omega^2} \to -\infty \\
\varepsilon_\perp &\to 1 - \frac{\omega_{pi}^2}{\omega^2 - \omega_{ci}^2} \equiv \varepsilon_{\perp_0} \\
\varepsilon_x &\to \left[\frac{\omega_{pi}^2}{\omega^2 - \omega_{ci}^2} + \frac{c^2}{v_A^2}\right]\frac{\omega_{ci}}{\omega} \equiv \varepsilon_{x_0},
\end{aligned} \tag{2.62}$$

hence $\varepsilon_\perp$ and $\varepsilon_\times$ remain finite while $\varepsilon_\parallel \to -\infty$. The coefficients b and f of the wave equation (2.36) also remain finite as $m_e \to 0$, but a and b are proportional to m_e^{-1}.

The radial propagation constant p_2 remains finite as $m_e \to 0$,

$$\lim_{m_e \to 0}\left(p_2^2\right) = \frac{k_0^4\left(\varepsilon_{\perp_0}^2 - \varepsilon_{\times_0}^2\right) + k_\parallel^4 - 2k_0^2 k_\parallel^2 \varepsilon_{\perp_0}}{k_0^2 \varepsilon_{\perp_0} - k_\parallel^2} \equiv p^2 , \tag{2.63}$$

while p_1 does not:

$$\lim_{m_e \to 0}\left(p_1^2\right) = \lim_{m_e \to 0}\left[\varepsilon_\parallel\left(k_0^2 - \frac{k_\parallel^2}{\varepsilon_{\perp_0}}\right)\right] \propto \frac{1}{m_e} , \tag{2.64}$$

where $\lim_{m_e \to 0}(p_1^2) < 0$ at least for $\omega_{ci} < \omega < \omega_{lh}$.

The solutions for the fields B_z and E_z are still given by equation 2.54. Noting that $\lim_{m_e \to 0}(p_1^2) = \lim_{m_e \to 0}(a)$ and that $\lim_{m_e \to 0}[J_m(p_1\rho)] = (i)^m \frac{e^{|p_1|\rho}}{\sqrt{2\pi|p_1|\rho}}$, it follows that

$$B_{z0} \equiv \lim_{m_e \to 0}\left(B_z\right) = i\gamma J_m(p\rho) \tag{2.65a}$$

and

$$E_{z0} \equiv \lim_{m_e \to 0}\left(E_z\right) = -iB_{z0} \cdot \lim_{m_e \to 0}\frac{b}{a} . \tag{2.65b}$$

Since $\lim_{m_e \to 0}\frac{b}{a} \propto \frac{1}{\varepsilon_\parallel} \propto m_e \to 0$, it follows that $E_{z0} = 0$. The above expressions are valid for $k_\parallel = 0$ as well, and $p^2 = f_0$ in that case. The other field components are obtained from equation 2.52, where it is noted that the factors in the matrix are all finite as $m_e \to 0$. The eigenmode equation (2.56) similarly reduces, as $m_e \to 0$, to

$$p\rho_0\left(k_\parallel^2 - k_0^2 \varepsilon_{\perp_0}\right) J_{m+1}(p\rho_0) = m\left[k_\parallel^2 - k_0^2\left(\varepsilon_{\perp_0} - \varepsilon_{\times_0}\right)\right] J_m(p\rho_0) , \tag{2.66}$$

which can be shown to be equivalent to the result derived by Gould [1960]. The

ρ and θ components of the particle current can be obtained from equations 2.61a and 2.61b, but the expression for the z component of the current given in 2.61c is indeterminate as $m_e \to 0$. The current in this case can be obtained more easily from the Maxwell equation:

$$J_z = \frac{c}{4\pi}\left(\nabla \times \mathbf{B}\right) \cdot \hat{\mathbf{z}}$$

$$= \frac{c}{4\pi\rho}\left(B_\theta + \rho \frac{\partial B_\theta}{\partial \rho} - im\, B_\rho\right) \qquad (2.67)$$

Numerical evaluation reveals that the zero-m_e approximation is quite accurate for most purposes. In particular, calculation of the eigenmode dispersion curves yielded the same results as the finite-m_e model within the accuracy of the numerical routine. The only significant differences in evaluating the field and current components involved E_z, J_z, and B_θ. E_z vanishes in the zero electron mass model, while the full calculation shows the actual magnitude of E_z and the form, which has a rapid transition near the wall. The current J_z calculated from the zero-m_e model also agrees with the full calculation except near the wall, where a significant difference occurs. J_z calculated from the finite-m_e model goes to zero at the wall, while the zero-m_e model yields a finite value there. An example for $\Omega = 2$ is shown in Figure 2-11a. The B_θ components calculated from the two models agree well except in a small region near the wall (Figure 2-11b); even there the difference is small.

2.3 Wave Damping

2.3.1 Introduction

The wave model discussed thus far includes no mechanism for energy dissipation and thus allows waves excited at a toroidal resonance to have unbounded amplitude. In fact, energy can be absorbed within the plasma by

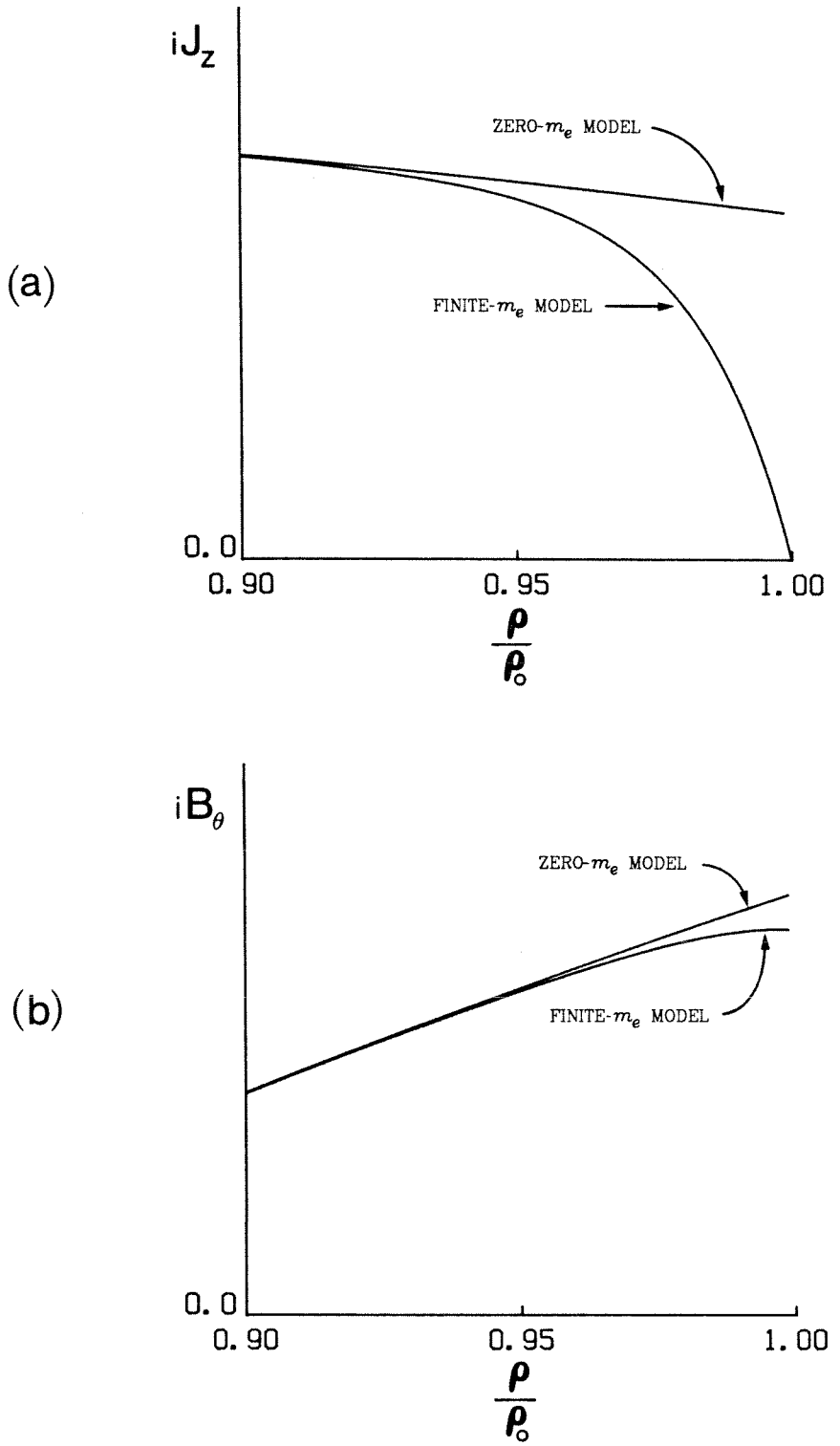

FIG. 2-11. Comparison of the zero-m_e and finite-m_e models applied to the calculation of a) j_z, and b) B_θ. This example is for an $N=1$, $m=1$, $l=1$ mode; $\Omega=2.0$ and $B_0=4.0$ kG.

both collisional and collisionless processes, and in the bounding structure which surrounds the plasma. Both the calculated and the observed damping are small in the experiments described in this thesis in the sense that a wave can propagate many times around the tokamak before losing an appreciable fraction of its energy; hence the concept of a toroidal eigenmode is still appropriate.

Energy dissipation in a weakly damped resonant cavity is often discussed in terms of the cavity "Q", defined as the time-averaged stored energy associated with the wave divided by the energy dissipated in one wave period. The Q of each toroidal eigenmode can be estimated experimentally by observing the width of the resonance in the wave field amplitude as the density increase sweeps through successive modes (see Chapter 7). Another approach is to consider the attenuation that a wave would undergo if it propagated from its point of excitation down an infinitely long cylinder, experiencing constant absorption per unit length. The wave fields would then decay as $e^{-\frac{z}{L_D}}$, where z is the distance along the cylinder axis and L_D is defined as the characteristic damping length. In the actual tokamak geometry, a useful model is to view the antenna as exciting waves which propagate toroidally in both directions [Stix, 1975]. Since the damping length is *not* small compared to the circumference of the tokamak, the waves interfere with each other and the wave amplitude at a given point is an infinite sum with contributions from each pass of the wave around the torus. In this view, the toroidal eigenmode resonances arise from the constructive interference which occurs when some integral multiple of the wavelength in the toroidal direction (which depends, of course, on the plasma density) becomes equal to the circumference of the torus. As pointed out by Takahashi [1979], the damping length L_D for a mode can be estimated experimentally from measurements of the wave field amplitude at a resonance and at an adjacent anti-resonance (see Chapter 7).

The cavity Q and the damping length, L_D, are both measures of the wave absorption, and are related [Takahashi, 1977] by the parallel (i.e., toroidal) group velocity of the wave:

$$L_D = \frac{2\,Q\,v_{g\parallel}}{\omega} \tag{2.68}$$

The group velocity, $v_{g\parallel}$, can be independently measured by a wave-packet technique which is also described in Chapter 7.

In the following sections, a variety of well-known damping mechanisms are briefly described, and expected cavity Qs are calculated for each for parameters appropriate to the Caltech Research Tokamak.

2.3.2 Cyclotron Damping

The perpendicular component of the orbit of an ion in a magnetic field consists, to first order, of simple Larmor precession at the cyclotron frequency, and it is natural to try to couple wave energy to this motion. If a circularly polarized electric field were imposed which rotated in the same sense and with the same frequency and phase as the ion motion, the ion would feel a constant acceleration and energy would be transferred from the wave to the particle. The velocity of the ion would increase linearly with time, and the ion Larmor radius would similarly increase until it suffered a collision either with another particle or with the vacuum chamber wall.

A prescribed electric field cannot, however, be simply imposed in the plasma volume. Rather, sources at the plasma edge excite waves which then propagate through the plasma according to the wave equations discussed earlier. Below the ion cyclotron frequency, both the slow and fast waves propagate. The slow wave has a resonance ($|\mathbf{k}|^2 \to \infty$) at ω_{ci} and does not propagate ($|\mathbf{k}|^2 < 0$) immediately above ω_{ci}; the fast wave propagates above and below ω_{ci} and is unaffected by the fundamental cyclotron resonance.

Absorption of the slow wave at the fundamental cyclotron resonance was used for heating in early stellerator experiments [Stix, 1960]. The waves were launched in a region of high magnetic field ($\omega < \omega_{ci}$) and propagated into a "magnetic beach" of lower field where a cyclotron resonant layer ($\omega = \omega_{ci}$) was present at which the wave was damped. In a tokamak geometry, however, the static magnetic field gradient is perpendicular to the static magnetic field direction, and the cyclotron resonance surface is a cylinder of constant radius. To take advantage of the fundamental resonance, the slow wave would probably have to be launched from the high field side of the torus, i.e., from the inside. Calculations suggest, however, that the slow wave does not propagate to the plasma core but is absorbed earlier in the plasma periphery by electron Landau damping [Klima, 1975; Colestock, 1983].

The fast wave, on the other hand, penetrates the plasma easily. Cold plasma theory predicts that the wave is completely right-hand circularly polarized at $\omega = \omega_{ci}$, the electric field vector rotating in the sense opposite to that of the ion precession. Hence, this simplest picture predicts no absorption of the fast wave at the fundamental cyclotron resonance. Hot plasma effects, however, prevent the wave from becoming completely right-hand polarized at $\omega = \omega_{ci}$, and the small left-hand component can then contribute to wave damping.

Calculation of the cyclotron damping in a tokamak configuration is complicated by several factors. The resonance surface is a cylinder of constant radius, and ions following the helical static magnetic field lines can pass through the resonant region at most twice during each poloidal revolution. If the wave field has a toroidal variation ($k_{\parallel} \neq 0$) then the resonance layer has effectively a finite width due to the velocity distribution of the ions and the variation of ω_{ci} with major radius. Taking into account the Doppler shift, an ion with a parallel (i.e., toroidal) velocity $v_{\parallel}$ experiences the fundamental

resonance layer when the condition $\omega - k_{\|} v_{\|} = \omega_{ci}$ is satisfied, where ω is the excitation frequency. For a toroidal magnetic field which varies as $1/R$ and a Maxwellian ion velocity distribution, the effective width of the resonant layer is given by

$$\Delta W = 2 \frac{k_{\|} v_{ti}}{\omega} R \,, \tag{2.69}$$

where $v_{ti} = \left(\frac{2 k_B T_i}{m_i} \right)^{\frac{1}{2}}$ is the ion thermal velocity. On each pass through the resonance layer, an ion (j) receives a "kick" $\Delta v_{\perp j}$ in its perpendicular velocity. Because the *phase* of the ion Larmor precession as it approaches the resonance region is assumed to be randomly distributed with respect to the phase of the wave field, the distribution of $\Delta v_{\perp j}$ is symmetric about zero: the ion perpendicular velocity is as likely to be increased after passing through the resonance zone as it is to be decreased. Net energy is still transferred to the ion population, however, since the average energy increment is given by $\langle \Delta E_j \rangle = \frac{1}{2} m_i \langle (\Delta v_{\perp j})^2 \rangle$, which is positive.

A simple calculation of fast wave cyclotron damping in tokamak geometry is given by Stix [1975], who averages over randomly-distributed initial orbit phases and assumes that collisions randomize the orbit phases between successive passes through the resonance zone. The analysis also assumes that the wave electric field (calculated from cold plasma theory) is constant along and across the resonance surface, that the parallel wavenumber is small enough that $v_{ph\|} = \frac{\omega}{k_{\|}} \gg v_A$, and that the cyclotron resonance layer passes through the center of the plasma. The result for the cavity Q is

$$Q_{\omega_{ci}} = \frac{\rho_0}{R} \frac{\omega_{ci}}{k_{\|}^2} \frac{\pi m_i}{2 k_B T_i} \,, \tag{2.70}$$

where k_B is Boltzmann's constant and T_i is the ion temperature; a similar

result was also obtained by Perkins [1972]. The Qs predicted from equation 2.70 are plotted in Figure 2-12 for the $N=1-5$, $m=1$, $l=1$ modes, as functions of the ion temperature. Note that the Q decreases with increasing ion temperature and also with increasing $k_{\parallel}$. The cyclotron frequency on axis was taken to be 8 MHz for this calculation, which corresponds to the lowest frequency used in the experiments described in Chapters 6 and 7. This implies that the static toroidal magnetic field on axis is 5.3 kG, which is nearly the upper limit to the field which can be obtained in the Caltech tokamak. For most of the wave propagation and coupling experiments, the excitation frequency was high enough that the fundamental cyclotron layer was not inside the tokamak vessel and fundamental absorption was not important.

Absorption can also take place at harmonics of the fundamental cyclotron frequency where the fast wave electric field has a finite left-hand component, even in cold plasma theory. This mechanism requires both a finite Larmor radius (i.e., non-zero temperature) and a spatial gradient in the wave field. Consider an ion precessing at frequency ω_{ci} in a magnetic field. If a uniform left-hand circularly polarized electric field at frequency $2\omega_{ci}$ were imposed, the ion would be accelerated during one half of its orbit and decelerated equally during the other half; the time-averaged energy change would be zero. If, however, the magnitude of the electric field had a gradient in the direction perpendicular to the static magnetic field, so that its magnitude varied over the orbit of the ion, then the acceleration and deceleration during the orbit would be unequal and a net transfer of energy from the wave to the ion could take place. The wave damping in this simple model is proportional to $\rho_L^2 \left| \nabla_\perp | \mathbf{E}_L | \right|^2$, where ρ_L is the Larmor radius and $\mathbf{E}_L$ is the left-hand component of the electric field, so harmonic damping favors high temperatures (large Larmor radii) and fields which vary rapidly in the transverse direction [Takahashi, 1977].

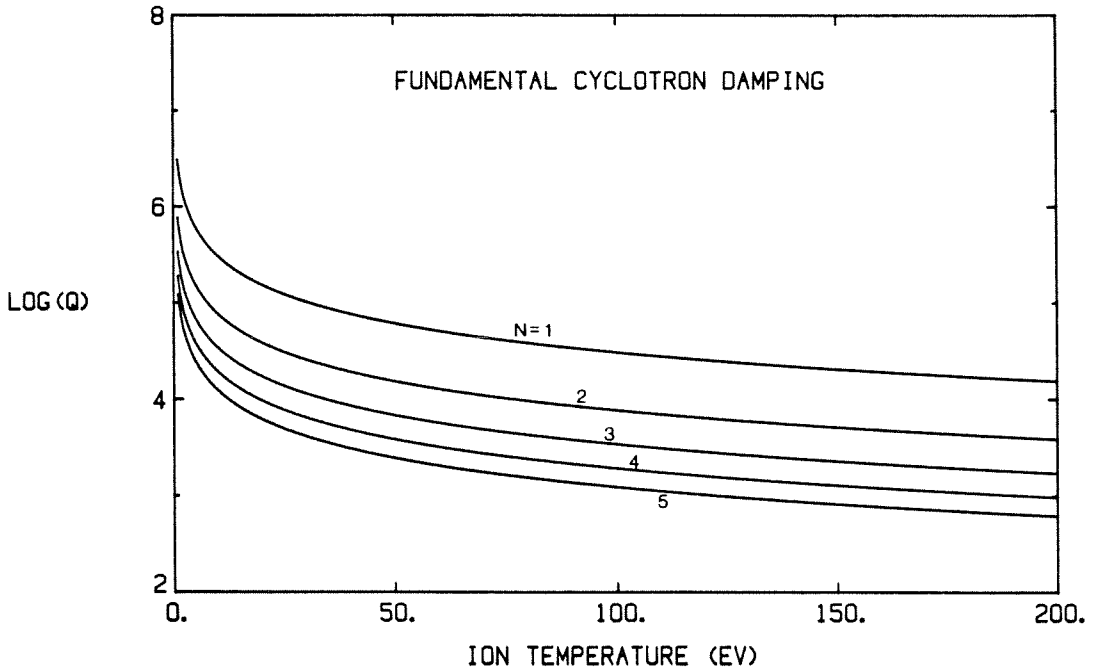

FIG. 2-12. Plots of the Qs of the $N=1-5$, $m=1$, $l=1$ toroidal eigenmodes, as functions of the ion temperature, for fundamental cyclotron damping. Here $\omega/2\pi=8$ MHz, $B_0=5.26$ kG, and the ion cyclotron resonance layer passes through the center of the plasma.

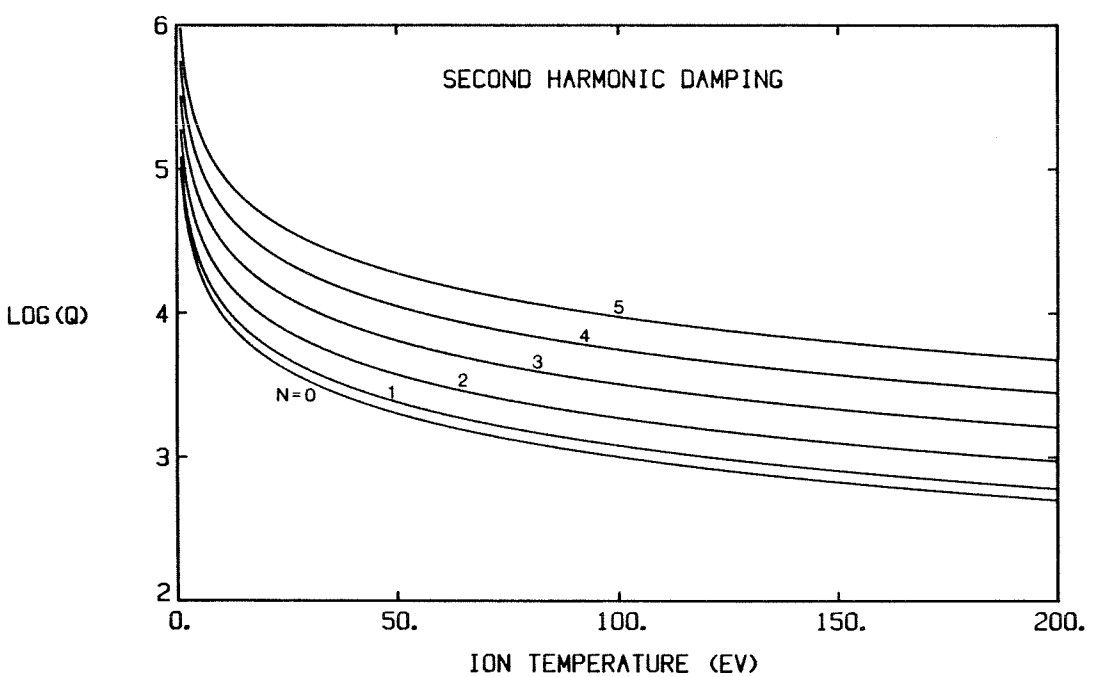

FIG. 2-13. Plots of the Qs of the $N=0-5$, $m=1$, $l=1$ toroidal eigenmodes, as functions of the ion temperature, for second-harmonic cyclotron damping. Here $\omega/2\pi=12$ MHz, $B_0=3.95$ kG, and the second-harmonic resonance layer passes through the center of the plasma.

An analysis of fast wave second-harmonic cyclotron damping in tokamak geometry is also given by Stix [1975] and uses the same approximations made for the fundamental damping calculation. The result for the cavity Q, assuming that the resonance layer is at the center of the plasma, is simply

$$Q_{2\omega_{ci}} = \frac{2\varepsilon}{\beta_{i\perp}} \tag{2.71}$$

where $\varepsilon \equiv \rho_0 / R$ is the inverse aspect ratio, and $\beta_{i\perp} \equiv B_0^2 / (8\pi n_i k_B T_{i\perp})$ is the perpendicular ion beta.

A more detailed calculation by Paoloni [1975a] includes the form of the toroidal eigenmode wave fields (using the model described in section 2.2.6) and does not restrict $k_\parallel$. The result, assuming again that the second-harmonic resonance layer passes through the center of the plasma column, is

$$Q_{2\omega_{ci}} = \frac{2\sqrt{\pi}}{\lambda_i} \left[\frac{p\,c}{2\,\omega_{pi}}\right]^2 \left[\frac{\rho_0}{R}\right] \frac{\left[\frac{1}{2p^2}\left[\left(\frac{k_A}{3}\right)^2 + k_\parallel^2\right](D+1)^2 + 1\right]}{(D-1)^2}, \tag{2.72}$$

where $\lambda_i = \frac{1}{2}(p\,\rho_L)^2$, $k_A = \frac{2\omega_{ci}}{v_A}$, $D = 2\frac{k_\parallel^2 + p^2}{k_A^2 - k_\parallel^2}$, and p is the radial wavenumber defined by equation 2.63. The Qs calculated from the above formula are plotted for several low order eigenmodes, as functions of the ion temperature, in Figure 2-13. Note that the Q decreases with ion temperature but increases with $k_\parallel$.

2.3.3 Landau Damping and TTMP

When there exists a population of particles in the plasma with thermal velocities parallel to the static magnetic field comparable to the parallel wave phase velocity, the wave can transfer energy to the particles via Landau damping [Stix, 1962]. For toroidal eigenmodes, the wave phase velocity is simply $v_{ph\parallel} = \frac{\omega}{k_\parallel} = \frac{\omega R}{N}$, and its amplitude decreases for successive toroidal modes.

For an $N=4$ mode, for example, at a frequency of 12 MHz, the phase velocity is $v_{ph\parallel} = 8.5\times10^8$ cm/sec. For a plasma in thermal equilibrium at a temperature of 100 eV, the electron thermal velocity is $v_{te} = 4.2\times10^8$ cm/sec, while the ion velocity is $v_{ti} = 9.8\times10^6$ cm/sec. Because the expression for the power absorbed due to Landau damping involves terms proportional to $e^{-\left[\frac{v_{ph\parallel}}{v_{t\alpha}}\right]^2}$, where $v_{t\alpha}$ is the electron or ion thermal velocity and a Maxwellian distribution is assumed, the damping by the ions is negligible compared to that due to the electrons. Further, the electron Landau damping decreases as the toroidal mode number decreases (because of the consequential increase in $v_{ph\parallel}$).

An analogous damping process for an electromagnetic wave propagating parallel to the static magnetic field is transit-time magnetic pumping (TTMP). Whereas the mechanism of Landau damping involves the interaction between the parallel component of the wave electric field and the electric charge of the particles ($\mathbf{F}=q\mathbf{E}_\parallel$), damping due to TTMP involves the interaction between the effective magnetic moment of the particle (due to its gyro-orbit) and a gradient in the wave magnetic field amplitude ($\mathbf{F}=-\mu\cdot\nabla\mathbf{B}$). Stix [1975] has shown that TTMP and electron Landau damping are coherent processes and must be calculated together; the result is that the net damping is equal to half of that due to TTMP alone. Paoloni [1975a] has calculated the expected toroidal eigenmode Q due to these processes, and finds

$$Q_{EL+TTMP} = \frac{1}{4\sqrt{\pi}}\frac{c^2}{v_{ph\parallel}v_{te}}\left(\frac{\omega_{ce}}{\omega_{pe}}\right)^2 e^{\left[\frac{v_{ph\parallel}}{v_{te}}\right]^2}\left[\frac{1}{2p^2}\left(\frac{k_A^2}{(\Omega+1)^2}+k_\parallel^2\right)(D+1)^2+1\right], \quad (2.73)$$

where $\Omega\equiv\omega/\omega_{ci}$. The Qs calculated for toroidal modes appropriate to the Caltech experiments are plotted as functions of electron temperature in Figure 2-14. The Qs decrease as the electron temperature increases (since there are then more particles with thermal velocity near $v_{ph\parallel}$) and also decrease as the

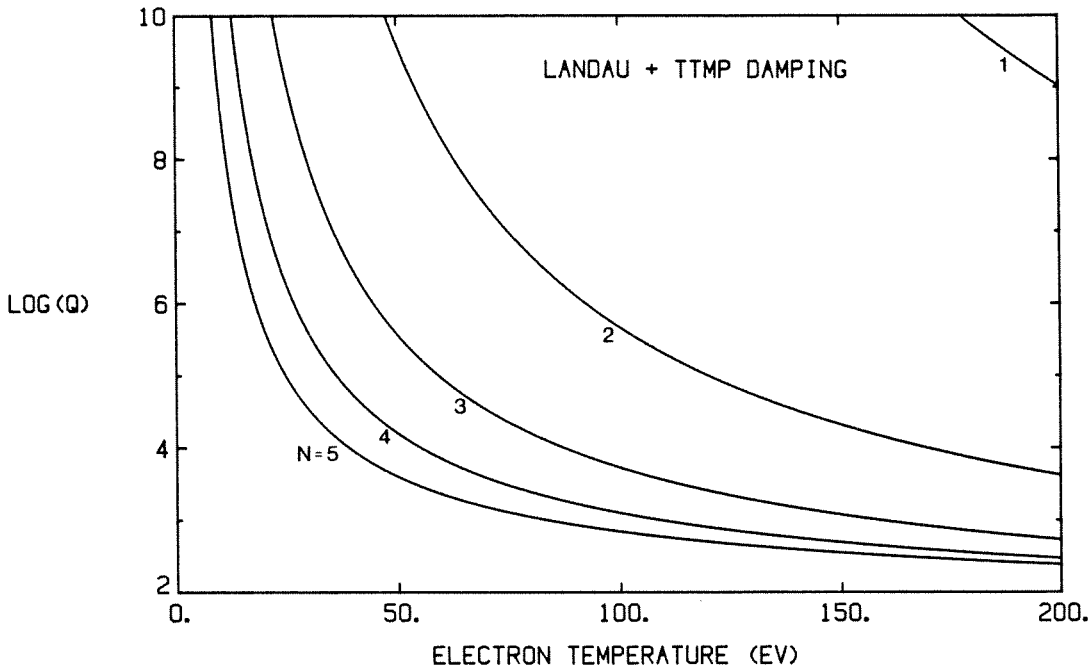

FIG. 2-14. Plots of the Qs of the $N=1-5$, $m=1$, $l=1$ toroidal eigenmodes, as functions of the electron temperature, for electron Landau damping and TTMP. Note that $Q=\infty$ for the $N=0$ mode. Here $\omega/2\pi=12$ MHz and $B_0=3.95$ kG.

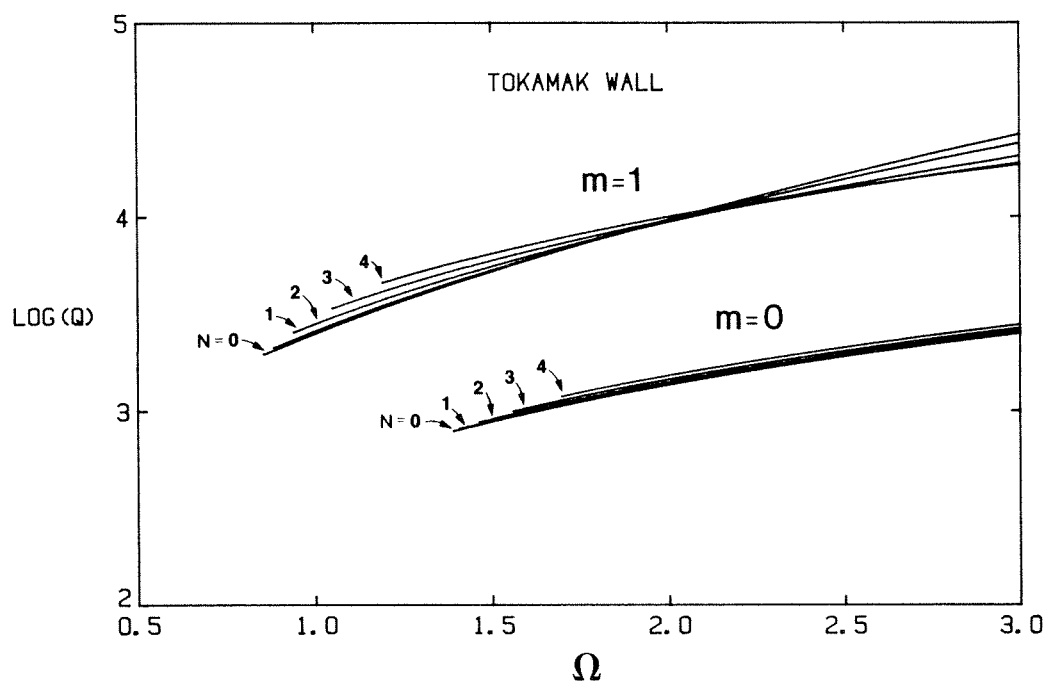

FIG. 2-15. Plots of the Qs of the $N=0-4$, $m=0, 1$, $l=1$ toroidal eigenmodes, as functions of Ω, for resistive wall damping. $B_0=3.95$ kG.

toroidal mode number (and hence $k_{\|}$) increases. The Q for the $N=0$ (cutoff) mode is infinite, since the parallel phase velocity is infinite and there is then no Landau damping.

2.3.4 Resistive Wall Damping

Wave damping can also occur due to ohmic losses in the conducting boundary surrounding the plasma. The wave model described earlier in this chapter assumed that the conductivity of the boundary was infinite, so that the RF fields vanish inside the wall. This requires that the tangential magnetic fields (B_z, B_θ) at the inner wall of the cylinder be balanced by surface currents flowing on the wall:

$$\mathbf{j}_s = -\frac{c}{4\pi}\hat{\rho}\times\mathbf{B}_t \ , \tag{2.74}$$

where $\mathbf{j}_s$ is the surface current, $\hat{\rho}$ is a unit vector in the radial direction, and $\mathbf{B}_t$ is the tangential component of the magnetic field at the surface of the conductor. In actuality, the conductivity of the tokamak vacuum vessel is finite, and the surface currents flow largely in a layer of thickness δ:

$$\mathbf{j}_s(\xi) = \mathbf{j}_{s0}\, e^{-\frac{\xi}{\delta}(1-i)} \ , \tag{2.75}$$

where ξ is the perpendicular distance into the conductor, measured from the surface, and δ, called the skin depth, is defined by $\delta = (\sigma\mu\omega)^{-\frac{1}{2}}$, where σ and μ are the conductivity and permeability of the conductor, respectively. Then the total power lost in the conductor, per unit surface area, is given by

$$P = \frac{1}{2\sigma} j_{s0}^2 \int_0^\infty e^{-2\frac{\xi}{\delta}}\, d\xi = \frac{1}{4} j_{s0}^2 \frac{\delta}{\sigma} \ , \tag{2.76}$$

where $j_{s0} = |\mathbf{j}_{s0}|$, while the total current flowing in the conductor, per unit length perpendicular to the direction of current flow, is

$$j_{tot} = \left| \int_0^\infty j_{s0} e^{-\frac{\pi}{\delta}(1-i)} d\xi \right| = \frac{\delta}{\sqrt{2}} j_{s0} . \tag{2.77}$$

Hence the power lost in the conducting wall, per unit area, is

$$P_{wall} = \frac{1}{2} j_{tot}^2 \frac{1}{\sigma\delta} \tag{2.78}$$

and it is apparent that $R_s \equiv \frac{1}{\sigma\delta}$ can be viewed as the effective surface resistance of the conducting boundary. Note that the surface resistance of stainless steel (of which the tokamak wall is made) at a frequency of 12 MHz is $R_s = 5.2 \times 10^{-3}$ Ω/square (mks units).

In calculating the power dissipated in the boundary, the usual approach [Jackson, 1962] is to assume that the fields in the plasma are, to first order, unchanged by the finite resistivity of the wall. The total currents flowing in the wall are then calculated from the tangential components of the wave magnetic field at the boundary, and the distribution of current in the metal is assumed to obey equation 2.75. The net power lost is then found by integrating equation 2.78 over the entire boundary surface. For tokamak geometry, the result is

$$P_{wall} = \frac{1}{2} R \rho_0 \frac{R_s c^2}{4} \left(|B_\theta(\rho_0)|^2 + |B_z(\rho_0)|^2 \right) . \tag{2.79}$$

In order to calculate the cavity Q for an eigenmode, the total stored energy associated with the wave, E_{tot}, is needed. This is obtained by integrating the expressions for the wave electric, magnetic, and kinetic energy densities (equations 2.20 - 2.22) over the plasma volume, using the field distributions appropriate for a particular eigenmode; the Q is then given by $Q_{wall} = \frac{2\pi}{\omega} \frac{E_{tot}}{P_{wall}}$. Calculated Qs for various eigenmodes appropriate to the Caltech tokamak are shown in Figure 2-15 as functions of Ω. Note that the dependence of the Q on the toroidal mode number (i.e., $k_\parallel$) is relatively small,

particularly near $\Omega = 2$.

2.3.5 Insulating Gap Damping

The tokamak must have an insulating gap at a particular toroidal location in order to prevent shorting out the electric field induced by the ohmic heating transformer (see Chapter 3). In the Caltech tokamak, this gap consists of an insulating spacer sandwiched between two stainless steel flanges welded to the vacuum vessel. The gap represents a perturbation to the boundary conditions of the wave-propagation problem and has apparently not been included in any theoretical models thus far. Besides potentially altering the wave fields within the plasma, the gap presents an additional mechanism for energy dissipation, viz., through dielectric losses. The insulating spacer on many tokamaks is made of alumina, but the Caltech tokamak utilizes Bakelite (phenol-formaldehyde). The dissipation factor (the reciprocal of the Q of the material, sometimes called the loss tangent) for Bakelite is relatively high: $D \approx 0.03$ at a frequency of 10 MHz (the value can change somewhat with ambient humidity).

The insulating spacer and the two adjacent flanges form a capacitor whose value is $C_G = 850$ pF in the Caltech tokamak. Surface currents induced on the inside of the tokamak wall due to the RF fields can flow through the spacer as displacement current, giving rise to dielectric losses; some of the current may also flow out the gap and around the outside of the tokamak vessel, causing energy loss through radiation. Only the former mechanism is considered here.

As an estimate of an upper bound of the energy loss in the insulating gap, we make the approximation that all of the current flowing in the toroidal direction on the inner wall flows through the gap as displacement current. The surface current is calculated, as before, from the periodic cylinder model, and the power dissipated in the dielectric is then

$$P_G = \frac{1}{2}|I_z|^2 R_G \,, \tag{2.80}$$

where I_z is the net current traversing the gap,

$$I_z = \int_0^{2\pi} \left| \mathbf{j}_s \cdot \hat{\mathbf{z}} \right| d\theta \,, \tag{2.81}$$

and $R_G \equiv \frac{D}{\omega C_G}$ is the effective resistance of the gap. The stored energy associated with the wave is calculated as described in section 2.3.4; the energy stored in the electric field in the dielectric gap is found to be small in comparison and is neglected.

The Qs for various eigenmodes resulting from dissipation in the gap are plotted as functions of Ω in Figure 2-16. Note that $m=0$ as well as $N=0$ modes have no component of B_θ, hence there is no z-component of surface current and no energy loss in the dielectric; these modes have infinite Q. The Qs of the $m=1$ modes decrease as N (or $k_\parallel$) increases; this is a result of the relative increase of B_θ as compared to B_z, at the plasma edge, as N is increased (cf. Figure 2-10). An increase in $B_\theta(\rho_0)$ causes an increase in j_{sz} which results in more current passing through the dielectric gap and more energy dissipation.

2.3.6 Collisional Damping

Wave energy can also be damped by collisions between particles in the plasma. Ohmic or joule damping arises from collisions between electrons and ions, described by "Spitzer resistivity" [Spitzer, 1962], while collisions with neutral particles can also lead to wave damping [Frank-Kamenetskii, 1960].

Paoloni [1975a] calculates the wave damping due to electron-ion collisions for the fast wave in a cylindrical geometry. Only fluid motion along the static magnetic field is considered, and E_z is approximated from the Maxwell equa-

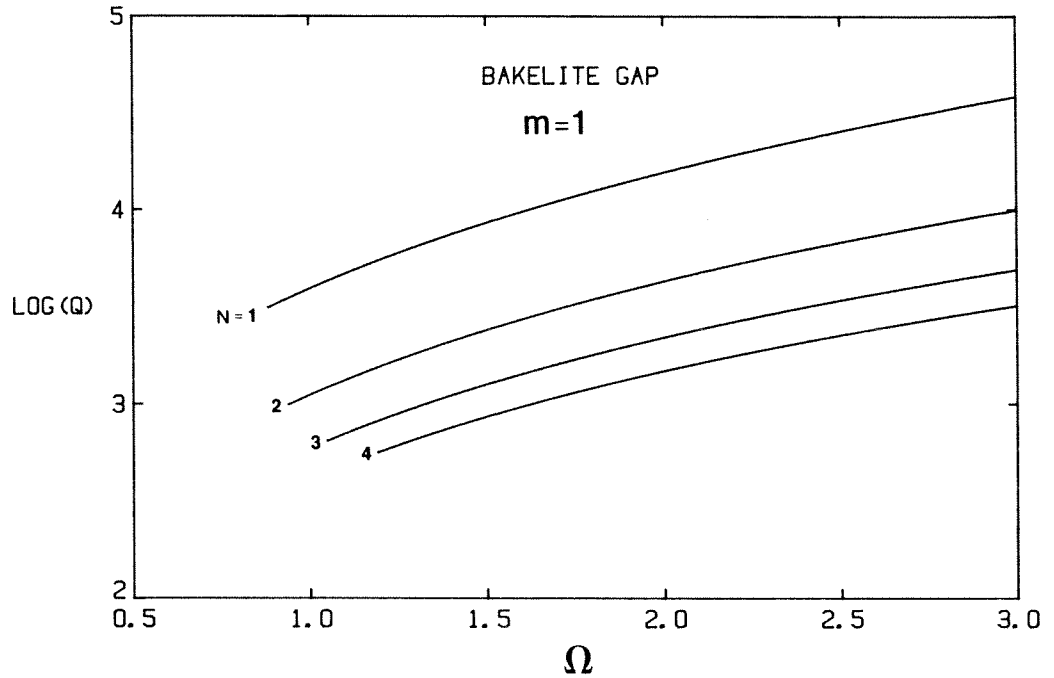

FIG. 2-16. Plots of the Qs of the $N=1-4$, $m=1$, $l=1$ toroidal eigenmodes, as functions of Ω, for damping due to dielectric losses in the insulating gap. Note that $Q=\infty$ for $N=0$ or $m=0$ modes. $B_0=3.95$ kG.

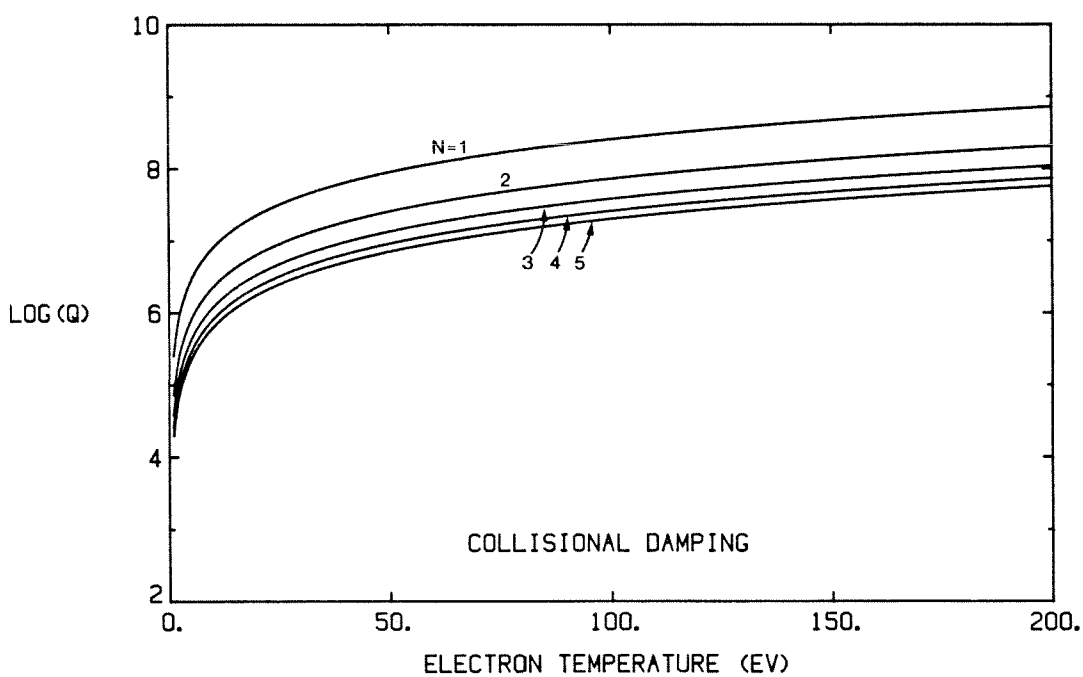

FIG. 2-17. Plots of the Qs of the $N=1-5$, $m=1$, $l=1$ toroidal eigenmodes, as functions of the electron temperature, for electron-ion collisional damping. Note that $Q=\infty$ for the $N=0$ mode. Here $\omega/2\pi=12$ MHz and $B_0=3.95$ kG.

tion for $\nabla \times \mathbf{B}$:

$$E_z = \frac{i\,c}{\omega\,\varepsilon_{\|}}(\nabla \times \mathbf{B})_z = \frac{\eta_{\|}\,c}{4\pi}(\nabla \times \mathbf{B})_z\,, \tag{2.82}$$

where $\mathbf{B}$ is calculated from the zero-m_e model and $\eta_{\|}$ is the parallel Spitzer resistivity (in units of statohm-cm). The ohmic power loss due to collisions is then just

$$P_{coll} = \int_V \frac{1}{2\eta_{\|}} |E_z|^2\, dV\,, \tag{2.83}$$

where the integration is over the volume of the tokamak. Paoloni calculates the stored wave energy as described in earlier sections, and finds the following expression for the Q for fast wave eigenmodes due to collisions:

$$Q_{coll} = \frac{4\pi\omega}{\eta_{\|}\,c^2\,k_{\|}^2}\left[\frac{1}{2p^2}\left(\frac{k_A^2}{(\Omega+1)^2} + k_{\|}^2\right)(D+1)^2 + 1\right]. \tag{2.84}$$

For parameters appropriate to the Caltech tokamak, the Qs for the $N=1-5$, $m=1$, $l=1$ eigenmodes are plotted as functions of the electron temperature in Figure 2-17. Note that the Qs decrease as N increases, but that even for the $N=5$ mode, for $T_e = 100$ eV, the Q is greater than 10^7.

2.3.7 Comparison

In the preceding section, six different wave damping mechanisms were considered: cyclotron fundamental, second harmonic cyclotron, electron Landau and TTMP, resistive wall, dielectric gap, and collisional damping. These mechanisms are compared, for some specific plasma parameters and frequencies, in Tables 2-1 and 2-2.

Table 2-1 compares the Qs for the different damping mechanisms for the case where $\omega = \omega_{ci}$ at the tokamak minor axis, i.e., the fundamental cyclotron resonance layer passes through the center of the plasma column. The excitation frequency is taken to be 8 MHz, so the toroidal field on axis is 5.26 kG. The

		log(Q)					
T (eV)	N	Fundamental	EL + TTMP	Collisional	Wall	Gap	Total
50	0	∞	∞	∞	3.58	∞	3.58
	1	4.79	14.7	7.77	3.59	3.83	3.37
	2	4.18	5.23	7.21	3.63	3.28	3.08
	3	3.83	3.59	6.93	3.68	3.01	2.80
	4	3.58	3.07	6.76	3.73	2.85	2.57
	5	3.39	2.85	6.63	3.78	2.75	2.42
100	0	∞	∞	∞	3.58	∞	3.58
	1	4.49	8.04	8.22	3.59	3.83	3.36
	2	3.88	3.45	7.67	3.63	3.28	2.90
	3	3.53	2.71	7.38	3.68	3.01	2.46
	4	3.28	2.51	7.21	3.73	2.85	2.28
	5	3.09	2.44	7.08	3.78	2.75	2.19

TABLE 2-1. Values of $\log(Q)$ predicted from various damping mechanisms (fundamental ion cyclotron, electron Landau + TTMP, electron-ion collisional, wall resistivity, and dielectric losses in the insulating gap) and the total Q, for the $N = 1 - 5$, $m = 1$, $l = 1$ toroidal eigenmode in the Caltech tokamak. Here $\omega/2\pi = 8$ MHz, $B_0 = 5.26$ kG, and the fundamental cyclotron layer passes through the center of the plasma; the second-harmonic resonance layer is not in the tokamak. Results of the calculations are shown for $T_e = T_i = 50$ and 100 eV.

		log(Q)					
T (eV)	N	$2\omega_{ci}$	EL + TTMP	Collisional	Wall	Gap	Total
50	0	3.30	∞	∞	3.98	∞	3.22
	1	3.38	>20	7.95	3.98	4.19	3.23
	2	3.57	9.61	7.41	3.98	3.63	3.21
	3	3.81	5.56	7.13	3.98	3.34	3.14
	4	4.05	4.19	6.96	4.00	3.17	3.03
	5	4.27	3.60	6.85	4.02	3.06	2.90
100	0	3.00	∞	∞	3.98	∞	2.96
	1	3.08	16.75	8.41	3.98	4.19	3.00
	2	3.27	5.67	7.86	3.98	3.63	3.06
	3	3.51	3.72	7.58	3.98	3.34	2.97
	4	3.75	3.10	7.41	4.00	3.17	2.76
	5	3.97	2.84	7.30	4.02	3.06	2.60

TABLE 2-2. Values of $\log(Q)$ predicted from various damping mechanisms (second-harmonic ion cyclotron, electron Landau + TTMP, electron-ion collisional, wall resistivity, and dielectric losses in the insulating gap) and the total Q, for the $N = 1 - 5$, $m = 1$, $l = 1$ toroidal eigenmode in the Caltech Tokamak. Here $\omega/2\pi = 12$ MHz, $B_0 = 3.95$ kG, and the second-harmonic resonance layer passes through the center of the plasma; the fundamental resonance layer is not in the tokamak. Results of the calculations are shown for $T_e = T_i = 50$ and 100 eV.

second harmonic resonance layer is then outside the tokamak and does not contribute to the damping. The Qs are shown for the $N=1-5$, $m=1$, $l=1$ toroidal eigenmodes, for temperatures of 50 and 100 eV (the electron and ion temperatures are taken to be equal). For small N (or $k_{\|}$), wall resistivity and dielectric losses in the gap are the major energy loss mechanisms; as N increases, fundamental cyclotron and electron Landau damping becomes more important. As the temperature increases, both fundamental and Landau damping increase; for $T=100$ eV and $N=5$, the most important mechanism is electron Landau damping. Collisional damping is negligible for all the cases shown (it is only of consequence for very low temperatures).

The total Q is also shown for each toroidal mode number and is obtained by summing the damping rates for each separate mechanism, assuming they are independent. The total Q is observed to decrease as N increases and is smaller for the higher-temperature case. As N varies from 0 to 5 (for $T=100$ eV), the total Q decreases from 3800 to 155.

An example where $\omega=2\omega_{ci}$ on axis is shown in Table 2-2. The excitation frequency is taken to be 12 MHz and the toroidal magnetic field is 3.95 kG. The fundamental cyclotron resonance layer is now inside the tokamak "hole" and does not contribute to the damping. For small N the most important dissipation mechanism is seen to be second-harmonic cyclotron damping; for larger N, electron Landau damping and dissipation in the dielectric gap become the dominant mechanisms. For large N, the total Q decreases, and for $N\approx 1-2$ the total Q reaches a maximum. For $T=100$ eV, the total Q varies from 1150 ($N=2$) to 398 ($N=5$).

2.4 Radial Density Profile

2.4.1 Numerical Model

The plasma density in the actual tokamak is not constant over the cross-section of the torus; it is generally peaked in the center. When the plasma density varies as a function of radius, the elements of the dielectric tensor $\overleftrightarrow{\boldsymbol{\varepsilon}}$ are no longer constants. The spatial derivatives of $\overleftrightarrow{\boldsymbol{\varepsilon}}$ must then be included in the derivation of the wave equations and simple analytic solutions are not feasible for arbitrary profiles. In this section a numerical approach is taken, solving for $\mathbf{E}$ and $\mathbf{B}$ by directly integrating Maxwell's equations. The periodic-cylinder model is again used, and the plasma density is allowed to be an arbitrary function of radius within some mild constraints.

We assume that $E_z = 0$ and that all field components vary as $e^{i(m\theta + \frac{N}{R}z) - i\omega t}$, where, as before, m and N are the poloidal and toroidal mode numbers and $k_\parallel = N/R$. Writing out the components of the Maxwell equation $\nabla \times \mathbf{E} = -\frac{1}{c}\frac{\partial \mathbf{B}}{\partial t}$ then yields:

$$\rho\text{-component:} \qquad -k_\parallel E_\theta = k_0 B_\rho \tag{2.85a}$$

$$\theta\text{-component:} \qquad k_\parallel E_\rho = k_0 B_\theta \tag{2.85b}$$

$$z\text{-component:} \qquad \frac{\partial E_\theta}{\partial \rho} = ik_0 B_z + \frac{im}{\rho} E_\rho - \frac{1}{\rho} E_\theta . \tag{2.85c}$$

while the ρ and θ components of the Maxwell equation $\nabla \times \mathbf{B} = -i\, k_0 \overleftrightarrow{\boldsymbol{\varepsilon}} \cdot \mathbf{E}$ are

$$\rho\text{-component:} \qquad -\frac{m}{\rho} B_z + k_\parallel B_\theta = k_0 \varepsilon_\perp E_\rho - ik_0 \varepsilon_\times E_\theta \tag{2.86a}$$

$$\theta\text{-component:} \qquad \frac{\partial B_z}{\partial \rho} = ik_\parallel B_\rho - k_0 \varepsilon_\times E_\rho + ik_0 \varepsilon_\perp E_\theta . \tag{2.86b}$$

The above constitute five equations in five unknowns, and it is easy to solve for the derivatives of E_θ and B_z in terms of E_θ and B_z alone:

$$\frac{\partial E_\theta}{\partial \rho} = \frac{1}{\rho}\left(\frac{m\varepsilon_\times k_0^2}{k_\parallel^2 - \varepsilon_\perp k_0^2} - 1\right) E_\theta + i k_0 \left(\frac{m^2}{\rho^2\left(k_\parallel^2 - \varepsilon_\perp k_0^2\right)} + 1\right) B_z \qquad (2.87a)$$

$$\frac{\partial B_z}{\partial \rho} = -i\frac{k_\parallel^4 - 2k_0^2 k_\parallel^2 \varepsilon_\perp + k_0^4\left(\varepsilon_\perp^2 - \varepsilon_\times^2\right)}{k_0\left(k_\parallel^2 - k_0^2\varepsilon_\perp\right)} E_\theta - \frac{1}{\rho}\frac{m\varepsilon_\times k_0^2}{\left(k_\parallel^2 - k_0^2\varepsilon_\perp\right)} B_z \,. \qquad (2.87b)$$

Note that $\varepsilon_\times$ and $\varepsilon_\perp$ are functions of density and that $k_\parallel^2 - \varepsilon_\perp k_0^2 > 0$ for $\omega_{ci} < \omega < \omega_{lh}$. We assume that the plasma density $n(\rho)$ satisfies $\left.\frac{\partial n(\rho)}{\partial \rho}\right|_{\rho=0} = 0$ and that $n(\rho)$ is everywhere sufficiently large that $\omega_{lh}(\rho) > \omega$.

Expanding the above equations near $\rho = 0$ yields the same solutions as for the constant density case:

$$B_z = \alpha J_m(p\rho) \qquad (2.88a)$$

$$E_\theta = \alpha\left[\frac{k_0 m}{\rho p^2}\left(1 - k_0^2\varepsilon_\times\right) J_m(p\rho) + \frac{k_0}{\rho} J_{m+1}(p\rho)\right], \qquad (2.88b)$$

where α is a constant and p is defined in equation 2.63. Equations 2.87a and 2.87b are then integrated by a simple numerical shooting code. First, the static magnetic field B_0, the frequency ω, and the functional form of $n(\rho)$ are chosen. An initial mean (i.e., line-averaged) density $\bar{n} = \frac{1}{\rho_0}\int_0^{\rho_0} n(\rho) d\rho$ is selected, and initial values of the fields to start the integration at $\rho = \delta\rho_0$ are found from equations 2.88a and 2.88b. The value of δ is typically chosen to be 10^{-4}; the solution is not sensitive to this choice provided δ is sufficiently small. The equations are then integrated from $\rho = \delta\rho_0$ to $\rho = \rho_0$ using a standard numerical routine, and the value of E_θ at $\rho = \rho_0$ is recorded. The mean density is then incremented and the procedure is repeated. The roots of the function $E_\theta(\rho_0; \bar{n})$ thus generated are the distinct densities at which the boundary condition $E_\theta(\rho_0) = 0$ is satisfied for the specified frequency ω. The frequency is then incremented and the process is continued, mapping out the

solutions within a specified area in density-frequency space. For a given frequency, once the eigendensity is found, the wave field components as functions of radius are found by integrating the equations for E_θ and B_z and by using equation 2.52 to find E_ρ, B_θ, and B_ρ.

Several density profiles were investigated with this model. A quadratic profile, often used in theoretical models, is given by

$$n_I(\rho;\alpha) = \frac{\overline{n}}{(1-\frac{\alpha}{3})}\left[1-\alpha\left[\frac{\rho}{\rho_0}\right]^2\right], \tag{2.89}$$

where α is a parameter related to the steepness of the profile. Another profile, designed to simulate coherent radial density perturbations, was composed by adding a J_0 Bessel function to a constant background density:

$$n_{II}(\rho;\alpha;m) = \frac{\overline{n}}{\lambda}\left[1+\alpha J_0\left(\xi_m \frac{\rho}{\rho_0}\right)\right], \tag{2.90}$$

where $\lambda = 1 + \frac{\alpha}{\xi_m}\int_0^{\xi_m} J_0(\eta)\,d\eta$ is the appropriate normalization factor and ξ_m is the m^{th} zero of the Bessel function J_0. Here α is related to the magnitude of the perturbation and m, to the period.

2.4.2 Effects on Eigenmode Dispersion Curves

Dispersion curves for modes using the quadratic density profiles are shown in Figures 2-18a and 2-18b for the first radial mode with $N=0, 4$ and $m=0, 1$. Figure 2-18a shows the results for the profile $n_I(\rho; 0.5)$, corresponding to a profile with a peak (center) density twice the edge density; Figure 2-18b is for the profile $n_I(\rho; 0.9)$, corresponding to a profile with a peak density of ten times the edge density. Results from the constant density profile model are also plotted (dashed lines) for comparison. The overall effect is that the curves are displaced downward (i.e., to smaller densities and frequencies),

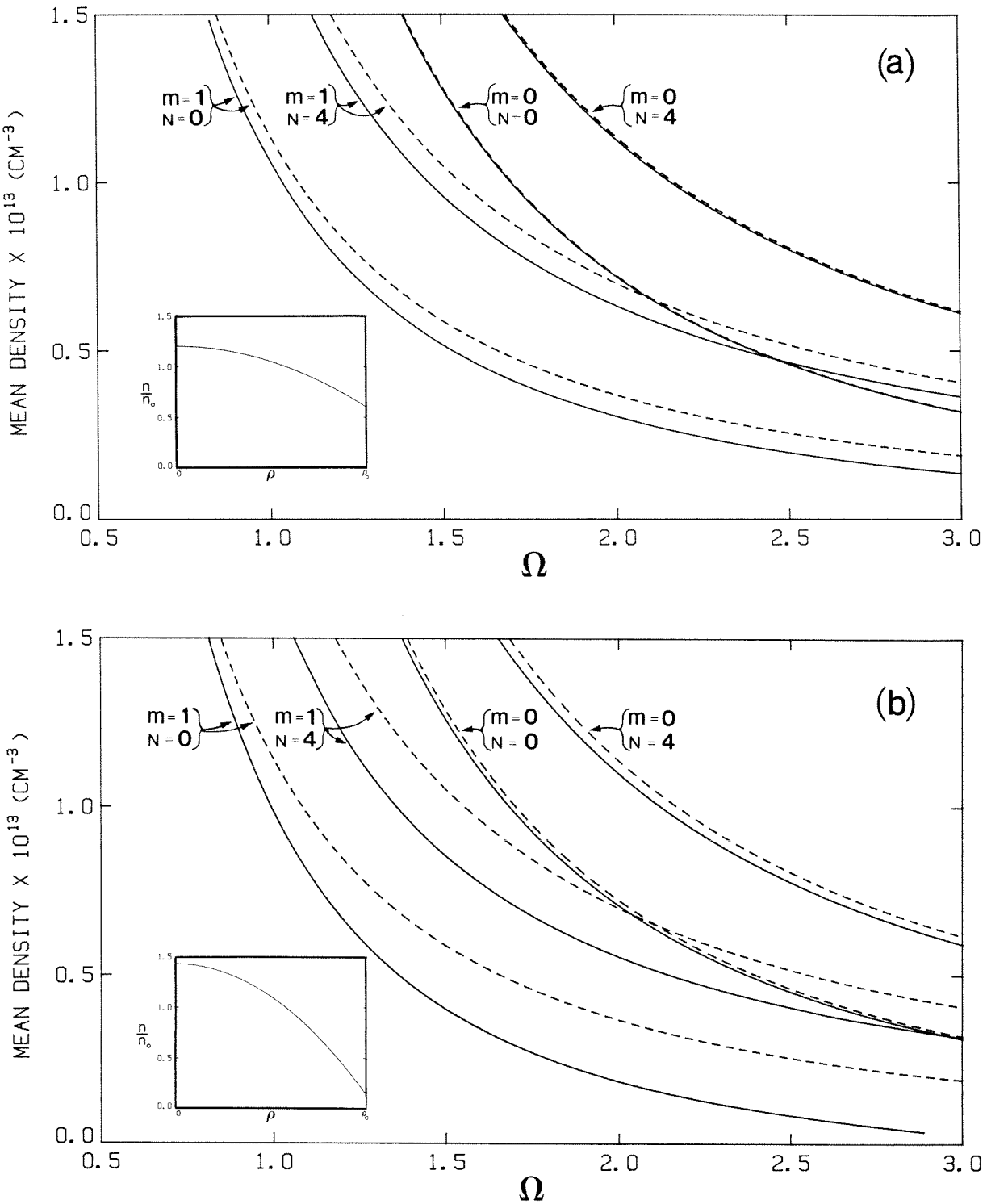

FIG. 2-18. Eigenmode curves for $N=0, 4$, $m=0, 1$, $l=1$ modes. Solid lines are for the quadratic density profile shown in the inset; dashed lines are the solutions for a constant density. a) $n_I(\rho; 0.5)$ density profile. b) $n_I(\rho; 0.9)$ density profile.

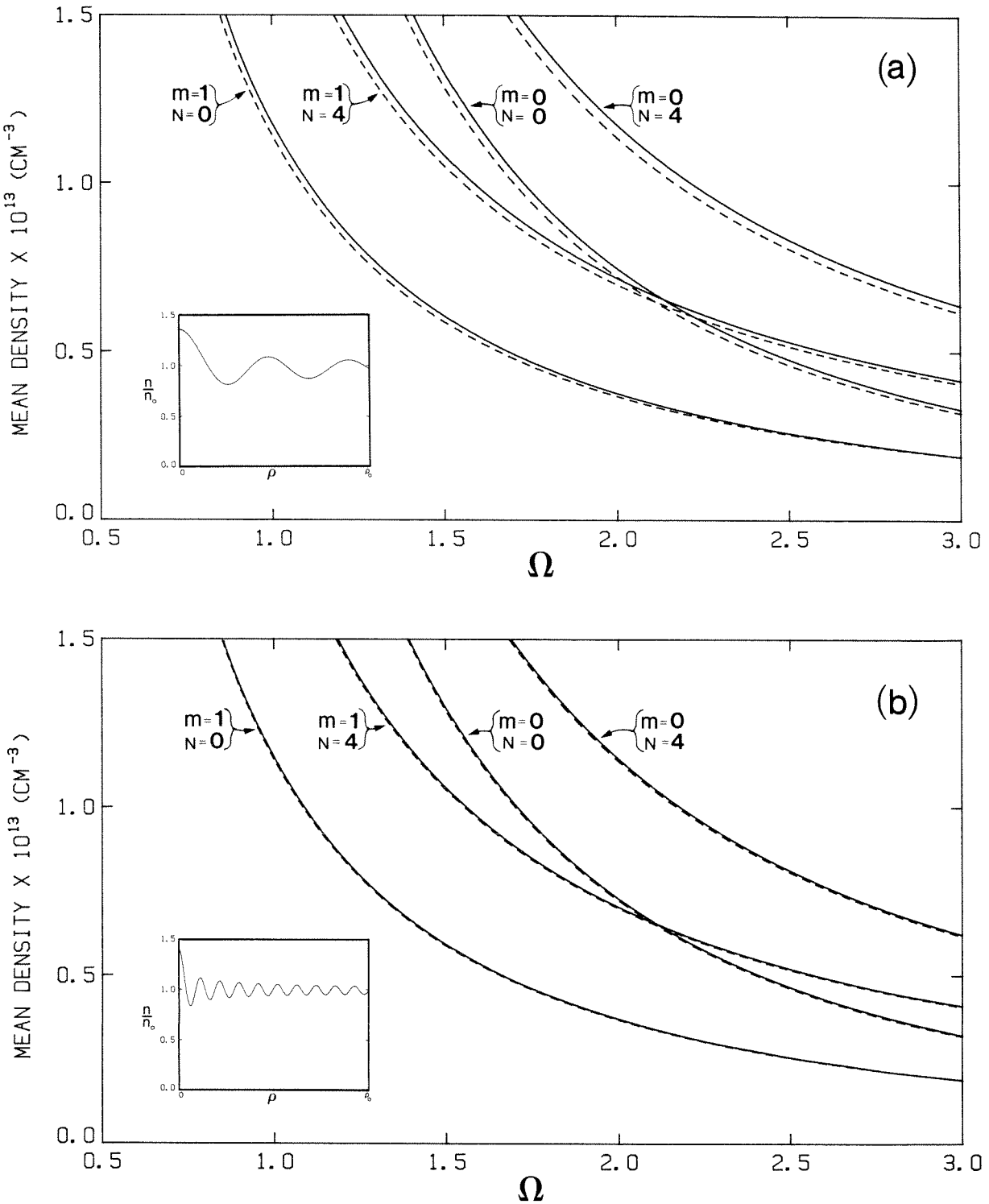

FIG. 2-19. Eigenmode curves for $N=0, 4$, $m=0, 1$, $l=1$ modes. Solid lines are for the oscillatory density profile shown in the inset; dashed lines are the solutions for a constant density. a) $n_{II}(\rho; 0.4; 5)$ density profile. b) $n_{II}(\rho; 0.4; 20)$ density profile.

the displacement being greater for the profile which is steeper. This means that, for a given frequency and mean density, the parallel wavenumber $k_{\|}$ is *increased* by changing the density profile from a constant to a quadratic form. Note that the effect is considerably larger for the $m=1$ modes than for the $m=0$ modes and that the relative displacement for the $m=1$ curves is substantial.

Eigenmode dispersion curves for two density profiles with oscillatory perturbations are shown in Figures 2-19a and 2-19b. Figure 2-19a pertains to the profile $n_{II}(\rho; 0.4; 5)$ which has 2.25 periods of oscillation radially; the density at the center of the plasma $(\rho=0)$ is ~ 1.4 times the mean density. The eigenmode curves are displaced slightly up in the frequency-density plane relative to their positions for the constant-density case. For a given frequency and density, then, the imposition of the oscillatory profile *decreases* $k_{\|}$; the effect, however, is rather small. The sign of the displacement is independent of the phase of the density perturbation: inverting the profile (i.e., changing its phase by π radians by changing the sign of α) still yields an upward displacement of the curves.

Figure 2-19b shows the results for the $n_{II}(\rho; 0.4; 20)$ density profile. The density at $\rho=0$ is still ~ 1.4 times the mean density, but there are now ~ 10 periods of oscillation in the radial profile. The eigenmode curves are still displaced upwards (i.e., lower $k_{\|}$ for fixed Ω and n) but the relative change is less than 1%. Thus, as the wavelength of the radial density perturbation decreases, the resulting effect on the location of the toroidal eigenmodes in density-frequency space diminishes.

2.4.3 Effects on Field Profiles

The radial profiles of the components of $\mathbf{B}$ and $\mathbf{E}$ for the $N=4$, $m=1$, $l=1$ eigenmodes, with a constant density profile, are shown in Figure 2-20a.

Here the electric field is plotted in terms of the right- and left-hand circularly polarized components: $E_R = E_\rho - i\,E_\theta$ and $E_L = E_\rho + i\,E_\theta$. The field profiles for the $n_I(\rho; 0.5)$ quadratic density function are shown in Figure 2-20b; the relative change in the fields is quite small.

Figures 2-20c and 2-20d show the field profiles using the $n_{II}(\rho; 0.4; 5)$ and $n_{II}(\rho; 0.4; 20)$ density functions. The effect on the field components is now quite noticeable: the components are perturbed with the same wavelength as the density perturbation. It is of particular interest that the left-hand component of the electric field, E_L, is altered markedly from its constant-density form. This is significant because it is the left-hand component of the field that is responsible for fundamental cyclotron damping, and second-harmonic damping is related to the transverse (radial) gradient of this field component.

Figure 2-21 shows the radial form of $\left|\nabla_\perp |\, \mathbf{E}_L \,|\right|^2$ for the density profile $n_{II}(\rho; \alpha; 20)$ as α is increased from 0.0 to 0.4. The transverse gradient of the field is seen to be extremely sensitive to the radial density perturbations: for the $\alpha = 0.4$ case, the peak of $\left|\nabla_\perp |\, \mathbf{E}_L \,|\right|^2$ is more than two-thousand times greater than the peak for the constant density ($\alpha = 0$) case.

The wave damping, of course, is dependent not only on the peak of the transverse gradient, but on some form of integral of the transverse gradient over the cyclotron resonance layer. A full calculation of the Qs expected for the eigenmodes using these density perturbations remains to be carried out. It is likely, however, that the dramatic increase of the transverse gradient of E_L will result in substantially increased damping and hence lower values for the Qs.

The preceding model of radial density perturbations is not presented as a realistic emulation of the tokamak environment; it is unlikely that such oscillatory density profiles as described actually exist. The model is intended only

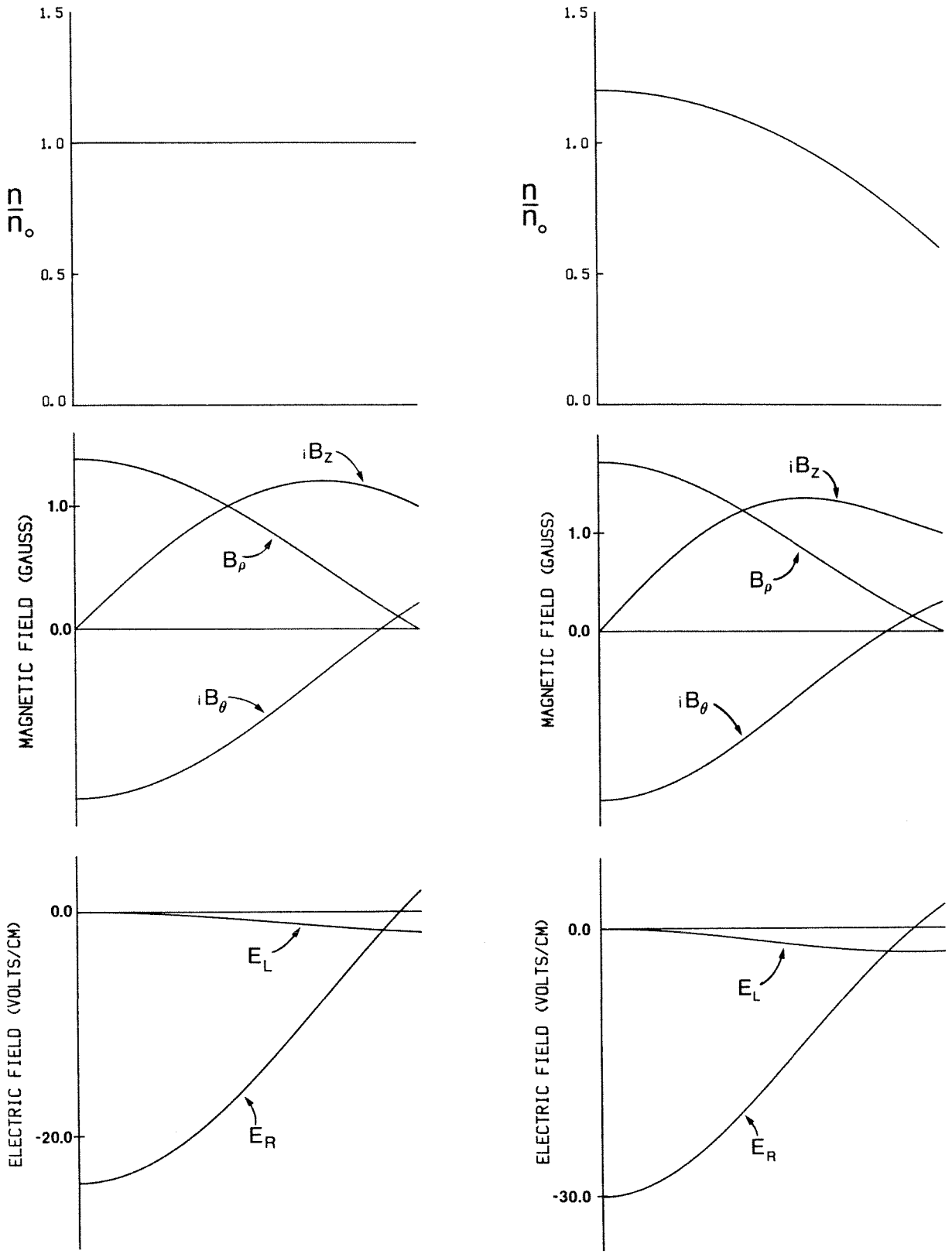

FIG. 2-20. Components of **B** and **E** as functions of radius for the $N=4$, $m=1$, $l=1$ toroidal eigenmode, for different density profiles. Here $\omega/2\pi=12$ MHz and $B_0=4$ kG. The horizontal axis in each plot is the radius ρ; the limits of the axis are 0 (left end) and ρ_0 (right end). The top plot in each column shows the density profile. a) Left-hand column - constant density profile. b) Right-hand column - quadratic density profile $n_I(\rho; 0.5)$.

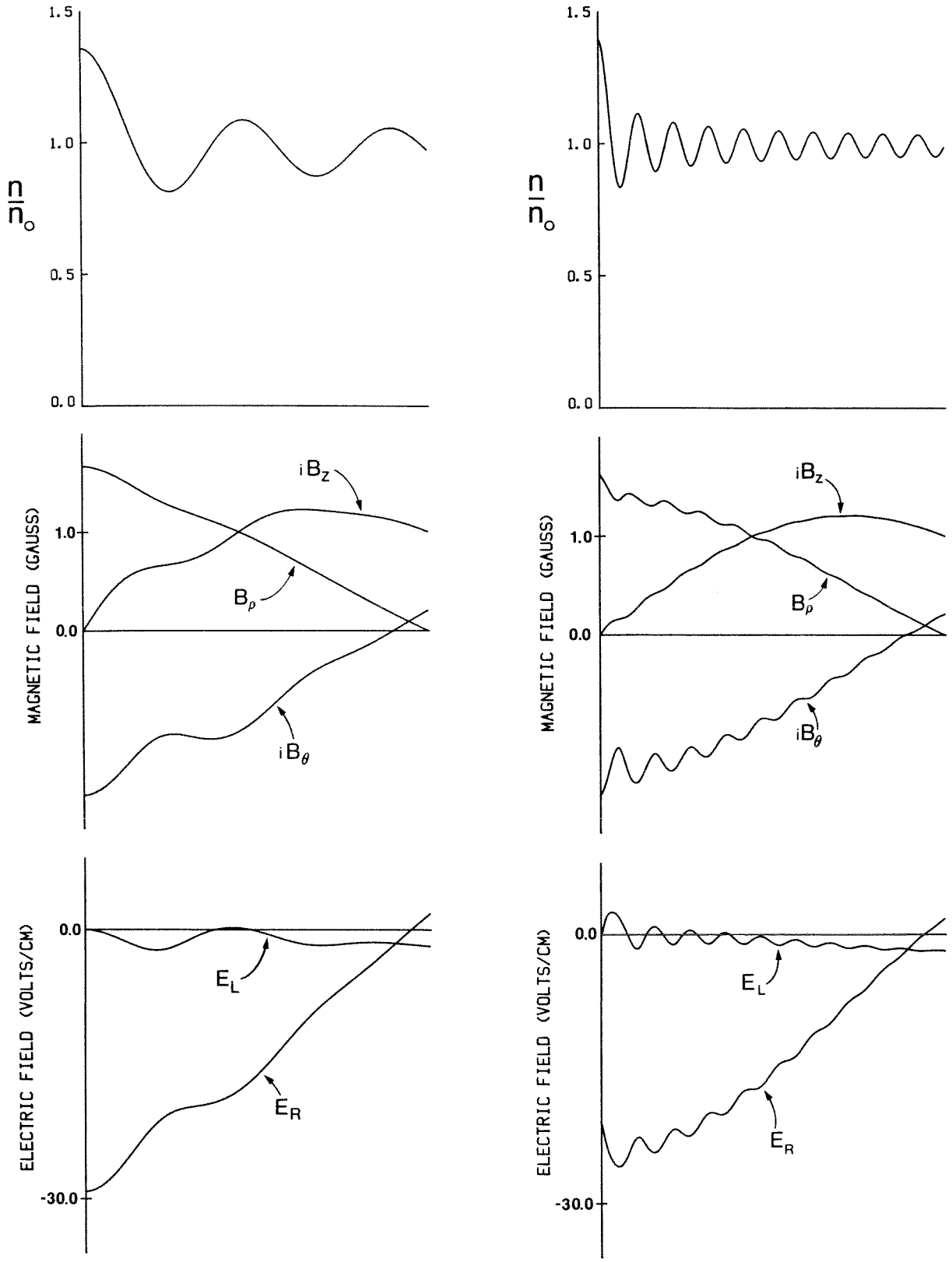

FIG. 2-20, continued. c) Left-hand column - oscillatory density profile $n_{II}(\rho; 0.4; 5)$. d) Right-hand column - oscillatory density profile $n_{II}(\rho; 0.4; 20)$.

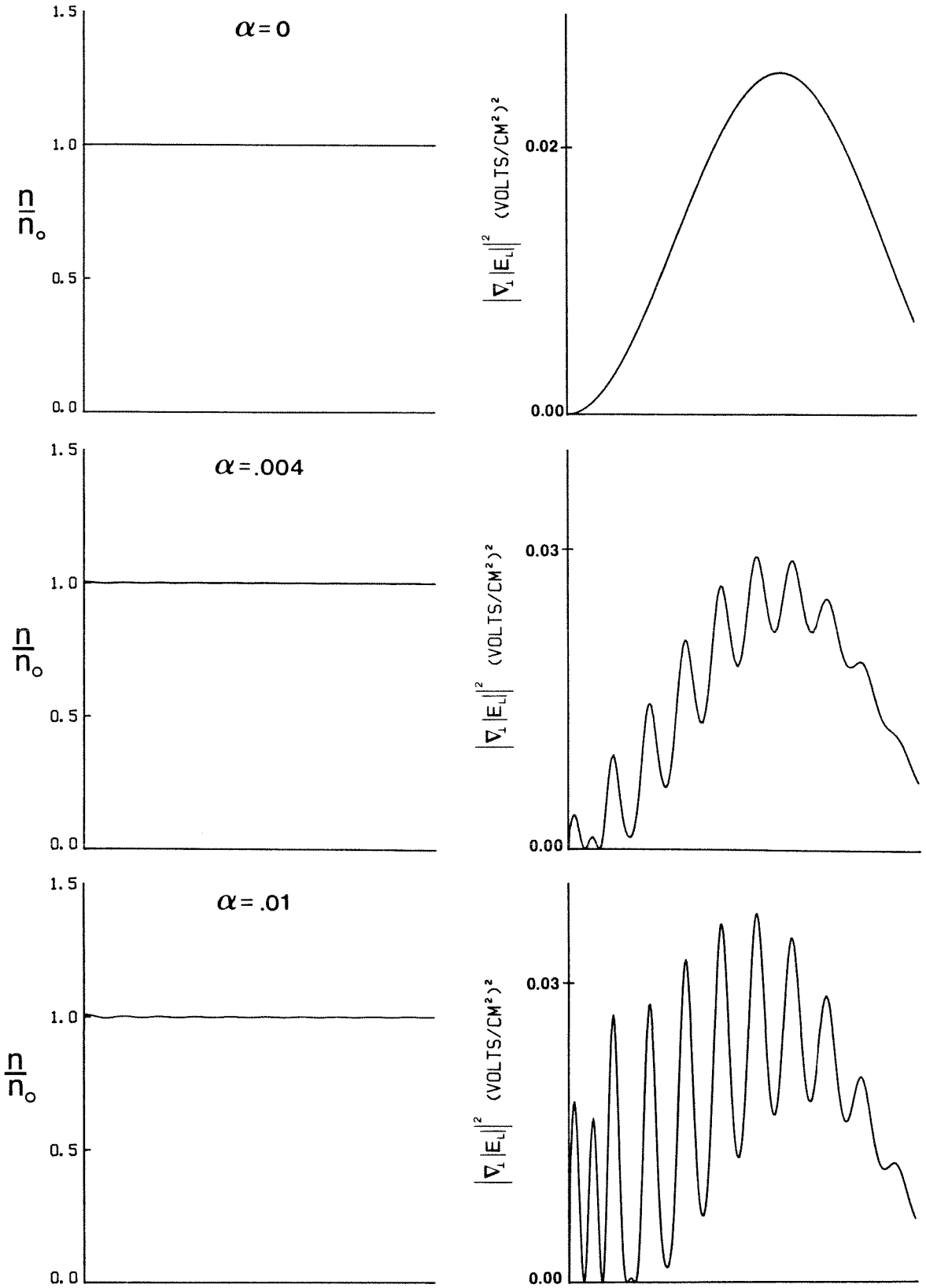

FIG. 2-21. Plots of the radial dependence of $|\nabla_\perp|\mathbf{E}_L||^2$ for the $N=4$, $m=1$, $l=1$ toroidal eigenmode and the $n_H(\rho;\alpha;20)$ oscillatory density profile, as α is increased from 0 to 0.4. Horizontal axis in each plot is the radius ρ; the axis limits are 0 (left end) and ρ_0 (right end). Here $\omega/2\pi = 12$ MHz and $B_0 = 4$ kG. Field distributions have been normalized so that $B_z(\rho_0) = 1$ G in each case.

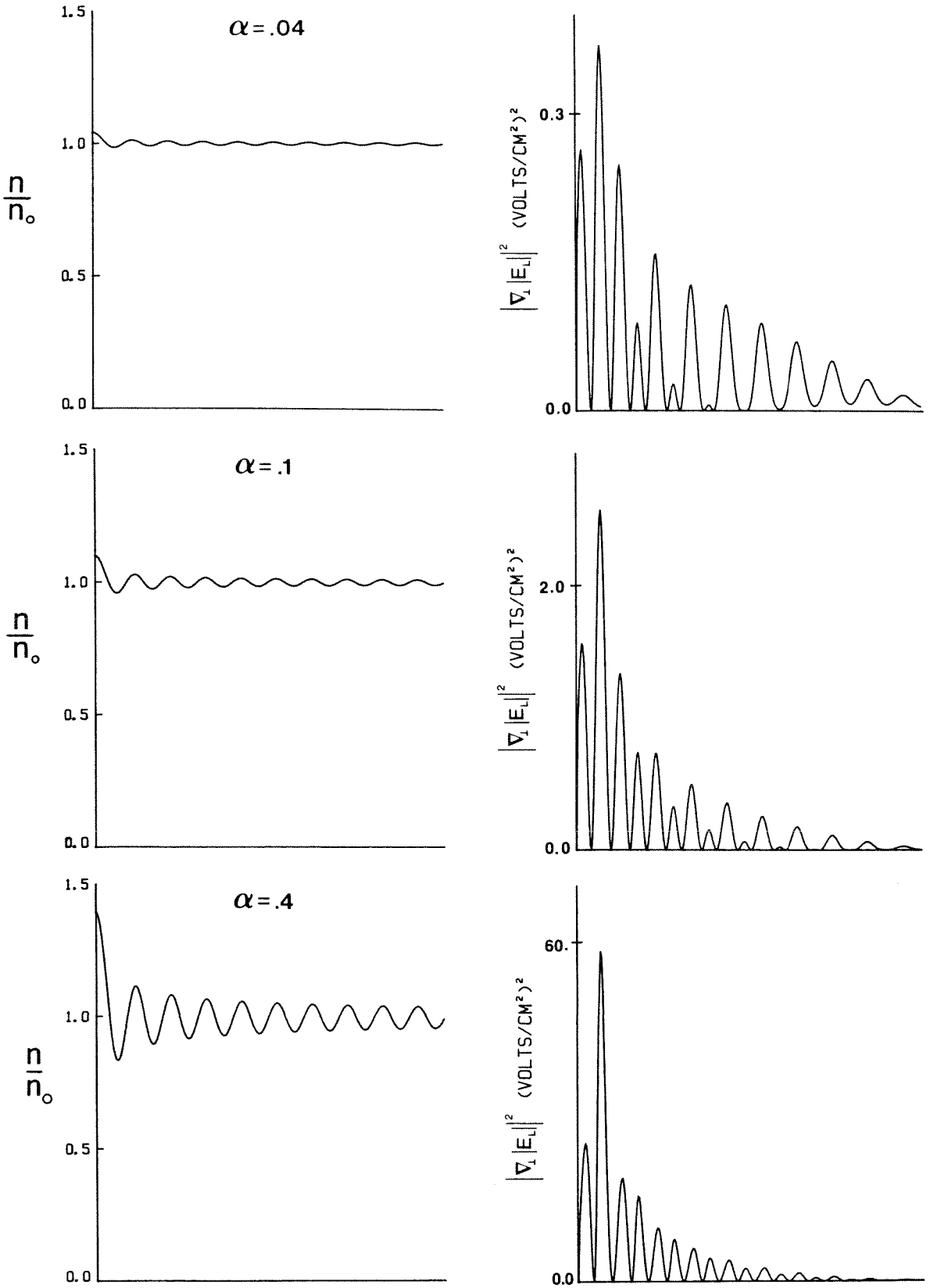

FIG. 2-21, continued.

to suggest that spatial density perturbations may be important to consider in calculations of cyclotron wave damping.

There is evidence that global density perturbations do exist in tokamaks. Low frequency ($\ll\omega_{ci}$) density fluctuations associated with global MHD modes have been observed in many tokamaks. The "sawtooth" oscillation, for instance, has been seen with an $m=0$ (poloidal) and $N=0$ (toroidal) structure; superimposed on this is a lower amplitude, higher m-number, higher frequency perturbation [Von Goeler, 1974; Jahns et al., 1978]. Many of the initial measurements were made with soft-X-ray detectors which respond to both electron temperature and density fluctuations. The T.F.R. group investigated the sawtooth fluctuations with a variety of external diagnostics in order to separate the density and temperature effects [T.F.R. Group, 1976]. They estimated typical values for the temperature fluctuations to be $\frac{\tilde{T}}{T}\sim 17\%$; for the density fluctuations, $\frac{\tilde{n}}{n}\lesssim 3\%$. Unfortunately, there is little information available about the *radial* profile of the density during sawtooth or other MHD oscillations.

Another kind of spatial density fluctuation occurring on a time scale much longer than $\frac{2\pi}{\omega_{ci}}$ has been observed in a number of tokamaks [Surko and Slusher, 1980; Mazzucato, 1982; Zweben and Gould, 1983]. These fluctuations, referred to as "microturbulence", typically have broad frequency spectra (below $\sim$200 kHz), significant amplitudes ($\frac{\tilde{n}}{n}\sim 0.01-0.5$) which depend on the radial position, and short correlation lengths ($\sim$1 cm). On the time scale of the RF period, then, the plasma density appears "grainy". It is conceivable that this form of density perturbation could also induce short-range fluctuations in the left-hand component of the wave electric field, resulting in enhanced cyclotron damping. Clearly, more work needs to be done to assess

this possibility.

2.5 Other Effects

2.5.1 Poloidal Magnetic Field

The discussion of toroidal eigenmodes has thus far neglected the poloidal component of the confinement magnetic field which is generated by the ohmic-heating plasma current. To first order, this field varies as $1/\rho$, where ρ is the minor radius, and its magnitude at the tokamak wall is typically 10% of the toroidal field.

The poloidal field breaks the degeneracy of the $\pm N$ eigenmodes: waves traveling in the direction of the plasma current see a different environment than waves traveling in the opposite direction. The net result is to change slightly the densities at which the $+N$ and $-N$ modes become resonant, leading to mode "splitting" [Takahashi, 1977]. The effect has been considered theoretically by several authors with similar results [Adam and Jacquinot, 1977; Messiaen, 1978]. Messiaen considers a uniform plasma with a poloidal field arising from a uniform plasma current density: $B_{pol} = \gamma B_0$, where $\gamma = \frac{\rho}{qR}$, R is the major radius, and q is the usual safety factor. Keeping only terms to first order in γ and neglecting the electron mass, a wave equation is derived for B_z:

$$\left[\nabla_\perp^2 + p^2 - 2\frac{m}{qR}\mu^2 k_\parallel\right] B_z = 0 \,, \tag{2.91}$$

where p has been defined previously (equation 2.63) and $\mu \equiv \frac{k_0^2 \varepsilon_x}{k_0^2 \varepsilon_\perp - k_\parallel^2}$. Note that for $q \to \infty$, corresponding to zero poloidal field, or if $m = 0$ or $k_\parallel = 0$, the wave equation reduces to the form found earlier (equation 2.40). Imposition of the appropriate boundary condition ($E_\theta(\rho_0) = 0$) yields, as before, an equation

which specifies the density for a mode given the frequency, i.e., equation 2.66 where p is replaced by $\left[p^2 - 2\frac{m}{qR}\mu^2 k_{\|}\right]^{\frac{1}{2}}$.

For parameters typical of the Caltech tokamak, the relative shift in density of the resonances associated with a plus and minus N toroidal mode number pair is small (typically < 5%). As will be mentioned in Chapter 7, resonance peak splitting which may be due to the poloidal field is sometimes, but not consistently, observed in actual experiments. Resonances due to a wave traveling in a single direction (i.e., a plus or minus N mode alone) are *traveling* wave resonances and the magnitude of the wave fields should not vary as a function of toroidal angle. If, however, the resonances due to the $\pm N$ modes substantially overlap (the resonances have finite width due to damping), then the modes become *standing* wave resonances and the amplitude of the fields should have nodes and peaks as a function of the toroidal angle.

2.5.2 Toroidal Geometry

The effects of toroidal geometry on fast wave propagation and eigenmodes have been considered by only a few authors [Pridmore-Brown, 1966; Gould, 1975; Swanson, 1975]. The most important effect of toroidal geometry is the inhomogeneous toroidal magnetic field which varies as $1/R$. Physically, this means that the absorption which may occur at the cyclotron fundamental and harmonic frequencies is confined to a cylindrical surface of constant major radius. Although this is clearly of great importance in calculating the wave damping, in cold plasma theory the fast wave has no dramatic transition at these frequencies and so this effect may not be important in determining gross propagation characteristics. Unfortunately, the wave equation in toroidal geometry cannot be solved by separation of variables; numerical methods are possible, but the problem is formidable.

Swanson considered a plasma-filled toroidal cavity of rectangular cross-section with the appropriate toroidal magnetic field. He calculated approximate fast wave eigenmode frequencies and found them to be within about 10% of the frequencies calculated from a straight rectangular model, for low order modes. It was noted, however, that there were in general no single mode solutions which simultaneously satisfied all of the boundary conditions.

Numerous questions remain about the theory of fast wave resonances in a truly toroidal cavity; no satisfactory analysis has yet emerged.

CHAPTER 3

The Caltech Research Tokamak†

The Caltech Research Tokamak is a small circular cross-section device with an air-core ohmic heating transformer. It has been used primarily for investigations of RF wave propagation near the ion cyclotron frequency [Hwang, 1979] and for studies of electric [Kubena, 1978] and magnetic [Levine, 1980; Hedemann, 1982] field fluctuations within the plasma outer edge. A recent focus of research has involved turbulence in the plasma edge and its relation to energy transport [Zweben et al., 1983]. The tokamak is in regular operation with toroidal fields of 3 - 6 kG, plasma currents of 15 - 35 kA, and plasma densities of $10^{12}-10^{13}$ cm^{-3}. Pulse lengths are typically 10 - 20 msec, and ion and electron temperatures are 50 - 100 eV.

3.1 Vacuum Vessel

The Caltech Research Tokamak was constructed during 1975 and 1976. The vacuum chamber was formed from four 7.5 mm thick stainless steel (316L) 90 degree elbows which were welded together to form two 180 degree flanged sections. Azimuthal copper water cooling channels were attached directly to the chamber (Figure 3-1). The completed torus had a major radius (R_0) of 45.7 cm (i.d.) and a minor radius (a) of 16.2 cm (i.d.); hence the aspect ratio was 2.8. The chamber, which had no plasma limiter, was evacuated by a

† This chapter is an updated version of the reference by Greene and Hedemann [1978]. The work described, except for the section on the charge-exhange diagnostic, represents the combined efforts of a number of individuals.

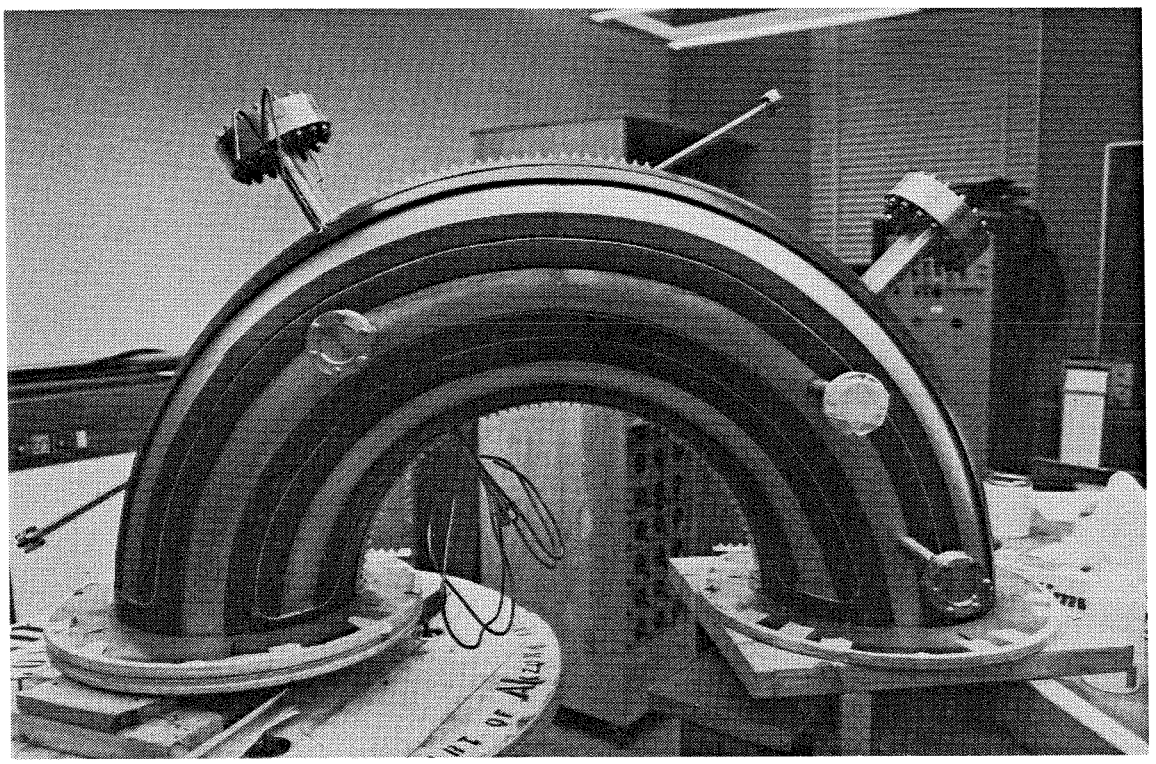

FIG. 3-1. Half of torus showing azimuthal water cooling channels and ports.

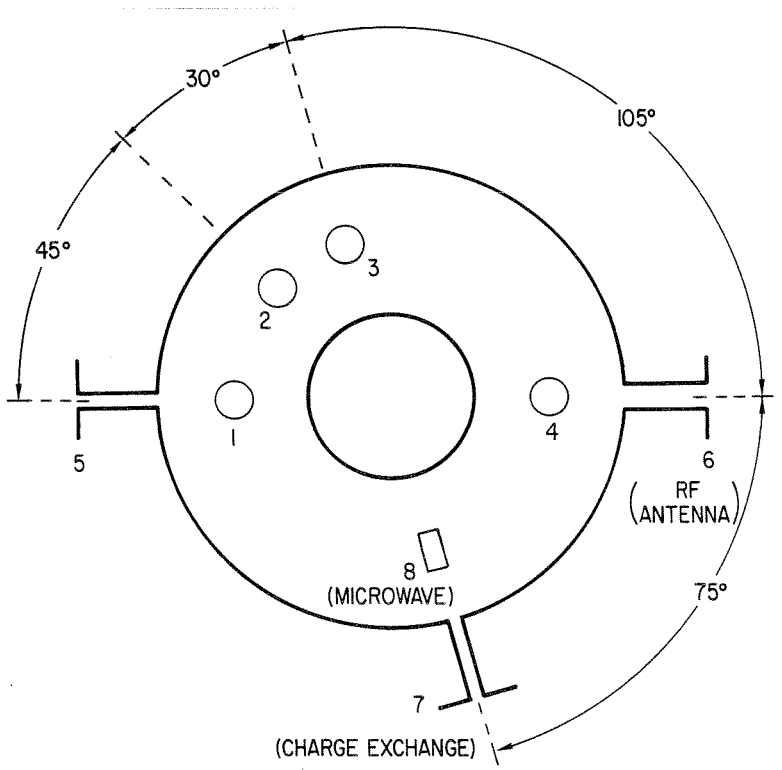

FIG. 3-2. Top view of tokamak, showing locations of ports used in these experiments. Ports #1-4 are 2.2 cm (i.d.), ports #5 and #7 are 9.8 cm tall × 2.2 cm wide, port #6 (the RF antenna port) is 9.8 cm tall × 4.7 cm wide, port #8 (one of the microwave interferometer ports) is rectangular, 2.2 cm × 3.5 cm. All ports are 15 cm long and end in high vacuum flanges.

Leybold-Heraeus turbomolecular pump, with a speed of 450 liters/sec, which permitted base pressures of 2×10^{-7} Torr to be attained without the use of a cold trap. Viton O-rings and copper gaskets were used throughout the vacuum system. The two halves of the torus were separated by a Viton O-ring backed by insulating Bakelite spacers in order to prevent azimuthal current flow.

A variety of ports were welded into the vacuum chamber. The largest, whose cross-section measured 9.8 cm tall × 4.7 cm wide, was connected, via a 14 cm i.d. elbow, to the high vacuum pump. A 10 cm i.d. port was later welded into the elbow to allow the use of the pumping port for the RF antennas. Five ports were available which measured 9.8 cm tall × 2.2 cm wide; they were located, like the pumping port, at the midplane around the outer radius of the chamber ($R = R_0 + a$). A number of pairs of 2.2 cm i.d. cylindrical ports were located along the top and bottom of the chamber, and a pair of rectangular ports, 2.2 cm × 3.5 cm, contained the horns for the microwave interferometer. All of the ports were about 15 cm long and ended in high vacuum flanges. The positions and orientations of the ports used in the experiments described in this thesis are shown in Figure 3-2.

3.2 Coil Design

The toroidal field coil was wound directly on the vacuum liner. It consisted of 480 turns of #1/0 AWG wire (nominally rated at 600 V!) wound in a double toroidal layer. Small inhomogeneities in the toroidal field coil winding (from ports projecting through the coil, etc.) resulted in horizontal and vertical field components (referred to as error field components) which significantly affected the plasma confinement time and the peak value of the plasma current.

Rather than measure the error fields inside the plasma volume, an

indirect procedure was used to infer these fields from measurements made outside the chamber. The toroidal field winding (minor radius = 17 cm) was modeled as a perfect current sheet with the addition of a number of azimuthal (i.e., toroidal) filamentary currents on the winding surface which were responsible for the error fields. To find the positions and amplitudes of these assumed currents, twelve one-turn azimuthal loops, spaced 30 degrees poloidally, were placed at a minor radius of 30 cm (i.e., outside the windings). The toroidal field was pulsed and the voltage induced in each loop was measured. From these data, the flux through each loop was obtained; this flux was attributed to the error currents, since an ideal winding would produce no flux external to the winding surface. By trial and error calculations, a set of five azimuthal ring currents was found which reproduced the measured fluxes (Figure 3-3). The error fields inside the vacuum chamber due to these currents were then computed. To cancel these fields, a set of azimuthal correction coils were designed which were located outside the toroidal field coil winding surface and which produced a field distribution inside the torus approximately equal and opposite to the error fields inferred by the above procedure (Figure 3-4). These error fields turned out to be largely horizontal in direction, hence the correction coils are referred to as horizontal field coils. Proper correction for all values of the toroidal field was insured by connecting the correction coil in series with the toroidal field winding. A second set of horizontal field correction coils was added to the tokamak several years after initial operations began in order to further increase the plasma lifetime. This set of coils was energized independently of the toroidal field by a separate DC supply. Correcting for the toroidal field errors had a large effect on the performance of the tokamak. Prior to field correction, the plasma pulse length was about 2 msec and the maximum plasma current was 10 kA; after field correction the maximum pulse length and plasma current rose to 20 msec and 35 kA, respectively.

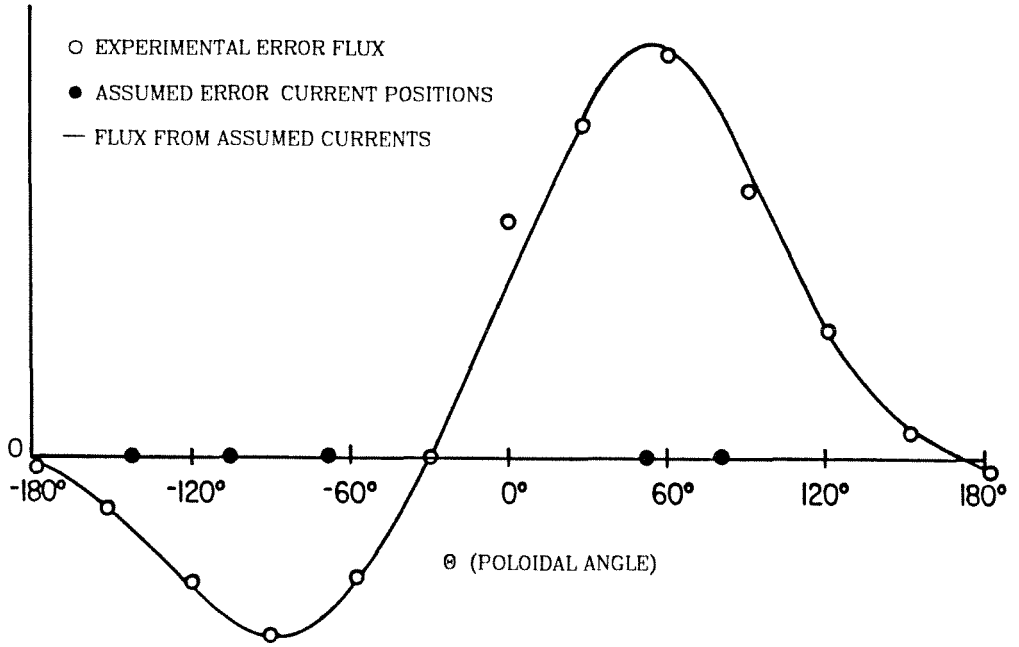

FIG. 3-3. Measured values of the flux versus poloidal angle and the flux due to the five assumed currents.

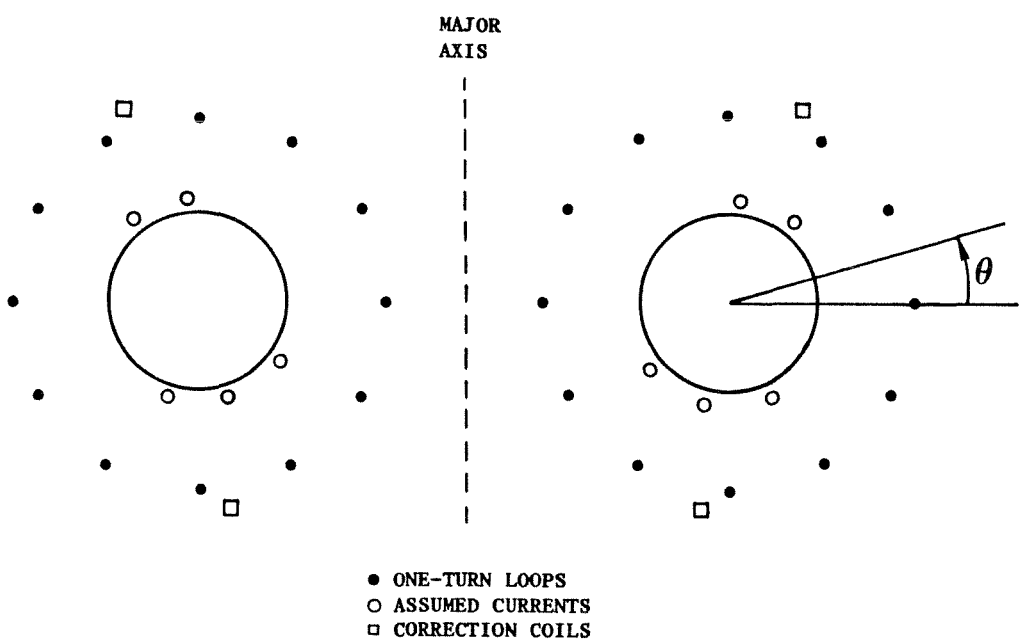

FIG. 3-4. Cross-section of the torus, showing locations of one-turn loop measurement coils, assumed currents and correction coils.

The design of the ohmic heating coil required little or no magnetic field inside the plasma due to the current in the coil (to avoid disturbing the plasma equilibrium), while it was desirable to have all windings lie on a single toroidal surface for ease of construction. To insure that the magnetic field inside the plasma was zero, the ohmic heating coil was designed to have a flux line coincide with the winding surface[1] (major radius = 45.7 cm, minor radius = 27.0 cm). The positions of the coil windings on this toroidal surface were calculated with the following simple model. A nearly circular flux line at the minor radius of the winding may be produced using only a few symmetrically placed azimuthal ring currents (Figure 3-5). The ring currents can be replaced by an assumed azimuthal sheet current on the winding surface, where the current at any point is taken to be proportional to the magnitude of the field from the ring currents at that point. The field outside the winding surface is then the same as that produced by the ring currents, while the field inside is zero. Breaking this sheet current into finite wires introduces only small error fields into the plasma volume.

The ohmic heating coil was wound on eight wooden frames clamped to the vacuum chamber, using #1 AWG cable. The error fields produced within the vacuum chamber due to this coil were calculated to be less than 1% of the ohmic heating field amplitude at the center of the torus (along the major axis).

The vertical field coils (used to control plasma radial position) were wound on the same frames which supported the ohmic heating coil and were designed to produce a slightly curved field within the plasma volume. The magnetic field index, $\eta = \frac{R}{B_v}\frac{\partial B_v}{\partial R}$, where B_v is the vertical field magnitude and R is the major radius, is a measure of the curvature of the field and was chosen to be

1. Then, from Ampere's law, it follows that the field must vanish inside the winding surface since there are no current sources there.

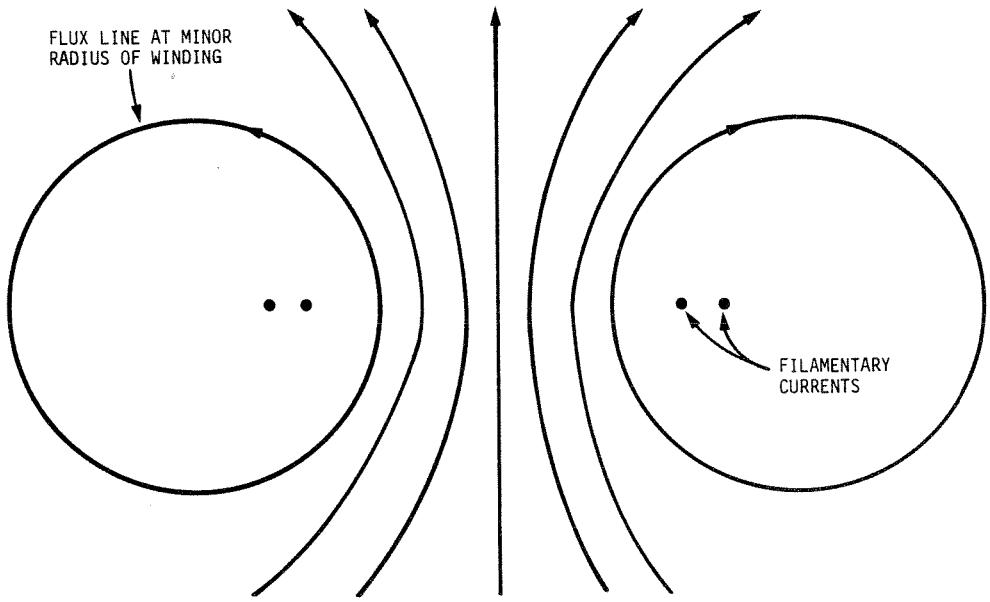

FIG. 3-5. Several flux lines of the ohmic heating field are shown, including the one at the minor radius of the winding. The flux lines are produced by a model consisting of two azimuthal filamentary ring currents of different magnitudes, flowing in the same direction, one at 0.63 R and the other at 0.75 R, where R is the major radius of the torus.

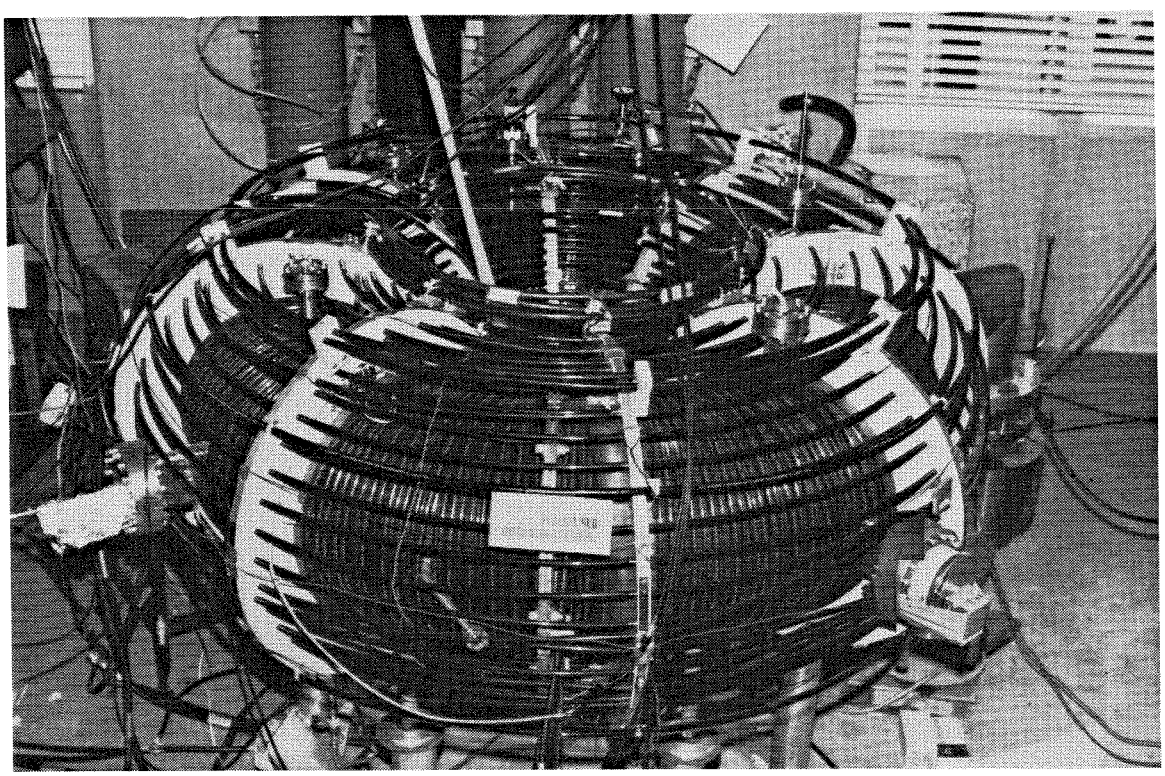

FIG. 3-6. The Caltech Research Tokamak, showing confinement and ohmic heating coils.

about -0.5 on the minor axis of the torus. The coils consisted of 40 azimuthal turns of #1 AWG cable, wound on the same toroidal surface as the ohmic heating coil. The turns were uniformly spaced poloidally, but the 20 turns on the inside ($R < 45.7$ cm) were wired so that the current flow through them was in the opposite direction to that in the 20 turns on the outside ($R > 45.7$ cm).

A photograph of the tokamak, showing the toroidal field, horizontal correction field, ohmic heating, and vertical field coils is shown in Figure 3-6.

3.3 Power Supplies

A tokamak shot involved the firing of a number of power supplies at specified times. A bank of digital timing modules in the power supply room provided easy adjustment of the relative timing. The repetition rate of the tokamak was limited by the toroidal field capacitor bank charging time and was generally set to a one minute cycle.

The sequence of events involved in firing the tokamak began with the switching on of a tungsten filament located in one of the bottom tokamak ports. The filament, biased $10-20$ V negative with respect to the tokamak chamber, provided a supply of free electrons and promoted consistent breakdown of the hydrogen filling gas. Several seconds after the filament was turned on, the toroidal field bank was switched into the toroidal field winding.

Power for the toroidal field coil was provided by a 240 kJ, 10 kV capacitor bank which was capable of providing a maximum field of about 13 kG on axis. Mechanical stresses in the coils became rather large at high fields, however, so in practice the toroidal field was rarely used above 5 kG. The bank was switched by ignitrons, and in order to prevent $L-C$ ringing during the plasma shot, a crowbar circuit was used. An ignitron shorted the toroidal field coil when the current in it reached a maximum, i.e., when the voltage across the

capacitor bank crossed zero after the first quarter-cycle of the $L-C$ ringing (the quarter-cycle period was typically ~9 msec). Thereafter, the dominant parameters of the circuit were the toroidal field coil inductance (L_{tc} = 7 mH) and resistance (R_{tc} = 0.17 Ω). The toroidal field amplitude then decayed exponentially with a time constant $\tau = \frac{L_{tc}}{R_{tc}}$ = 42 msec.

The ohmic heating coil was energized by a power supply which consisted of two capacitor banks, referred to as the "fast" and "slow" banks, which were switched into the ohmic heating coil through ignitrons. The two banks, which had different capacitances and could be charged to different voltages, provided some degree of flexibility in shaping the ohmic heating current waveform.

It was desirable for the ohmic heating field to have a fast initial rise time in order to generate a large electric field in the tokamak chamber to promote complete breakdown of the plasma. Since the rise time of the current was $\tau = \frac{\pi}{2}\sqrt{L_{OH}C_{OH}}$, where L_{OH} and C_{OH} are the inductance of the ohmic heating coil and the capacitance of the bank, respectively, the fast bank had a smaller capacitance and was operated at higher voltages than the corresponding slow bank. The fast bank was fired first (about 2 msec before the peak of the toroidal field current), and the slow bank fired when the voltage on the fast bank had decayed to the point where the voltages on the two banks were equal. The fast bank capacitance was 650 mF and could be charged to a maximum of 2.5 kV, while the slow bank consisted of two halves each of which had a capacitance of 0.22 F at up to 450 V. The two halves of the slow bank could be connected in series or in parallel to provide further flexibility.

Transient supressors were used at each end of the coaxial transmission lines (RG-215) which connected the ohmic heating and toroidal field coils to the power supplies, located in an adjacent room. These simple $R-C$ combinations reduced the voltage spikes which occurred due to reflections from the

impedance mismatch at the ends of the cables.

The vertical field coils were also energized by a power supply consisting of "fast" and "slow" capacitor banks. The fast bank consisted of 2 μF of capacitance, was typically charged to 100 – 200 V, and was discharged into the vertical field coil through an SCR. The slow bank, consisting of 400 μF of capacitance, was charged to 40 – 60 V and was switched into the coil when the voltage on the fast bank had decayed to the level of the voltage on the slow bank. The vertical field fast bank was fired about 100 μsec after the ohmic heating fast bank.

To provide for reliable initial breakdown of the plasma, a 1.5 mF capacitor, charged to 6 - 9 kV, was discharged into the ohmic heating coil about 2 msec before the firing of the main ohmic heating bank. This "preionization" supply resulted in an oscillating current in the ohmic heating coil with a frequency of about 13 kHz and a duration of about 1 msec. The oscillating magnetic flux produced a large toroidal electric field in the tokamak, causing initial breakdown of the gas by accelerating the electrons provided by the tungsten filament.

3.4 Data Acquisition

The data acquisition system was housed in the control cabinet which also included the RF diagnostics electronics (Figure 3-7). The data system evolved through many incarnations, but only the most recent (and that used for most of the experiments described in this thesis) will be described.

The four signals which were generally most useful in diagnosing the plasma global behavior (the one-turn loop voltage signal, the plasma current signal, the soft-UV monitor output, and the microwave interferometer detector output) were recorded on a four-channel waveform recorder (Biomation model

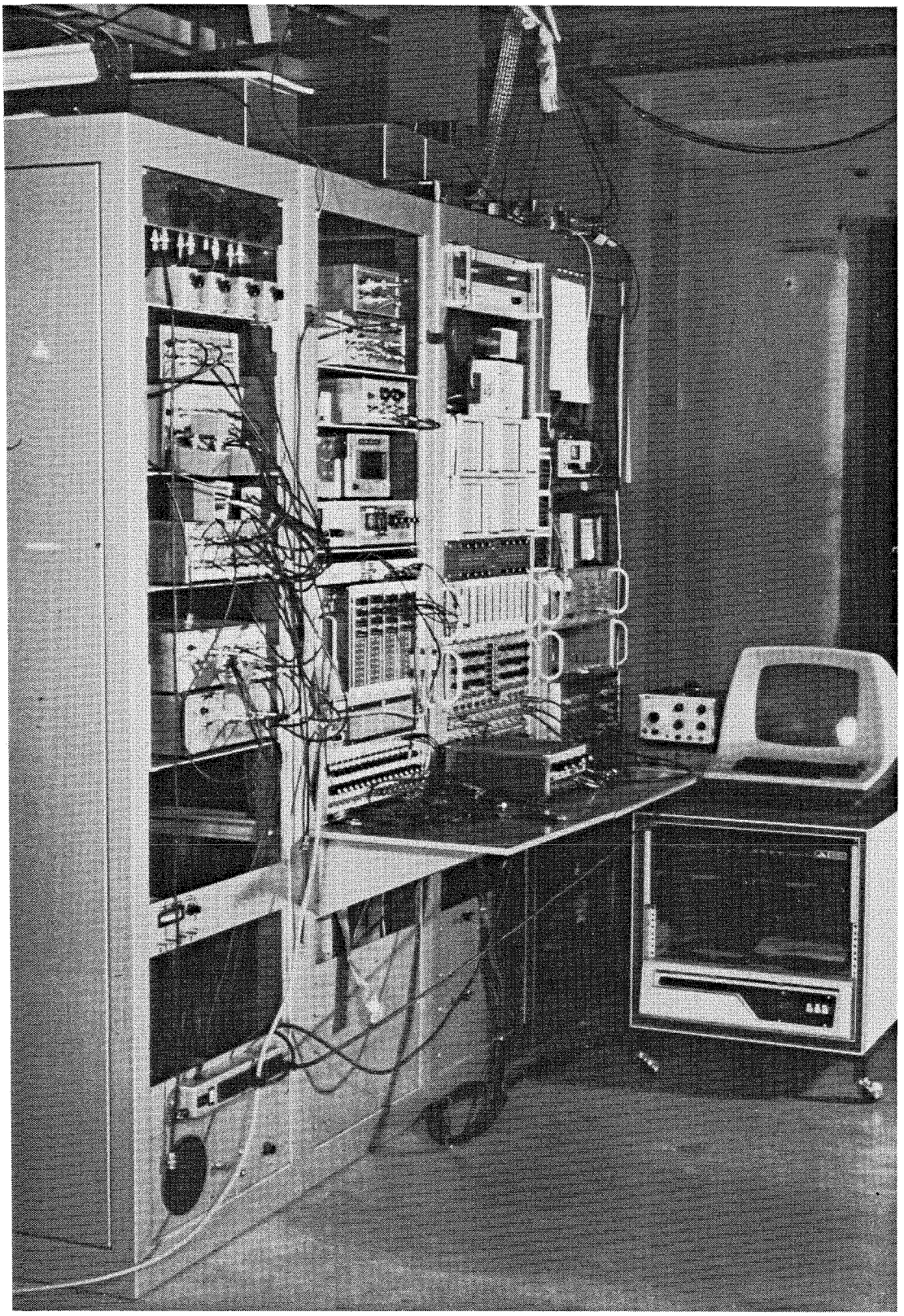

FIG. 3-7. Data acquisition system (center) and RF electronics (left-most cabinet). The dedicated LSI-11 computer is visible at the right.

1015). Each channel had a memory of 1024 bytes and a resolution of 8 bits. The sampling rate of the Biomation recorder was usually set to 50 kHz so that the record length, 20 msec, was sufficient to cover all but the longest plasma shots. The time variation of the above-mentioned signals was quite slow, so that anti-aliasing filters were in general not required. The four channels were displayed on a CRT monitor immediately after each tokamak shot, and an interface allowed transfer of the data to a DEC LSI-11/03 computer which was dedicated to data collection. Data transferred to the computer were stored on floppy disks for later analysis with an LSI-11/23 computer.

A CAMAC crate containing a number of LeCroy A-D modules was used for recording other experimental signals. Two LeCroy model 2264 transient recorders provided up to sixteen channels of 8-bit data recording capability with a record length for each channel of 4 kilobytes and a maximum sampling rate (in the sixteen channel mode) of 500 kHz. A plug-in module for the CAMAC crate[2] allowed display of the sixteen data channels on CRT monitors automatically after the tokamak shot and also permitted transfer of the data to the computer. Because the LeCroy modules had only fixed full-scale inputs of ±256 mV, a series of sixteen buffer-amplifiers with attenuators were constructed which provided calibrated full-scale inputs from 0.2 V to 20.0 V and also included offset adjustments. Twelve of the buffers had -3 db bandwidths of 250 kHz; the other four had bandwidths of 1 MHz. Since the sampling rate used for most of the experiments was either 50 or 100 kHz, low-pass filters (with cut-off frequencies of about 20 and 40 kHz, respectively) were sometimes used to eliminate the possibility of aliasing from higher-frequency signal components.

2. Designed and built by F. Cosso, E.E. (Caltech).

3.5 Diagnostics

A variety of standard tokamak diagnostics for measuring average macroscopic plasma parameters were available; they are described here only briefly (for further information, see DeMichelis [1978] or Cross [1977]).

Plasma current was measured with a Rogowski coil which encircled the chamber poloidally. The signal from the Rogowski coil was proportional to $\frac{\partial I_p}{\partial t}$, where I_p is the net plasma current, and was integrated electronically to provide an output of 0.5 V/kA.

Plasma position (in an average sense) was monitored by "up-down" and "in-out" coils. These coils were similar to Rogowski coils, but the number of turns per unit length was made proportional to $\cos(\theta)$ or $\sin(\theta)$ (where θ is the poloidal angle) with the direction of winding reversing appropriately as the cosine or sine changed sign. The integrated voltage from the coils was divided by the plasma current electronically, and the resulting voltage was roughly proportional to the vertical or horizontal plasma mean-center displacement. The in-out coil was used primarily as an aid in adjusting the charging voltages for the vertical field capacitor banks.

The plasma loop voltage V_p (the "one-turn voltage") is the integral of the electric field in the plasma around the tokamak toroidally. Coupled with the plasma current I_p, this yields a value for the plasma resistance, R_p, from which the electron temperature can be deduced. The loop voltage was measured indirectly using a single loop of wire placed on top of the torus. The voltage V measured by this loop is not the same as the plasma loop voltage, V_p, due to the poloidal flux between the plasma and the wire. The measurement, however, may be used to calculate the plasma resistance from

$$R_p = \frac{V}{I_p} - \frac{1}{I_p^2}\frac{d}{dt}\left(\frac{1}{2} L_p I_p^2\right),$$

where L_p is the effective inductance of the toroidal plasma [Dimock et al., 1973]. The electron temperature is then related to R_p by

$$R_p = 2.09 \times 10^{-3} Z_{eff} \frac{\ln\Lambda}{T_e^{3/2}} \quad (\Omega),$$

where $Z_{eff} = (\sum_\alpha Z_\alpha^2 n_\alpha)/(\sum_\alpha Z_\alpha n_\alpha)$ is the effective atomic number of the plasma (n_α is the density of ionic charge species α, in cm^{-3}, and Z_α is its atomic number), T_e is the electron temperature in eV, and $\Lambda = 1.54 \times 10^{10} T_e^{-3/2} n_e^{-1/2}$. Solution for the electron temperature is carried out by numerical integration.

A microwave interferometer operating at 75 GHz measured the average electron density along a vertical chord through the center of the tokamak. The additional phase shift of the microwave signal passing through the tokamak chamber, due to the presence of the plasma, is approximately

$$\Delta\Phi = \frac{4\pi e^2}{2c\,\omega m_e} \int_{-\rho_0}^{\rho_0} n_e(\xi)\, d\xi ,$$

provided $\omega_{pe}^2(\xi) \ll \omega^2$ for $-\rho_0 \leq \xi \leq r0$. Defining the line-averaged electron density $\bar{n}_e$, it follows that

$$\bar{n}_e = \frac{1}{2a} \int_{-\rho_0}^{\rho_0} n_e(\xi)\, d\xi = \frac{m_e c\, \omega \Delta\Phi}{4\pi e^2},$$

so the electron density is linearly proportional to the phase shift or to the number of fringes observed on the output of the interferometer's crystal detector (one fringe corresponds to a phase shift of 2π radians). For $\frac{\omega}{2\pi} = 75$ GHz, the constant of proportionality is approximately 1.8×10^{12} cm^{-3}/fringe.

The microwave source was a Hughes Impatt oscillator (model 41343H-001) which provided about 75 mW of power and had to be well shielded (see section 4.1.3). The interferometer was constructed from WR-15 waveguide plumbing;

the detector was a 1N53 diode in a Baytron 1V-30 mount. The detector functioned as a homodyne mixer, and the output was proportional to $\sin(\Delta\Phi + \Phi_0)$, where Φ_0 is a constant. One fringe shift therefore corresponded to a change in $\Delta\Phi$ of 2π radians. The *sign* of the phase shift could not, however, be directly determined, and this sometimes led to ambiguity in determining the density evolution during part of a tokamak shot. The art of reconstructing $n_e(t)$ from the interferometer output is discussed by Levine [1980].

Two light detectors were used to provide general indications of impurity levels in the plasma. A visible light detector utilized a phototransistor (Fairchild FPT 120A) with a spectral response from 500 to 1000 nm. This detector was generally mounted on an optical port on the RF antenna feedthru flange and was used to register signs of arcing from the RF antennas. A soft-UV vacuum photodetector [Zweben et al., 1979] was very useful in determining global relative impurity levels. The detector consisted simply of a bare plate of tungsten, located in one of the bottom tokamak ports and appropriately shielded from the plasma. The photoelectric current from the plate was measured and was proportional to the incident flux of UV photons; the response of the detector was roughly from 20 to 120 nm (the "soft" UV region). The detector response during a tokamak shot was apparently largely dominated by radiation from oxygen impurity lines. The magnitude of the signal correlated inversely with the peak plasma current and plasma shot duration: low level signals indicated clean plasmas and vice versa. This diagnostic was used routinely to estimate the relative "cleanliness" of the machine after various probes were introduced.

3.6 Discharge Cleaning

The inside wall of the tokamak was regularly cleaned by procedures

recommended by R. J. Taylor [Oren and Taylor, 1977]. The ohmic heating coils were pulsed with a 3 kW, 30 kHz oscillator for 30 – 50 msec, at a repetition rate of about 2 Hz. During the discharge cleaning, a current of 70 – 80 A was passed through the toroidal field coil, producing a magnetic field on axis of about 150 G and lengthening the confinement time of the plasma. The gas fill pressure was $5 - 10 \times 10^{-4}$ Torr of hydrogen which was admitted to the tokamak, as during regular plasma shots, through a leak valve on the forepump side of the turbopump[3].

Through processes that are poorly understood, the low density plasma knocks low-Z impurities off of the walls of the vacuum vessel. The primary impurities, carbon and oxygen, then combine in the plasma to form methane and water vapor which are pumped out through the turbopump. Although the dynamics of the chemical processes occurring in the plasma have not been well characterized, the overall effect on the tokamak performance is dramatic. Without discharge cleaning, the tokamak plasma shots are limited to a duration of only a few msec and to plasma currents of about 10 kA; after sufficient discharge cleaning, the shots last 10 - 20 msec with currents of up to 35 kA.

Evolution of impurity levels in the tokamak neutral gas during discharge cleaning was monitored with a quadrupole residual gas analyzer (Varian VGA-100); relative impurity levels required for clean operation of the tokamak were established through experience. Daily discharge cleaning of 4 – 6 hours was generally sufficient, but after opening the tokamak to air (to change a probe, for instance), cleaning for 15 – 25 hours was usually necessary.

3. Since the pumping speed of the turbopump was considerably smaller for hydrogen than for higher mass impurities, admitting the gas on the forepump side served to increase the purity of the gas reaching the tokamak.

3.7 Gas Puffing

When the tokamak was fired, the plasma density rose rapidly (<1 msec) to a peak value of $5-10\times10^{12}$ cm^{-3}. The density then decayed over a period of about $1-2$ msec to a level of $\sim10^{12}$ cm^{-2} where it remained for the rest of the shot. The peak density was smaller by a factor of $2-3$ than what would be expected if all of the hydrogen gas in the chamber were ionized: a typical filling pressure of 3.5×10^{-4} Torr[4] would yield an electron density of 2.5×10^{13} cm^{-3} if fully dissociated and ionized (the volume of the tokamak was 237 liters). Since optical measurements indicated a nearly fully ionized plasma, the discrepancy was probably due to hydrogen being driven into the tokamak walls or into the ports. There was some evidence that the background neutral gas pressure in the ports rose during the plasma shot.

The density fall following the initial rise was presumably due to the loading of the inner wall with hydrogen. In order to increase the plasma density again, a fast-opening (~1 msec) piezoelectric gas valve (Veeco model PV-10) was installed. The valve was located on one of the bottom tokamak ports, and was connected to a hydrogen reservoir which was typically kept at a pressure of $500-800$ Torr. The duration and temporal position of the voltage pulse which opened the valve were controlled by two digital timing modules. The valve was typically pulsed for $2-8$ msec, beginning $2-5$ msec after the start of the tokamak shot.

The additional gas introduced by the piezoelectric valve was quickly ionized by the plasma and caused the plasma density to rise. A short pulse of gas typically resulted in an approximately linear rise in density, over a period of $3-6$ msec, up to a peak of $1.0-1.5\times10^{13}$ cm^{-3}. While the density rise after gas

4. The ionization gauge used to measure gas pressure in the tokamak was calibrated for nitrogen; its sensitivity for hydrogen gas was smaller by a factor of about 0.43. This pressure, and all other pressures reported in this thesis, are ***corrected*** ion gauge pressures.

puffing was fairly reproducible from shot to shot, the subsequent fall in density sometimes was not. With a clean machine, the density decay would occasionally virtually mirror the rise; more often, however, the fall was much more abrupt. Gas puffing also shortened the overall plasma lifetime. Without gas puffing, shot lengths of 20 msec were easy to obtain; with gas puffing to a density of about 10^{13} cm^{-3}, the maximum shot lengths were 10 – 15 msec.

3.8 Plasma Characteristics

Records of the one-turn voltage, the plasma current, the soft-UV monitor output, and the plasma density for a typical clean tokamak shot (with gas puffing) are shown in Figure 3-8. For comparison, a shot in which a contaminated probe was in the plasma is shown in Figure 3-9.

The one-turn loop voltage is a useful monitor as it provides confirmation of the proper firing of the ohmic-heating fields. The first oscillation observed, at around $t = 1.5$ msec, is due to the preionization capacitor being discharged into the ohmic heating winding. About one msec later, the loop voltage signal goes off scale; this results from the fast bank being fired. After an interval of another msec, the fast bank voltage has decayed sufficiently that the slow bank fires; this transition is evident on the trace. Misfirings due, for instance, to insufficient preionization voltage or a faulty ohmic heating supply ignitron are easily diagnosed using the loop voltage signal.

The plasma current increases abruptly (within about 0.5 msec) to a level of 10 – 15 kA immediately after the ohmic heating fast bank is fired. The current then increases slowly over a period of 3 – 5 msec, peaks at a current of 20 – 30 kA, and begins to decrease. In a clean tokamak, the current decay is smooth; in a dirty machine the decay is much more abrupt and the plasma shot length is decreased.

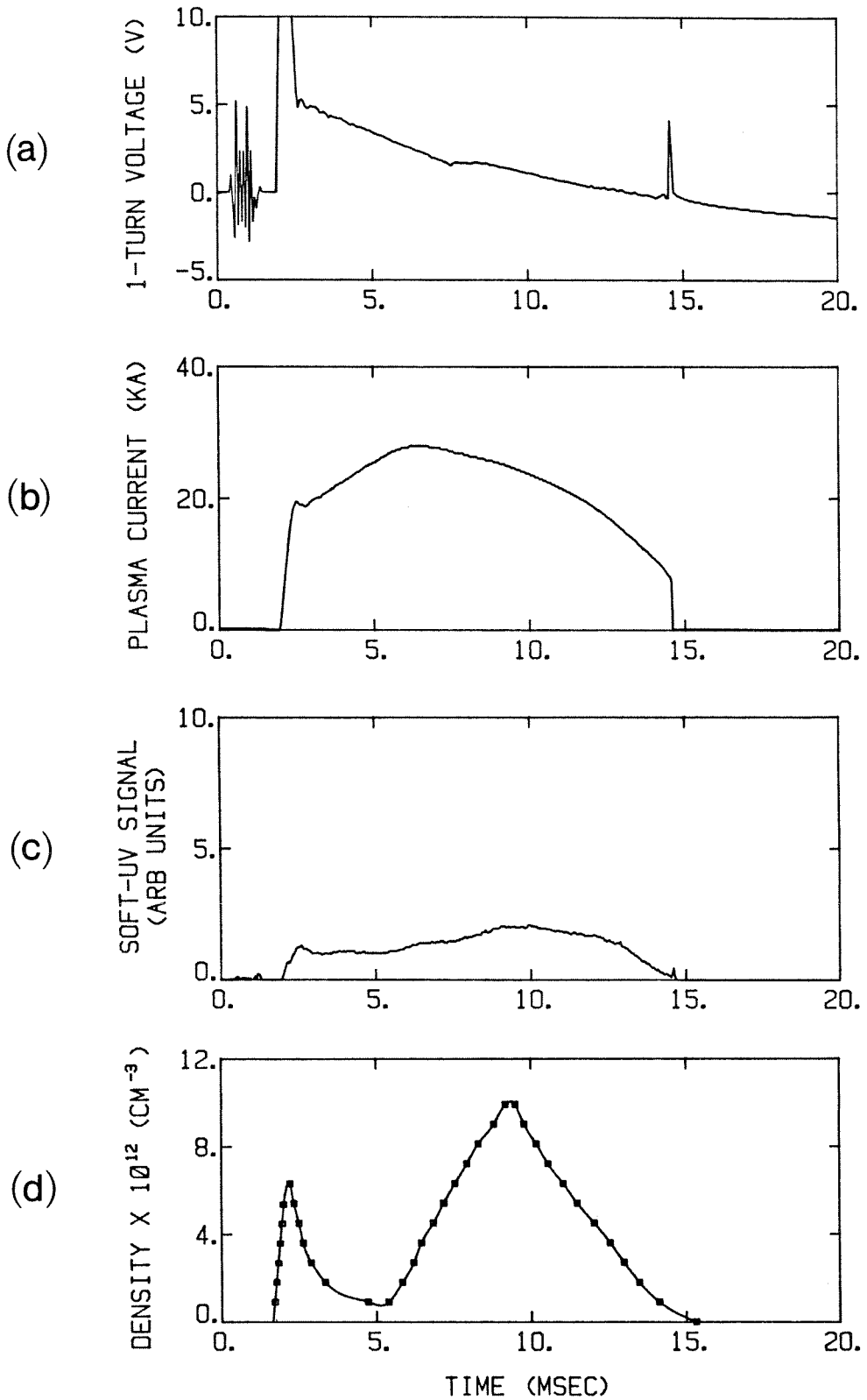

FIG. 3-8. Typical "clean" plasma discharge. a) One-turn loop voltage. b) Plasma current. c) Soft-UV signal. d) Plasma density, derived from the interferometer output. Squares indicate half-fringe increments.

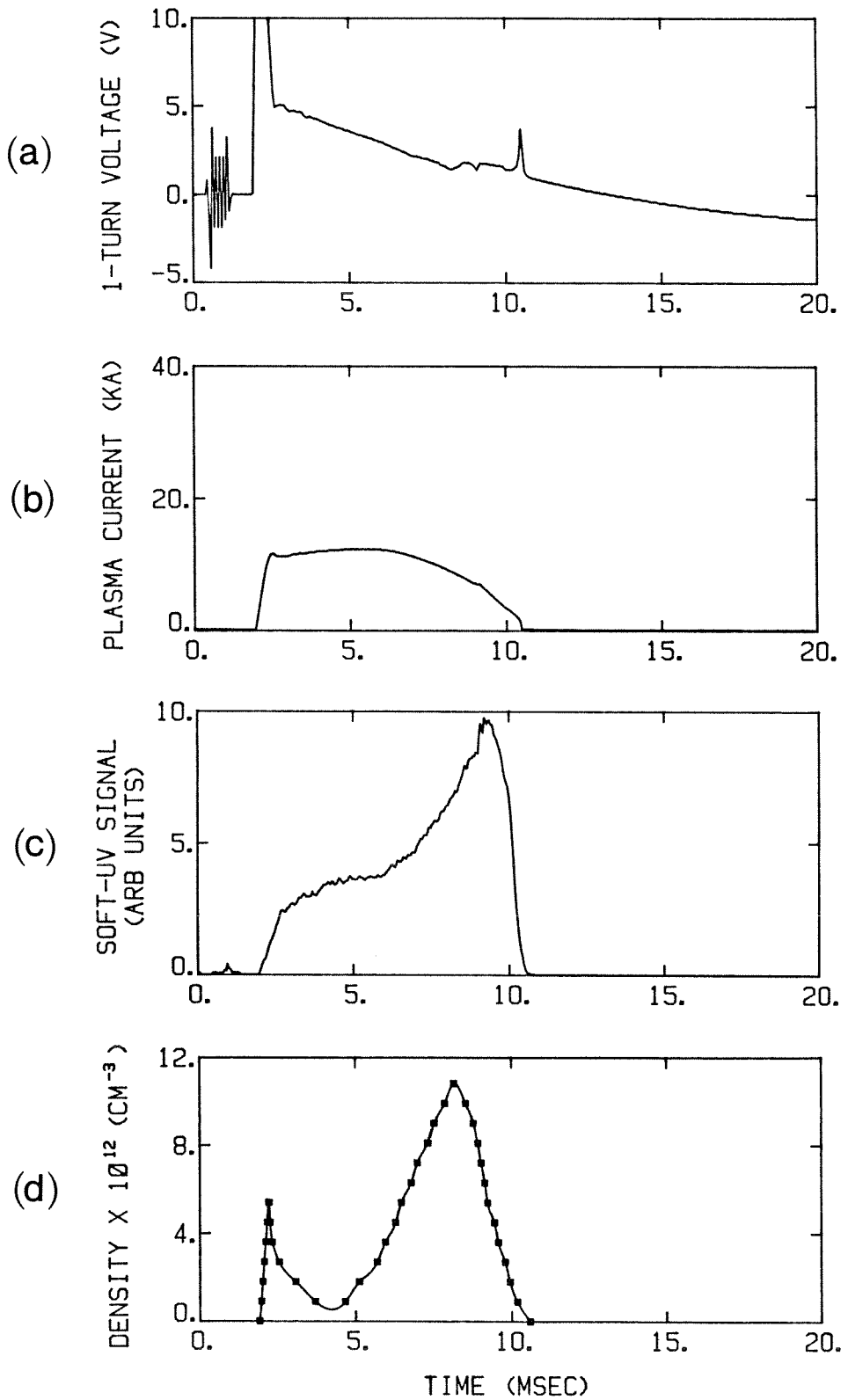

FIG. 3-9. Typical "dirty" plasma discharge. a). One-turn loop voltage. b) Plasma current. c) Soft-UV signal (units are the same as in Figure 3-8c). d) Plasma density.

The soft-UV signal is the most useful indicator of the impurity level of the machine. When the tokamak is clean, the signal is small and varies slowly during the plasma shot, roughly following the plasma density evolution. In a contaminated machine, however, the UV signal is much larger and may increase dramatically throughout the abbreviated plasma shot. The behavior shown in Figure 3-9 is often characteristic of a probe "burning up" in the plasma.

The density evolution shown in Figure 3-8 is characteristic of a clean plasma discharge; the gas puff causes a linear increase in density up to a peak of around 10^{13} cm^{-3} followed by a similar density decay. The density evolution of the dirty discharge shows a fast increase and an abrupt fall. Occasionally dirty discharges yield very high peak densities but the shots are rarely repeatable.

Reproducibility of even a clean tokamak discharge was sometimes a problem. Typically, about 10% of the shots during a run simply did not form a plasma due to failure of one of the ignitrons to fire properly. About 15% of the remaining shots were usually unsatisfactory because their density or current evolution were abnormal.

3.9 Charge-Exchange Diagnostic

3.9.1 Introduction

An estimate of the ion temperature in the Caltech Research Tokamak was obtained using a charge-exchange diagnostic. Neutral atoms of hydrogen within the plasma undergo charge-exchange collisions with energetic ions ($H + H^+ \rightarrow H^+ + H$) resulting in a population of neutral atoms with an energy distribution similar to that of the plasma ions. The energetic neutrals are not confined by the magnetic field and their spectrum can be measured outside the tokamak.

Although the tokamak plasma is nearly fully ionized, there is always a small background of neutral hydrogen, even at the plasma center [Goldston, 1982]. These neutrals arise from desorption of gas from the tokamak wall and from recombination. Neutrals diffusing into the plasma from the wall region are generally cold ($T<5$ ev) and have short mean free paths for electron impact ionization. Before being ionized, however, they can undergo charge-exchange collisions with the hotter plasma ions (since the rate coefficient for charge-exchange is larger than that for impact ionization at energies less that $\sim$10 keV). The charge-exchange reactions produce energetic neutrals which can penetrate farther into the plasma and undergo further charge-exchange reactions. Through this cascade of charge-exchange reactions, cold neutrals from the wall can reach the hot plasma core.

The neutral particle energy spectrum, observed with a diagnostic outside the plasma, is related to the ion energy distribution, but interpretation is complicated by a number of factors. The spectrometer sees a chord through the plasma and hence receives neutral particles which were "born" throughout the plasma. The plasma density and temperature are peaked at the center, while the neutral atom density is largest at the periphery. Furthermore, neutrals produced through charge-exchange collisions in the plasma may be attenuated on their way out by impact ionization or further charge-exchange.

Most of the charge-exchange neutral flux received by the diagnostic arises from the low temperature region near the plasma edge. Hence, to observe the charge-exchange energy distribution characteristic of the core plasma, it is necessary to look at the high-energy part of the spectrum, i.e., energies greater than that corresponding to the plasma core temperature [Eubank, 1979].

If the neutral particle distribution was uniform and homogeneous in space and Maxwellian in energy, the energy distribution of the flux entering the charge-exchange spectrometer, $F(E_\perp)$, would be simply proportional to

$\sqrt{E_\perp}\, e^{-\frac{E_\perp}{kT_i}}$, where T_i is the ion temperature, k is Boltzmann's constant, and $E_\perp$ is the kinetic energy component along the chord which the spectrometer views. A plot of $\frac{1}{E_\perp}\ln\left[\frac{F(E_\perp)}{\sqrt{E_\perp}}\right]$ then yields a straight line of slope $-\frac{1}{kT_i}$ from which the temperature is found. In practice, this is what is generally plotted from the charge-exchange data [Afrosimov et al., 1961; Eubank, 1979] although the resulting curve is, not surprisingly, generally not a straight line. In fact, observations on tokamaks often yield a "two-temperature" distribution resembling a broken line with two slopes, the higher slope (i.e., lower temperature) part of the curve occurring at lower energies. This form of spectrum apparently results from the inhomogeneous density and temperature profiles present in the actual tokamak [Parsons and Medley, 1974]. In particular, the large number of low-energy atoms which undergo their final charge exchange reaction (i.e., the last before emerging from the tokamak and being detected) in the outer edge of the plasma (where the neutral density is highest) are responsible for the large flux observed at low energies. The high-energy part of the spectrum is thought to be representative of the central ion energy distribution.

3.9.2 Design and Construction

A neutral particle spectrometer was constructed in order to measure the energy spectrum of the neutral flux from the Caltech Research Tokamak. In general, these devices function by converting the neutral atoms back into ions (once they are outside the magnetic fields of the tokamak) and performing energy analysis on the ions. The neutrals are ionized by passing them through a "stripping cell" containing a relatively high pressure of some gas such as hydrogen, nitrogen or helium, or through an oven containing an alkalai metal vapor such as cesium. Inelastic scattering results in ionization of some

fraction of the neutrals (through a reaction such as $H + N_2 \rightarrow H^+ + N_2 + e^-$) and the ions are then dispersed in energy by any of a variety of schemes. Energy dispersion has been accomplished using electrostatic deflection (parallel plate analyzers, cylindrical analyzers, etc.), using combined electric and magnetic fields (when mass-sensitive energy dispersion is required), and using time of flight measurements.

The ions must be detected after energy selection, and this is usually accomplished with a channeltron [Barnett and Ray, 1972] or via secondary electron emission from a metal target [Fleischmann and Tuckfield, 1968]. The channeltron [Goodrich and Wiley, 1962] is a high gain ($\sim 10^8$) tubular continuous electron multiplier which has a high efficiency for counting a wide variety of particles (e.g., electrons, ions, and photons). The mouth and inside of the tube are coated with a material which has a high secondary electron emission coefficient; a potential of about 2.8 kV is applied between the ends of the device, with the mouth of the channeltron biased negative with respect to the other end. Incident particles striking the funnel-shaped mouth of the tube generate secondary electrons which are then accelerated through the tube, making multiple collisions with the wall. A single incident particle results in an output pulse containing about 10^8 electrons, which are detected with a collector cup near the end of the tube.

The neutral atom spectrometer constructed for the Caltech Research Tokamak[5] followed a design first described by Barnett and Ray [1972]. A schematic of the spectrometer is shown in Figure 3-10. The spectrometer was attached to port #7 of the tokamak (Figure 3-2). A turbomolecular pump (with a speed of 450 liters/sec) and a series of baffles maintained the pressure in the charge-exhange spectrometer chamber during operation at about 5% of the

5. Part of the neutral particle spectrometer system was manufactured by Z. Lucky Enterprises, Los Angeles, Ca.

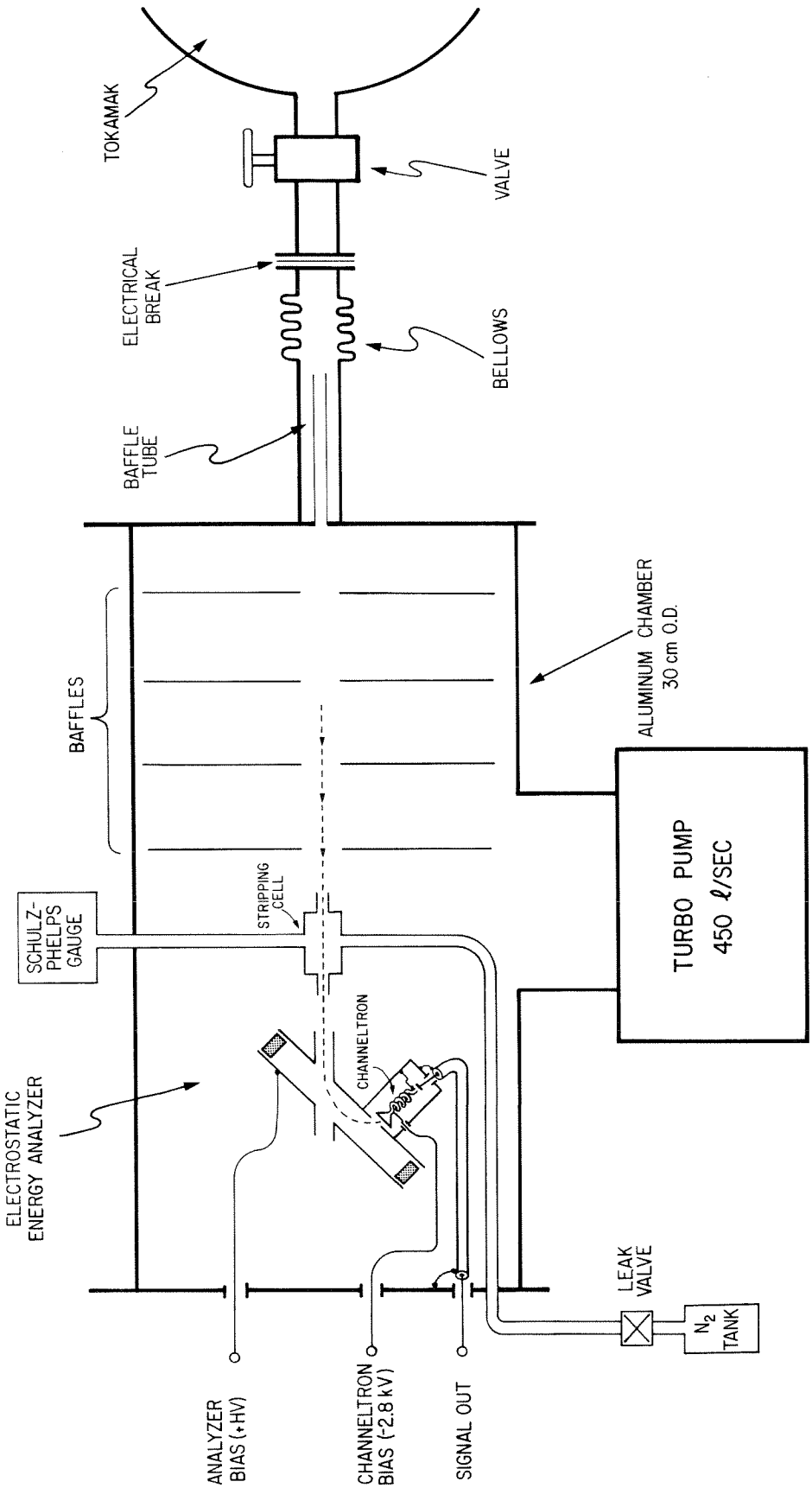

FIG. 3-10. Schematic diagram of the charge-exchange spectrometer.

pressure in the tokamak. Neutral atoms from the tokamak were collimated and entered the nitrogen stripping cell which was fed continuously from a reservoir through a leak valve. The pressure in the stripping cell was monitored approximately by a Schulz-Phelps ionization gauge; the cell was usually operated at a pressure of about 2×10^{-3} Torr.

Ions emerging from the stripping cell then passed into a 45° parallel plate electrostatic energy analyzer. This type of analyzer, first described by Harrower [1955], utilizes a uniform electric field created by applying a potential between the two plates. The plate closer to the stripping cell was grounded to the chamber wall, as was the stripping cell itself. Ions entering the input aperture travel in parabolic paths, and those with energies within a specific range emerge through the exit aperture. The energy of those ions that exit the analyzer is linearly proportional to the potential difference between the plates; the relation is $U_0 = q_i V_b \frac{s}{2d}$, where U_0 is the kinetic energy of the ion entering the analyzer, V_b is the bias potential, d is the separation between the plates, s is the linear distance between the input and exit apertures, and q_i is the ion charge. For the analyzer constructed here, the relation is $U_0 = 1.5 e\ V_b$. The resolution of the analyzer depends on the size of the apertures, on the spacing between them, and on the range of angles the incident particles make with respect to the entrance aperture. For the analyzer described here, the relative energy resolution was calculated to be better than 12%. A channeltron (Galileo model 4039) faced the exit aperture; it was mounted within a shielded box to reduce background noise from UV photons.

The energy spectrum was obtained by varying the analyzer bias from shot to shot. (Some experiments using a fast (=1 msec) high voltage sweeper were also performed, but the total particle flux was too small to provide adequate counting statistics.) In order to relate the signal from the channeltron to the actual energy spectrum of the incoming neutrals, the energy dependence of

each component of the system had to be examined. The cross section for ionization in the nitrogen stripping cell was strongly dependent on the neutral particle energy, decreasing rapidly below about 1 keV. Calibration curves for the stripping efficiency between 10^2 and 10^4 eV were presented by Barnett and Ray [1972] and were used here in unfolding the spectrum. The energy dependence of the parallel plate analyzer has already been discussed, but that of the channeltron must be considered. For a channeltron operating with its entrance aperture at ground potential, the counting efficiency drops off rapidly below about 800 eV [Iglesias and McGarity, 1971]. The technique of preacceleration [Burrous et al., 1967] greatly reduced this energy dependence. The channeltron was simply biased so that the mouth of the multiplier was at a potential of -2.8 kV with respect to the grounded plate of the analyzer. Then any ions emerging from the exit aperture received an additional 2.8 keV of energy before striking the channeltron. Burrous et al. [1967] have measured the relative efficiency as a function of incident proton energy for a preaccelerated channeltron detector and found a variation of less than 10% between 200 eV and 18 keV.

The exit end of the channeltron was grounded; the collector was a small copper cap suspended about 1 mm from the end of the channeltron tube. Because of decreased gain at high input fluxes, the channeltron was used in a pulse counting mode. A discriminator followed by a one-shot multivibrator and a low-pass filter was used to insure that each detected ion contributed equally to the output signal. The electronics limited the maximum counting rate to about 1 MHz.

A photograph of the tokamak lab which shows the installed charge-exchange spectrometer is shown in Figure 3-11.

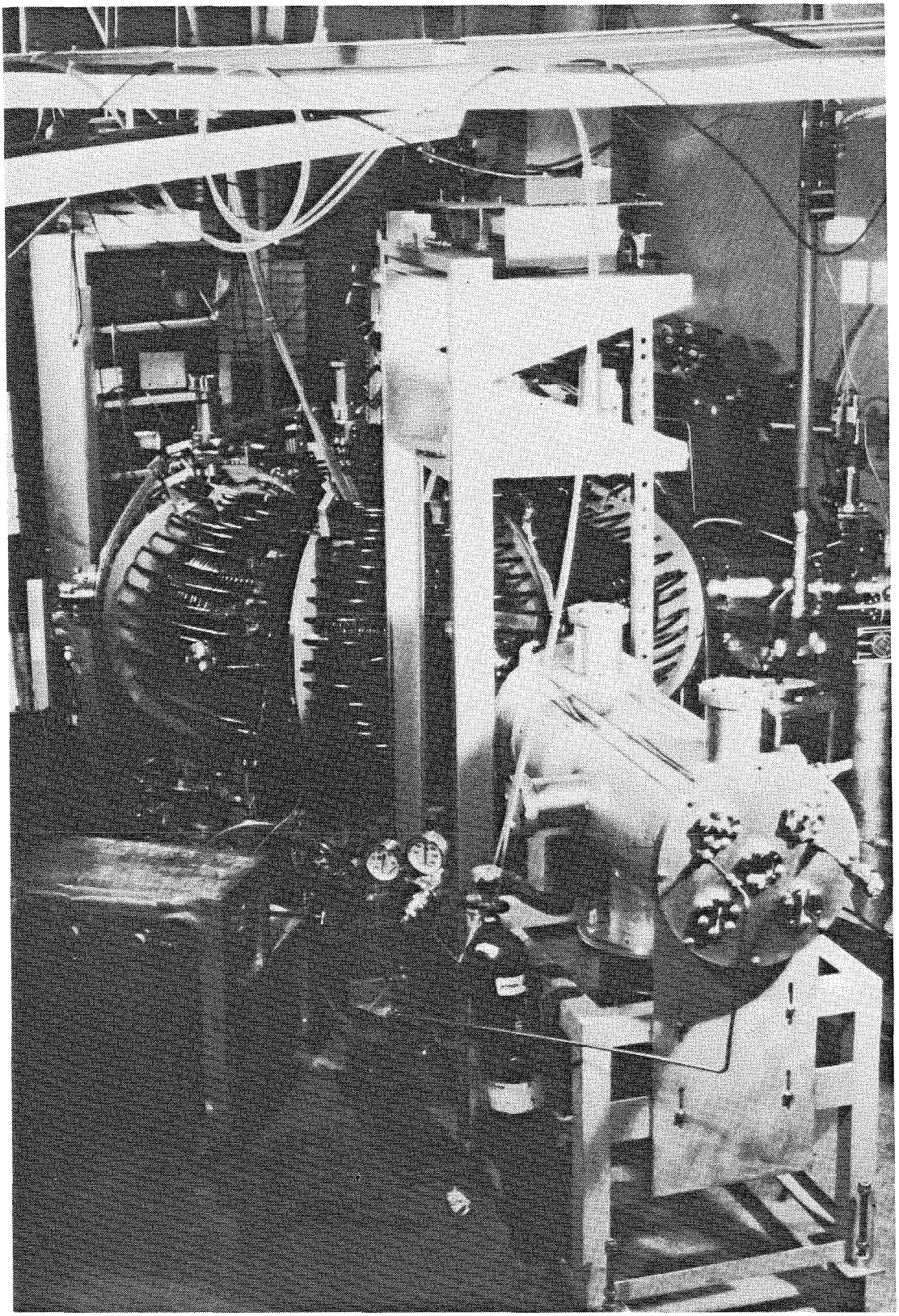

FIG. 3-11. The tokamak lab, showing the charge-exchange spectrometer (the cylindrical chamber at lower right) attached to the tokamak. The RF antenna port is on the right side of the tokamak.

3.9.3 Operation

No problems were observed with contamination of the tokamak from nitrogen from the stripping cell. In fact, the nitrogen peak on the residual gas analyzer did not change noticeably when the charge exchange system was opened to the tokamak, indicating that the differential pumping of the chamber was adequate.

A series of tokamak shots was recorded while changing the analyzer bias between 100 V and 600 V in increments of 50 V; about 4-6 shots were recorded at each voltage. Typical shots at analyzer voltages of 150 and 400 V (corresponding to particle energies of 225 and 600 eV, respectively) are shown in Figures 3-12 and 3-13. Consider the charge-exchange signal in Figure 3-12. The peak at around 4.5 msec corresponds to the density minimum following the initial gas breakdown. As the gas puffing begins to increase the plasma density, the charge-exchange signal decreases initially but reaches a minimum at around 6.5 msec (while the plasma density is still rising) and increases again. Figure 3-13 shows almost the same initial rise and fall of the charge-exchange signal, but the magnitude of the signal after the gas puff begins is substantially lower; this implies cooling of the plasma due to the gas puff.

The full charge-exchange spectrum was plotted out for two points in the discharge: at the density minimum occurring at around 4.5 msec, and at the density peak occurring at around 8.5 msec. The results are shown in Figure 3-14; the characteristic "two-temperature" spectrum is evident. The energy spectra coincide for low energies but diverge for energies above about 350 eV. Fitting a straight line (by least squares) to the higher-energy parts of the two curves yields an estimated ion temperature of 80 eV for the high density case and 130 eV for the low density case. Hence the gas puffing cools the plasma substantially. Measurements by Levine [1980] of the electron temperature (from the plasma resistivity) also indicate a decrease in temperature as the

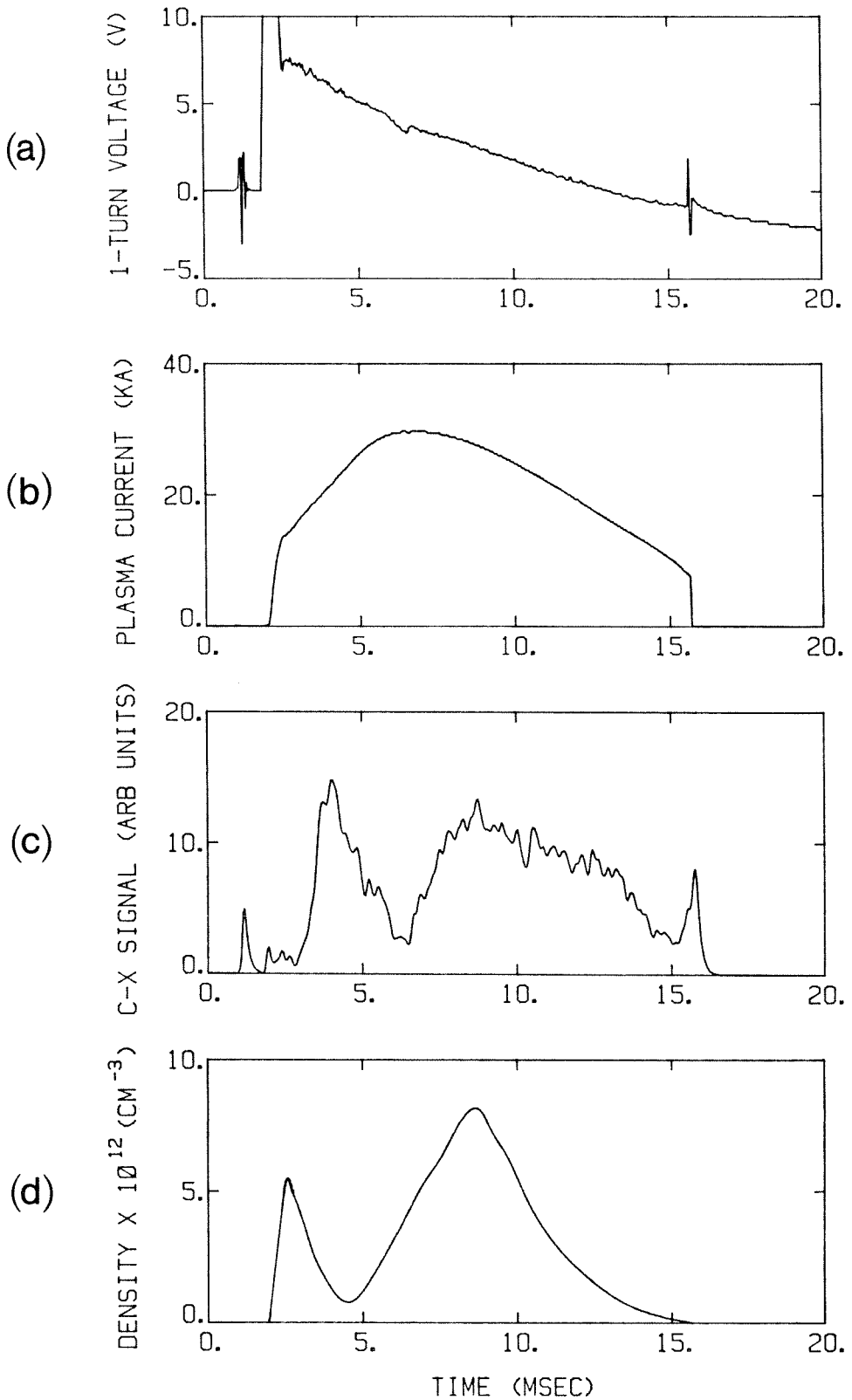

FIG. 3-12. Typical tokamak shot; analyzer bias = 150 V. a) 1-turn voltage. b) Plasma current. c) Charge exchange spectrometer output signal (from discriminator). d) Plasma density (from microwave interferometer).

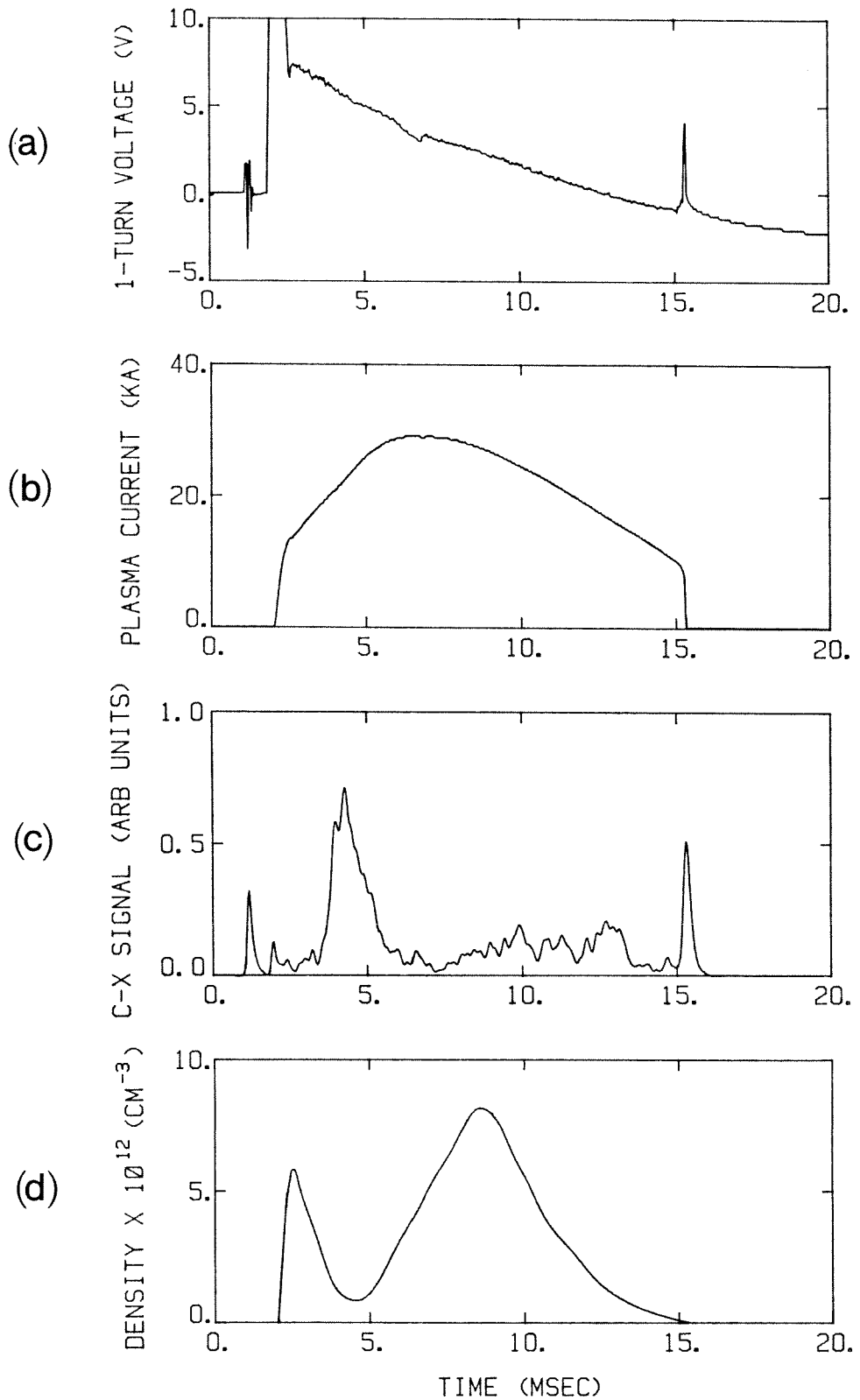

FIG. 3-13. Typical tokamak shot; analyzer bias = 400 V. a) 1-turn voltage. b) Plasma current. c) Charge exchange spectrometer output signal (from discriminator). d) Plasma density (from microwave interferometer).

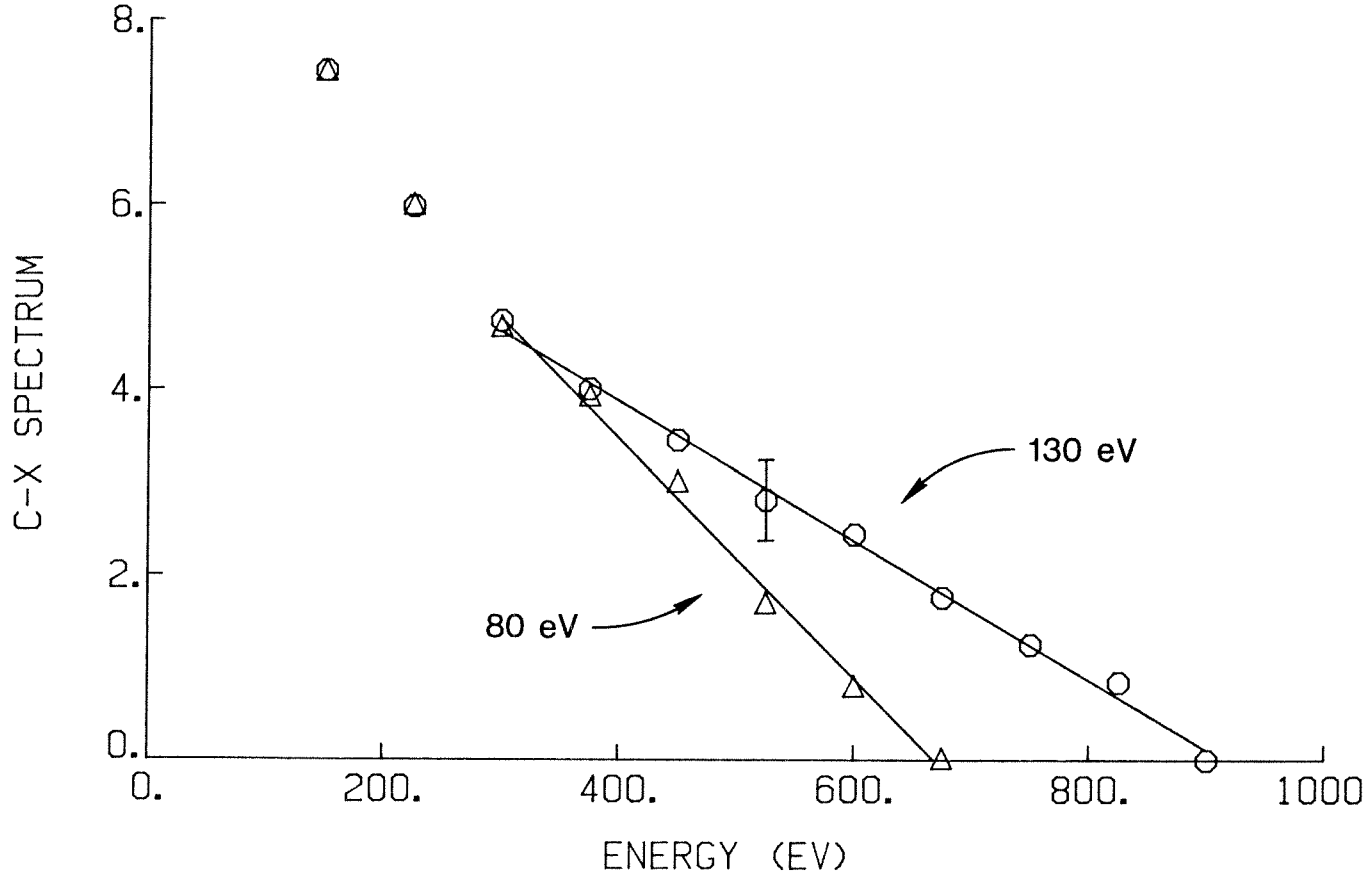

FIG. 3-14. Plots of the charge exchange spectrum at low density (○) and high density (△) points during the discharge. Vertical axis is $\ln[F(E)/\sqrt{E}]+C$, where $F(E)$ is proportional to the counting rate of the spectrometer (corrected for the stripping cell efficiency) when the analyzer bias is set for energy E, and C is an arbitrary constant. Least-squares fits to the high energy part of the curves yield temperatures of 130 eV (low density) and 80 eV (high density).

density increases during gas puffing under similar circumstances: the decrease noted was 22%, a somewhat smaller change than that observed for the ions.

CHAPTER 4

RF Apparatus

A large quantity of RF equipment was constructed by the author during the course of these experiments because the required devices were generally not commercially available. A number of changes also had to be made in the tokamak and its electrical systems and diagnostics in order to permit operation of the RF experiments. This chapter describes the design, construction and installation of the RF system, including the high-power amplifier, directional coupler, impedance-matching system, and amplitude and phase detectors.

4.1 RF System Design

4.1.1 RF Exciters

Several different RF amplifiers were used in these experiments. The signal source, gating circuitry, and first stage of amplification were the same in all cases, but the output stages varied depending on the application.

The RF signal generator was a Hewlett-Packard 8601A which provided an output of up to 20 dbm (referenced to 50 Ω). The signal was gated by an RF switch consisting of a double-balanced mixer (Minicircuits model ZAY-3) whose IF port was driven by a square pulse from a pulse generator (Systron-Donner model 101). The generator, which had easily adjustable pulse width and delay controls, could be triggered by a low-frequency signal generator (0.001 - 10 Hz) for testing purposes. During an experiment, it was triggered, via a fiber-optic

link, from a timing module in the tokamak power supply room.

The output from the RF switch passed through a series of three 50 Ω RF attenuators which provided 0 - 100 db attenuation in 0.1 db steps. The signal was then amplified by a broadband (0.15 - 300 MHz), 10 W, 40 db gain amplifier (ENI model 411LA) and was passed through a 30 MHz low-pass filter (Miller model C-511-T) to attenuate harmonics generated by the RF switch. At this point, the signal could be amplified by one of three systems, or it could be used directly.

For low-power wave propagation and impedance measurement experiments, the RF pulse was amplified by a 300 W broadband (0.35 - 30 MHz) power amplifier (ENI model A-300). This amplifier was very convenient to use as it required no tuning and was unconditionally stable (i.e., stable for arbitrary load impedance).

For operation at higher power levels (up to 1 kW), an amateur-radio linear amplifier was employed (Dentron Clipperton-L). The signal was amplified to an appropriate driving level (~60 W) by a 100 W broadband (7 - 30 MHz) linear amplifier (Marko model 100), passed through another harmonic attenuation network, and was fed to the Dentron input. The Dentron amplifier utilized four 572B tubes in parallel in a grounded-grid design, with an untuned input and a π-network output tank circuit. The output networks for the 40 and 20 meter bands were modified to allow operation from 8 - 12 and 14 - 16 MHz. In addition, power supply regulation was improved substantially to reduce 60 Hz modulation of the output.

For operation at power levels up to 100 kW, a high power class C amplifier was constructed (section 4.2). The 1 kW RF source described above was used to drive the larger amplifier. Both the high power amplifier and the driver system components were housed in a large cabinet in a room adjoining the tokamak lab. Approximately 20 m of RG-17 50 Ω coaxial cable connected the high power

amplifier to the impedance-matching network which was mounted on the end of the antenna feeder tube; RG-8 was used to connect the lower-power systems.

Directional couplers were used to monitor forward and reflected power, both at the output of the amplifier system being used and at the input of the impedance-matching box. For power levels lower than 1 kW, Bird model 4266 dual broadband couplers (-30 db, 2 - 32 MHz) were used; for the high-power amplifier, a special dual coupler was built into the RG-17 transmission line itself (section 4.3).

4.1.2 System Grounding

Identification and elimination of ground loops throughout the RF generator, tokamak, and data acquisition systems was a tedious but essential task. Large transient magnetic fields are present throughout the laboratory during a tokamak shot, largely from the preionization and ohmic heating power supplies. Topological loops formed by multiple grounding connections or by the interconnecting shields of coaxial cables can lead to pickup of spurious signals. The changing magnetic flux intercepted by such a loop generates an EMF around the loop which can be falsely interpreted as a genuine signal.

The pickup problem was serious enough to require complete reconfiguration of the tokamak laboratory grounding system. The tokamak vacuum vessel was connected directly to the building earth ground in the power supply room via a 2.5 cm diameter copper tube. This was done in order to reduce the danger from a potential catastrophic failure of the toroidal field winding insulation which could result in an arc to the vacuum chamber. This connection formed the only path from the chamber to the building ground. The power supplies of equipment which had to be connected to the vacuum chamber (i.e., the tokamak turbopump, the data acquisition system console,

and the RF source cabinet) were isolated from the building ground using electrostatically-shielded isolation transformers. The chassis ground of the data aquisition console was connected to the tokamak system ground by a 3.8 cm diameter copper tube which attached to the RF impedance-matching box. The RF source cabinet ground was connected to the tokamak system ground only through the sheath of the RF output transmission line which also attached to the impedance-matching box. A schematic of the grounding system is shown in Figure 4-1.

The only signal cables whose sheaths were required to make contact with the tokamak vessel (and thus form ground loops) were those running from the data acquisition system console to the impedance-matching box (i.e., cables for forward and reflected voltage, and RF antenna current and voltage signals). The potential ground loops that these cables could form was avoided by routing them through the copper tube that provided the chassis ground connection, and by bundling them tightly together.

All other signal cables leading to tokamak diagnostics were isolated from making electrical contact with the tokamak vessel. The plasma current, loop voltage, and visible light monitors did not require physical connection to the tokamak vessel; mylar washers at waveguide junctions isolated the microwave interferometer. The vacuum flange that housed the UV light monitor was isolated from the tokamak chamber by a teflon spacer; the magnetic probes were also isolated from the chamber.

4.1.3 RF Shielding

Interference and pickup from the RF generator also caused significant problems, particularly at high power levels. Initial operation with the high power amplifier generally saturated most of the tokamak diagnostics. Two approaches were taken to eliminate these problems: reduction of the RF

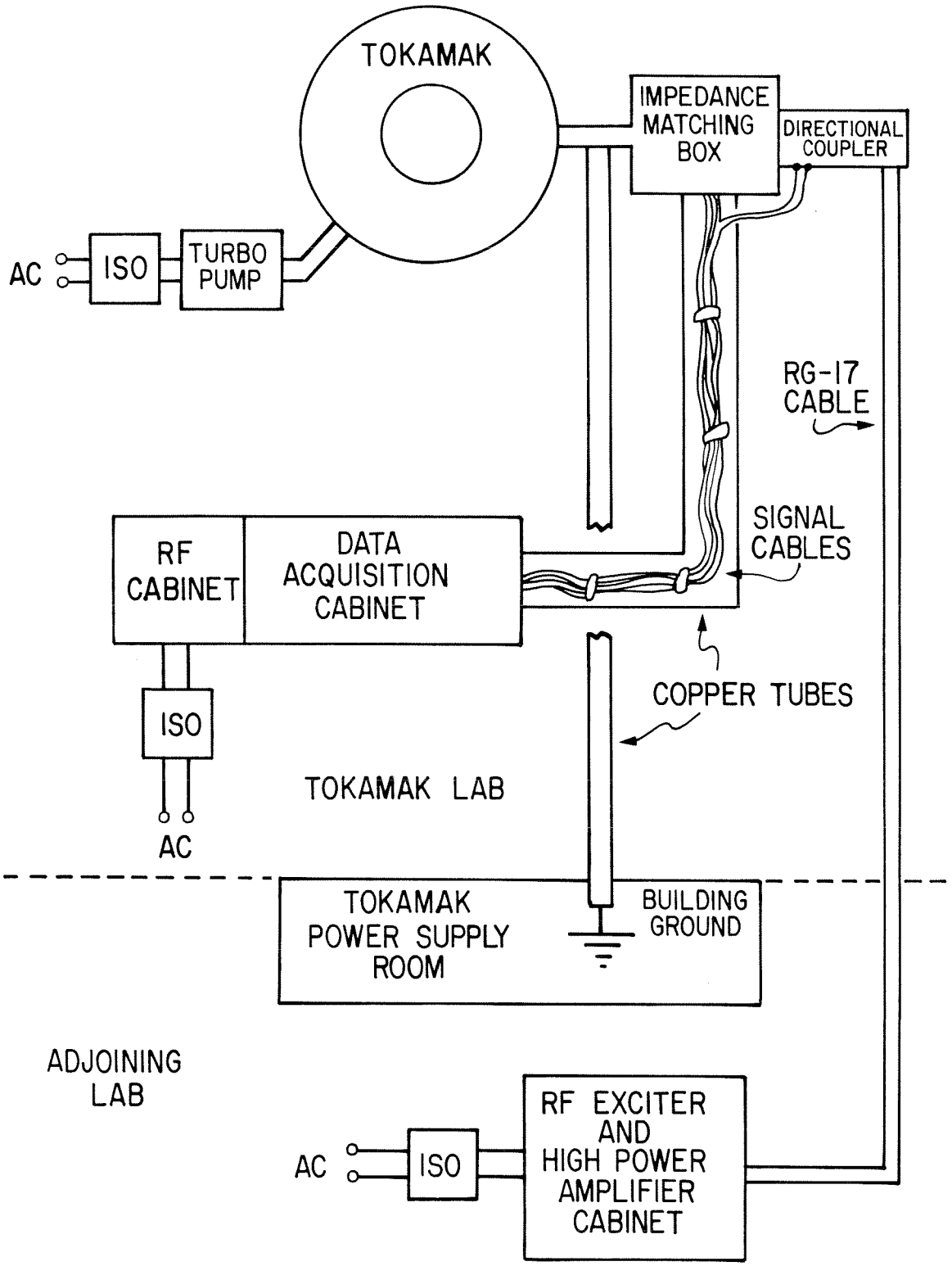

FIG. 4-1. Grounding configuration of tokamak and RF system. ISO = electrostatically-shielded isolation transformer with RF bypass filter.

leakage, and shielding of the diagnostics and data acquisition system.

RF leakage can occur at joints in the amplifier cabinet or impedance-matching box, at the terminating connectors of the transmission line connecting the two, from the transmission line itself, or from the antenna-tokamak assembly. Radiation from imperfect electrical contact between the frames of the cabinets and their covers was minimized by using wide mating surfaces (generally 5 cm) and fastening them with closely spaced screws. Critical joints in the amplifier cabinet were sealed with a conductive RF caulk.[1]

The vacuum O-ring seal assembly through which the antenna tube passed into the tokamak was found to be a path through which RF currents were flowing, giving rise to substantial radiation. Nylon bushings had been installed in the O-ring holders to prevent scoring of the antenna tube; these actually insulated the tube from the tokamak chamber and resulted in the antenna "floating" with respect to the tokamak wall. This problem was solved by installing a spring-finger grounding assembly, at the end of the tube, which provided a very good RF seal to the tokamak port.

RF pickup through the data acquisition system, the tokamak diagnostics, and the RF electronics cabinet (containing amplifiers, amplitude and phase detectors, and physically connected to the data acquisition cabinet) was investigated by exciting, at low power, a dipole antenna which was strung across the lab. This flooded the lab with RF radiation and its effect on the various electronic systems could be easily observed. EMI filters (Corcom model 10R1) were added to the power supplies of all of the electronic systems to eliminate RF pickup from the power lines.

The plasma current integrator box was rebuilt to afford better shielding and was moved from its location overhanging the tokamak (which required a

1. Eccoshield VY-C, manufactured by Emerson & Cuming, Canton, MA.

long power supply cable) to the data aquisition cabinet. The plasma current Rogowski coil was connected by a 50 Ω coaxial cable to the integrator box where it was terminated in 50 Ω. A 100 kHz, 50 Ω low-pass filter preceded the termination and eliminated RF pickup from the Rogowski coil. The loop voltage monitor was similarly terminated at the data acquisition cabinet with a 50 Ω low-pass filter.

The visible light detector was found to be easily saturated by low levels of RF radiation, and it was completely rebuilt. The phototransistor and a preamplifier were housed in a small aluminum box which was mounted (via an insulating, light-tight tube) to an optical window on the antenna feedthru flange. The hole in the box that allowed light to enter was shielded with a 200-mesh stainless steel screen, affixed with a conductive silver epoxy (Emerson & Cuming Eccobond 66C). The signal and power lines from the detector box were brought back to an amplifier in the data acquistion cabinet via a shielded multi-conductor cable. The cable shield (aluminum-coated polyester) was sealed to both the detector box and the amplifier box using the silver epoxy.

The microwave interferometer system also required some modification to eliminate severe interference from the RF generator. The Impatt oscillator was enclosed in a steel box to shield it electrically and magnetically (the oscillator was sensitive to DC magnetic fields as well as RF interference). Power lines leading to the oscillator were heavily filtered and the oscillator was electrically isolated from the waveguide forming the interferometer with a mylar disc. The output of the detector diode was connected to a 50 Ω coaxial cable which led back to the data acquisition system cabinet where it was terminated with another 100 kHz, 50 Ω low-pass filter. The diode detector mount was also electrically isolated from the rest of the microwave system.

During the course of testing the microwave system, it was discovered that the detector output was quite sensitive to physical vibration of the detector

mount. Vibrations of the waveguide, caused by the jump of the tokamak chamber that occurs during a shot, were causing a large signal in the 1 - 10 kHz range on the detector output. This vibration-induced noise, which had plagued earlier operation of the microwave system [Levine, 1980], made interpretation of the interference fringes difficult. The noise was greatly reduced by clamping lead weights to various parts of the waveguide in order to damp out the unwanted vibrations.

4.2 High Power Amplifier

4.2.1 Introduction

A high-power RF amplifier was built in order to have a wide range of power available for investigating coupling and antenna-plasma interactions. A class C amplifier was designed around an Eimac 4CW100,000E water-cooled ceramic envelope power tetrode and provided output power of up to 100 kW for pulses of 5 - 10 msec duration. The amplifier could be tuned over a frequency range of 5 - 20 MHz using different tank coils.

In a class C design, the tube is biased to conduct for only a small fraction of the total RF cycle. The tube applies current pulses to the output tank circuit, which therefore must be of sufficiently high Q to keep the tank current flowing when the tube is cut-off. This non-linear behavior of the tube means that the amplifier efficiency can be high, exceeding the 50% limit of a linear amplifier [Martin, 1955].

A tetrode tube was chosen for several reasons. The control grid - anode feedback capacitance is very small for tetrodes (~0.3 pF in this case) due to shielding by the screen grid, so neutralization is not generally required. Tetrode amplifiers also can be driven with considerably less power than a triode, minimizing the requirements of the driver section [Sutherland, 1967].

4.2.2 RF Design

A simplified schematic of the amplifier is shown in Figure 4-2; it will be referred to in the following discussion of the amplifier design and construction.

A grounded cathode design was employed for simplicity, since the filament transformer was then at RF ground potential and did not require large, high-current RF chokes. Because the Eimac tetrode was physically large (~ 20 cm o.d. × 29 cm long), its input (control grid - cathode) and output (anode - cathode) capacitances were correspondingly high (430 pF and 100 pF, respectively). The input and output RF tuned circuits had to be designed to incorporate these added reactances.

The grid tuned circuit was a parallel resonant $L-C$ network in which the variable capacitor was, at RF frequencies, effectively in parallel with the tube input capacitance and thus simply added to it. A 1500 Ω non-inductive resistor[2] fixed the real part of the grid input impedance in order to swamp out variations in impedance at high power due to secondary grid emission. An impedance step-up was necessary to match the impedance of the driver amplifier (50 Ω) to that of the grid circuit (1500 Ω). This was accomplished using two bifilar-wound broadband RF transformers in series [Ruthroff, 1959; Sevick, 1976].

Grid bias was applied through the same 1500 Ω resistor through an RF bypass filter; a 0.01 μF capacitor blocked the DC voltage from the input tuned circuit. RF grid drive was obtained from the 1 kW Dentron amplifier described in section 4.1.1.

The output tank circuit consisted of a $C-L-C$ π-network which transformed the resonant plate impedance of the tube ($R_p \sim 600\ \Omega$ for typical operating conditions[3]) to the desired output impedance ($R_L = 50\ \Omega$). Note that

2. Most of the non-inductive resistors used in this amplifier were provided by the Carborundum Company, Niagara Falls, N.Y.

3. Calculated from Eimac constant-current tube curves.

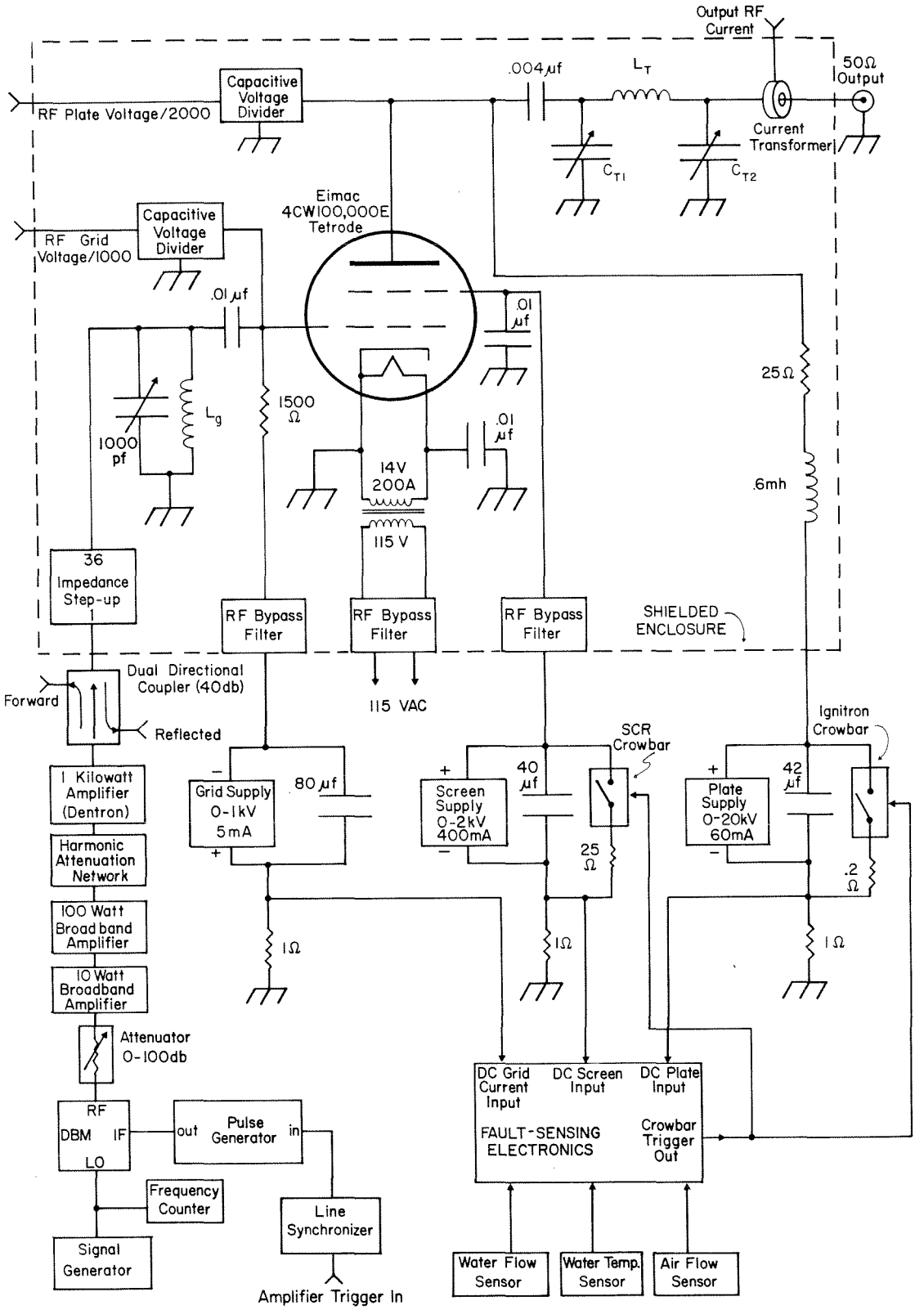

FIG. 4-2. Schematic of high-power RF amplifier.

the output capacitance of the tube was effectively in parallel with the first capacitor of the tank, C_1, since the impedance of the 0.004 μF DC-blocking capacitor was negligible at the frequencies being considered (5 - 20 MHz).

The loaded Q of the output tank circuit, Q_L, is of some importance. If Q_L is too small, the harmonic content content of the output will be high; if Q_L is too large, power losses from the circulating current in the tank will be excessive, reducing the amplifier efficiency. A loaded Q between 10 and 20 is generally chosen in order to balance the two effects [DeMaw, 1979]; a design value of 12 was chosen for this amplifier. Once the resonant plate impedance R_P, the load impedance R_L, the operating frequency $\omega/2\pi$, and the loaded Q are selected, the component values for the tank circuit (C_{T1}, C_{T2}, L_T) may be found using the impedance transformation relations of a π-network [DeMaw, 1978]:

$$C_{T1} = \frac{Q_L}{\omega R_L}, \tag{4.1a}$$

$$C_{T2} = \frac{1}{\omega R_L}\left[\frac{R_L(Q_L^2 + 1) - R_T}{R_T}\right]^{\frac{1}{2}}, \tag{4.1b}$$

and

$$L_T = \frac{Q_L R_T + (R_T)^{\frac{1}{2}}\left[R_L(Q_L^2 + 1) - R_T\right]^{\frac{1}{2}}}{\omega(Q_L^2 + 1)} \tag{4.1c}$$

Plate voltage was applied through a high voltage RF choke (see below), and a 25 Ω series resistance limited plate current in the event of an internal tube arc.

4.2.3 Construction

The amplifier was built within an aluminum frame (2.0 m high × 1.2 m wide × 0.7 m deep) which was covered with aluminum sheet panels (Figure 4-3).

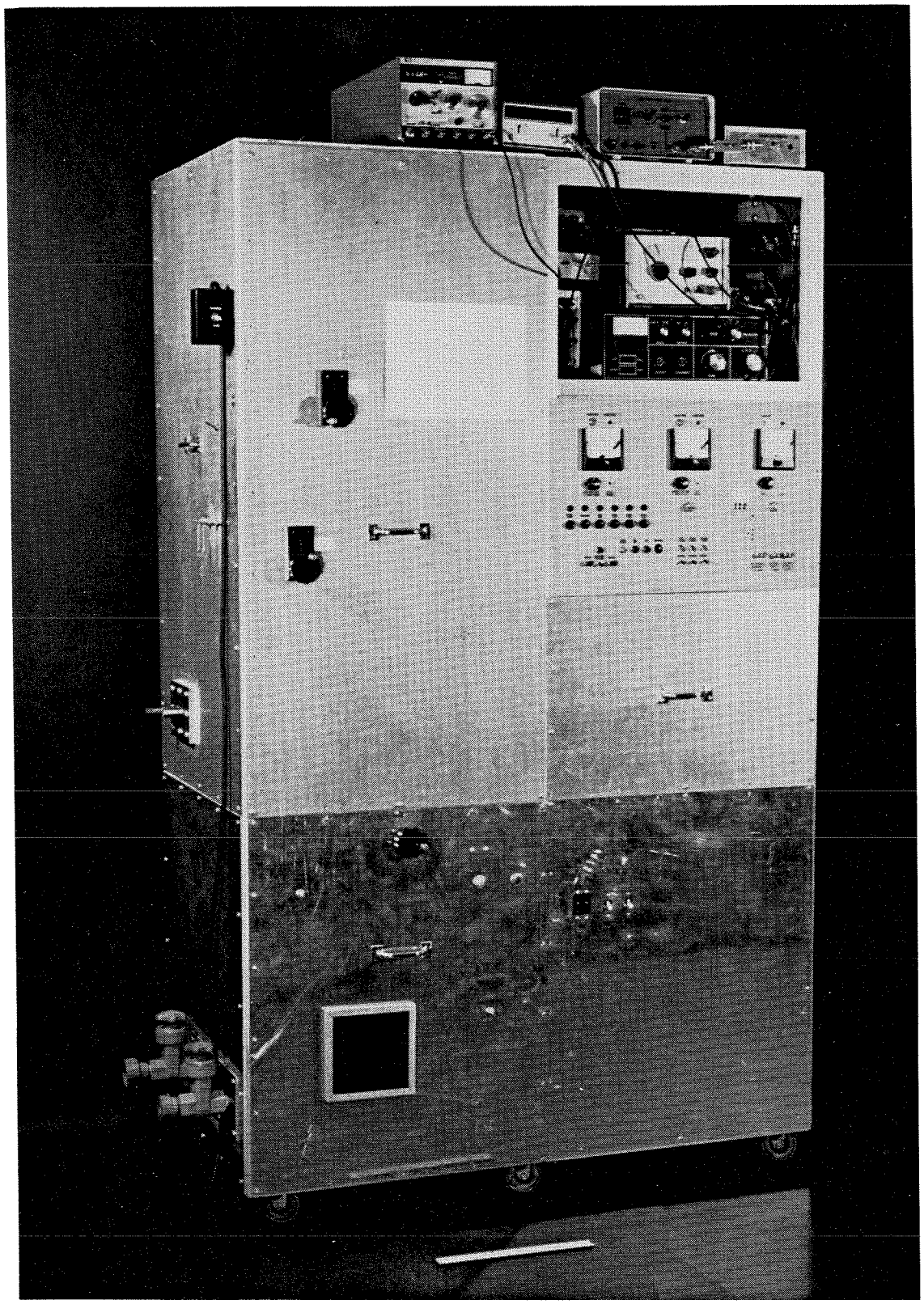

FIG. 4-3. Front view of RF amplifier. Exciter compartment is at upper right, water cooling connections are at lower left. Rule at bottom is 30 cm long.

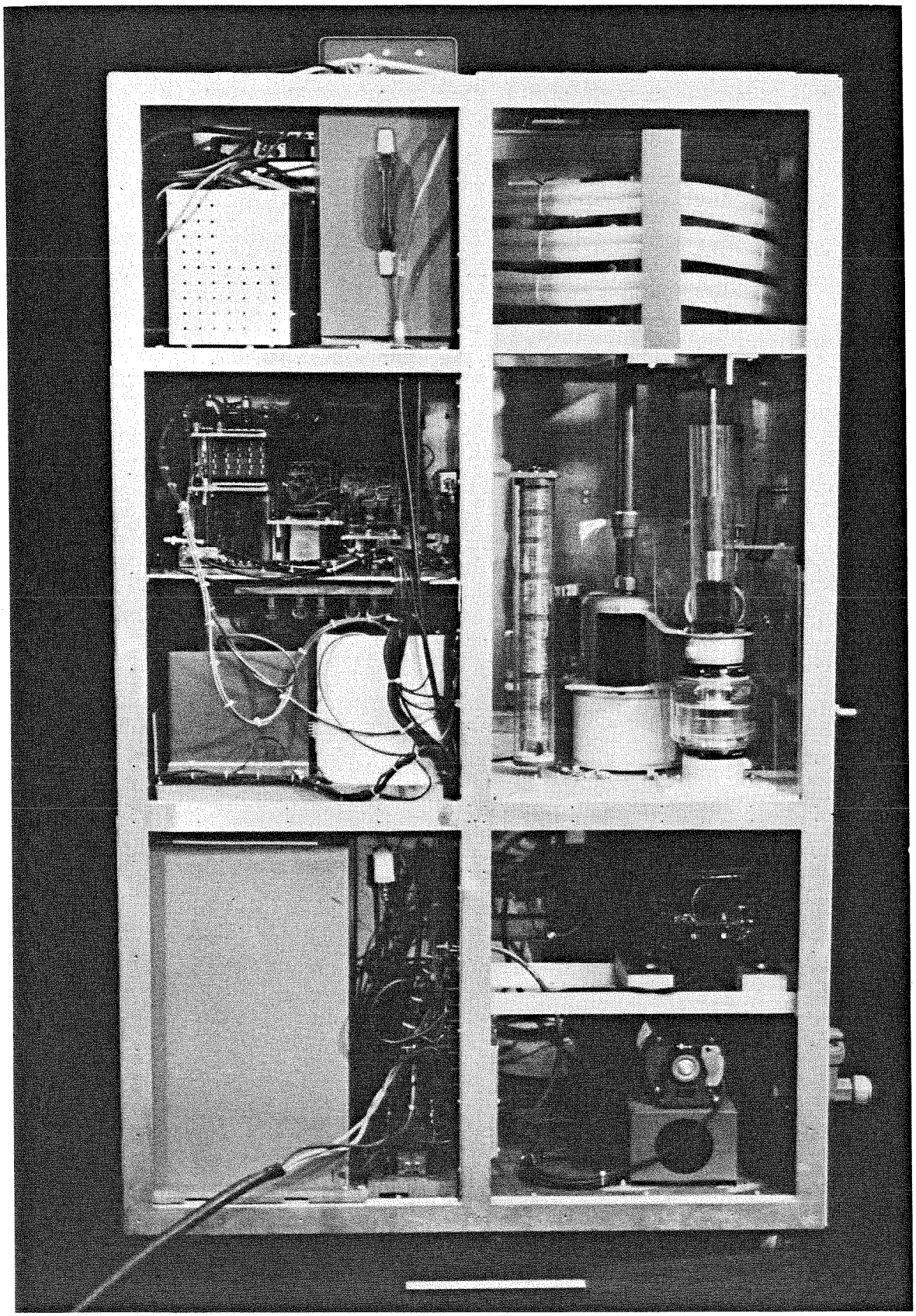

FIG. 4-4. a) Back view of RF amplifier (cover panels removed).

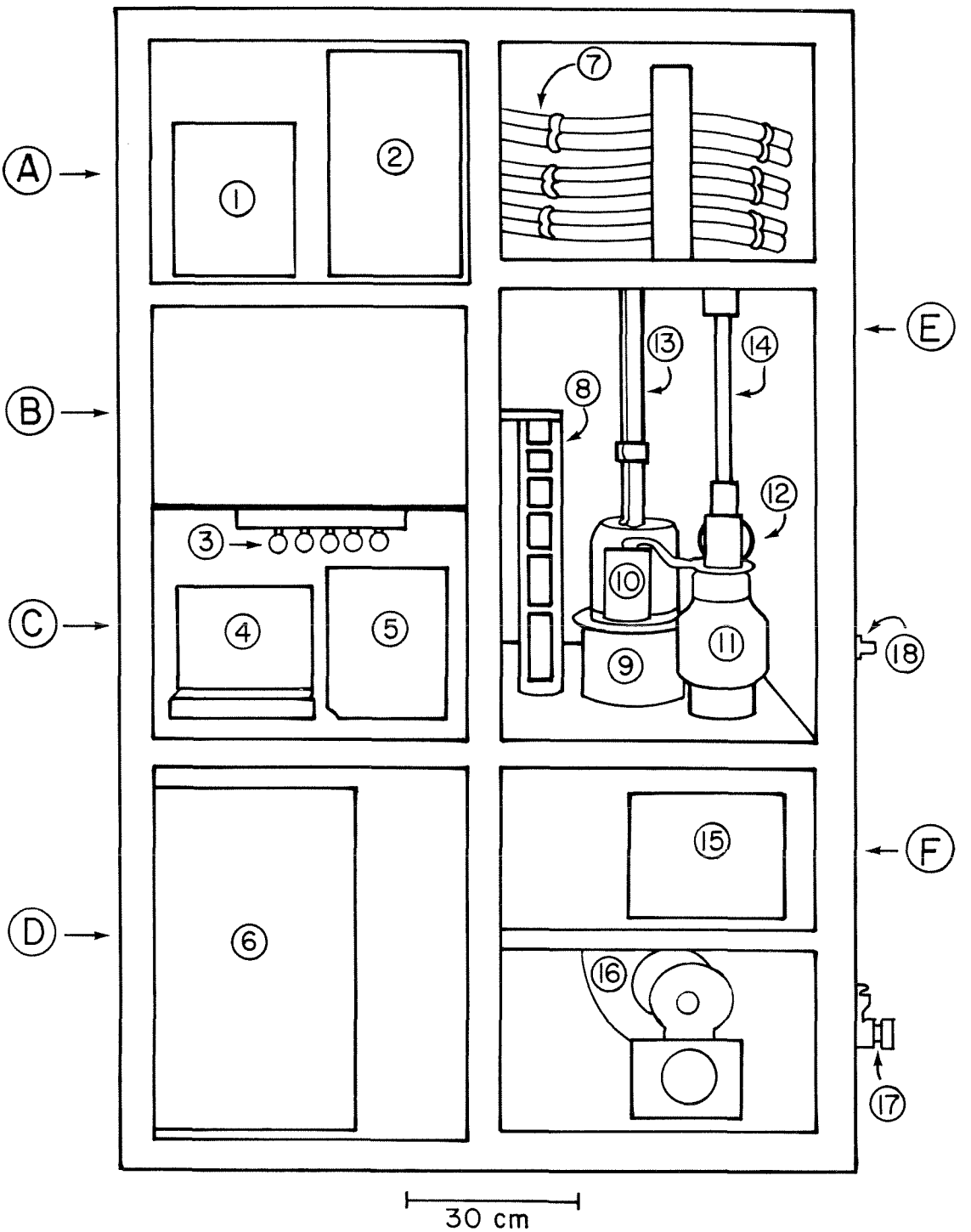

FIG. 4-4. b) Schematic of FIG. 4-4a. **A** - RF exciter and gating electronics compartment. **B** - Grid bias power supply and control logic compartment. **C** - Plate and screen bias supplies and crowbar compartment. **D** - Capacitor bank compartment. **E** - Plate tank circuit compartment. **F** - Grid tuned circuit compartment. **1** - Power supply for Marko 100 W amplifier. **2** - ENI 10 W amplifier. **3** - Screen supply bleeder resistors. **4** - Ignitron crowbar. **5** - 20 kV plate power supply. **6** - Plate supply capacitors. **7** - Water system coils. **8** - Plate supply RF choke. **9** - Eimac 4CW100000E tetrode. **10** - DC-blocking capacitor. **11** - Tank circuit vacuum capacitor (C_{T1}). **12** - Tank circuit inductor (L_T). **13** - Water cooling lines. **14** - Capacitor adjustment mechanism. **15** - Filament transformer. **16** - Tube base cooling blower. **17** - Water system connections. **18** - RF output connector.

The chassis was divided into six shielded and isolated sections: the output tank circuit compartment, the input grid tuned circuit compartment, the plate and screen power supplies and crowbar compartment, the plate supply capacitor bank compartment, a compartment for the grid bias power supply and control electronics, and one for the exciter and RF gating electronics (Figures 4-4a,b). Good shielding between the compartments was essential as the overall gain of the whole system (including the exciter) was greater than 60 db.

The tube was mounted in an Eimac SK-2000 air-cooled socket on an aluminum partition which separated the input and output RF compartments. A blower mounted below the socket provided a forced-air flow of 5 m^3/min. The air intake, in the grid compartment, and the exhaust, in the plate compartment, used RF shielded air filters[4] to prevent RF leakage through the large apertures. The tube socket contained an integral bypass capacitor for the screen grid electrode, so external RF bypassing of the screen power supply was not necessary.

The layout of the RF components was very important because of their large physical size. Stray inductances and capacitances associated with the various elements could be substantial and had to be taken into account in the design.

The control-grid tuned circuit was mounted directly below the tube socket and consisted of a 0 - 1000 pF, 3 kV vacuum variable capacitor and an inductor wound from copper strap. A capacitive voltage-divider allowed monitoring of the grid RF voltage.

The plate tank circuit was constructed on the same partition that held the tube socket. The π-network consisted of two 0 - 1000 pF, 15 kV vacuum capacitors[5] and a plug-in inductor wound from 0.95 cm o.d. silver-plated copper

4. Teckcell filters, manufactured by Tecknit, Santa Barbara, CA.

5. Manufactured by the Jennings Corp., Palo Alto, CA.

tubing. Since the inductance LT predicted from equation 4.1c was small ($< 1\ \mu H$) for the operating parameters of interest, it was necessary to mount the tube and the two capacitors close together in order to minimize the stray inductances associated with the capacitor bodies. Teflon sheet insulation was used when necessary to prevent RF breakdown.

The plate supply choke was wound on a phenolic tube 5 cm o.d. × 50 cm long. It consisted of 400 turns of #18 AWG magnet wire, wound in six sections of decreasing width (this served to increase the resonant frequencies of the choke which arose from capacitive coupling between adjacent turns). The measured inductance was 0.65 mH, the resistance, 1.2 Ω. A high voltage cable led from the bottom of the RF choke, through a shielded tube, to the plate supply capacitor bank compartment.

An RF plate voltage monitor was constructed using a shielded vacuum voltage divider capacitor (Jennings model VDF-2.8-60S) whose input capacitance was ~2.8 pF; the division ratio was chosen to be 2000. The output RF current was monitored using a high frequency current transformer (Ion Physics Co. model CM-1-S).

The filament power supply consisted of a step-down transformer which provided 14 V (rms) at 200 A. The transformer[6] was designed with an air gap in the core so that the leakage inductance was high. This limited the short-circuit current to insure that the filament specifications were not exceeded during the filament warm-up period (the resistance of the cold filament was much lower than the resistance at operating temperature). The transformer was mounted directly below the tube socket, in the grid tuned-circuit compartment, so that the connecting straps could be kept very short. Connections on the secondary side were silver plated to minimize contact resistance. The pri-

6. Built by Teledyne - Crittenden Transformer Works, Los Angeles, CA.

mary power (115 V, 30 A) was passed through an RF filter at the point where it entered the grid compartment (as were all other power lines entering the chamber) in order to prevent RF energy from being conducted onto the AC power lines.

The grid bias supply used a sealed transformer/rectifier unit (Plastic Capacitor Co. model HV50-502M) to provide up to 1 kV at 5 mA. The DC grid current drawn during an RF pulse was usually negligible.

The screen bias supply used a transformer and diode bridge to provide up to 2.5 kV at 400 mA. Secondary electron emission from the screen grid can lead to reverse screen current under some operating conditions. It was therefore important to provide a low-impedance path for this current in order to keep the screen voltage constant during the RF pulse [Sutherland, 1967]. This was accomplished by bleeding the supply with a resistor between the output and ground; a bleeder current of 80 mA was found to be sufficient. The screen grid supply voltage was maintained during the RF pulse by the 80 μF capacitor across its output.

The plate bias power supply was composed of a 15 kV (rms), 60 mA current-limited transformer (originally used to light a neon sign!), a rectifier stack, and a capacitor bank. Full wave bridge rectification was employed, using four pairs of 10 kV, 300 mA diodes (International Rectifier #30AV100). The case of the transformer had to be insulated since it was connected to the center-tap of the secondary. The capacitor bank consisted of three low-inductance energy storage capacitors in parallel, totaling 42 μF and rated at 20 kV. This was sufficient to keep the plate voltage sag during an RF pulse to less than 10%.

Voltage adjustment and regulation were accomplished in the same fashion for the grid, screen, and plate supplies.[7] A triac was used to modulate the

7. The voltage regulator circuitry was designed and built by F. Cosso, E.E. (Caltech).

power delivered to the transformer primary; the triac was in turn triggered from a feedback loop which sensed the high voltage DC output through a resistive voltage divider. This enabled full charging current to be applied to the capacitors immediately after an RF pulse, thus increasing the maximum repetition rate (which was helpful during tuning of the amplifier). Regulation of the bias supply voltages was typically held to 1%.

The Eimac tube could be damaged by excessive anode current, by internal arcing to one of the grids, or by heat from the filament without sufficient cooling. As the grids could be damaged by an arc carrying an energy of only ~50 joules,[8] it was necessary to provide adequate protection circuitry. The screen and plate currents were monitored, and, if they rose above preset limits (15 A for the plate, 1.2 A for the screen), crowbars were triggered which discharged the capacitors within ~2 μsec. The plate supply crowbar consisted of an ignitron (General Electric model GL7703) in series with a 0.2 Ω non-inductive resistor connected across the capacitor bank. The resistor was chosen to critically damp the resulting L–C–R circuit (where L arose from the inductance of connecting leads). The screen supply crowbar consisted simply of an SCR and a damping resistor.

Three other interlocks were provided which discharged the capacitors and shut off the filament power: an air flow switch (for the blower cooling the tube base), a water flow switch (for the anode cooling system described below), and a water temperature switch. Control circuitry was arranged so that the cooling systems continued to operate for several minutes after the amplifier was turned off.

The Eimac tube required both forced air and anode water cooling, even at the low duty cycle used here, due to the large continuous filament power being

8. Conversation with R. Artego, Eimac Division of Varian, San Carlos, CA.

dissipated (~3 kW) and the fact that 20 - 30 % of that power ended up in the anode. The water jacket which covered the tube anode was at a DC potential of 15 - 20 kV during operation of the amplifier. It was therefore necessary to build a deionized water system which could maintain the water specific resistivity at a sufficiently high value (>0.5 MΩ-cm), both to prevent current from flowing through the water channels and to prevent electrolysis which could damage the tube anode.[9]

A schematic diagram and a photograph of the cooling system are shown in Figures 4-5a,b. A 360 liter polypropylene tank was used for the water reservoir. All plumbing and components were made of plastic or stainless steel to eliminate corrosion. One water pump provided 20 liter/min for anode cooling and another provided 2 liter/min for the purifying loop, which included a 1 micron particle filter, a mixed-bed deionizing cartridge, and an oxygen-removal cartridge.[10]

The deionized water system was cooled by a water-to-water heat exchanger consisting of 25 m of 2.5 cm i.d. copper tubing, welded into a grid, nickel-plated, and suspended within the polypropylene tank. The heat exchanger was connected to a recirculating water cooling system which serviced the building and required a flow of 8 liter/min during operation of the amplifier.

In order to provide a water path of sufficient resistivity and yet allow adequate water flow, it was necessary to coil 6 m of 1.9 cm i.d. plastic tubing inside the amplifier tank circuit compartment. The water was grounded to the cabinet through conductive feedthrus, and under operating conditions the current flow through the water channel was less than 0.5 mA.

---

9. Eimac Application Bulletin 16, "Water Purity Requirements in Liquid Cooling Systems".

10. The filters were manufactured by the Barnstead Co., Boston, MA.

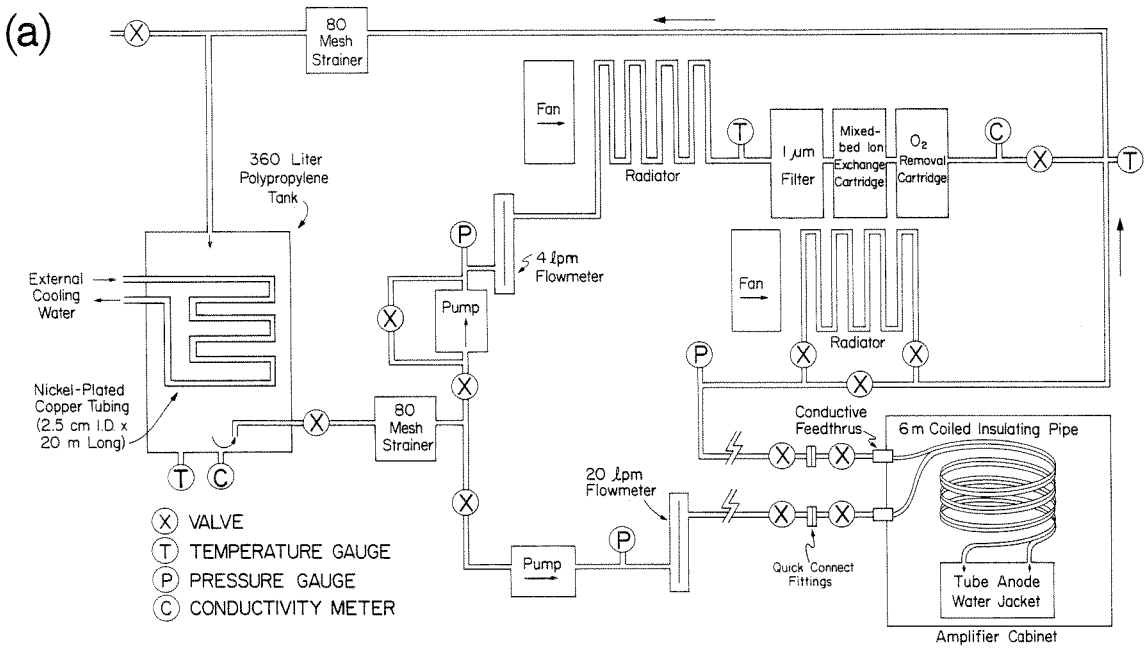

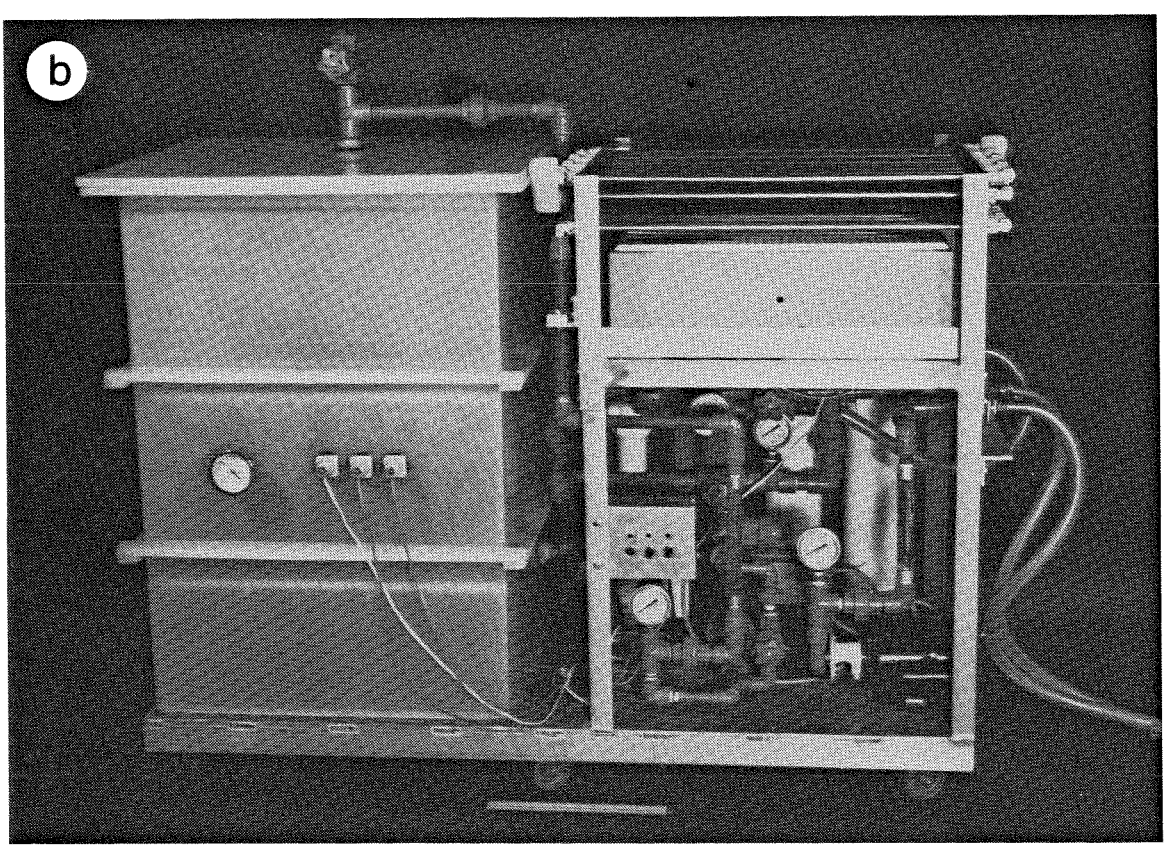

FIG. 4-5. a) Schematic diagram of high-purity water cooling system b) Photograph of water cooling system. Rule at bottom is 30 cm long.

4.2.4 Operation

The amplifier had to be tuned before the Eimac tube could be energized. Grid tuning was adjusted using the directional coupler in the driver line. The driver system was operated at low power and the grid tuning capacitor was adjusted to minimize the reflected power. During operation, the resonant grid impedance was considerably higher than the 1500 Ω which paralleled it, so little readjustment was usually necessary.

Plate tuning was accomplished by connecting a 50 Ω signal generator and directional coupler to the 50 Ω *output* cable of the amplifier. Now, however, the resonant plate impedance of the tube had to be simulated. The impedance was calculated at the desired operating point using the tube constant-current curves, and a non-inductive resistor of approximately the same value was connected between the anode and cathode of the tube. The two π-network capacitors were adjusted (without energizing the tube) to minimize the reflected signal from the directional coupler. The resistor and the signal generator were then removed and the filament power and high voltages were applied.

The 1 kW Dentron amplifier had some residual 60 Hz output ripple, so it was found useful to synchronize the amplifier pulses to the line voltage. When a trigger pulse was received, an output pulse was generated at the next zero-crossing of a line voltage reference. The tokamak timing cycle was also modified so that it fired at a zero-crossing of the line reference.

Initial testing of the amplifier was performed by connecting a non-inductive, air-cooled 50 Ω resistor to the output cable. The amplifier was pulsed at a repetition rate of ~0.5 Hz with a pulse width of 2 - 5 msec. RF plate and grid voltages were monitored during operation as well as output RF current and DC plate current. The DC plate voltage and current gave the tube input power, while the output RF current together with the load impedance yielded the output power.

Some low frequency ($\sim$50 kHz) parasitic oscillations were observed during early operation of the amplifier. They were traced to a resonant circuit composed of the grid bypass capacitor together with an RF choke in the grid bias power supply. The problem was solved by replacing the choke with an $R-C$ network. It was also necessary to shape the input RF gating pulse to slow its rise time to $\sim$0.2 msec. No high frequency parasitics were observed.

The tube was typically operated with a plate potential of +15 kV, a screen potential of +1.5 kV, and a grid potential of -540 V. Under these conditions, an output power of 160 kW was achieved (at 14 MHz). The DC input power was 230 kW, yielding an efficiency of 70%. Lower powers (down to $\sim$4 kW) were also easy to deliver.

4.3 Directional Coupler

The solutions to Maxwell's equations applied to a coaxial transmission line are traveling waves proceeding in both directions. A directional coupler is a device which generates an output signal proportional to the amplitude of the wave traveling in a *single* direction along the line. This was a necessary instrument for tuning the impedance matching network (section 4.4) which transformed the amplifier output impedance to the impedance presented by the RF antenna. A perfect match was indicated by a vanishing reflected wave amplitude.

Much of the developmental work on directional couplers (sometimes referred to as reflectometers) was done in the 1940's; an excellent bibliography of the work was given by Schwartz [1954]. Many of the coupler schemes utilized at microwave frequencies (e.g., multiple hole or slot couplers) are not practical to implement at lower RF frequencies ($<$100 MHz). In this range, several authors have presented designs which involve a loop coupled both

electrically and magnetically to a coaxial line section [Pistolkors and Neumann, 1941; Parzen, 1949; Boff,1951]. The basic idea is that the voltage across the loop is the result of contributions from capacitive coupling to the center element of the coaxial line and from magnetic coupling to the current carried by the center element. The contributions are in phase or out of phase with each other, depending on the direction of the wave on the line. If the coupling coefficients are adjusted appropriately, the two contributions will cancel when out of phase, leading to zero output for a wave traveling in one direction.

If the dimensions of the coupler are very small compared to a wavelength, a lumped-element equivalent circuit model may be justified. A schematic drawing and a simple circuit for a loop-type coupler are shown in Figures 4-6a,b. Here L represents the mutual inductance between the center conductor and the loop, C_1 and C_2 represent the capacitances between the loop and the center and outer conductor, respectively, R_T is the resistive termination on the sensing side of the loop (usually a terminated 50 Ω coaxial cable), and Z is the impedance terminating the other side of the loop. V_1 is the potential between the inner and outer conductors and V_2 is the voltage induced across the loop due to the current in the center conductor. Solutions for the current (I) and voltage (V) waves on a coaxial line [Chipman, 1968] are given by

$$I = \frac{V_f}{R_0} e^{-ikx+i\omega t} - \frac{V_r}{R_0} e^{ikx+i\omega t} \tag{4.2a}$$

$$V = V_f e^{-ikx+i\omega t} + V_r e^{ikx+i\omega t}, \tag{4.2b}$$

where the subscripts "f" and "r" refer to waves propagating from left to right, and from right to left, respectively (as in Figure 4-6a). R_0 is the characteristic impedance of the transmission line and k is the wave number.

Taking the loop position to be at position $x = 0$, it follows that $V_1 = V_f + V_r$ and $V_2 = \frac{i\omega L}{R_0}(V_f - V_r)$. Using Kirchhoff's equations, the solution for the

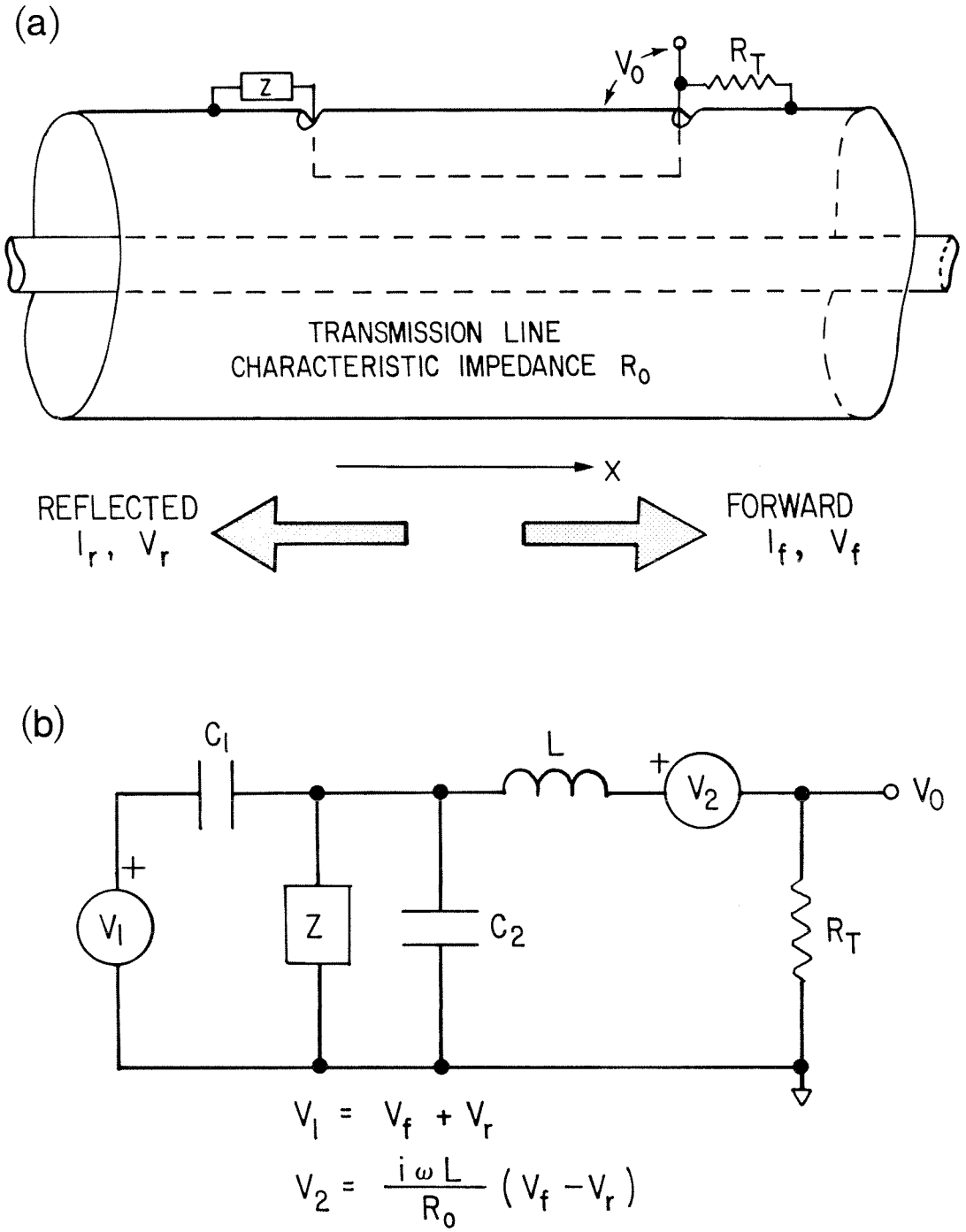

FIG. 4-6. a) Schematic of loop-type directional coupler. b) Equivalent circuit model of loop-type coupler. The "+" symbols indicate relative phasing of the two voltage sources.

output voltage is

$$V_0 = R_T \frac{V_2\left(Z' - \frac{i}{\omega C_1}\right) - Z' V_1}{(R_T + i\omega L + Z')\left(Z' - \frac{i}{\omega C_1}\right) - Z'^2}, \tag{4.3}$$

where $Z' = \frac{Z}{1 + i\omega C_2 Z}$ is the impedance of the parallel combination of Z and C_2. When there is only a forward traveling wave on the line, the numerator of (4.3) vanishes provided

$$Z' = \frac{L}{C_1 (R_0 + i\omega L)}. \tag{4.4}$$

If the coupling parameters can be arranged so that relation 4.4 is satisfied, then a forward-traveling wave will produce no signal at V_0, while a wave traveling in the reverse direction *will* yield a non-zero output. The loop then functions as a directional coupler.

If the area enclosed by the loop is sufficiently small that $\omega L \ll R_0$ is a valid approximation, and if the ratio $\frac{C_2}{C_1}$ is not too large, so that $\frac{C_2}{C_1}\frac{\omega L}{R_0} \ll 1$ is still valid, then C_2 can be neglected, $Z' \to Z$, and relation 4.4 becomes simply

$$Z = \frac{L}{C_1 R_0}, \tag{4.5}$$

a result first derived by Parzen [1947]. The coupling factor in the reverse direction is then found from equation 4.3,

$$\left|\frac{V_0}{V_r}\right| = \frac{\omega L R_0 C_1}{L + R_0^2 C_1}, \tag{4.6}$$

where we have set $R_T = R_0$. The predicted coupling therefore increases linearly with frequency.

Some loop-type directional couplers are available commercially, but those capable of handling high power levels (100 kW) are expensive and designed for

large-diameter rigid coaxial air-line. Since the duty cycle of the RF amplifier was very low (always <1%), a relatively small (2.2 cm o.d.) flexible 50 Ω coaxial cable (RG-17A/U) was used to connect it to the impedance matching network in the tokamak lab. An extremely simple dual directional coupler was built into the cable itself.

A diagram of the dual coupler is shown in Figure 4-7a. The coaxial line section for the coupler was just a 10 cm length of the RG-17 cable. The loop was formed by simply inserting an insulated wire between the outer conductor (copper braid) and the dielectric insulation of the cable. It was found, however, that the resistive termination Z specified by equation 4.5 was not adequate; much higher directivity was obtained by adding a small trimmer capacitor in parallel with the resistance.[11] The necessity for this complex impedance termination probably arose from stray reactances due to the physical size of the elements (not included in the model) or from the approximations used in the derivation of equation 4.5.

One end of the loop was terminated with a miniature non-inductive variable resistor (100 Ω) in parallel with a trimmer capacitor (5 – 60 pF) and soldered to the copper braid; the other end was soldered to a small 50 Ω cable which led to a BNC connector. Two couplers were built into the same section of coaxial line and were oriented in opposite senses in order to measure both the forward and reflected waves. The entire assembly was enclosed in a copper box to eliminate external interference.

The couplers had to be adjusted initially to optimize their directivity. The procedure for tuning the reflected wave coupler will be described; the other coupler was adjusted in a similar fashion. The ends of the RG-17 cable were attached to low-VSWR connectors. The left-hand end of the cable (referring to

11. Similar couplers built using the much smaller RG-58 for the coaxial line did not require the additional parallel capacitance.

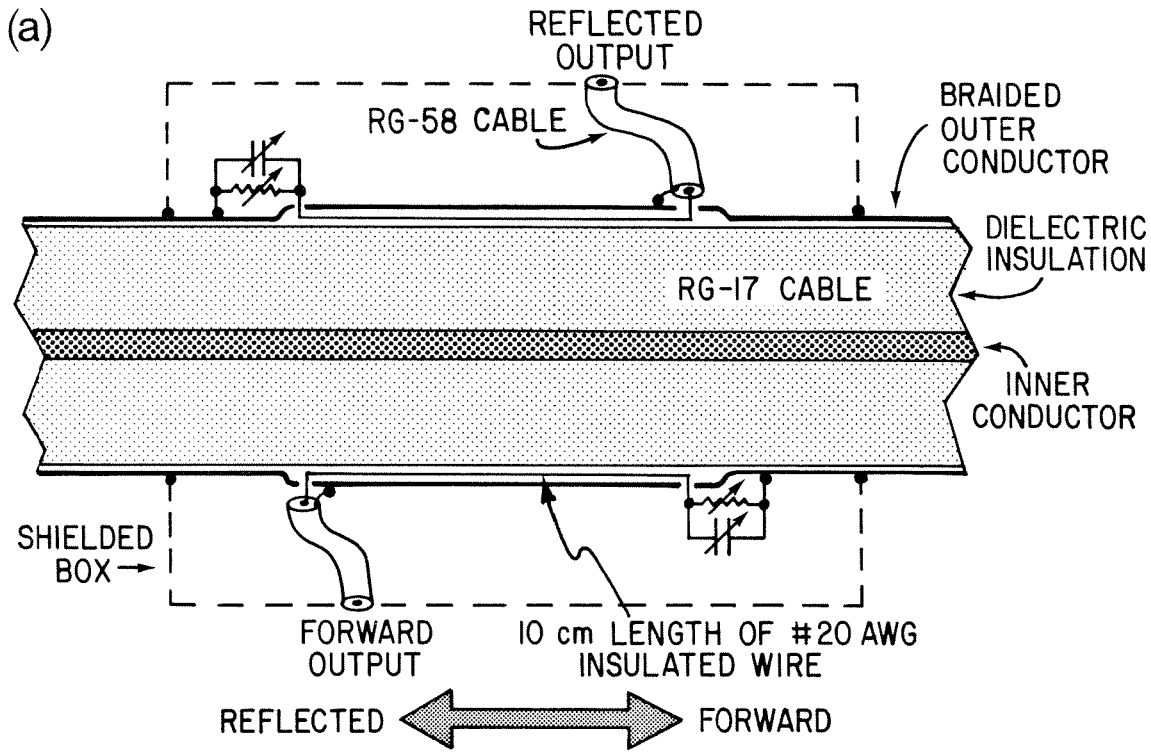

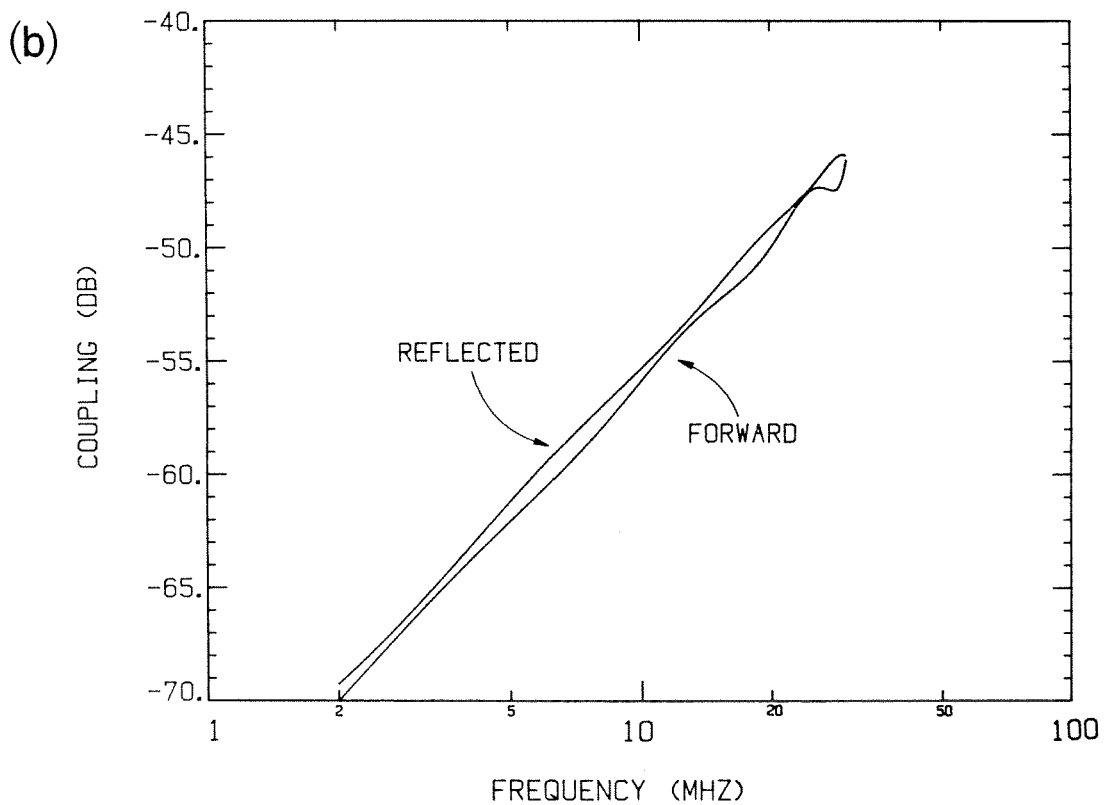

FIG. 4-7. a) Diagram of dual directional coupler built into RG-17 cable (not to scale). b) Forward and reflected coupler calibrations.

Figure 4-7a) was connected to a 50 Ω signal generator (capable of several watts of output power) which was swept from 1 - 30 MHz, while the right-hand end was connected to a 50 Ω termination. There were then only forward traveling waves propagating in the coax. The sensing side of the reflected wave coupler was connected to an oscilloscope via a 50 Ω terminated line, and the variable resistor and capacitor were adjusted simultaneously to minimize the output signal over the entire frequency range.

The coupling coefficient is plotted as a function of frequency for the two couplers in Figure 4-7b and the form agrees well with the linear frequency prediction of equation 4.6. The directivity of the couplers was typically greater than 30 db, while the power handling capability (>2 MW) was limited only by the breakdown voltage of the coaxial line. Impedance measurements on the coaxial line indicated that the perturbation of the characteristic impedance of the coupler section by the wire beneath the braid was negligible.

A photograph of the completed coupler (without the copper shield) is shown in Figure 4-8.

4.4 Impedance Matching Network

4.4.1 Introduction

In order to efficiently transfer RF energy to the plasma, it is necessary to match the impedance of the generator (50 Ω) to that presented by the antenna in the plasma. This is in general accomplished with some sort of passive reactive network placed between the generator and the antenna.

If the antenna impedance were constant, it would be a relatively easy matter to design a network to transform the impedances appropriately. However, since the plasma waves launched by the antenna are not highly damped, resonant toroidal eigenmodes can develop which cause peaks to appear in the

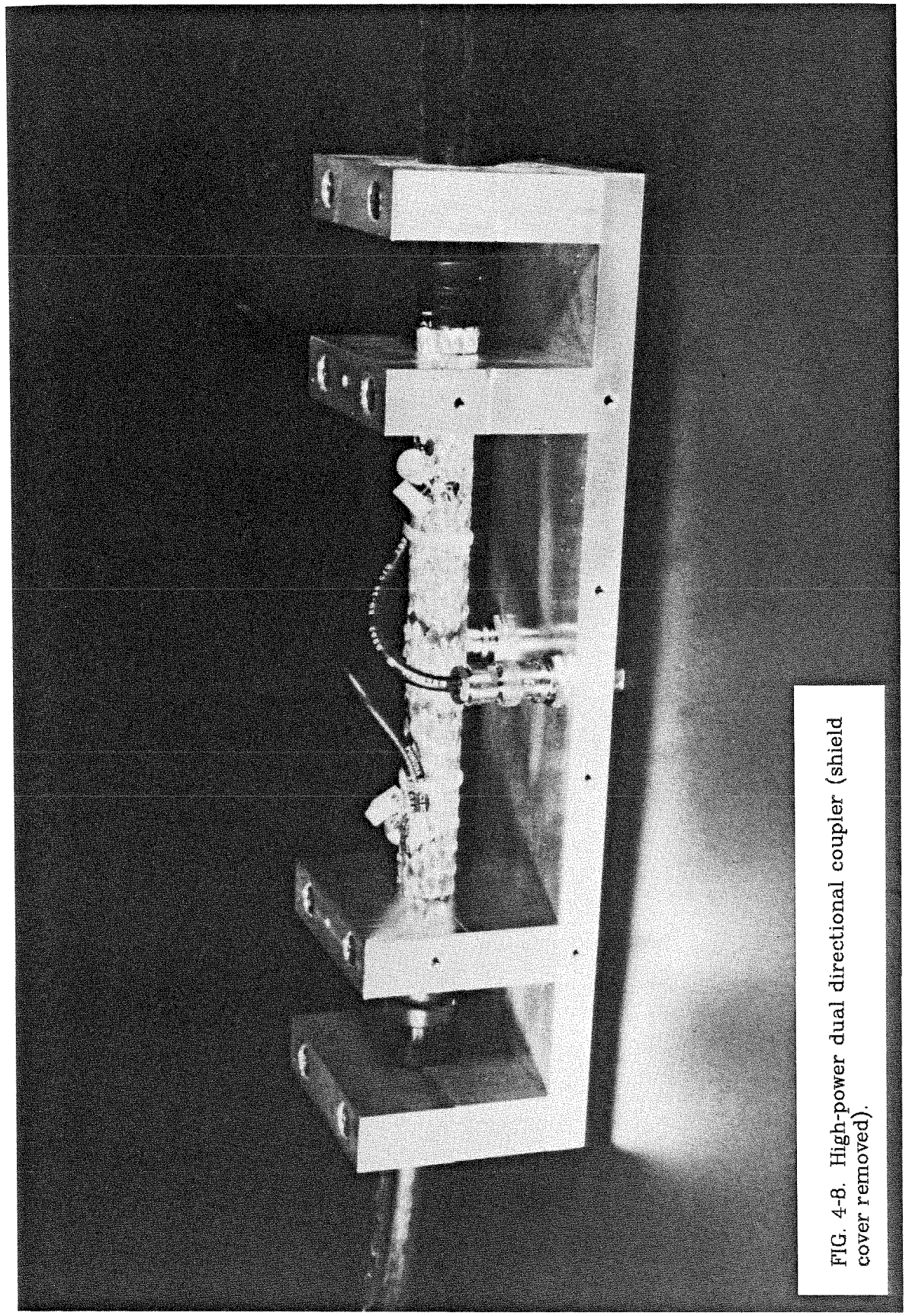

FIG. 4-8. High-power dual directional coupler (shield cover removed).

real part of the antenna input impedance (for shielded loop antennas) at particular values of the plasma density. These peaks can be 5 - 10 times the off-resonance loading resistance (see Chapter 6). Unshielded antennas do not exhibit eigenmode peaks in the input resistance (probably because it is swamped out by the increased background loading) but do exhibit a loading resistance which increases (for magnetic antennas) or decreases (for electric antennas) as the plasma density increases, typically changing by a factor of 2 – 5 during the tokamak shot. The reactive part of the antenna impedance generally decreases slightly as the plasma density increases (for all of the antennas) but rarely by more than ~ 10%.

Ideally, the impedance-matching network would be active, its elements changing value as the load impedance changed in order to maintain a perfect match. In practice, this has not been feasible because of the time scale over which the antenna impedance changes (half-widths of eigenmode peaks are typically 50 - 500 μsec in these experiments) and the mechanical difficulties associated with automatically adjusting large inductors and vacuum capacitors.

Most of the work directed towards plasma heating with ICRF waves has been done using shielded loop antennas which, in one-component plasmas, give rise to toroidal eigenmodes and corresponding peaks in the antenna input resistance. It is desirable, from the point of view of heating, to stay locked to a single resonance peak, as the increased loading resistance leads to better coupling efficiency. Since the occurrence of a particular eigenmode depends on the plasma density and the RF frequency, several approaches have been tried to keep the system locked to a resonance. The PLT group has used precise control of plasma density as well as active frequency feedback to stay tuned to a mode [Hwang et al., 1978b]. The matching network, which utilized stub tuners, was fixed. Several other groups [Bhatnagar et al., 1978b; Biddle, 1980]

have attempted, with mixed results, to solve both the impedance matching and mode tracking problems by incorporating the antenna impedance into the tank circuit of a high power RF oscillator.

Since the major thrust of the work presented here was to study wave propagation and coupling, and not heating, no attempt was made to track a particular eigenmode. The RF frequency was fixed during the plasma shot, as was the matching network.

4.4.2 Design

Some of the simple reactive impedance-matching networks which were considered were π-networks, T-networks and quarter-wave transformers. An $L-C-L$ T-network was chosen (Figure 4-9), as it let to component values which were easily implemented (this was an important factor, since the available high voltage vacuum capacitors were limited to values $\lesssim 1000$ pF) and exhibited reasonable insensitivity to changes in the load impedance (see below).

A typical value for the loop antenna impedance (with plasma), used for preliminary design of the matching network, was $Z_{L0} \approx 0.5 + 5.0i\ \Omega$ (at 12 MHz). The impedance seen by the matching network, however, was the antenna impedance Z_{L0} as transformed by the antenna feeder tube. This frequency-dependent transformation is discussed in detail in Chapter 6; here we simply call the resulting impedance $ZP = R' + i\,X'$. Once the source impedance ($R_g = 50\,\Omega$) and the load impedance (ZP) for the matching network are specified, there are still an infinite number of ways to select L_1, L_2, and C to achieve a perfect match at a particular frequency. The families of component values which provide an impedance match are usually specified in terms of a parameter Q_L (which is called the loaded Q of the network). Solutions for the components [DeMaw, 1978] are then given by

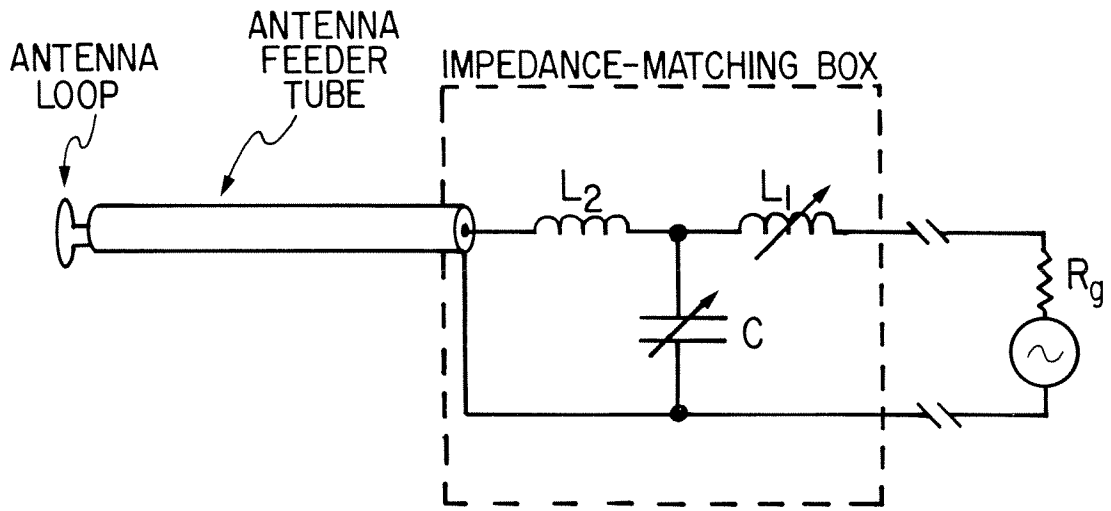

FIG. 4-9. Schematic of $L-C-L$ impedance-matching network.

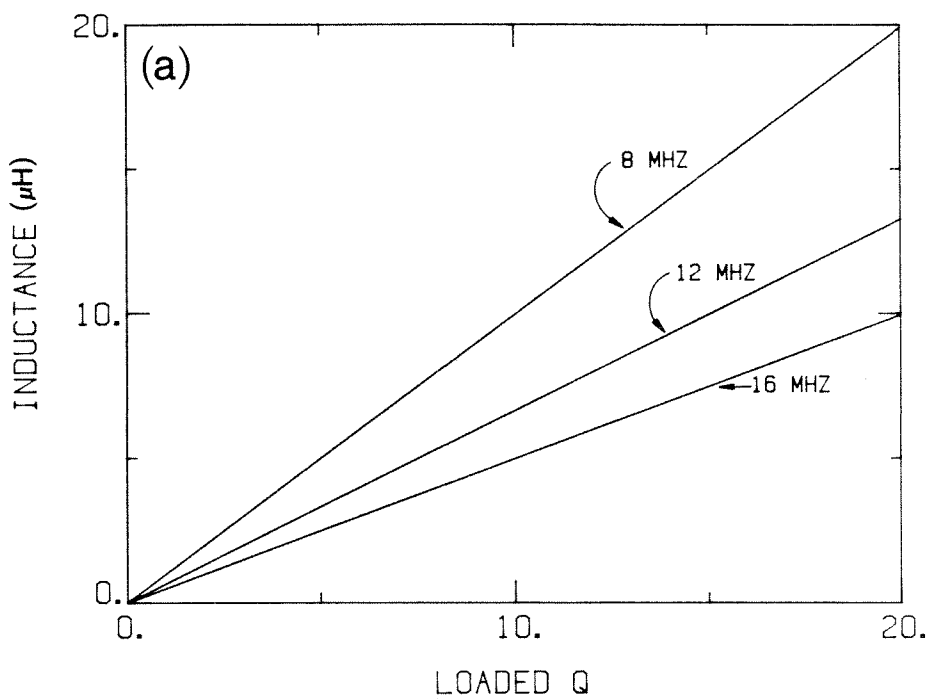

FIG. 4-10. a) Solutions at three frequencies for impedance-matching network inductance L_1 as a function of Q_L. Matching-network load impedance is $Z_{LO} = 0.5 + 0.42fi$ ohms, where f is the frequency in MHz. Network transforms the load impedance to 50 ohms.

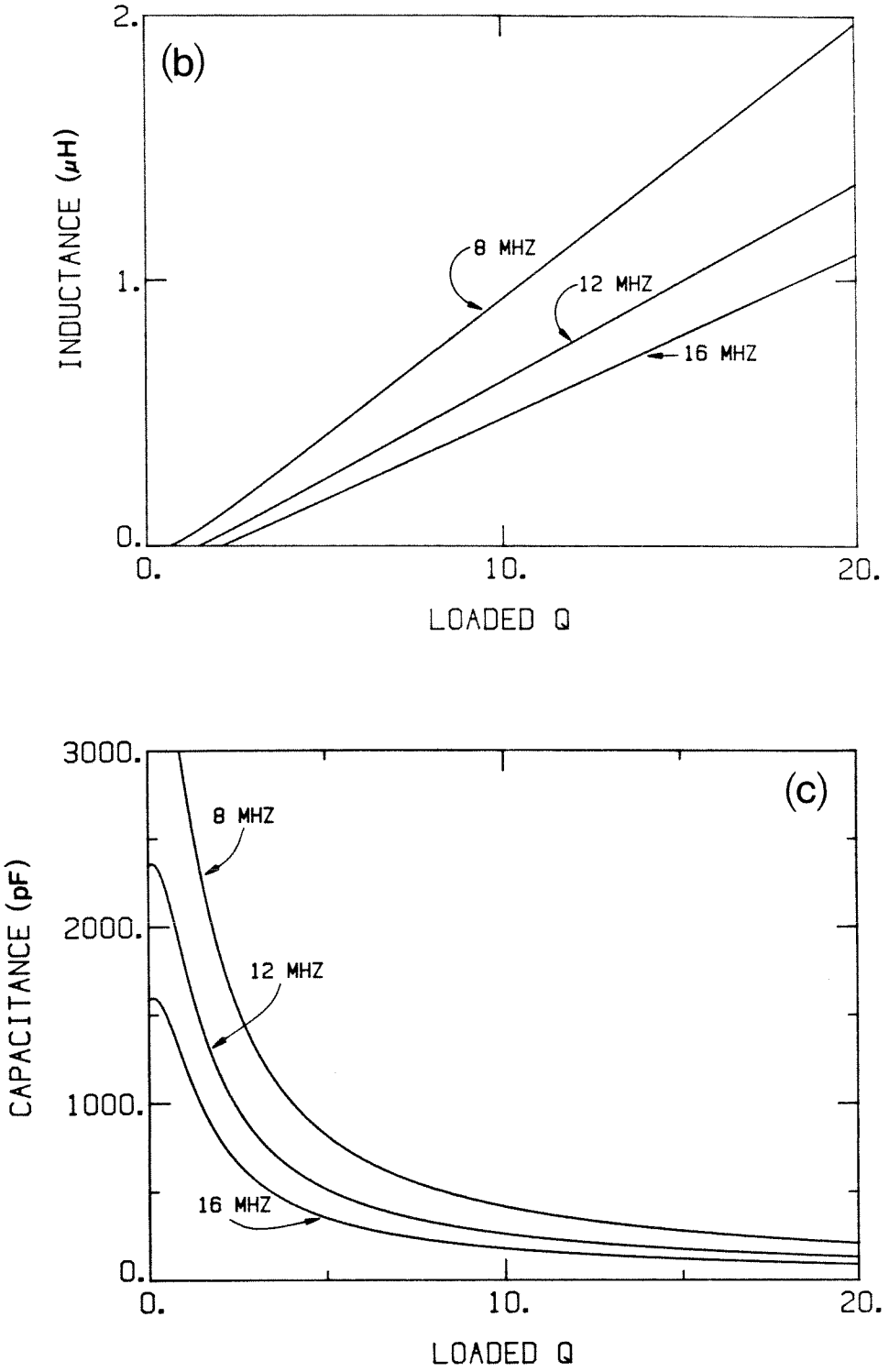

FIG. 4-10, continued. b) Solution for impedance-matching network inductance L_2 as a function of Q_L. c) Solution for impedance-matching network capacitance C as a function of Q_L.

$$L_1 = \frac{R_g\, Q_L}{\omega}$$

$$L_2 = \frac{R'\, B - X'}{\omega} \qquad (4.7)$$

$$C = \frac{Q_L + B}{A\,\omega},$$

where $A = R_g(1 + Q_L^2)$ and $B = \left(\frac{A}{R'} - 1\right)^{\frac{1}{2}}$. Solutions for L_1, L_2, and C, as functions of Q_L, are shown in Figure 4-10 for the three operating frequencies typically used (8, 12 and 16 MHz). In order to keep component values within practical limits, a Q_L of 5 - 10 was generally selected.

Once having chosen an assumed antenna impedance ($Z_{L0} = R_{L0} + iX_{L0}$) and Q_L, the values of the components of the matching network are determined. With these values fixed, the fraction P of the power available from the generator which is deposited in the load decreases as the antenna resistance R_L or reactance X_L varies. Plots of P as functions of RL and X_L are shown in Figures 4-11a,b for several different values of the design antenna impedance Z_{L0}. Note that for each curve, the factor P is unity only when $Z_L = Z_{L0}$, since that is the impedance for which the network is tuned.

For a typical Z_{L0} ($0.5 + 5.0i\ \Omega$), Figure 4-11a shows that greater than 70% of the available power is delivered to the load provided $0.14\,\Omega < R_L < 1.70\,\Omega$ (for $X_L = X_{L0}$). Hence the matching network is not extremely sensitive to the changes in R_L which we expect to see during the actual plasma shot. If R_L is held fixed at R_{L0}, and X_L is varied, Figure 4-11b shows that greater than 70% of the available power is delivered to the load if $4.3\,\Omega < X_L < 5.7\,\Omega$. This is a much smaller (14%) relative allowable change than was found for the case where R_L was varied, but fortunately during a plasma shot X_L changes by less than 10%. Hence a simple T-network, appropriately tuned, can provide sub-

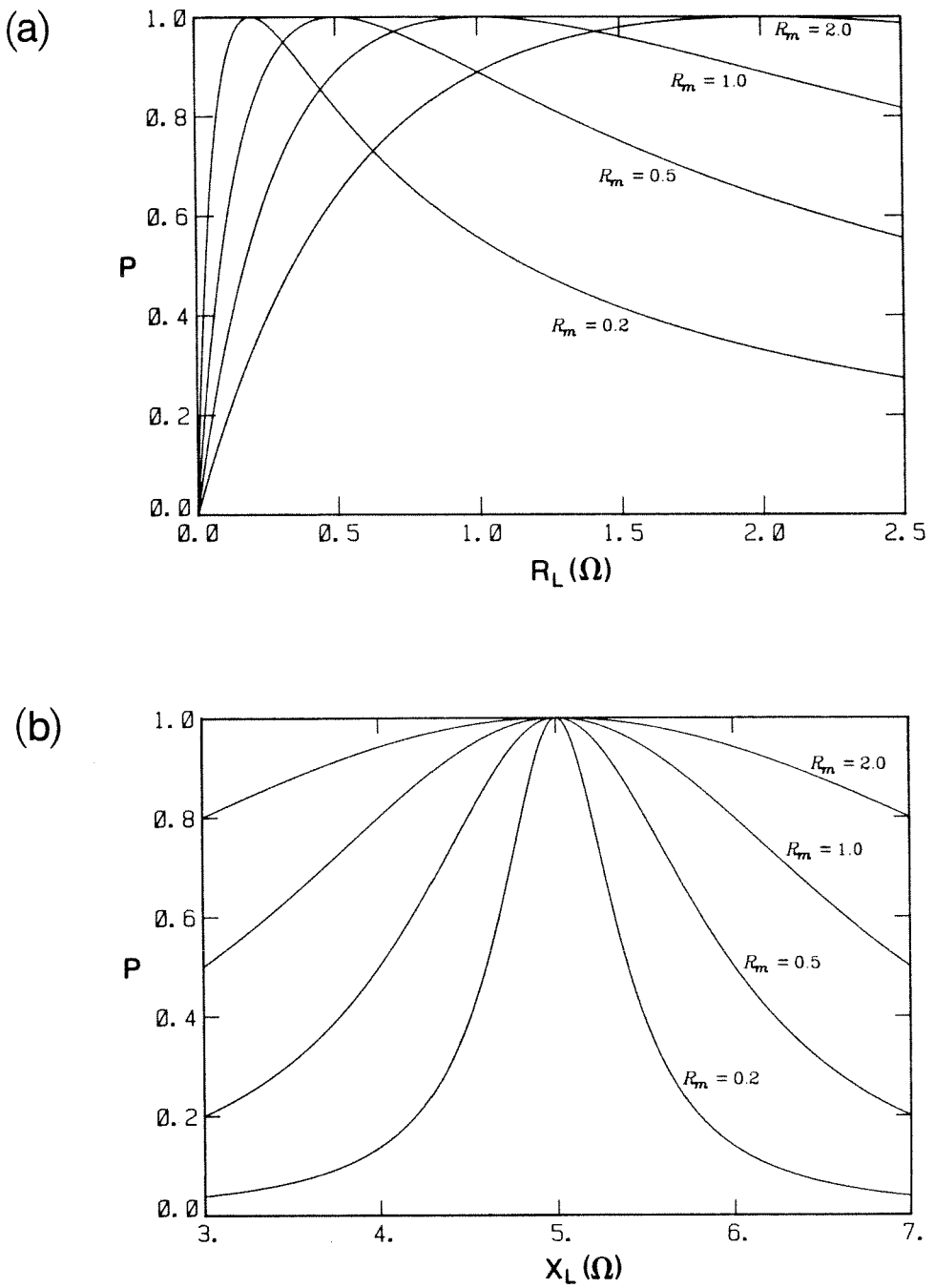

FIG. 4-11. Calculated sensitivity of impedance-matching network to changes in load impedance. a) Fraction P of power available from generator which is deposited in load for fixed matching network parameters, as a function of R_L. The frequency is 12 MHz and the load resistance is 0.5 Ω. Four different curves are shown, corresponding to setting the impedance-matching network for a perfect match at $Z_L = R_m + 5.i$ Ω, where R_m = 0.2, 0.5, 1.0 and 2.0 Ω. b) Fraction P as a function of X_L, for fixed load resistances R_m. For each curve, the matching network has been set to yield a perfect match at $Z_L = R_m + 5.i$ Ω.

stantial amounts of power to the antenna-plasma load even with the impedance changes that occur during the shot.

It should be pointed out that the above discussion assumed that the generator impedance, R_g, remained constant as the load impedance changed. This was true for some of the RF exciters (e.g. the ENI A-300 amplifier), but the effective output impedance of the high power tetrode amplifier did depend on the power level and the load mismatch. Although the impedance matching network design may not have been optimal for the high-power amplifier, large amounts of power were still successfully coupled to the plasma.

4.4.3 Construction

The T-network matching system (Figures 4-12 and 4-13) was built within an aluminum box which measured 55 × 65 × 42 cm, and was, during operation, mounted adjacent to the RF antenna on a table next to the tokamak. The RF input cable and the antenna feeder tube attached to the box via specially constructed RF-tight fittings.

The input cable center conductor was connected to the middle of a two-position high voltage air-powered switch. The switch consisted of two 2.2 cm o.d. brass cone-shaped plugs connected to flexible copper braid and facing opposite sides of a central cylindrical brass electrode which had conical depressions machined in each end. The fixed center electrode was mounted in a hole bored perpendicularly through a 7.6 cm o.d. plexiglass pillar which was bolted to the bottom of the aluminum box. The two movable electrodes were mounted, via plexiglass insulators, to the ends of air cylinders which were in turn mounted on two facing sides of the box. The air cylinders had strokes of about 10 cm and were pneumatically connected via solenoid valves to an air source and arranged so that when one was extended, the other was withdrawn. The large separation was necessary to prevent RF arcs when operating at high

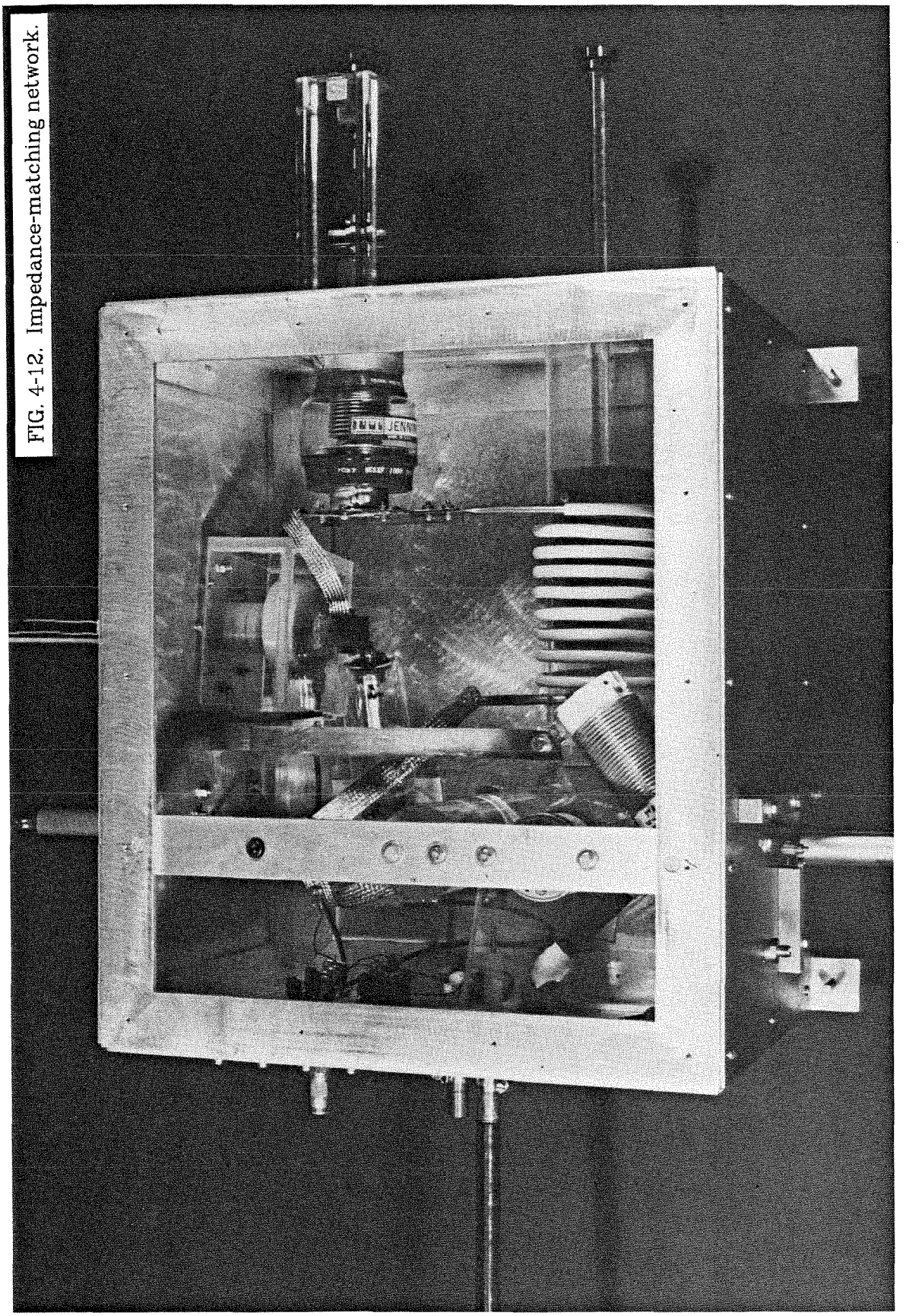

FIG. 4-12. Impedance-matching network.

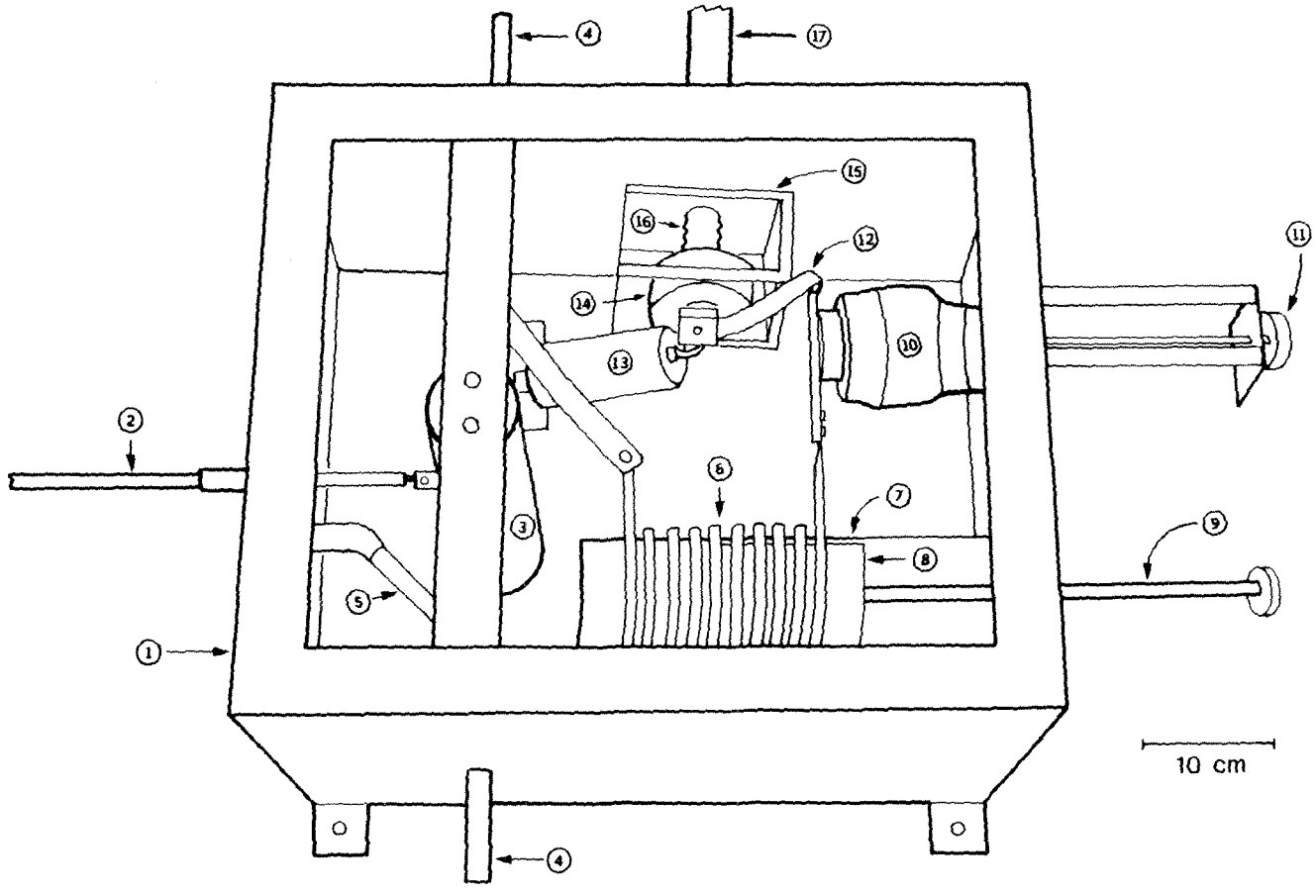

FIG. 4-13. Schematic of Figure 4-12. **1** - Aluminum housing (cover removed). **2** - RF input cable (RG-17 A/U) which plugs into center electrode of high voltage switch. **3** - Plexiglass pillar housing center electrode of high voltage switch which connects input either to a dummy load or to inductor L_1. The switch itself is hidden beneath the bracket supporting the pillar. **4** - Air cylinders which drive the high voltage switch. **5** - 50 Ω dummy load resistor. **6** - Inductor (L_1). **7** - Plexiglass insulating tube. **8** - Sliding brass cylinder to vary L_1. **9** - Adjustment rod for brass cylinder. **10** - Vacuum capacitor (C). **11** - Adjustment knob for vacuum capacitor. **12** - Inductor (L_2). **13** - Vacuum voltage divider capacitor. **14** - RF current monitor. **15** - Plexiglass housing to insulate current monitor. **16** - Ceramic insulator of antenna feeder tube. **17** - Antenna feeder tube.

power levels. The electrodes, which had a contact area of about 3.5 cm^2, were silver-plated to minimize contact resistance. One side of the switch was connected to an air-cooled 50 Ω non-inductive resistor which served as a dummy load for testing purposes; the other side led to the inductor L_1 of the impedance-matching network. The switch could be activated remotely from the amplifier cabinet so that the high power amplifier could be easily tuned using the dummy load before attempting to tune the matching network.

Capacitor C was a 0 - 1000 pF, 15 kV vacuum capacitor, one flange of which was mounted to the aluminum box wall. The inductor L_1 was wound from 1.3 cm o.d. soft copper tubing, insulated with heat-shrink tubing, and mounted on a 10 cm diameter plexiglass tube. The coil used for most of the experiments consisted of nine turns over a length of 18 cm and had an inductance of 5 μH (at 12 MHz). The inductance was varied (i.e., decreased) by sliding a copper tube, 8.9 cm in diameter, inside the plexiglass tube underneath the coil windings. Since the tube was much thicker than a skin depth, flux was excluded from its interior (through the induction of appropriate surface currents) and the net flux linking the coil was reduced. The tube also increased the stray capacitance between turns of the coil, changing the self-resonant frequency. In practice, the coil reactance could be lowered by up to ~50% using this method, and although the Q of the coil itself was reduced, there was no significant decrease in the overall matching network Q (indicating that power losses in the sliding tube were not important). Inductor L_2 was not adjustable and consisted simply of the strap connecting the vacuum capacitor to the center conductor of the antenna feeder tube.

RF antenna current was measured with a current monitor (Ion Physics Co. model CM-100-L) mounted in a plexiglass shield directly over the ceramic insulator at the end of the antenna feeder tube; the sensitivity of the monitor, connected to a 50 Ω terminated cable, was 0.1 V/A. RF voltage was measured

with a capacitive voltage divider (similar to that described in section 4.2.3) which was connected to the antenna tube inner electrode at the point where it emerged from the O-ring seal at the end of the ceramic insulator. The output of the divider, also connected to a 50 Ω terminated cable, was 0.55 mV/V at 12 MHz. The divider had a nearly flat frequency response over the range of interest but was calibrated at each frequency used.

4.5 Linear RF Detectors

In order to record the amplitudes of RF signals (forward and reflected voltages, antenna voltage and current, magnetic probe outputs) on the low-frequency (<1 MHz bandwidth) digital transient recorders, amplitude or envelope detectors were required. Square-law diode detectors were originally used but resulted in compressing the 48 db dynamic range of the 8-bit transient recorders to only 24 db. Since the magnetic probe signals may vary by 10 db more than this, a linear detector was desirable. The availability of a linear detector–video amplifier integrated circuit (designed for radar signal-processing applications) provided a simple solution.

A ten-channel RF detector system was constructed; the schematic for a single channel appears in Figure 4-14a. A broadband 1:4 RF transformer coupled the input signal (terminated in 50 Ω) to the detector's long-tailed pair input. Some R–C filtering was required at the video amplifier output to prevent spurious oscillations and was followed by a low frequency 20 db gain amplifier. The time response of the detector was determined by the R–C filter and was typically set to ~2 μsec. The frequency response was quite flat, varying by less than 0.5 db from 1 to 100 MHz (Figure 4-14b). The input-output voltage calibration curve for a typical detector is shown in Figure 4-14c; it is reasonably linear over a 40 db range.

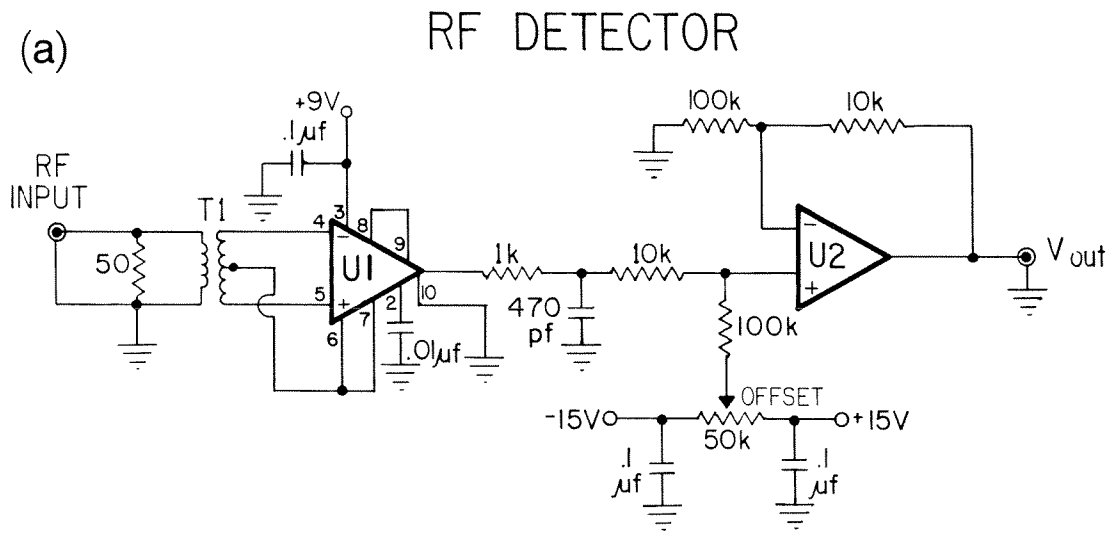

U1 – Plessey SL510C

U2 – LF 356

T1 – 1:4 broadband RF transformer
(Minicircuits T1-1T)

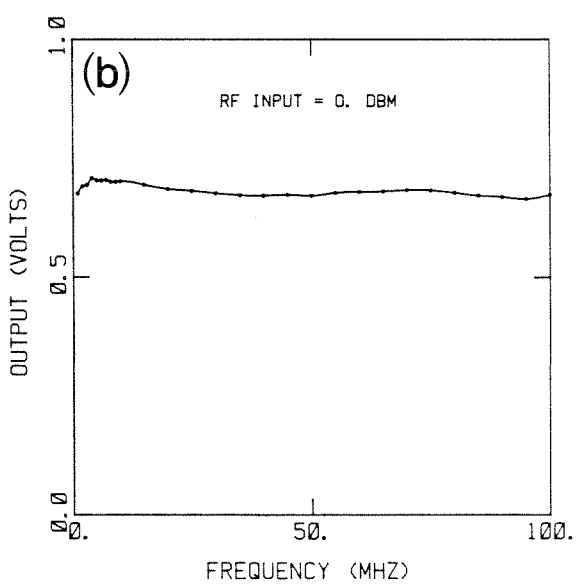

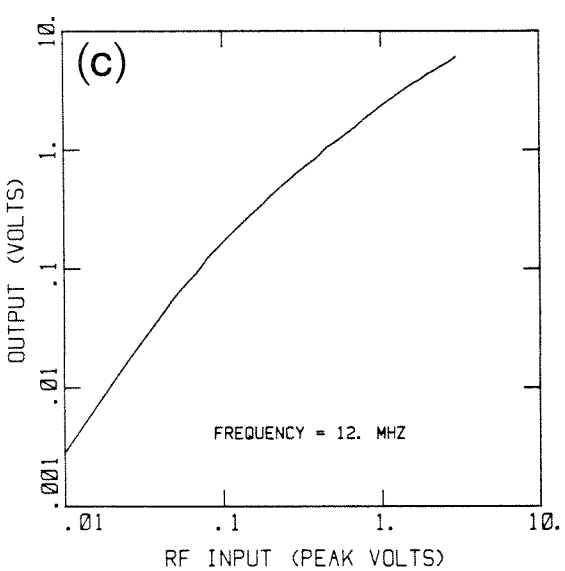

FIG. 4-14. a) Schematic of linear RF detector (one channel). b) Frequency response of detector: DC output voltage versus frequency for fixed input amplitude. c) Linearity of detector: DC output voltage versus RF input peak voltage for a fixed frequency.

The actual calibration curves for the detectors were stored on disk and used during data analysis to accurately unfold the RF amplitude signals.

4.6 RF Phase Detectors

4.6.1 Introduction

RF phase detectors were required both for measuring the phase between the antenna current and voltage (for impedance measurements) and for measuring the phase of the wave fields detected by various probes around the tokamak. The different applications imposed different constraints on the phase detectors.

When an eigenmode came into resonance, the magnetic probe signal magnitude could increase by a factor of up to 25 - 35 db (see Chapters 6 and 7). The temporal width of the resonance was determined by the Q of the mode and by the rate of change of plasma density. The half-width of the resonance peaks on the probe signals was typically 50 - 500 μsec in these experiments, during which the phase of the signal could undergo transitions of up to about 2π radians.

The characteristics of the RF signals from the antenna voltage and current monitors were somewhat different. Sharp peaks associated with eigenmodes were seen with some antennas, but the change in signal magnitude during the plasma shot was generally less than 10 db. However, the change in phase between the voltage and current signals was very small - less than 1 degree in some experiments. In this case, therefore, phase noise and dependence on input amplitude had to be minimized.

4.6.2 DBM Phase Detector

Several approaches to the problem of phase detection were considered. Double-balanced mixers (DBMs) are commonly used as phase detectors at RF frequencies [Mini-Circuits Laboratory, 1980] and were used here in early impedance-measuring experiments. When two signals of the same frequency are applied to the RF and LO (local oscillator) ports of a DBM, the DC component of the output at the IF (intermediate frequency) port is a function of the phase difference between the signals. The approximate phase characteristic of this kind of detector is $V_{out} = A_1 A_2 \cos\varphi$, where A_1 and A_2 are the amplitudes of the input signals, φ is the relative phase difference between them, and provided A_1 and A_2 are well below the compression level of the mixer. In order to unambiguously determine the phase over a 2π radian range, a quadrature system using two DBMs must be used (Figure 4-15). The phase difference between the input signals may then be found from

$$\varphi = \tan^{-1}\left(\frac{V_2}{V_1}\right) + \frac{\pi}{2}\left[1 - \mathrm{sgn}(V_1)\right], \tag{4.8}$$

where $\tan^{-1}$ is the principal branch and $-\frac{\pi}{2} < \varphi < \frac{\pi}{2}$. This approach has the advantage of simplicity, good harmonic rejection, and lack of active components but suffers from several drawbacks. The phase characteristic function ($\sim\cos\varphi$) is only an approximation; its actual form must be found by careful calibration and depends somewhat on input power level. The dynamic range of the system (important for magnetic probe measurements) is limited because of the proportionality of the output voltage to the input signal amplitude (the data recording system has a fixed dynamic range of 48 db). Finally, a single phase signal requires two data channels, which are often a scarce commodity.

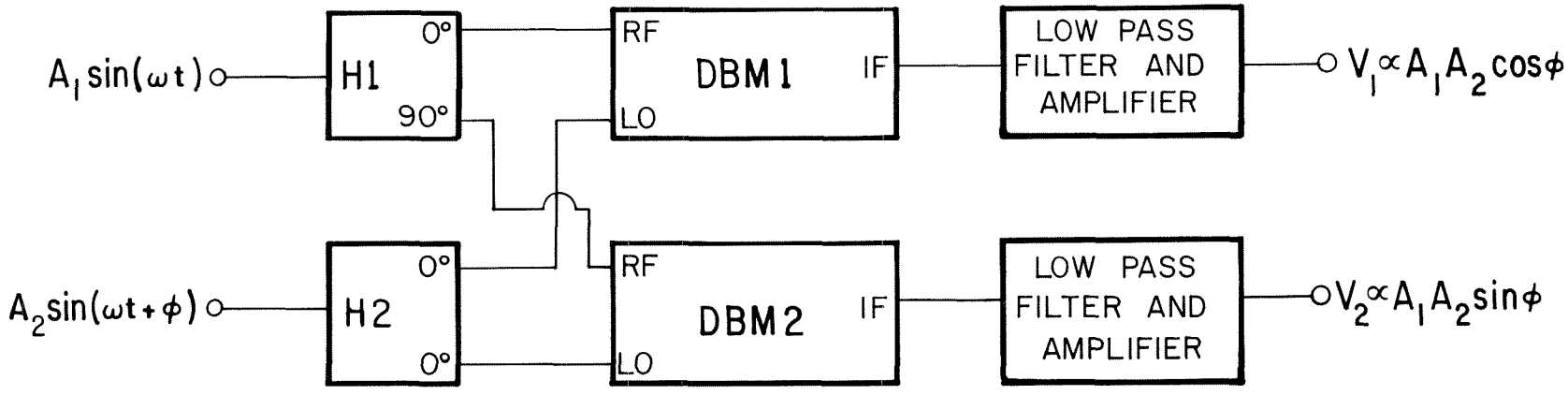

H1 - Wide bandwidth quadrature hybrid (Anzac JH-6-4)

H2 - 0° Power splitter (Minicircuits ZSC - 2 - 1)

DBM1, 2 - Matched pair, high compression level double-balanced mixers (Minicircuits ZAY - 3 - 1)

FIG. 4-15. Quadrature phase detector using two double-balanced mixers.

4.6.3 Digital Phase Detector

A simple digital phase detector has been devised which circumvents the above problems. The relative phase between two RF' sinusoids is proportional to the time interval τ_{zc} between successive positive (or negative) - going zero-crossings of the signals: $\varphi = 2\pi\tau_{zc}/\tau_{rf}$, where τ_{rf} is the RF' period. An ideal phase detector could therefore consist of a two-state "black box" which would be set high whenever one input signal had a positive-going zero-crossing and would be set low whenever the other signal had a positive-going crossing. The output of this device would then consist of a train of pulses whose duty-cycle would be proportional to the input phase difference. The phase information could be extracted by low-pass filtering the output.

The design of a four-channel, 2π radian range phase detector for use with the magnetic probe signals is shown in Figure 4-16. Because τ_{rf} could be as short as 50 nsec (at a frequency of 20 MHz), circuitry with very fast switching times was required. ECL (emitter-coupled logic), with transition times on the order of 1 nsec, was found adequate. The function of the above-mentioned "black box" and the subsequent low-pass filtering was realized using an ECL comparator, two ECL D-type flip-flops, and a low-frequency differential amplifier. The sinusoidal input signals were converted to square waves of constant amplitude by the comparators. Each flip-flop had only one input which was positive-edge triggered: the clock (Ck) input. The other inputs (R (reset), and S (set)) were state-sensitive.

Consider the function of flip-flop $U3a$ in Figure 4-16. As long as the positive-going transition at the Ck input occurs while R is low, the output at Q is a pulse-width modulated square wave whose duty-cycle is linearly proportional to the phase difference between the inputs at Ck and R. During π radians of the phase characteristic, however, the transition at Ck occurs while R is high, and so the output Q remains low. The operation of flip-flop $U3b$ is

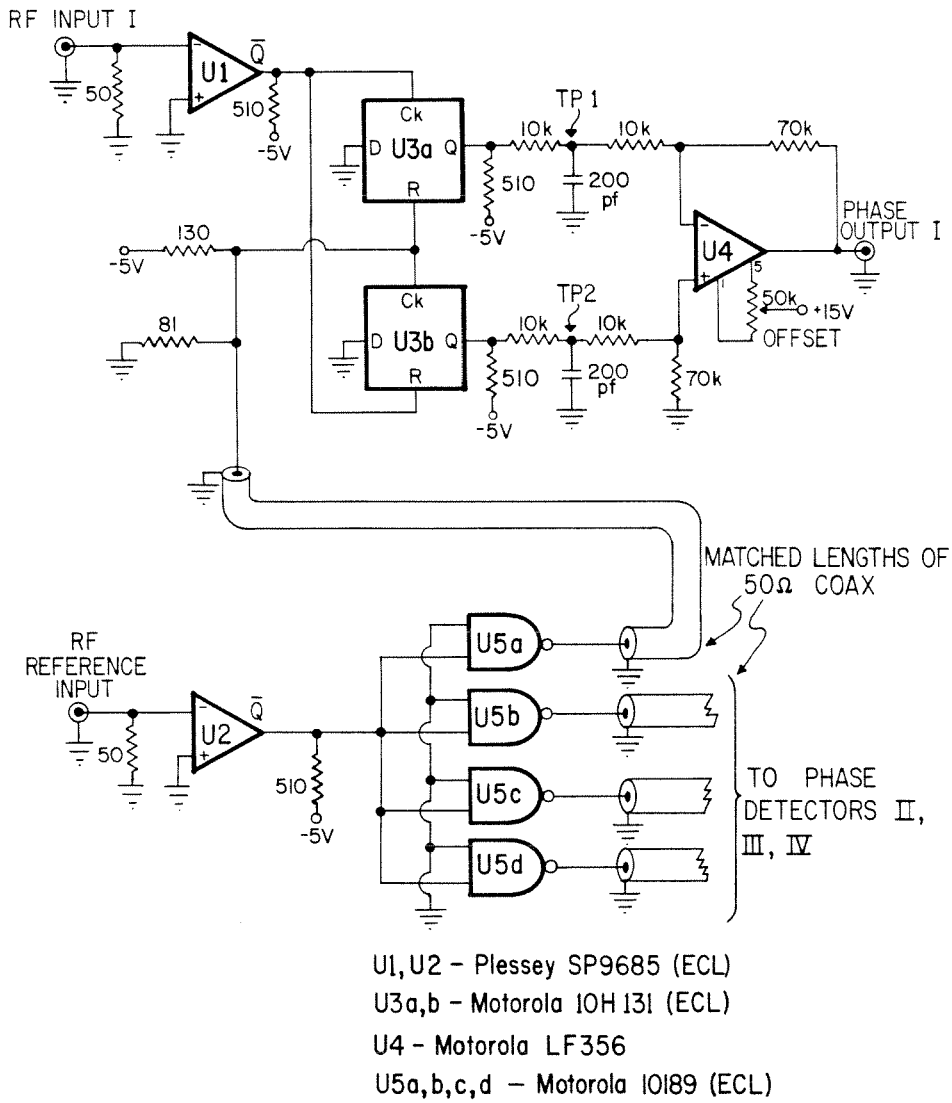

FIG. 4-16. Schematic diagram of 2π radian range digital phase detector (one channel shown). Compact layout of ECL circuitry was crucial to optimize performance.

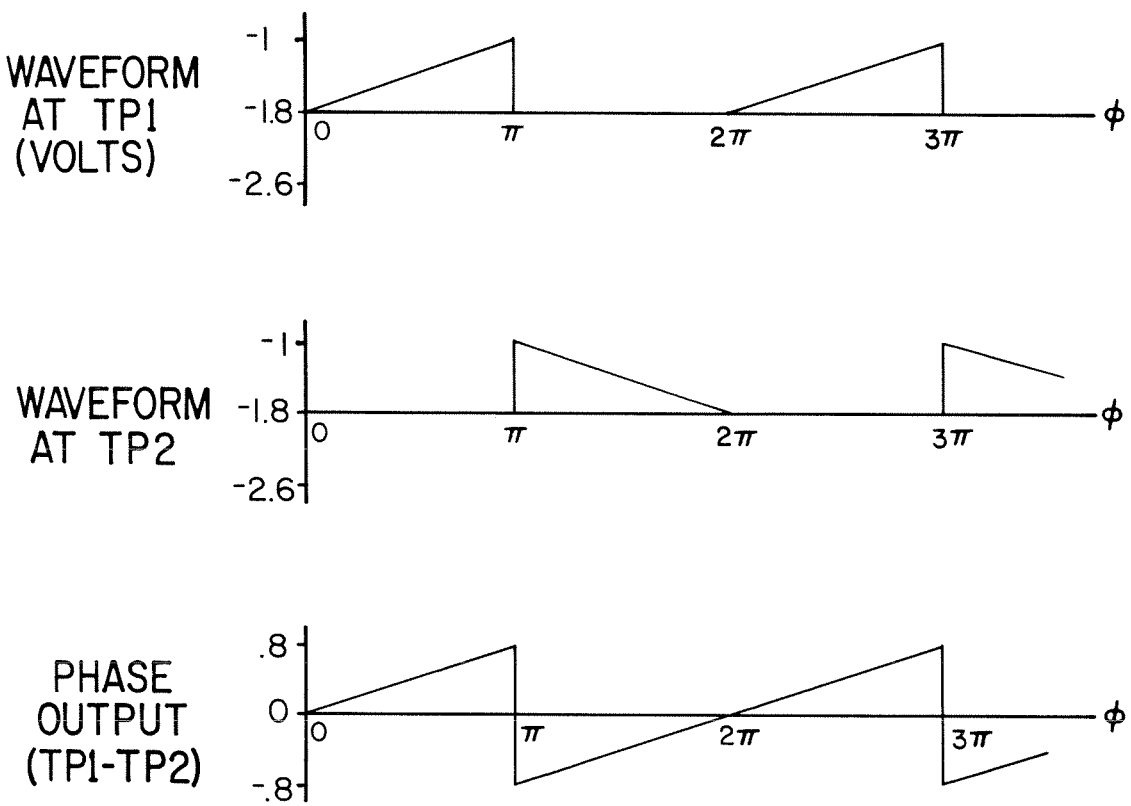

FIG. 4-17. Waveforms at *TP*1 and *TP*2 (in FIG. 4-16) as functions of the phase difference between the input signals. Subtracting the two waveforms provides a phase characteristic with a 2π radian range.

identical except that its Ck and R inputs are interchanged with respect to $U3a$. Therefore, output Q of $U3b$ provides a pulse-width modulated output during the π radian portion of the characteristic when Q of $U3a$ remains low, and conversely it remains low during the π radian portion when $U3a$ is functional. The flip-flop outputs are low-pass filtered by an $R-C$ combination and are subtracted by a differential amplifier ($U4$). The variation of filtered outputs (at $TP1$, $TP2$ in Figure 4-16) with input phase difference is shown in Figure 4-17, and it is clear that subtracting the two provides a linear phase output characteristic with a 2π radian range.

The time response of the phase detectors to a step change in phase was determined by the time constant of the low-pass filter and was generally set to $\sim 5\,\mu$sec. The frequency range over which the phase detector operated was limited on the upper end by the rise and fall times of the ECL logic. Distortion of the phase characteristic begins to occur when the rise and fall times become a substantial fraction of the RF period. Typically these phase detectors functioned at frequencies of up to about 70 MHz.

4.6.4 Harmonic Distortion

The digital phase detector is, however, sensitive to the presence of harmonics on the input signals. To obtain an estimate of the magnitude of this effect, consider an idealized comparator, with no input offset or hysteresis, whose output changes state as the input voltage passes through zero:

$$V_{\text{out}} = V_L + \left[V_H - V_L\right] \text{sgn}(V_{\text{in}}) \,, \tag{4.9}$$

where V_H and V_L are the two output voltage states of the comparator. If a sinusoid $A_0 \sin(\omega_0 t)$ is applied to the input, the output will change states at times $t = n\pi/\omega_0$, where n is an integer. If a harmonic of the fundamental frequency is added to the input, the transition times will be shifted. For an input

$V_{in} = A_0 \sin(\omega_0 t) + A_n \sin(n\omega_0 t + \varphi_n)$, the positive-going zero-crossing which had occurred at $t = 0$ before the introduction of the harmonic now occurs approximately at time

$$t_{zc} = \frac{-A_n \sin\varphi_n}{A_0 \omega_0 \left[1 + n \frac{A_n}{A_0} \cos\varphi_n\right]} \tag{4.10}$$

The shift in transition time is a function of the relative phase of the harmonic, φ_n, and its maximum occurs at $\varphi_n = \pi/2$, for $nA_n \ll A_0$, leading to a maximum possible shift in zero-crossing time of $\Delta t_{zc} = \frac{A_n}{A_0 \omega_0}$. This corresponds to the introduction of a phase error of A_n / A_0 radians. Thus, to keep the error introduced by a harmonic to a level less than 0.1 degree (which is necessary in some of the impedance-measuring experiments), the amplitude of the harmonic should be at least 55 db below the fundamental. Experimental simulations agree reasonably with this estimate.

By observing the RF antenna current and voltage signals during plasma shots with a spectrum analyzer, it was found that the second (2ω) and third (3ω) harmonic amplitudes were generally lower than 30 db below the fundamental. This was sufficient, however, to require additional filtering preceding each input to the phase detector. A pair of 50 Ω, six-pole bandpass filters were constructed for each fundamental operating frequency using image-parameter design. A typical 12 MHz filter had a 3 db bandwidth of 2 MHz and an attenuation of 60 db above 23 MHz, which was more than sufficient to reduce the effect of input signal harmonics on the phase detector output to a negligible level.

4.6.5 Dynamic Range

The dynamic range of the phase detection system can be defined as the ratio of maximum to minimum input signal amplitude (at constant input

phase) over which the detector output varies by less than a given amount. Variation of the detector output as the input amplitude is decreased is primarily a consequence of the input offset voltage and finite gain of the comparators. The upper limit (A_{max}) to the allowable input amplitude is typically slightly less than half of the comparator power supply voltage swing. As the input signal envelope decreases, the point during each cycle at which the comparator triggers the subsequent ECL logic changes. This introduces a phase error whose magnitude can be simply estimated.

The voltage transfer function for a comparator may be modeled as

$$V_{out}(V_{in}) = \frac{V_H + V_L}{2} + (V_{in} + V_{off})\cdot\Psi(V_{in}) , \tag{4.11a}$$

where

$$\Psi(V) = \begin{cases} G\cdot V & \text{for } V_L/G < V < V_H/G \\ V_H & \text{for } V > V_H/G \\ V_L & \text{for } V < V_L/G \end{cases} \tag{4.11b}$$

Here G is the comparator voltage gain and V_{off} is the input offset voltage. Let the input voltage be $V_{in} = A\sin(\omega t)$ and the positive-going voltage at which the subsequent ECL switches, V_s. Then the time t_s at which the transition occurs is given by the solution of

$$V_s = G\cdot\left[A\sin(\omega t_s) + V_{off}\right] + \frac{V_H + V_L}{2} . \tag{4.12}$$

The apparent phase shift $\Delta\varphi$ introduced by changing the input signal amplitude from A_{max} to A_{min} is then

$$\Delta\varphi = 2\pi \frac{\Delta t_s}{\tau_{rf}}$$

$$= \sin^{-1}\left(\frac{V_s' - G\,V_{off}}{G\,A_{min}}\right) - \sin^{-1}\left(\frac{V_s' - G\,V_{off}}{G\,A_{max}}\right), \qquad (4.13)$$

where $V_s' = V_s - (V_H + V_L)/2$. Parameters appropriate to the Plessey SP9685 (one of the fastest comparators available) are: $G = 650$, $V_{off} = 3.0$ mV, $V_s = 0.15$ V, $A_{max} = 4.0$ V.[12] For a phase error of less than 10 degrees, then, equation 4.13 yields a dynamic range of 48 db. For an error of less than 0.1 degree, the dynamic range is reduced to 11 db. The phase detector system described was quite adequate for the magnetic probe measurements where a 2π radian range was used and the signals varied by at most 35 db. For the impedance measurements, however, where a 1 degree full scale range was often used, the dynamic range was marginal and had to be increased.

Improvements in dynamic range can be made by increasing the gain of the input stage and by reducing the input offset voltage. A phase detector was constructed for the impedance measurements which incorporated input offset adjustments and another stage of RF amplification for each comparator. The Plessey SL532 low phase-shift limiting amplifier was used, providing an additional 12 db of gain and increasing the estimated dynamic range to 23 db, which was adequate for the impedance measurements.

In laboratory simulations, the observed dynamic ranges of the phase detectors were somewhat larger than predicted. In addition, the magnitudes of the current and voltage signals for the impedance measurements changed in close synchrony during the plasma shot (since $|Z_{ant}|$ did not change very much) which tended to reduce phase errors.

12. Radar and Radio Communications IC Handbook, 1981, published by Plessey Semiconductors, Irvine, CA.

CHAPTER 5

RF Antennas and Plasma Probes

The structure which couples energy to the plasma, the RF antenna, is of crucial importance in the design of any ICRF system which transfers energy to plasma waves, yet the interactions between the antenna and the plasma remain poorly understood. An area of current controversy, for example, is the role of the Faraday shield for traditional magnetic loop antennas [Faulconer, 1981; Messiaen and Weynants, 1982]; another is the nature of the anomalous density-dependent antenna loading resistance which is seen in some tokamaks [Buzankin et al., 1976; Bhatnagar et al., 1978a; Taylor and Morales, 1978].

This chapter begins with a description of a series of RF antennas which were built in order to illuminate various features of the antenna-plasma coupling problem. The antennas were of small poloidal extent because of the limited size of the tokamak ports and were easily changed through an air-lock. Three magnetic loop antennas (bare, insulated, and Faraday-shielded) and two electric field antennas (bare plate, "T") are described. The vacuum fields associated with the magnetic loop antennas are displayed, showing some of the effects of the Faraday shield. Magnetic probes are then discussed in some detail as they were the major source of information regarding wave propagation in the plasma. A brief mention is made of several conventional Langmuir probes which were used both to measure radial density profiles and to investigate the modification of the probe $I-V$ characteristic in the plasma near an antenna due due to application of RF power. The chapter then concludes with

a section on the design and construction of a RF plasma current probe and the rotatable antenna with which it was used.

5.1 RF Antennas

5.1.1 Antenna Feedthru Assembly

The tokamak port used for the introduction of RF antennas had the largest cross-section of any port on the machine (9.8 cm high × 4.7 cm wide) and also functioned as the pumping port (Figure 5-1). The antennas had to be about 1 m long in order to pass through all of the vacuum plumbing into the tokamak chamber. The portion of the antenna which provided this length was a 3.8 cm o.d. coaxial line section which will be referred to as the antenna feeder tube. The RF coupling structure was mounted on one end of this tube; the other end consisted of an alumina high voltage insulator with an O-ring vacuum seal through which the center conductor emerged (Figure 5-2). The end with the insulator plugged into the impedance-matching box (Figure 5-3) where it was electrically connected to the T-network (section 4.4).

The center element of the feeder tube was removable and was contiguous with the radiating element at the end of the tube. A close-fitting Pyrex tube was slid into the feeder tube to provide high voltage insulation between the coaxial elements. The loop antennas required a low impedance feeder tube (see Chapter 6) and the center element of these antennas consisted of a 2.54 cm o.d. copper tube, yielding a characteristic impedance of 16 Ω. The electric field antennas, however, used a higher impedance section (99 Ω) for which the center element of the feeder tube was a 6.4 mm o.d. copper rod.

A vacuum seal was made on the outside of the antenna feeder tube through double, differentially-pumped O-ring seals which allowed sliding motion and rotation of the tube. The differential pumping was found to be

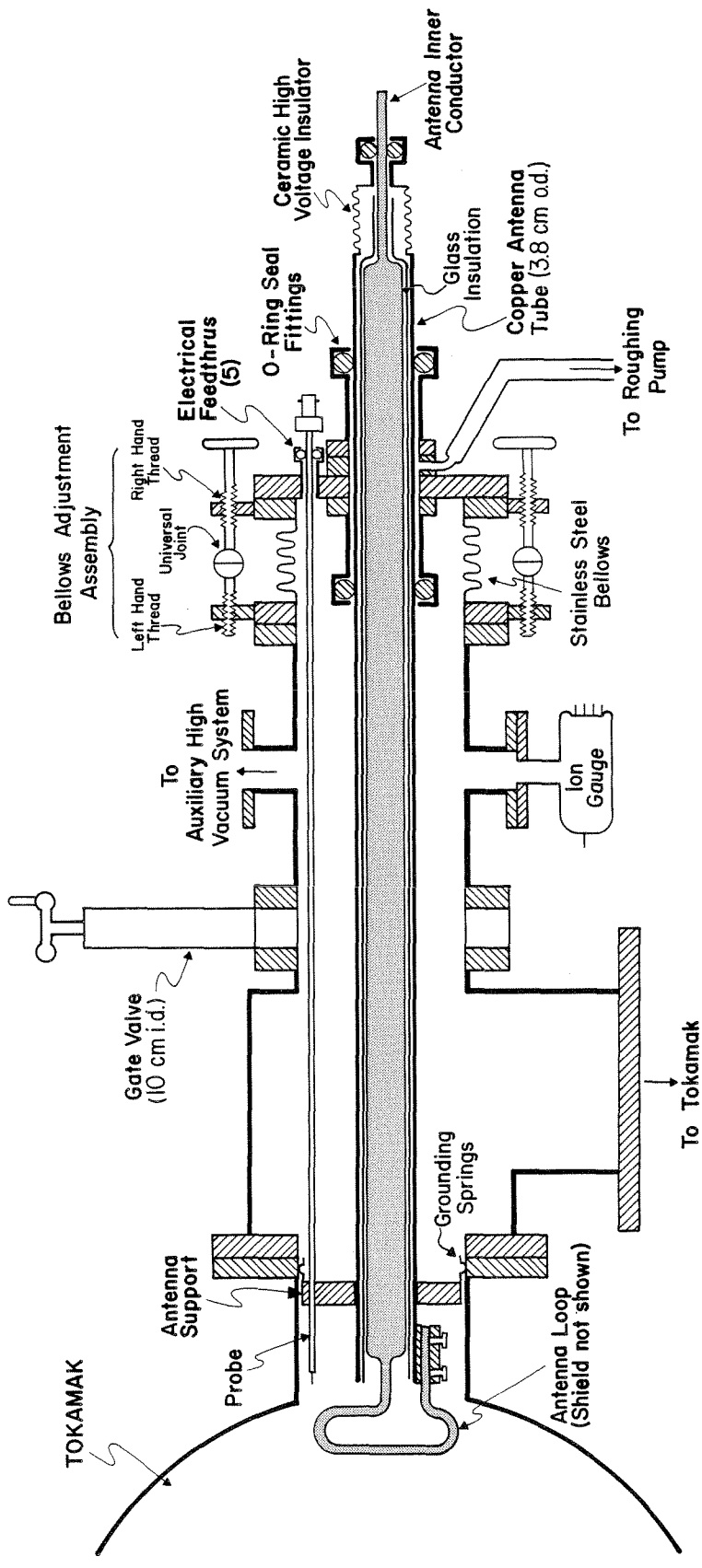

FIG. 5-1. Schematic of antenna assembly.

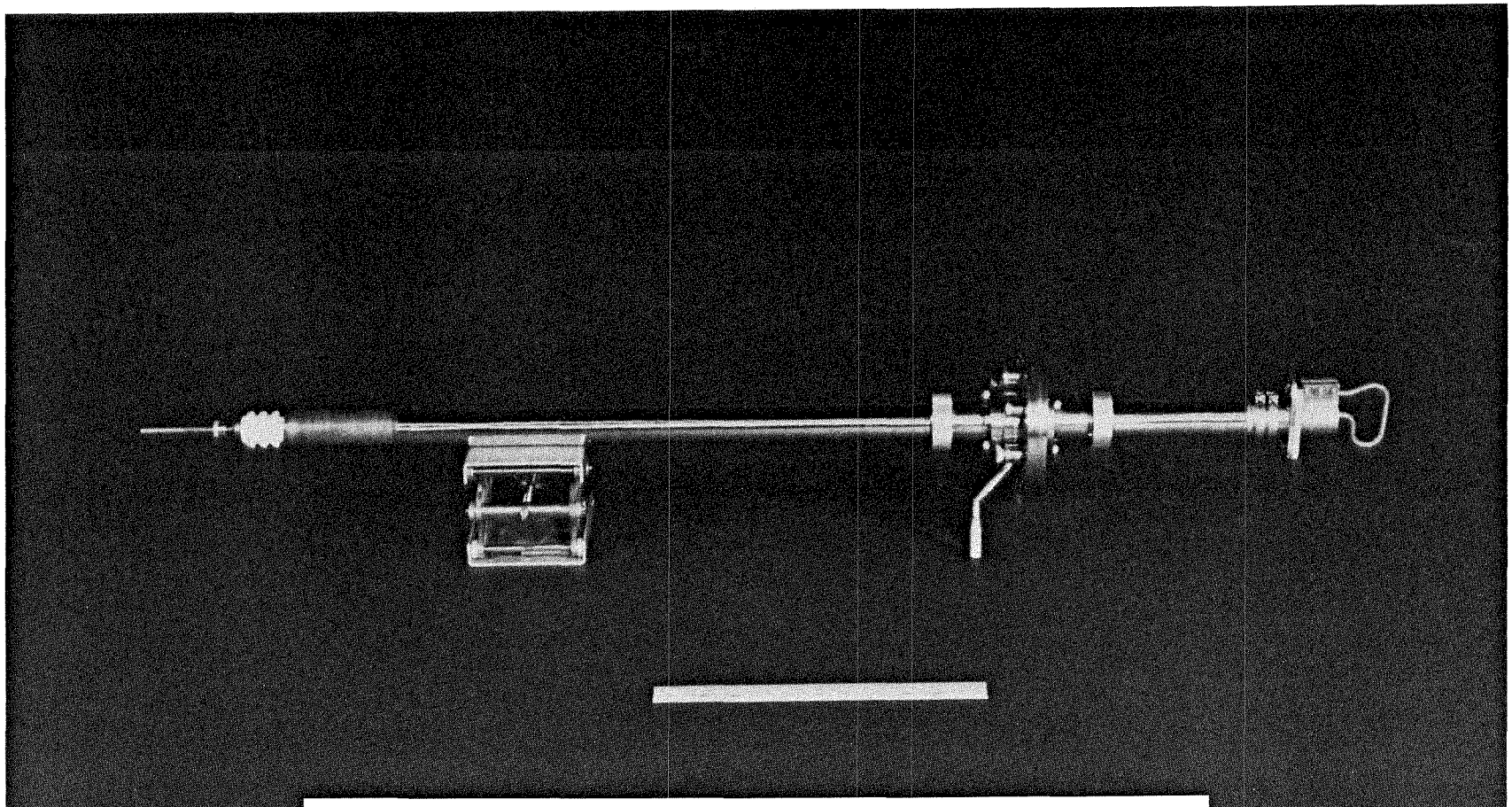

FIG. 5-2. RF antenna, showing (from right to left) loop coupling structure, feeder tube with differentially-pumped double O-ring seal feedthru flange, and ceramic insulator with O-ring seal for inner conductor. Rule is 30 cm long.

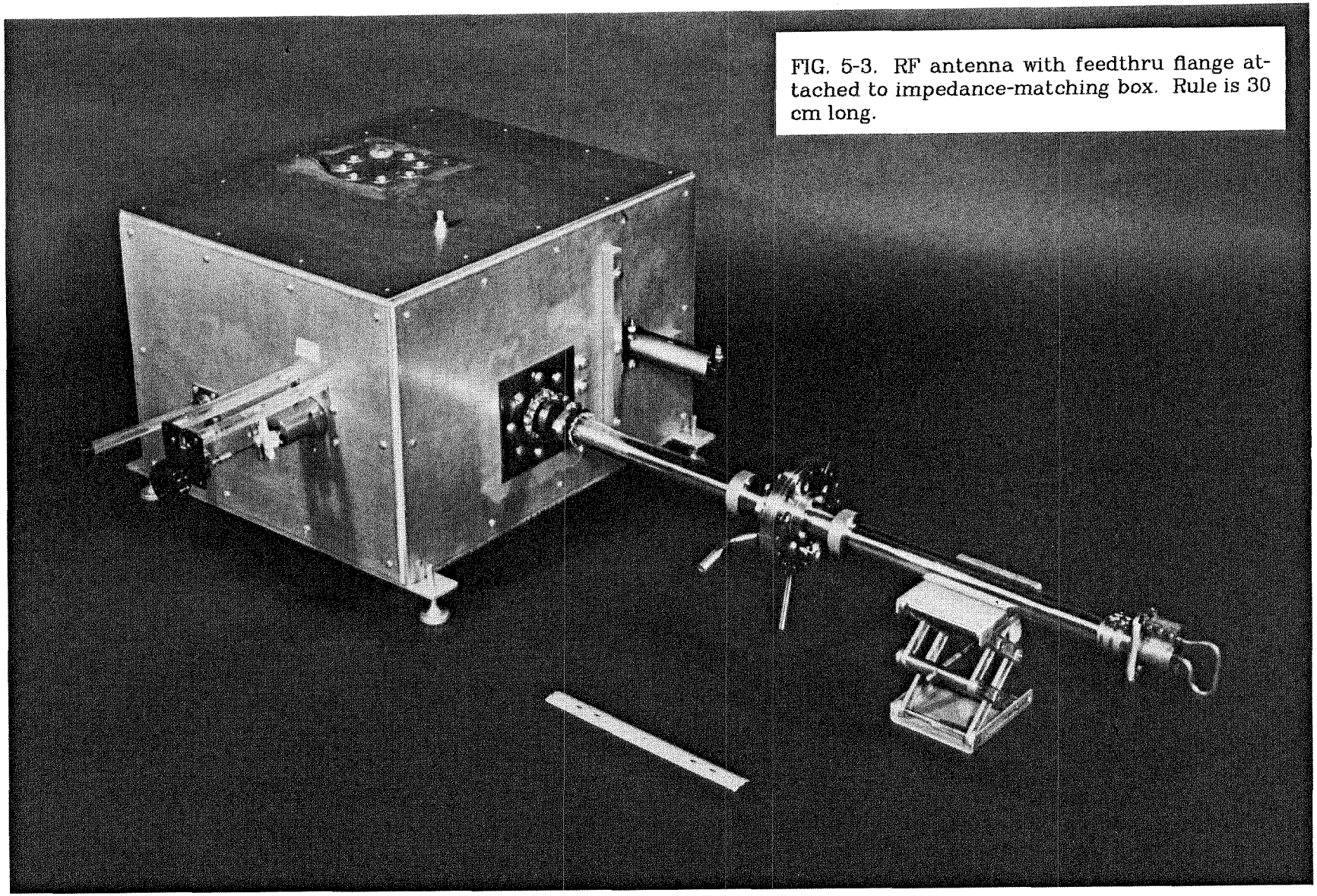

FIG. 5-3. RF antenna with feedthru flange attached to impedance-matching box. Rule is 30 cm long.

necessary in order to prevent large bursts air from leaking in past the seal when inserting the antenna. The surface of the copper feeder tube was soft and easily scored by the O-ring fittings, causing small leaks to occur. This problem was solved by plating the outside of the tube with a 25 micron layer of hard chrome; nylon bushings were also added to the insides of the O-ring fittings to decrease the lateral play in the seals. The double O-ring seal assembly was part of a 15.2 cm o.d. vacuum flange which also had five small O-ring vacuum seals for viewing ports and electrical feedthrus (Figure 5-4). This flange was mounted on a bellows assembly which allowed the antenna support structure (described below) to be aligned with the tokamak port as it was being inserted, thus preventing binding. The bellows assembly was, in turn, bolted to an 18 cm long, 10 cm i.d. air-lock chamber which had a gate valve at its end. The air-lock chamber allowed antennas to be easily changed without opening the tokamak to air; it was pumped down to the 10^{-5} Torr level with an auxiliary vacuum system before opening it to the tokamak. The antenna assembly, attached to the tokamak and the impedance-matching box, is shown in Figure 5-5.

The antenna feeder tube was grounded to the tokamak port by means of a clamp-on support structure (visible in Figure 5-4) which had spring-finger contact strips[1] along its edges. The support was machined to conform to the contours of the tokamak port, and large areas were milled through its face to maximize the pumping speed through it. An effective RF seal was made when the structure was slid into the port, compressing the silver-plated fingers. The support structure also served as a base for attachment of the Faraday shield and the Langmuir probes.

1. Manufactured by the Instrument Specialties Co., Little Falls, N.J.

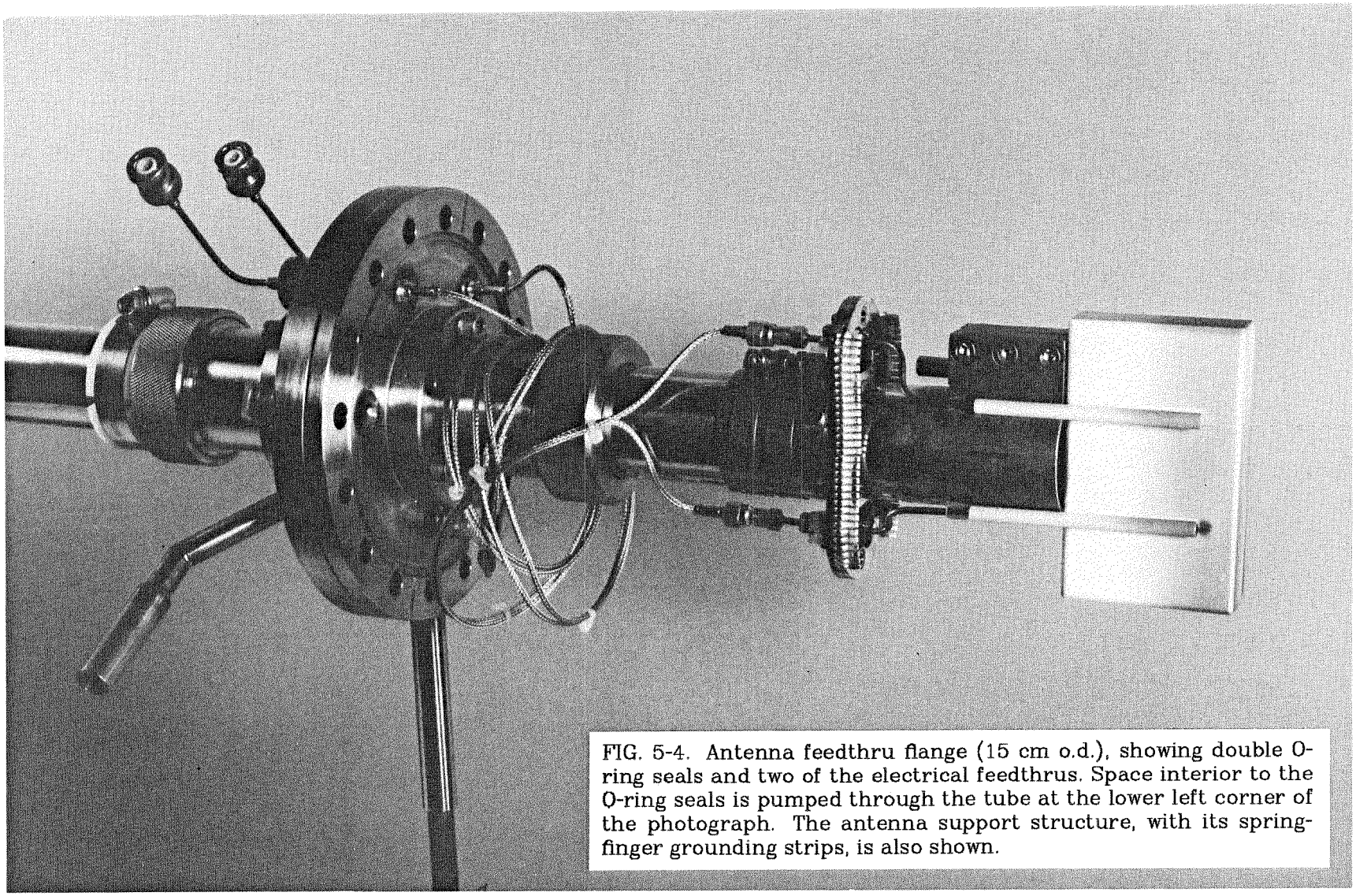

FIG. 5-4. Antenna feedthru flange (15 cm o.d.), showing double O-ring seals and two of the electrical feedthrus. Space interior to the O-ring seals is pumped through the tube at the lower left corner of the photograph. The antenna support structure, with its spring-finger grounding strips, is also shown.

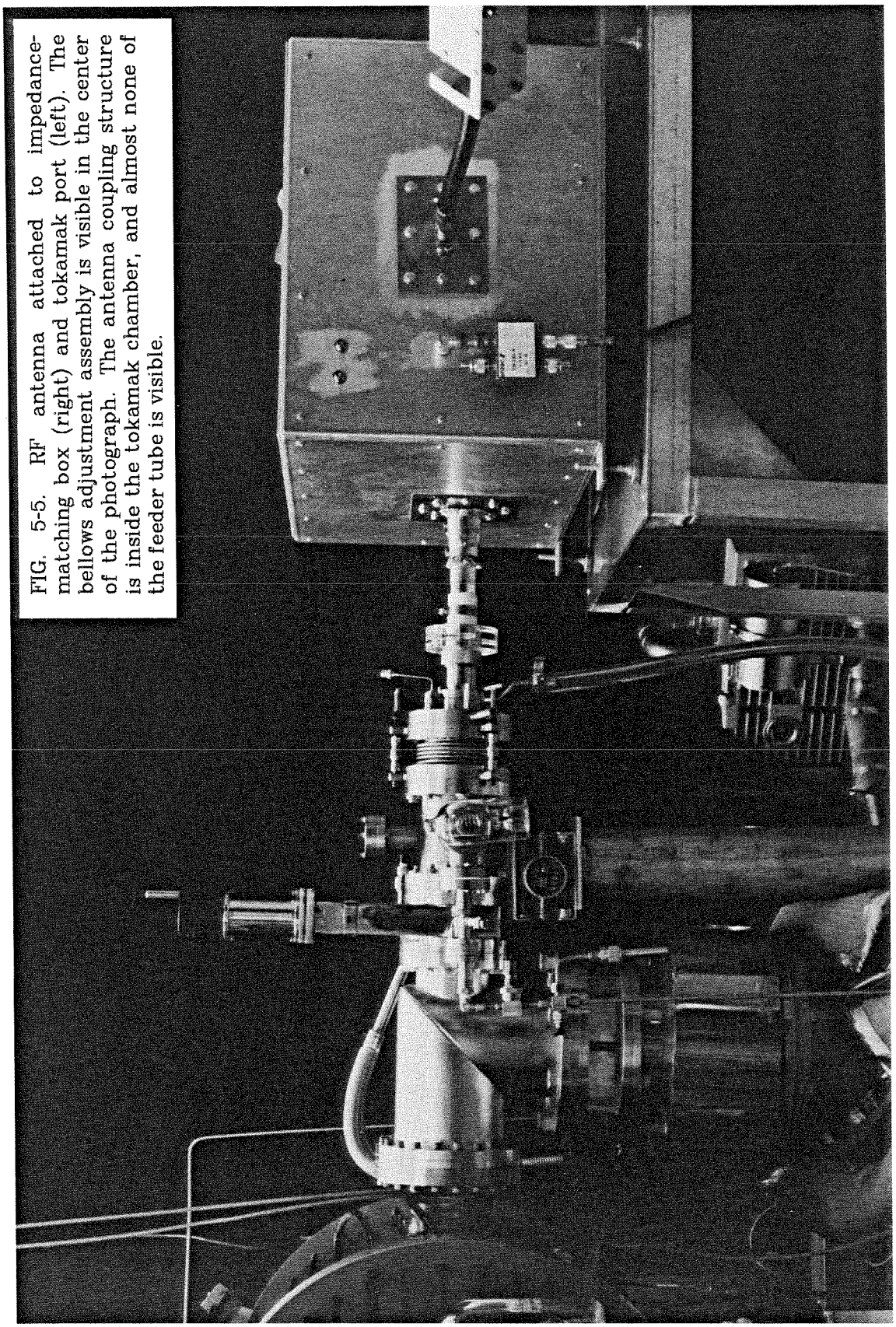

FIG. 5-5. RF antenna attached to impedance-matching box (right) and tokamak port (left). The bellows adjustment assembly is visible in the center of the photograph. The antenna coupling structure is inside the tokamak chamber, and almost none of the feeder tube is visible.

5.1.2 Bare Loop Antenna

The simplest magnetic loop antenna consisted of a bare loop of 6.4 mm o.d. OFHC copper rod. One side of the loop was welded to the 2.54 cm o.d. center conductor of the antenna feeder tube; the other side was clamped in a split copper block which was welded to the outer conductor of the feeder tube. The hole through the block, and the end of the loop which fit into it, were silver-plated to reduce contact resistance. A photograph and diagram of the antenna are shown in Figure 5-6.

The antenna could be inserted about 5 cm into the plasma (measured from the inner wall of the tokamak to the leading edge of the loop) with virtually no effect on the global plasma parameters. This distance corresponded to the end of the feeder tube being flush with the tokamak inner wall. The loop was usually left in the tokamak during the discharge-cleaning procedure and no outgassing problems were observed. Note that the entire antenna feeder tube was under vacuum, the seal being at the end which was attached to the impedance-matching box.

The Q of the antenna (the ratio of its reactance to its resistance), including the antenna feeder tube, was measured using the method described by DeMaw [1976]. A high Q (~800) variable vacuum capacitor was connected with copper strap directly across the input to the feeder tube, and a 50 Ω signal generator and a 50 Ω oscilloscope were loosely coupled to the resonant circuit through 1.0 pF capacitors. The vacuum capacitor was adjusted to achieve resonance at the desired frequency, and the frequency was then varied to find the -3 db points from which the Q was simply calculated ($Q = \frac{\omega}{\Delta\omega_{3db}}$). A value of 157 was obtained at 12 MHz with the antenna front edge 5 cm into the tokamak; this decreased to 148 with the loop withdrawn into the tokamak port (the decrease was due to induction of eddy currents in the stainless steel

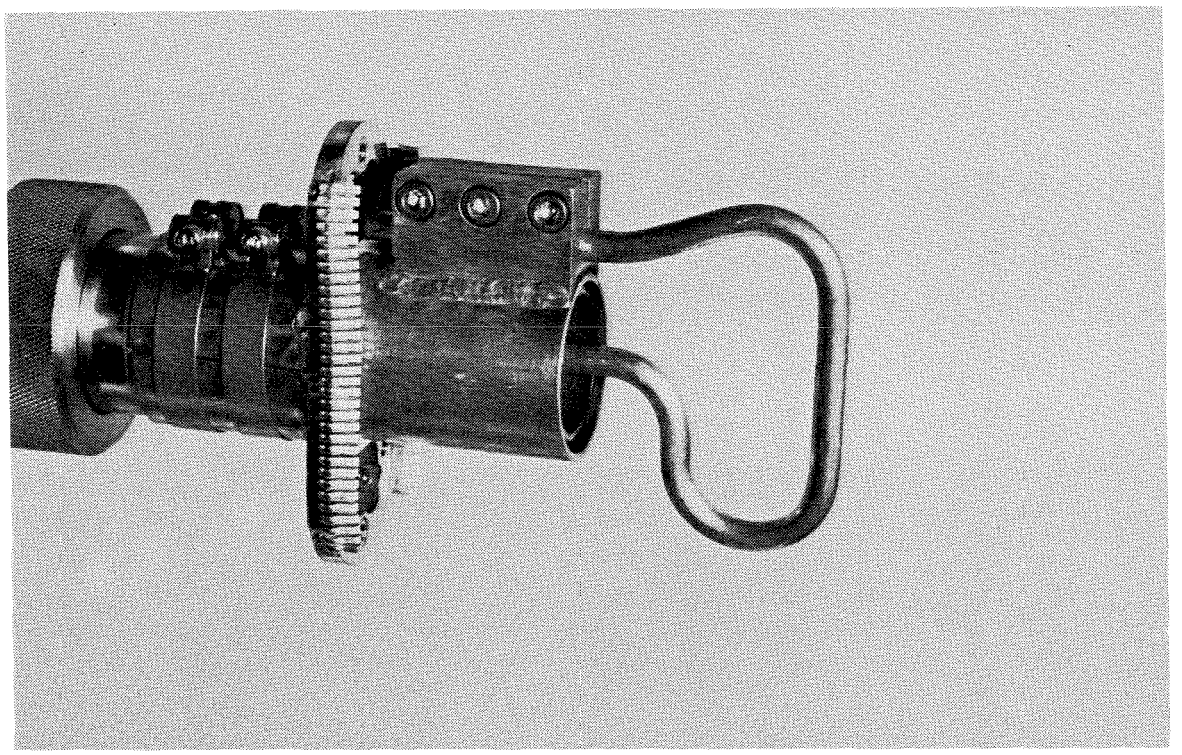

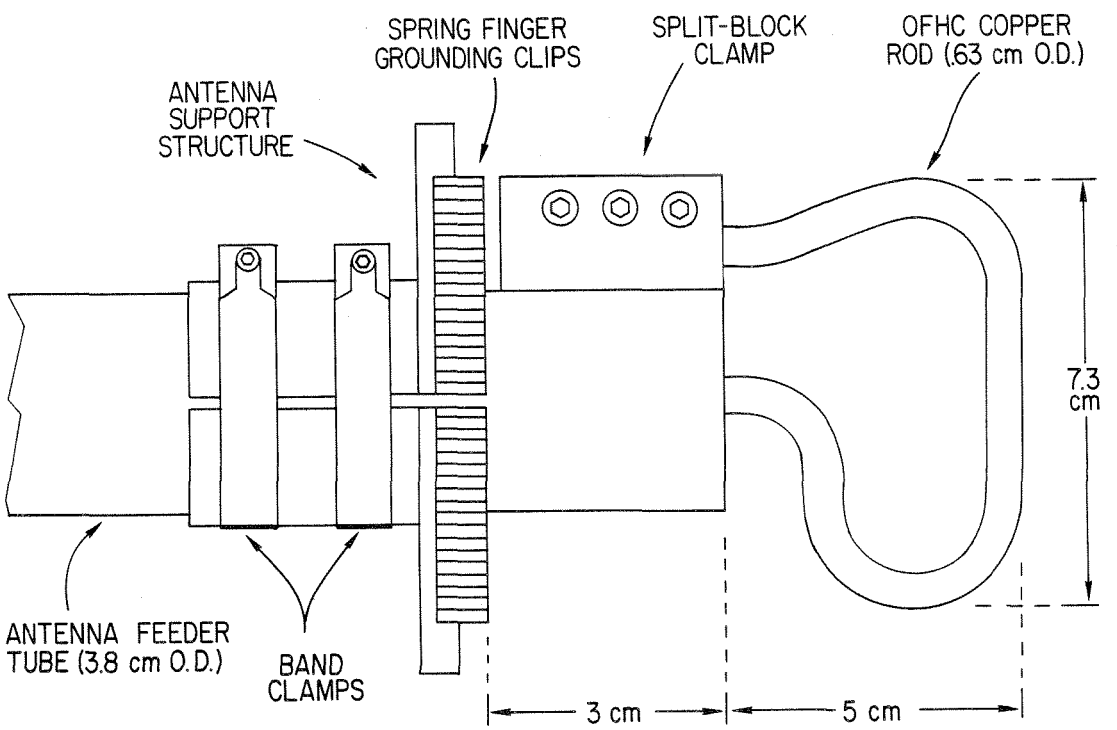

FIG. 5-6. Bare loop antenna.

port which increased the resistive part and decreased the reactive part of the loop impedance). Since the input reactance was approximately 18 Ω, the Q measurement implied an antenna resistance of about 0.1 Ω.

Calculations of the antenna resistance at 12 MHz based on its geometry, however, yielded a figure of about 0.02 Ω, a factor of 5 lower than observed. This implied that the major power losses in the antenna occurred not from distributed resistance, but from connections (i.e., between the feeder tube and the matching box, and at the clamp for the loop rod at the tokamak end of the tube). No effort was made to increase the antenna Q, however, since the losses in the antenna were sufficiently small for the experiments being performed.

5.1.3 Ceramic-Insulated Loop Antenna

The ceramic-insulated loop antenna was a modification of the bare loop antenna which prevented plasma from reaching the antenna element. A five-sided hollow box was constructed from 3 mm thick Macor[2] sheet; the outside dimensions of the box were 8.9 cm high × 5.4 cm wide × 1.9 cm thick. The edges of the Macor pieces were lapped to a smooth finish and they were assembled in a jig. The box was then glued together from the *inside* using a thin bead of low vapor pressure epoxy which was applied though a hypodermic syringe. The very close fit of the pieces of the box insured that no plasma was able to reach the epoxy. The box was then slid over the bare loop and epoxied in place, also from the inside. The completed assembly is shown in Figure 5-7.

The Macor was conditioned by leaving it in the discharge-cleaning plasma. After such cleaning, it could typically be inserted about 4 cm past the wall without adversely affecting the tokamak plasma. After several months of use, the side of the box which faced the electron runaways was noticeably

2. Macor, a machineable glass-ceramic, is manufactured by Corning Glass Works, Corning, N.Y.

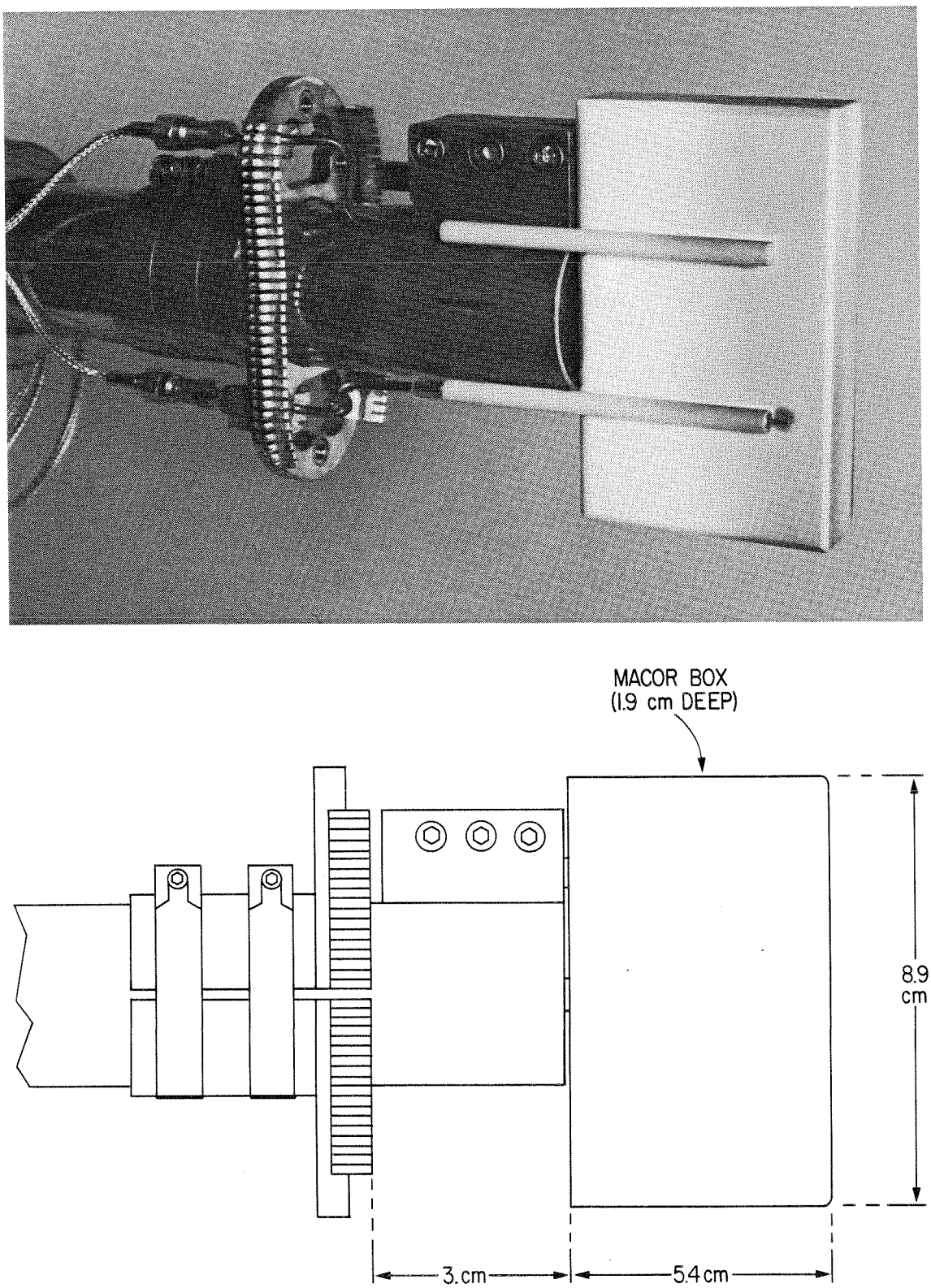

FIG. 5-7. Ceramic-insulated loop antenna, showing probes attached to the side of the antenna.

blackened. The discoloration affected only the outer 20 - 30 microns of the Macor and did not seem to affect the plasma discharge.

Several small probes were built which could be attached to the side of the Macor box (a magnetic and a Langmuir probe are shown in Figure 5-7). The bodies of the probes were 2.18 mm o.d. 50 Ω semi-rigid coax which could easily be bent to the desired contour. The last 10 cm of the probe was sheathed in an alumina tube to protect the teflon insulation of the cable and to minimize current flow to the outer conductor of the cable. The coaxial cables were clamped to the antenna support structure where they ended in SMA connectors. Lengths of a small, flexible 50 Ω cable (RG-178), whose insulating jackets had been stripped off (to decrease outgassing), connected the probes to vacuum feedthrus on the antenna feedthru flange (Figure 5-4).

5.1.4 Faraday-Shielded Loop Antenna

A Faraday shield was built for the bare loop antenna to reduce the electric field components produced by the antenna. There could be a large potential difference across the loop antenna due to its finite inductance: an RF potential of 1000 V applied to the input of the antenna feeder tube (at 12 MHz) produced a potential difference of about 140 V between the top and bottom of the loop. The large toroidal electric fields which could thus be generated are thought to couple to unwanted electrostatic modes [Messiaen and Weynants, 1982].

The Faraday shield consisted simply of strips of metal covering the loop and effectively shorted out the z-component of the electric field. The shield, shown in Figure 5-8, was welded from 0.8 mm thick copper sheet. Four strips, 2.0 cm tall, were bent to form a 2.1 cm wide box covering the loop. The strips were separated by 2.0 mm wide gaps which extended 3.8 cm along the sides of the shield. The slots were baffled in order to prevent plasma streaming along the magnetic field lines from reaching the inner loop through the gaps. The

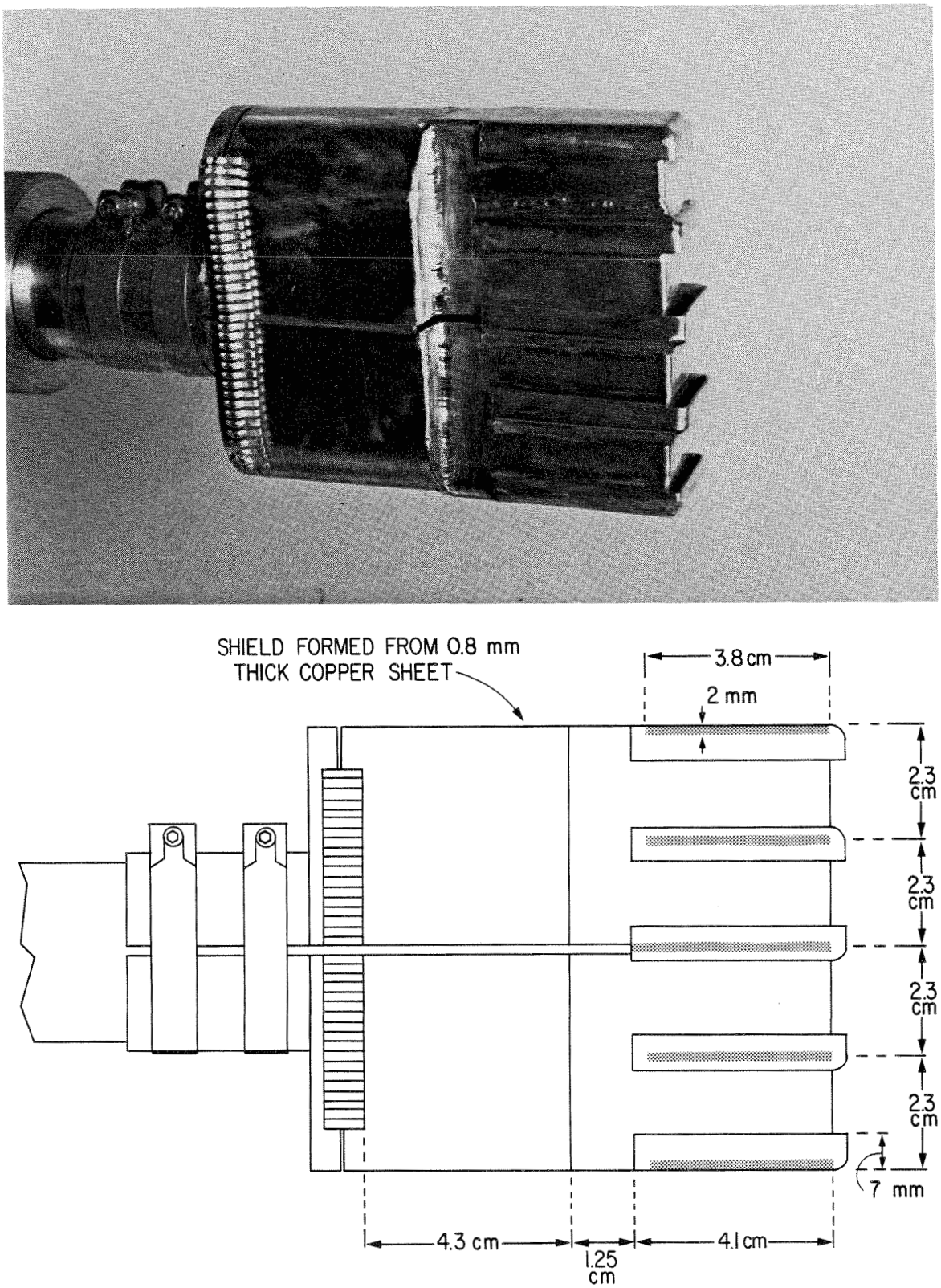

FIG. 5-8. Loop antenna with Faraday shield. The shaded areas in the scale drawing represent the slots in the shield which are hidden in the photograph by the baffles.

shield assembly was bolted to the antenna support structure, and a gap of 4.0 mm separated the front of the loop from the inside front of the shield.

The shield decreased the Q of the antenna to about 126 at a frequency of 12 MHz, due to the decrease in inductance of the loop (by about 12%) and the increase in resistance (by about 9%) because of eddy current losses. The Faraday shield also had the unfortunate effect of almost completely blocking the port, vastly reducing the pumping speed of the tokamak turbopump. It was necessary to use the turbopump from the charge-exchange diagnostic, pumping on another port of the tokamak, to achieve adequate pumping speed. The shielded antenna could be inserted about 4 cm past the tokamak wall before the global plasma properties were affected.

5.1.5 Bare Plate Antenna

In order to investigate the effect of the electric fields generated by the loop, several antennas were designed to maximize these fields. The first such structure investigated consisted of a bare rectangle of copper (5.1 cm long × 3.8 cm wide × 1.5 mm thick) connected to the inner element of the antenna feeder tube (Figure 5-9). For this antenna, the inner element consisted of a 6.3 mm o.d. copper rod which was centered within the feeder tube with a single teflon spacer at the midpoint of the tube. In operation, then, the plate was simply being driven at an RF potential with respect to the tokamak wall.

This type of antenna is referred to here as an electric field antenna because, in the absence of plasma, the antenna produces essentially no magnetic field. It is recognized, of course, that in the plasma environment the antenna may drive currents (through the plasma) which then produce magnetic fields; nevertheless the label "electric field antenna" will be used to distinguish this design from the loop antennas.

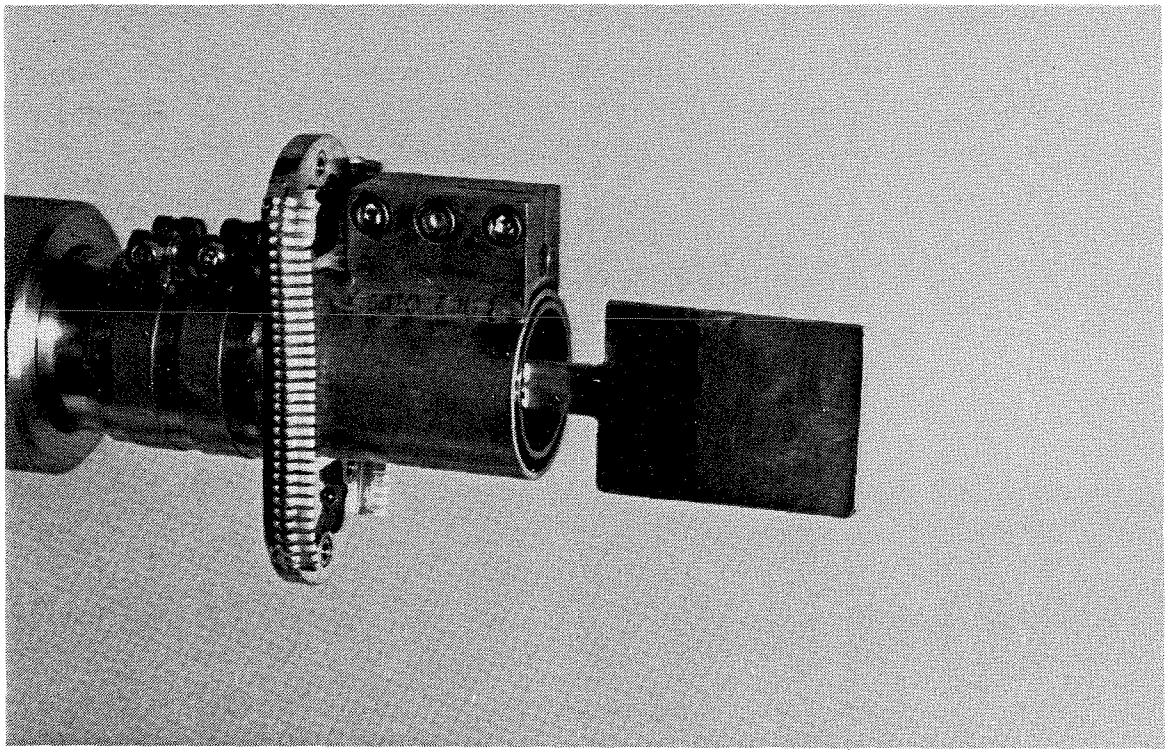

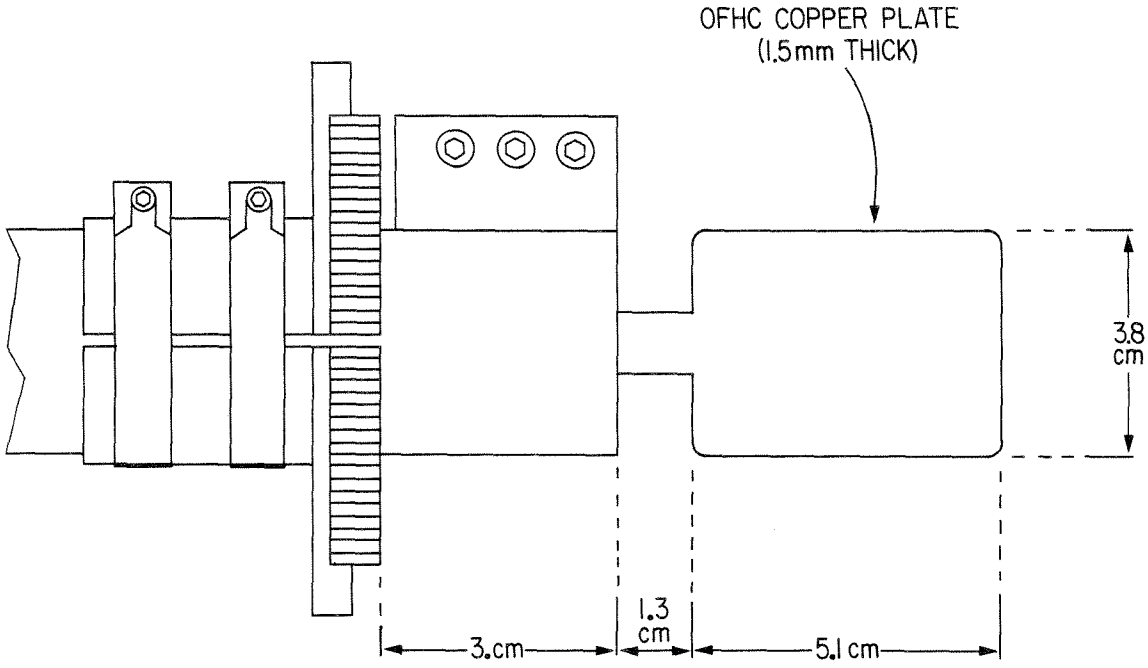

FIG. 5-9. Bare plate antenna.

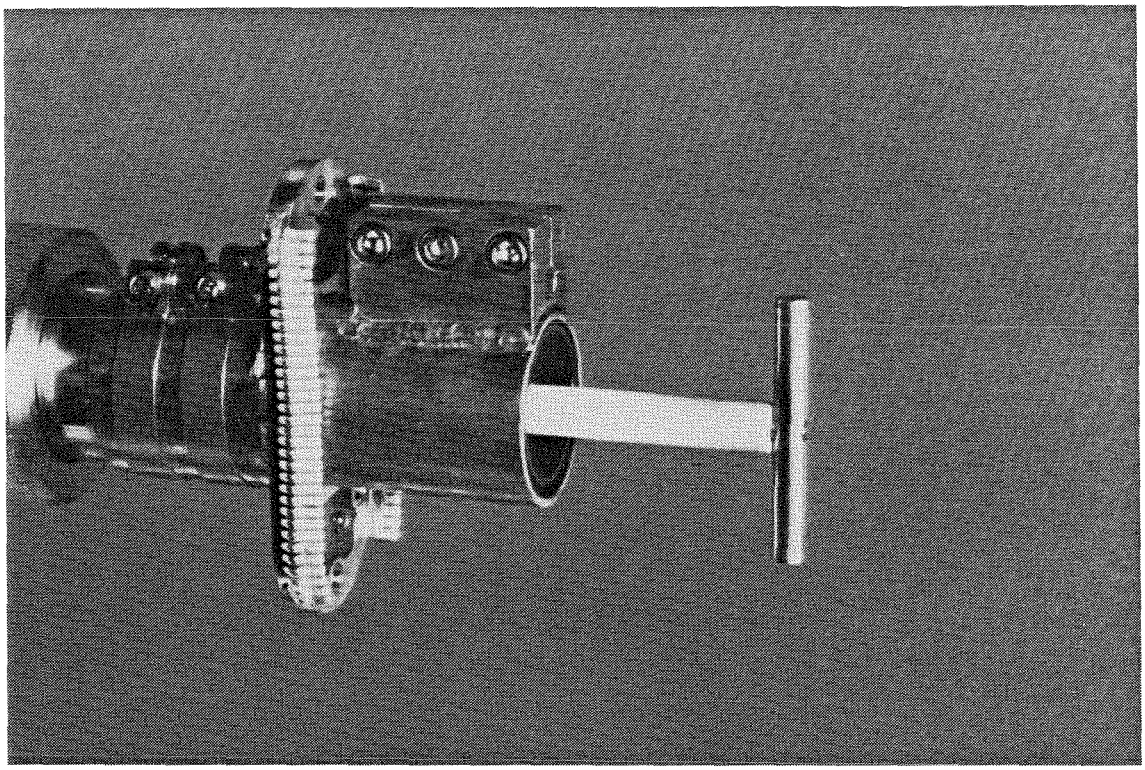

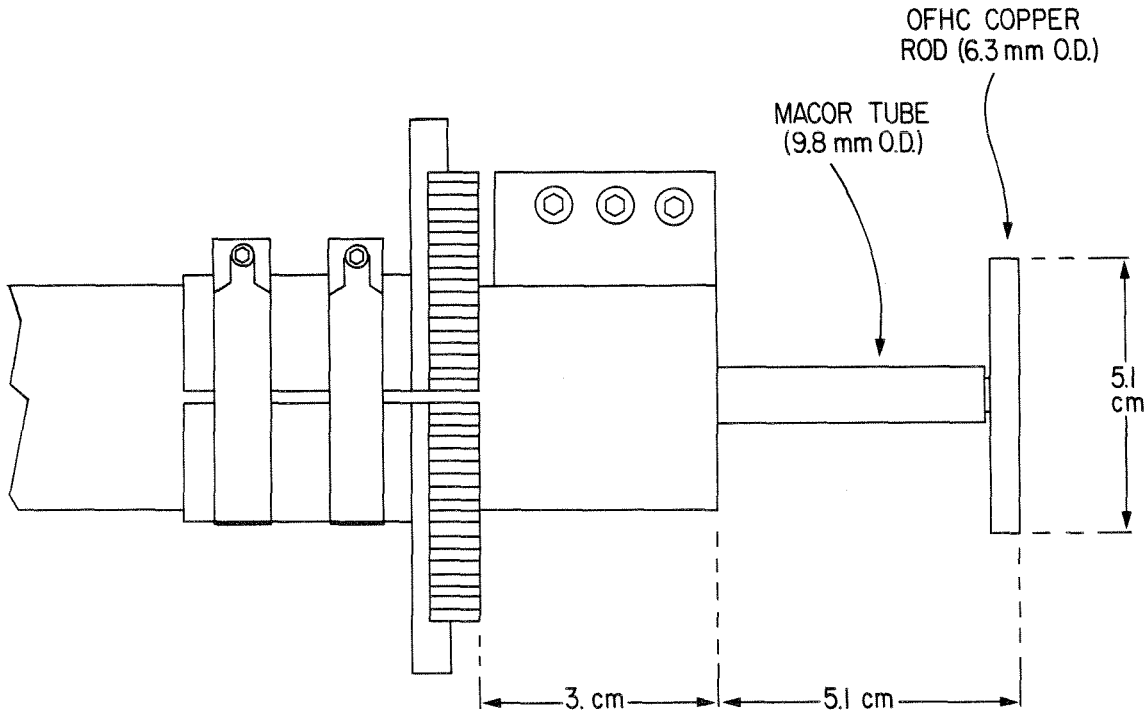

FIG. 5-10. "T" antenna.

5.1.6 "T" Antenna

The possibility that the bare plate antenna was being "shorted out" by plasma in the mouth of the tokamak port led to the construction of a modified electric antenna. This antenna consisted of a rod of copper (6.3 mm o.d. × 5.1 cm long), attached at its midpoint to another rod which in turn was connected to the inner conductor of the 99 Ω antenna feeder tube (Figure 5-10). The middle rod was insulated with a Macor tube which insured that any current flow driven in the plasma by the antenna came from the bar at its end (displacement current through the Macor was negligible). The inner element of the feeder tube could be rotated to align the cross bar of the "T" parallel or perpendicular to the toroidal magnetic field.

Both electric field antennas could be inserted 5−6 cm past the tokamak wall without any adverse effects. Both of the antennas could also be operated either "floating" (i.e., with a series capacitor between the matching network and the RF input) or at DC ground with respect to the tokamak wall (using an RF choke between the matching network input and ground). When isolated, the antennas assumed the plasma floating potential, while when at DC ground they generally drew a net electron current from the plasma.

5.2 Vacuum Fields

Measurements were made in a test jig to examine the effect of the Faraday shield on the loop antenna fields in vacuum (or air, to be precise).

The antenna feeder tube was mounted through a large sheet of brass which served as a ground plane. The sheet was located 12 cm behind the tip of the loop (Figure 5-11), and the end of the feeder tube was connected coaxially to a signal generator. The fields produced in this test set-up were, of course, different from those produced in the tokamak chamber because of the

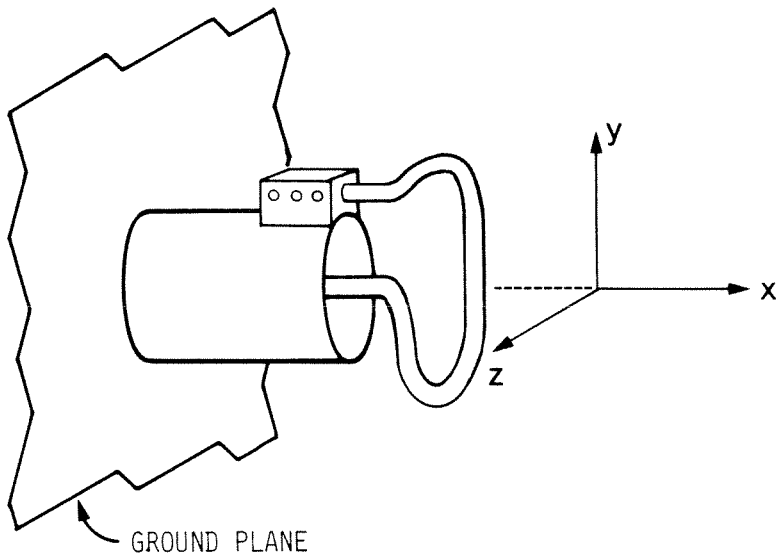

FIG. 5-11. Diagram of the test configuration for measurement of the antenna vacuum magnetic fields. The $x-$axis is collinear with the center element of the feeder tube; the $y-$axis lies in the plane of the antenna loop. The front edge of the loop is located at $x = -2.5$ cm.

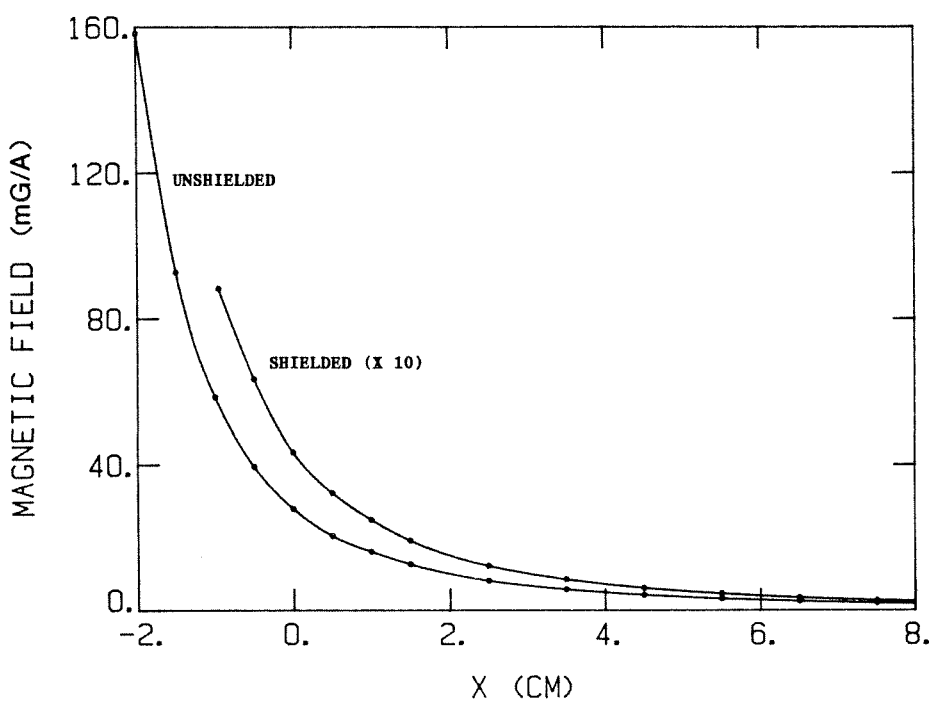

FIG. 5-12. Plots of normalized $|B_z(x,0,0)|$ for shielded and unshielded loop antennas. The dots are the experimental points. Vertical scale units are milligauss per ampere of antenna current, where the current is measured at the input to the antenna feeder tube. Data points for the shielded antenna have been multiplied by 10.

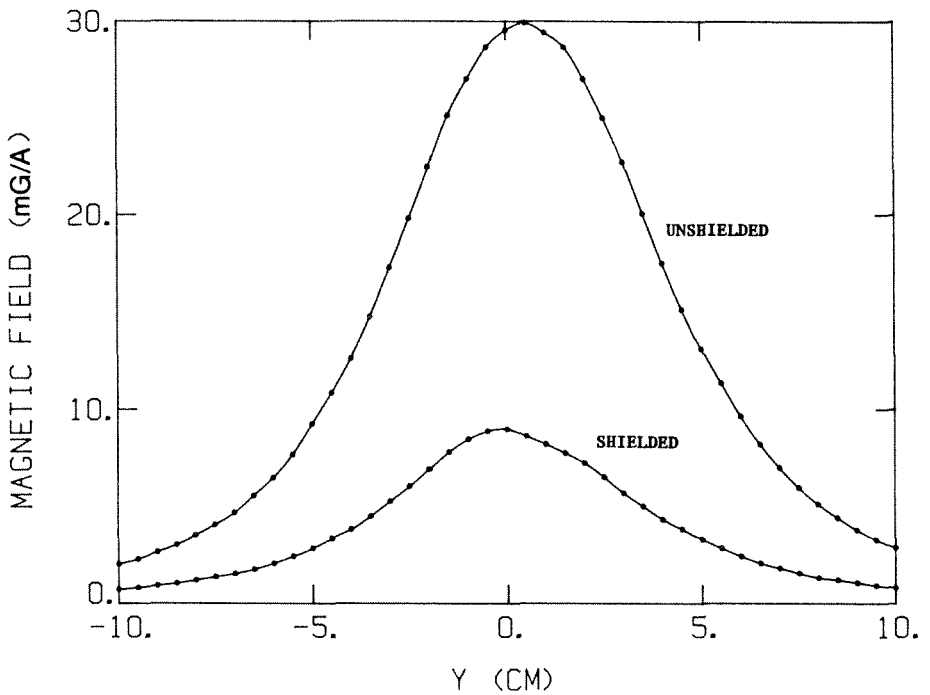

FIG. 5-13. Plots of normalized $|B_z(0,y,0)|$ for shielded and unshielded loop antennas.

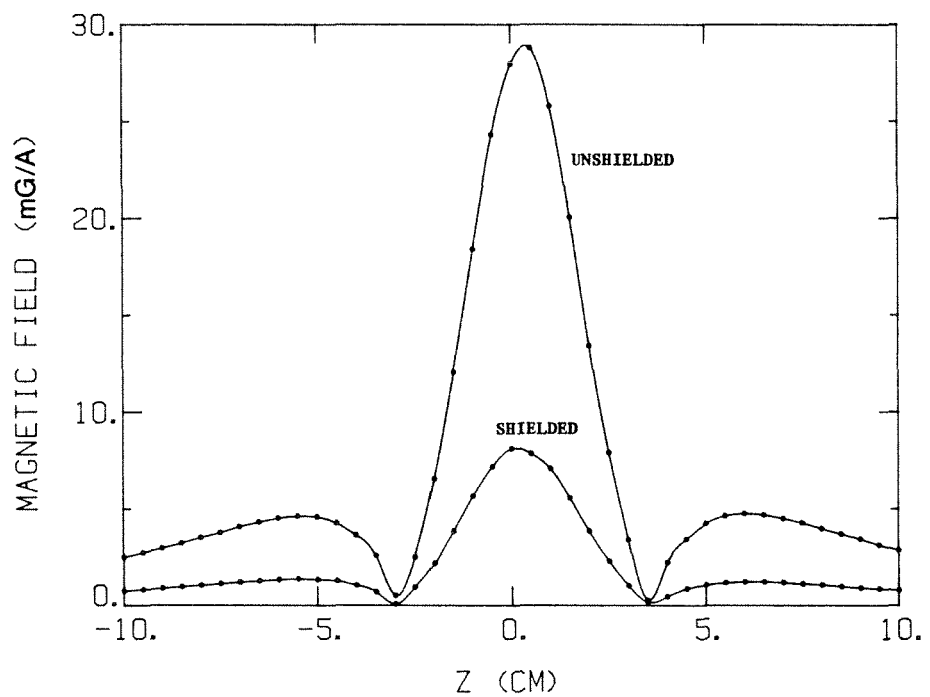

FIG. 5-14. Plots of normalized $|B_z(0,0,z)|$ for shielded and unshielded loop antennas.

different geometry, yet useful information was still obtainable from measurements near the antenna where boundary effects were less important.

Measurements of the z-component of the magnetic field (analogous to the toroidal direction in the tokamak) were made along each of the three axes shown in the figure. The x-axis of the coordinate system was colinear with the axis of the antenna feeder tube, and the tip of the loop was located in this system at $x = -2.5$ cm. When the Faraday shield was added, the loop position remained fixed and the front edge of the shield was then located at $x = -2.0$ cm. The magnetic field probes described in section 5.3 were used for these measurements, which were made at a frequency of 12 MHz.

The amplitude of B_z is shown for the shielded and bare loop antennas, as a function of position along the three axes, in Figures 5-12, 5-13 and 5-14. The field falls off rapidly in the x-direction (roughly as $1/r$, where r is the distance to the current-carrying element) and displays a localized peak around the origin in the y- and z-directions. The most notable feature of these measurements was that the introduction of the shield reduced the magnetic field amplitude by a factor of about $3-4$ and had little effect on its spatial dependence. The fact that the loop was about 5.0 mm behind the front edge of the Faraday shield meant that the maximum magnetic field seen by the plasma (that at the front edge of the antenna) was even lower for the shielded antenna - about 10% of the field seen at the front edge of the bare loop antenna, for a given excitation current. This reduction of magnetic flux available for coupling to the ICRF waves was responsible for the very low loading resistances observed with the shielded antenna (see Chapter 6).

One of the supposed advantages of the Faraday shield for ICRF work is the reduction of E_z produced by the potential difference between the loop and the wall. By covering the loop with metal strips running in the z-direction, which present a low-impedance path to the wall, E_z near the antenna surface is

greatly reduced. The Faraday shield allows B_z to pass through by the induction of surface currents in the strips. To first order, the current flows up the outside surface of the strips in the y-direction, through the gaps between the strips, and back down the inside surface. The current distribution on the inside of the strips is just what is needed to cancel the field produced by the loop so that there is no field inside the conducting strips themselves. The currents running along the outer surfaces of the strips therefore generate the magnetic field seen outside the antenna so that, in a sense, the low-inductance shield *becomes* the radiating element of the antenna.

Although the inductance associated with the current path on the outside of the shield is small, there still must exist a potential difference between the top and bottom of the shield. To first order, the electric fields produced by the shield are in the x- and y-directions (corresponding to the radial and poloidal directions in the tokamak geometry), but the fringing fields associated with any antenna of finite toroidal width produce components of E in the z-direction as well.

The potential differences across the gaps between strips of the shield were measured experimentally. A vector voltmeter with a 10:1 divider probe was used to measure the potentials across the five gaps at 1.0 cm intervals along the gaps (Figure 5-15). The probe ground clip was bent to be parallel and very close to the probe tip so that the induced EMF from magnetic flux threading the probe part of the circuit was negligible; the RF generator was also floated to minimize any RF ground loop currents. The results are shown in Figure 5-16 where S represents the path length along the gap (the front center of a 2 cm wide strip corresponds to $S = 0$, while $S = \pm 1$ cm corresponds to the corners of the shield, etc.). The potentials across the gaps are peaked along the front of the shield ($|S| \lesssim 1$ cm) and the largest potential jumps are across the central gap (i.e., the gap along the midline of the antenna). Summing the potentials

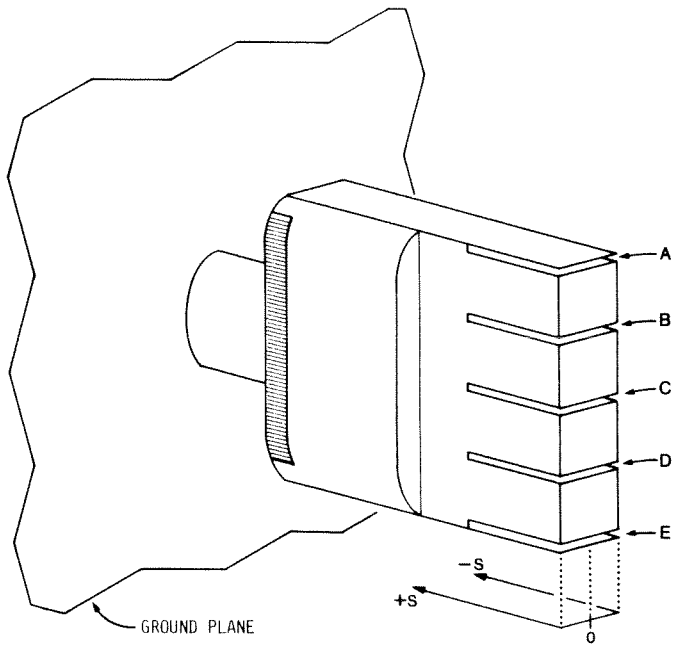

FIG. 5-15. Diagram of the test configuration for measurement of poten- tials across the Faraday shield gaps. S is the path length along each gap and $S = 0$ corresponds to the front center of the shield. The five gaps are labeled A - E. The baffles which cover each gap are not shown.

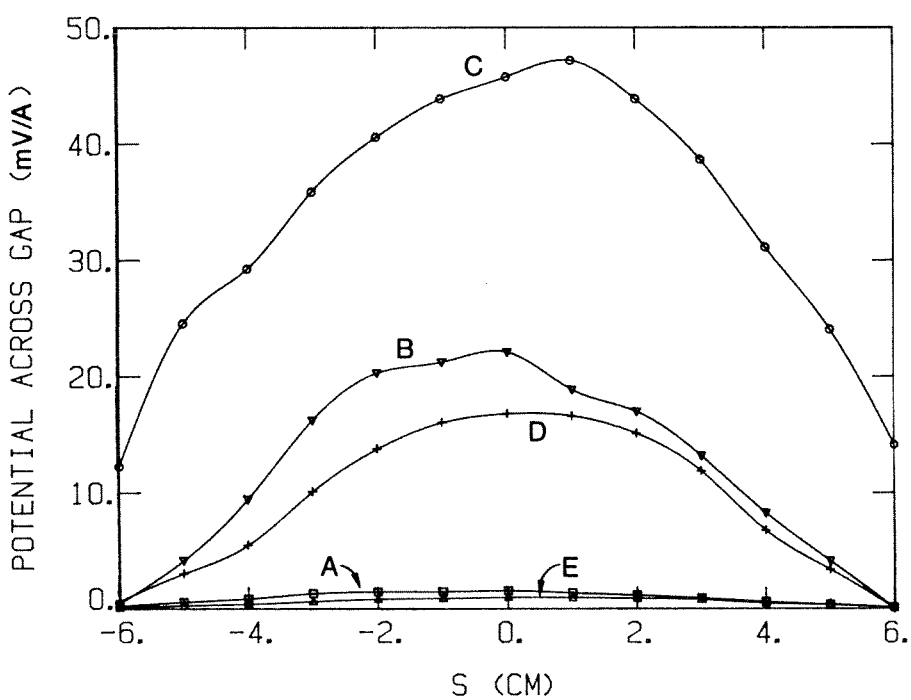

FIG. 5-16. Measured RF potentials across the five gaps of the Faraday shield, as functions of S. Vertical scale units are millivolts per ampere of antenna current, where the current is measured at the input to the antenna feeder tube.

across the five gaps at $S=0$ yields an estimate of the potential difference between the top and bottom of the front of the shield: 87 mV (per ampere of antenna current, measured at the input to the feeder tube). This should be compared to the potential difference of about 2.5 V/A between the top and bottom of the bare loop. Hence the electrostatic potentials seen by the plasma are substantially smaller with the Faraday shield in place, even after normalization to the same magnetic flux at the front edges of the two antennas. This is actually just a result of the lowered inductance of the effective current path due to the introduction of the shield. The same result could presumably be obtained by simply using a very wide antenna loop conductor.

5.3 Magnetic Probes

5.3.1 Introduction

Magnetic probes are a routine diagnostic for investigating the field structure of plasmas [Lovberg, 1965]. The most common type of magnetic probe, and the type to be discussed here, consists of a small loop or coil of wire encased in an insulating jacket which is inserted into the plasma. Other approaches are possible, such as charged particle beam probes or optical methods, but are generally much more complex experimentally.

If the dimensions of the coil are small compared to the characteristic lengths over which the magnetic field changes, then the voltage output of the coil gives an indication of the time rate of change of a component of the magnetic field at the location of the coil. It is necessary, however, to consider how the field that the probe senses is related to the field that would have been at that point in the plasma in the absence of the probe. The probe interacts with the plasma in a number of ways: local plasma which intercepts the probe is cooled; the presence of the probe perturbs the flow of plasma and hence the

particle currents which generate the wave magnetic fields; impurities from boil-off or erosion of the surface of the probe envelope may diffuse through the plasma bulk and cool it substantially through bremsstrahlung radiation. Other problems include destruction of the probe due to the large heat flux incident on it and frequency response limitations due to the self-inductance of the coil.

The effect of the probe on the bulk plasma can be monitored by observing the global plasma diagnostics: the visible light and soft-UV detectors, the plasma current and loop voltage monitors, and the microwave interferometer. If these signals change negligibly as the probe is pushed into the plasma, it may be assumed that the probe is not interacting greatly with the bulk plasma. If the probe is pushed too far into the plasma, or if it is contaminated, the soft-UV and visible light signals increase substantially during the plasma shot, the plasma current may be reduced, and the density evolution is typically substantially changed. A test of the effect of a probe on the large-scale propagation of the waves being observed was performed by using two probes separated toroidally by a large fraction of the tokamak circumference and exciting one of the RF antennas. One probe was fixed in the plasma and the wave fields were measured. The other probe was then inserted into the plasma and any resulting effect on the signals from the first probe was observed. In fact, no effect was found until the second probe was inserted far enough into the plasma to affect the global plasma diagnostic signals by itself (4 - 6 cm).

The effect of the probe on local plasma and the resulting effect on the magnetic fields at the probe are difficult to analyze [Ecker et al., 1962; Malmberg, 1964; Lovberg, 1965]. These effects were likely to be small in this experiment because the fields being measured arose from global plasma properties and the scale length over which the fields and eigenmodes varied was large compared to the dimensions of the probe. Experimental confirmation,

however, was not available.

Physical damage to probes inserted into the plasma was a common problem. The Pyrex envelopes used to house magnetic probes withstood the plasma environment moderately well, generally lasting many months (>1000 plasma shots) before requiring replacement. Damage was almost entirely confined to the side of the probe which faced electron runaways. Deterioration of the probe began with discoloration from clear to amber, followed by progressively worse fracturing and flaking of the glass surface. Other probe envelope materials were tried, with mixed results. An alumina tube[3] inserted 2 cm into the plasma was severely eroded after only 100 plasma shots. Boron nitride[4] and Macor withstood a similar test much better, showing only some discoloration and very slight erosion. Pyrex was chosen because it was easy to repair and vacuum-tight glass-to-metal seals were readily available.

5.3.2 Description of Probes

The magnetic probes used in these experiments consisted of small coils wound on insulating forms and protected from the plasma by a Pyrex tube. Two types of probes were constructed: single-coil and triple-coil probes. The single-coil probes were oriented with the magnetic axis of the coil perpendicular to the probe shaft. These probes could measure B_θ or B_z by simply rotating the probe shaft by 90 degrees (where θ corresponds to the poloidal angle and z corresponds to the toroidal direction in the tokamak). The triple-coil probe consisted of three coils whose magnetic axis were mutually orthogonal; these probes measured all three components of the magnetic field at a single point. Construction of the triple-coil probes is described here; the single-coil

3. Alumina tubes were obtained from the Coors Co., Boulder, Col.

4. Boron nitride, grade HPC, was obtained from Union Carbide Corp., Carbon Products Division, New York, N.Y.

probes were built in a similar fashion.

The probe shaft was a 1.27 cm o.d. × 0.83 cm i.d. stainless steel tube whose surface was polished. One end of this tube was welded to a 0.95 cm o.d. stainless-to-Pyrex transition, and the end of the Pyrex tube was closed forming a vacuum-tight envelope. The probe was introduced into the plasma through a single O-ring seal which allowed the probe to slide and rotate (Figure 5-17). A well-polished surface was found to aid in preventing bursts of air from leaking into the tokamak as the probe shaft was inserted. Since the Pyrex could be damaged by extended discharge cleaning, the probe tips were generally left in the ports 3 – 5 cm from the inner wall of the tokamak and were pushed in past the wall prior to a tokamak run.

The three orthogonal coils were wound on a 3 mm o.d. phenolic form with seven turns each of #34 AWG magnet wire (Figure 5-18). The two leads from each coil were twisted to prevent pickup and were epoxied to the side of the form. At the end of the form each pair of wires was soldered to a 2.18 mm o.d. semi-rigid 50 Ω coaxial cable (which had a solid copper outer conductor), taking care to keep the two wires extremely close to each other to minimize any enclosed area. The three coaxial cables were soldered together along their length and were centered in, and epoxied to, a 1.15 cm o.d. phenolic tube which could then be slid into the stainless steel probe shaft. The coils, and the rod they were wound on, were completely covered with a thin coating of a high-temperature epoxy. The epoxy also covered the gap between the rod and the semi-rigid coax, and the end of the coaxial cable bundle itself. The epoxy-coated end of the probe, along with about 1 cm of the adjoining coaxial cable bundle, was given three coats of a colloidal silver lacquer (Emerson & Cuming Eccocoat CC-2). The surface resistance of the resulting film was about 1 Ω/square and provided an effective electrostatic shield. The silver coating, however, was easily scratched and was protected by a high-temperature teflon-

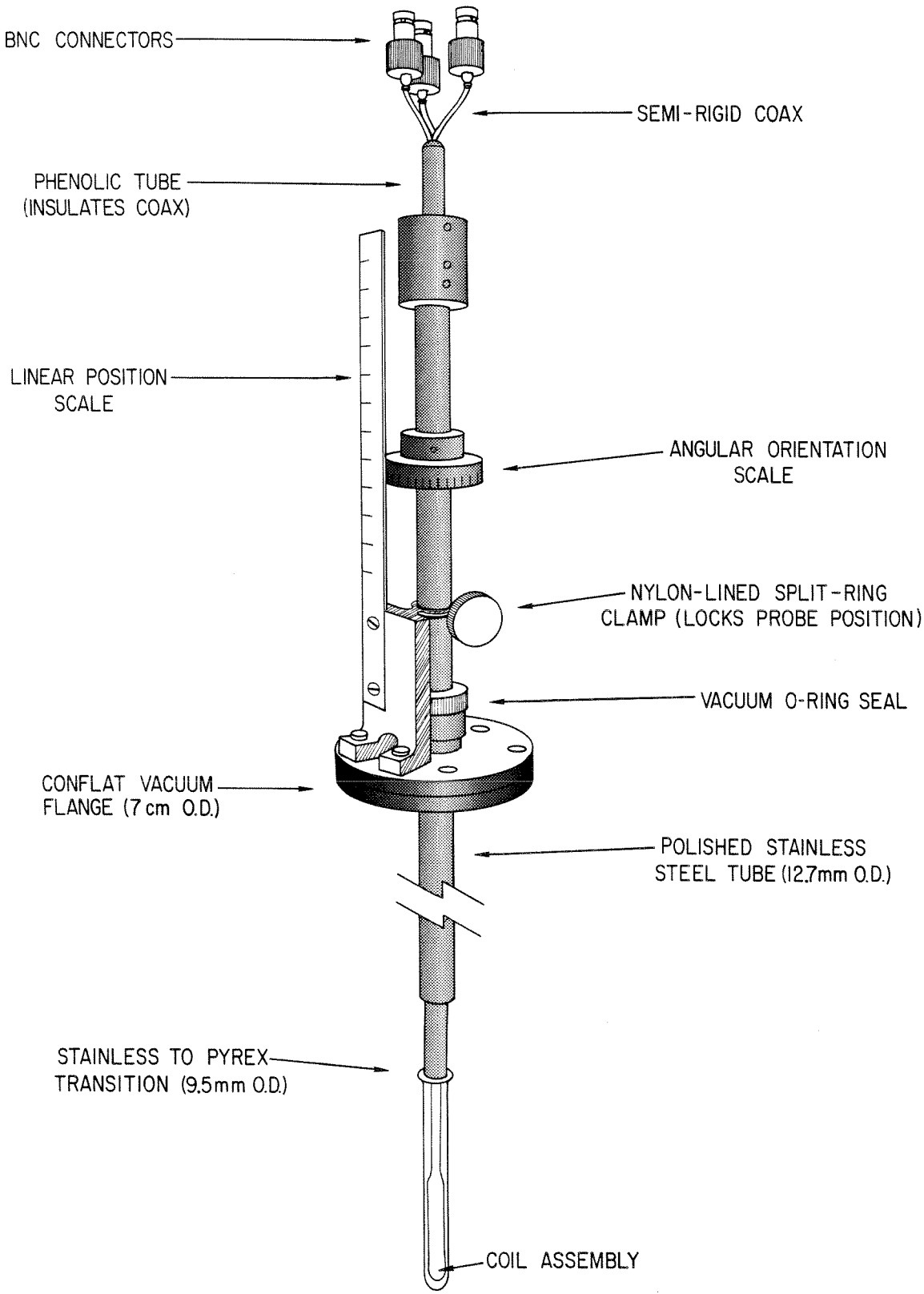

FIG. 5-17. Magnetic probe holder.

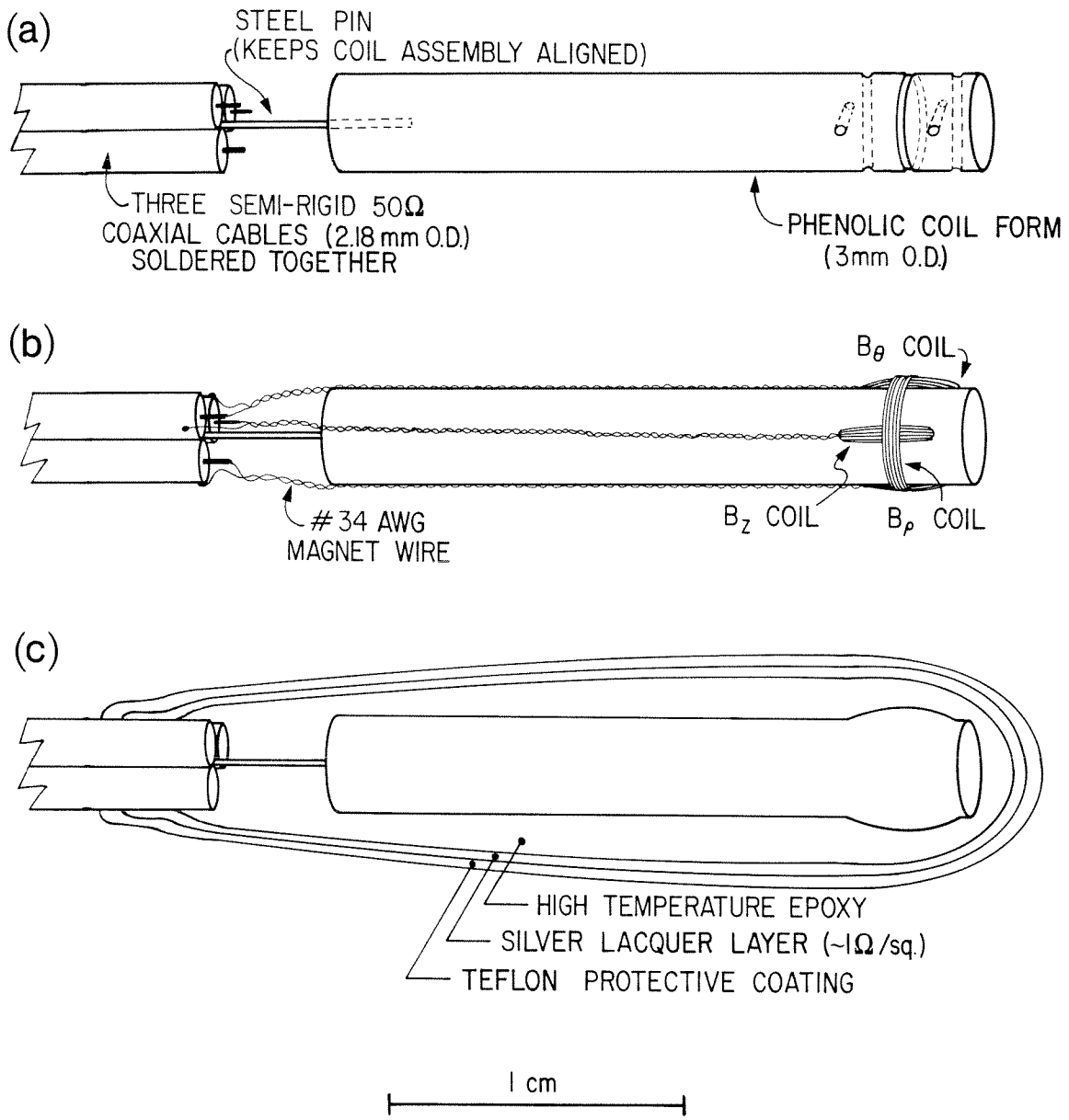

FIG. 5-18. Magnetic probe construction. a) Bare phenolic form fixed in place with stainless steel pin. b) Coils wound on mutually orthogonal axes. c) Electrostatic shield applied.

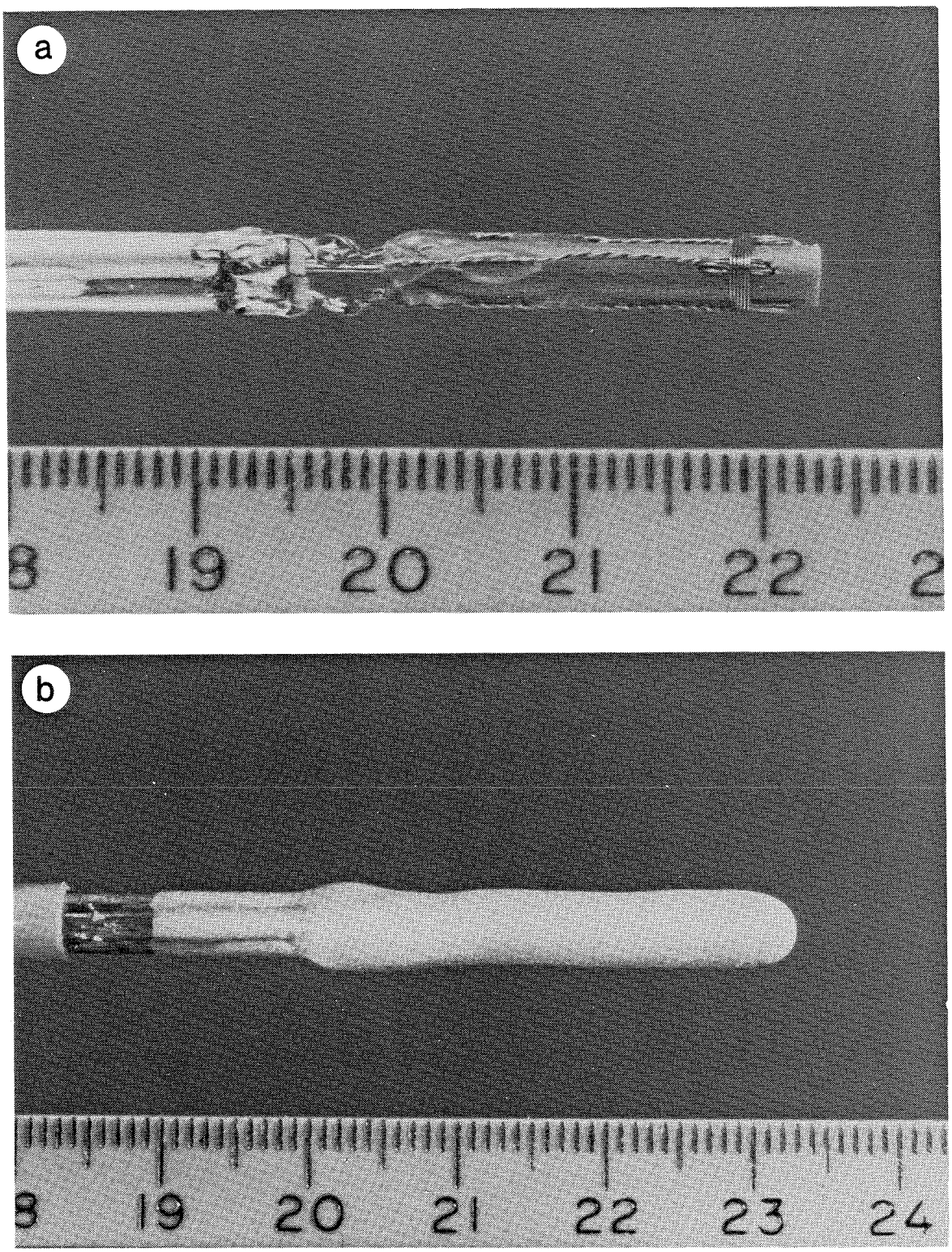

FIG. 5-19. a) Magnetic probe before shielding. b) Probe after coating with epoxy and silver lacquer.

based coating.[5] Application of the electrostatic shield is shown in Figure 5-19. Output ends of the three semi-rigid cables were soldered to BNC jacks, and the completed assembly could withstand temperatures of 300 °C (probe tip temperatures greater than 100 °C have been observed in some experiments).

5.3.3 Circuit Model of Magnetic Probe

The wavelengths of the fields that the probe senses are generally much greater than the dimensions of the probe. Therefore, a lumped-element circuit model is used to investigate the response of the probe [Ramo and Whinnery, 1944].

A simple equivalent circuit used by a number of authors [Segre and Allen, 1960; Ashby et al., 1963; Decker and Honea, 1972] is shown in Figure 5-20. Here L_p represents the self-inductance of the coil, R_p is the resistance of the coil (which is frequency-dependent due to the skin effect), C_p is an effective capacitance representing the stray capacitance of the coil and its leads, and R_L is the load impedance. V_p is the EMF generated by the external magnetic fields; it is proportional to the number of turns N, to the coil area A, and to the time rate of change of flux linking the coil. It is assumed that the coil area A is small compared to the scale length over which the magnetic field changes.

The probes are used to detect waves with a sinusoidal time variation, and V_p is then given by $V_p = -i\omega NAB$, where B is the magnitude of the magnetic field component parallel to the axis of the coil at the location of the coil, and B and V_p vary as $e^{+i\omega t}$. The output voltage V_0 is then related to the magnetic field B by

$$V_0 = \frac{-i\omega NAB\, e^{i\theta}}{\left[\left(1 - \omega^2 L_p C_p + \frac{R_p}{R_L}\right)^2 + \left(\omega R_p C_p + \frac{\omega L_p}{R_L}\right)^2\right]^{\frac{1}{2}}} \qquad (5.1a)$$

5. TFE Coating #6065, manufactured by Crown Industrial Products Co., Hebron, Ill.

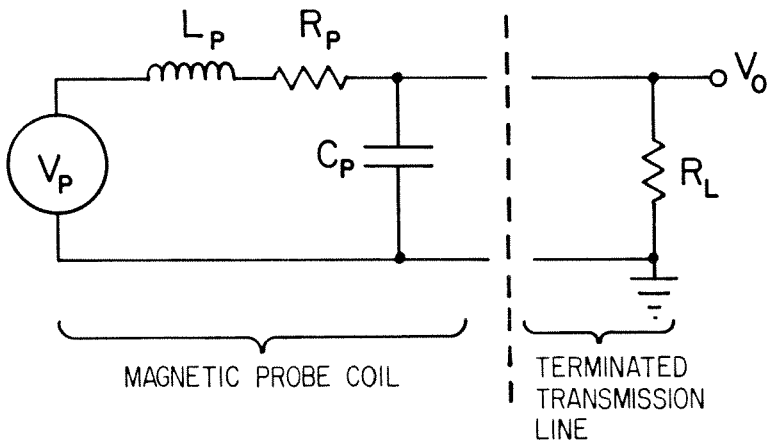

FIG. 5-20. Magnetic probe equivalent circuit model.

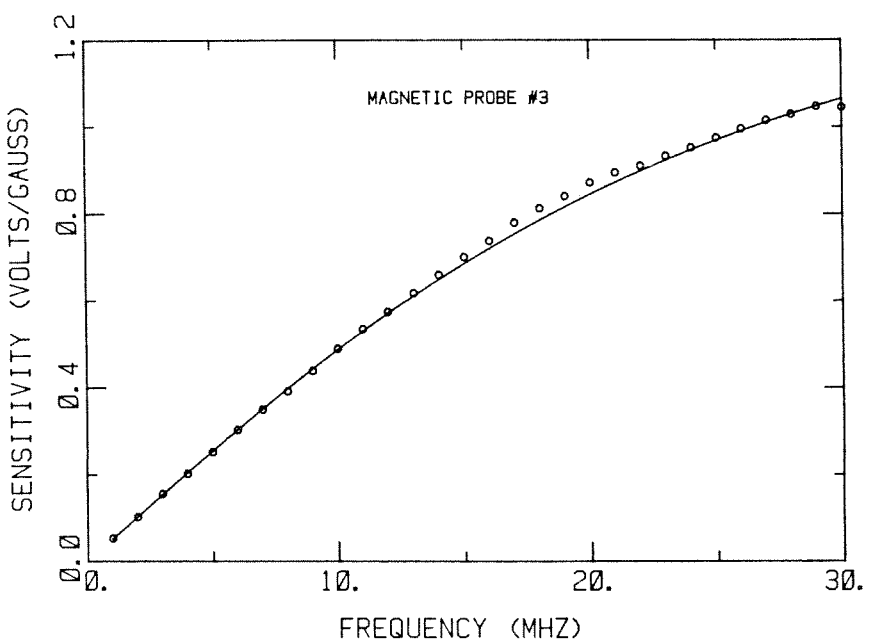

FIG. 5-21. Typical magnetic probe calibration as a function of frequency. Sensitivity is defined as the rms voltage output of the probe (terminated in 50 Ω) divided by the rms magnetic field amplitude (in gauss). Circles are the measured points; the solid line is the result of equation 5-2a with $NA = 0.82$ cm^2 and $L_p = 0.28$ μH.

where

$$\theta = \tan^{-1}\left[\frac{\omega R_p C_p + \frac{\omega L_p}{R_L}}{1 - \omega^2 L_p C_p + \frac{R_p}{R_L}}\right]. \qquad (5.1b)$$

The RF resistance of the coil was generally small and could be neglected provided $R_p \ll R_L, \frac{1}{\omega C_p}$. The radius of the wire used to wind the coils (a) was 80 microns. Since this was still large compared to the skin depth (δ) at the frequencies of interest (5 - 20 MHz), the resistance per unit length was given by $\rho = \eta/(2\pi a \delta)$, where η is the DC resistivity. At a frequency of 12 MHz, this yields a resistance of $\rho = 0.018\ \Omega$/cm. The total length of wire used for each coil was about 12 cm, so the RF resistance of a coil at 12 Mhz was $R_p = 0.2\ \Omega$. It was convenient to use standard terminated 50 Ω transmission line to connect the magnetic probe output to the RF electronics; hence $R_L = 50\ \Omega$ and the condition $R_p \ll R_L$ was satisfied.

The coil capacitance C_p was at most a few picofarads, and its effect was negligible provided $C_p \ll (\omega^2 L_p)^{-1}, (\omega R_p)^{-1}$. The coil self-inductance L_p was on the order of 0.3 μH and therefore both R_p and C_p could be neglected in equation 5.1, yielding

$$V_0 = \frac{-i\omega NAB\, e^{i\theta}}{\left[1 + \left[\frac{\omega L_p}{R_L}\right]^2\right]^{\frac{1}{2}}}, \qquad (5.2a)$$

where

$$\theta = \tan^{-1}\left[\frac{\omega L_p}{R_L}\right]. \qquad (5.2b)$$

The wave fields detected by these probes were often small, and to improve the signal-to-noise ratio it was desirable to maximize the sensitivity of the probe. The output of the probe for a given field amplitude could be increased

by enlarging the area of the coil. This had to compete, however, with the necessity of minimizing the perturbation of the plasma by the probe, which required small probe dimensions.

For a fixed frequency and coil diameter, the sensitivity of the probe, defined as $S = V_0 / B$ volts per gauss (V/G), is a function of N and can be maximized by choosing N appropriately. The self-inductance of the coil is given approximately by $L_p = N^2 L_0$, where L_0 is the inductance of one turn (~6 nH for these probes). The magnitude of the voltage source V_p increases as N, but the coil inductance forms a voltage divider with the load impedance R_L, and the voltage division ratio increases as N^2 for large N. It is easy to show that the sensitivity of the probe (at a given frequency) is maximized for

$$N = N_{\max} = \left(\frac{R_L}{\omega L_0} \right)^{\frac{1}{2}} , \tag{5.3}$$

and the maximum value is just

$$S_{\max} = \frac{\omega N A}{\sqrt{2}} \times 10^{-8} \quad V/G , \tag{5.4}$$

where the units of A are cm^2. For a frequency of 12 MHz, then, $N_{\max} = 8$ and $S_{\max} = 0.7$ V/G. The sensitivity can be maximized as a function of the number of turns only for a single frequency, so in practice a compromise value of $N = 7$ was chosen.

5.3.4 Experimental Probe Response

A small Helmholtz coil was built in order to calibrate the magnetic probes. It was necessary to keep the length of the current-carrying conductors much smaller than a wavelength at the frequencies being used. Each coil of the Helmholtz pair was a one-turn loop wire with a diameter of 7.6 cm; the pair yielded a field of 0.24 G/A (gauss per ampere of current flowing through the coil) in the central region between the coils. The Helmholtz coil current was

monitored with a high-frequency current transformer at the input to a coil. Magnetic probes could be inserted through guides either along the axis or between the Helmholtz coils, allowing calibration of all three coils in a triple-coil probe. A typical frequency response curve for a probe is shown in Figure 5-21. The expected response from equation 5.2 is also plotted and agrees well with the experimental results.

Isolation between the coils of a triple-coil probe is a measure of the actual orthogonality of the coil axes as well as intra-coil capacitive coupling. Isolation between two coils can be defined as the ratio, expressed in db, between the output of one coil when the external field is parallel to its axis and the output of the other coil (which ideally would be zero). Isolation between the B_z and B_θ coils was typically 45 db; between the B_z and B_ρ coils, 30 db.

Large electrostatic fields in the plasma may couple to the magnetic probe coils (which are not balanced) and generate spurious signals. The silver coating described earlier encloses the coils in a continuous grounded electrostatic shield, greatly reducing the coil-plasma capacitance which can lead to pick-up. However, the effect of the silver lining on the magnetic signals must be considered. A perfect conductor encasing the magnetic probe coils would shield out external fields entirely. If, however, the conductivity and thickness of the silver layer are chosen so that the skin depth in the layer is much larger than its thickness, then the layer will have a negligible effect on the magnetic fields being measured.

The effectiveness of the shielding was tested in the laboratory. Copper foil was wrapped tightly around the last few centimeters of the Pyrex envelope of the probe shaft. An RF potential was applied between the foil and the probe coaxial cable shield emerging from the end of the stainless shaft. The electrostatic coupling factor was defined as the ratio, expressed in db, between the potential applied to the foil cap and the output from a magnetic probe coil

(terminated, as always, in 50 Ω). An unshielded probe exhibited a coupling factor, at 12 Mhz, of 64 db. Shielding the probe with a silver coating with a conductivity of about 1 Ω/square improved the coupling factor to 90 db. The frequency response of the probe was unchanged by the shielding, as expected, since the skin depth in the silver layer ($\sim$1 mm) was much larger than the thickness of the layer ($\sim$0.03 mm).

5.4 Langmuir Probes

Langmuir probes [Langmuir and Mott-Smith, 1924] have long been used to measure electron temperature, plasma density, and floating and space potentials [Chen, 1965]. In its simplest form, the probe consists of an insulated wire, whose tip is exposed, which is inserted into the plasma and biased with respect to the walls of the confinement chamber. The bias is varied (either swept or from shot to shot) and the $I-V$ characteristic is recorded, from which the various plasma properties are inferred.

Although the measurement is very simple to perform, the results must be interpreted with considerable caution. The presence of the probe perturbs the plasma (as discussed in section 5.3.1) and there is some evidence that current-drawing probes may generate plasma fluctuations [Lecioni, 1968; Schmidt, 1968]. The probe theory which is used to interpret the $I-V$ characteristic is very complicated in the presence of a magnetic field [Chen, 1965]. Some observed effects of a strong magnetic field are a decrease in the ratio of electron to ion saturation currents and a disappearance of a sharp knee in the $I-V$ characteristic which ordinarily occurs at the plasma space potential [Sato, 1972]. Probes have nevertheless been used even in the edge plasma of large tokamaks [Budny, 1982]. The usual approach is to use field-free probe theory, provided $\rho_i \ll \rho_p$ (where ρ_i is the ion Larmor radius and ρ_p is the

cylindrical probe radius), and to correct for the area of the probe (since the plasma tends to stream along the magnetic field lines, the effective area of the probe is reduced). It should be recognized, however, that interpretation of the probe characteristic requires the assumption of a distribution function, and the usual simple Maxwellian may not be adequate in a tokamak environment (due to mirroring, for instance).

Probe results in this thesis include measurements of entire $I-V$ characteristics as functions of radial position (section 6.3.1) and, for the probe mounted on the side of the ceramic-insulated loop antenna, as functions of RF antenna current (section 6.3.2). Also investigated were the effects of inserting an RF antenna on the ion saturation current of a distant probe and the dependence of the antenna probe floating potential on various parameters.

The probe tips were made from 1.0 mm o.d. tungsten rod and had an exposed length of 3.8 mm. The tungsten rod (about 5 cm long) was crimped to the inner conductor of a 2.18 mm o.d. semi-rigid coaxial cable. The probes used for radial profile scans were insulated with an alumina tube which was in turn inserted inside a stainless steel tube (3.0 mm o.d.) as shown in Figure 5-22. The alumina insulator was recessed about 1 mm from the end of the stainless tube, and the tungsten was well centered in order to prevent arcing to the stainless tube when drawing large probe currents. The Langmuir probe which attached to the side of the ceramic-insulated loop antenna (section 5.1.3) was built in the same way except that an additional ceramic tube covered the stainless steel jacket to prevent RF currents from flowing along it.

The probes were connected via coaxial cable to a 0.2 F capacitor which was charged to the desired bias voltage. Care was taken in the routing of the signal cables to insure that ground-loop signals were negligible. Probe current was measured either by the voltage drop across a 1.0 Ω resistor in the output line or with a current monitor which had an $I-t$ saturation product of about

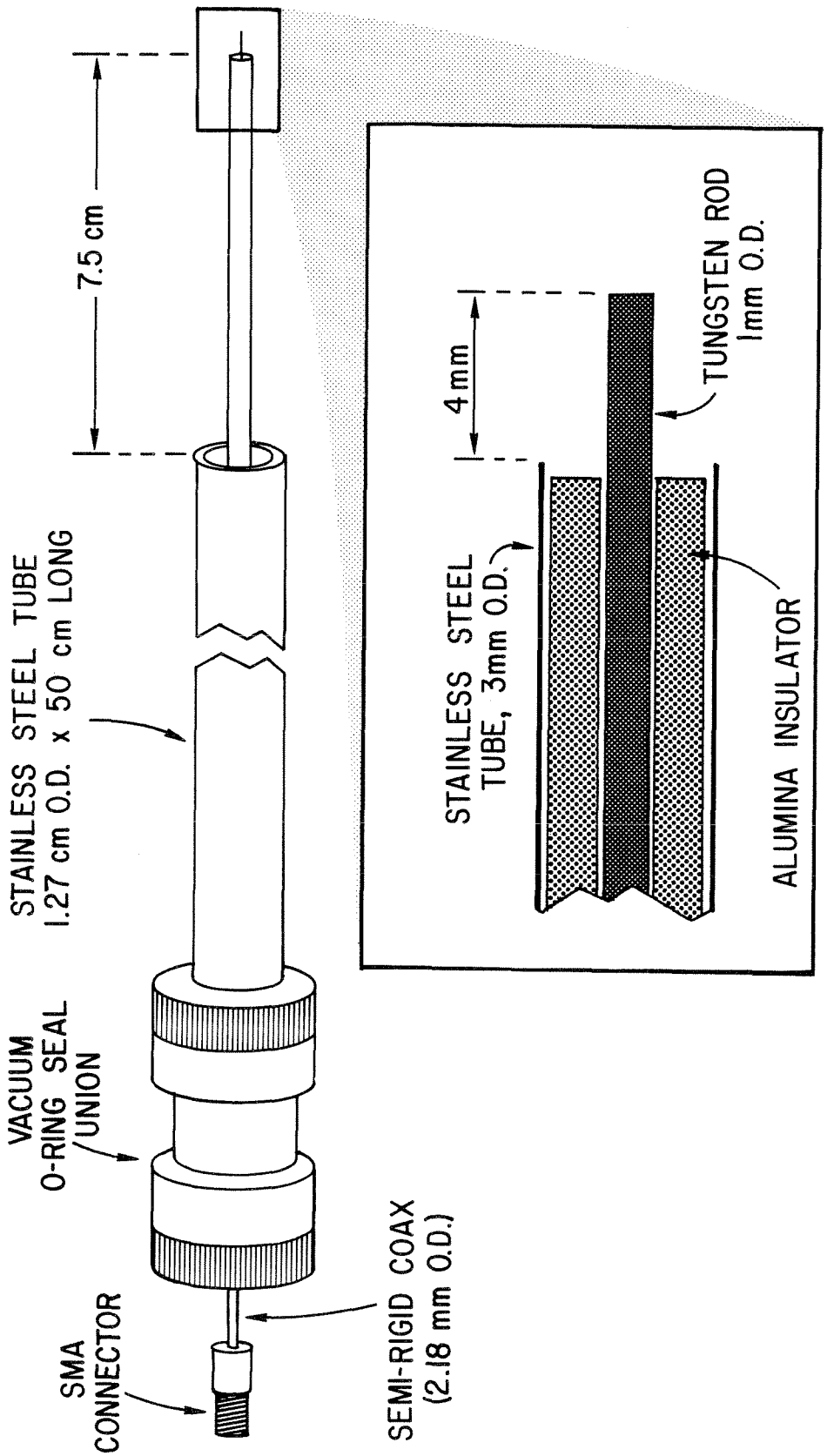

FIG. 5-22. Langmuir probe construction.

1 A-sec. The probe $I-V$ characteristic was mapped out by varying the bias from shot to shot.

5.5 RF Plasma Current Monitor

5.5.1 Introduction

A current probe was constructed in order to investigate the distribution of RF current flowing in the tokamak plasma near an RF-excited electric field antenna. The probe had to be capable of operating at RF frequencies, be sufficiently sensitive, and be compatible with the plasma plasma environment. This section describes the design and construction of such a probe, based on the familiar Rogowski coil [Rogowski, 1912].

The Rogowski current monitor consists of a uniform toroidally-wound coil which measures some function of the total current passing through its aperture and has the advantage that no physical contact with the current-carrying medium is necessary. The Rogowski coil, in various forms, has been used extensively in plasma physics research, primarily to measure the large currents flowing through various magnetic field coils. It is also routinely wrapped around tokamaks, in the poloidal direction, and used as a diagnostic of the total plasma current [DeMichelis, 1978].

There has, however, been very little use of the Rogowski coil to directly measure current distributions inside a plasma; indeed only four references in the literature have been found. The earliest was a Russian group [Golovin et al., 1958] which used three fixed concentric Rogowski coils in a cylindrical Z-pinch experiment to obtain information on the plasma current radial distribution. Two groups have discussed the use of a Rogowski monitor in mapping the plasma current distribution inside an MPD (magnetoplasmadynamic) arc jet [Schneiderman and Patrick, 1967; Belinski, 1973]. Finally, an Italian group

[Piperno and Solaini, 1975] has also used a small Rogowski coil to probe the current density profile in a Z-pinch device. In all of the above cases, the Rogowski coil was used to investigate the background (i.e., low-frequency or DC) component of the current; no attempt was made to observe plasma currents associated with high-frequency waves.

Like all physical probes introduced into a plasma, the Rogowski coil does, to some extent, perturb the plasma and thus the current it is trying to measure. As with other probes, the extent and effect of this perturbation are difficult to assess. The comments made earlier in relation to magnetic probes (section 5.3) apply here as well. As a minimum condition, it is necessary for the global plasma properties (density, current, etc.) to remain largely unaffected by the insertion of the probe. Also, since the Rogowski coil measures current passing through its aperture, it is desirable to maximize the aspect ratio of the coil while still keeping the major diameter small compared to the plasma characteristic size. In a tokamak, the plasma flows largely along the magnetic field lines, and so to minimize the perturbation of the plasma flowing through the aperture of the coil, the normal to the plane of the aperture should be oriented parallel to the background magnetic field. If the normal to the plane of the aperture was oriented perpendicular to the field, the only plasma passing through it would be that due to cross-field diffusion (although that in itself could suggest a useful experiment).

5.5.2 Design of the Current Monitor

A schematic diagram of a simple Rogowski coil is shown in Figure 5-23. The toroidal solenoid consists of N turns, uniformly spaced, and the return lead is brought back through the winding (in order to prevent a net single loop which would respond to $\frac{\partial B_z}{\partial t}$). From Faraday's law, the EMF induced around

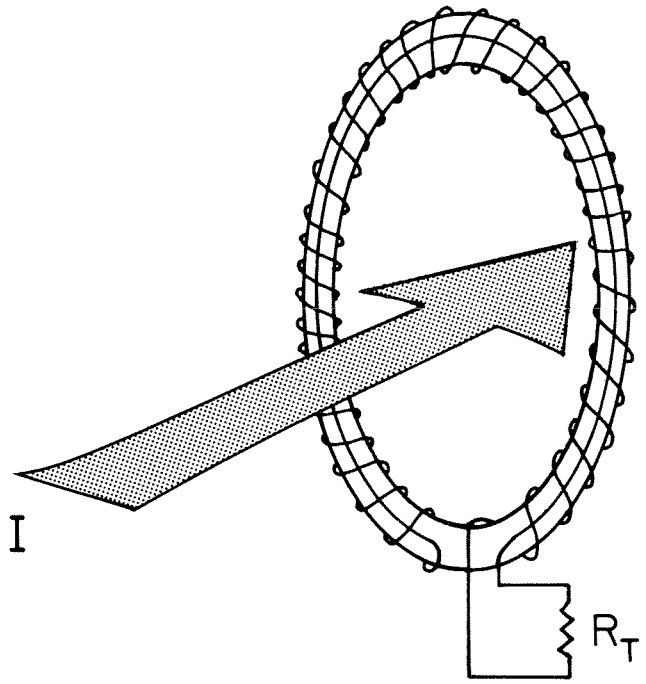

FIG. 5-23. Schematic of a simple Rogowski coil.

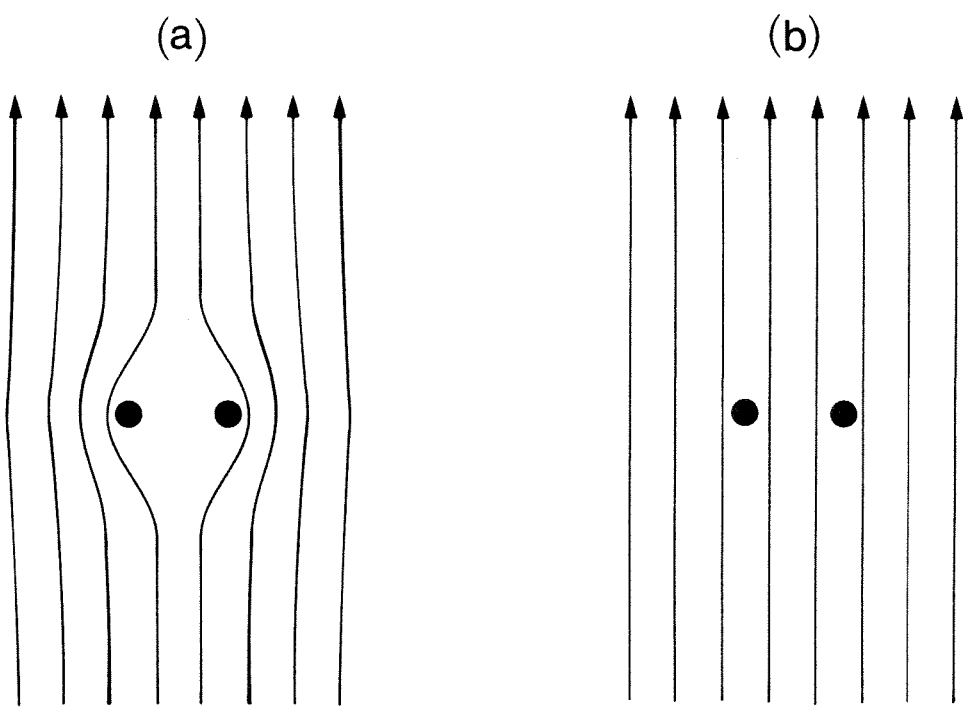

FIG. 5-24. Sketch of the diffusion of magnetic field lines through the Rogowski coil shield. a) Flux is excluded from the aperture for $t \ll \tau_d$. b) Flux penetrates the aperture for $t \gg \tau_d$.

any one turn is approximately

$$\Delta V_R = -A \frac{\partial}{\partial t}(\mathbf{B}\cdot\hat{\mathbf{n}}) , \tag{5.5}$$

where $\mathbf{B}$ is the magnetic field, $\hat{\mathbf{n}}$ is a unit vector directed along the minor axis of the torus at the position of the turn, A is the area of the loop and mks units are being used. Then the total voltage induced around the Rogowski coil is just the sum over all of the turns,

$$V_R = -A \sum_{j=1}^{N} \frac{\partial}{\partial t}(\mathbf{B}_j \cdot \hat{\mathbf{n}}_j) . \tag{5.6}$$

For large N, the sum can be approximated by an integral:

$$V_R = -\frac{A}{\Delta l} \frac{\partial}{\partial t} \sum_{j=1}^{N} \mathbf{B}_j \cdot (\hat{\mathbf{n}}_j \Delta l)$$

$$\rightarrow -\frac{A}{\Delta l} \frac{\partial}{\partial t} \int_C \mathbf{B}\cdot d\mathbf{l}$$

$$= -\frac{NA}{l} \frac{\partial}{\partial t} \left[\mu_0 \int_S \mathbf{j}\cdot d\mathbf{s} + \frac{1}{c^2} \frac{\partial}{\partial t} \int_S \mathbf{E}\cdot d\mathbf{s} \right] . \tag{5.7}$$

where S is a closed surface bounding the closed curve C, and $l = N\Delta l$ is the major circumference of the toroidal coil. The second term in equation 5.7 is due to displacement current and is ordinarily neglected, although in some special circumstances it can be important [Klein, 1975]. The displacement current due to a charged particle beam traveling towards a Rogowski monitor has been investigated by Stygar and Gerdin [1982], who show that the major effect is an increase in the rise time of the output signal (on the order of 1 nsec for a 25 keV beam). The effect is negligible for conditions likely to be encountered in the Caltech tokamak. The induced voltage around the coil then becomes

$$V_R = -\frac{\mu_0 NA}{l} \frac{\partial I}{\partial t} , \tag{5.8}$$

where I is the total current passing through the aperture of the torus.

Hence, in its simplest form, the Rogowski coil may be modeled as a voltage source, given by V_R, in series with the self-inductance of the coil, L_R, and terminated by a load impedance impedance R_T. The resistive load R_T used here was always a 50 Ω terminated coaxial cable. The time response of the Rogowski coil is then, with this model, limited only by the inductive time constant, $\frac{L_R}{R_T}$. Since the coil is designed to look for RF currents, we assume that all fields and currents vary as $e^{+i\omega t}$. The output voltage, V_0, is then given by

$$V_0 = \frac{-i\,\mu_0 NA\,\omega I}{l\left[1 + \left(\frac{\omega L_R}{R_T}\right)^2\right]^{\frac{1}{2}}}, \tag{5.9}$$

hence the sensitivity of the current monitor is a linear function of frequency if the inductance is sufficiently small ($\omega L_R \ll R_T$).

In practice, several other effects must be considered in the design of the coil. Large currents are often accompanied by large electrostatic potentials, and capacitive coupling to the coil windings can lead to spurious output signals, particularly at high frequencies. To protect against this problem, high frequency current monitors are usually encased in a toroidal conducting shell which is then grounded. A perfect shield, however, excludes all time-varying magnetic flux from the interior of the torus where the coil is situated; the shield is therefore slotted toroidally in order to allow B_θ to enter. The shield also performs another useful function: it prevents any z-component of the RF magnetic field from penetrating to the inside of the coil where it could otherwise generate spurious signals due to inhomogeneities in the winding [Anderson, 1971]. A grounded shield, however, could substantially alter the current distribution within the plasma by providing an alternate route for current flow. For this reason, the shielded Rogowski coil built for these experiments was

encased in an insulating shell; displacement current through the shell was negligible.

The high frequency behavior of the coil departs from that given by equation 5.9 when resonances due to the distributed capacitance between the turns of the coil, and between the coil and the shield, become important. A more realistic model of the device, that of a distributed delay line, has been analyzed by several authors [Cooper, 1963; Nassisi and Luches, 1979] who also discuss methods of increasing the coil self-resonant frequencies. The resonant frequencies of the coil built here, however, turned out to be much higher than the operating frequencies of interest even without taking special precautions.

A more important consideration, from the point of view of the Rogowski coil as a tokamak diagnostic, is the effect of the coil and its shield on the confining magnetic fields. Although it is desirable for the shield to prevent the penetration of any RF components of B_z, it is crucial to allow the penetration of the low frequency (essentially static) external confining field (B_{z0}, $B_{\theta 0}$) into the coil aperture. If the conductivity of the shell were infinite, even the low frequency confining fields would be excluded by the surface currents which would be set up in the shield. The result would be that the net confining field would bend around the coil and none of it would thread the aperture (Figure 5-24); consequently, plasma would be excluded as well. It is therefore important to make the diffusion time of the confining magnetic field lines through the shield short compared to the characteristic duration of the tokamak shot. In the present design, this was accomplished by making the shield from sufficiently thin copper (0.25 mm). The time constant (τ_d) appropriate for diffusion of field lines through a conducting cylindrical shell whose axis is parallel to the field is given by Lovberg [1965]: $\tau_d = \mu r \delta \sigma / 2$, where μ and σ are the permittivity and DC conductivity of the material, respectively, r is the radius of the cylinder, δ is the wall thickness, and mks units are being employed. Using the

dimensions of the Rogowski coil which was built for the Caltech tokamak, the above yields $\tau_d = 0.13$ msec. Perhaps a more appropriate method for calculation of the diffusion time of the field lines through the shield, given its geometry, is to calculate the inductive time constant L/R for a solid ring whose cross-sectional area is the same as the total cross-sectional area of the shield, and whose o.d. is the same as that of the shield. This approach yields a similar value for the diffusion time: $\tau_d = 0.15$ msec. Hence the diffusion time of the field lines through the shell is short compared to the plasma lifetime of $10-20$ msec.

5.5.3 Construction of the Current Monitor

The mechanical design of the current monitor had to take into account some special constraints: it had to be compatible with the high vacuum environment (i.e., not outgas) and had to be capable of withstanding the plasma and the heat deposited by it. The construction of a monitor which satisfied these criteria is shown in Figures 5-25 and 5-26.

The coil was wound with 100 equally spaced turns of #34 AWG teflon-insulated wire on a ceramic (Macor) ring of square cross section (31 mm o.d. × 1.6 mm × 1.6 mm). The return lead was brought back underneath the winding through a groove in the outer face of the ring. The electrostatic shield, machined from copper bar, was made in two pieces (a body and a cover) and had a wall thickness of 0.25 mm. The pieces of the shield, when joined together by a pressure fit, left a 0.5 mm gap between them at the inner wall (see Figure 5-25). The coil lay within the body of the shield, and one of its output leads was joined to the inner conductor of a 2 m long, 3.58 mm o.d., semi-rigid 50 Ω coaxial cable which fit through a hole in the outer edge of the shield. The other output lead, and the outer conductor of the coaxial cable, were joined to the copper shield body. The three connections were made with minute

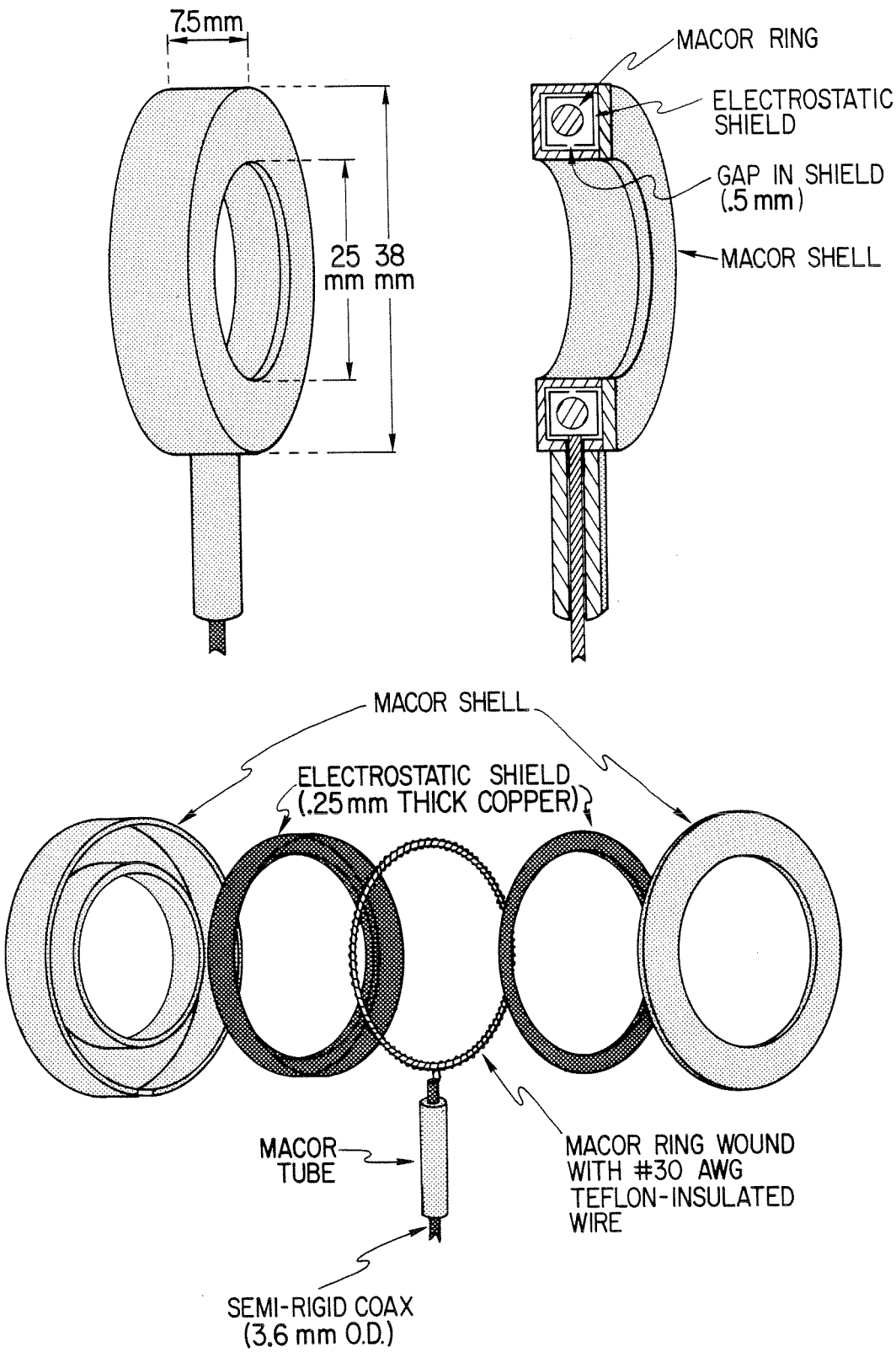

FIG. 5-25. Schematic diagram of RF plasma current monitor.

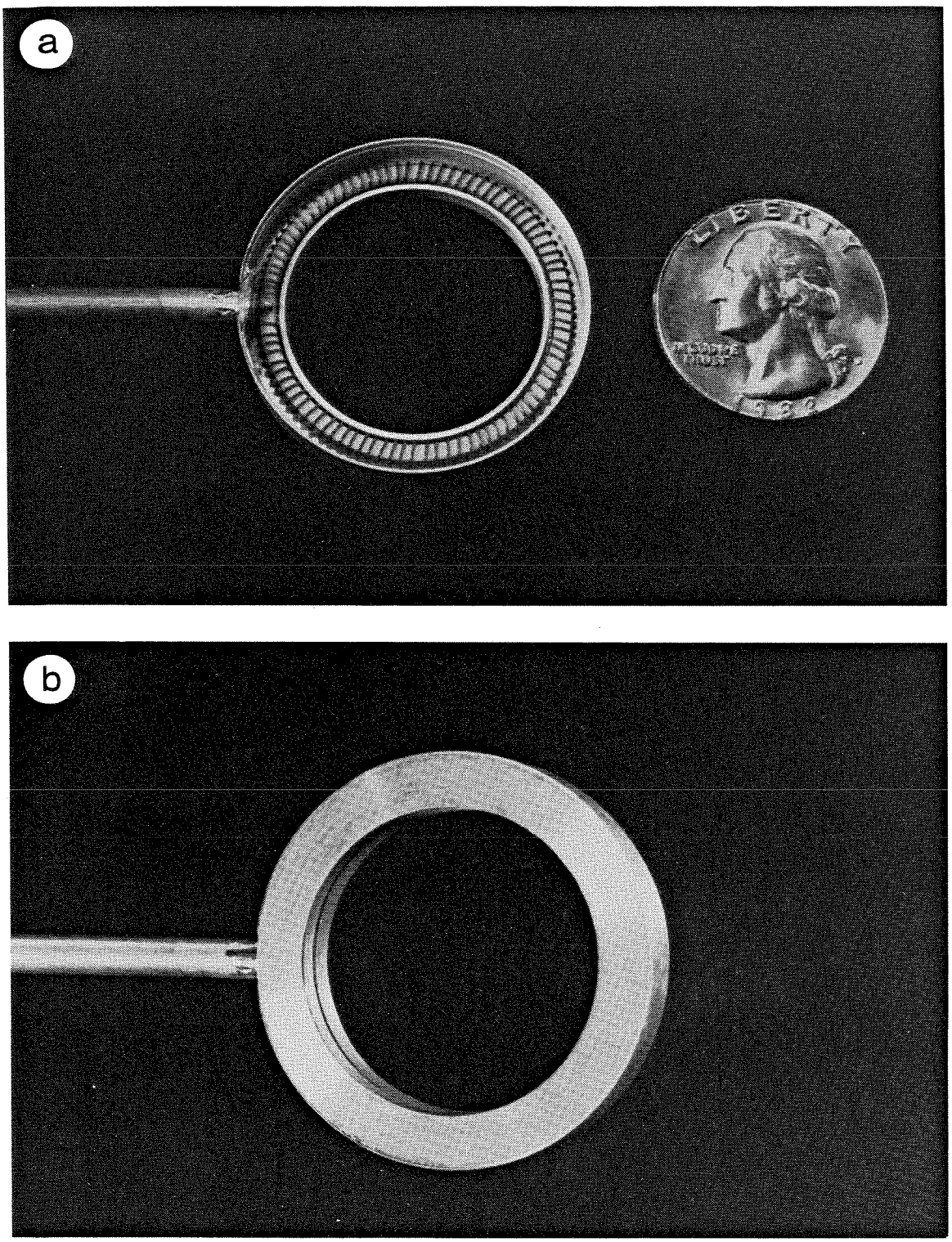

FIG. 5-26. Construction of RF plasma current monitor. a) Macor ring wound with 100 turns of #34 AWG teflon-insulated wire. Return lead is brought back around coil through groove in ring. Coil is installed in one half of electrostatic shield. b) Split electrostatic shield in place. Gap (0.5 mm) between two halves of shield is visible.

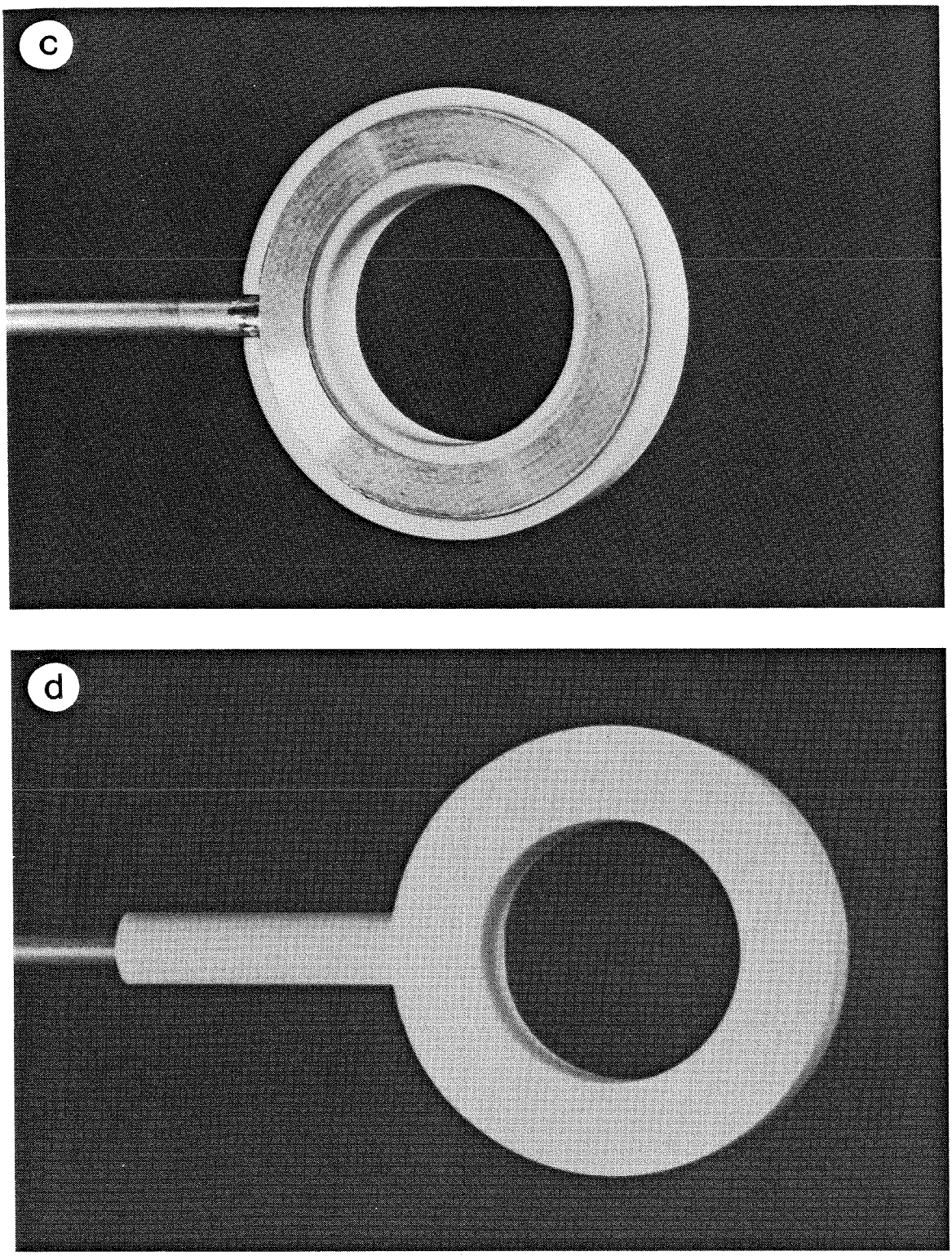

FIG. 5-26, continued. c) One half of ceramic shell attached to electrostatic shield. d) Completed ceramic insulation of current monitor.

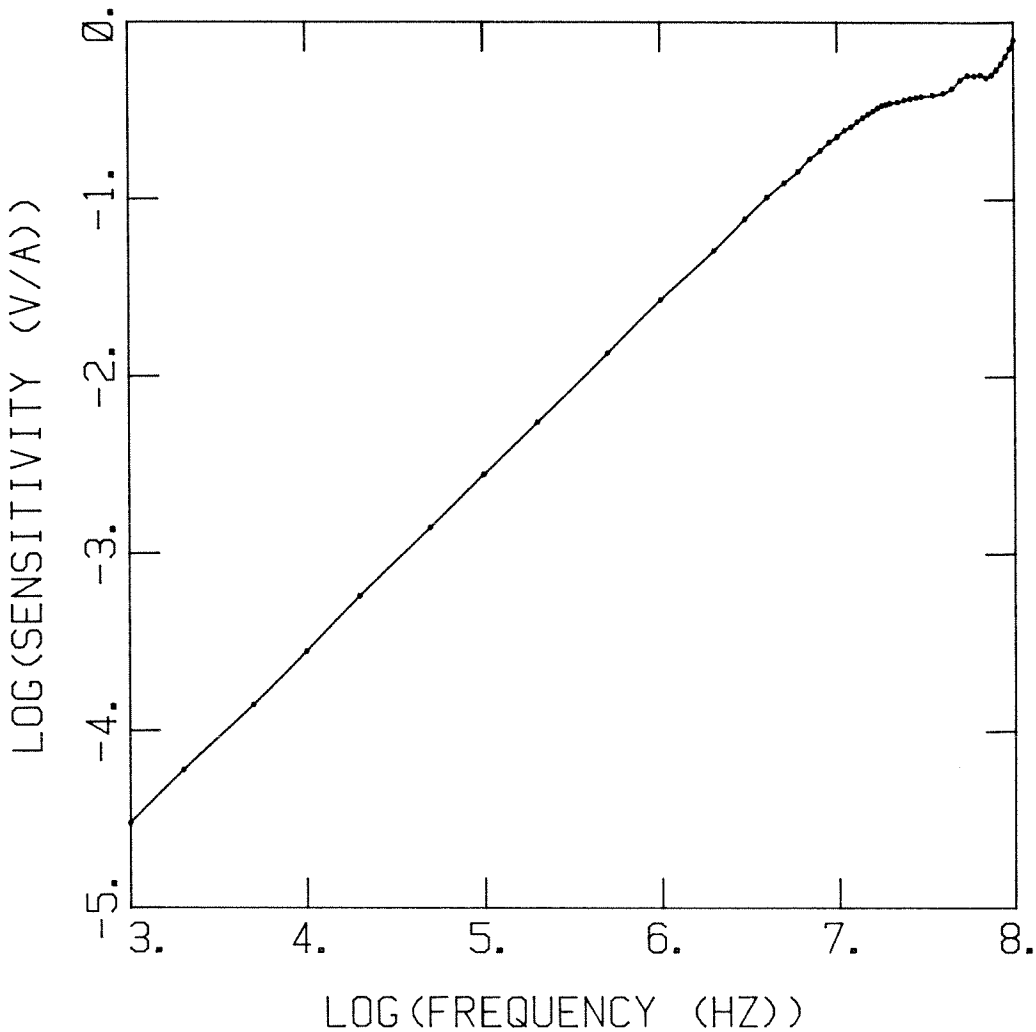

FIG. 5-27. Frequency response of current monitor.

amounts of a high-melting point solder, and the assembly was throughly cleaned and degreased. The electrostatic shield containing the coil was then insulated with a close-fitting two-piece ceramic shell, both to limit the temperature rise of the teflon insulation of the wire inside and to minimize the effect of the grounded shield on the RF current distribution within the plasma. The shell was machined from Macor and had a wall thickness of 1.6 mm. The overall dimensions of the finished current monitor were 38 mm o.d. × 25 mm i.d. × 7.5 mm thick. The cover of the ceramic shell was affixed to the body of the copper shield with several small dots of high-vacuum epoxy. The epoxy was kept centered between the i.d. and the o.d. of the ring, well away from the mating surfaces of the Macor pieces which had been lapped to a smooth finish (this insured that the plasma was kept well away from the epoxy).

The sensitivity of the coil was calibrated from 1 kHz to 100 MHz with a coaxial fixture similar to that described by Vignone [1968]. The result is shown in Figure 5-27; no serious resonances are present within this range. The coil response begins to depart from linearity with frequency at about 20 MHz, which is consistent with calculations using equation 5.9 (the inductance of the coil in its shield was about 0.3 μH).

5.5.4 Rotatable Antenna Fixture

The current monitor probe was built in order to try to investigate the current distribution near an electric field type RF antenna. This was mechanically difficult, however, due to the awkward geometry and small ports of the tokamak. One approach would have been to simply rotate the Rogowski coil around the antenna, but this would not have allowed the Rogowski coil major axis to remain parallel to the background confinement field (which was largely in the toroidal direction, since the poloidal magnetic field generated by the plasma ohmic-heating current was less than 10% of the toroidal field at the

outer wall). Instead, a small antenna was designed to rotate about a fixed current probe.

A schematic and photographs of the assembly are shown in Figures 5-28 and 5-29. The transmitting antenna was simply a short cylindrical plug of copper (1.0 cm o.d. × 1.0 cm long) which was connected to the center conductor of a 50 Ω semi-rigid coaxial cable. The coaxial line passed through a vacuum flange which was attached to the end of a 1 m long, 3.81 cm o.d. stainless steel tube that supported both the transmitting antenna and the current monitor. The support tube passed through the same differentially-pumped double O-ring seal flange that was used for the other RF antennas; the tube could thus be rotated and linearly translated. The semi-rigid coax was bent as shown in the diagram to offset it from the central axis of the support tube. About 7 cm of the coax adjacent to the copper antenna was encased in a Macor sheath to prevent the shield of the coax from exciting waves or driving current in the plasma (since the shield of the cable was grounded to the tokamak wall some 12 cm away, the shield at the antenna end of the cable was not necessarily at wall potential). The offset bends were made appropriately to maximize the diameter of the circle that the copper plug traced out when the support tube was rotated, while still allowing the assembly to fit through the tokamak port when the copper plug was oriented vertically above the current monitor (this circle diameter turned out to be ~8.9 cm).

The semi-rigid cable from the current monitor passed through a vacuum O-ring seal which was welded to the flange on the end of the support tube; hence it could be rotated or translated independently of the transmitting antenna. The copper plug antenna could therefore be rotated around the Rogowski coil while keeping the orientation of the coil fixed. Angular scales attached to the support tube and to the end of the semi-rigid coax from the current monitor allowed accurate setting of the orientations of the

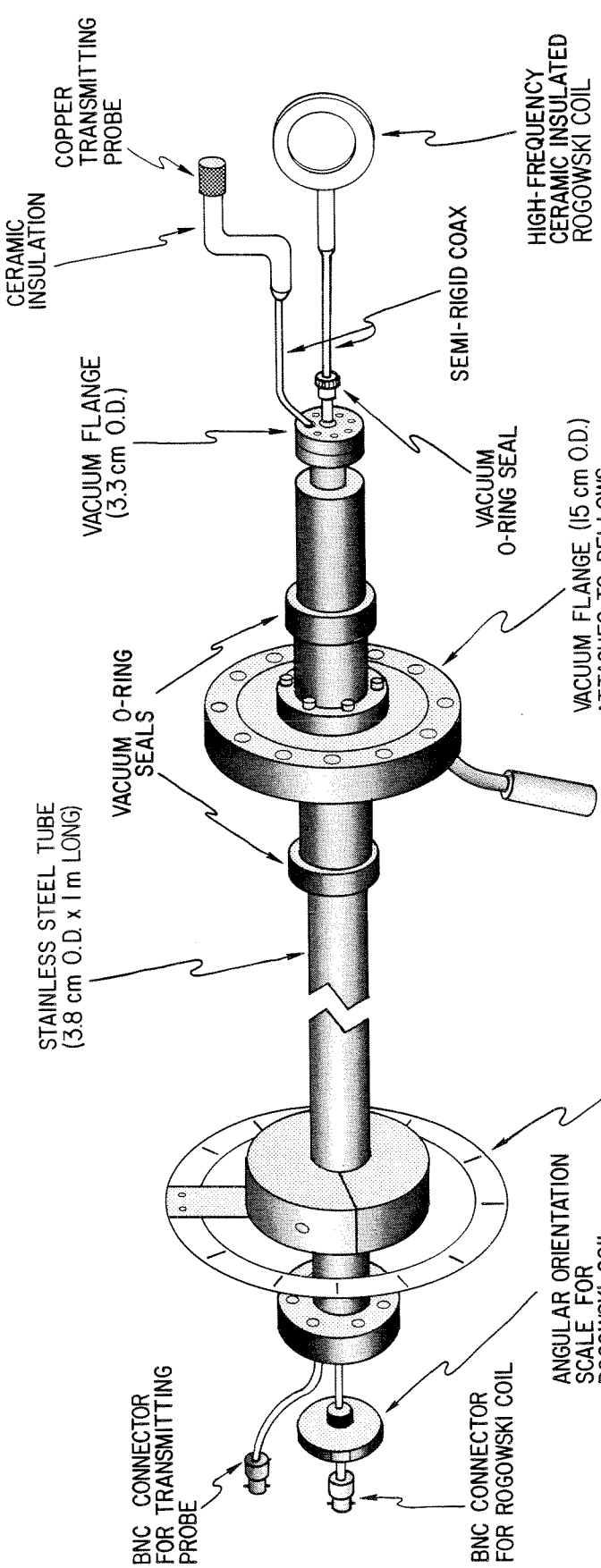

FIG. 5-28. Schematic diagram of rotatable antenna assembly. Both transmitting probe and current monitor can be independently rotated and linearly translated.

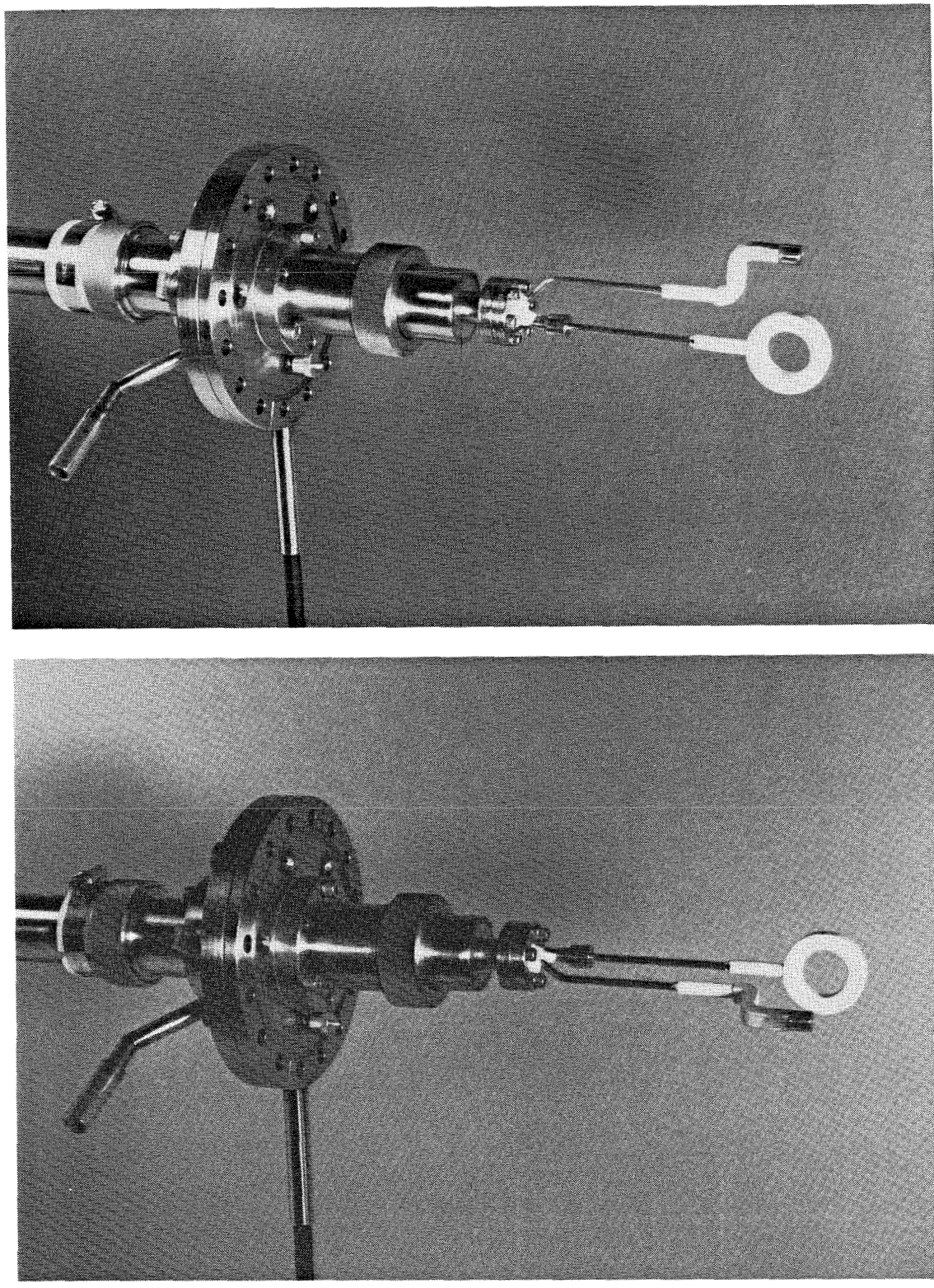

FIG. 5-29. Rotatable antenna assembly, showing two positions of the transmitting probe as it rotates around the current monitor.

transmitting antenna and the current monitor. The transmitting probe connector was attached, via a short length of flexible coax, to the output of the impedance matching box; the output of the Rogowski monitor led to an amplifier in the RF electronics cabinet.

In operation, the transmitting probe was fixed radially at a position corresponding to the probe tip being located 3.0 cm past the inner wall of the tokamak. No outgassing or contamination problems were observed from the transmitting probe. The Rogowski coil, however, required substantial conditioning through discharge-cleaning and tokamak shots. Eventually it could be inserted approximately 3.8 cm past the wall without affecting the global properties of the plasma (corresponding to the entire coil being just past the inner wall of the tokamak).

CHAPTER 6

Impedance Measurements

A fundamental diagnostic of the interaction between the plasma and the RF antenna is the antenna impedance. The antenna may launch waves and excite cavity resonances in the tokamak plasma and may interact with local plasma through particle collection; these effects in turn change the input impedance of the antenna. Knowledge of the antenna input impedance and its variation with plasma parameters is necessary for the design of impedance-transformation networks which efficiently couple energy to the plasma and can also illuminate the physics of the coupling process.

This chapter presents the results of impedance studies made on the series of RF antennas described in the preceding chapter. The experimental approach to the measurements is described in detail, and the transformation necessary to relate the measured impedance to the impedance at the input to the coupling structure is developed. Typical tokamak shots and associated raw impedance data are displayed for each of the five antennas. Density-dependent background loading (apparently unconnected with wave excitation) is clearly seen with all of the uninsulated antennas; the insulated and shielded antennas show peaks on the input loading resistance associated with eigen-mode production. Studies of the effects of various parameters (plasma density, antenna insertion, excitation frequency, toroidal magnetic field, and antenna current) on the complex input impedance are presented.

Langmuir probe $I-V$ curves (at DC) taken with and without high power RF

antenna excitation are discussed, and the dramatic change of the floating potential near an insulated RF antenna is noted. Finally, a simple model is presented which explains some features of the observed loading of the uninsulated antennas solely in terms of particle collection.

6.1 Experimental Method

6.1.1 General Considerations

The antenna impedance Z_a is defined here as $Z_a = V_a / I_a$, where V_a and I_a are the RF voltage across and current through the antenna at a specified point (an $e^{+i\omega t}$ time dependence is assumed, and all quantities are complex). A convenient point at which to measure the impedance for comparison with theoretical analysis is at the input to the antenna coupling structure, although in practice this may not be feasible.

RF excitation systems generally consist of the same three elements, whether they be for high power heating or low power wave-launching experiments: a coupling structure (referred to here as the RF antenna), an impedance-matching system, and an RF generator (Figure 6-1). In order to prevent unwanted radiation and power loss, the three sections are connected by transmission lines of various kinds. The RF antenna is usually close to or in the plasma, and power must be conducted to it through a transmission line which includes a vacuum-air transition.

The impedance which the antenna presents to the matching system is, of course, a function of the plasma interaction with the coupling structure and in general changes with plasma parameters. The RF generator, on the other hand, is almost always designed to operate into a specified load impedance, equal to the internal impedance of the generator Z_g (usually 50 Ω). To optimize power transfer between the generator and the antenna (crucial for

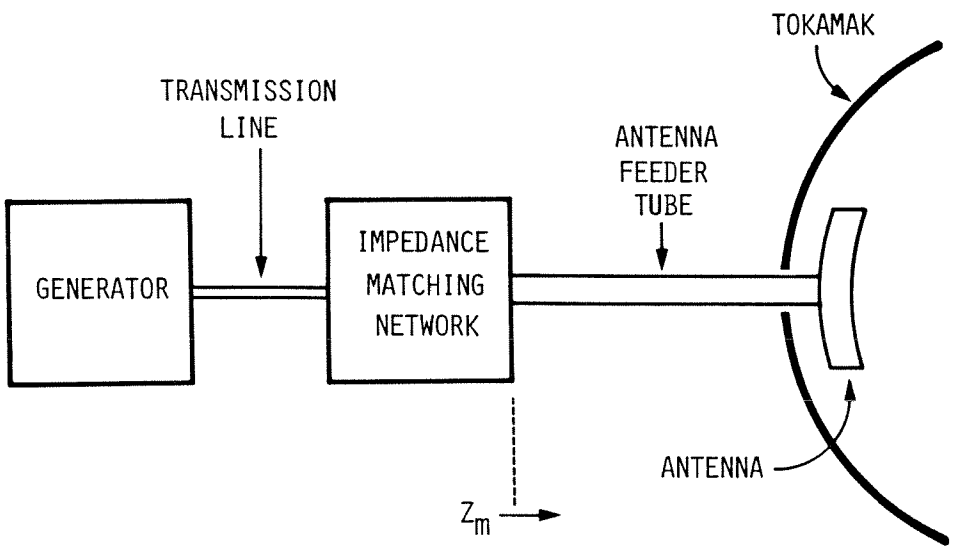

FIG. 6-1. General configuration for RF heating or wave propagation experiments, showing the generator, impedance-matching network, antenna feeder tube, and antenna. The impedance Z_m is measured at the input to the antenna feeder tube; the impedance is later transformed to the antenna-end of the feeder tube.

plasma heating experiments), the matching system must transform the impedance of the antenna so that $Z_a = Z_g^*$, where the "*" represents the complex conjugate.

The antenna input impedance in the absence of a plasma, $Z_0 = R_0 + iX_0$, is largely reactive for magnetic loop antennas but inevitable losses from the finite conductivity of the metals used in the antenna, from connecting joints, and from eddy currents induced in the stainless steel tokamak ports all contribute to R_0. It was difficult in practice to keep the effective antenna background resistance much below 0.1 Ω.

The change in antenna impedance due to the presence of a plasma, ΔZ_a, generally has both real and imaginary (resistive and reactive) components: $\Delta Z_a = \Delta R_a + i\Delta X_a$. The power dissipated in the impedance Z_a is then $P_a = \frac{1}{2}|I_a|^2(R_0 + \Delta R_a)$, where I_a is the peak RF antenna current. The term $\frac{1}{2}|I_a|^2 R_0$ represents energy lost in joule heating of the antenna, while the term $\frac{1}{2}|I_a|^2 \Delta R_a$ represents additional power dissipated due to the presence of the plasma. This additional power will occasionally be referred to here as power dissipated "by the plasma", although the destination of this power is not always clear. The power may be deposited in the plasma bulk via damping of waves launched from the antenna; it may heat the plasma surface; it may, through some interaction with local plasma, simply be heating the antenna itself.

The ratio of the power dissipated by the plasma to the power input to the RF antenna, a measure of power transfer efficiency, is just $\Delta R_a/(R_0 + \Delta R_a)$. Thus to reduce losses in the antenna structure to, say, 25% of the total dissipated power, the ratio $\frac{R_0}{\Delta R_a}$ must be kept less than 0.33. ICRF experiments are usually characterized by small values for ΔR_a, typically ranging from a few

tenths of an ohm to a few ohms. Efficient coupling of power to the plasma is possible, then, provided some care is taken to minimize losses in the antenna. Similarly, losses in the transmission line section connecting the antenna with the matching system, and in the matching network itself, must be kept small.

Ohmic losses in the antenna, transmission line, and matching network arise from joule heating of the conductors. Both the RF resistance of the current-carrying conductors (governed by the skin effect) and contact resistance at mechanical connections contribute to these losses. The distribution of high frequency current density in a conductor is given by $j \propto e^{-\frac{x}{\delta}}$, where x is the distance into the conductor measured from and perpendicular to its surface. δ, called the skin depth, is defined by $\delta = 1/\sqrt{\sigma\mu\omega}$ where μ and σ are the permeability and conductivity of the material, respectively, and it has been assumed that $\delta \ll a$, where a is the thickness of the conductor. Under these conditions, the particular geometry of the cross section of the conductor is unimportant; the current flows largely in a layer of thickness δ at the surface of the conductor. It is the surface area that determines the high-frequency resistance of a conductor, hence physically wide straps are used to interconnect elements in the impedance-matching network. Note that the surface resistance of copper at a frequency of 16 MHz is about 1 mΩ/square.

6.1.2 Experimental Approach

A simple and direct approach was used in these experiments to measure the complex antenna impedance. The magnitudes of the RF antenna current (I_m) and voltage (V_m) and the relative phase between the two (φ_m) were measured at the input to the short transmission line section (the antenna feeder tube) which connected the impedance-matching system to the antenna; the experimental arrangement is shown in Figure 6-2. The current and voltage

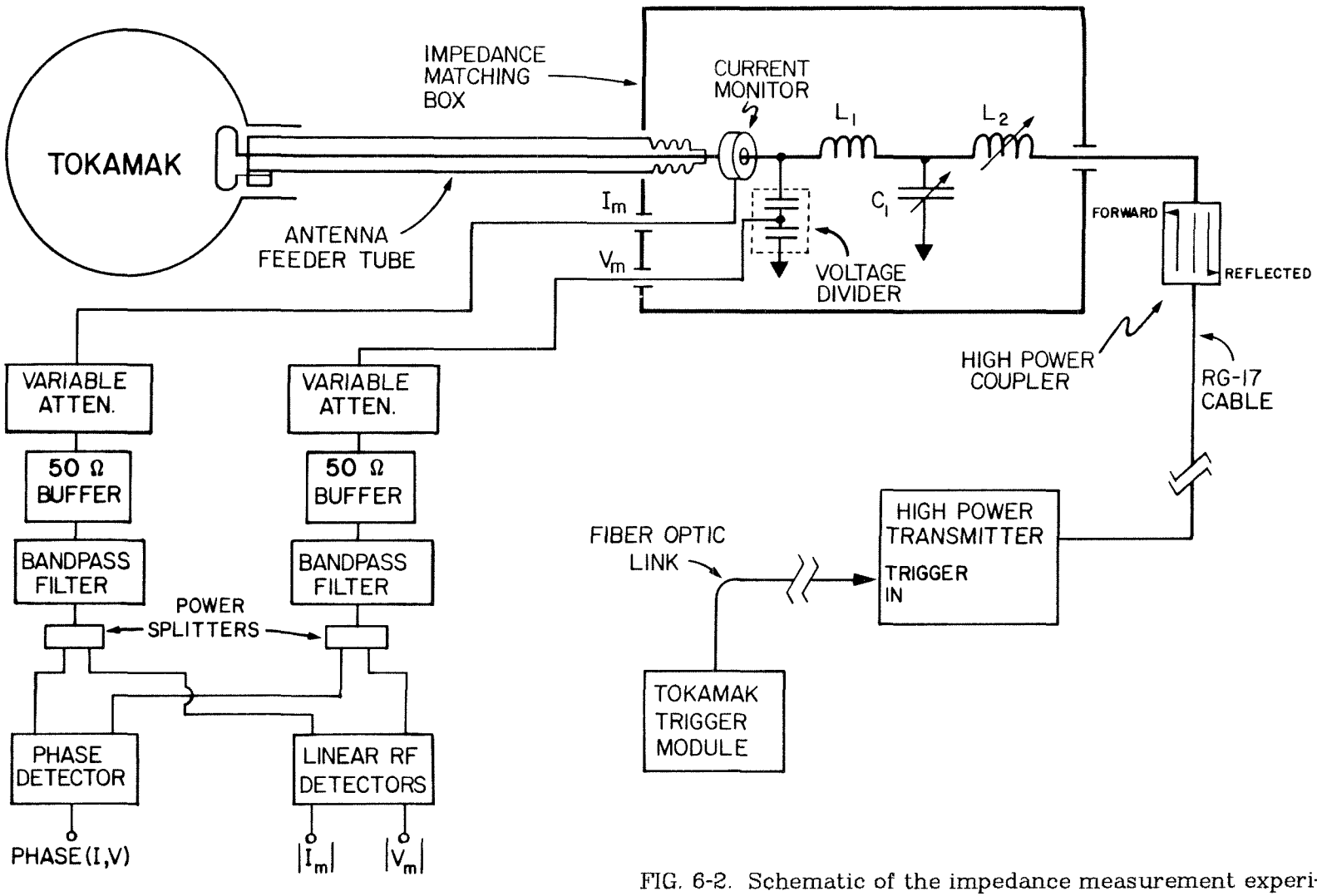

FIG. 6-2. Schematic of the impedance measurement experiment. The RF current and voltage and the phase between the two are measured on the antenna-side of the matching network, at the input to the feeder tube.

signals were first passed through variable attenuators to reduce the signal levels, if necessary, and were then led to buffer amplifiers which served to present a constant (50 Ω) impedance to the voltage and current monitors. The outputs of the buffers were passed through bandpass filters (with typical bandwidths of 1 MHz) to reduce any harmonics on the signals, then to power splitters which led to the amplitude and phase detectors. The characteristic impedance of all of the system components was 50 Ω. For low-power experiments, the buffer amplifiers were replaced with +30 db wide-band RF amplifiers (TRW CA3020).

The impedance looking into the transmission line section was then given by $Z_m = \frac{V_m}{I_m} e^{i\varphi_m}$, and the power dissipated by the antenna and its feeder tube was just $P_m = \frac{1}{2} V_m I_m \cos(\varphi_m)$. The primary advantage of this approach was that the measurements were made on the *antenna* side of the matching network and were thus independent of the tuning of the network. The measurements were simple to interpret since there was no need to transform the measured impedance across a high-ratio impedance-matching network in order to find the antenna impedance.

The reflection-coefficient method used by Hwang [1980] measures the complex reflection coefficient (ρ) at the input (i.e., the generator side) of the matching network; a directional coupler is used to measure the forward and reflected wave amplitudes on the transmission line and the phase between them. The input impedance at the location of the coupler can then be found: $Z_{in} = Z_c \frac{1+\rho}{1-\rho}$, where Z_c is the characteristic impedance of the transmission line (in which the directional coupler is located) leading from the generator to the matching network. This method requires the matching network to be reasonably well tuned to the RF antenna in order for ρ to be determined with sufficient accuracy. The method also requires accurate characterization of the impedance- transformation properties of the matching network for each new

setting of the network. Since the transformation ratios across the network for the components of the impedance are large (the resistive part of the generator impedance is 50 Ω, while that of the antenna impedance is typically <1 Ω; the reactive part of the generator impedance is typically <1 Ω, while that of the antenna impedance may be $15-30$ Ω), small errors in determining the transformation properties of the matching network can lead to significant errors when mathematically relating the measured impedance to the impedance on the antenna-side of the network. On the other hand, the reflection-coefficient method does have greater sensitivity to the relatively small changes in the imaginary part of the antenna impedance that occur during the plasma shot.

The independence of the impedance measurements from the particular setting of the matching network in the experiments described here means that the only effect of the matching network tuning is on the level of power delivered to the plasma.

6.1.3 Antenna Feeder Tube Transformations

The short transmission-line section which connects the RF antenna structure with the matching network does transform the impedance of the antenna somewhat, and it is desirable to unfold this transformation. The feeder tube is a coaxial section which also serves as the vacuum feedthru. The voltage and current measurements are made in air, at the end of the feeder tube which terminates in the matching network housing. The geometry of the feeder section is precisely known; hence the impedance transformation between the point at which the voltage and current monitors are located and the other end of the feeder tube (where the antenna coupling structure is located) can be derived from transmission-line theory.

The feeder transmission line consists of concentric copper tubes separated by a glass insulating tube (section 5.1); the geometry of a cross-section of the line is shown in Figure 6-3. The characteristic impedance of such a line is easily calculated. The distributed capacitance is found to be

$$C = \frac{2\pi\varepsilon_0}{\ln\left(\frac{bd}{ac}\right) + \frac{1}{\varepsilon_1}\ln\left(\frac{c}{b}\right)} \quad \text{Farad/meter,} \tag{6.1}$$

and the distributed inductance is

$$L = \frac{\mu_0}{2\pi}\ln\left(\frac{d}{a}\right) \quad \text{Henry/meter.} \tag{6.2}$$

where ε_0 and μ_0 are the permittivity and permeability of free space, respectively, and ε_1 is the permittivity of the glass tube. The characteristic impedance is then $Z_c = \sqrt{L/C}$, and the phase velocity of a wave on the line is $v_{ph} = 1/\sqrt{LC}$. The line was uniform except near the end of the tube at the vacuum break. Two different feeder transmission lines were actually used in the experiments: a low-impedance section ($Z_c \simeq 15\ \Omega$) used with the magnetic loop antennas, and a higher impedance section ($Z_c \simeq 99\ \Omega$) used with the electric field antennas. The dimensions of the two sections are given in Figure 6-3.

The effect of the electrically very short transition region at the vacuum break can be modeled by a series of transmission-line sections of different characteristic impedances. Consider the main transmission-line section, with characteristic impedance Z_{c_1}, and let it be terminated at its end by the antenna coupling structure with impedance Z_{a_0}. Then Z_{a_0} is related to the input impedance of this section (Z_{a_1}) by

$$Z_{a_0} = \frac{Z_{a_1} - iZ_{c_1}\tan(\beta_1 l_1)}{1 - i\,\frac{Z_{a_1}}{Z_{c_1}}\tan(\beta_1 l_1)}, \tag{6.4}$$

where l_1 is the length of the section and β_1 is the wavelength in the section

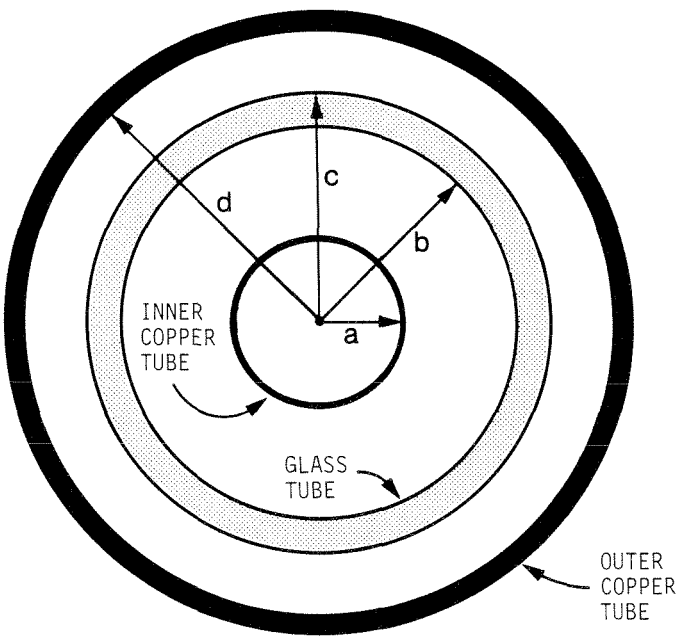

FIG. 6-3. Geometry of the cross-section of the main section of the antenna feeder tube. For the low-impedance feeder tube, $a = 1.27$ cm, $b = 1.40$ cm, $c = 1.59$ cm, $d = 1.75$ cm. For the high-impedance feeder tube, $a = 0.32$ cm, $b = 1.40$ cm, $c = 1.59$ cm, $d = 1.75$ cm. The dielectric constant of the glass was ~ 4.8.

[Chipman, 1968]. The transformation of impedance across any section may be written as

$$Z_{a_j} = F_j\left(Z_{a_{j+1}}\right), \tag{6.5}$$

where

$$F_j(\xi) = \frac{\xi - i\, Z_{c_j} \tan(\beta_j l_j)}{1 - i\, \frac{\xi}{Z_{c_j}} \tan(\beta_j l_j)}.$$

The impedance at the input to any section j may then be related to the impedance at the antenna-end of the line by

$$Z_{a_0} = F_1\left(F_2\left(F_3\left(\cdots\left(F_j\left(Z_{a_j}\right)\right)\cdots\right)\right)\right). \tag{6.6}$$

The low-impedance line, for example, is modeled by four serial sections, shown in Figure 6-4, and the antenna impedance is given by $Z_{a_0} = F_1(F_2(F_3(F_4(Z_{a_4}))))$, where Z_{a_4} is the actual quantity measured in the experiment.

The transformation can be simplified considerably because the lengths of sections 2, 3, and 4 are very small compared to a wavelength. For section j, we have

$$Z_{a_{j-1}} = F_j\left(Z_{a_j}\right) \simeq Z_{a_j} - i\, Z_{c_j} \beta_j l_j \left[1 - \left(\frac{Z_{a_j}}{Z_{c_j}}\right)^{\frac{1}{2}}\right], \tag{6.7}$$

provided $\beta_j l_j \ll 1$, and the inverse transformation is then given by

$$Z_{a_j} = F^{-1}\left(Z_{a_{j-1}}\right) \simeq Z_{a_{j-1}} + i\, Z_{c_j} \beta_j l_j \left[1 - \left(\frac{Z_{a_{j-1}}}{Z_{c_j}}\right)^{\frac{1}{2}}\right]. \tag{6.8}$$

Thus adding a short section of transmission line to the input of the line is equivalent to adding a small amount of inductive or capacitive reactance in series with the input, depending on whether the input impedance is less than or greater than the characteristic impedance of the added section.

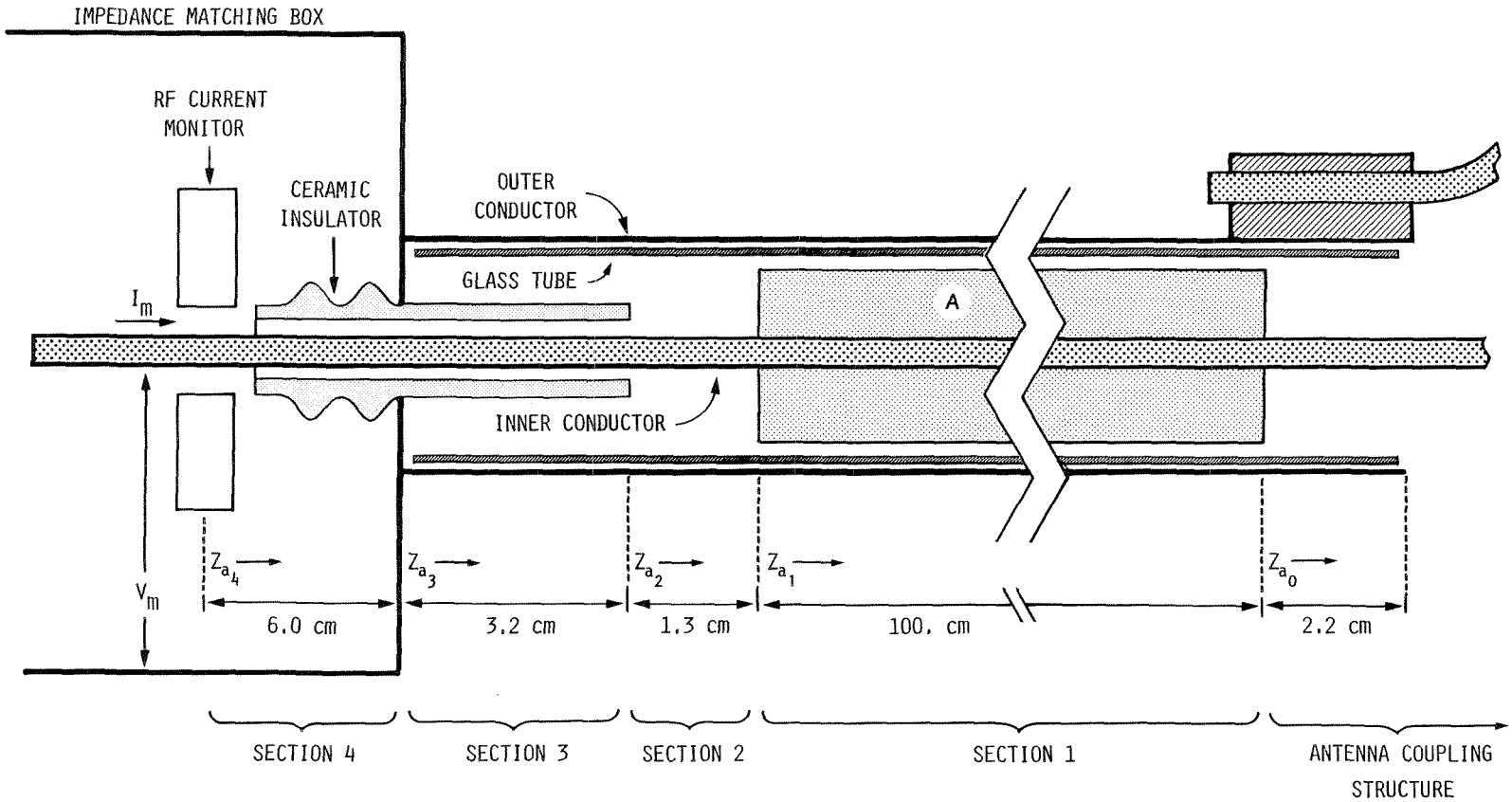

FIG. 6-4. Geometry of the antenna feeder tube used to calculate the impedance transformation relations, showing the separation into four sections. The area marked "A" is the 2.54 cm o.d. copper tube used for the low-impedance line; this tube is absent for the high-impedance line. Z_{a_4} represents the measured impedance, Z_{a_0}, the antenna impedance.

The low-impedance line was used only with the loop antennas and, for all experiments with these, the relation $|Z_{a_j}/Z_{c_j}|^2 \ll 1$ was satisfied ($j = 2, 3, 4$). Therefore, the transformation for the short sections can be approximated as $Z_{a_{j-1}} \simeq Z_{a_j} - iZ_{c_j}\beta_j l_j$, and, for the composite transform,

$$Z_{a_1} \simeq Z_{a_4} - i\left[\sum_{j=2}^{4} Z_{c_j}\beta_j l_j\right]. \tag{6.9}$$

The above equation is then used with equation 6.4 to relate the measured impedance (Z_{a_4}) to the antenna impedance (Z_{a_0}). The small sections each act as a series imaginary impedance proportional to frequency, i.e., as an inductance with value $Z_{c_j} l_j \sqrt{L_j C_j}$.

Some examples of the specific transformations between the measured impedance ($Z_m \equiv Z_{a_4}$) and the antenna impedance (Z_{a_0}) are shown for the high and low impedance lines in Figures 6-5 and 6-6. Note that the ratio of the real part of the antenna impedance to the real part of the measured impedance depends somewhat on the imaginary part of the measured impedance and is generally between one and two for the range of parameters appropriate to the experiments described here. The transformation of the imaginary part of the measured impedance depends slightly on the real part of the measured impedance; the overall effect is largely to add a constant reactance to the antenna impedance.

The measured impedance during the plasma shot, for the low-impedance line and a loop antenna, typically varied over the range: $\mathrm{Re}(Z_m) \approx 0.1 - 2.0\ \Omega$, $\mathrm{Im}(Z_m) \approx 15. - 20.\ \Omega$. Therefore the phase measured between the voltage and current, $\varphi_m = \tan^{-1}\left[\mathrm{Im}(Z_m)/\mathrm{Re}(Z_m)\right]$, was quite close to 90 degrees and varied by only a small amount (0.1 − 4.0 degrees) during the plasma shot. A sensitive and noise-free phase detection system was needed for this measurement; the detector is discussed in detail in section 4.6.

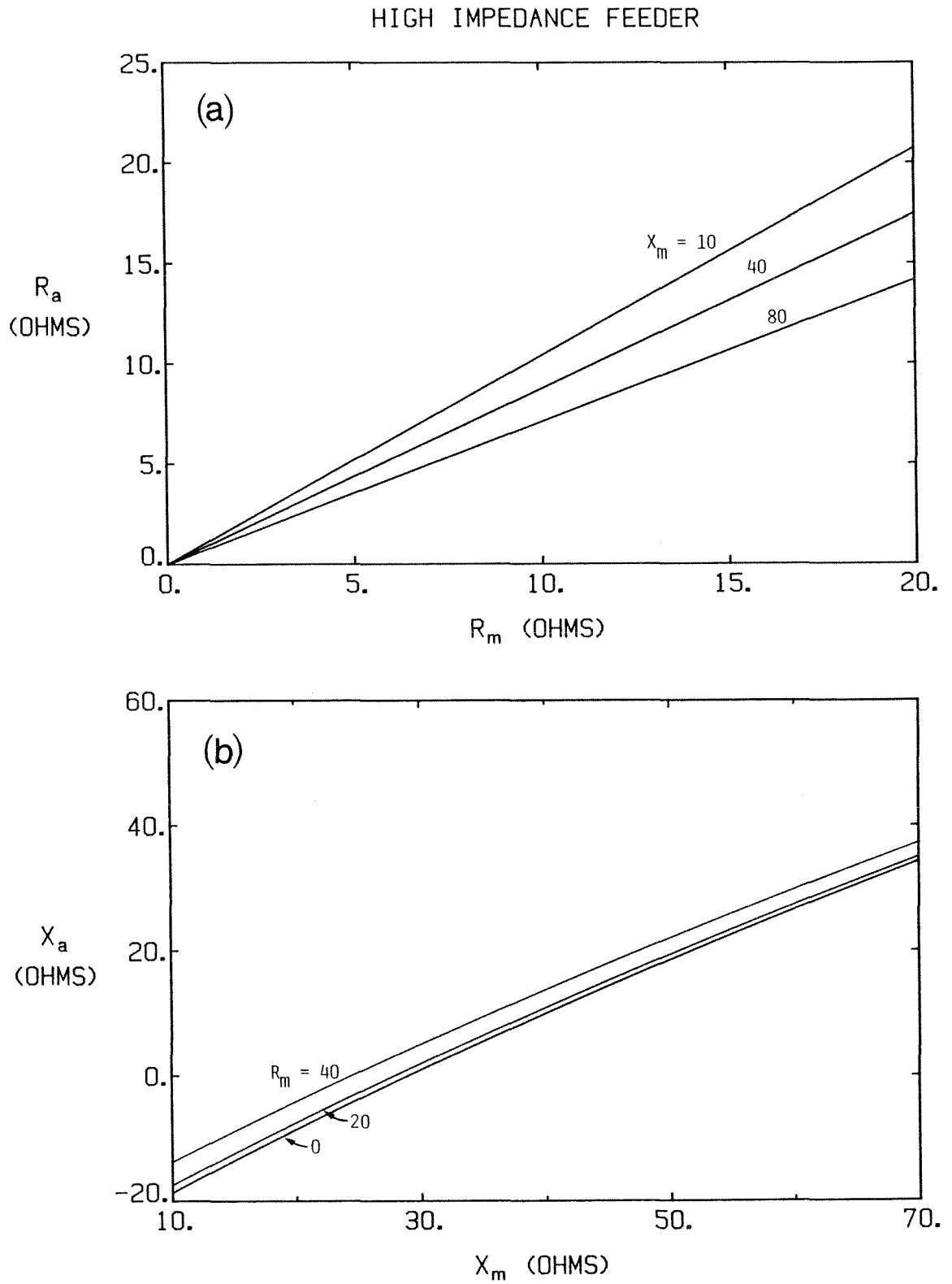

FIG. 6-5. Examples of the transformation between the measured impedance ($Z_m = R_m + iX_m$) and the impedance at the input to the antenna coupling structure ($Z_{a_0} = R_a + iX_a$) for the high-impedance feeder tube. a) R_a vs. R_m for various values of X_m. b) X_a vs. X_m for various values of R_m.

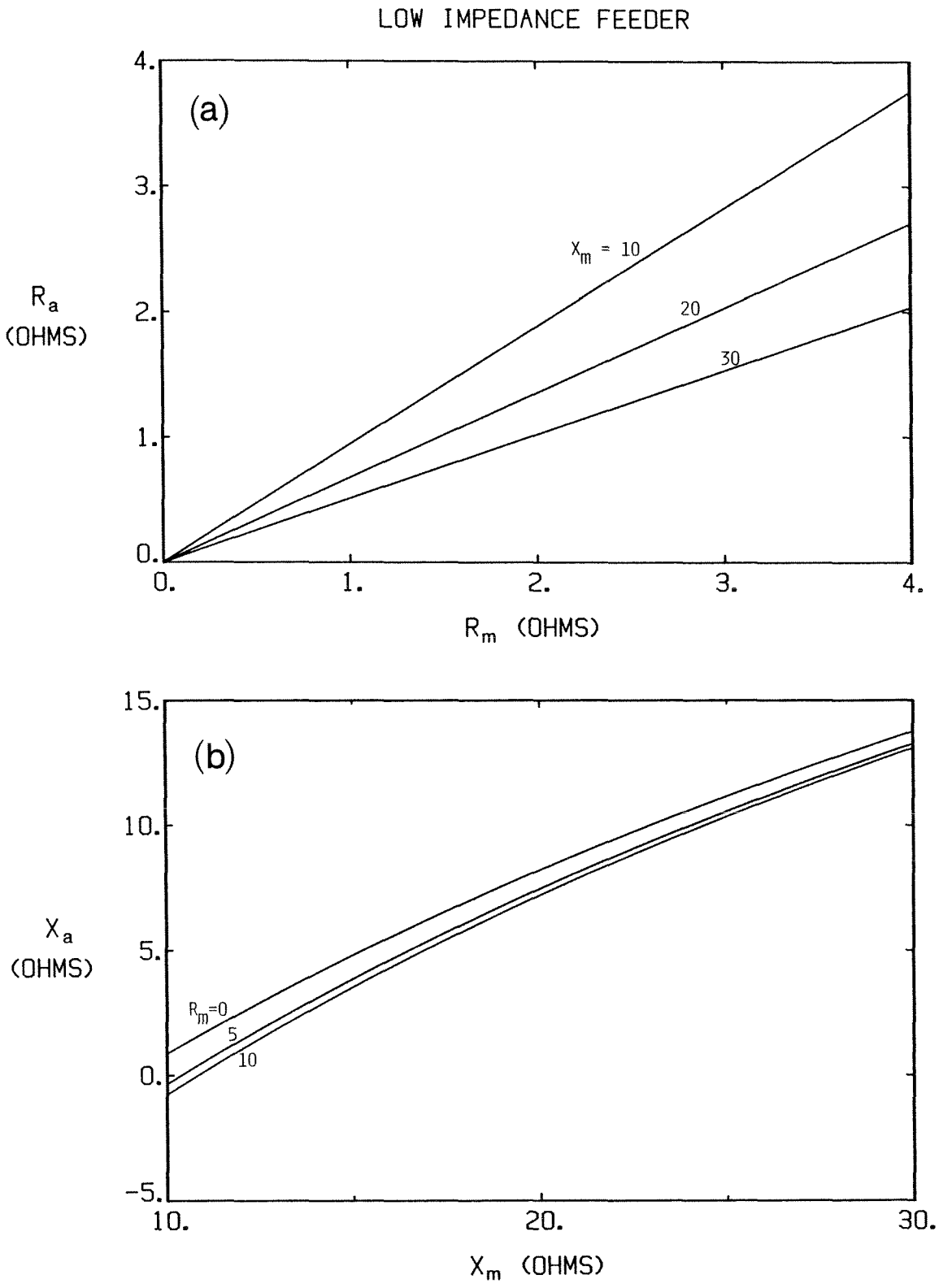

FIG. 6-6. Examples of the transformation between the measured impedance ($Z_m = R_m + iX_m$) and the impedance at the input to the antenna coupling structure ($Z_{a_0} = R_a + iX_a$) for the low-impedance feeder tube. a) R_a vs. R_m for various values of X_m. b) X_a vs. X_m for various values of R_m.

In summary, the voltage-current-phase measurement of impedance close to the RF antenna eliminates the problem of accurately characterizing the high-ratio impedance-matching network. The remaining transformation across the feeder tube from the measurement point to the antenna coupling structure is independent of the tuning of the matching network and leads to small transformation ratios.

6.1.4 Data Collection and Analysis

Data collection was accomplished with the sixteen-channel LeCroy A-D system and the four-channel Biomation waveform recorder as described in section 3.4. During impedance measurements, the following signals were always recorded: one-turn voltage, plasma current, soft-UV signal, microwave interferometer output, forward and reflected RF voltages (from the directional coupler), and the RF voltage, current, and phase, measured at the input to the antenna feeder tube. Additional channels often recorded included the visible light (from a photodetector) and X-ray (from a PIN diode) signals, the outputs from various magnetic probes, and the gas-puff valve voltage waveform. In addition, the hydrogen gas pressure and the settings of the toroidal field, vertical field, horizontal field, and ohmic-heating field power supplies were recorded (manually) for each shot.

Each recorded channel generally consisted of 1024 equally-spaced samples of eight-bit resolution. The data from each plasma shot were transferred, between shots, from the transient recorder memory, through an LSI-11/03 computer, to storage on 8-inch floppy disks. The data archived from all of the experiments described in this thesis comprise some 3000 tokamak shots and occupy $\sim$40 megabytes of disk space.

A typical tokamak run began with extensive discharge cleaning (section 3.6) to lower the level of impurities adsorbed on the tokamak walls. After

sufficient cleaning, as judged from the quadrupole residual gas analyzer, tokamak shots were started. The tokamak usually required several shots to settle into a repeatable discharge mode. The piezoelectric gas-puff valve voltage waveform was then adjusted, together with the voltage and timing of the tokamak power supplies, to try to achieve the desired plasma current and density evolution. After considerable experience, combinations of the various parameters were found which usually led to fairly reproducibly discharges with the desired plasma properties. Three factors which acted to make the discharge less reproducible were identified: problems with the gas-puff valve (due to the piezoelectric diaphragm "sticking"), irregular firing of the ohmic-heating or preionization power supply ignitrons, and insufficiently clean walls.

Data collection was begun once the tokamak was firing in a mode which was both reproducible and had similar properties to previously recorded discharges with which the data run was to be compared. Generally three to seven shots were recorded for each setting of the experimental parameters (e.g., RF antenna position, excitation frequency, etc.). The tokamak could typically be run for two to five hours before impurity adsorption on the walls increased to the point where the plasma shots became noticeably shortened and less reproducible. The collected raw data sets were then plotted out in compact form (eight data channels per page) to provide for rapid review of the experiment.

Calibration curves for the directional coupler, the RF detectors, and the current and voltage monitors were used in the computer programs which were written to analyze the data; the curves were interpolated as necessary using a cubic-spline fit. The signal attenuation due to the connecting coaxial cables, buffer amplifiers, bandpass filters, and power splitters was also measured at each frequency used and entered into the programs.

Analysis of a series of similar plasma shots for the dependence of the impedance on a particular parameter yields a set of data points for each setting of the experimental parameter. The mean of the set is usually plotted as the experimental point associated with the particular experimental parameter; the scatter in the data is indicated with "error bars" of amplitude $\pm\sigma$, where σ is the standard deviation of the data set. In general, the scatter in the data from shot to shot was greater than the actual "error" due to, for instance, instrumental background noise, calibration error, or quantization error (from the eight-bit resolution of the data system). In cases where the scatter in the data did not vary much as the experimental parameter was changed, the vertical lines denoting the scatter may be omitted from some of the plotted points. High-frequency noise was also present on some of the signals associated with the impedance measurement; this appeared to be due to density fluctuations in the plasma intercepting the antenna. This noise was sometimes reduced using some simple digital filters [Hamming, 1977].

6.2 Impedance Measurement Results

This section presents the results of impedance measurements on the five antennas described earlier. For each antenna, an impedance analysis for a typical shot is first shown. Eight of the raw data channels are displayed, followed by the results from the analysis program: the antenna current and voltage, the power dissipated by the antenna, and the real and imaginary parts of the complex antenna impedance (all transformed from the point of measurement to the antenna-end of the feeder tube). Following this display of a characteristic plasma shot, the dependence of the real and imaginary parts of the antenna impedance on various parameters is shown. The curves drawn through the experimental points in these plots are generally fits to low-order polynomials and are meant to "guide the eye". Comparison of some of the data

with theoretical models is discussed in section 6.4.

6.2.1 Bare Loop Antenna

Raw data channels for a typical tokamak shot using the bare loop antenna are shown in Figure 6-7. The excitation frequency was 12 MHz, the toroidal magnetic field on axis was 4.0 kG, and the front edge of the antenna loop was 2.5 cm past the tokamak wall. The matching network was tuned to match the generator impedance to the antenna impedance; from the forward and reflected voltage signals it is apparent that, during the plasma shot, most of the incident RF power is being absorbed by the antenna-plasma system. The line-averaged density measured by the microwave interferometer ramps up almost linearly after the gas puff begins (at $t \simeq 4$ msec); the density fall is also fairly linear. The phase signal decreases by ~ 4 degrees as the plasma density increases; the antenna current and voltage vary by a factor of almost two during the plasma shot. Although the amplitude variations of the RF antenna current and voltage were considerably less than the dynamic range of the phase detector (which was greater than 20 db for a change in output corresponding to 0.1 degree), the independence of the phase detector output on the input signal amplitude was checked in each experiment under actual operating conditions and signal levels.

The raw phase signal provides a useful indication of the resistive part of the antenna loading impedance. Because the antenna current and voltage track each other fairly closely, it follows that $|Z_m|$ does not change very much during the plasma shot. Also, the phase φ_m remains close to $\pi/2$ radians during the shot. Writing $\varphi_m = \pi/2 - \delta\varphi_m$, it follows that

$$Z_m = |Z_m| e^{i\varphi_m} \simeq |Z_m| (\delta\varphi_m + i) . \qquad (6.10)$$

where terms of order $(\delta\varphi_m)^2$ and higher have been dropped. The antenna

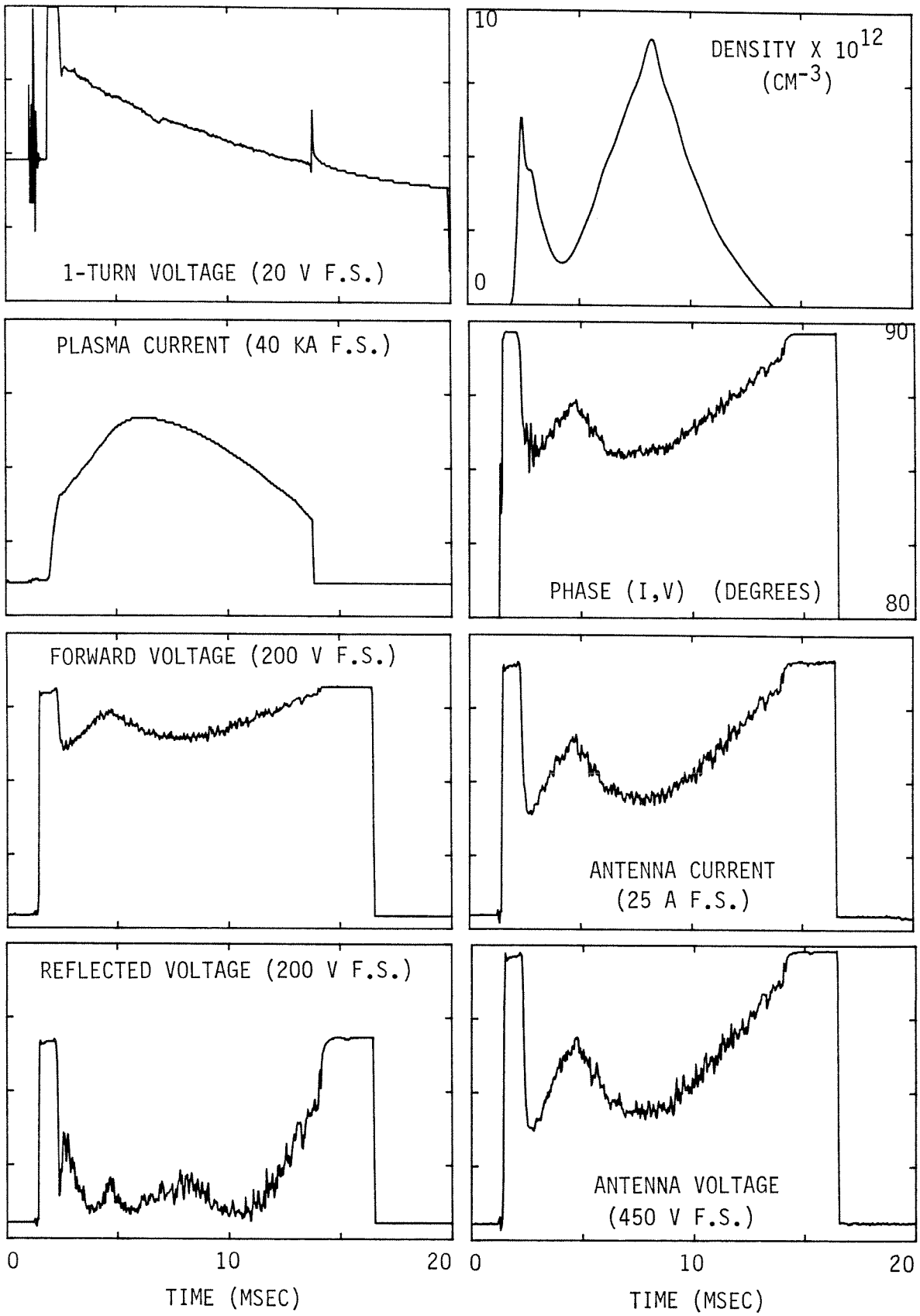

FIG. 6-7. Raw data from a tokamak shot using the bare loop antenna. Here $\omega/2\pi = 12$ MHz, $B_0 = 4.0$ kG, and the leading edge of the loop was 2.5 cm past the tokamak wall. Note the good impedance match indicated by the small reflected voltage signal during the discharge. The density curve is plotted from analysis of the microwave interferometer signal.

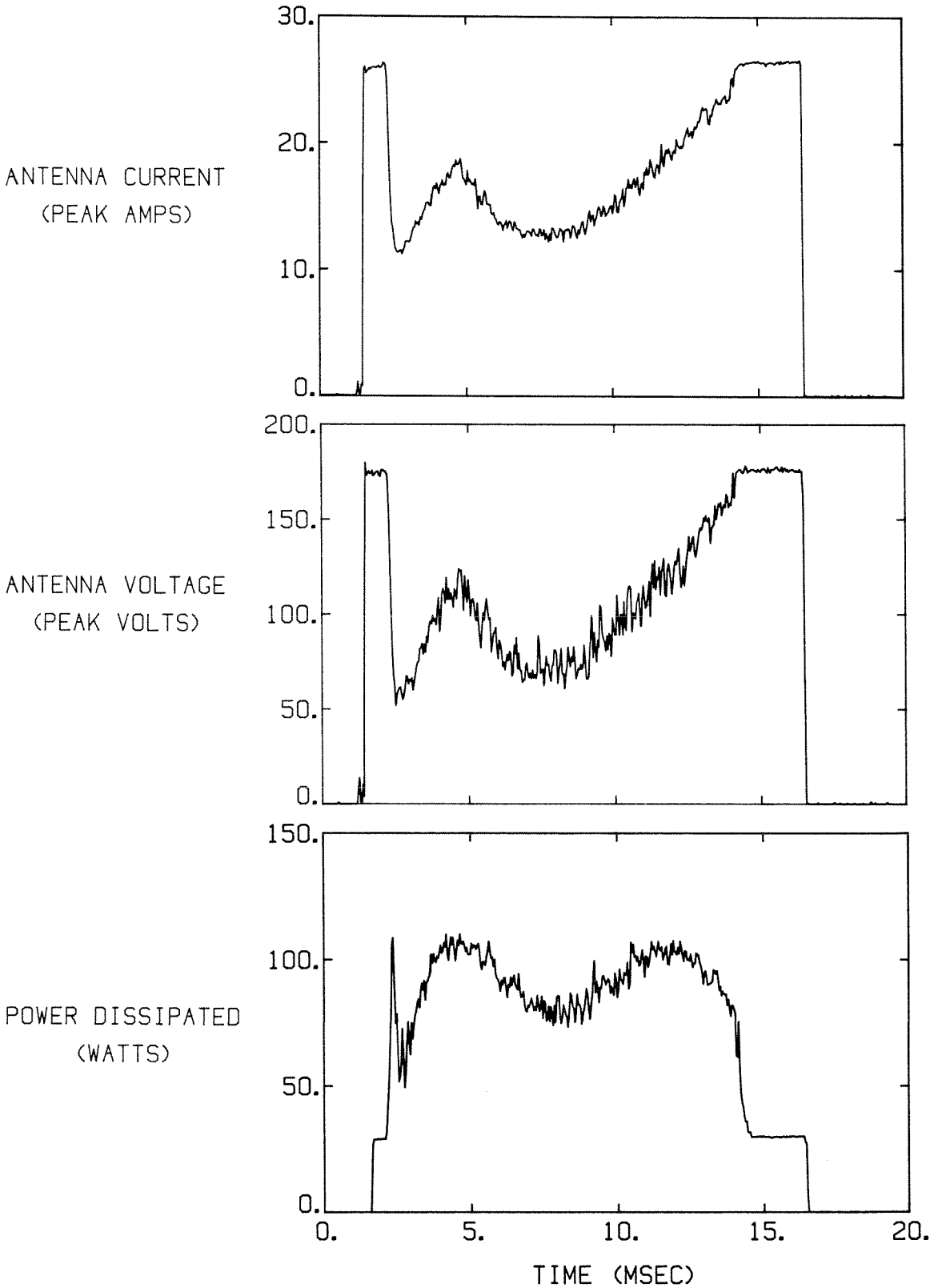

FIG. 6-8. Results for the antenna current, voltage, and dissipated power from the computer analysis of the raw data for the tokamak shot shown in Figure 6-7. The results have been transformed from the measurement location to the antenna-end of the feeder tube. Note the dissipation of ~30 watts in the background antenna resistance after the discharge has ended.

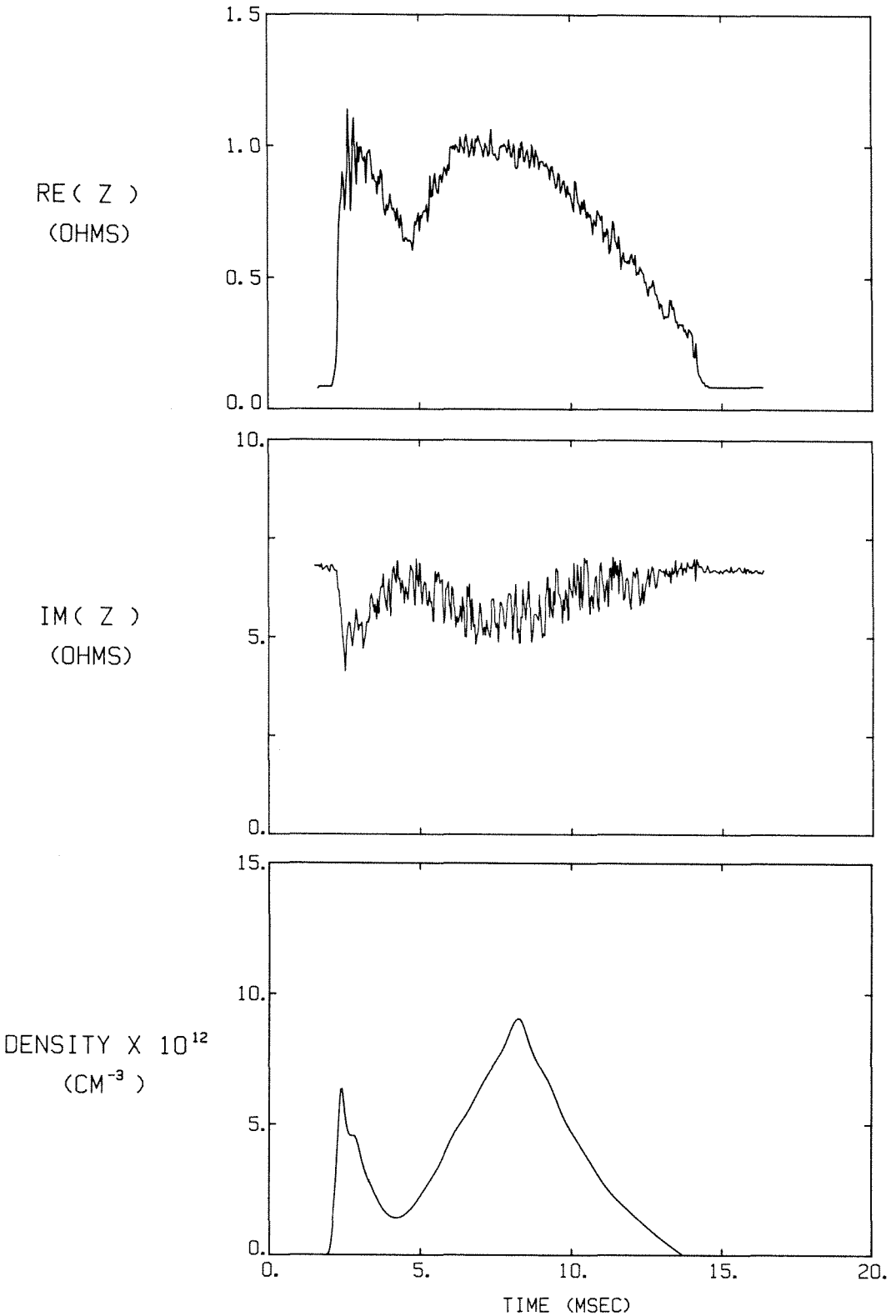

FIG. 6-9. Real and imaginary components of the bare loop antenna impedance, and the plasma density, for the tokamak shot shown in Figure 6-7. The analysis program has tranformed the impedance to the antenna-end of the feeder tube.

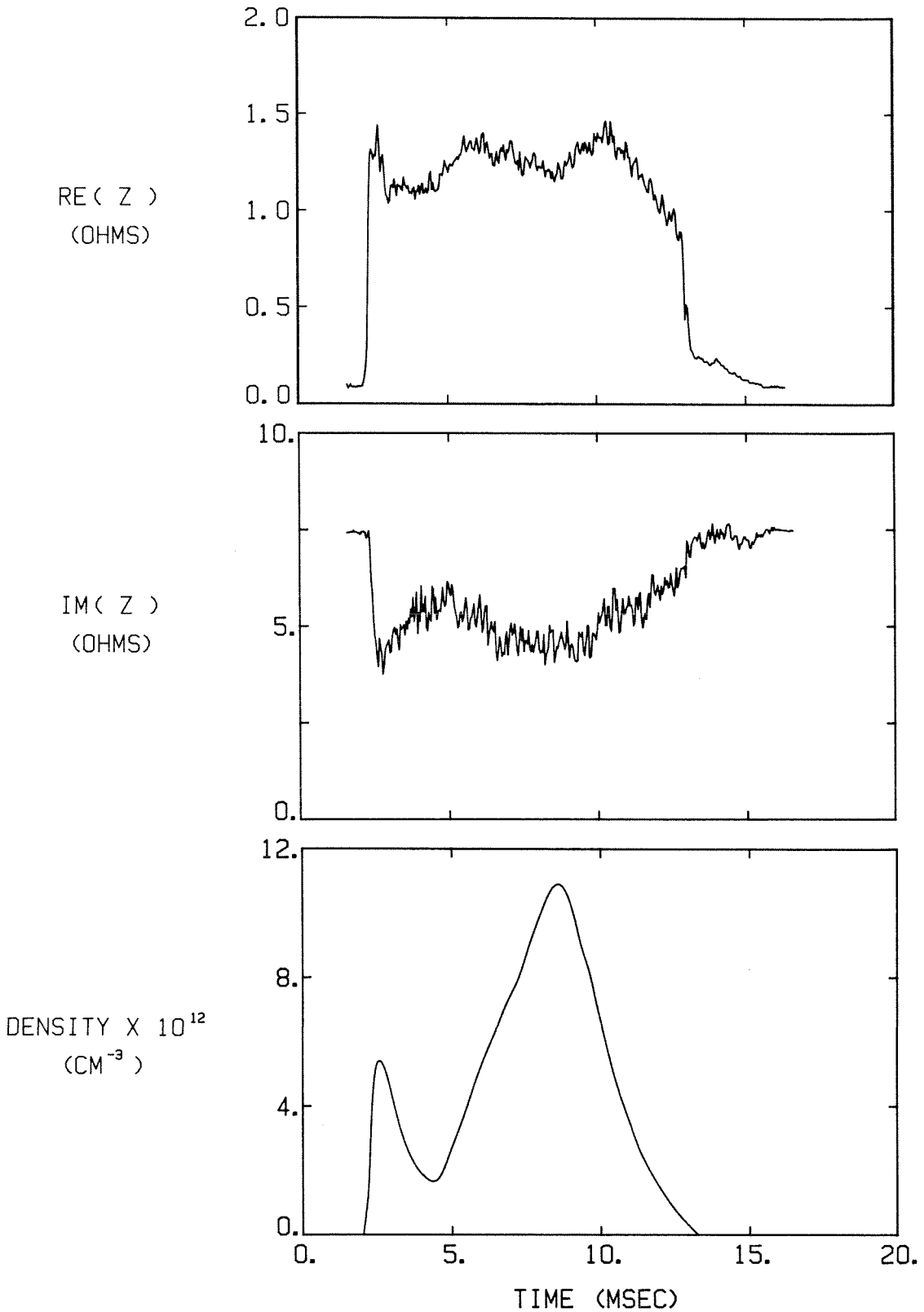

FIG. 6-10. Results of the impedance analysis for another tokamak shot where the leading edge of the loop was 5.0 cm past the tokamak wall; again $\omega/2\pi = 12$ MHz and $B_0 = 4.0$ kG. The increase in the real part and the decrease in the reactive part of the impedance are both larger than for the previous shot.

loading resistance, measured at the input to the antenna feeder tube, is then just $R_m \simeq |Z_m| \, \delta\varphi_m$. Hence, the raw phase signal in Figure 6-7, viewed upside-down, is approximately proportional to the antenna loading resistance.

The RF antenna current and voltage, transformed to the input of the antenna coupling structure using the computer analysis program, are shown in Figure 6-8; also shown is the net power dissipated by the antenna and plasma. Note that the transformed antenna current is somewhat larger than the raw current signal, and the transformed voltage is substantially smaller than the raw signal (because of the large inductance added to the antenna loop by the feeder tube).

The real and imaginary parts of the antenna impedance (transformed to the end of the antenna feeder tube), together with the plasma mean density, are plotted in Figure 6-9. Note that the real part of the impedance does in fact follow the form suggested by the raw phase signal. The background loading resistance (due to ohmic losses in the system) is $\sim$80 mΩ. The loading resistance increases with density but appears to saturate at $n \simeq 5-7 \times 10^{12}$ cm^{-3}, somewhat before the density reaches its peak. The peak of the loading resistance is nearly 1.0 Ω.

The imaginary (reactive) part of the antenna impedance is $\sim 7\,\Omega$ in the absence of plasma; this merely reflects the inductance of the antenna loop. The reactive part of the impedance decreases during the plasma shot, the decrease being roughly proportional to the increase in plasma density. The relative noise on the plot of Im(Z) in Figure 6-9 is large, i.e., comparable to the change in the mean of the signal. This is typical of the reactive impedance measurements, and the source of the noise appears to be related to plasma density fluctuations. As with fluctuations associated with Langmuir probe ion saturation current measurements, the relative level of the fluctuations in the imaginary part of the antenna impedance decreases as the antenna is moved

farther into the tokamak plasma.

The results of the impedance analysis for another shot where the front edge of the antenna loop was 5.0 cm past the tokamak wall are shown in Figure 6-10. Although the density evolution is comparable to that of the previous shot (Figure 6-7), the density seen by the antenna is now higher because it is further into the plasma; the plasma density profile is peaked in the center of the tokamak. The real part of the antenna loading impedance is now larger, reaching a peak of $\sim 1.4\ \Omega$. The evolution of the antenna resistance with density, however, shows a new feature. After the initiation of the gas puff at $t \simeq 4.5$ msec, the density begins an approximately linear increase. The antenna resistance also begins to increase, but reaches a peak at $t \simeq 6$ msec, corresponding to a mean plasma density of $n \simeq 5.5 \times 10^{12}\ \mathrm{cm}^{-3}$. After this point, the antenna resistance slowly *decreases* until it reaches a minimum of $\sim 1.2\ \Omega$ at a time corresponding to the density *maximum*. This behavior is approximately repeated during the density fall, with the antenna resistance first increasing and then decreasing as the density decays.

The imaginary part of the antenna impedance in the absence of the plasma is now $\sim 7.5\ \Omega$. The slight increase in this background reactance, as compared with the shot shown in Figure 6-9, is due to the loop being slightly less shielded by the tokamak port and walls. The antenna reactance again decreases with the appearance of plasma, the decrease still being roughly proportional to the plasma density increase. The magnitude of the change is somewhat larger for this shot, the reactance reaching a minimum of $\sim 4.5\ \Omega$ at a time corresponding to the density peak. Note that the relative fluctuation level of the antenna reactance is smaller than that of the previous shot.

The variation of the complex antenna impedance with different parameters is shown in Figures 6-11 to 6-15. In each case, the data points shown in the plots represent the mean of the experimental points accumulated from a

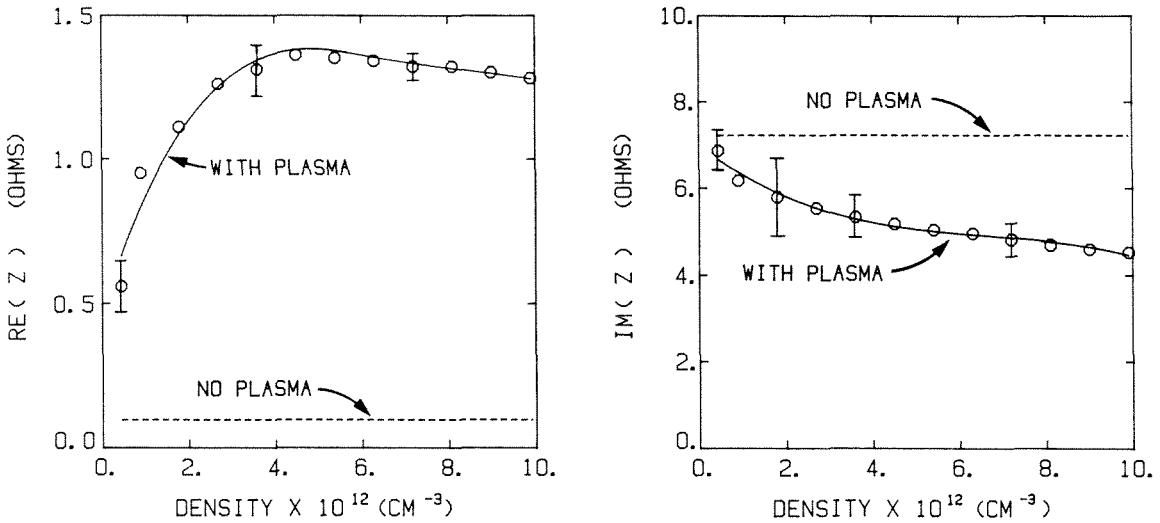

FIG. 6-11. Variation of the complex impedance of the bare loop antenna with plasma density, as measured with the microwave interferometer. $\omega/2\pi = 12$ MHz, $B_0 = 3.5$ kG, and the antenna was inserted 5.1 cm past the wall. The dashed line represents the background impedance measured without any plasma.

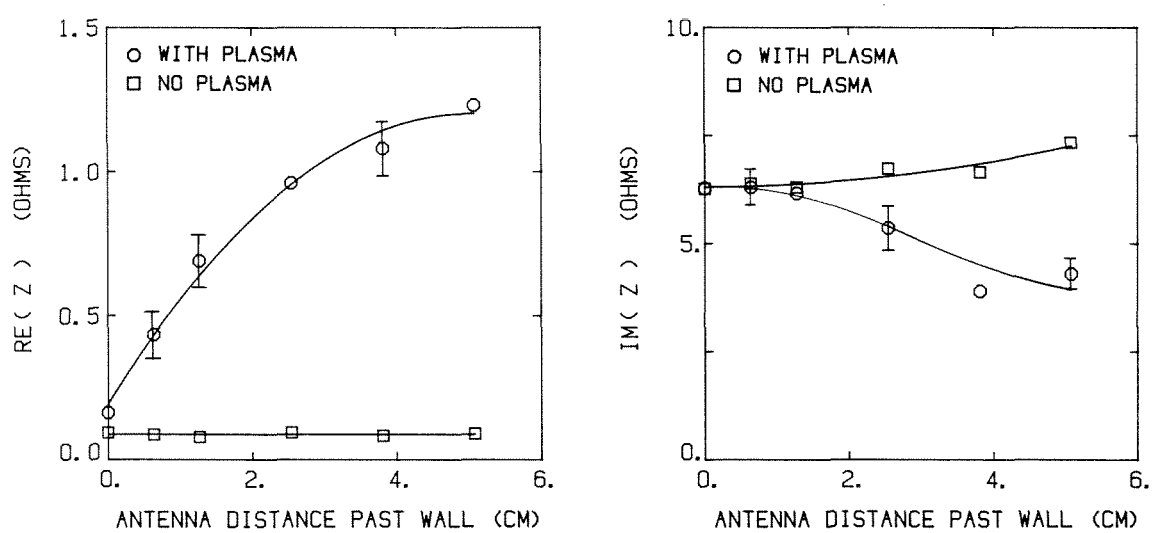

FIG. 6-12. Variation of the complex impedance of the bare loop antenna with insertion of the antenna past the tokamak wall. The horizontal axis is the distance from the front edge of the antenna loop to the tokamak wall. Here $\omega/2\pi = 12$ MHz, $B_0 = 4.0$ kG, and the data set was taken at a plasma density of $n \simeq 6.0 \times 10^{12}$ cm^{-3}. The background impedance (without plasma) is also plotted.

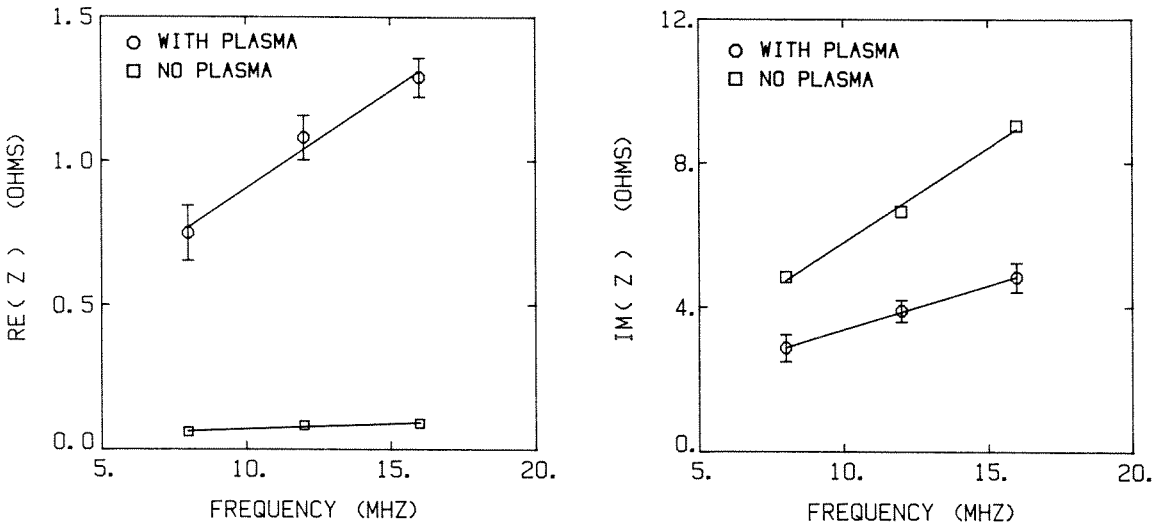

FIG. 6-13. Variation of the complex impedance of the bare loop antenna with excitation frequency. The front edge of the antenna was 3.8 cm past the tokamak wall, the data set was taken at a plasma density of $n \simeq 8.0 \times 10^{12}$ cm^{-3}, and $B_0 = 4.0$ kG. The background impedance (without plasma) is also plotted.

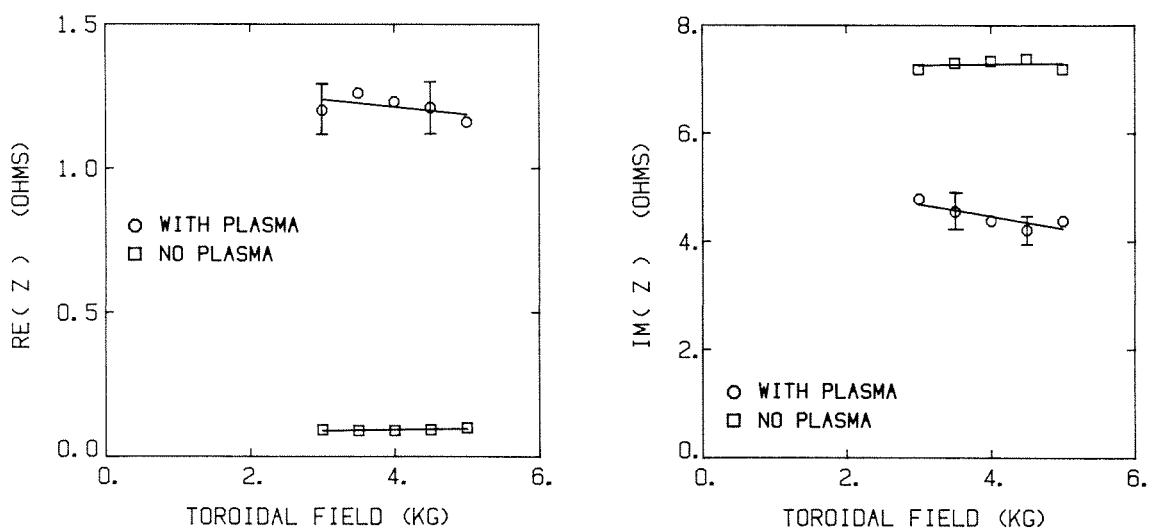

FIG. 6-14. Variation of the complex impedance of the bare loop antenna with toroidal magnetic field. The front edge of the antenna was 5.1 cm past the tokamak wall, the data set was taken at a plasma density of $n \simeq 8.1 \times 10^{12}$ cm^{-3}, and $\omega/2\pi = 12$ MHz. The background impedance (without plasma) is also plotted.

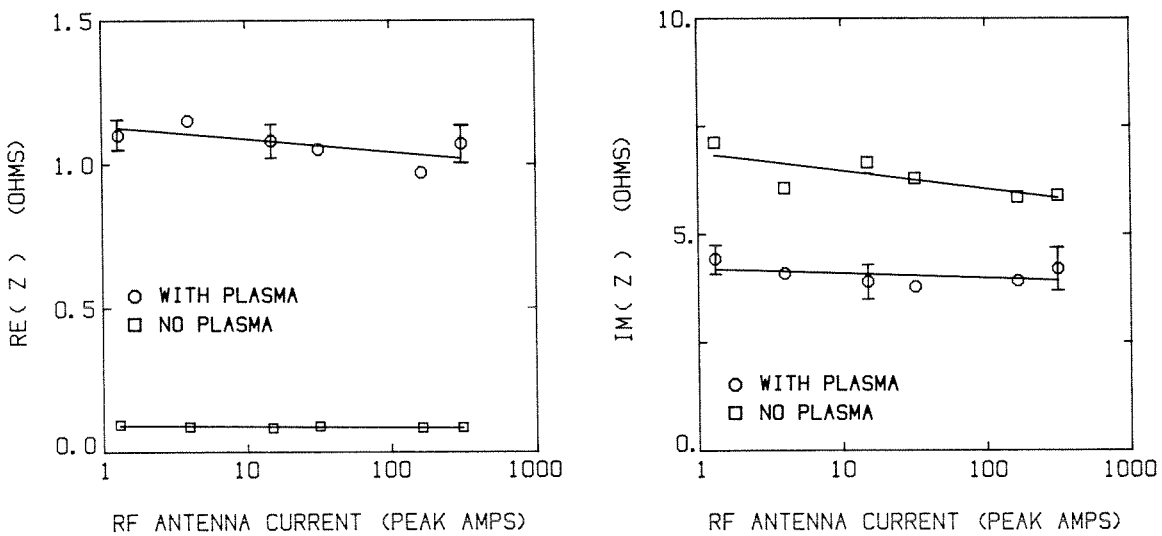

FIG. 6-15. Variation of the complex impedance of the bare loop antenna with RF excitation current. The front edge of the antenna was 3.8 cm past the tokamak wall, the data set was taken at a plasma density of $n \simeq 8.1 \times 10^{12}$ cm^{-3}, $\omega/2\pi = 12$ MHz, and $B_0 = 4.0$ kG. The background impedance (without plasma) is also plotted.

series of similar tokamak shots; vertical bars denoting the scatter of the data are also shown for some points. The lines marked "no plasma" are the results of the loading measurements when no plasma was present. In all cases, the impedance results plotted have been transformed to the antenna-end of the feeder tube, using the expressions derived in section 6.1.3.

The variation of the complex antenna impedance with mean plasma density (as measured with the microwave interferometer) is shown in Figure 6-11. For this experiment, the front edge of the antenna loop was 5.1 cm past the tokamak wall, the excitation frequency was 12 MHz, and the toroidal magnetic field was 3.5 kG. The variation of antenna impedance with plasma density was measured during the density rise following the initiation of the gas puff. The real part of the impedance initially rises as the density increases, then reaches a peak and decreases slightly. The imaginary part of the antenna impedance decreases monotonically as the plasma density rises.

Variation of the antenna impedance with insertion of the antenna past the tokamak wall is plotted in Figure 6-12. Here the excitation frequency was 12 MHz, the toroidal magnetic field was 4.0 kG, and the data set was taken during the density rise following the gas puff, when the density reached a value of $n \simeq 6.0 \times 10^{12}$ cm^{-3}. The real part of the antenna impedance increases monotonically as the antenna is inserted into the plasma, although its rate of rise decreases as it moves farther in. In the absence of plasma, the imaginary part of the impedance increases slightly as the antenna moves into the tokamak chamber due to decreased shielding of the antenna loop. In the presence of plasma, the imaginary part of the impedance decreases somewhat as the antenna is inserted.

The effect of the excitation frequency on the complex antenna impedance is shown in Figure 6-13. The front edge of the antenna loop was now 3.8 cm past the tokamak wall, the toroidal magnetic field on axis was 4.0 kG, and the

data set was taken at a plasma density of $n \simeq 8.0 \times 10^{12}$ cm^{-3}. Because of the extensive calibrations that had to be carried out at each new excitation frequency, in general only three different frequencies were used in these investigations: 8, 12, and 16 MHz. Even with only three points on the plots, some trends are evident. The real part of the antenna impedance clearly increases with frequency, changing by a factor of ~ 1.7 as the frequency doubles. The background resistance does not change significantly over this frequency range (it increases slightly, due to the skin effect). Both the antenna background reactance and the reactance in the presence of plasma increase as the frequency is raised, the increase being approximately linear within the accuracy of the measurement.

The variation of the antenna impedance with the toroidal magnetic field is displayed in Figure 6-14. For this experiment, the front edge of the antenna loop was 5.1 cm past the tokamak wall, the excitation frequency was 12 MHz, and the data set was taken at a mean plasma density of $n \simeq 8.1 \times 10^{12}$ cm^{-3}. Within the scatter of the data points, there is no significant change in either the real or imaginary parts of the impedance as the toroidal magnetic field varies from 3.0 to 5.0 kG.

Finally, the variation of the antenna impedance with the level of RF current exciting the antenna is shown in Figure 6-15. The excitation frequency for this experiment was 12 MHz, the toroidal magnetic field was 4.0 kG, and the data set was taken at a point during the plasma shots corresponding to a mean density of $n \simeq 8.1 \times 10^{12}$ cm^{-3}. The RF antenna current (transformed, as always, to the end of the antenna feeder tube) was varied from ~ 1 A (peak) to ~ 300 A (peak) using a variety of amplifiers ranging from the 10 watt ENI amplifier to the 100 kilowatt tetrode amplifier. Over this range of excitation current, no significant change is observed in either the real or imaginary part of the complex antenna impedance.

6.2.2 Bare Plate Antenna

Typical raw signals from a tokamak shot using the bare plate antenna are shown in Figure 6-16. For this shot, the excitation frequency was 12 MHz, the toroidal magnetic field on axis was 4.0 kG, and the leading edge of the copper antenna plate was 3.8 cm past the tokamak wall. Also, the antenna was oriented so that the plane of the surface of the plate was normal to the toroidal magnetic field lines. The antenna was operated with an RF bypass choke to ground (inside the impedance-matching box) so that the plate was at DC ground potential (or more accurately, at tokamak wall potential). The impedance-matching network was tuned for a fairly good match: the reflected wave voltage (from the directional coupler) is a small fraction of the forward wave voltage during most of the plasma shot. The phase signal now has a rather different form from that observed with the bare loop antenna. As the plasma density increases, the phase also increases, i.e., moves closer to 90 degrees. This means that the real part of the impedance *decreases* as the density rises, in contrast to the *increase* observed with the bare loop antenna.

Results from the computer analysis of the RF antenna current and voltage and the dissipated power (transformed to the end of the feeder tube) are shown in Figure 6-17. Again, the voltage at the input to the antenna coupling structure is substantially smaller than that measured by the voltage divider because of the inductance associated with the antenna feeder tube. The antenna current is largely unchanged by the transformation.

The complex impedance at the antenna-end of the feeder tube is plotted along with the density evolution for this shot in Figure 6-18. The real part of the impedance scales approximately as the reciprocal of the mean plasma density, and its peak value (at low density) is $\sim 5\ \Omega$. At low density, the imaginary part of the antenna impedance is quite noisy; these fluctuations diminish as the density increases during the shot. The mean value of the imaginary part of

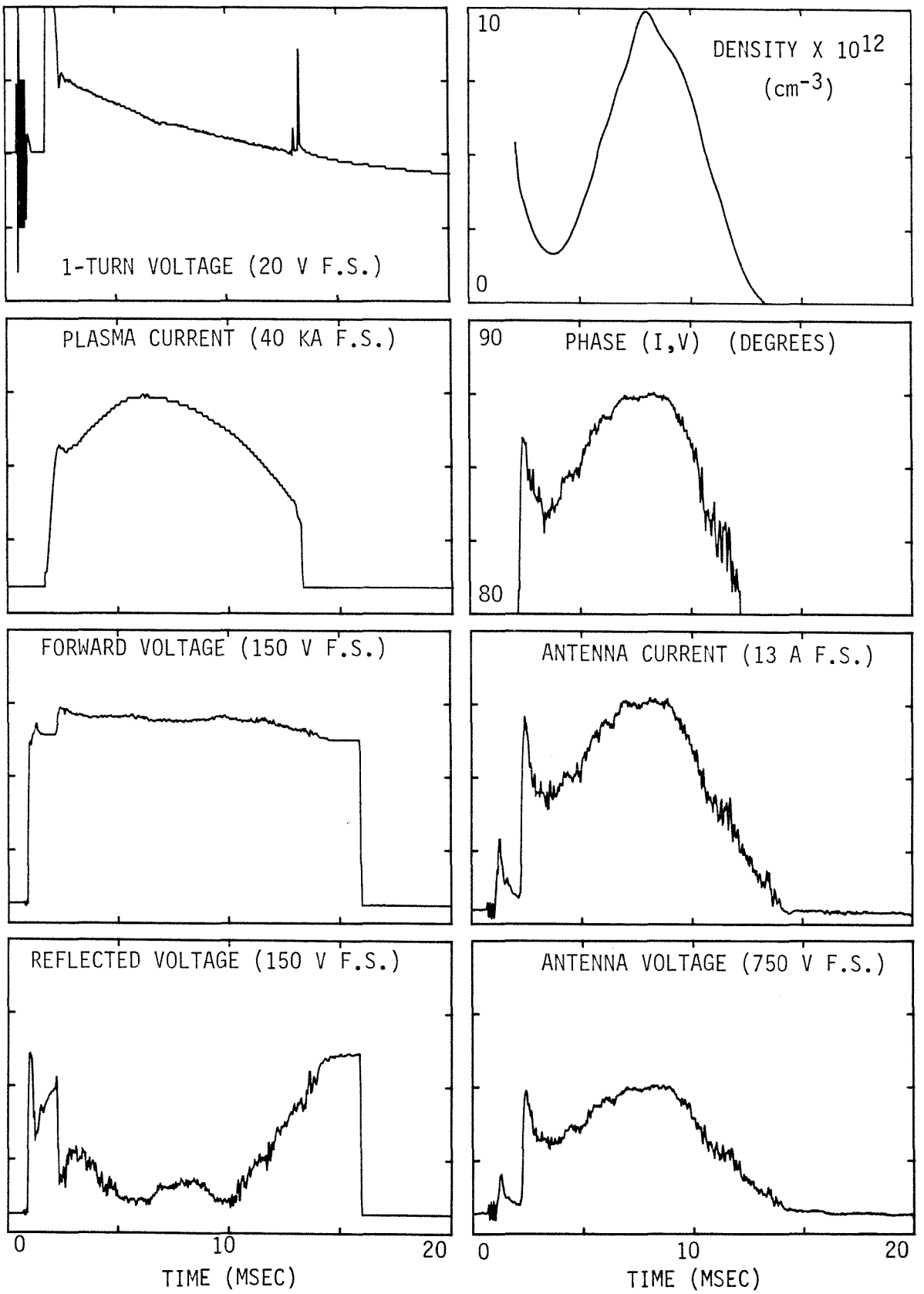

FIG. 6-16. Raw data from a tokamak shot using the bare plate antenna. Here $\omega/2\pi = 12$ MHz, $B_0 = 4.0$ kG, and the leading edge of the plate was 3.8 cm past the tokamak wall. The plane of the surface of the plate was normal to the toroidal field lines, and the antenna was at DC ground potential.

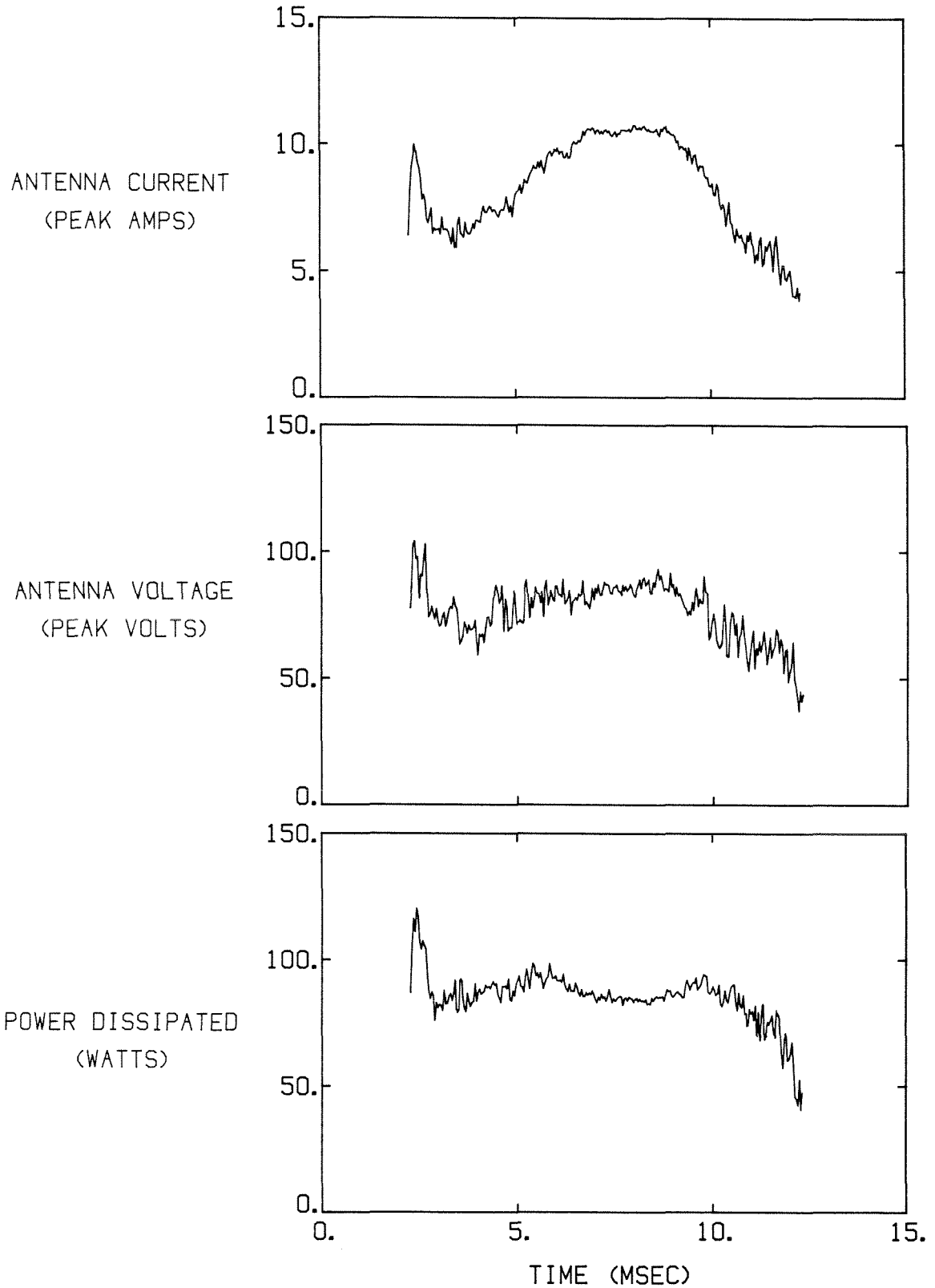

FIG. 6-17. Results for the antenna current, voltage, and dissipated power from the computer analysis of the raw data for the tokamak shot shown in Figure 7-16. Note that results can only be plotted for the period during the plasma shot when the raw phase signal is on-scale (i.e., $80° < \varphi_m < 90°$).

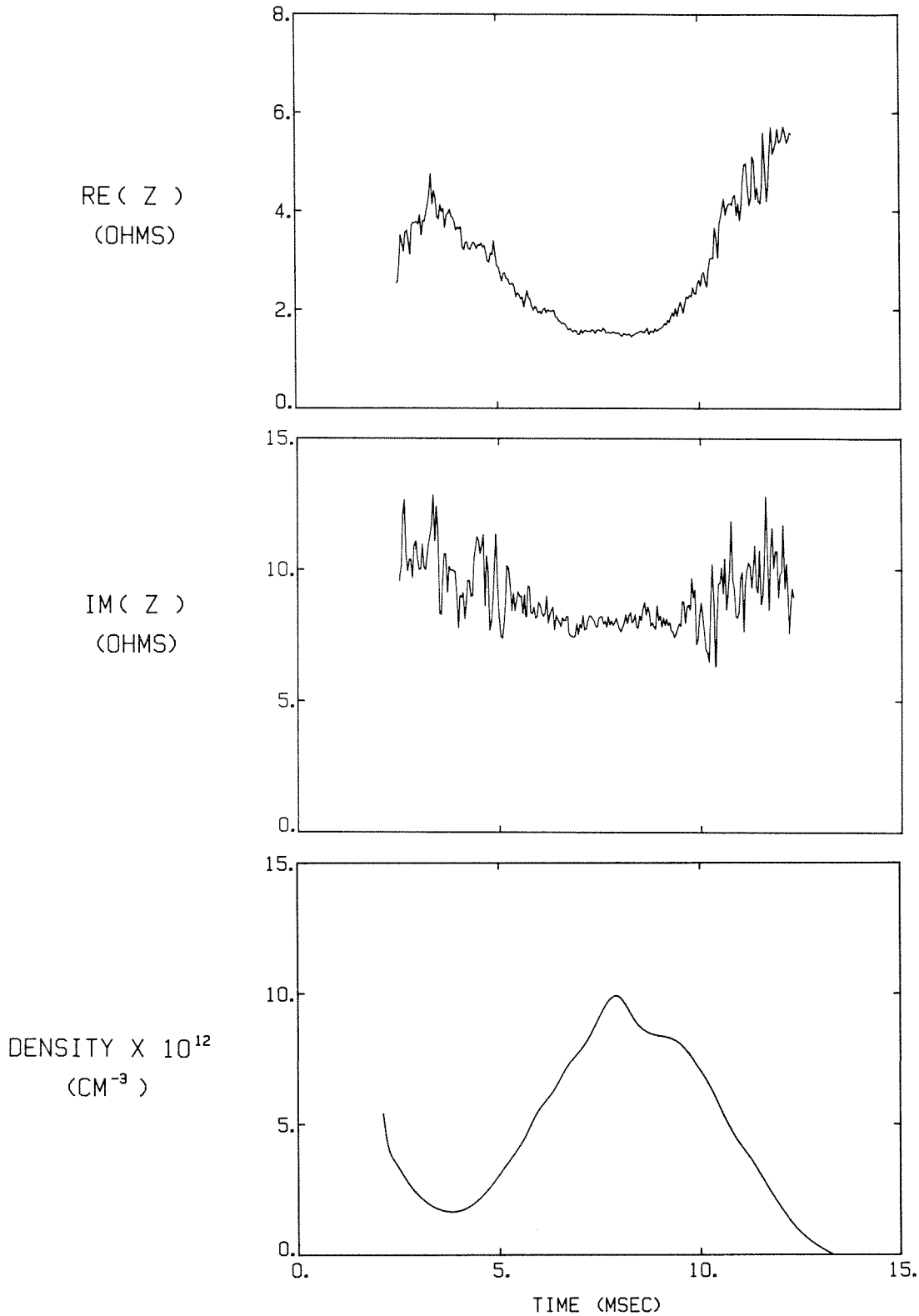

FIG. 6-18. Real and imaginary components of the bare plate antenna impedance, and the plasma density, for the tokamak shot shown in Figure 7-16. The analysis program has transformed the impedance to the antenna-end of the feeder tube.

the impedance decreases slightly as the density increases.

Several effects are noticed when the antenna is floated by removing the DC grounding choke. With no application of RF power and without changing any of the tokamak settings, if the antenna is changed from a grounded to a floating configuration, the plasma density and current evolution change markedly. Figure 6-19 shows the density and current evolution for two successive tokamak shots during an otherwise reproducible run: for the first shot, the antenna was grounded; for the second, it was floating. In both cases, the plane of the antenna plate was normal to the toroidal magnetic field lines, and the leading edge of the plate was 3.8 cm past the tokamak wall. The density during the second shot (antenna floating) reaches a peak value of only ~60% of that observed during the first shot (antenna grounded). The plasma current is somewhat larger for the shot with the antenna floating, and the discharge duration is considerably longer. Increasing the gas puff with the antenna floating can simulate conditions that occur with the antenna grounded, i.e., adding more gas externally with all other parameters fixed increases the peak density during the shot and decreases the discharge duration.

The origin of this effect is not understood. One explanation involves absorption of hydrogen by the copper plate. When the antenna is floating, there is no net current to it. Since the floating potential is, in these experiments, always negative with respect to the wall potential, a grounded antenna draws a net DC electron current (typically 20−30 amps). It is possible that surface heating due to this current, or some other effect of the increased electron flux striking the surface, causes absorbed hydrogen in the metal to evolve more rapidly during the discharge. This would then increase the density, for a constant gas puff, with respect to the case with the antenna floating.

The effects of grounding or floating the bare plate antenna, and of changing its orientation with respect to the toroidal magnetic field, on the plasma

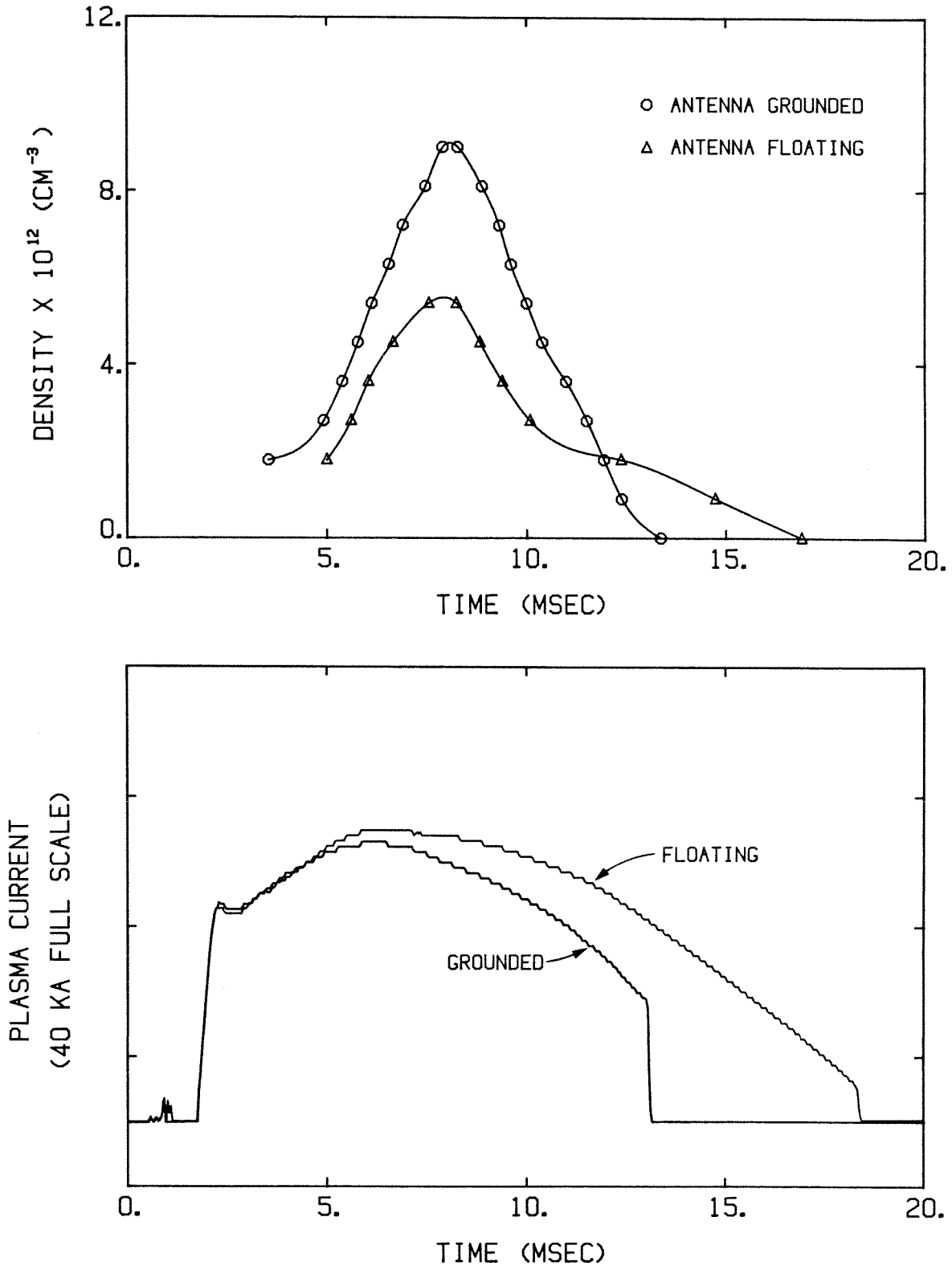

FIG. 6-19. Evolution of the plasma density (from the microwave interferometer signal) and plasma current for two successive tokamak shots: one with the bare plate antenna grounded, the other with the antenna floating. The leading edge of the plate was 3.8 cm past the tokamak wall and the plane of the surface of the plate was normal to the toroidal axis; also, $B_0 = 4.0$ kG.

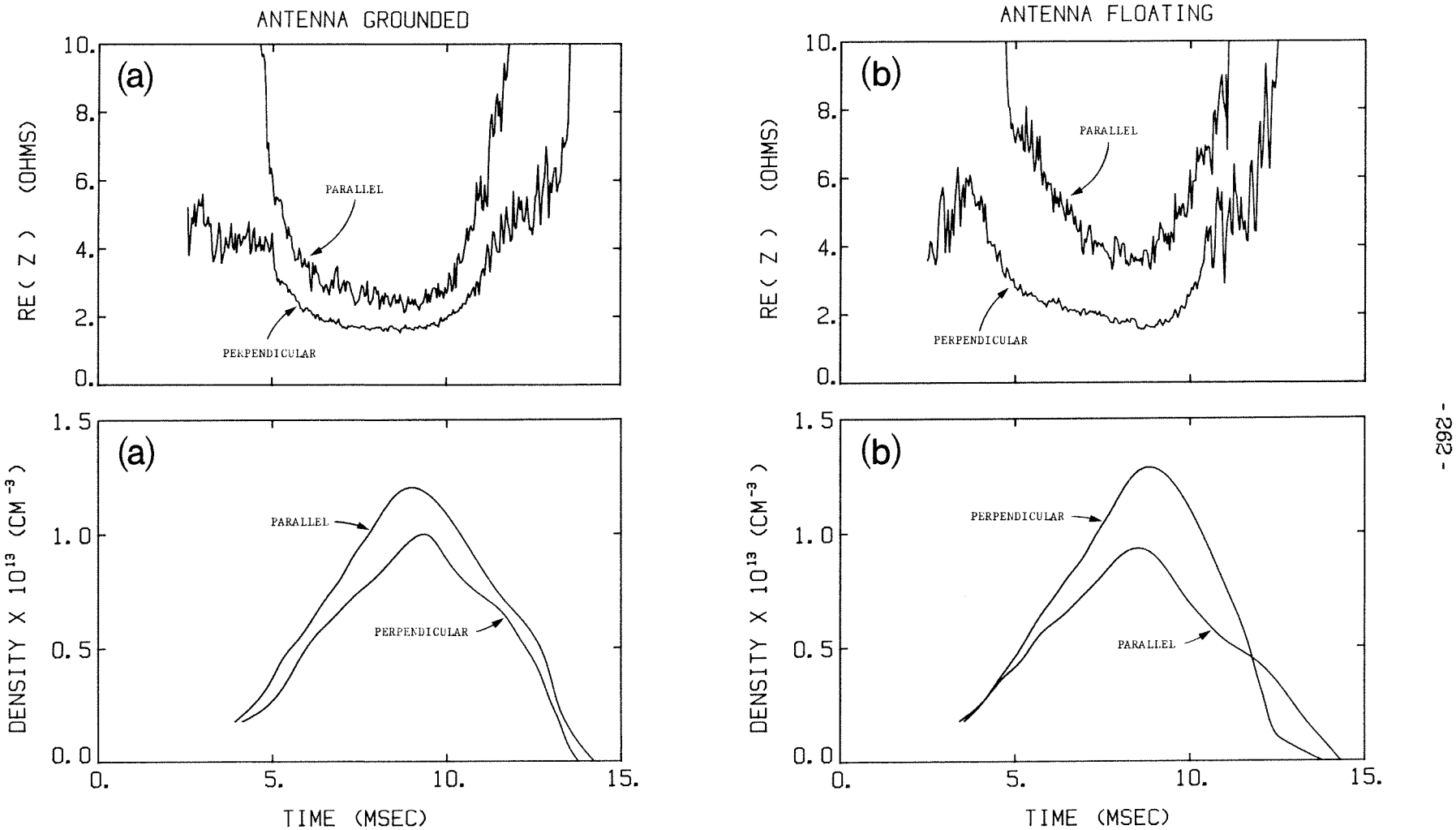

FIG. 6-20. Effects of grounding and floating the bare plate antenna on the real part of the antenna impedance and on the plasma density evolution, with the plane of the surface of the plate oriented perpendicular and parallel to the toroidal axis. Here $\omega/2\pi = 12$ MHz, $B_0 = 4.0$ kG, and the leading edge of the plate was 2.5 cm past the tokamak wall. a) Antenna grounded. b) Antenna floating.

density evolution and the real part of the antenna impedance are shown in Figures 6-20a and 6-20b; no significant effect was observed on the imaginary part of the impedance. These shots were taken with an excitation frequency of 12 MHz and a toroidal magnetic field on axis of 4.0 kG, and the leading edge of the antenna plate was 2.5 cm past the tokamak wall. In these figures, the curves labeled "perpendicular" refer to the antenna orientation where the toroidal magnetic field lines are normal to the plane of the surface of the antenna plate; the label "parallel" refers to the orientation where the toroidal field lines are parallel to the surface of the plate.

The antenna was at DC ground potential in Figure 6-20a; on the two successive shots shown, the orientation of the antenna was changed from perpendicular to parallel leaving all other parameters unchanged. Thus, for the grounded antenna, changing the orientation from perpendicular to parallel increases the plasma density at a given time and also increases the antenna resistance at a given density. When the antenna is floating (Figure 6-20b), changing the orientation from perpendicular to parallel decreases the density but still increases the antenna resistance, by a somewhat larger ratio than that observed for the grounded antenna. Note that the gas puff was increased between the shots with the antenna grounded and those with it floating in order to counteract the density decrease discussed previously. For all of the following plots of impedance data from the bare plate antenna (Figures 6-21 to 6-25), the orientation of the plate was perpendicular to the toroidal field direction.

The variation of the complex antenna impedance (transformed to the antenna end of the feeder tube) with plasma density is shown in Figure 6-21. The excitation frequency was 12 MHz, the toroidal field on axis was 4.0 kG, the leading edge of the antenna plate was 3.8 cm past the tokamak wall, and the antenna was at DC ground potential. The real part of the impedance decreases

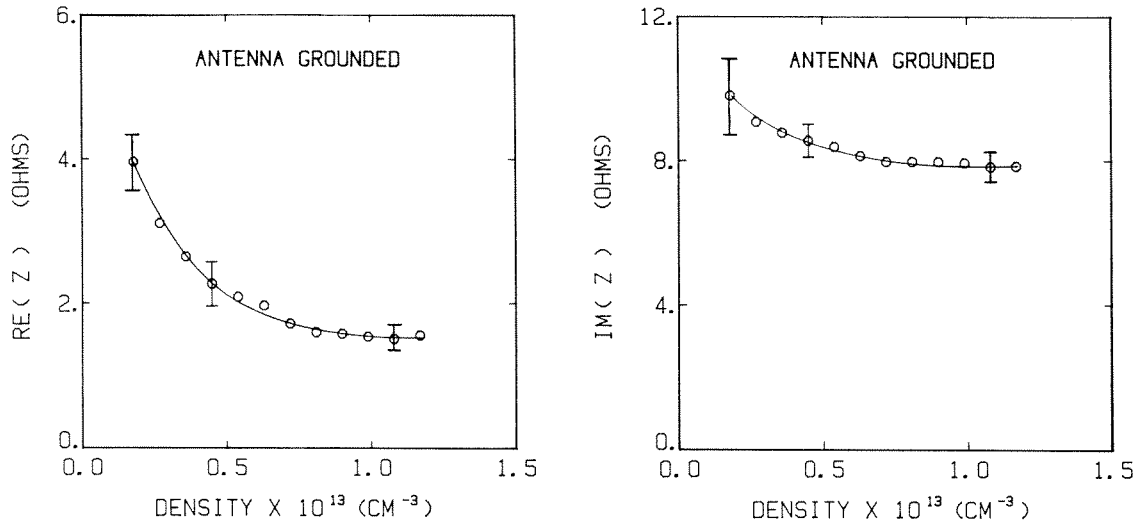

FIG. 6-21. Variation of the complex impedance of the bare plate antenna with plasma density. Here $\omega/2\pi = 12$ MHz, $B_0 = 4.0$ kG, the leading edge of the plate was 3.8 cm past the tokamak wall, and the antenna was at DC ground potential.

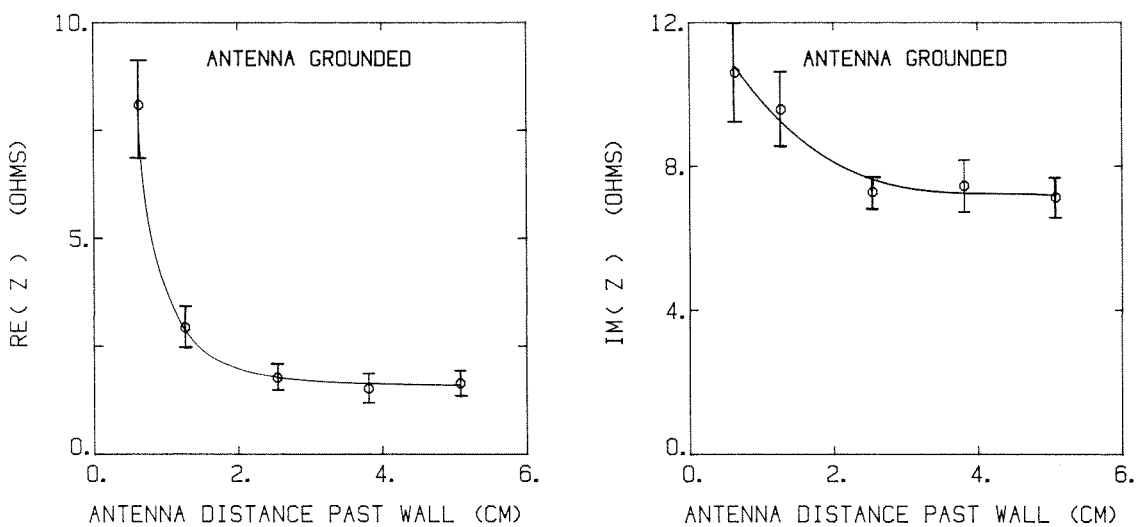

FIG. 6-22. Variation of the complex impedance of the bare plate antenna with insertion of the antenna past the tokamak wall. The horizontal axis is the distance between the leading edge of the plate and the tokamak wall. Here $\omega/2\pi = 12$ MHz, $B_0 = 4.0$ kG, and the data set was taken at a plasma density of $n \simeq 8.1 \times 10^{12}$ cm^{-3}; also, the antenna was at DC ground potential.

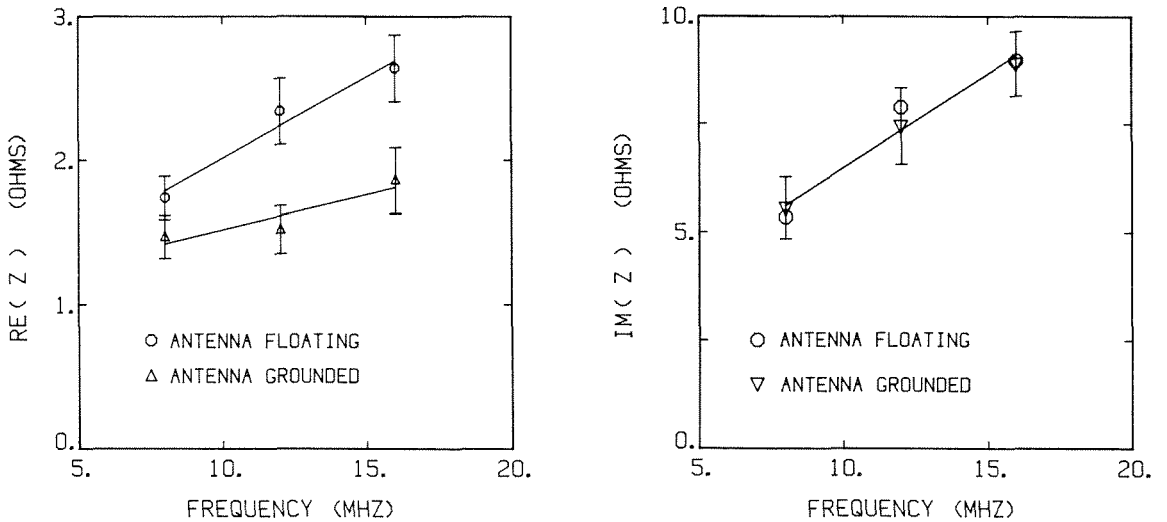

FIG. 6-23. Variation of the complex impedance of the bare plate antenna with excitation frequency, for both grounded and floating configurations. The leading edge of the plate was 3.8 cm past the wall, the data set was taken at a plasma density of $n \simeq 8.1 \times 10^{12}$ cm^{-3}, and $B_0 = 4.0$ kG.

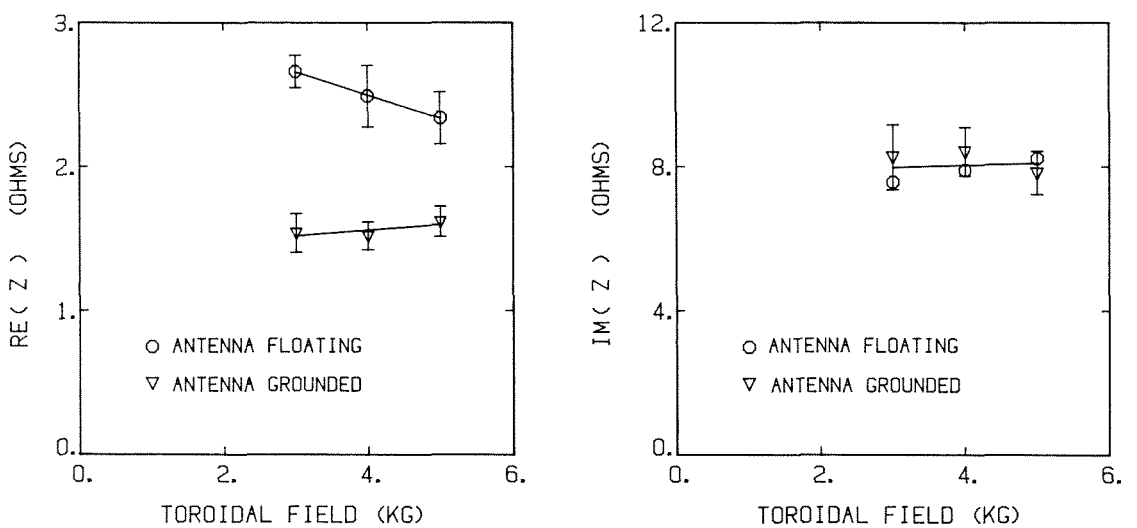

FIG. 6-24. Variation of the complex impedance of the bare plate antenna with toroidal magnetic field, for both grounded and floating configurations. The leading edge of the plate was 3.8 cm past the wall, the data set was taken at a plasma density of $n \simeq 8.1 \times 10^{12}$ cm^{-3}, and $\omega/2\pi = 12$ MHz.

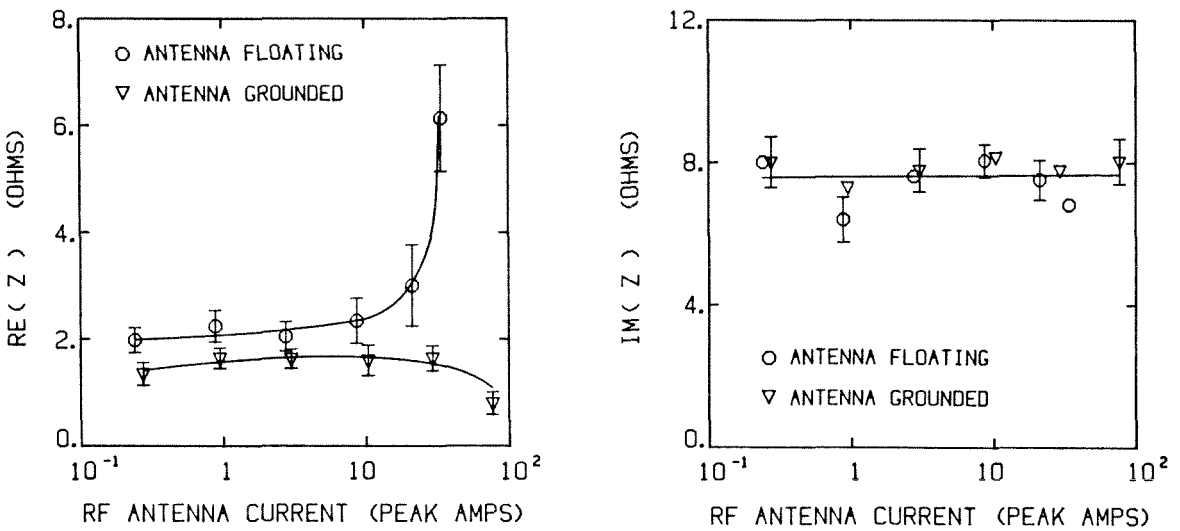

FIG. 6-25. Variation of the complex impedance of the bare plate antenna with RF excitation current, for both grounded and floating configurations. The leading edge of the plate was 3.8 cm past the tokamak wall, and the data set was taken at a plasma density of $n \simeq 8.1 \times 10^{12}\ \mathrm{cm}^{-3}$; also $\omega/2\pi = 12$ MHz and $B_0 = 4.0$ kG. Note that the measured antenna current has, as in all of the plots, been transformed to the current at the antenna-end of the feeder tube.

substantially and monotonically as the plasma density increases; the imaginary part of the impedance exhibits a small decrease.

Variation of the antenna impedance with insertion of the antenna past the tokamak wall is plotted in Figure 6-22. The excitation frequency was 12 MHz, the toroidal field was 4.0 kG, and the data was taken at a mean plasma density of $n \simeq 8.1 \times 10^{12}$ cm^{-3}; also, the antenna was at DC ground potential. The real part of the antenna impedance decreases abruptly as the antenna enters the plasma; the rate of this fall decreases as the antenna moves farther into the tokamak. The reactive part of the impedance also decreases as the antenna is inserted, but the relative decrease is much smaller.

The dependence of the complex impedance of the bare plate antenna on excitation frequency is shown in Figure 6-23. The toroidal magnetic field was 4.0 kG, the leading edge of the antenna plate was 3.8 cm past the tokamak wall, and the data set was taken at a plasma density of $n \simeq 8.1 \times 10^{12}$ cm^{-3}. As with the bare loop antenna, both the real and imaginary parts of the antenna impedance increase as the frequency is raised. The results are presented for the antenna both floating and grounded. The imaginary part of the impedance for the two cases is almost identical; however, the real part of the impedance, and the rate of rise with frequency, is greater for the floating antenna than for the grounded antenna.

Variation of the complex antenna impedance with toroidal magnetic field is shown in Figure 6-24. Here the excitation frequency was 12 MHz, the leading edge of the antenna plate was 3.8 cm past the tokamak wall, and the plasma density was $n \simeq 8.1 \times 10^{12}$ cm^{-3}. Again, the results are presented both for floating and grounded antennas. The real part of the impedance for the floating antenna shows a small decrease as the toroidal magnetic field is raised from 3.0 to 5.0 kG; none of the other plots show significant changes within the limits of the measurement.

Finally, the change in antenna impedance with antenna excitation current is presented in Figure 6-25, for both floating and grounded antennas. The excitation frequency for this experiment was again 12 MHz, the toroidal magnetic field was 4.0 kG, the antenna insertion was 3.8 cm, and the data set was taken at a plasma density of $n = 8.1 \times 10^{12}\ \mathrm{cm}^{-3}$. The imaginary part of the impedance for both the floating and grounded antennas shows no significant change with excitation current; the real part of the impedance of the grounded antenna also shows little change. The real part of the floating antenna impedance, however, shows a dramatic increase as the current increases past ~ 10 amps. The maximum current that was driven with the floating antenna was ~ 30 amps; as the current increased further, the antenna resistance increased beyond the range over which the impedance matching network was useful.

6.2.3 "T" Antenna

Raw signals from a typical tokamak shot using the "T" antenna are shown in Figure 6-26. For this shot, the excitation frequency was 12 MHz, the toroidal magnetic field was 4.0 kG, and the leading edge of the "T" was 3.8 cm past the tokamak wall. The general features of the RF signals are similar to those of the bare plate antenna (Figure 6-16). In particular, note that the phase signal has the same general form with respect to the density evolution. In all experiments using the "T" antenna, the cross-bar of the "T" was oriented vertically, i.e., with its axis perpendicular to the direction of the toroidal field; also, the "T" was grounded via an RF choke in the impedance-matching box.

Results of the computer analysis of this shot for the antenna current and voltage and the dissipated power are shown in Figure 6-27. The large increase in power dissipation during the density rise is due to the increase in antenna current as the antenna impedance becomes better matched to the generator.

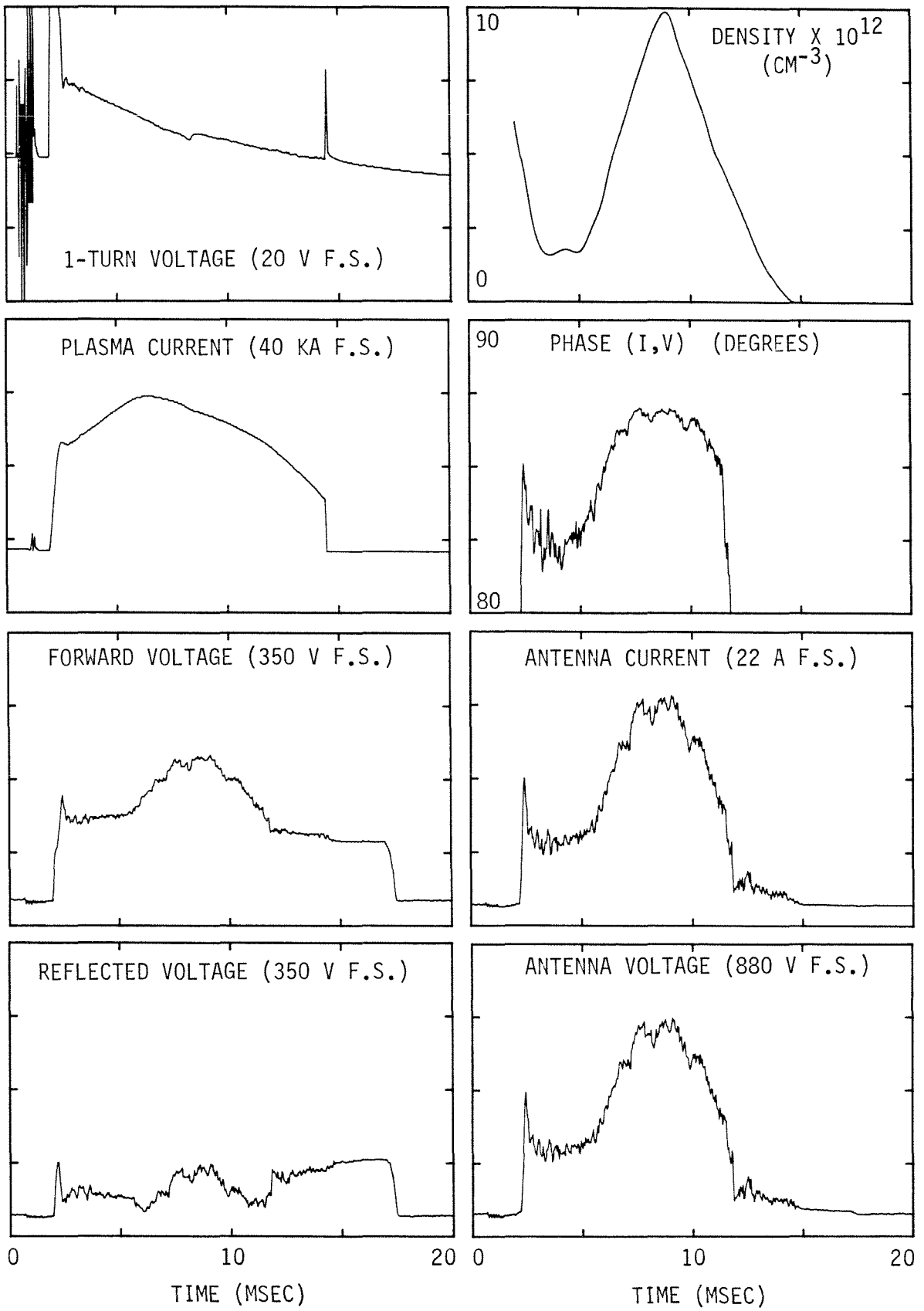

FIG. 6-26. Raw data from a tokamak shot using the "T" antenna. Here $\omega/2\pi = 12$ MHz, $B_0 = 4.0$ kG, and the front edge of the cross-bar of the "T" was 3.8 cm past the wall. The cross-bar was oriented perpendicular to the toroidal field direction, and the antenna was at DC ground potential.

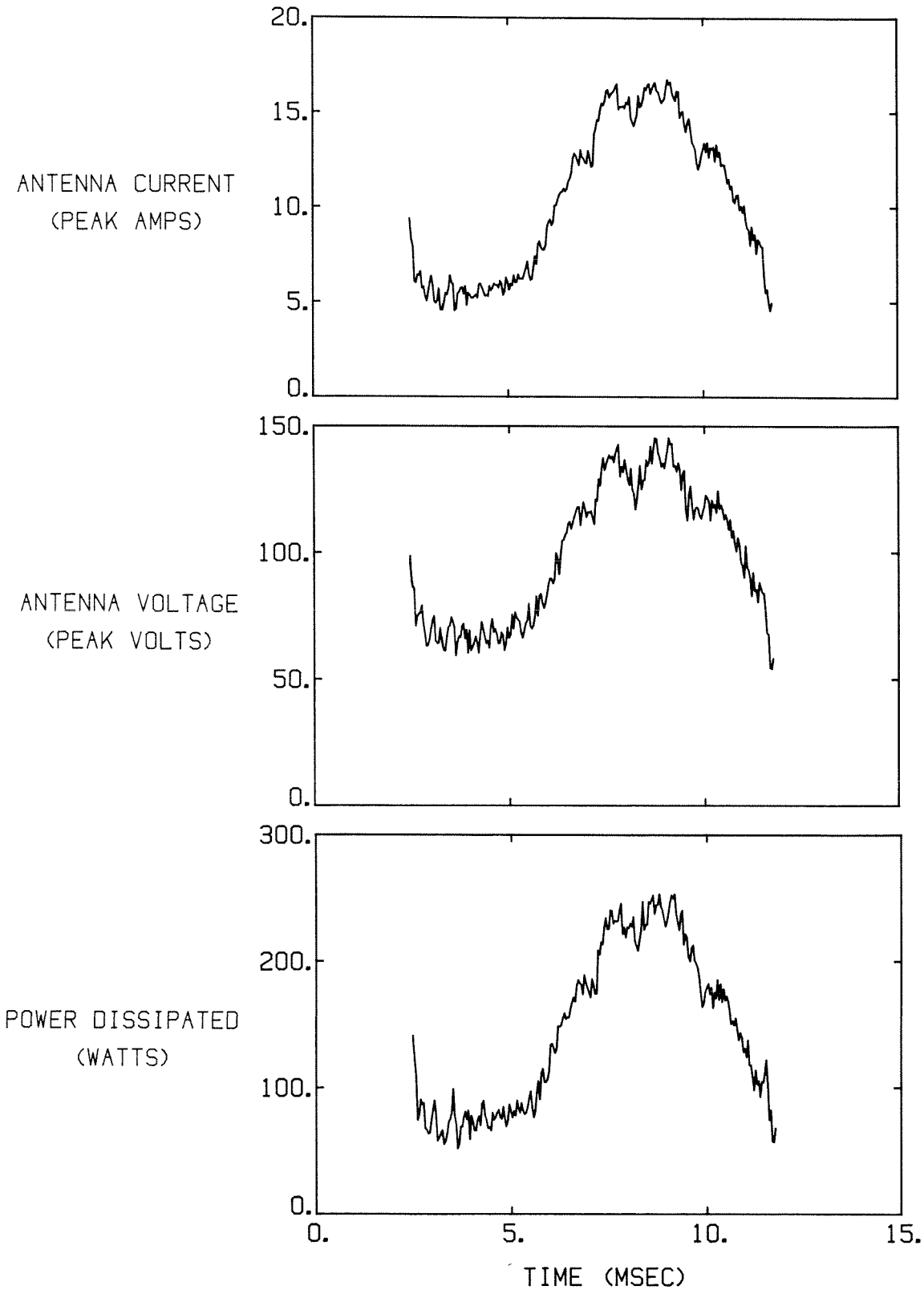

FIG. 6-27. Results for the antenna current, voltage, and dissipated power from the computer analysis of the raw data for the tokamak shot shown in Figure 6-26. The results are plotted for the period during the plasma shot when the raw phase signal is on-scale (i.e., $80° < \varphi_m < 90°$).

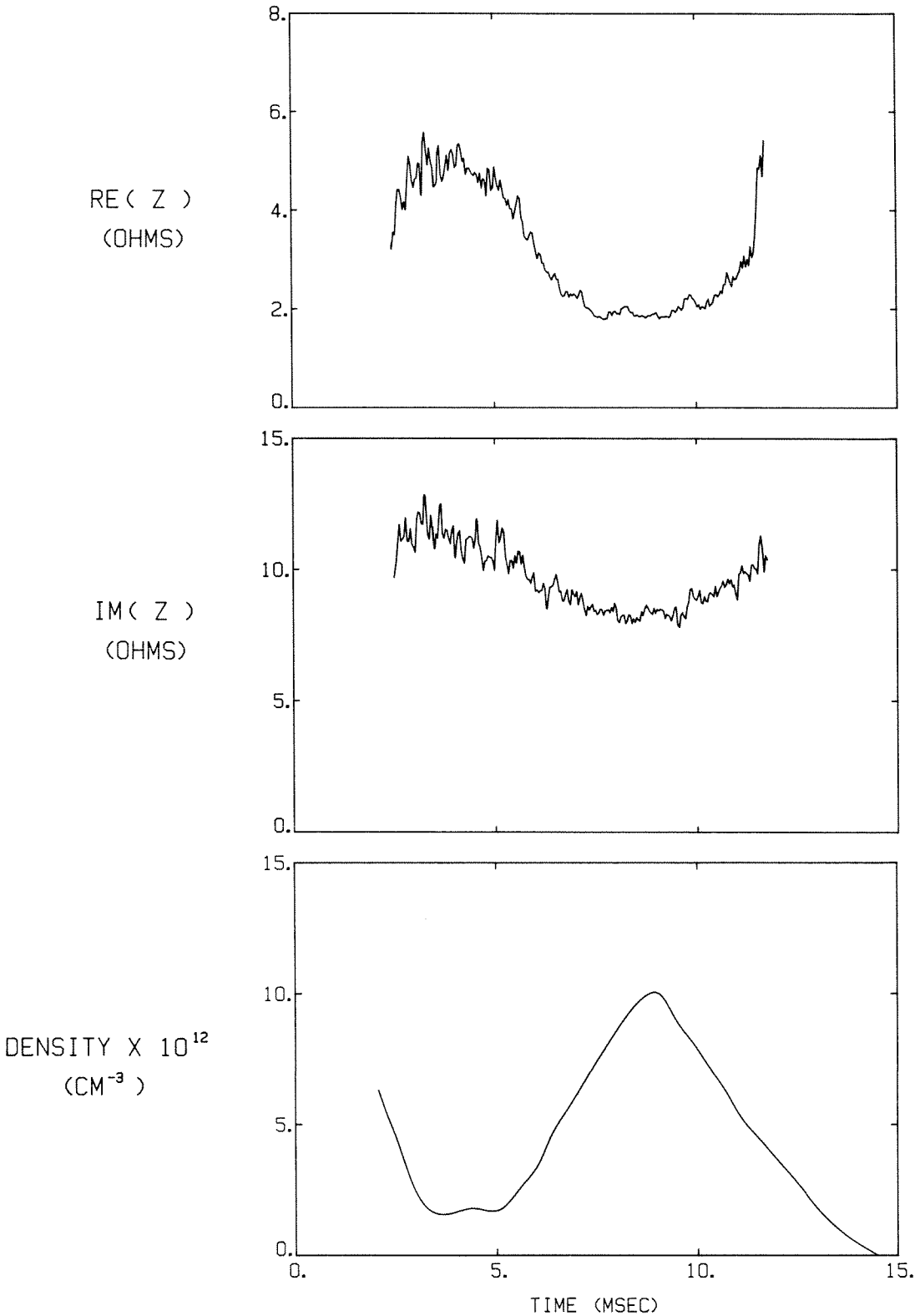

FIG. 6-28. Real and imaginary components of the "T" antenna impedance, and the plasma density, for the tokamak shot shown in Figure 6-26. The analysis program has transformed the impedance to the antenna-end of the feeder tube.

Note that the power incident on the matching network, related to the square of the forward voltage signal shown in Figure 6-26, also increases during the density rise. The power outputs of most of the RF generators were dependent on the load impedance which they saw and thus changed in a complicated fashion as the antenna load impedance changed during the plasma shot; only the ENI broadband power amplifiers were capable of delivering a constant incident (or forward) power to an arbitrary load.

The complex impedance analysis for this characteristic shot is shown in Figure 6-28; the results are quite similar to those shown for the bare plate antenna (Figure 6-17). Again, the real part of the impedance decreases substantially as the density rises; the relative decrease of the imaginary part of the impedance is somewhat smaller.

The variation of the antenna impedance with plasma mean density is shown in Figure 6-29. For this experiment, the excitation frequency was 8.5 MHz, the toroidal magnetic field was 3.6 kG, and the front edge of the "T" was 3.8 cm past the tokamak wall. Note that both the magnitude and the functional form of the real part of the impedance are quite similar to that found for the bare plate antenna (Figure 6-18), with the antenna resistance varying approximately as the reciprocal of the plasma density. The imaginary part of the impedance also decreases somewhat as the density increases; the magnitude of the reactance, for a given plasma density, is slightly smaller than that found for the bare plate antenna. It should be recalled, however, that the data set for the bare plate antenna was taken at a frequency of 12 MHz and a toroidal field of 4.0 kG.

The variation of antenna impedance with the insertion of the antenna past the tokamak wall is shown in Figure 6-30. For these data points, the excitation frequency was 12 MHz, the toroidal field was 4.0 kG, and the plasma density was $n \simeq 8.1 \times 10^{12}$ cm^{-3}. As with the bare plate antenna, the real part of

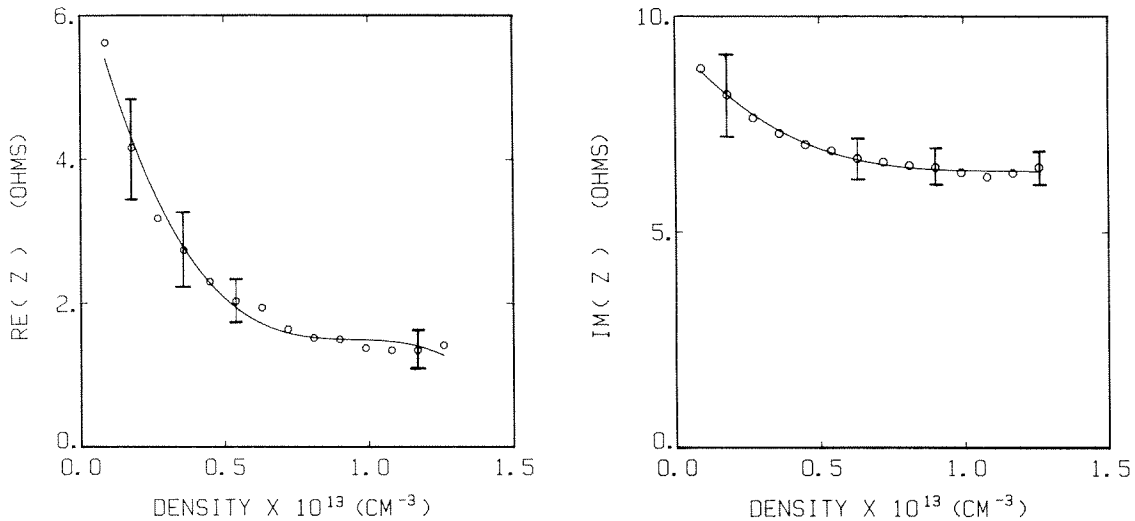

FIG. 6-29. Variation of the complex impedance of the "T" antenna with plasma density. Here $\omega/2\pi = 8.5$ MHz, $B_0 = 3.6$ kG, and the front edge of the cross-bar of the "T" was 3.8 cm past the tokamak wall.

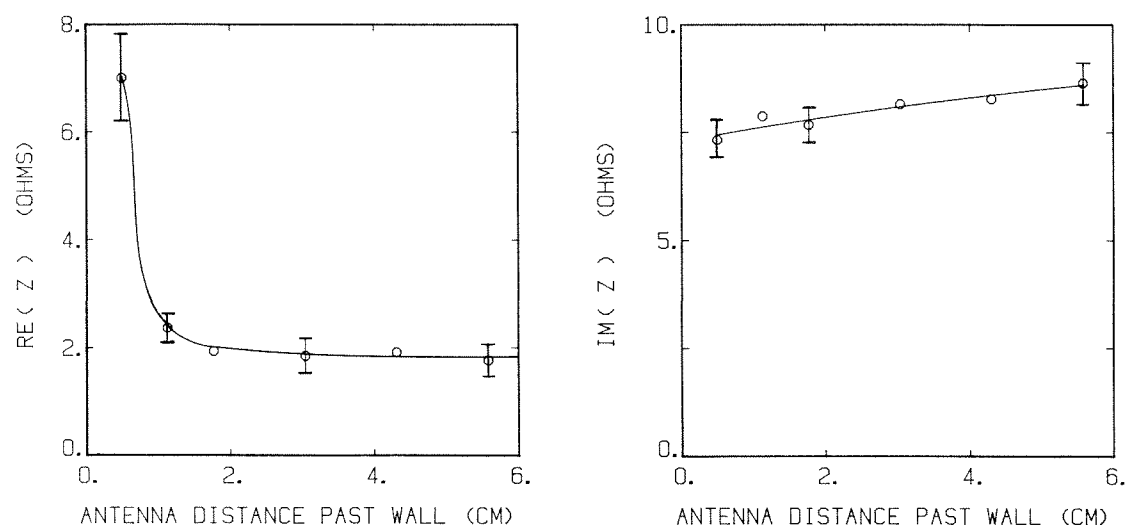

FIG. 6-30. Variation of the complex impedance of the "T" antenna with insertion of the "T" past the tokamak wall. The horizontal axis is the distance between the leading edge of the cross-bar of the "T" and the tokamak wall. Here $\omega/2\pi = 12$ MHz, $B_0 = 4.0$ kG, and the data set was taken at a plasma density of $n \simeq 8.1 \times 10^{12}$ cm^{-3}.

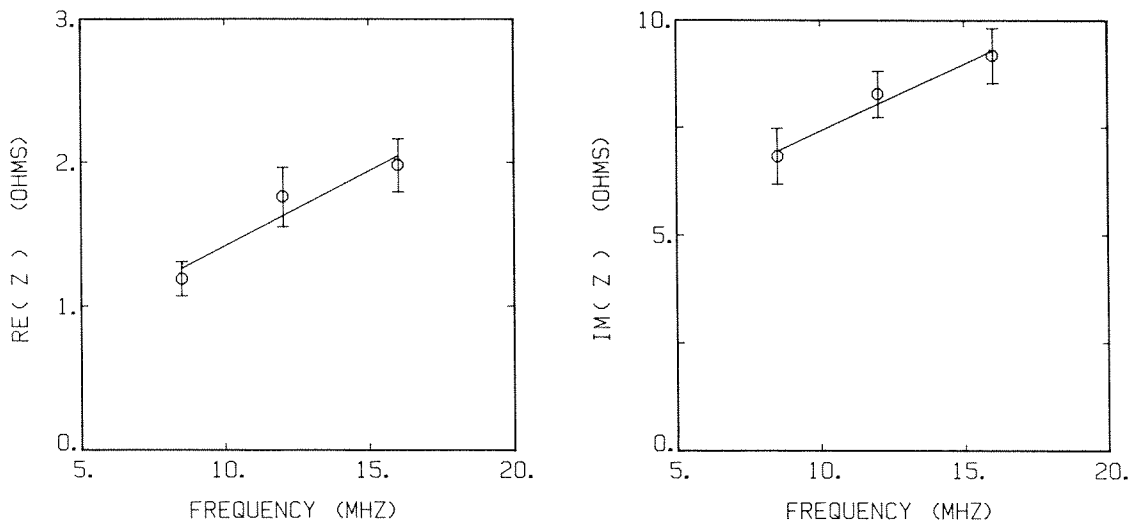

FIG. 6-31. Variation of the complex impedance of the "T" antenna with excitation frequency. The leading edge of the "T" was 3.8 cm past the tokamak wall, the data set was taken at a plasma density of $n \simeq 8.1 \times 10^{12}\ \mathrm{cm}^{-3}$, and $B_0 = 4.0$ kG.

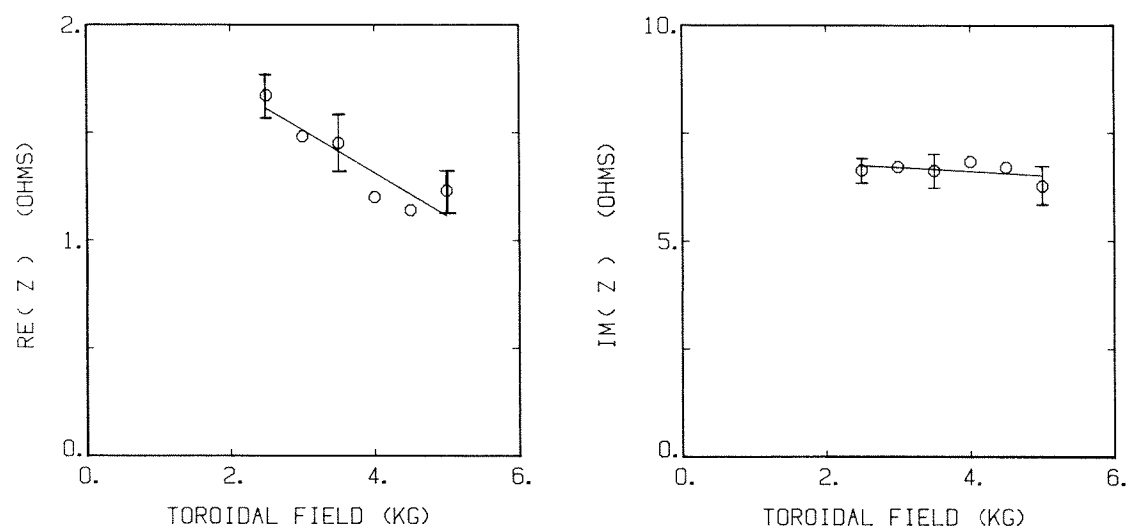

FIG. 6-32. Variation of the complex impedance of the "T" antenna with toroidal magnetic field. The leading edge of the "T" was 3.8 cm past the tokamak wall, the data set was taken at a plasma density of $n \simeq 8.1 \times 10^{12}\mathrm{cm}^{-3}$, and the excitation frequency was $\omega/2\pi = 8.5$ MHz.

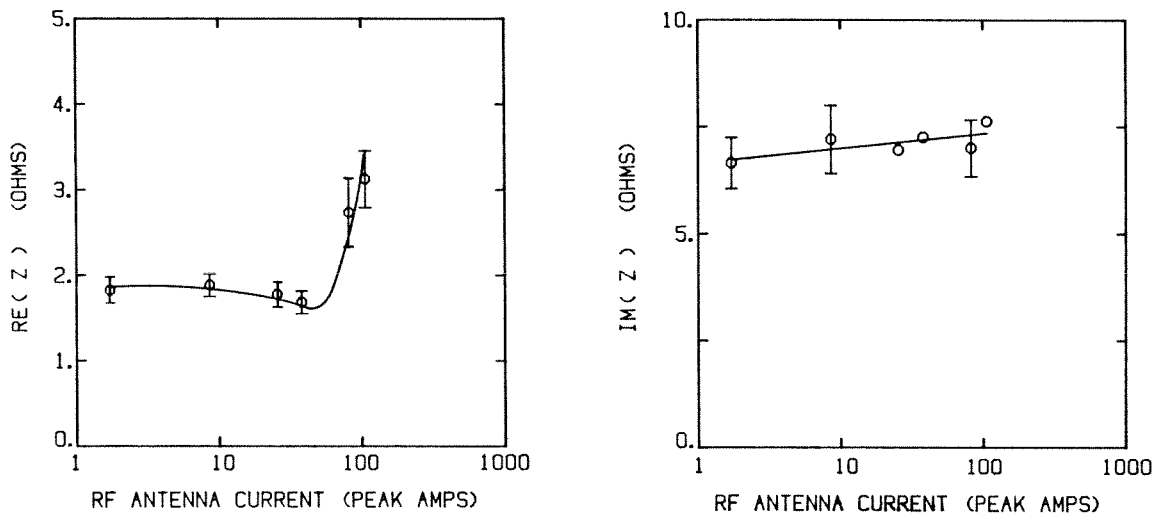

FIG. 6-33. Variation of the complex impedance of the "T" antenna with antenna excitation current. Here $\omega/2\pi = 12$ MHz, $B_0 = 4.0$ kG, the leading edge of the "T" was 3.8 cm past the tokamak wall, and the data set was taken at a plasma density of $n \simeq 8.1 \times 10^{12}$ cm^{-3}.

the impedance decreases abruptly as the antenna leading edge moves past the tokamak wall, but does not decrease below ~2 Ω. The dependence of the imaginary part of the impedance on the antenna insertion is somewhat different from that found for the bare plate antenna. For the "T" antenna, the reactive part of the impedance increases only slightly (from ~7.3 Ω to ~8.6 Ω) as the antenna leading edge is inserted from 0.5 to 5.6 cm past the wall. In contrast, the reactive part of the impedance of the bare plate antenna decreases by ~30% over a similar range of antenna insertion.

The effect of excitation frequency on the grounded "T" antenna is shown in Figure 6-31. Here, again, the toroidal field was 4.0 kG, the leading edge of the "T" was 3.8 cm past the tokamak wall, and the data was taken at a plasma density of $n \simeq 8.1 \times 10^{12}$ cm^{-3}. The general trend is again evident: both the real and imaginary parts of the antenna impedance increase as the frequency increases.

The variation of antenna impedance with toroidal magnetic field is plotted in Figure 6-32. The excitation frequency was 8.5 MHz, the leading edge of the antenna was 3.8 cm past the tokamak wall, and the data set was taken at a plasma density of $n \simeq 8.1 \times 10^{12}$ cm^{-3}. There is virtually no change in the imaginary part of the antenna impedance as the toroidal field is varied from 2.5 to 5.0 kG; the real part of the impedance, however, decreases by about 30% over the same range.

Lastly, the variation of antenna impedance with antenna excitation current is shown in Figure 6-33. For this experiment, the excitation frequency was 12 Mhz, the toroidal field was 4.0 kG, the antenna insertion was 3.8 cm, and the plasma density was again $n \simeq 8.1 \times 10^{12}$ cm^{-3}. No significant variation of the imaginary part of the impedance is observed as the excitation current is varied from ~ 2 A to ~100 A; the real part of the impedance increases slightly, but the increase is not much greater than the scatter in the data.

6.2.4 Ceramic-Insulated Loop Antenna

Raw signals from a typical tokamak shot utilizing the ceramic-insulated loop antenna are shown in Figure 6-34. The excitation frequency for this shot was 16 MHz, the toroidal magnetic field on axis was 4.0 kG, and the front edge of the Macor box surrounding the loop was 2.5 cm past the tokamak wall. The phase signal has a rather different form from those discussed previously. The overall phase change during the plasma discharge is small: the full-scale range of the phase plot in the figure is 2.0 degrees. As the density rises, a series of sharp spikes in the phase signal (in the direction of decreasing phase) are encountered. From the discussion of section 6.2.1, this implies that real part of the loading resistance has a series of sharp peaks as the density increases; this will be seen more clearly when the computer analysis of the data is discussed. Coincident with the negative-going peaks in the phase signal, the antenna current and voltage also have sharp minima, decreasing by up to ~40%. The impedance-matching network was tuned to match the antenna impedance to the generator at the peaks in the loading resistance. The sharp minima in the reflected voltage signal coincide with the peaks in the phase signal (i.e., the peaks in the antenna resistance) and show that at the peaks, the reflection coefficient can be made very small. Detuning the impedance-matching network so that the reflected and incident voltage signals are nearly equal eliminates the effect of the antenna loading on the impedance which the generator sees. In this case, the antenna current and voltage signals do not show sharp minima, yet the phase signal is largely unchanged, demonstrating that in fact the phase detector is not sensitive to input amplitude variations.

Results of the computer analysis of the raw data for the antenna current, voltage, and dissipated power, transformed to the end of the antenna feeder tube, are shown in Figure 6-35. The sharp minima in the current and voltage signals are evident, as are some peaks in the dissipated power. The peaks in

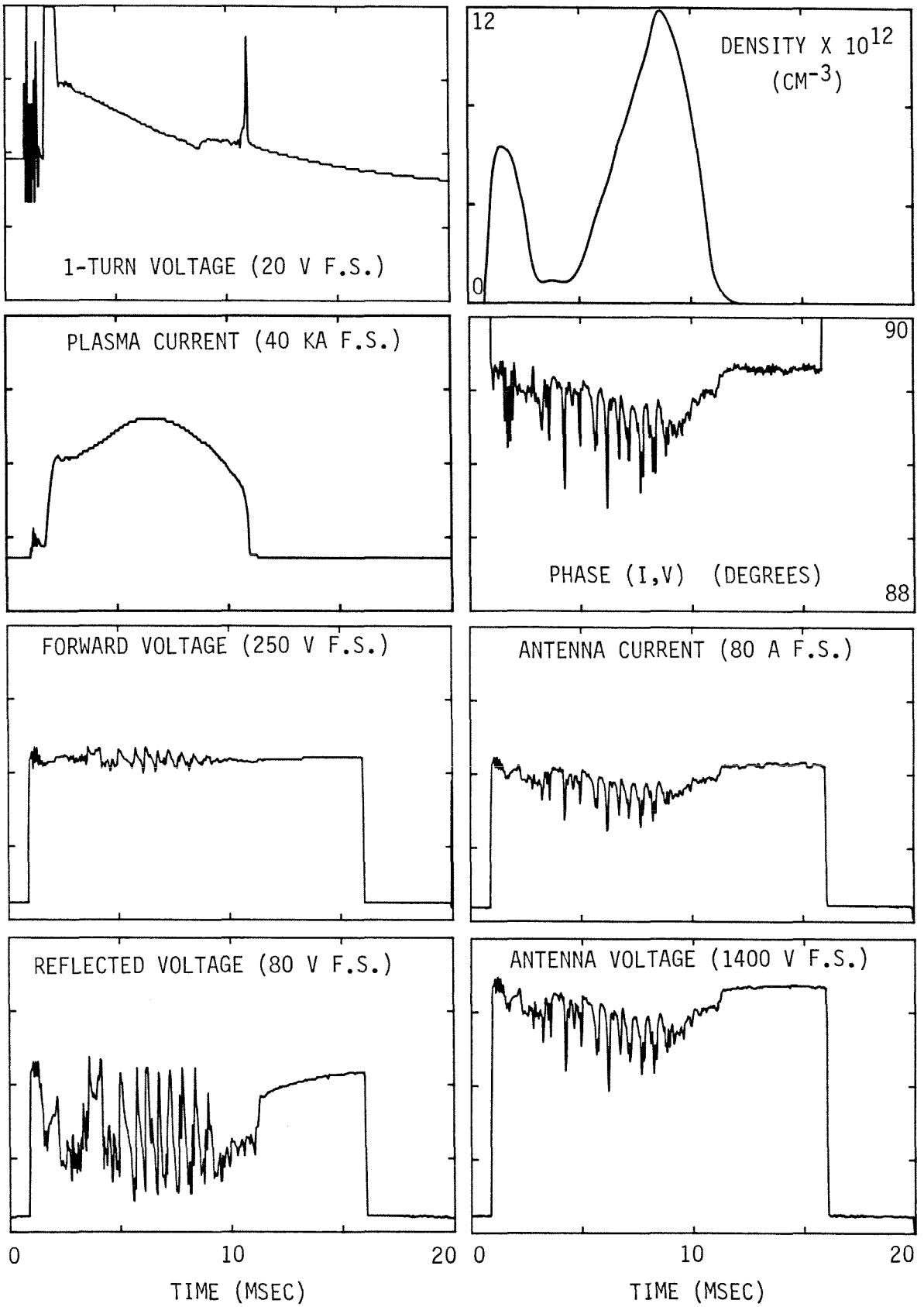

FIG. 6-34. Raw data from a tokamak shot using the ceramic-insulated loop antenna. Here $\omega/2\pi = 16$ MHz, $B_0 = 4.0$ kG, and the front edge of the Macor box surrounding the loop was 2.5 cm past the tokamak wall. Note that the full-scale range of the phase plot is 2.0 degrees.

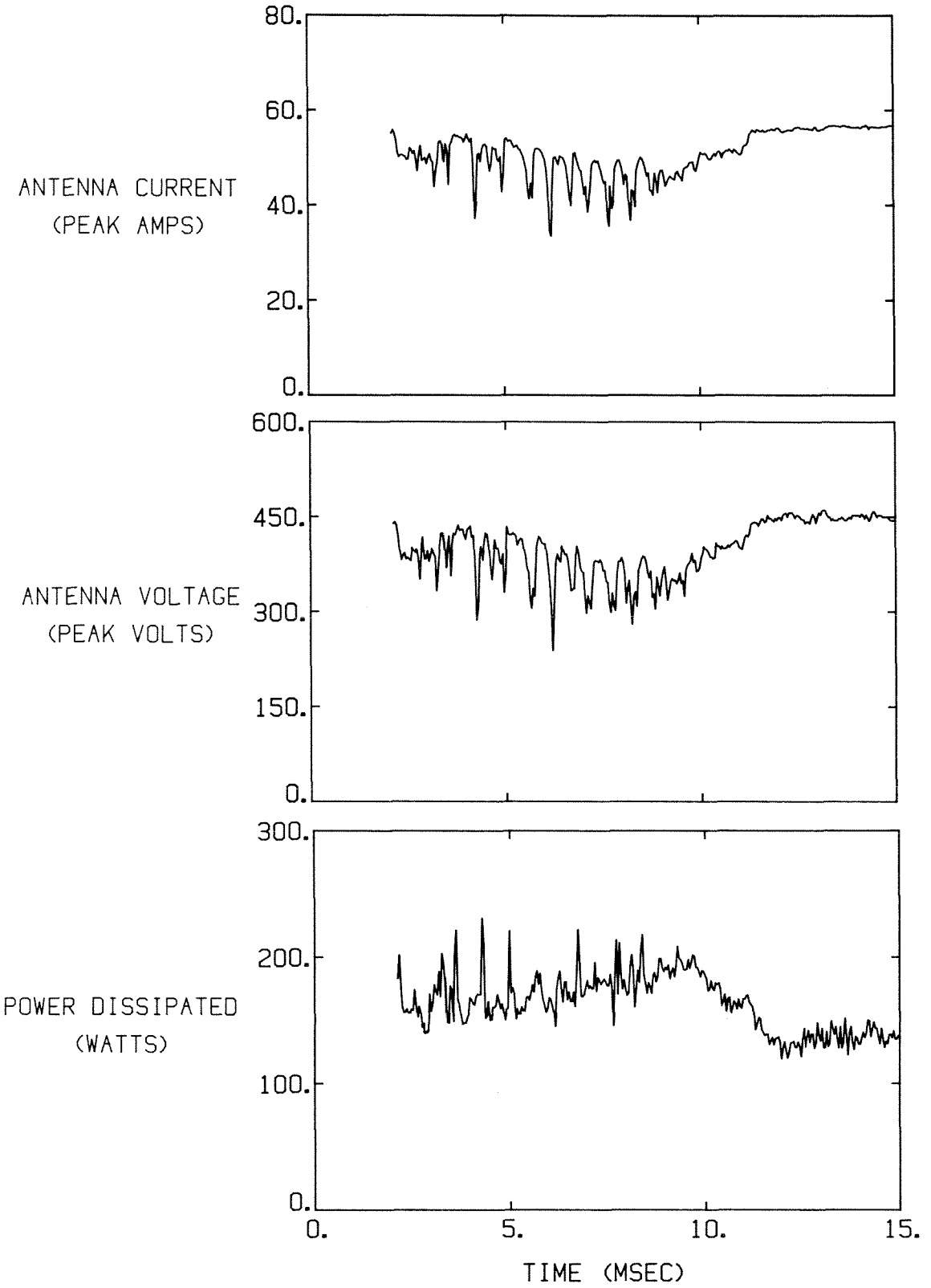

FIG. 6-35. Results for the antenna current, voltage, and dissipated power from the computer analysis of the raw data for the tokamak shot shown in Figure 6-34.

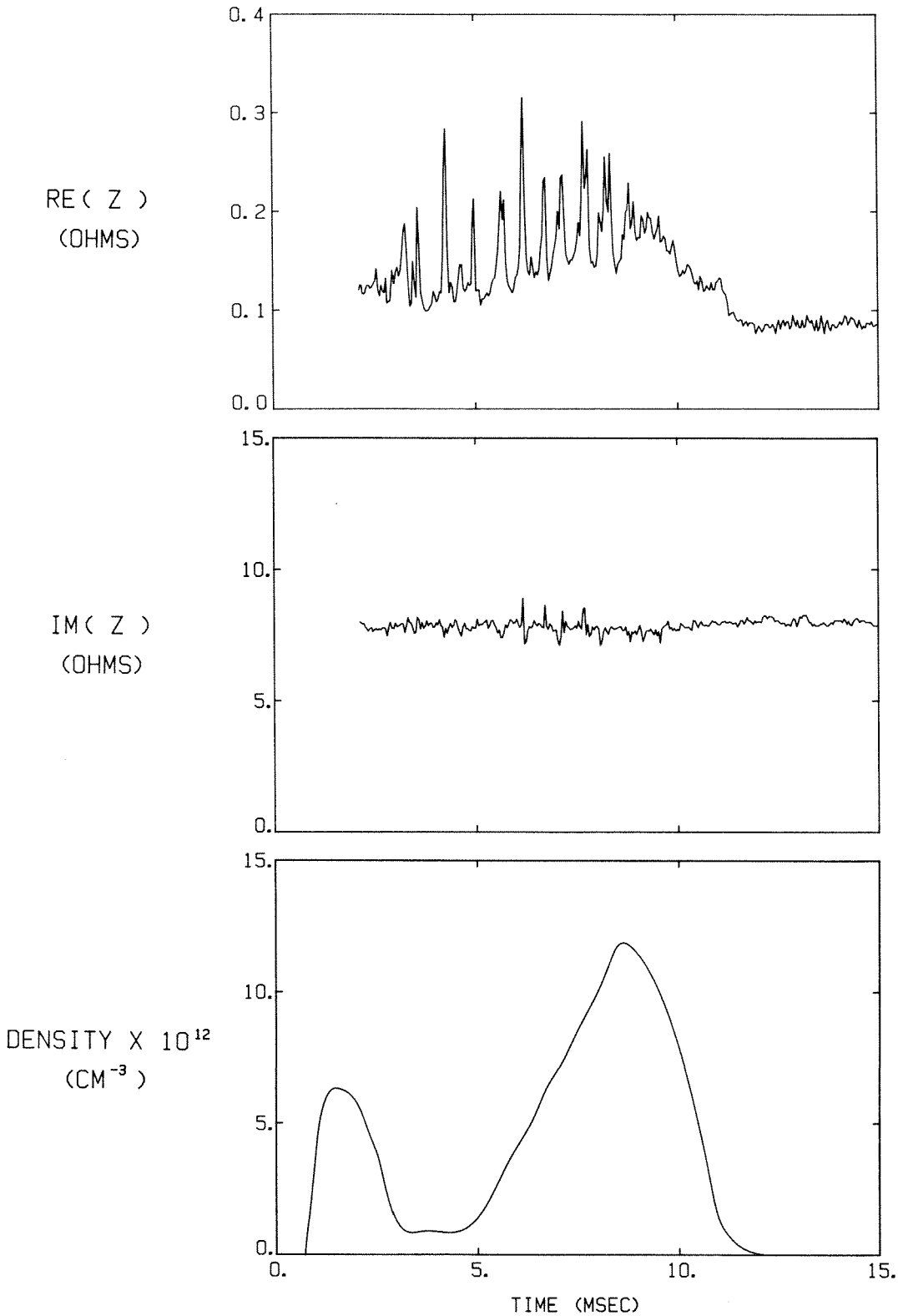

FIG. 6-36. Real and imaginary components of the ceramic-insulated loop antenna impedance, and the plasma density, for the tokamak shot shown in Figure 6-34. The sharp peaks in the real component of the impedance are coincident with the excitation of toroidal eigenmode resonances.

the power arise because, even though the antenna current and voltage may have minima at that point, the real part of the antenna impedance has a maximum.

Results of the analysis for the complex impedance are plotted in Figure 6-36. The distinct sharp peaks on the real part of the impedance (corresponding to the minima of the phase signal) are clearly seen. The background antenna resistance is ~ 80 mΩ, and the instrumental noise associated with the measurement is ~ 15 mΩ. The largest peak in the antenna resistance has an amplitude of ~ 0.32 Ω, which is approximately four times the background loading resistance. The imaginary part of the antenna impedance does not change significantly during the plasma discharge, although two or three small peaks, just above the noise level, which coincide with peaks on the real part of the impedance can be discerned.

The sharp peaks in the RF signals are, of course, related to the excitation of toroidal eigenmode resonances in the tokamak cavity. Details of the wave fields associated with the eigenmodes are presented in Chapter 7. Here we merely note that, in general, there is a one-to-one correspondence between the peaks seen on the real part of the antenna impedance and the peaks in the wave fields around the tokamak as detected with magnetic probes. The magnitude of the peaks in the antenna resistance seen in Figure 6-36 can vary from shot to shot by up to $\sim 50\%$. Lowering the excitation frequency or plasma density, or raising the toroidal magnetic field, reduces the number of modes which appear during the plasma shot (which is in agreement with the discussion of Chapter 2) and also broadens the modes and enhances their reproducibility.

Figures 6-37 and 6-38 present the variation of the amplitudes of the peaks of the real part of the antenna impedance with antenna insertion and frequency, respectively. For both of these plots, the density of modes during the discharge was sufficiently high that an individual mode could not be

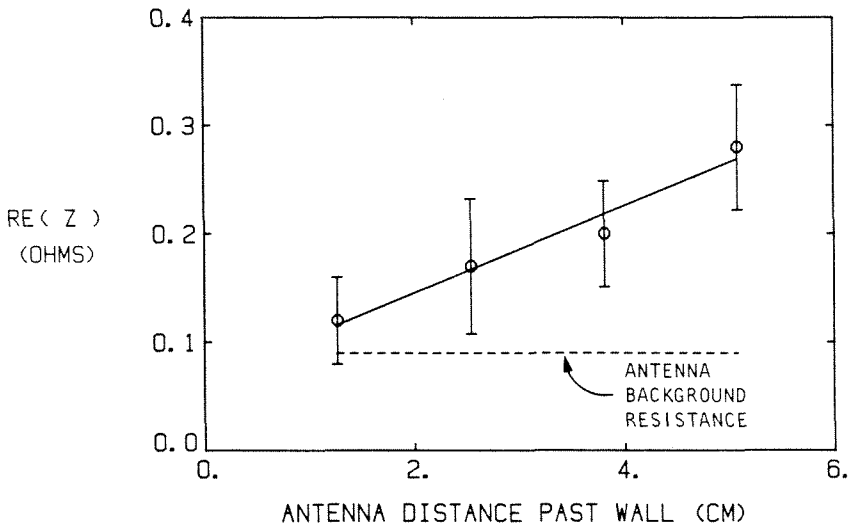

FIG. 6-37. Variation of the amplitudes of the peaks of the real part of the ceramic-insulated loop antenna impedance as a function of the insertion of the antenna. The horizontal axis is the distance between the front edge of the ceramic box surrounding the antenna loop and the tokamak wall. The points plotted represent the averages of the second, third, and fourth peaks observed after the initiation of the gas puff. Here $\omega/2\pi = 12$ MHz and $B_0 = 4.0$ kG. The antenna background resistance (without plasma) is also plotted.

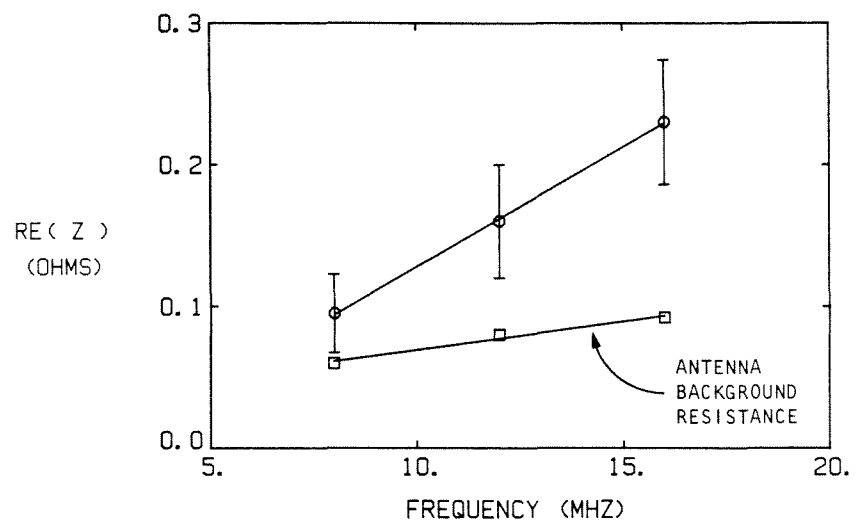

FIG. 6-38. Variation of the amplitudes of the peaks of the real part of the ceramic-insulated loop antenna impedance as a function of the excitation frequency. The points plotted represent the averages of the second, third, and fourth peaks observed after the initiation of the gas puff. The leading edge of the insulating box was 3.2 cm past the tokamak wall and $B_0 = 4.0$ kG. The antenna background resistance (without plasma) is also plotted.

confidently identified from shot to shot. Consequently, the points plotted in these graphs are the averages of second, third, and fourth modes observed after the start of the density rise associated with the gas puff. Each experimental point plotted represents data from five to ten tokamak shots. The vertical bars are the standard deviation of the data set composed of the average, for each shot, of the peak amplitudes of the three modes.

The variation of the amplitudes of the peaks with antenna insertion is shown in Figure 6-37. The excitation frequency was 12 MHz and the toroidal magnetic field on axis was 4.0 kG. Although the scatter in the data is large, the peaks clearly increase in amplitude as the antenna moves into the tokamak. Similarly, Figure 6-38 presents the data for the variation of the peak amplitudes as a function of the excitation frequency. For these shots, the leading edge of the antenna was 3.2 cm past the tokamak wall and the toroidal magnetic field was 4.0 kG. The amplitude of the peaks is seen to increase significantly as the frequency is raised.

Carefully controlling the plasma density evolution by adjusting the gas puff valve waveform to slow the rate of gas injection permits identification of particular eigenmodes from shot to shot. The particular density at which a mode occurs is a function of the toroidal field and the excitation frequency, and the eigenmode dispersion curves can be mapped out through careful experiments as described in Chapter 7. Figure 6-39 presents the amplitudes of the peaks on the real part of the antenna impedance, as functions of the toroidal magnetic field, for the first five modes which occur after the gas puff. For this experiment, the excitation frequency was fixed at 12 MHz and the leading edge of the antenna was 3.2 cm past the tokamak wall. The scatter in the data is large, but the amplitudes of the peaks in the loading resistance clearly increase substantially for the modes occurring at higher density. The variation of peak amplitude on the toroidal field strength is not significant, except

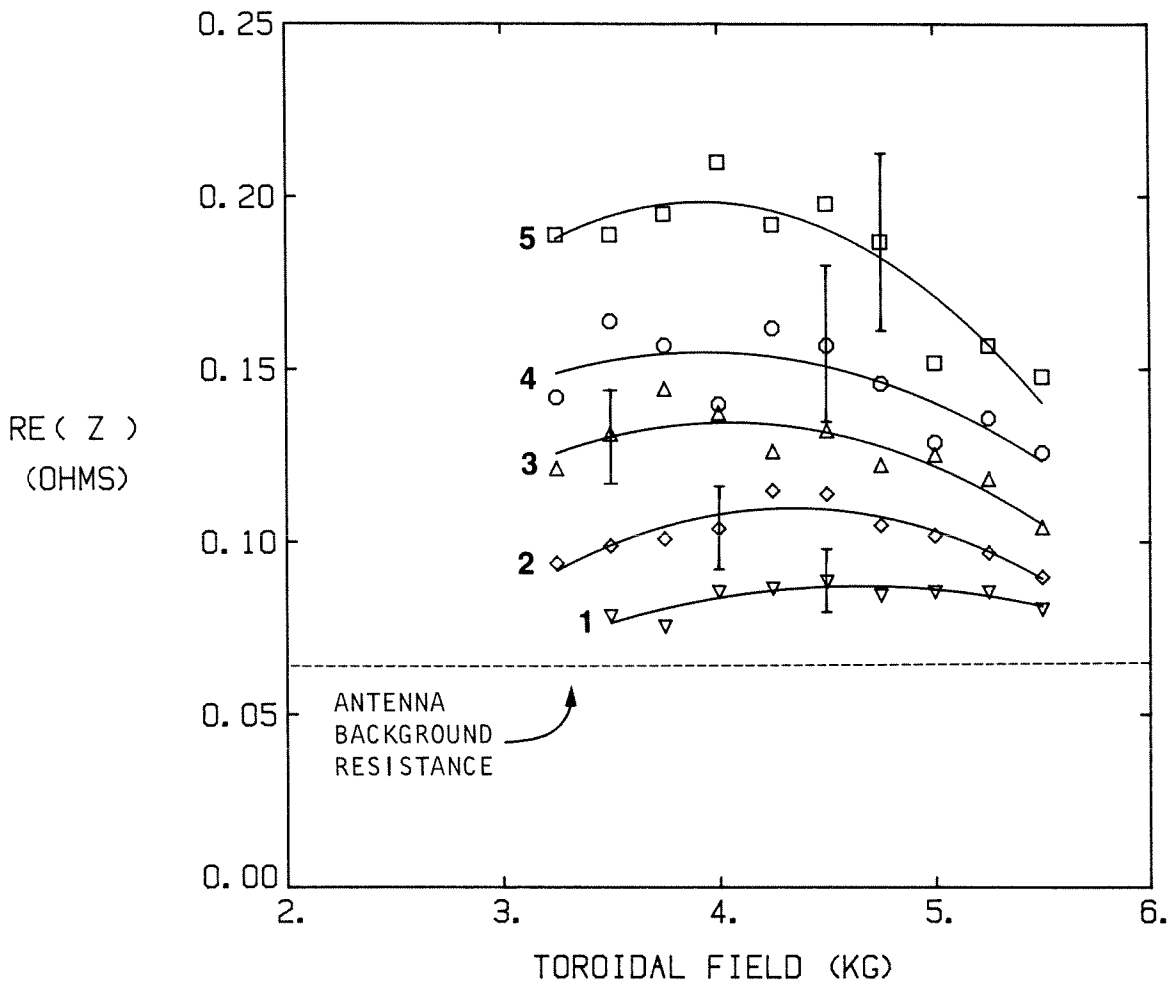

FIG. 6-39. Variation of the amplitudes of the peaks of the real part of the ceramic-insulated loop antenna impedance as a function of the toroidal magnetic field, for the first five modes which appear after the initiation of the gas puff. The leading edge of the insulating box surrounding the antenna loop was 3.2 cm past the tokamak wall and $\omega/2\pi = 12$ MHz. The curves for each mode are labeled from 1 to 5, in order of their appearance during the density rise. The antenna background resistance (without plasma) is also plotted.

perhaps for the fifth mode, where a decrease in peak amplitude is noticed as the toroidal field increases.

6.2.5 Faraday-Shielded Loop Antenna

Raw signals from a typical tokamak shot using the Faraday-shielded loop antenna are shown in Figure 6-40. The excitation frequency for this shot was 12 MHz, the toroidal magnetic field was 4.0 kG, and the front edge of the shield was 5.1 cm past the tokamak wall. In order to see any effect of the plasma on the antenna impedance, the antenna had to extend fairly far into the plasma ($\gtrsim 3-4$ cm). With the antenna 5 cm into the plasma, the impurity levels began to increase and the plasma discharge duration began to decrease. Inserting the antenna any further than this resulted in abrupt increases in impurities, as measured by the soft-UV detector, and early disruptions of the plasma current.

The change of the phase signal due to the appearance of plasma is now very small: the full-scale range of the phase plot is only one degree. The phase signal after the plasma terminates, at $t \simeq 12$ msec, shows the instrumental noise associated with the phase detector - the rms phase noise is less than 0.04 degree. Note that the amplitudes of the raw antenna current and voltage signals vary during the plasma shot by less than 2 db, a factor small enough to ensure that the phase signal was not being affected by the input amplitude variations, even at this sensitivity. The phase signal during the discharge exhibits a small decrease which appears to be proportional to the mean density rise; superimposed on this are several negative-going peaks which are coincident with the excitation of eigenmodes as seen on magnetic probes (and discussed in Chapter 7).

Figure 6-41 shows the results of the computer analysis for the antenna current and voltage and the dissipated power, transformed to the antenna end

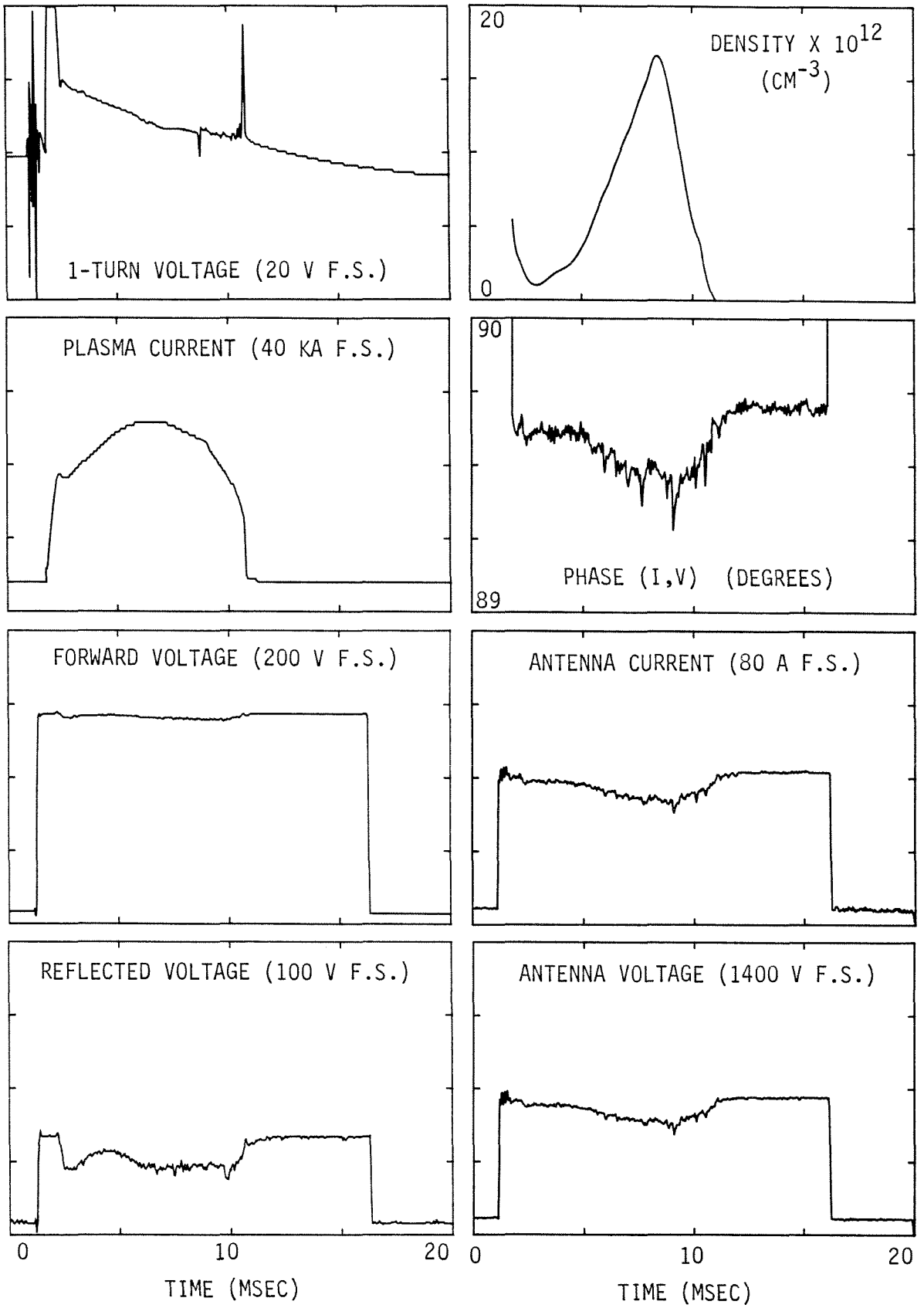

FIG. 6-40. Raw data from a tokamak shot using the Faraday-shielded loop antenna. The leading edge of the ceramic box surrounding the antenna loop was 5.1 cm past the tokamak wall, also $\omega/2\pi = 12$ MHz and $B_0 = 4.0$ kG. Note that the full-scale range of the phase plot is 1.0 degree.

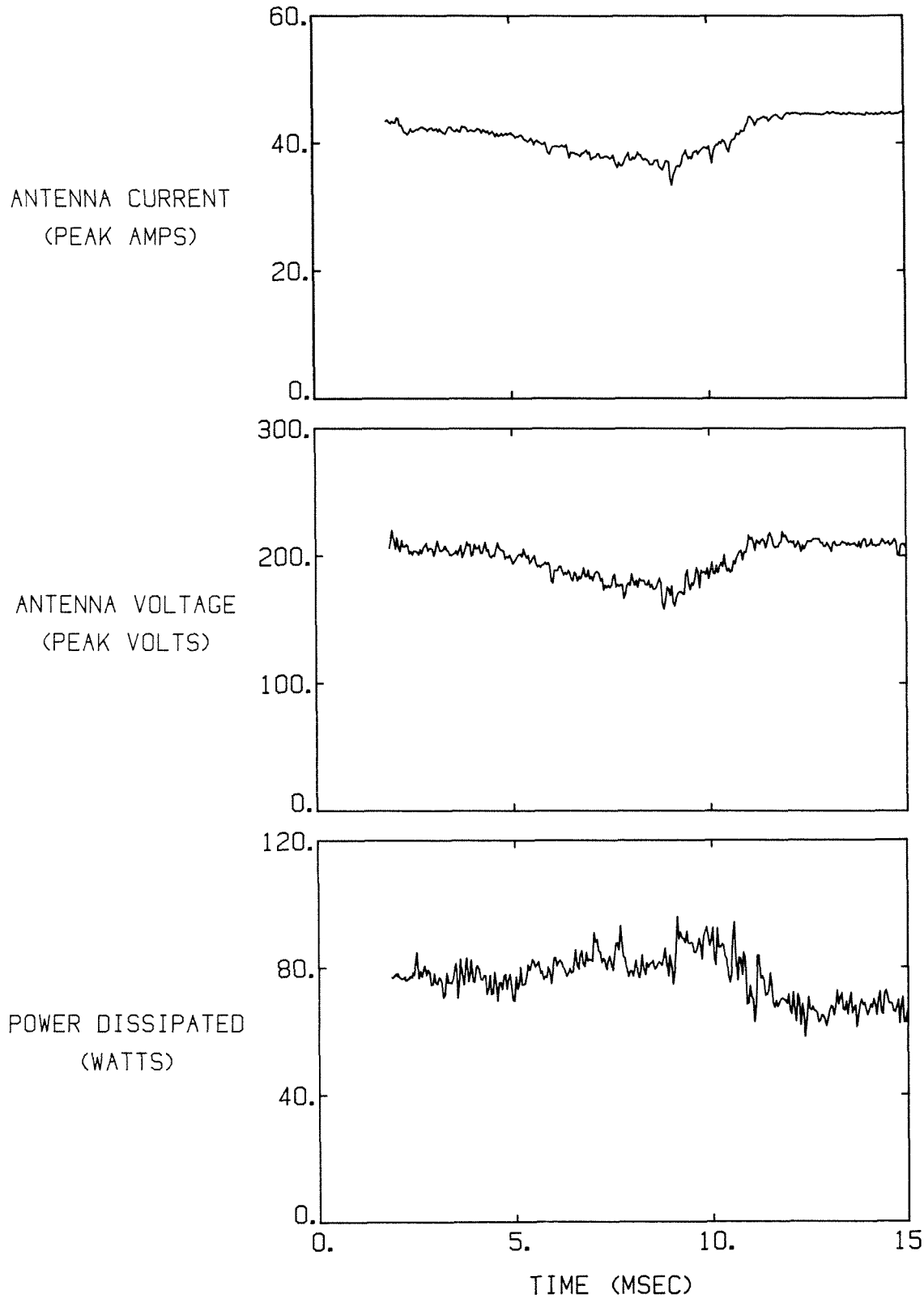

FIG. 6-41. Results for the antenna current, voltage, and dissipated power from the computer analysis of the raw data for the tokamak shot shown in Figure 6-40.

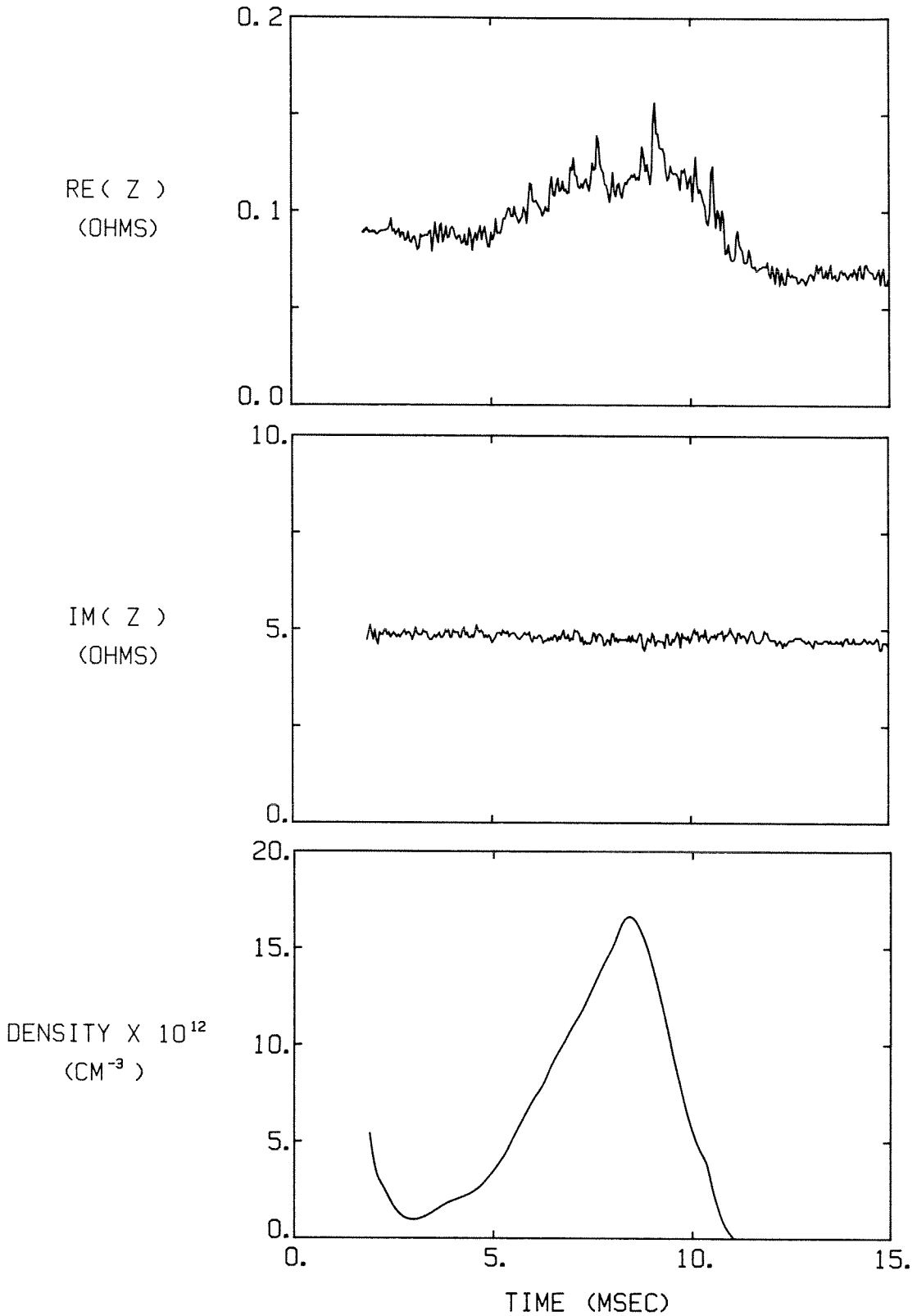

FIG. 6-42. Real and imaginary components of the ceramic-insulated loop antenna impedance, and the plasma density, for the tokamak shot shown in Figure 6-40.

of the feeder tube. The plots are unremarkable; the increase of the dissipated power with the appearance of plasma is only just above the noise level. This is a reflection of the very small increase in the real part of the antenna impedance in the presence of plasma. Figure 6-42 shows the actual complex impedance resulting from the computer analysis. The real part of the impedance follows the general form suggested by the phase signal of Figure 6-40: a small density-dependent background loading with a few small peaks discernible from the noise. Note that the background antenna resistance is ~70 mΩ and that the largest loading observed during the shot is only ~80 mΩ larger than this. The imaginary part of the impedance shows no change above the noise level during the tokamak discharge.

Because the loading was so small, and the reproducibility was poor, the data sets from the Faraday-shielded antenna were not analyzed further.

6.3 Langmuir Probe Studies

Langmuir probes were used both to study edge plasma properties with and without RF power applied to an antenna, and to provide the I–V curve data for the impedance model to be discussed in section 6.4. Construction of the probes is described in section 5.4; the probes were operated at a fixed bias and probe curves were mapped out by varying the bias from shot to shot.

The basic features of an idealized Langmuir probe curve have been discussed by many authors [Langmuir and Mott-Smith, 1924; Chen, 1965]. As the probe is biased negative with respect to the actual plasma space potential at the probe location, virtually all of the ions whose paths intersect the probe are collected, but fewer and fewer of the electrons have sufficient energy to reach the probe. In this region, the net current collected by the probe is approximately given by

$$I_p \simeq \frac{neA}{4}\left(U_e\, e^{\frac{e(V_p - V_s)}{k_B T_e}} - U_i \right) \qquad (V_p < V_s)\,, \tag{6.11}$$

where n is the plasma density, e is the electronic charge, A is the probe area, V_p is the probe potential, V_s is the space potential, T_e is the electron temperature, k_B is Boltzmann's constant, U_e is the mean electron thermal speed (a Maxwellian distribution is assumed), and U_i is the ion sound speed (roughly equal to the ion thermal speed if the ion and electron temperatures are equal) [Budny, 1982]. A logarithmic plot of this electron-repelling part of the probe curve (after subtracting off the ion saturation current) then yields a straight line of slope $-\frac{1}{k_B T_e}$ from which the electron temperature is found. As the probe bias becomes more positive than V_s, almost all of the electrons but fewer and fewer of the ions are collected by the probe. The ion-repelling region of the probe curve ($V_p > V_s$) is difficult to analyze theoretically, but the following simple form is sometimes useful in unmagnetized plasmas:

$$I_p \simeq \frac{neA}{4}\left(U_e - U_i\, e^{\frac{e(V_p - V_s)}{k_B T_i}} \right) \qquad (V_p > V_s)\,. \tag{6.12}$$

The ion saturation current (for $V_p \ll V_s$) is then given by $I_{si} \simeq -\frac{neA}{4} U_i$, while the electron saturation current (for $V_p \gg V_s$) is $I_{se} \simeq \frac{neA}{4} U_e$. Thus, the saturation currents are proportional to the plasma density and to the square root of the temperature. In the presence of a magnetic field, however, the electron saturation current is usually significantly smaller than predicted by this simple expression.

When the probe floats with respect to the plasma, the net current to it must vanish. Because the flux of electrons striking a probe at the space potential is much larger than the flux of ions (due to their higher thermal velocity) a floating probe charges up to a sufficiently negative potential (with respect to

the space potential) to retard the flux of electrons and render the electron and ion currents equal. The floating potential can be found from equation 6.11:

$$V_f \simeq V_s - \frac{k_B T_e}{e} \ln\left(\frac{U_e}{U_i}\right) \simeq V_s - 3.76 \frac{k_B T_e}{e}, \qquad (6.13)$$

where a hydrogen plasma of equal electron and ion temperatures has been assumed. Hence, the difference between the space potential (if it can be identified) and the floating potential can yield information on the electron temperature. Unfortunately, in the presence of a magnetic field, the space potential (usually identified as a "knee" in the curve) often becomes obscured [Sato, 1972], and generally only the electron-repelling part of the probe curve is useful.

6.3.1 Probe Results Away From RF Antenna

A typical tokamak shot showing the ion-saturation probe current is shown in Figure 6-43. The probe tip was 4.0 cm past the tokamak wall and the probe bias was -200 volts (with respect to the tokamak chamber). Note that there is substantial noise on the signal (and this trace has already been filtered somewhat); these fluctuations are characteristic of Langmuir probe traces. The magnitude of the current roughly follows the mean density inferred from the microwave interferometer, except that the probe current reaches its peak shortly before the mean density peaks. This is probably because the plasma moves slightly inward toward the end of the discharge (as seen with the in-out coils [section 3.5]) and the Langmuir probe was located on the outside of the torus. With proper adjustment of the vertical field power supplies, the mean density and the probe saturation current roughly track each other during most of the discharge. Note that the ratio of the peak mean density to the density just before the gas puff begins is somewhat larger than the ratio of the saturation currents at the corresponding times. Part of the explanation for

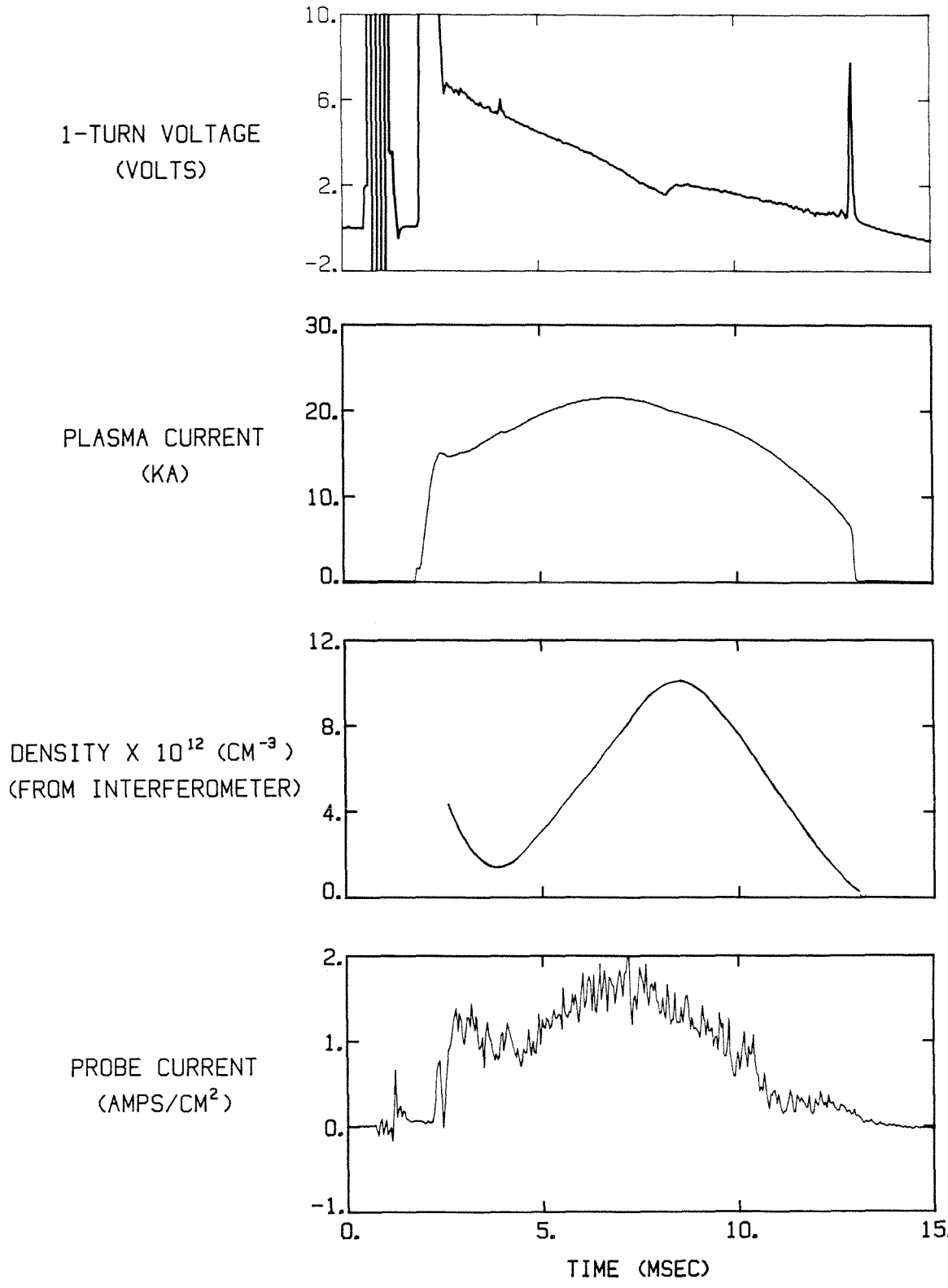

FIG. 6-43. A typical tokamak shot, showing the one-turn voltage, the plasma current, the plasma density (from the microwave interferometer signal) and the ion-saturation Langmuir probe current. The probe tip was 4.0 cm past the tokamak wall and the bias was -200 V with respect to the tokamak chamber. The probe was located in tokamak port #1 (cf. Figure 3-1), and the RF antenna was withdrawn from the tokamak.

this observation may lie in the dependence of the saturation current on both the density and the temperature. As mentioned in section 3.9, both the electron and ion temperatures of the bulk plasma are observed to decrease during the gas puff. The edge plasma where the probe is located is probably cooled at least as much as the bulk plasma, leading to reduced saturation current.

A Langmuir probe $I-V$ curve is shown in Figure 6-44a. Here the probe tip was 1.0 cm past the tokamak wall, and the data points were taken when the mean plasma density reached $n \simeq 7.0 \times 10^{12}$ cm^{-3}. Fitting an exponential to the electron-repelling part of the curve yields an electron temperature of ~ 9.5 eV; together with the ion saturation current, this implies a density of $\sim 0.51 \times 10^{12}$ cm^{-3}. Similar plots of the $I-V$ curve for probe insertions of 2.0 cm and 4.0 cm past the tokamak wall are shown in Figures 6-44b and 6-44c. As the probe moves farther into the plasma, the slope of the transition region of the curves decreases, which means that the electron temperature increases. The ion saturation current also increases, by a larger factor than would be expected from the temperature increase alone; hence the density must also be increasing as the probe moves in. Plots of the electron temperature and density, derived from the $I-V$ curves using the simple theory discussed above, are shown in Figure 6-45 as functions of the probe insertion. Thus, the temperature and density profiles appear to be almost linear functions of radius near the plasma edge. At the most interior point investigated (4.0 cm past the wall), the electron temperature was ~ 32 eV and the density was $\sim 4.1 \times 10^{12}$ cm^{-3}, or some 60% of the line-averaged plasma density as measured by the microwave interferometer.

Langmuir probe curves are perhaps most useful in establishing general trends in plasma density and temperature. Due to the significant complexities and uncertainties of probe theory in the presence of a magnetic field, the absolute values of plasma parameters derived from the probe traces should be

(a)

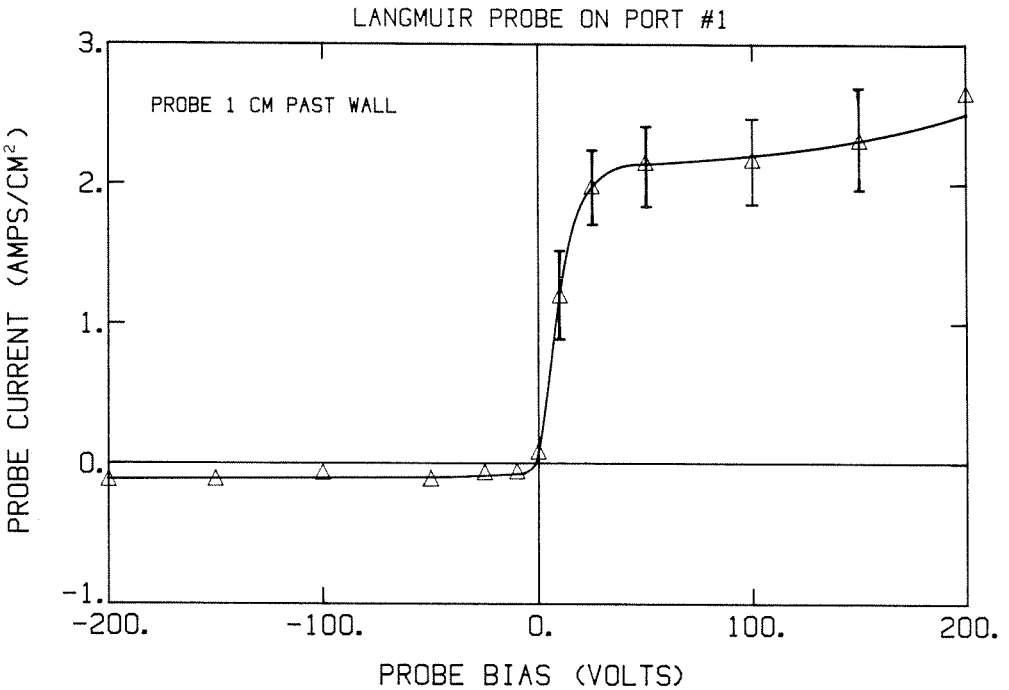

(b)

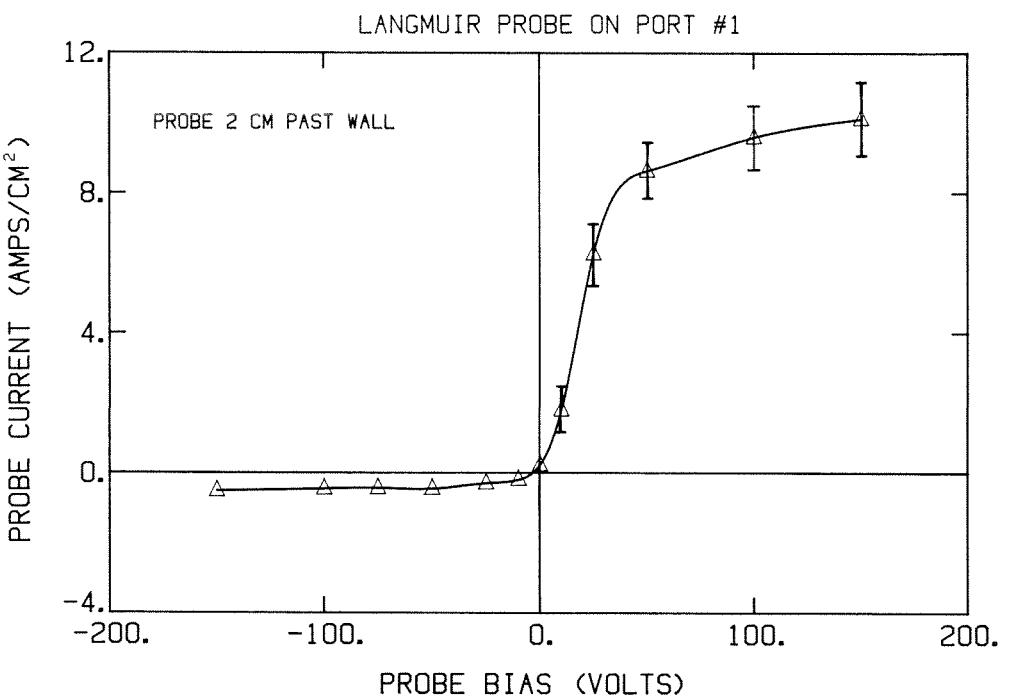

FIG. 6-44. Langmuir probe $I-V$ curves. The probe was located in tokamak port #1, and the data sets were taken at a mean plasma density of $n \simeq 7.0 \times 10^{12}$ cm^{-3}. The exposed area of the probe tip was 0.12 cm^2. For plots a), b), and c), the RF antenna was withdrawn from the plasma. a) Probe tip 1.0 cm past the tokamak wall. b) Probe tip 2.0 cm past the tokamak wall.

(c)

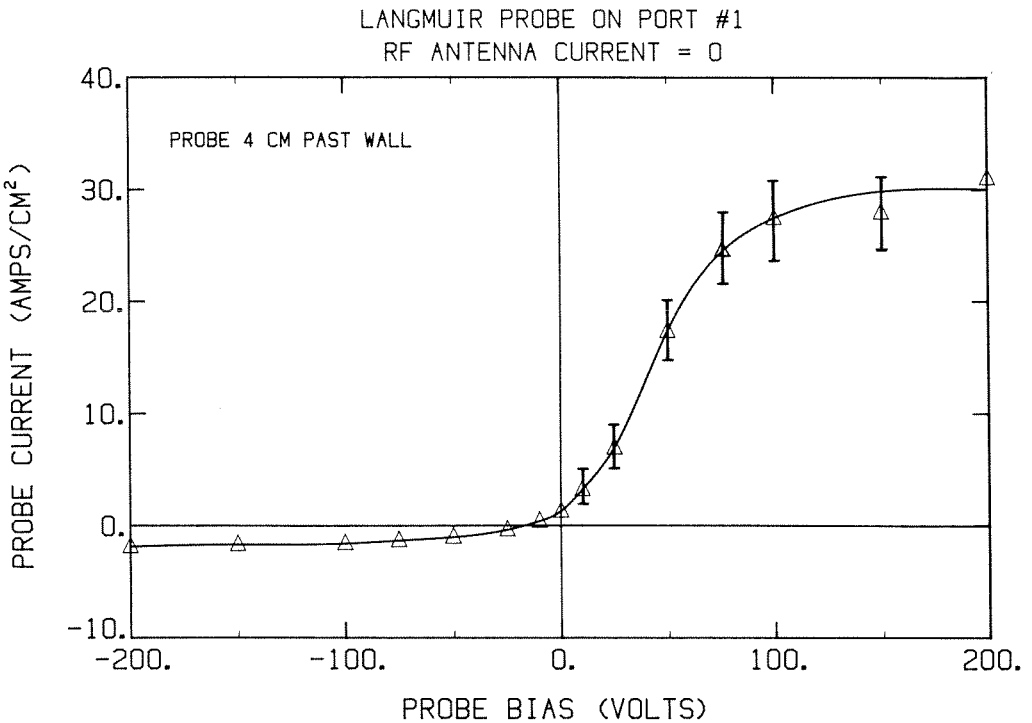

(d)

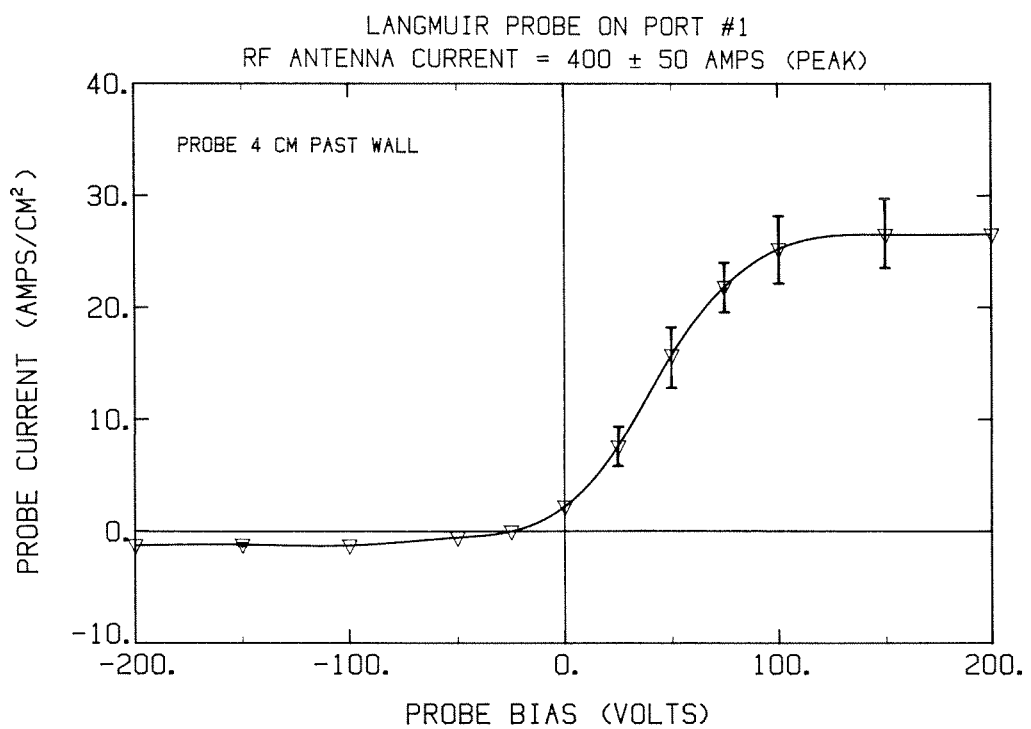

FIG. 6-44, continued. c) Probe tip 4.0 cm past the tokamak wall. d) Probe tip 4.0 cm past the tokamak wall, and the ceramic-insulated loop antenna was inserted 3.2 cm past the wall and excited with ~400 A of RF current at $\omega/2\pi = 12$ MHz.

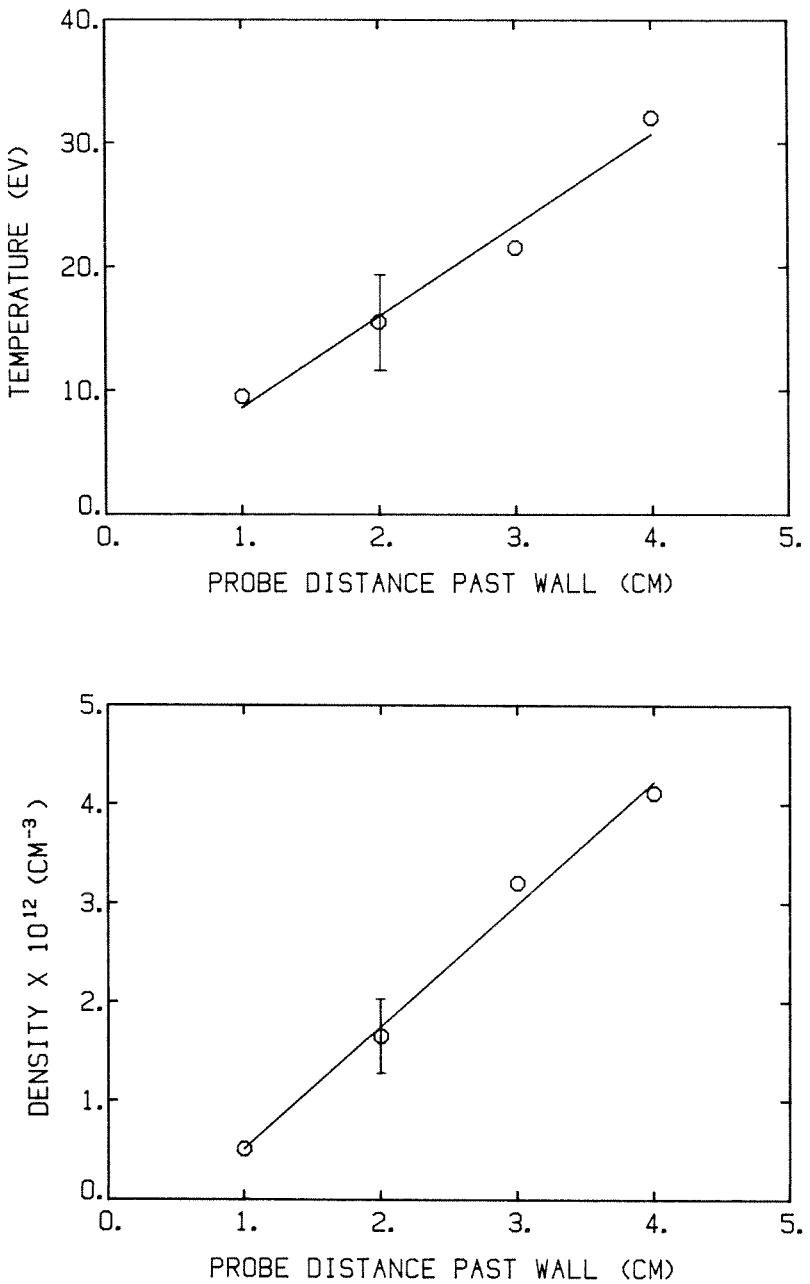

FIG. 6-45. The electron temperature and density, derived from the Langmuir probe plots using simple theory, as a function of radial position.

regarded with at least moderate skepticism. In this spirit, then, an investigation of the effect of insertion of the Macor-covered loop antenna on the plasma edge density is presented in Figure 6-46. The question being addressed was whether or not the the Macor box acted as a limiter, depressing the edge density globally around the tokamak. A Langmuir probe was mounted on tokamak port #1 (Figure 3-2), which was 180 degrees toroidally away from the RF antenna port, and was biased at -200 V with respect to the tokamak chamber in order to draw ion saturation current. For each of three positions of the Macor box (the leading edge of the box being 0.0, 2.5, or 5.0 cm past the tokamak wall), the Langmuir probe was inserted from 0.0 to 8.0 cm past the wall in 1.0 cm steps, and at each probe position, 3 – 7 plasma shots were recorded. It should be noted that at a probe insertion of ~7 cm or greater, the impurity levels in the plasma (observed with the soft-UV detector) began to increase markedly, indicating contamination of the plasma by the probe. For each plasma shot, the probe current was recorded at a mean plasma density of $n \simeq 6.0 \times 10^{12}$ cm^{-3}.

The results in Figure 6-46 show, surprisingly, that the ion saturation current at a particular radial position actually *increased* when the Macor-shielded antenna was moved into the plasma. Since it was unlikely that the plasma temperature increased upon insertion of the Macor, this implies that the plasma density increased. However, the differences observed between the saturation currents when the Macor box was 2.5 or 5.0 cm past the wall were not significant. Since the mean (line-averaged) plasma density measured by the microwave interferometer was the same for all of the data points, this plot suggests that the plasma density profile (normally peaked in the center) was being flattened or broadened by the insertion of the Macor. However, this supposition cannot be substantiated without a reliable radially-resolved density diagnostic (such as a multi-channel microwave interferometer). The defensible

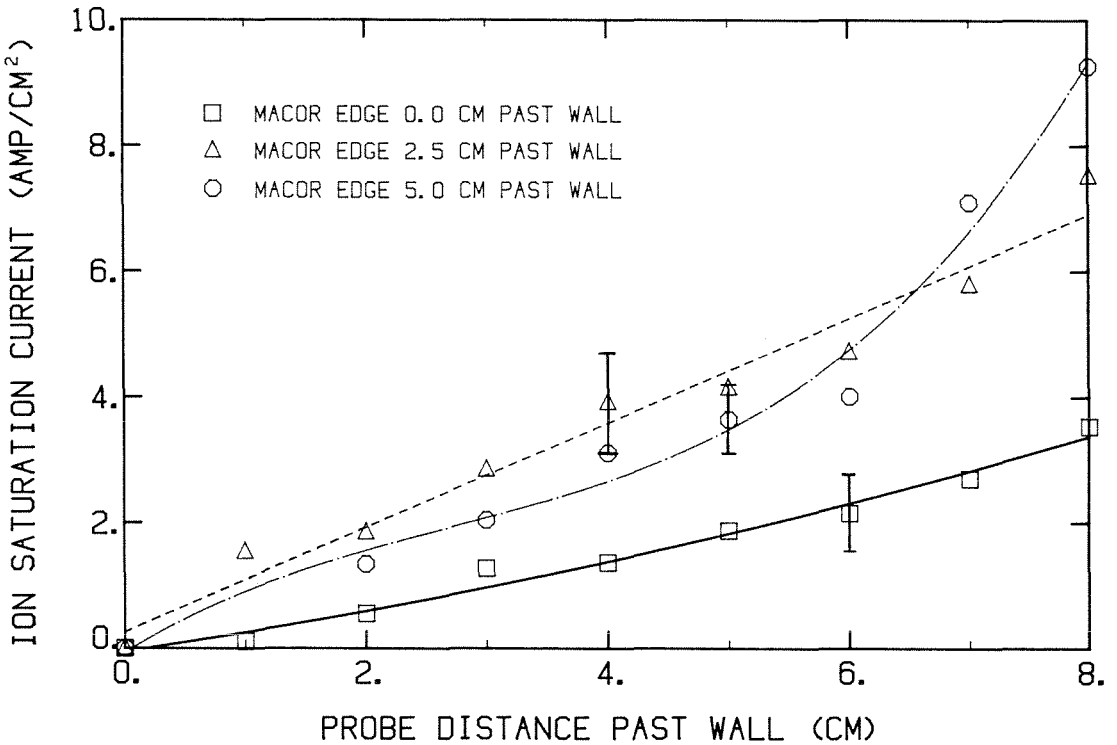

FIG. 6-46. Effect of the insertion of the ceramic-insulated loop antenna on the radial dependence of the ion saturation current of a Langmuir probe. The probe was located in tokamak port #1 (180° toroidally away from the RF antenna) and was biased at -200 V with respect to the tokamak chamber. The leading edge of the Macor box was positioned at 0.0, 2.5, and 5.0 cm past the tokamak wall; there was no RF excitation.

conclusion of this experiment is simply that the insertion of the Macor-insulated antenna does *not* diminish the plasma edge density.

The effect of high-power RF excitation on the Langmuir probe $I-V$ curve was investigated using the probe on port #1. For this experiment, the probe was inserted 4.0 cm past the tokamak wall and the bias was again varied from shot to shot. The RF antenna used was the Macor-insulated loop antenna, inserted 3.2 cm past the tokamak wall. The excitation frequency was 12 MHz, the toroidal magnetic field was 4.0 kG, the RF antenna current (transformed to the antenna end of the feeder tube) was approximately 400 A (peak), and the data points were taken at a mean plasma density of $n \simeq 7.0 \times 10^{12}$ cm^{-3}. The resulting $I-V$ curve is plotted in Figure 6-44d; comparison with the curve of Figure 6-44c (taken with the same experimental parameters but with no RF current) shows that RF excitation with the insulated antenna produces no noticeable effect on the $I-V$ curve far away from the antenna.

6.3.2 Probe Results Near RF Antenna

This section presents the results of investigations with a Langmuir probe attached to the side of the Macor-insulated loop antenna (section 5.1.3). The tip of the probe was 1.0 cm back from the front edge of the Macor box and the perpendicular distance from the probe axis to the Macor surface was 2 mm.

An $I-V$ curve taken with this probe, without any RF excitation, is shown in Figure 6-47a. The leading edge of the Macor box was 3.2 cm past the tokamak wall; hence the tip of the Langmuir probe on the side of the box was 2.2 cm past the wall. The toroidal magnetic field on axis was 4.4 kG, and the data points were taken when the microwave interferometer indicated a plasma mean density of $n \simeq 7.2 \times 10^{12}$ cm^{-3}. The part of the curve below the floating potential is similar to that of Figure 6-44b (which was taken with a Langmuir probe 2.0 cm past the wall, located 180 degrees toroidally away from the RF

(a)

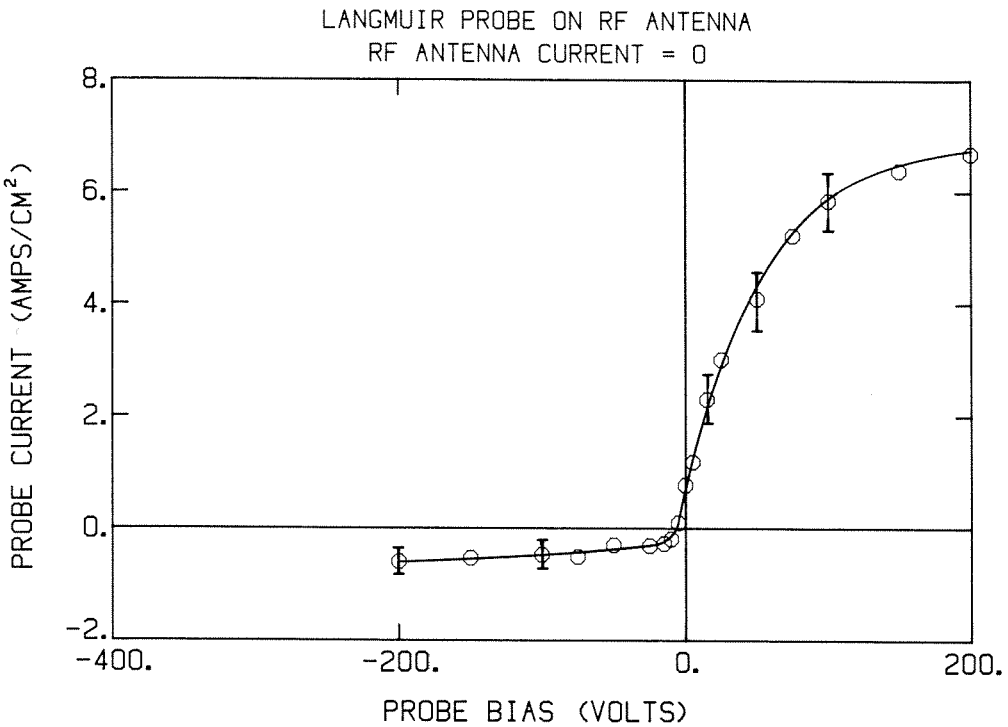

(b)

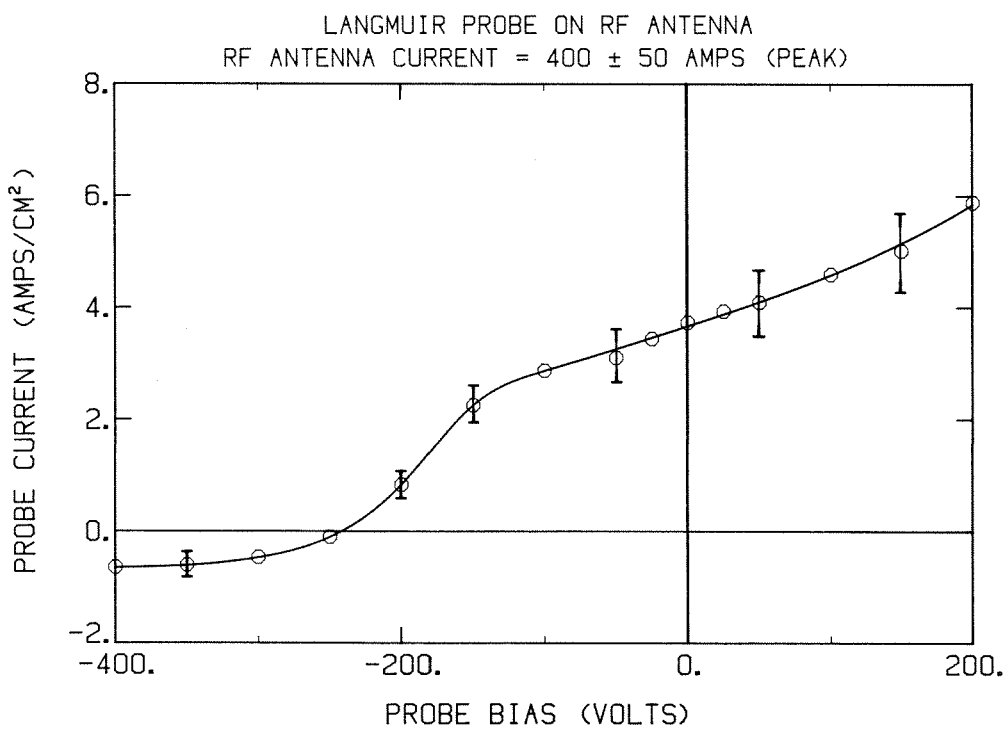

FIG. 6-47. $I-V$ characteristics of a Langmuir probe mounted on the side of the ceramic-insulated loop antenna. The probe tip was located 1.0 cm back from the front edge of the ceramic box, which in turn was located 3.2 cm past the tokamak wall. The data sets were taken at a mean plasma density of $n \simeq 7.2 \times 10^{12}$ cm^{-3}, and $B_0 = 4.4$ kG. a) Langmuir probe curve with no RF excitation. b) Langmuir probe curve with RF antenna current of ~400 A (peak) at a frequency of 12 MHz.

antenna). The part of the curve above the floating potential, however, exhibits some differences. The current does not appear to have saturated, even at +200 V bias, and the "knee" which appears in the other $I-V$ curves is no longer clear. The ion saturation currents for the two curves are almost equal. Neglecting possible temperature changes, this implies that the density 1.0 cm back from the leading edge of the ceramic box is comparable to the density at the same location in the absence of the antenna, for the same mean plasma density.

Excitation of the RF antenna with a large current changes the Langmuir probe characteristic markedly. Figure 6-47b shows the $I-V$ curve obtained with an RF current of $\sim$400 A (peak) at a frequency of 12 MHz; the other plasma and tokamak parameters were unchanged from those of Figure 6-47a. The entire $I-V$ curve appears to have been shifted to the left; the floating potential now occurs at ~ -240 V. The ion current still appears to saturate for potentials below ~ -350 V, and the value of the saturation current is about the same as for the curve taken without RF current (Figure 6-47a). The slope of the curve in the transition region, however, is significantly smaller than for the curve without RF current. Also, the electron current does not appear to saturate, increasing almost linearly with the probe bias above ~ -100 V.

The dramatic change of the floating potential with the application of RF current to the insulated loop antenna led to further explorations of this effect. A typical plasma shot is shown in Figure 6-48; the antenna and tokamak parameters were unchanged from those given above. The antenna probe floating potential remains fairly constant throughout the shot. Note that the RF pulse begins slightly before the ohmic-heating banks fire (which is coincident with the sudden rise of plasma current). The floating potential also decreases immediately with the onset of the RF current which suggests the possibility that the effect is simply electrostatic pickup by the probe. In fact, this is not

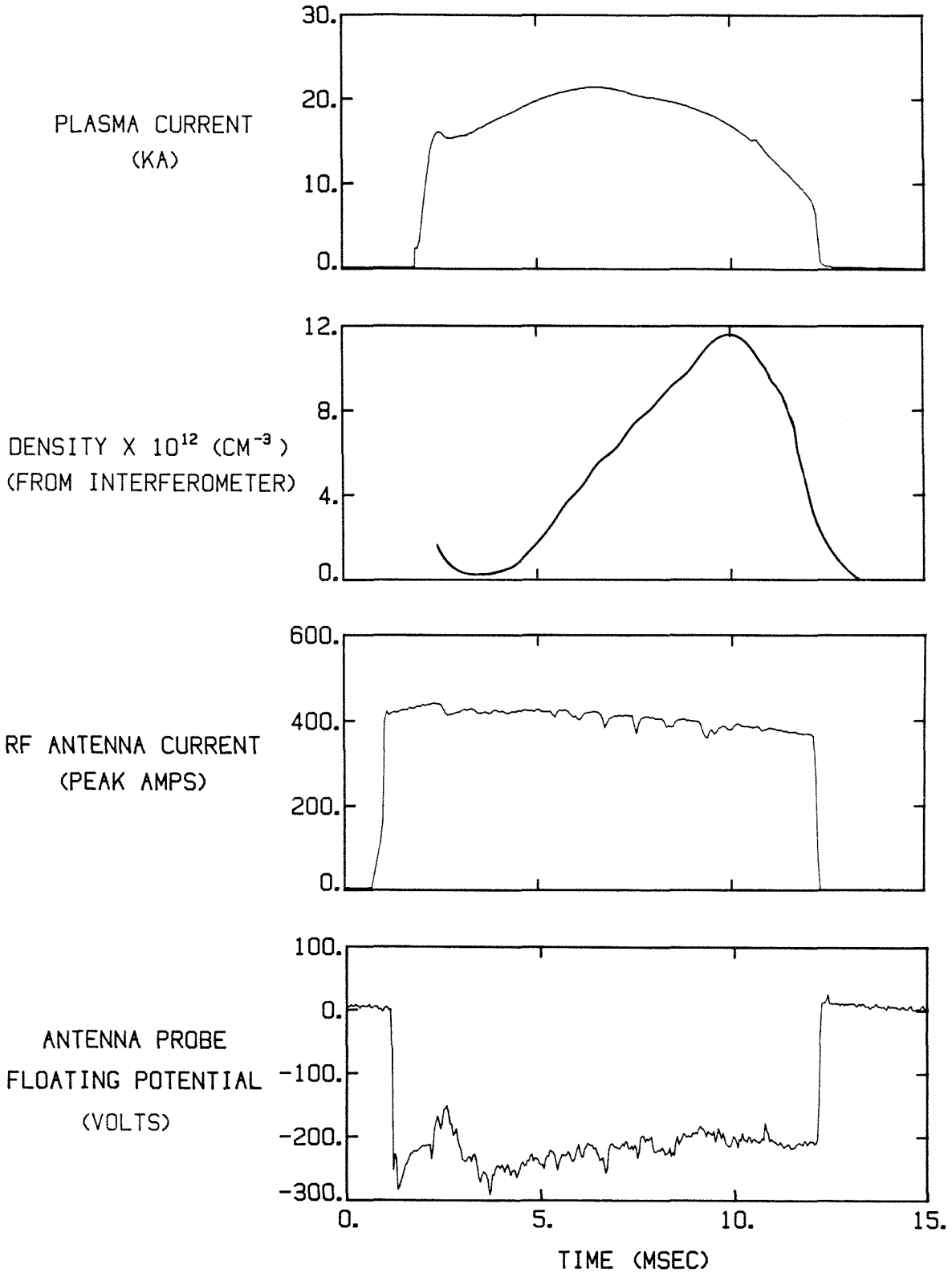

FIG. 6-48. Typical raw data for a tokamak shot, showing the plasma current, the plasma density, the RF antenna current, and the floating potential of the Langmuir probe on the side of the ceramic-insulated loop antenna. The leading edge of the ceramic box was 3.2 cm past the tokamak wall, $\omega/2\pi = 12$ MHz, and $B_0 = 4.4$ kG.

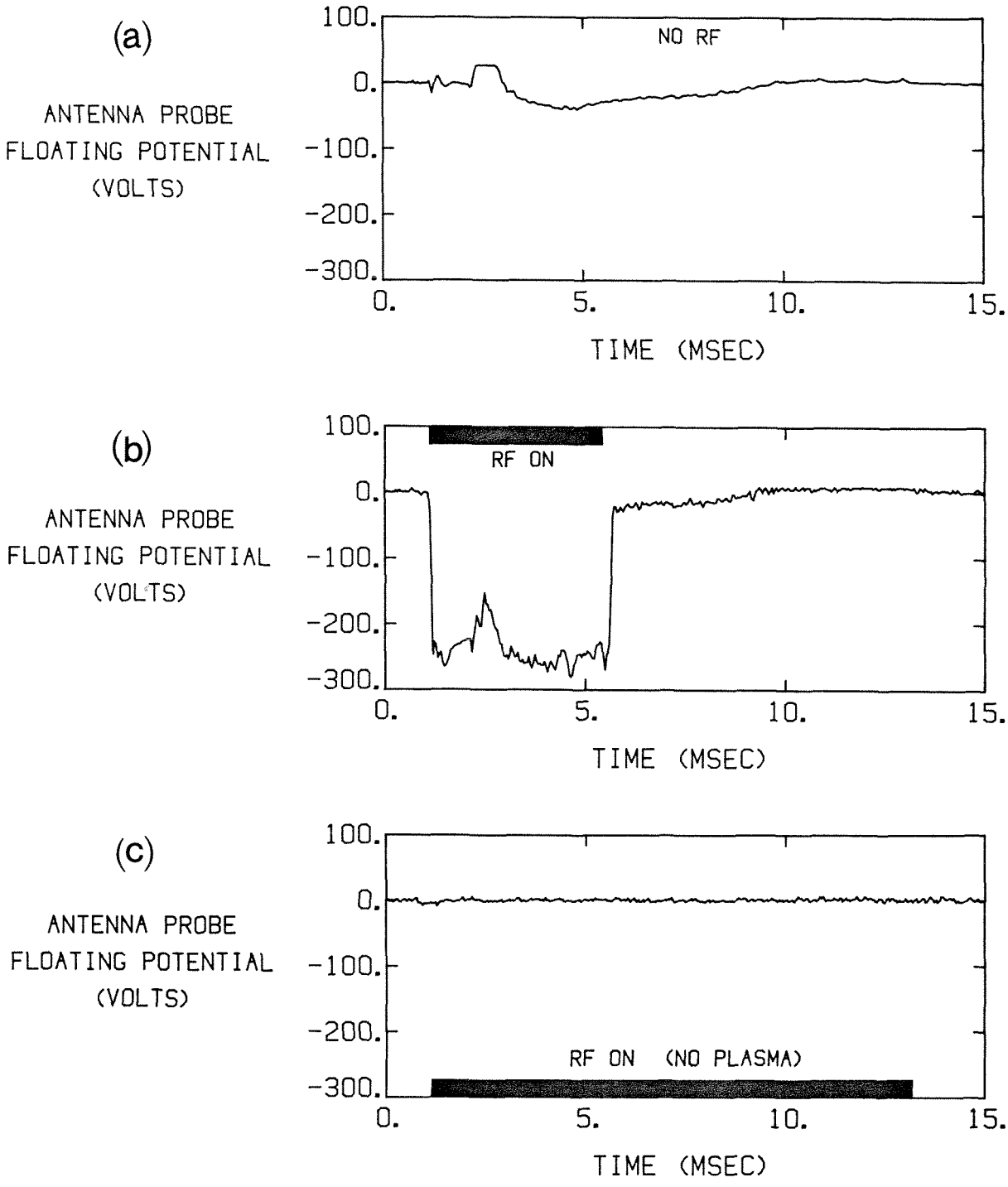

FIG. 6-49. Floating potential of the Langmuir probe on the side of the ceramic-insulated loop antenna. The leading edge of the ceramic box was 3.2 cm past the tokamak wall. a) Floating potential with no RF current applied to the loop. b) Floating potential with a loop current of ~400 A (peak) at a frequency of 12 MHz. The horizontal bar shows the duration of the RF pulse. c) Floating potential with RF excitation and with all tokamak fields firing, but with no gas and hence no plasma.

the case. Figures 4-49a, 4-49b, and 4-49c show the antenna probe floating potential for three different tokamak shots. In the first plot (Figure 6-49a), no RF current is applied, and the floating potential varies during the shot by less than 50 V. Note that these potentials are, of course, the potentials with respect to the tokamak wall, and not with respect to the space potential. Figure 6-47b shows the antenna probe potential for a similar discharge with ~400 A of RF current applied during only part of the shot. The floating potential change upon application of the RF current has a very short rise-time; the decay-time when the RF pulse ends (at which point the plasma is still present) is equally short. Finally, Figure 6-47c shows the floating potential of the antenna probe with the application of the RF current and with all tokamak fields firing, but without any gas in the machine and consequently no plasma. There is no discernible pickup by the probe.

The question then remains as to why the probe floating potential drops suddenly upon the application of RF current in the shot shown in Figure 6-46, apparently before the formation of the plasma. The answer is that there actually is a low-density plasma in the tokamak for some time before the ohmic-heating bank begins to drive the large plasma current. The preionization power supply discharges into the ohmic-heating coils several milliseconds before the ohmic-heating bank is fired, in order to initially break down the gas (section 3.3). This preionization can, in fact, be observed with a visible light detector. The preionization plasma density has not been measured directly, but it is estimated to be in the range of $10^{11} - 10^{12}$ cm^{-3}. This suggests, then, that the change in the antenna Langmuir probe floating potential with application of RF current to the antenna is rather insensitive to the plasma density. This argument is further supported by the observation that the floating potential changes little during the tokamak shot shown in Figure 6-48, while the plasma mean density varies by a large factor during the gas puff.

The relation between the change in floating potential seen by the antenna Langmuir probe and the magnitude of the RF current exciting the antenna loop was also investigated. Figure 6-50 shows the floating potential of the probe as a function of the peak RF current for two excitation frequencies: 12 and 16 MHz. The data set was taken at a plasma density of $n \simeq 7.2 \times 10^{12}$ cm^{-3}, although, as mentioned before, the signal was not very sensitive to the density. Here the leading edge of the Macor was again 3.2 cm past the wall of the tokamak, and the toroidal magnetic field on axis was 4.5 kG. The floating potential drops monotonically and almost linearly as the antenna RF current increases, with the change for the excitation frequency of 16 MHz being slightly larger than for the 12 MHz case.

Finally, the relation of the floating potential during the RF pulse to the toroidal magnetic field is displayed in Figure 6-51. Here the excitation frequency was 12 MHz, the RF antenna current was approximately 185 A (peak), and the toroidal field was varied from 3.6 to 5.2 kG. Each point plotted in this graph represents data from three to six tokamak shots. As the toroidal field increases, for fixed RF excitation current, the change in floating potential is observed to decrease slightly. The decrease is on the order of 25% over the range of toroidal field used.

6.4 Discussion

6.4.1 General Impedance Characteristics

The impedance measurements on the five RF antennas present a variety of different features. Qualitatively, the results from the bare plate and "T" antennas were similar to each other, as were results with the ceramic-insulated and Faraday-shielded loop antennas. These two sets of antennas, however, behaved quite differently from each other and from the bare loop antenna. Those

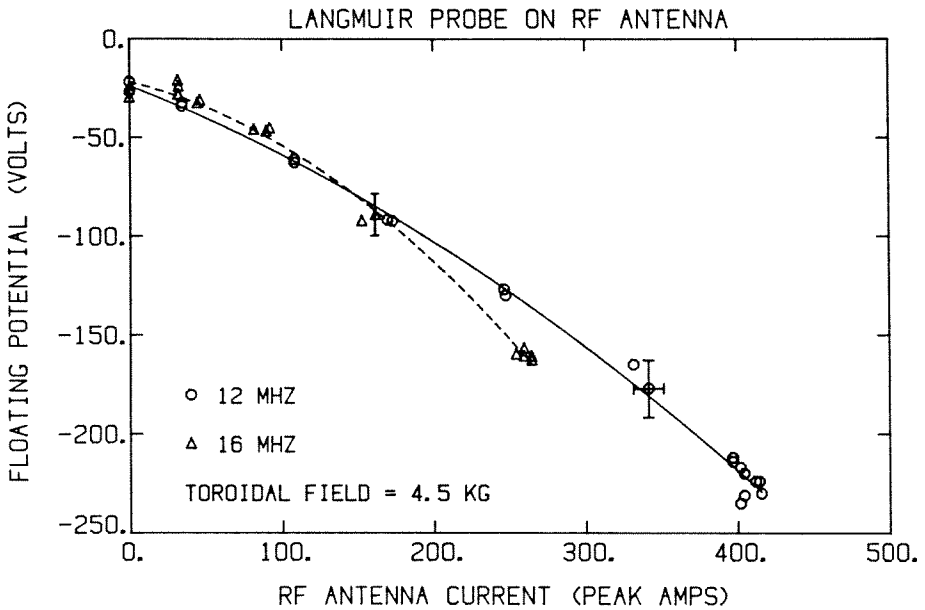

FIG. 6-50. Floating potential of the Langmuir probe on the side of the ceramic-insulated loop antenna, as a function of the RF antenna current, for two frequencies: 12 and 16 MHz. The leading edge of the ceramic box was 3.2 cm past the tokamak wall, the data set was taken at a plasma mean density of $n \simeq 7.2 \times 10^{12}$ cm^{-3}, and $B_0 = 4.5$ kG.

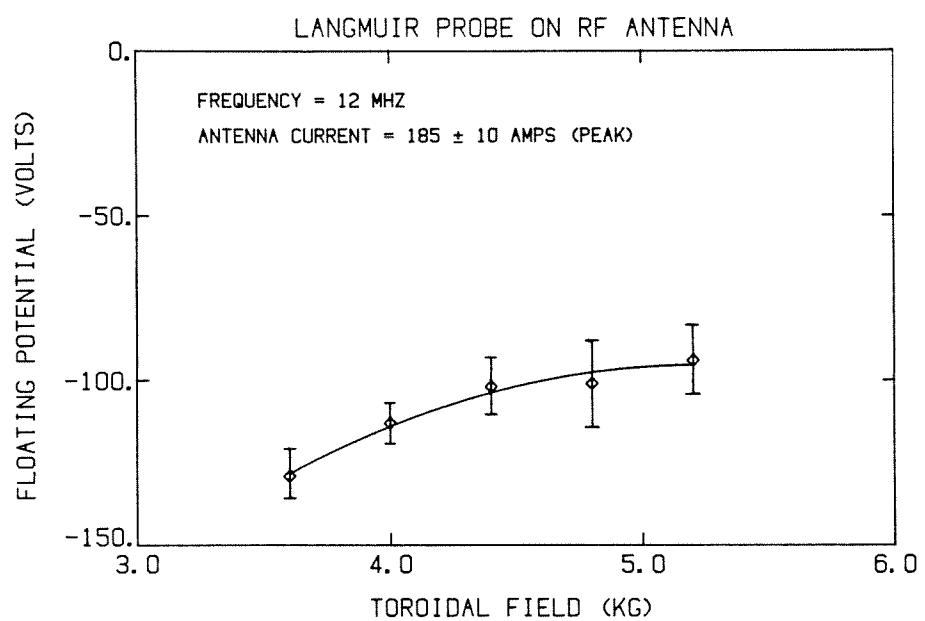

FIG. 6-51. Floating potential of the Langmuir probe on the side of the ceramic-insulated loop antenna, as a function of the toroidal magnetic field. The excitation frequency was 12 MHz, and the RF antenna current was ~185 A (peak). The leading edge of the ceramic box was 3.2 cm past the tokamak wall, and the data set was taken at a plasma mean density of $n \simeq 7.2 \times 10^{12}$ cm^{-3}.

antennas with the center current-carrying element exposed directly to the plasma (i.e., the bare loop, bare plate and "T" antennas) exhibited a large density-dependent loading loading resistance. The loading increased with plasma density for the bare loop antenna but decreased with density for the bare plate and "T" antennas; the magnitude of the resistance was typically $2-8\ \Omega$. In contrast, the dominant feature of the characteristic loading resistance of the ceramic-insulated loop antenna was a series of sharp peaks, as the density rose, which were typically $0.1-0.3\ \Omega$ in amplitude, or $2-3$ times the background resistance due to ohmic antenna losses. There was also a small continuous component of the loading which was roughly proportional to density, typically $0.05-0.10\ \Omega$ in amplitude. The input resistance of the Faraday-shielded loop antenna was similar in that the density-dependent loading was present, although somewhat smaller in magnitude (typically $<0.04\ \Omega$). The peaks on top of the background loading observed with the insulated antenna were also seen with the Faraday-shielded antenna but were of considerably smaller amplitude ($<0.05\ \Omega$).

The effect on the loading resistance of moving the antennas farther into the plasma (with the measurements made at constant mean density) was comparable to the effect of a density increase at a fixed antenna location. Thus moving the bare loop antenna farther past the tokamak wall increased the measured resistance; moving the bare plate or "T" antennas farther in decreased the resistance. For the ceramic-insulated and Faraday-shielded antennas, the magnitudes of both the loading resistance peaks and of the background continuous loading increased with density.

All of the antennas exhibited an increase in loading resistance as the excitation frequency increased; the increase was generally smaller than a factor of two as the frequency was doubled.

The loading resistance of the "T" antenna decreased by ~30% as the toroidal magnetic field was raised by a factor of two. None of the other antennas showed any significant change in impedance as the toroidal field was varied.

The bare loop and ceramic-insulated loop antennas showed no significant variation of loading resistance with antenna current. The bare plate and "T" antennas, however, exhibited a substantial increase in resistance as the current increased above a certain level.

The parametric dependence of the imaginary part of the antenna impedance was similar for the bare loop, bare plate, and "T" antennas. The antenna reactance decreased as the density increased or as the antenna was moved farther into the plasma; the decrease was typically 10−30% over the range of parameters measured. Similarly, these antennas all exhibited an increase in reactance as the excitation frequency was raised; the increase was typically 30−100% as the frequency was doubled. None of these three antennas showed any significant change in reactance as either the excitation current or the toroidal magnetic field were varied. The insulated and Faraday-shielded antennas showed no significant change in reactance at all, in the presence of the plasma.

The sharp, discrete peaks observed on the loading resistance of the insulated and shielded antennas have a different physical origin from the continuous density-dependent loading seen with the bare exposed antennas. As mentioned in Chapter 7, the sharp peaks coincide with the appearance of peaks in the RF magnetic fields observed globally around the tokamak (the toroidal eigenmodes). As discussed below, some features of the observed peaks in the loading can then be understood in terms of wave generation and damping.

Although the bare antennas also excite discrete eigenmodes, there is no continuous wave excitation corresponding to the density-dependent loading. It

is likely that the continuous density-dependent loading results not from wave excitation and subsequent damping but rather from particle collection effects in the immediate vicinity of the antenna.

6.4.2 Particle Collection Model

When a conductor is placed in the tokamak and biased with respect to the chamber wall, a space charge sheath forms around the electrode and, if the fluxes of electrons and ions collected by the electrode are unequal, a net current will flow. Simple Langmuir probe theory which describes the relation between the applied DC potential and the DC current drawn by the electrode was discussed earlier. This section models the bare plate and "T" antennas as Langmuir probes driven with periodic excitation.

At an electron temperature of 30 eV and a plasma density of 2×10^{12} cm^{-3}, the Debye length, a measure of the thickness of the space charge sheath surrounding the electrode, is very small ($\sim$0.03 mm). The thermal velocities are sufficient for even ions to traverse the sheath in a very small fraction of an RF period ($\tau_{RF}\sim$100 nsec). We then assume the steady state (DC) $I-V$ characteristic to be valid instantaneously during the periodic excitation. In addition to conduction (particle) current, displacement current can flow through the capacitance arising from charge separation across the sheath region. Simple estimates of the plasma sheath capacitance suggest that the resulting shunt reactance seen by the antenna is large compared to the experimentally observed impedance values; hence this sheath capacitance is probably not important in the frequency and plasma parameter region of interest.

For the purposes of this model, an analytical function was needed to fit the experimentally observed Langmuir probe $I-V$ curves. The function developed was

$$I_p(V_p) = \frac{neAU_i}{4}\left[\alpha e^{\frac{e(V_p - V_f + k_B T_e \ln\alpha)}{k_B T_e}} - 1\right] \qquad (V_p < 0) \qquad (6.14a)$$

$$I_p(V_p) = \frac{neAU_i}{4}\left[(2\alpha - 1) - \alpha e^{-\frac{e(V_p - V_f + k_B T_e \ln\alpha)}{k_B T_e}}\right] \qquad (V_p > 0), \qquad (6.14b)$$

where V_p and V_f are the probe potential and the floating potential, respectively, measured with reference to the tokamak wall, and I_p is the probe current (other symbols are defined in section 6.3). Here α is related to the ratio of electron (I_{se}) to ion (I_{si}) saturation currents by

$$\alpha = \frac{1}{2}\left[\frac{I_{se}}{I_{si}} + 1\right], \qquad (6.15)$$

and the experimental value for α is typically ~10. Once V_f and α are fixed (from the experimental probe traces), this functional form scales appropriately with temperature, density, and probe area and models well the curves of Figure 6-44.

If a sinusoidal voltage, $V_{RF}\cos(\omega t)$, is applied to the antenna electrode, the resulting current depends on the fashion in which the electrode is connected to the generator. Two cases are discussed here: the electrode is either grounded with respect to the chamber wall (by means of a low-pass filter) or is left floating (via an isolation capacitor). These cases correspond to the two operating modes of the bare plate and "T" antennas.

Figure 6-52 shows a typical Langmuir probe $I-V$ curve plotted from equation 6-14, with $T_e = 30$ eV, $n = 4\times10^{12}$ cm^{-3}, $A = 12$ cm^2, $\alpha = 10$ and $V_f = -20$ V. Also plotted is an example of the applied voltage for a grounded antenna, $V_p(t) = V_{RF}\cos(\omega t)$, and the resulting antenna current. The antenna current response is clearly non-sinusoidal, and there is a net DC time-averaged current flow.

If the electrode is allowed to float by removing all DC current paths to it, a

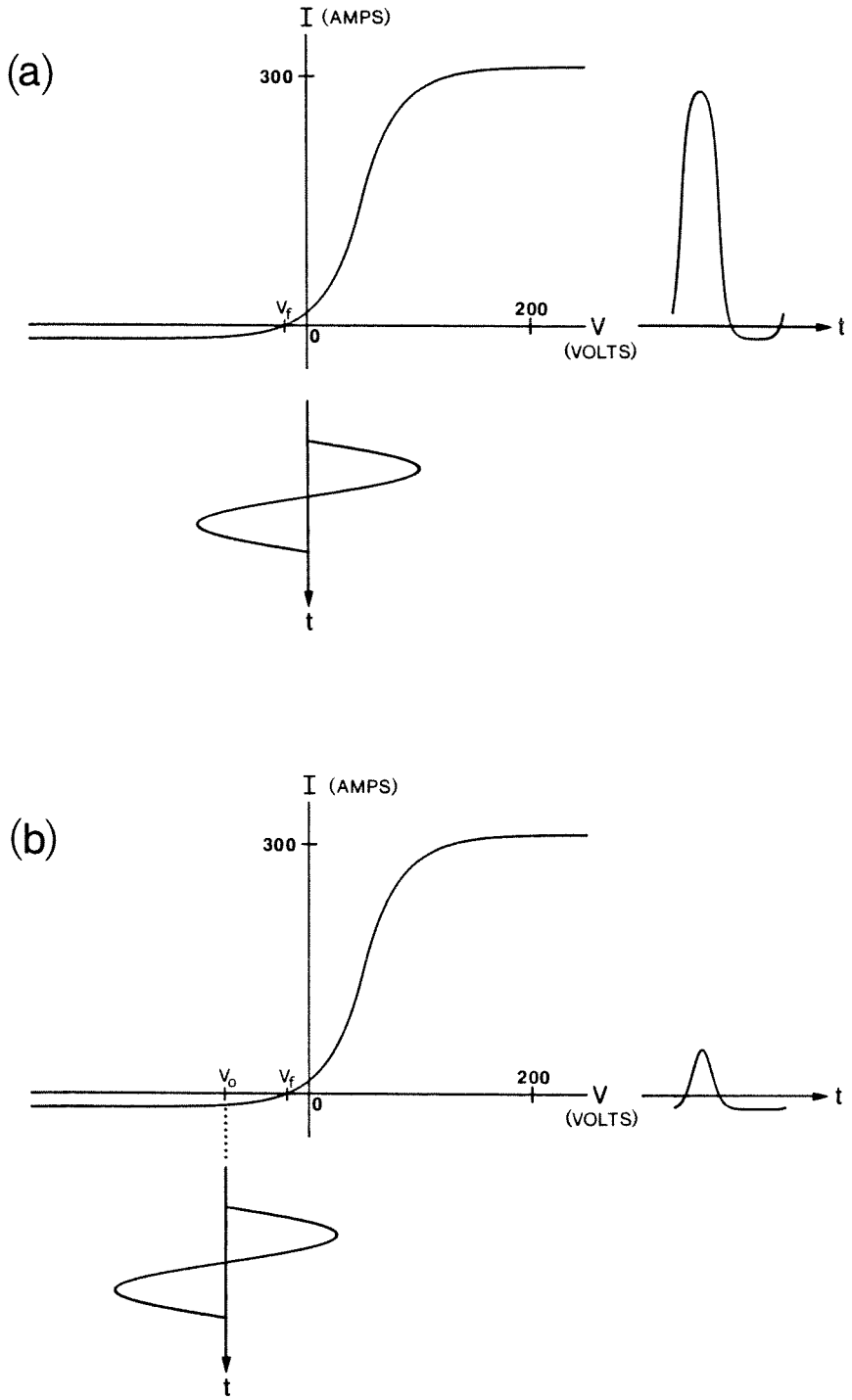

FIG. 6-52. Periodic excitation of a Langmuir probe. The static $I-V$ curve is shown together with one period of the imposed sinusoidal probe voltage (100 V peak) and the resulting current drawn by the probe. The $I-V$ curve is from equation 6-14, with $T_e = 30$ eV, $n = 4\times10^{12}$ cm^{-3}, $A = 12$ cm^2, and $V_f = -20$ V. a) Probe at DC ground potential. Note that the probe draws a net DC current. b) Probe floating. The probe charges to potential V_0 such that the DC component of the resulting current vanishes. Note that for the same excitation voltage, the peak current is reduced for the floating probe.

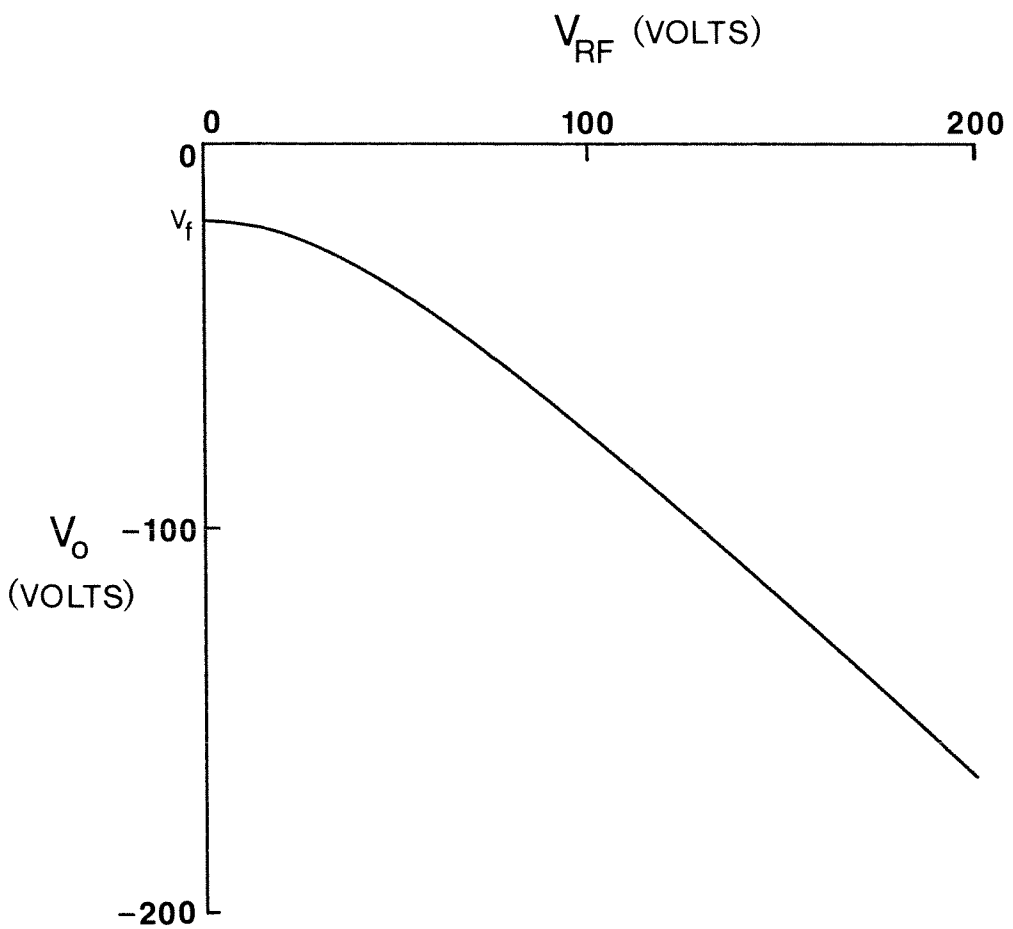

FIG. 6-53. The antenna bias potential, V_0, plotted as a function of the RF excitation amplitude, V_{RF}, for the $I-V$ curve shown in Figure 6-52.

charge will build up which shifts the operating point on the $I-V$ curve. The condition that the antenna float requires the integral of the current over one RF period to vanish. Figure 6-52b graphically illustrates this condition. The excitation voltage is the same as in Figure 6-52a, but the floating antenna charges up to a sufficiently negative potential that the areas under the positive and negative parts of the current waveform are equal. Note that this results in a substantially lower peak current as well. Mathematically, the condition describing a floating antenna can be written as

$$\int_0^\tau I_p\Big(V_0 + V_{RF}\cos(\omega t)\Big)\,dt = 0\,, \tag{6.16}$$

where V_0 is the bias potential resulting from charge buildup on the antenna, and τ is the RF period. The above integral equation can be solved numerically for the self-charging bias potential, V_0, as a function of the excitation amplitude, V_{RF}. As an example, for the $I-V$ curve in Figure 6-52, a plot of V_0 vs. V_{RF} is shown in Figure 6-53. Note that when the excitation voltage vanishes, the bias voltage is simply the DC floating potential, V_f.

The DC bias potential of the bare plate or "T" antenna during RF excitation was not directly measured experimentally. A related experiment, however, was performed with the ceramic-insulated loop antenna, as described in section 6.3.2. In the absence of RF excitation, the surface of an insulator will also charge up to the DC plasma floating potential, since the time-averaged current to it must vanish. When the loop is excited with an RF current, an RF potential exists between the loop and the tokamak wall due to the finite inductance of the loop; the magnitude of the potential varies with location around the loop. Although the Macor ceramic was 3 mm thick, displacement current could still flow through the resulting capacitance and into the plasma, resulting in the potential of the surface of the ceramic being driven at the RF frequency. Thus, in some respects, this situation is the same as a floating bare plate or "T"

antenna.

The potential near the surface of the ceramic on the side of the loop antenna was investigated with a floating Langmuir probe. The relation between the measured probe potential and the RF excitation current in the loop is shown in Figure 6-50. Note the similarity between the form of the curve and the theoretical calculation shown in Figure 6-53. A strict comparison cannot be made, however, for several reasons. The Langmuir probe axis was 2 mm from the Macor, so the potential seen by the probe was not necessarily the same as that at the surface of the ceramic. Both capacitive coupling between the loop element and the probe, and particle currents between the probe and the plasma and between the probe and the ceramic surface contribute to the potential measured by the probe. Further, the relation between the antenna excitation current and the potential developed on the outside of the ceramic is not linear. Since the impedance presented by the capacitance due to the ceramic is substantially higher than that presented by the plasma or by the loop itself, the insulator acts as a voltage divider, and the potential on the plasma-side of the ceramic should be proportional to the plasma impedance (which changes with excitation level).

Bare Plate and "T" Antenna Impedance

The simple model of the bare plate and "T" antennas as driven Langmuir probes can be used to find the expected antenna RF impedance. The actual impedance experiments measured the ***fundamental*** components of the RF voltage and current, and the phase between them. The current response, I_p, to a periodic voltage excitation, $V_{RF}\cos(\omega t)$, will, of course, have harmonic components; these are eliminated in the experiment using bandpass filters. The fundamental component of the impedance due to particle collection by the antenna is then simply the excitation voltage divided by the fundamental com-

ponent of the current:

$$Z(V_{RF}) = \frac{V_{RF}}{\frac{2\omega}{\pi}\int_0^{\frac{\pi}{\omega}} I_p\Big(V_0 + V_{RF}\cos(\omega t)\Big)\cos(\omega t)\,dt}\,, \qquad (6.17)$$

where V_0 is given as a function of V_{RF} by the solution of equation 6.16 for a floating antenna, or $V_0 = 0$ for a grounded antenna. Note that this impedance is purely real, i.e., a resistance. An inductive component of the impedance in series with this real part arises due to the geometry of the return current path between the electrode and the tokamak wall. This will not be considered theoretically, but evidence that the current leaving these antennas is spatially localized along the toroidal field lines is presented in Chapter 7.

Since the current I_p is linearly proportional to plasma density, the RF impedance given by equation 6.17 should vary inversely with density. The variation of the real part of the impedance of the "T" antenna with plasma line-averaged density is shown in Figure 6-54. The solid line is a least-squares fit to a $1/n$ density dependence. The agreement is reasonable, considering that the average density measured by the microwave interferometer does not strictly track the density in the outer plasma where the antenna is located. Note also that this model neglects possible temperature effects due to cooling of the plasma during the gas puff or due to heating of the plasma by the RF fields.

The qualitative behavior of the impedance as the bare plate antenna is rotated from a parallel to a perpendicular orientation can be understood in terms of this model. From equation 6.14, the current I_p is proportional to the antenna electrode area. In a strong magnetic field the plasma particles, to first order, stream along the field lines. Then, since the ion gyro-radius ($\rho_i \sim 1$ mm) is much smaller than the antenna dimensions, the area that enters into equation 6.14 is the projected area perpendicular to the field direction. Reducing this area by rotating the antenna then has the same effect as

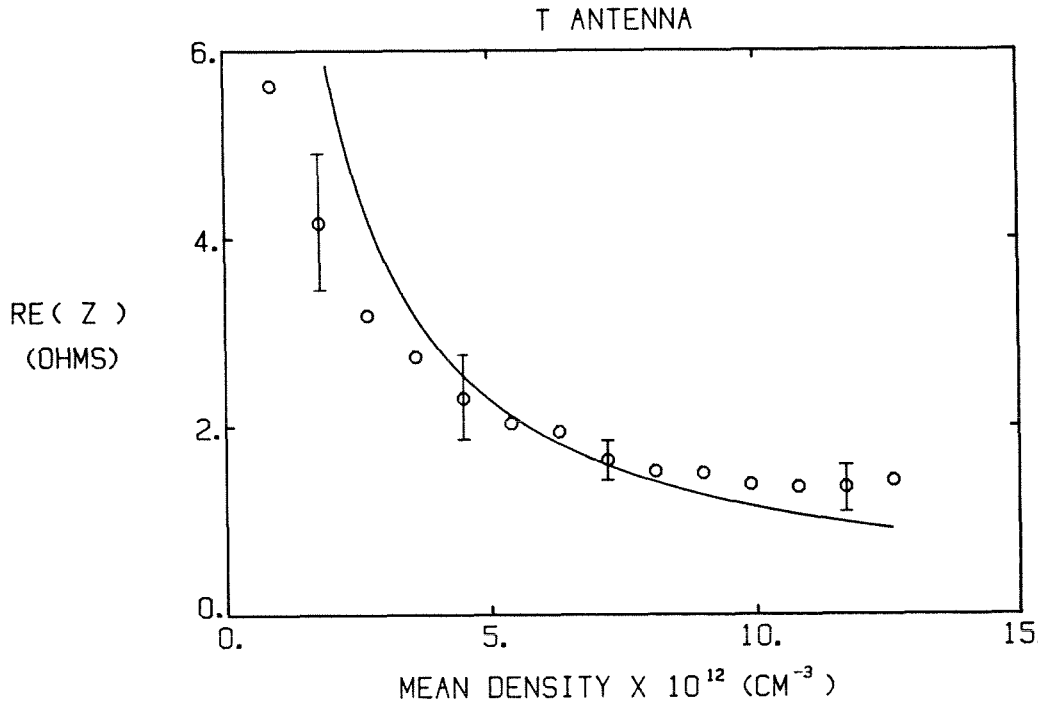

FIG. 6-54. Variation of the real part of the impedance of the "T" antenna as a function of the mean (line-averaged) plasma density. The experimental points are from the data of Figure 6-29; the solid line is a least-squares fit to a $1/n$ density dependence.

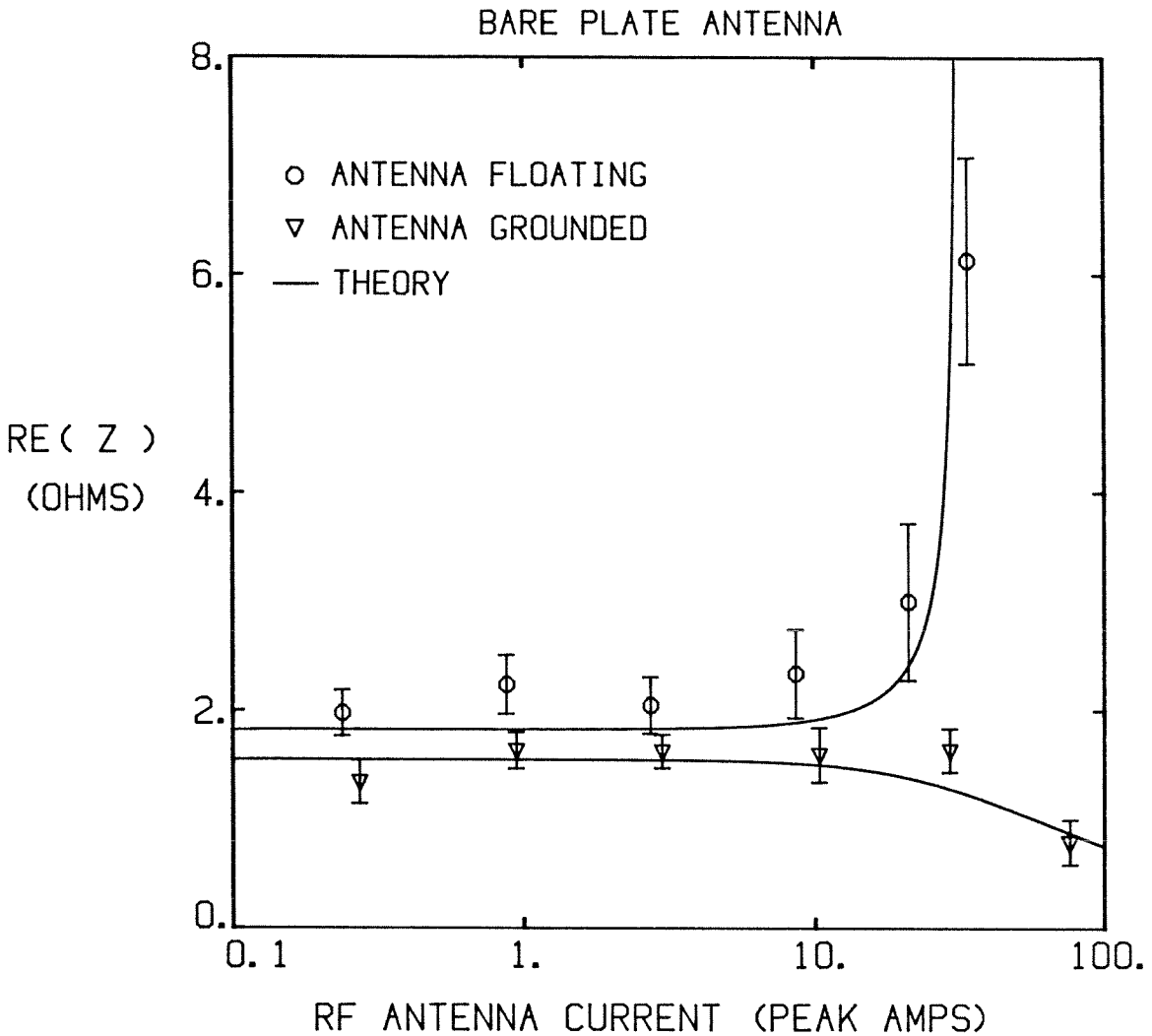

FIG. 6-55. Variation of the real part of the bare plate antenna impedance as a function of the antenna excitation current, for both floating and grounded configurations. The experimental points are from Figure 6-25; the solid lines are the results calculated from equation 6.17, with $n = 4 \times 10^{12}$ cm^{-3}, $T_e = 30$ eV, $A = 12$ cm^2, and $V_f = -5$ V.

lowering the density: the antenna current decreases and hence the impedance increases. This effect was confirmed by the experiment illustrated in Figure 6-20. The impedance of both the floating and grounded antennas increases substantially for the orientation where the projected antenna area is much smaller.

A more severe test of the model involves the predicted dependence of the impedance on the excitation amplitude. The real part of the impedance of the bare plate antenna is plotted as a function of the fundamental component of the antenna excitation current in Figure 6-55 for both grounded and floating antennas. The leading edge of the plate was 3.8 cm past the tokamak wall. A reasonable density to assume, based on Langmuir probe profiles, was $n \sim 4 \times 10^{12}\ \mathrm{cm}^{-3}$; the temperature at this location was typically $\sim$30 eV. Using these values and an effective antenna area of $12\ \mathrm{cm}^2$, the impedance was calulated from equation 6-17 and is also plotted in the figure. Note that the horizontal axis of the plot is the fundamental component of the excitation current rather than the excitation voltage. The agreement between the theoretical curves and the experimental results is rather good, especially considering the simplicity of the model and the uncertainties in establishing the various parameters. It should be noted that the lower curve, for the grounded antenna, eventually turns up sharply as the current is raised further. This follows intuitively, since for very large excitation voltages, the current approaches saturation both on the positive and negative excursions and hence the impedance must increase as the voltage is raised further. Note again that this model does not consider possible heating of the local or bulk plasma at high excitation current levels. Some evidence that the plasma actually is heated is seen in Figure 6-47b, where the slope of the transition region of the $I-V$ curve is considerably smaller than for the case without RF power.

Bare Loop Antenna Impedance

The simple particle collection model appears to account reasonably well for some of the observed impedance characteristics of the bare plate and "T" antennas. The impedance of the bare loop antenna, however, has the opposite behavior with respect to plasma density and antenna insertion. Because of the loop inductance, the potential of the antenna varies around the loop. Each point on the loop which is in contact with the plasma will draw a particle current which depends on the density at that point and the potential of that point with respect to the wall. A very simple model of the loop antenna which nevertheless proves useful is shown in Figure 6-56. Rather than considering the more difficult distributed-impedance problem, the effect of the plasma is lumped into a real impedance Z_p which shunts the loop at its midpoint. L_A is the loop inductance and L_f is the stray inductance representing that part of the loop not in the plasma. The input impedance of the antenna is then given by

$$Z_{ant} = \frac{\omega^2 L_A{}^2 Z_p}{4\left[Z_p^2 + \left[\frac{\omega L_A}{2}\right]^2\right]} + i\left[\frac{\omega L_A}{2} + \frac{\omega L_A Z_p^2}{2\left[Z_p^2 + \left[\frac{\omega L_A}{2}\right]^2\right]}\right]. \qquad (6.18)$$

It is clear from the circuit model that the real part of the antenna impedance has a maximum for a particular value of the plasma shunt impedance, Z_p. When the shunt impedance is very small (at high plasma density), most of the current flows through it and the input impedance is small. When the shunt impedance is very large (at low plasma density), most of the current flows through the inductance which is in parallel with Z_p, and since the inductor is lossless, the input impedance is still small. The maximum of $\mathrm{Re}(Z_{ant})$ occurs when $Z_p = \omega L_A / 2$ and has the value $\omega L_A / 4$.

The model was applied to the experimental impedance data for the bare loop antenna. The antenna loop inductance was approximated, from its

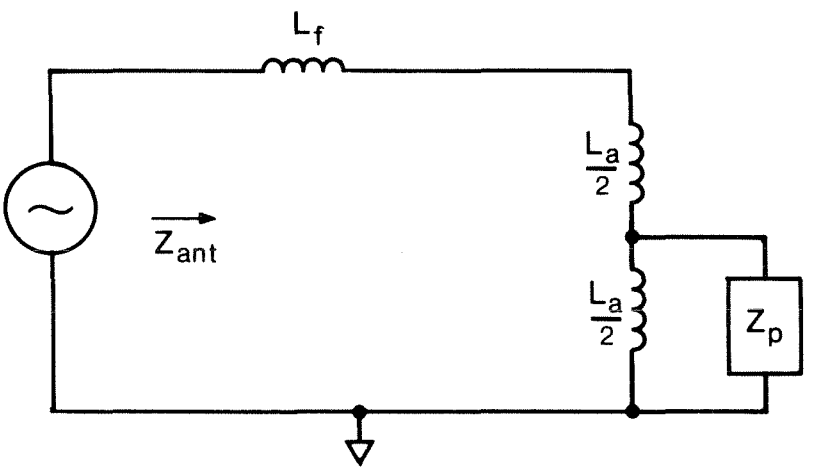

FIG. 6-56. Simple equivalent circuit model for calculation of the impedance of the bare loop antenna. Z_p represents the plasma impedance, L_A is the loop inductance, and L_f is the distributed stray inductance.

geometry, as 80 nH. The plasma shunt impedance, from the previous discussion, was taken to be inversely proportional to the plasma density: $Z_p = \eta / n$, where η is a constant. The shunt impedance arises from the parallel contributions of the distributed impedance along the loop and is dominated by the impedance of that part of the loop in the region of highest density plasma, i.e., the front or leading part of the loop. Since the height of the loop and the length of the cross-bar of the "T" antenna were comparable, a reasonable value for the constant η was taken from the impedance data of the "T" antenna: $\eta \sim 1.4 \times 10^{13}\ \Omega\text{-cm}^{-3}$. Taking the value of the stray inductance to be $L_f = 75$ nH, the results from equation 6-18 for the real and imaginary parts of the antenna impedance are plotted in Figure 6-57; the experimental points are from the data of Figure 6-11.

The reasonable agreement between the theoretical curves and the experimental data supports the hypothesis that the impedance of bare loop antenna is dominated by a shunting of the loop reactance due to plasma particle collection.

6.4.3 Impedance Due to Eigenmodes

The input loading resistance of the ceramic-insulated loop antenna was dominated by a series of sharp peaks associated with eigenmode excitation. Such peaks were first observed on the TO-1 tokamak in Moscow [Ivanov, 1973] and on the ST tokamak at Princeton [Adam et al., 1974] and have since been seen in a number of other experiments.

The peaks on the impedance are a direct result of the damping of waves in the high-Q toroidal cavity. As discussed in Chapter 2, the fast waves excited in the frequency and plasma parameter range of concern are only weakly damped; interference effects of waves traveling around the torus in both directions leads to a spectrum of discrete cavity resonances at which the wave

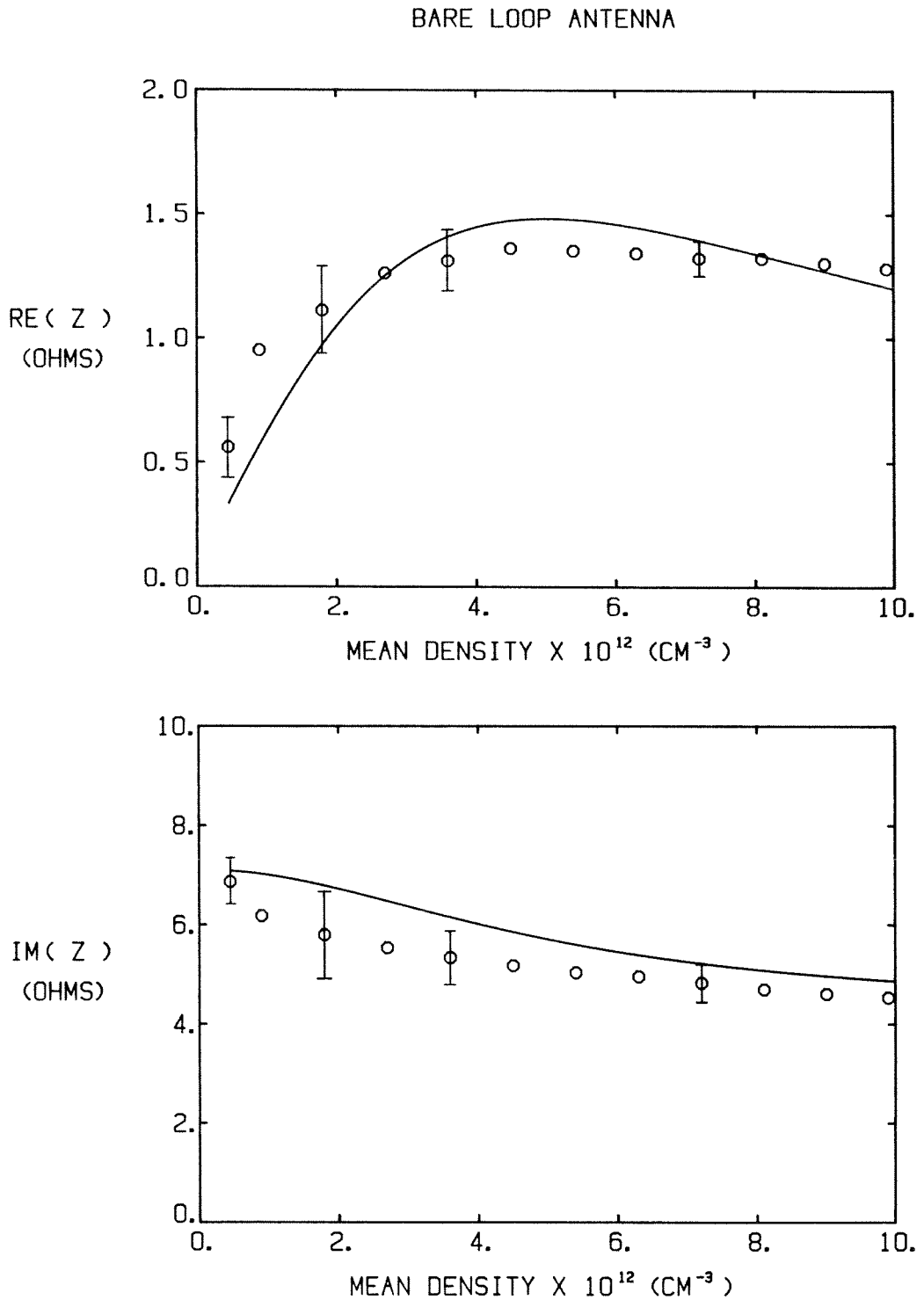

FIG. 6-57. Real and imaginary components of the impedance of the bare loop antenna, as a function of the mean plasma density. The experimental points are from the data of Figure 6-11; the solid lines are the results of the theoretical model described by equation 6.18.

fields can build up to large amplitudes. The input impedance of the antenna can be written as the ratio of the power dissipated by the antenna to the square of the antenna current:

$$Z_{ant} = \frac{1}{I_{ant}{}^2} \int \mathbf{E}_s \cdot \mathbf{J}_s \, dS \,, \tag{6.19}$$

where I_{ant} is the antenna current, $\mathbf{E}_s$ and $\mathbf{J}_s$ are the electric field and current on the surface of the antenna loop element, and the integral is taken over the loop. For a given antenna current, the lower the damping in the cavity, the higher will be the amplitude of the wave electric field throughout the cavity (at a resonance), and, in particular, the higher will be the back-EMF at the antenna loop itself. Thus, *lower* damping in the cavity leads to *higher* input loading resistance at the resonances. Stix [1975] has shown that the loading resistance is $2/\alpha$ times higher in the periodic-cylinder model than it would be for an infinite cylinder with no interference effects, where $e^{-\alpha}$ is the attenuation the wave suffers in traveling a length equal to the circumference of the tokamak.

The discussion in Chapter 2 treated the boundary value problem without external sources and solved for the normal modes of the system. To solve the problem including the RF antenna requires solutions of Maxwell's equations with the appropriate source terms. In order for the fields to remain finite at the resonances, appropriate wave damping must be included. The fields in the cavity can be written as a summation over all of the eigenmode solutions of the corresponding source-free problem. The coefficients of the individual terms can then be found in principal by imposing the boundary conditions on the conducting wall and on the antenna element. For high-Q, well separated eigenmodes, the situation can be simplified somewhat. When the excitation frequency is near a resonant frequency for a particular eigenmode, the amplitude of the resonant term dominates the response, and contributions from the

other modes can be neglected. Paoloni [1975a] has carried out a perturbation expansion about the eigenmodes and arrives at a simple expression for the input impedance of a loop antenna when the excitation frequency is equal to the resonant frequency for an eigenmode:

$$Z_{ant} = \frac{Q\,\omega\,\Phi^2}{2\,W}, \tag{6.20}$$

where W is the total time-averaged wave energy for the mode and Φ is the eigenmode flux linked by the loop. Here W and Φ are evaluated using the source-free dissipationless field solutions, and Q is defined, as before, as the ratio of the time-averaged wave energy to the energy dissipated in one wave period for the particular mode. Thus the magnitude of the antenna resistance at an eigenmode is directly proportional to the Q of that mode. Note that the term $\frac{\Phi^2}{2W}$ does not depend on the magnitude of the field, but only on the radial form of the field and on the antenna geometry.

The reason for the increase in loading at the peaks of the modes as the antenna is moved into the plasma (Figure 6-37) is now apparent. As the antenna moves in, Φ increases because more of the loop is past the wall and because the magnitude of the component of the wave field which links the loop, B_z, is a decreasing function of minor radius in the outer plasma for the modes of interest (cf. Figure 2-10).

The variation of the antenna loading at the eigenmode peaks as a function of the excitation frequency, toroidal magnetic field, or mode number is more difficult to analyze because Q and W are no longer constant. The term $\frac{\Phi^2}{2W}$ was calculated for the $N=0-5$, $m=1$, $l=1$ toroidal eigenmodes as a function of $\Omega \equiv \omega/\omega_{ci}$ using the periodic-cylinder, constant-density, zero-electron mass model described in Chapter 2. The flux Φ was calculated by integrating the z-component of the wave magnetic field over the area inclosed by a polygon

approximation to the loop boundary; the front edge of the loop was taken to be 2.5 cm past the tokamak wall. The results are plotted in Figure 6-58. For $\Omega \lesssim 2.3$, the value of $\frac{\Phi^2}{2W}$ decreases with increasing toroidal mode number; the term decreases with Ω for $N = 0, 1, 2$ and varies little with Ω for $N = 3, 4, 5$.

In order to calculate the input loading resistance, the Qs of the modes must be known. As is discussed in the following chapter, the theoretical calculations for the mode Qs which were presented in Chapter 2 do *not* correctly predict the observed values; the theoretical values are generally too high. Estimates of the mode Qs based on wave field measurements are presented in the following chapter. Drawing on those results in advance, the expected antenna impedance can be calculated as a function of the mode number. Table 6-1 presents the theoretical and experimental data for the first five modes encountered as the density rises, for a toroidal field of 4.0 kG. Specifically, the experimental value of Q and the theoretical evaluation of $\frac{\Phi^2}{2W}$ are used in equation 6.20 to calculate the predicted antenna eigenmode impedance. Except for the first mode, the results agree within a factor of about 50%, with the predicted value being consistently lower than the observed result. The agreement, except for the first mode, is reasonable considering the large scatter in the data for the Qs and for the antenna impedance. Phase measurements also presented in Chapter 7 confirm, as expected from the discussion of Chapter 2, that the observed eigenmodes are $m = 1$ modes of successively increasing toroidal mode number. The toroidal mode numbers were not identified absolutely, however, so the assumption in the table that the first observed mode was an $N = 0$ mode may be incorrect. However, even if the first observed mode were an $N = 1$ or $N = 2$ mode, the change in the values for $\frac{\Phi^2}{2W}$ and hence the change in the predicted impedance would be relatively small.

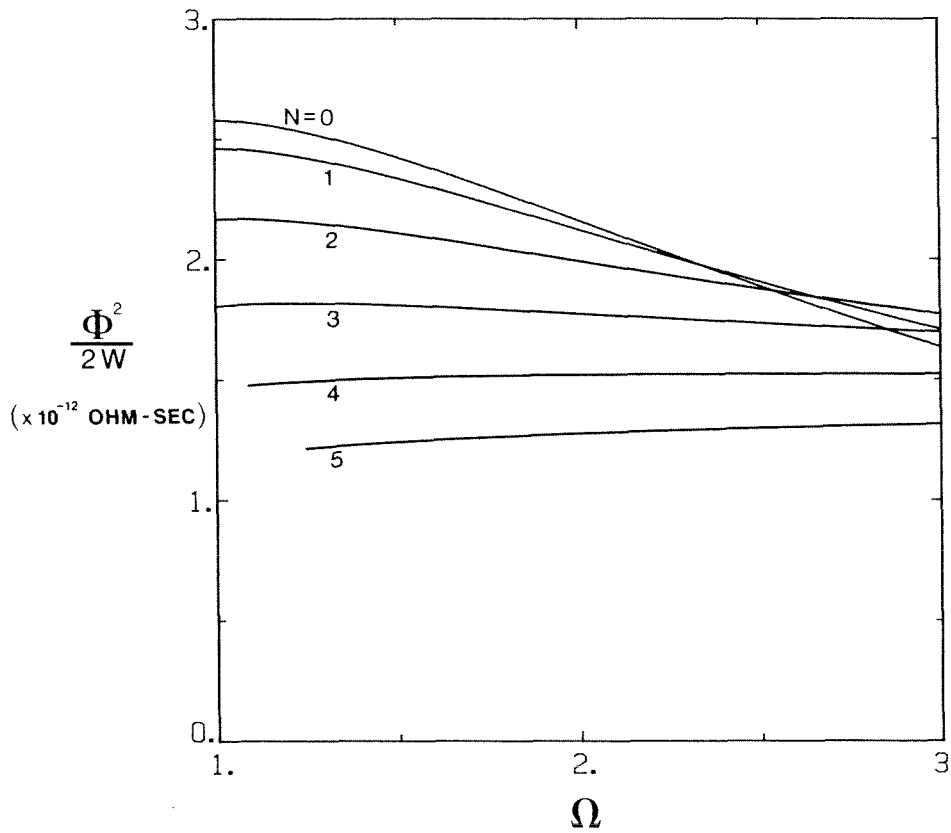

FIG. 6-58. Calculation of the quantity $\Phi^2/(2W)$ as a function of $\Omega = \omega/\omega_{ci}$ for the $N = 0 - 5$, $m = 1$, $l = 1$ toroidal eigenmodes. The wave fields and wave energy W are found from the zero-electron mass, constant-density model described in Chapter 2; the flux Φ is found by integrating the z-component of the magnetic field over the area inclosed by the loop antenna. The front edge of the loop is 2.5 cm past the tokamak wall and its boundary is approximated by a polygon.

Antenna Loading due to Eigenmodes					
Mode Order	N	Q	$\Phi^2/(2W)$ ($\times 10^{-12}$ ohm-sec)	Re(Z_{ant}) (milliohms)	Re(Z_{ant}) (milliohms)
(observed)	(assumed)	(observed)	(calculated)	(calculated)	(observed)
1	0	27	2.17	4.	19.
2	1	155	2.13	25.	43.
3	2	309	1.99	46.	70.
4	3	537	1.77	72.	91.
5	4	891	1.51	101.	134.

TABLE 6-1. Comparison of expected values (from equation 6.20) and observed values (from Figure 6-39) of the real part of the insulated loop antenna impedance at the eigenmode peaks. Here Q is taken from the data presented in Chapter 7 and $\Phi^2/(2W)$ is calculated from the wave model of Chapter 2. The column labeled "Mode" lists the order of the observed eigenmodes, and N is the assumed toroidal mode number associated with each mode. Also, $\omega/(2\pi) = 12$ MHz, $B_0 = 4.0$ kG, and the front edge of the loop is taken to be 2.5 cm past the tokamak wall. Note that the background loading due to ohmic losses in the antenna has been subtracted from the observed values for Re(Z_{ant}).

CHAPTER 7

Wave Experiments

Waves associated with toroidal eigenmodes in a tokamak plasma were first observed in the TM-1-Vch and TO-1 tokamaks at the Kurchatov Institute [Ivanov et al., 1971; Vdovin et al., 1971] and have since been seen in a variety of other machines. The most detailed investigations were carried out on the ST and ATC tokamaks at Princeton [Adam et al., 1974; Takahashi, 1979], on the T.F.R. tokamak at Fountenay-aux-Roses [T.F.R. Group, 1977] and on the Erasmus tokamak in Brussels [Messiaen et al., 1978]. In several experiments, the spectrum of the modes in density-frequency space was mapped out, and mode identification was carried out in some cases using phase measurements of the wave magnetic fields at the plasma edge.

Toroidal eigenmodes were first observed in the Caltech Research Tokamak by Hwang [1979] who characterized the general location of the modes in density-frequency space. Mode identification was not carried out, however, as the major emphasis of the work involved complex antenna impedance measurements.

This chapter presents the results of a series of experiments designed to investigate the waves launched in the Caltech tokamak, using the RF antennas and magnetic probes previously described. The chapter is divided into three main sections. The first reports observations of the magnetic fields associated with the toroidal eigenmodes. The most surprising result is that the all of the antennas, including the bare plate, bare loop, and "T" antennas, excited the

eigenmodes with comparable efficiency in terms of wave amplitude normalized to the antenna current. Eigenmode dispersion curves were mapped out by tracking the density at which various modes occurred as the magnetic field was incremented. Probes which were separated toroidally and poloidally were used to estimate the mode structure of the waves, and radial profiles of the fields were obtained as well. Finally, the wave field amplitude evolution was analyzed for the various modes to obtain estimates of the cavity Q and the damping length for each mode as a function of the toroidal magnetic field.

The second section of this chapter describes a new approach to the investigation of ICRF waves propagating in a tokamak. The antennas were excited with very short bursts (4-5 cycles) of RF current, generating waves on a time scale short compared to the formation time for the eigenmodes. The wave packets thus launched by the antenna were observed with the magnetic field probes and could be seen to propagate several times around the machine. The time delay between the peaks of the excitation and received signal envelopes gave direct information about the group velocity of the waves in the toroidal direction. The group velocity was investigated as a function of a variety of plasma parameters for comparison with theoretical models. Both the ceramic-insulated loop antenna and the "T" electric field antenna were used in these experiments and yielded similar results.

The last section of this chapter presents an investigation of the RF current density distribution in the outer tokamak plasma near a very small electric field antenna, using the RF current probe discussed earlier (section 5.5). The experiment apparently represents the first direct measurement of RF particle current in a plasma. The current leaving the antenna was found to be quite localized along the toroidal field direction; the result suggests a mechanism for the good coupling to eigenmodes observed with the electric field antennas.

7.1 Eigenmode Observations

The experimental configuration of the tokamak and RF system was basically the same as that described for the impedance measurement experiments (section 6.1). The wave fields were detected with the magnetic probes detailed in section 5.3. The probes were mounted on various tokamak ports as necessary for the particular experiment; up to four probes could be used simultaneously. Each probe was connected to a 50 Ω attenuator and a +30 db broadband RF amplifier. The output of each amplifier led to a power splitter, one output of which led to a linear RF detector and the other to an input of the four-channel phase detector. The reference input of the phase detector could be connected to any of the probe signals but was usually used with the antenna current signal. The outputs of the amplitude and phase detectors were recorded with the data system described previously (section 3.4). In many experiments, the antenna impedance was monitored simultaneously, as described in section 6.1, both as an aid in tuning the matching system and to observe the relation between the eigenmode wave field peaks and the peaks on the antenna loading resistance. Impedance information was also required for the Q measurements in order to convert the measured (loaded) Q to the unloaded cavity Q.

The loop antennas were always positioned so that the plane of the loop was normal to the toroidal direction. This orientation was chosen in part because the toroidal component of the magnetic field associated with the eigenmodes was the largest component of the field near the wall where the antenna had to be positioned, and it was desirable to maximize the eigenmode flux linked by the loop in order to increase the coupling efficiency. The bare plate and "T" antennas, however, could be rotated throughout a full 360° range.

7.1.1 Typical Probe Data

An example of the magnitude of the signal from a magnetic probe is plotted in Figure 7-1, along with the plasma density derived from the microwave interferometer signal. The ceramic-insulated loop antenna was used, the front edge of the antenna was 3.2 cm past the tokamak wall, the excitation frequency was 8.5 MHz, and the toroidal magnetic field on axis was 3.8 kG; hence $\omega/\omega_{ci} \simeq 1.5$ at the plasma center. The coil axis of the probe was located 2.0 cm past the wall, in tokamak port #1 (180° toroidally away from the RF antenna), and the orientation of the coil was such as to measure the toroidal component of the wave magnetic field. Four eigenmodes are clearly visible during the density rise; the same modes can also be seen during the density fall. Several qualitative features can be seen from this plot. The eigenmodes occur at approximately the same density during the rising and falling portions of the density curve; this implies that they are in fact the same modes. The amplitudes of the modes increase as the density increases; also the amplitudes of the modes during the density fall are smaller than those occurring during the density rise. The density rises and falls approximately linearly with time, and it is clear that the temporal width of the resonances decreases as the density rises. From shot to shot there was considerable variation in the amplitude of each mode, but the general features described above were characteristic. In many cases, the density fall was much more abrupt than the rise, and the modes occurring during the fall were not easily identifiable.

A surprising result of this investigation was that *all* of the RF antennas were capable of exciting eigenmodes, including the bare plate and "T" antennas. In previous work at other laboratories, only loop antennas of various sorts have been used to excite ICRF waves.

Typical probe signals for the various RF antennas are shown in Figures 7-2, 7-3, and 7-4, for excitation frequencies of 8.5, 12, and 16 MHz, respectively.

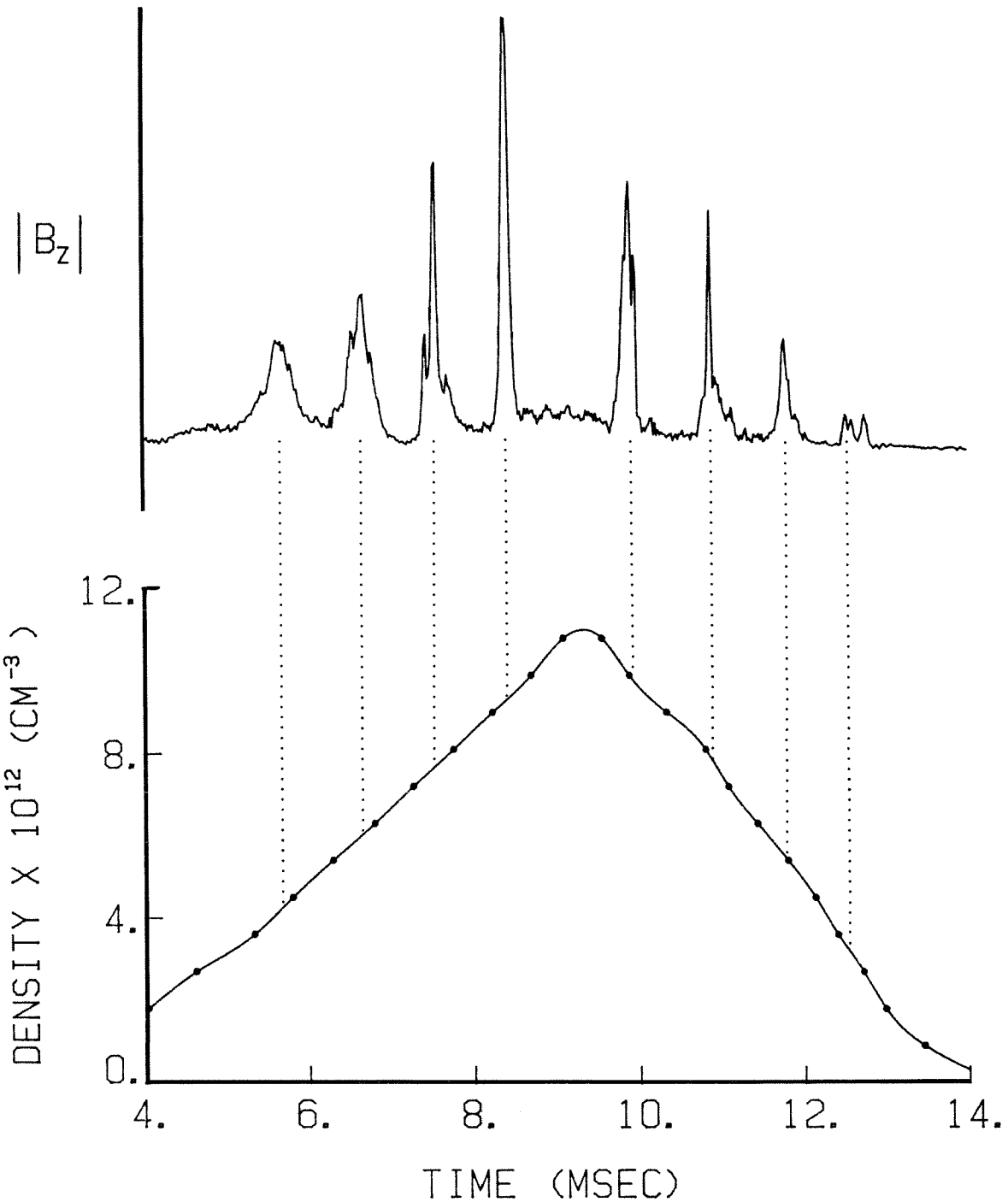

FIG. 7-1. Magnitude of the toroidal component of the wave magnetic field for a typical tokamak shot, as measured with a magnetic probe, and the density evolution following the gas puff. The ceramic-insulated loop antenna was excited at a frequency of 8.5 MHz and the static toroidal magnetic field on axis was 3.8 kG. The magnetic probe was located 180° toroidally away from the RF antenna and the axis of the probe coil was 2.0 cm past the wall. The four modes observed during the density rise occur at approximately the same densities as those seen during the density fall.

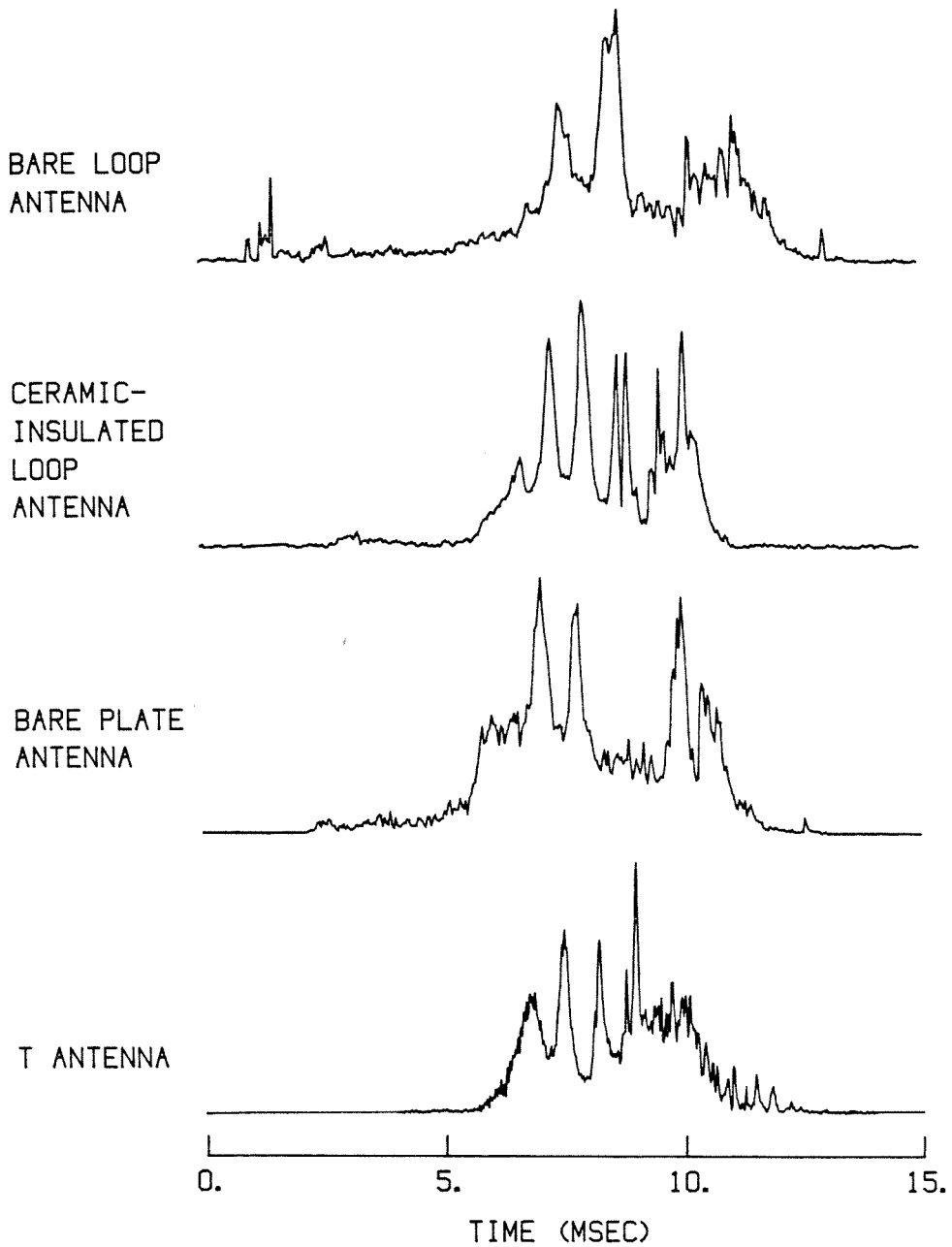

FIG. 7-2. Typical magnetic probe signal amplitudes for the bare loop, ceramic-insulated loop, bare plate, and "T" antennas. The excitation frequency was 8.5 MHz and the static magnetic field on axis was 4.0 kG (hence $\omega/\omega_{ci} \simeq 1.4$ at the plasma center). The probe, oriented to measure the toroidal component of the wave magnetic field, was located in tokamak port #2, 180° toroidally and 90° poloidally away from the RF antenna. The density evolution and peak density were different for each shot.

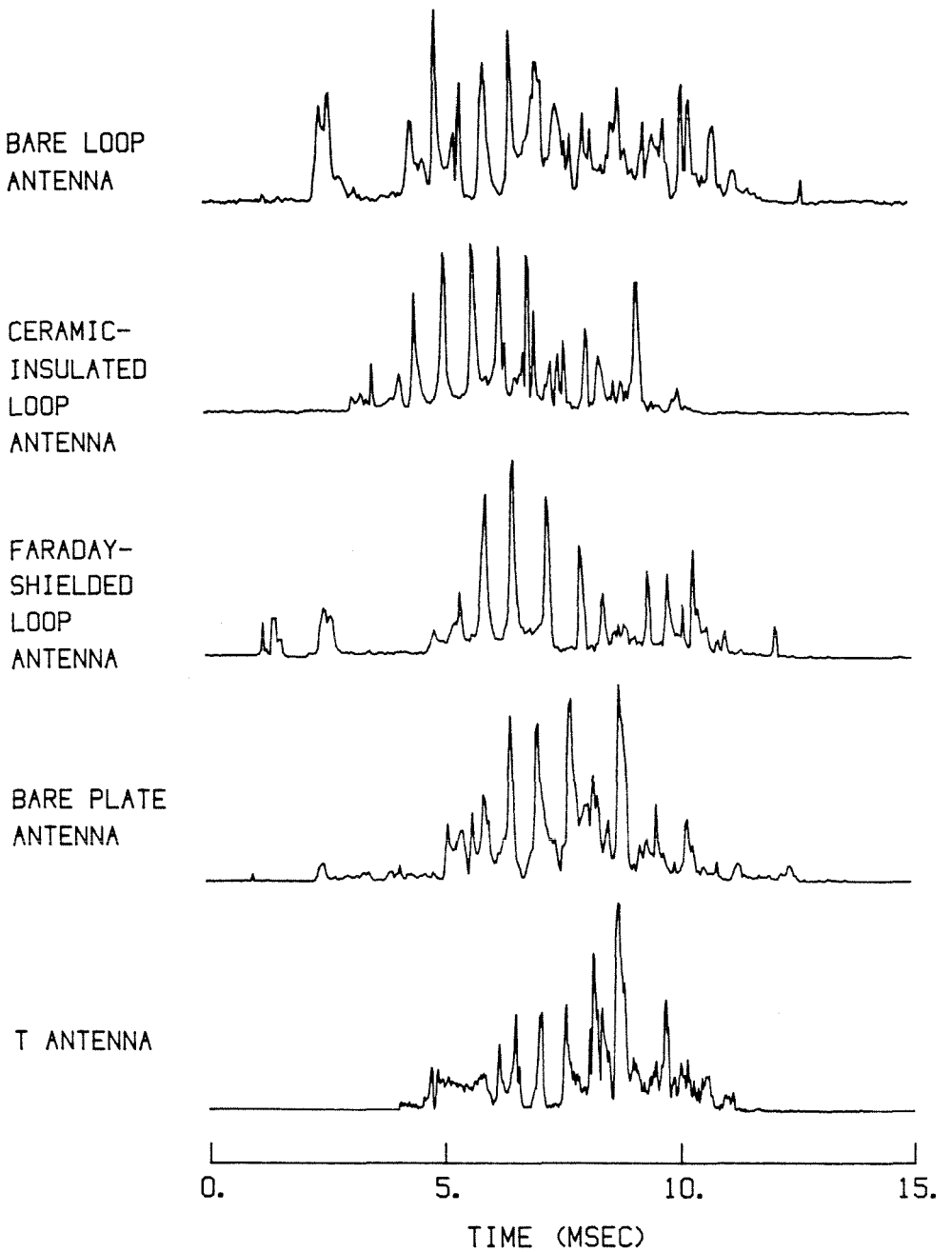

FIG. 7-3. Typical magnetic probe signal amplitudes for the bare loop, ceramic-insulated loop, Faraday-shielded loop, bare plate, and "T" antennas. The excitation frequency was 12. MHz and the static magnetic field on axis was 4.0 kG (hence $\omega/\omega_{ci} \simeq 2.0$ at the plasma center). The probe, oriented to measure the toroidal component of the wave magnetic field, was located in tokamak port #2, 180° toroidally and 90° poloidally away from the RF antenna. The density evolution and peak density were different for each shot.

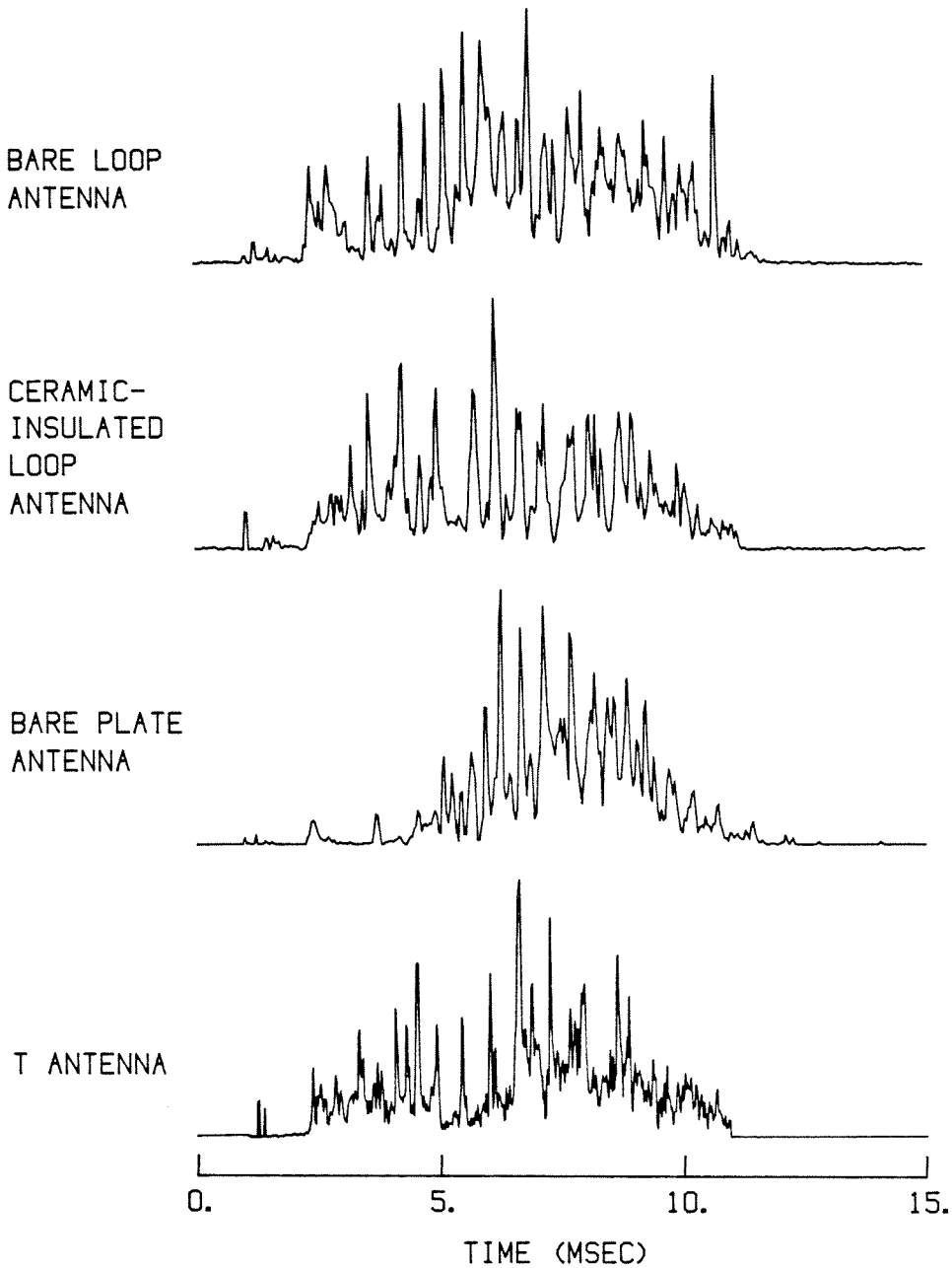

FIG. 7-4. Typical magnetic probe signal amplitudes for the bare loop, ceramic-insulated loop, bare plate, and "T" antennas. The excitation frequency was 16. MHz and the static magnetic field on axis was 4.0 kG (hence $\omega/\omega_{ci} \simeq 2.6$ at the plasma center). The probe, oriented to measure the toroidal component of the wave magnetic field, was located in tokamak port #2, 180° toroidally and 90° poloidally away from the RF antenna. The density evolution and peak density were different for each shot.

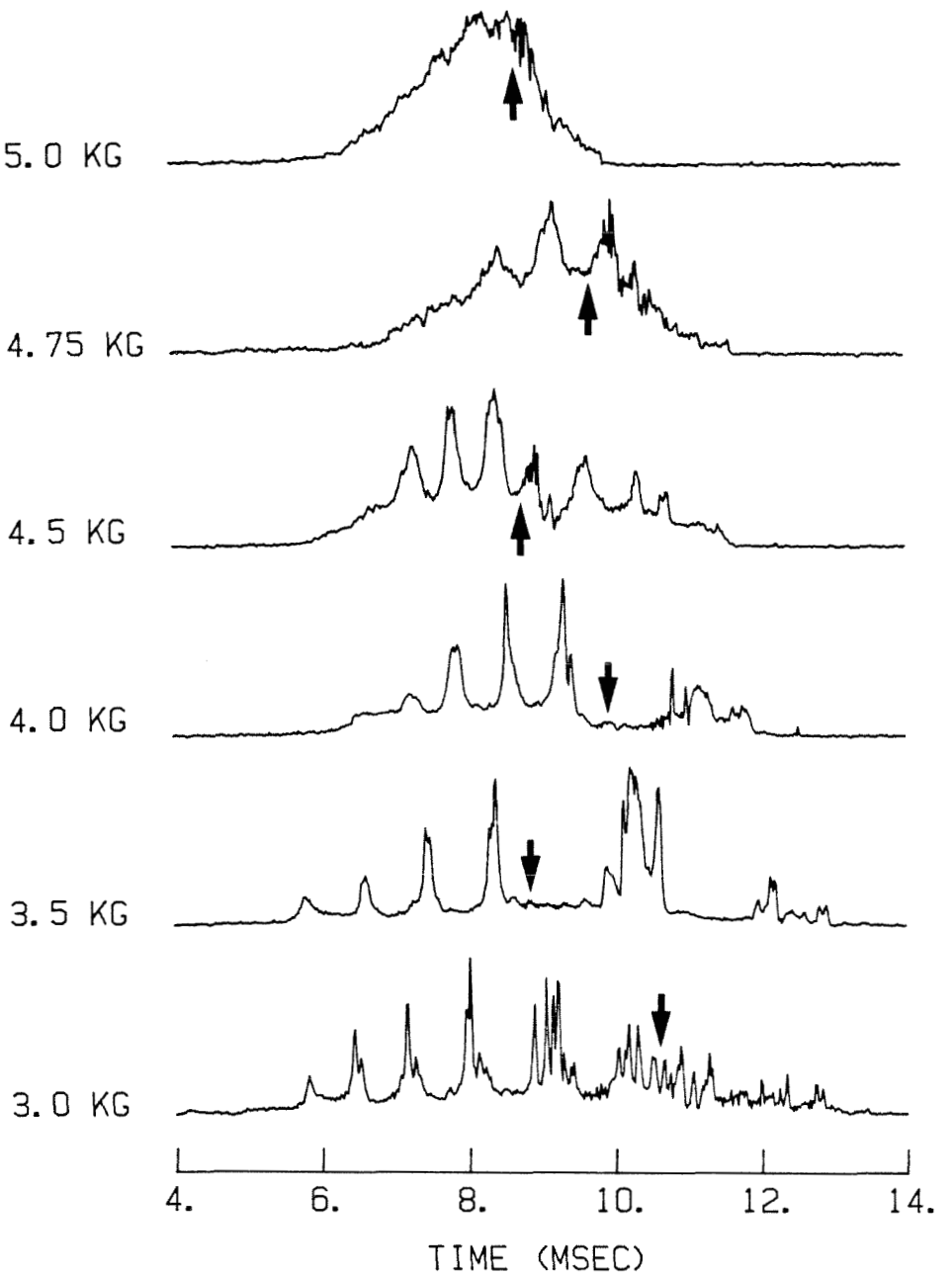

FIG. 7-5. Effect of the static toroidal magnetic field on the magnetic probe signal amplitudes, for a fixed excitation frequency of 8.5 MHz. The ceramic-insulated loop antenna was used and the magnetic probe was located in tokamak port #1 (180° toroidally away from the antenna). The density evolution was different for each shot; the arrows indicate the time at which the plasma density reached its maximum value. The peak densities were similar for all of the shots: $n \simeq (8 \pm 2) \times 10^{12}$ cm^{-3}.

The toroidal magnetic field was 4.0 kG in all cases, hence $\omega/\omega_{ci} = 1.4$, 2.0, and 2.6 at the plasma center for the three frequencies. The leading edge of each antenna was 3.8 cm past the tokamak wall, and the density evolution was different for each shot. Several effects are worthy of comment. As the frequency is raised, the modes become more densely spaced in time, more modes are observed, and the temporal width of the modes decreases. For each frequency, the character of the modes for each antenna is similar. The modes at each frequency do not occur at identical times or even in exactly the same numbers because the density evolution and the peak density associated with each curve are different; the plasma density profiles may differ as well.

Typical behavior of the eigenmodes as the toroidal magnetic field was varied is shown in Figure 7-5. The ceramic-insulated loop antenna was used, and the excitation frequency was 8.5 MHz; the ratio ω/ω_{ci} at the plasma center was thus varied from 1.1 to 1.9. The plasma density evolution could change significantly as the confinement field was varied, and the time at which the density reached its peak is indicated for each curve with an arrow. The peak densities achieved in each shot were the same within ~20%. The density decay for these shots was much faster and more abrupt than the density rise; thus the eigenmodes appearing to the right of the arrows cannot in general be matched with those occurring during the density rise. The plot shows the dramatic effect of changing the magnetic field: as the field is raised, fewer and fewer modes come into resonance during the density rise. In addition, the modes that do appear become broader and broader. We shall see subsequently that this is an indication of increased wave damping.

The effect of raising the toroidal magnetic field on the characteristics of the modes is thus qualitatively the same as the effect of lowering the excitation frequency. This is consistent with the simple theoretical models described in Chapter 2: in the frequency and plasma parameter range of interest, the wave

dispersion relation depends only on the ratio ω/ω_{ci} rather than on ω or B_0 separately.

The average wave excitation efficiencies for the five RF antennas are shown in Figure 7-6, as functions of the peak antenna current. For these measurements, the excitation frequency was 12 MHz, the toroidal magnetic field was 4.0 kG (hence $\omega/\omega_{ci} \simeq 2.0$ on axis) and the leading edge of each antenna was 3.8 cm past the tokamak wall. The toroidal component of the wave magnetic field was measured with a probe in tokamak port #2 (180° toroidally and 90° poloidally away from the antenna); the center of the coil was 2.0 cm past the wall. The excitation efficiency is defined here as the peak eigenmode field amplitude measured by the probe, divided by the antenna current. The amplitudes of the second, third, and fourth modes to appear after the initiation of the gas puff were divided by the currents at the corresponding times, and the results were averaged. Each point on the plot represents the average of 5 – 10 tokamak shots analyzed in this fashion.

The ceramic-insulated loop antenna was the most efficient coupler; the Faraday-shielded antenna was the least efficient. The bare loop, bare plate, and "T" antennas all showed comparable efficiencies, ranging from 50 – 70% of the ceramic-insulated antenna efficiency. The efficiency of the Faraday-shielded loop antenna was only ~30% that of the ceramic-insulated antenna. This was expected, since the vacuum field measurements (section 5.2) showed that the magnetic flux available for coupling to the eigenmodes was substantially reduced by the imposition of the shield. None of the antennas showed significant variation in coupling efficiency as the antenna current changed over a wide range. Note that even at the highest antenna current, using the most efficient antenna, the wave field amplitude measured by the probe was only ~0.7 gauss, a small fraction of the toroidal or poloidal confinement field magnitude. Hence the linearization of the fluid momentum equation (2.1a) for

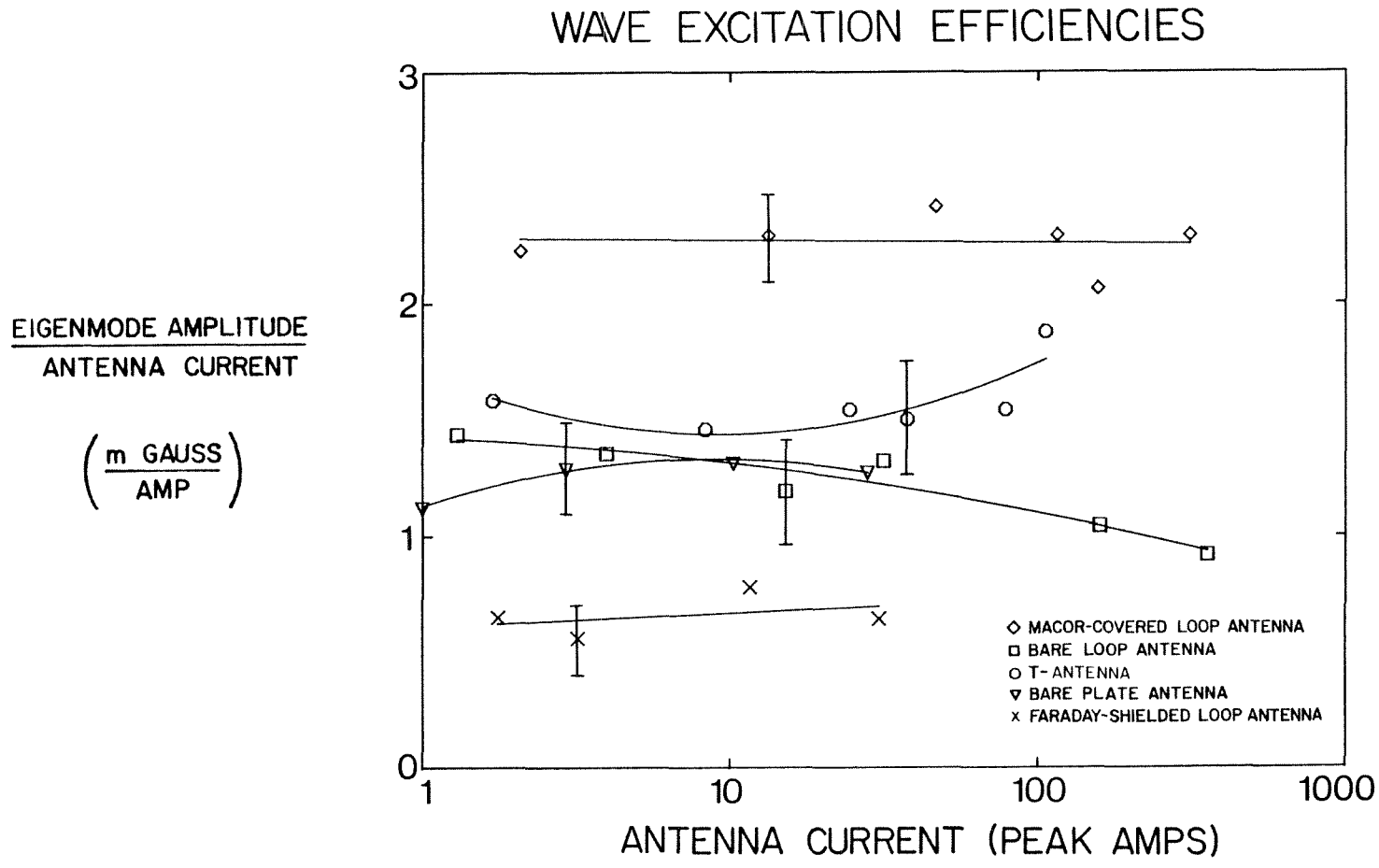

FIG. 7-6. Eigenmode excitation efficiences as functions of the antenna current, for the bare loop, ceramic-insulated loop, Faraday-shielded loop, bare plate, and "T" antennas. The magnetic probe, located in tokamak port #2, was oriented to measure the toroidal component of the wave magnetic field; the axis of the probe coil was 2.0 cm past the wall. The excitation frequency was 12 MHz, and the front edge of each of the antennas was located 3.2 cm past the wall. The experimental points represent the averages of the excitation efficiencies for the second, third, and fourth modes to appear after the initiation of the gas puff; each point is the average of 5 – 10 tokamak shots analyzed in this fashion.

small wave amplitudes is experimentally justified.

7.1.2 Eigenmode Dispersion Curves

At a given excitation frequency and toroidal magnetic field, the specific densities at which eigenmode resonances appear can be found in principle from the dispersion characteristics of the waves in the bounded system. As discussed in Chapter 2, the form of the radial density profile can substantially affect these eigendensities. It was found that, for the same line-averaged density (which is what the microwave interferometer measures), the more peaked the profile, the lower the eigendensity. Since the actual radial density profile in the Caltech tokamak plasma has not been measured except at the plasma edge, direct comparison with theory is not possible; nevertheless, comparison of the general features of the eigenmodes is useful.

Eigenmode curves (i.e., plots of the density at which a specific mode appears as a function of ω/ω_{ci}) were mapped out experimentally. In the range of parameters appropriate to the experiments considered here, the theoretical curves depend only on the ratio ω/ω_{ci}. For convenience in the experiments, ω/ω_{ci} was changed by varying the toroidal magnetic field rather than the RF frequency. The experiments required considerable care in adjusting the density evolution via the gas puff valve voltage waveform. A slowly rising, smooth density was necessary in order to have clean, well-separated modes for identification from shot to shot. Probe signals such as the one shown in Figure 7-1 were analyzed, recording the density corresponding to each of the eigenmode peaks occurring after the initiation of the gas puff. The toroidal magnetic field was then adjusted slightly and the procedure repeated. Typically 4 – 6 shots were recorded at each field strength; the eigendensities for each mode were averaged.

The resulting eigenmode dispersion curves for the ceramic-insulated loop antenna are shown in Figure 7-7a. The excitation frequency was 12 Mhz, and the leading edge of the ceramic box shielding the antenna was 3.2 cm past the tokamak wall. The probe used to measure the wave fields was located in tokamak port #2, and the probe coil axis, oriented to measure the toroidal component of the field, was 2.0 cm past the wall. Generally only the first $5-6$ modes occurring during the density rise were sufficiently reproducible and clearly separable; the curves for the first five modes are plotted in the figure. As expected from the discussion in Chapter 2, the eigendensities decrease as ω/ω_{ci} increases. The labels $1-5$ identifying the modes represent the observed order in which they appear after the initiation of the gas puff.

Also plotted in the figure is a curve calculated from theory, using the quadratic density profile $n_I(\rho; 0.9)$ discussed in section 2.4, for the $N=0$, $m=1$, $l=1$ toroidal eigenmode (dashed line). The theory of Chapter 2 predicts that this is the lowest cutoff mode, i.e., that there are no eigenmodes occurring at densities below the curve. The density profile used in the calculation is a quadratic function of minor radius, with a peak density at the center ten times that at the edge and consequently a line-averaged density of seven times the edge density. This curve is plotted only as an indication that the observed modes do in fact occur within the region of density-frequency space predicted by simple cold-plasma theory. Because the exact location and spacing of the modes depends strongly on the radial density profile chosen, mode identification cannot be carried out by comparison of the theoretical and experimental curves. Note that the theoretical curves for a constant density model (plotted in Figure 2-9) are more closely spaced near the cutoff; this is true for the quadratic density profile model as well. In contrast, the spacing of the observed modes in Figure 7-7a is relatively uniform. One explanation for this effect is that the $N=0$ or 1 modes are simply not excited sufficiently to

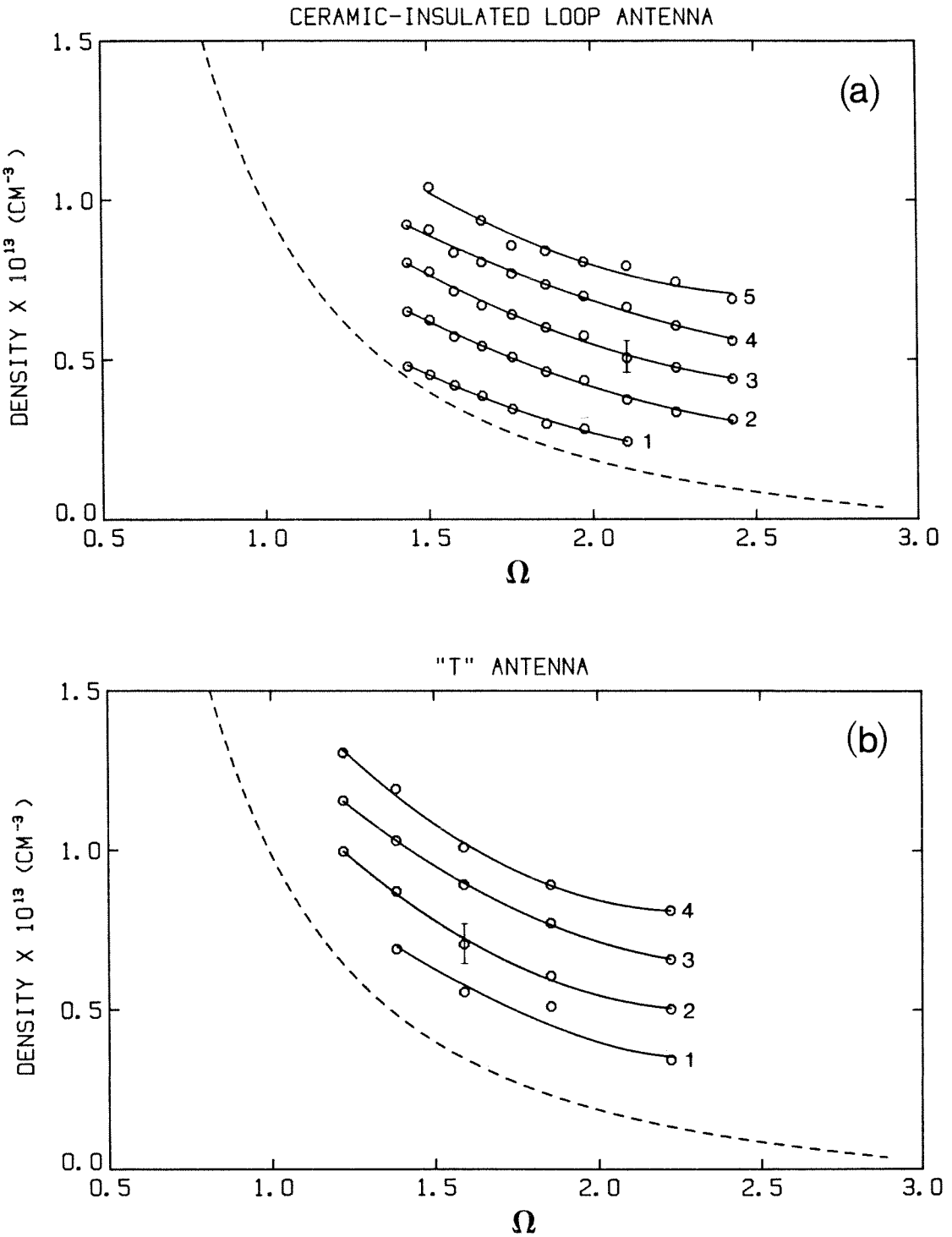

FIG. 7-7. Eigenmode dispersion curves for the ceramic-insulated loop antenna and the "T" antenna. The mean density (from the microwave interferometer) at which the modes apear is plotted as a function of $\Omega \equiv \omega / \omega_{ci}$. Each experimental point (circles) represents the average of the eigendensities for that particular mode from 4-6 tokamak shots. For comparison, the theoretical result for the cutoff mode ($N = 0$, $m = 1$, $l = 1$) using the $n_I(\rho, 0.9)$ quadratic density profile is plotted (dashed line). a) Ceramic-insulated loop antenna, excited at a frequency of 12 MHz. b) "T" antenna, excited at a frequency of 8.5 MHz.

observe and that the first modes seen are $N=2$ or higher order modes. Another possibility involves the presence of a very low density region at the tokamak wall - plasma interface. As will be seen later in this chapter when the group velocity results are discussed, inclusion of a vacuum layer at the plasma edge can substantially modify the modes near cutoff.

Similar results with the "T" antenna are displayed in Figure 7-7b. In this experiment, the excitation frequency was 8.5 MHz and the front edge of the cross-bar of the "T" was 2.8 cm past the wall; the magnetic probe used was the same as described above. The spacing of the modes and their general location in density-frequency space are similar to the results obtained with the loop antenna, except that the first observed mode occurs at a somewhat higher density.

7.1.3 Global Characteristics: Amplitude and Phase

The amplitude evolution of the wave magnetic field associated with the eigenmodes was similar at all locations investigated. Figure 7-8 displays signals from four magnetic probes, at different locations, taken during a single tokamak shot. The ceramic-insulated loop antenna was used to excite the waves at a frequency of 12 MHz, and the toroidal magnetic field on axis was 4.0 kG. The probes were located in tokamak ports #1, 3, 4, and 5; their location with respect to the RF antenna is shown in Figure 3-1. The probe coils were all oriented to observe the toroidal component of the wave magnetic field and the axes of the probe coils were 2.0 cm past the tokamak wall. The gas puff began at $t \simeq 3$ msec and the plasma density reached its peak at $t \simeq 12$ msec. The first five modes are clear and well separated, and the signals from all four probes are quite similar. The relative amplitudes of the successive modes vary somewhat from one probe to another and from shot to shot. The signal amplitudes from the B_ρ and B_θ probe coils were quite similar to

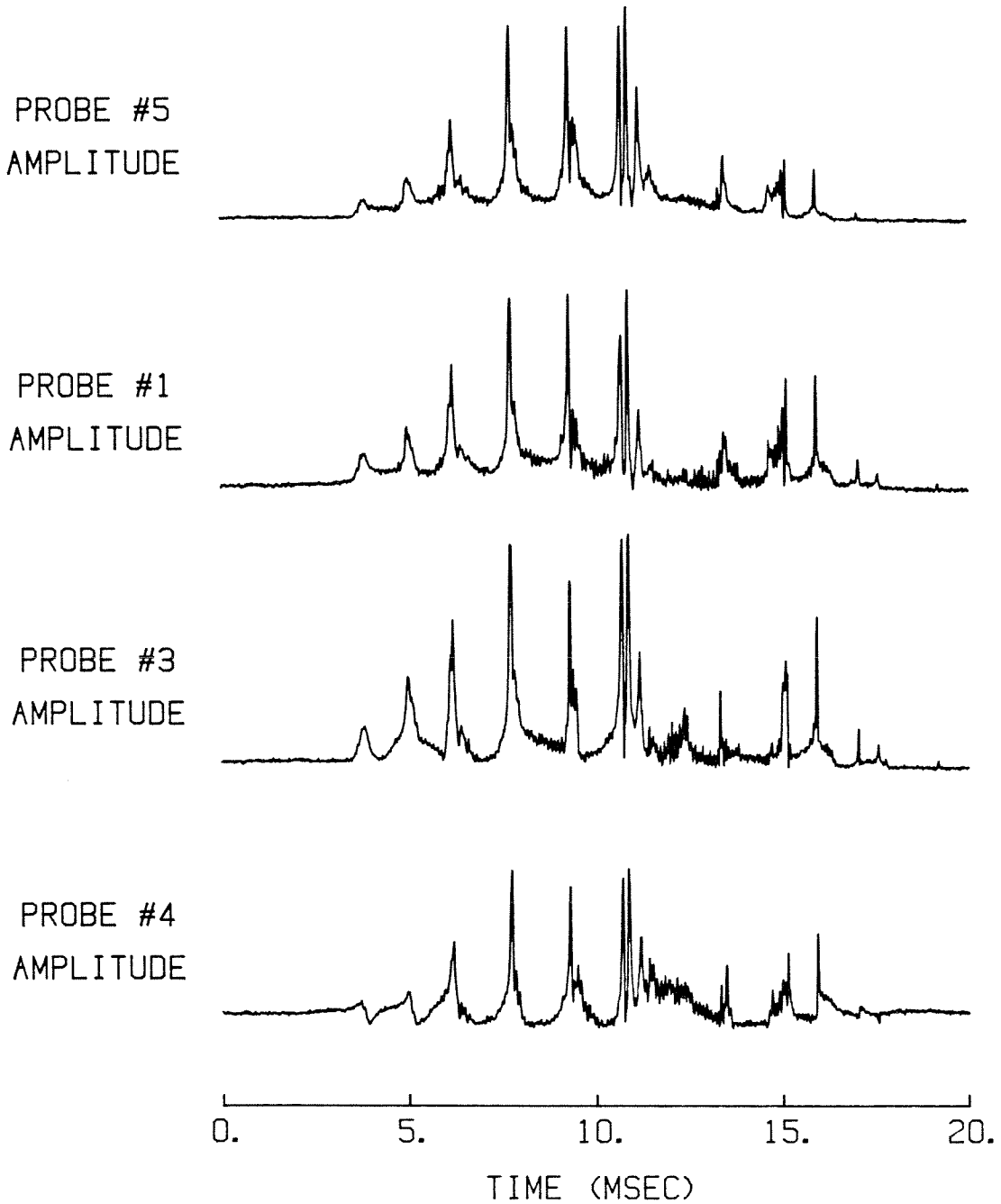

FIG. 7-8. Magnetic probe signal amplitudes from four probes during a typical single tokamak shot. The probes were located in tokamak ports #1, 3, 4 and 5 and were oriented to measure the toroidal component of the wave magnetic field. The ceramic-insulated loop antenna was used to excite the modes at a frequency of 12 MHz; also $B_0 = 4.0$ kG on axis.

those from the B_z coil, except for an overall change in magnitude.

The eigenmodes are thus seen to be global modes, which implies that the wave damping length is, as expected, large compared to the tokamak circumference.

Phase measurements were carried out in order to further identify the mode structure. The phase detector used in this experiment was described in section 4.6; it had an unambiguous range of 2π radians and sufficient dynamic range to track the phase during the large wave amplitude peaks at the eigenmode resonances. The phase detector reference input signal was taken from the antenna RF current monitor signal using a 0° power splitter. A signal from one of the magnetic probes could also be used as the reference input.

A typical tokamak shot showing the phase detector output signals from two magnetic probes is shown in Figure 7-9; the phase reference signal was the RF antenna current. Also shown for comparison is the amplitude of the signal from one of the probes. The probes were located in tokamak port #1 (180° toroidally and 90° poloidally away from the RF antenna) and in port #4 (90° poloidally away from the RF antenna and at the same toroidal location as the antenna). The probes were positioned 2.0 cm past the tokamak wall and were oriented to measure the toroidal component of the wave magnetic field. The ceramic-insulated loop antenna was used for the measurements, with an excitation frequency of 12 MHz, and the toroidal magnetic field on axis was 4.0 kG.

The first four eigenmodes after the initiation of the gas puff (at $t \simeq 4.5$ msec) are clearly visible on the trace of the signal amplitude. The very abrupt jumps in the phase signals from −180° to +180° represent the mapping of the actual continuous phase signal into a 360° range by the phase detector electronics. Due to the fast response of the detector ($\tau \simeq 5\,\mu$sec), these phase jumps generally occur within one sample period of the data

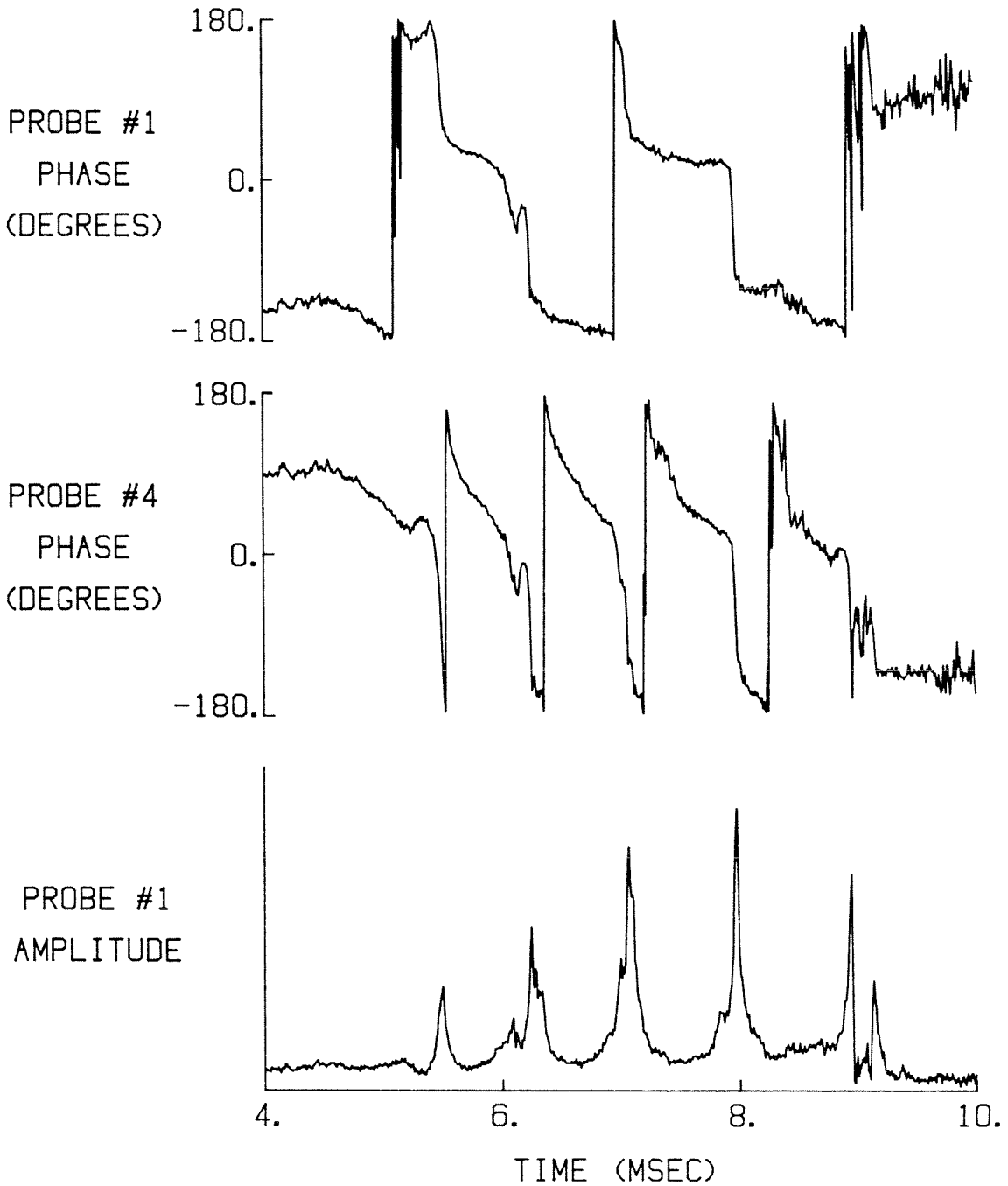

FIG. 7-9. Phase detector output signals for the magnetic probes in tokamak ports #1 and #4, and the amplitude of the signal from probe #1, for a typical tokamak shot. The phase detector reference signal was the RF antenna current. The ceramic-insulated loop antenna was excited at a frequency of 12 MHz, the toroidal magnetic field on axis as 4.0 kG, and the magnetic probes were oriented to measure the toroidal component of the wave magnetic field.

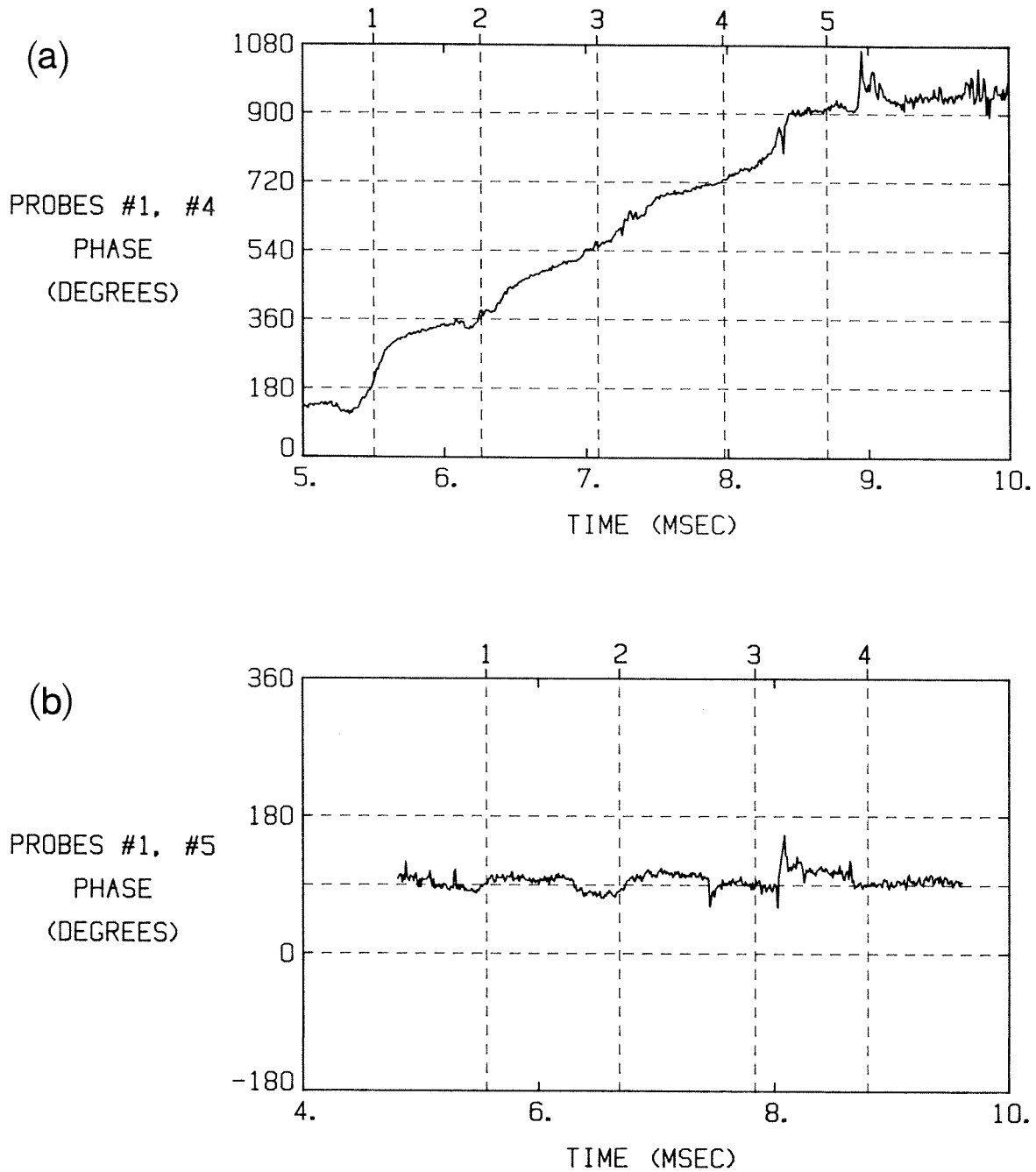

FIG. 7-10. Relative phase between pairs of magnetic probes. The vertical dashed lines mark the times at which the eigenmode peaks in the wave amplitude occur; the lines are labeled in order of appearance of the modes after the gas puff. The waves were excited with the ceramic-insulated loop antenna at a frequency of 8.5 MHz; the toroidal magnetic field on axis was 3.5 kG. a) Phase between two probes separated by 180° in the toroidal direction. b) Phase between two probes separated by 90° in the poloidal direction.

recording system and can be easily separated from the actual phase variation of the signals. Note that these 360° phase jumps are not coincident with the eigenmode amplitude peaks.

The phase between the signal from magnetic probe #4 and the antenna current changes by ~360° from one mode to the next. The phase undergoes a fairly rapid transition of ~180° during the eigenmode amplitude resonance and a slower variation between mode peaks. The phase of the signal from probe #1 shows similar behavior except that the rate of change of phase is smaller by a factor of ~2.

The phase signals were generally quite clean and reproducible from shot to shot. Note that because the magnetic probes were all constructed identically and the connecting cables were matched (within ~0.5 cm), the relative phase difference between the signal from probes #1 and #4 therefore represents the actual phase difference between the wave magnetic fields at the probe locations.

A more useful representation is to display the relative phase between pairs of probes. A computer program was written which removes the 360° phase detector jumps and then subtracts the phase signals from each other. Figure 7-10a shows the resulting phase difference between two probes separated by 180° toroidally during the part of the tokamak shot following the gas puff. Note that the phase at the beginning of the plot was chosen to lie in the 0°−360° interval; this choice was arbitrary to an additive constant of an integral multiple of 360°. The vertical dashed lines mark the times at which the eigenmode resonances occurred on the probe signal amplitude; for this particular shot, five modes were clearly identifiable. The labels 1−5 at the top of the plot simply identify the order of appearance of the modes after the initiation of the gas puff.

The phase difference between the two probes continuously increases as the density rises. At each eigenmode resonance (the intersection of the dashed vertical line with the phase curve), the phase difference is an almost exact multiple of 180°, with the phase increasing by 180° between successive modes. This result is consistent with the wave theory described in Chapter 2, which predicted that the first $4-5$ modes accessible in the Caltech tokamak would have successively increasing toroidal mode numbers. If the wave fields at toroidal eigenmodes vary as $e^{iN\varphi}$, where N is the toroidal mode number and φ, the toroidal angle (note that $\varphi = z/R_0$ in the periodic cylinder model), then the predicted phase difference between two locations separated toroidally by 180° is precisely that which was observed: successive increases of 180°. Because only two probes were used, the toroidal mode number can only be identified absolutely as even or odd. According to Figure 7-10a, then, the first observed mode is odd, probably an $N=1$ or $N=3$ mode. Physically, the parallel (i.e., toroidal) wavelength of the fields in the plasma decreases as the density rises; eigenmodes occur when the wavelength is such that an integral number of waves can fit around the tokamak. The cold plasma theory does not describe the behavior of the wave fields between eigenmode resonances as wave damping must then be considered.

The phase difference between two probes at the same toroidal location, but separated by 90° poloidally, is shown in Figure 7-10b for another tokamak shot. The experimental arrangement was as described above but the probes were located in tokamak ports #1 and #5, 180° toroidally away from the RF antenna. The vertical dashed lines again denote the times at which the eigenmode resonances occur.

The phase difference is very close to 90° at each of the eigenmodes, and it varies little between modes. If the wave fields vary, as assumed in the periodic cylinder model, as $e^{im\theta}$, where m is the poloidal mode number and θ is the

poloidal angle, then this result implies that $m = 1 + 4l$, where l is some integer. Thus, the measurement is consistent with values for m of 1, 5, −3, 9, −7, etc. The simple cold-plasma theory predicts that the plasma densities required to reach even the $m = 5$ or $m = -3$ modes are beyond the limits of the Caltech tokamak, for the frequency range of interest (cf. Figure 2-9d), and that other lower-order m modes would be excited first. Therefore, it is reasonable to conclude that the observed waves have an $m = +1$ poloidal mode structure.

In conclusion, phase measurements of the wave magnetic fields support the predictions of the simple periodic-cylinder, cold-plasma model that the first modes encountered are $m = +1$ modes of low and successively increasing toroidal mode numbers.

7.1.4 Wave Amplitude Radial Profiles

The radial profiles of the amplitudes of the magnetic field components associated with the eigenmodes were investigated experimentally. A three-coil magnetic probe was located in tokamak port #1 to provide a measurement of the toroidal, poloidal, and radial components of the magnetic field simultaneously. The ceramic-insulated loop antenna was used to excite the eigenmodes at a frequency of 8.5 MHz and the toroidal static magnetic field was 3.5 kG on axis; hence $\omega/\omega_{ci} \simeq 1.6$ at the plasma center. After conditioning the probe with discharge cleaning and tokamak shots, it could be inserted almost 4 cm past the wall without seriously affecting the plasma discharge. During the wave measurements, the probe was inserted into the plasma in increments of 0.5 or 1.0 cm. The plasma density evolution was adjusted carefully, via the gas puff valve voltage waveform, so that the first $4-5$ eigenmodes were distinct and clearly separated, and the tokamak discharge was fairly reproducible. At each position of the magnetic probe, $3-6$ shots with similar plasma current and

density evolution were recorded. At each eigenmode peak, the components of the magnetic field were normalized to the antenna current at that time; the data for each field component from the tokamak shots at each probe location were averaged.

The results of this field component survey are displayed in Figures 7-11a,b,c, and d for each of first four eigenmodes to for each of the first four eigenmodes to appear after the initiation of the gas puff. Notice that the radial form of the field components is quite similar for each of the modes, apart from an overall scale factor. Over most of the radial range, B_z is the largest component of the wave field, and it increases monotonically as the probe is inserted radially into the plasma. The ρ-component of the field also increases as the probe moves into the plasma, but its magnitude is considerably less than that of the z-component. Note that as the probe moves in, the rate of rise of B_ρ increases, while that of B_z decreases; for the first mode at the maximum probe insertion, B_ρ becomes larger than B_z. The θ—component of the field is approximately constant over the range of the probe position for all four of the modes. The overall coupling efficiency to the modes (the field amplitude divided by the antenna current) increases for each successive mode.

The experimental results can be compared with the theoretical field profiles which are shown in Figure 2-10. These profiles are calculated from the zero-electron mass, constant-density, periodic-cylinder model. For the $m = 1$ poloidal mode and the first radial mode, the profiles for the $N = 0, 1, 4$ toroidal modes are plotted. From the discussion of the phase measurements in the previous section, the poloidal mode number of the observed modes in the tokamak is $m = 1$, and the toroidal mode number of the first observed mode is probably $N = 1$ or $N = 3$, with successive modes having integrally increasing toroidal numbers.

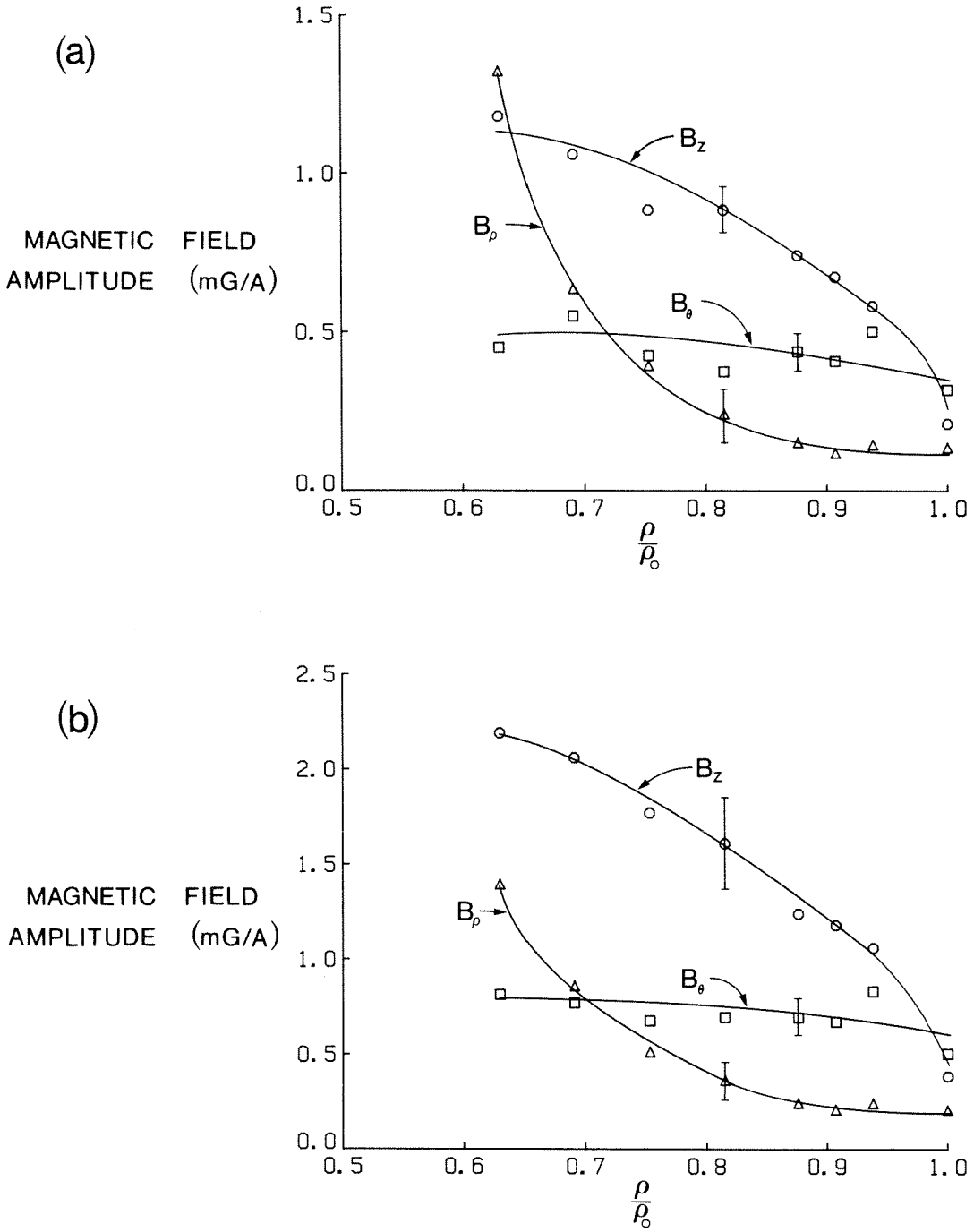

FIG. 7-11. Radial profiles of the magnetic field components of the eigenmode fields, for the first four modes observed after the initiation of the gas puff. The ceramic-insulated loop antenna was used to excite the waves at a frequency of 8.5 MHz and the toroidal magnetic field on axis was 3.5 kG. a) Field profiles for the first mode. b) Field profiles for the second mode.

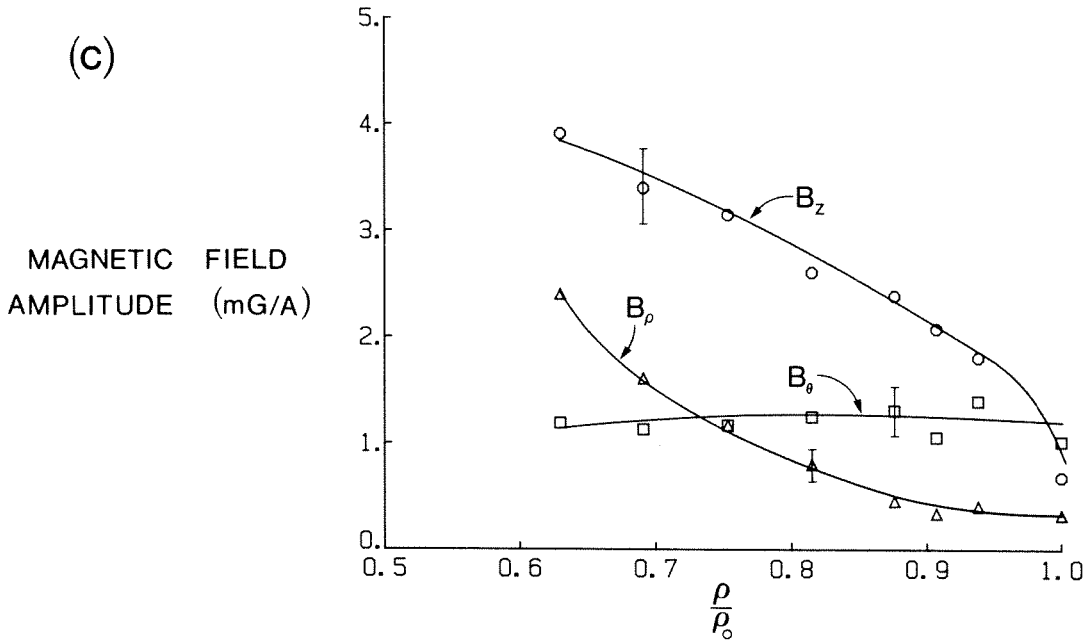

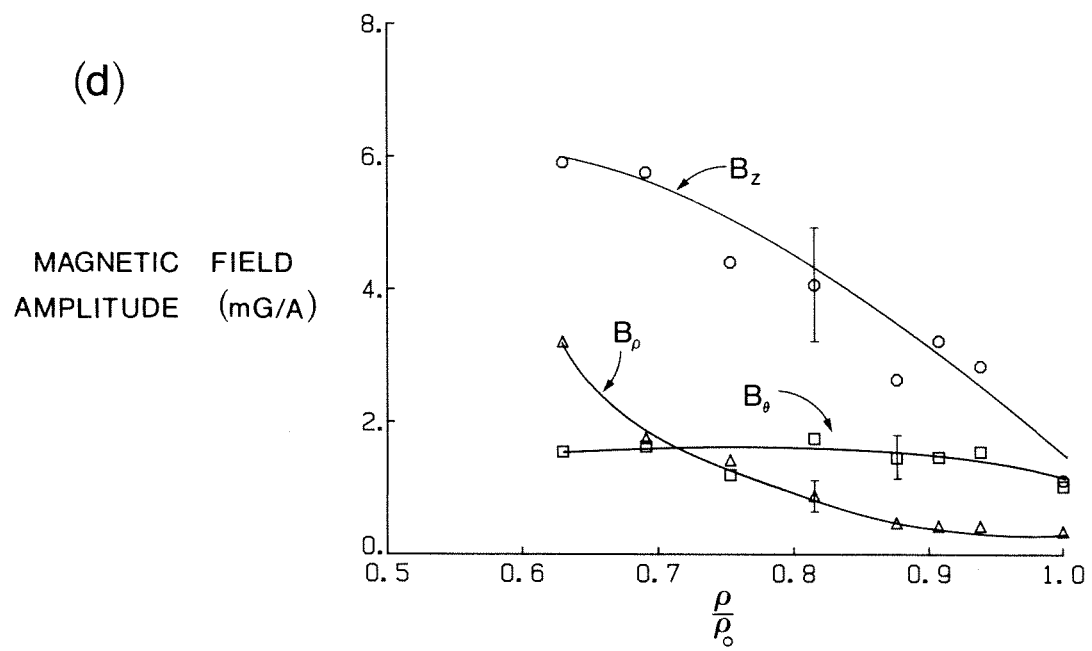

FIG. 7-11, continued. c) Field profiles for the third mode. d) Field profiles for the fourth mode.

The general form of the ρ- and z-components of the field over the range of the measurement ($0.75 < \rho/\rho_0 < 1.00$) agrees roughly with the calculated form: B_z and B_ρ both increase as ρ decreases, B_z is considerably larger than B_ρ, and the rate of increase of B_ρ is larger than that of B_z as ρ decreases. The major difference in the form of the calculated profiles as the toroidal mode number increases is a relative decrease in the magnitude of B_z compared to the other components. This effect is not observed experimentally: the observed relative magnitude of B_z with respect to B_ρ is approximately constant for the four modes. The calculated curves exhibit several other features which do not agree with the measurements. The theory predicts that B_ρ should vanish at $\rho = \rho_0$ in order to satisfy the boundary conditions of a perfectly conducting wall. The measurements show a small but finite value for B_ρ when the probe coil is at minor radius ρ_0. This is not surprising, however, because the probe does not actually measure the field component at the surface of the conducting boundary. The probe is located in the center of a 2.2 cm i.d. cylindrical port; this perturbation to the boundary will certainly alter the radial component of the field near it. Another point is that the wall, being made of stainless steel, is not a perfect conductor; in fact, the conductivity of the wall is not too different from the parallel conductivity of the plasma at the temperatures typically encountered in the tokamak. The effect of the finite wall conductivity on the field profiles near the wall has not yet been considered theoretically. Finally, the low plasma density at the plasma-wall interface in the actual tokamak also affects the eigenmode fields near the wall.

Another point of disagreement involves the θ—component of the wave field. The experimental results show that B_θ is fairly constant as the probe is moved in as far as 4.0 cm past the wall. The theoretical curves in Figure 2-10, for the $m = 1$, $N = 1, 4$ modes, show B_θ monotonically decreasing as the minor

radius decreases, passing through zero at some point. The change in sign of B_z simply means that the phase has changed by 180°; the appropriate quantity for comparison with the experiment is the absolute value of the B_θ curve. It is not clear why the experimental and theoretical results are distinctly different. Besides some of the effects mentioned above which can alter the wave fields near the plasma edge, a possible explanation involves the poloidal component of the confinement magnetic field. The total static magnetic field in the tokamak is the sum of the toroidal and poloidal components (the component from the vertical field coils is negligible). At typical plasma currents of 25 kA and toroidal magnetic fields of 3.5 kG, the angle between the toroidal direction and the direction of the total confinement field at the plasma edge is ~5°. If we assume, as a first approximation, that the wave fields are tied to the total static magnetic field [Messiaen, 1978], then the parallel component of the wave field will also contribute to the signal measured with a probe oriented to measure the θ–component of the field (in the tokamak toroidal coordinate frame). Simple misalignment of the probe would yield the same effect. The three probe coils were orthogonal within ~5°, and the alignment of the B_z coil with the toroidal axis of the tokamak was also accurate within ~5°. Nevertheless, even 5° of error due to misalignment or due to the poloidal field effect would be sufficient to substantially alter the θ–component of the field measured by the probe, particularly if the actual ratio of B_z to B_θ was large.

In conclusion, some of the features of the eigenmode magnetic field radial profile measurements are in agreement with predictions of the simple theoretical model presented in Chapter 2 for $m = 1$ modes. The z- and ρ-components of the field have roughly the expected form, although the θ–component does not. The overall agreement, however, is much better than for modes with $m \neq 1$. The four successive eigenmodes investigated all have similar field profiles, further supporting the conclusions of the section 7.1.3 that the field

structure is that of $m = 1$ modes of successively increasing toroidal mode number.

7.1.5 Wave Damping Measurements

The disposition of the energy lost in the antenna-plasma system is of considerable importance, both for understanding the physics of the wave coupling and propagation, and for the more practical motivation of optimizing the plasma heating. For the fast wave near the ion cyclotron frequency in the Caltech tokamak, the wave attenuation is small so that cavity resonances dominate the field response. Measurements involving the form of these resonances can yield information about the damping processes in the plasma.

Eigenmode Q Measurements

The cavity Qs expected for a variety of damping mechanisms were calculated for different eigenmodes in section 2.3. In a simple cavity resonator, the Q of a mode may be found by observing the response as the frequency is swept through the resonance: $Q = \frac{\omega_{res}}{\Delta\omega}$, where ω_{res} is the resonant frequency for a particular mode and $\Delta\omega$ is the difference in frequency between the points at which the field amplitudes are reduced from their peak value by a factor of $1/\sqrt{2}$. Although the driving frequency could in principle be swept, it is easier to utilize the changing plasma density. It can be shown that, at a fixed frequency, the Q of a mode is approximately given by $Q \simeq \frac{2 n_{res}}{\Delta n}$, where n_{res} is the density at which the resonance peak occurs, and Δn is the difference in density between points at which the field amplitudes are reduced by $1/\sqrt{2}$ [Takahashi, 1977]. The cavity Qs for each mode can then be estimated by careful analysis of the density and magnetic field amplitude traces. Because the cavity is loaded by the RF antenna, however, the Q estimated in this

fashion is the *loaded* Q; the theoretical calculations are for the *unloaded* Q. If the RF antenna were coupled very weakly to the eigenmode, then there would be no difference between the two. In many experiments, however, the antenna is tuned to maximize the coupling to the eigenmodes. If the antenna were perfectly matched to the mode, so that at resonance there was no power reflected back to the generator from the antenna, it can be shown that the loaded Q would be smaller than the unloaded Q by a factor of two. Hwang [1979] has shown that the loaded and unloaded cavity Qs can be related by measurement of the antenna impedance:

$$Q_{UL} = Q_L \left[1 + \frac{R_{res} - R_0}{2 R_{off}} \right], \tag{7.1}$$

where Q_L and Q_{UL} are the loaded and unloaded Qs, R_{res} is the antenna resistance at the eigenmode resonance, R_0 is the background antenna resistance (in the absence of plasma), and R_{off} is the antenna resistance off-resonance, i.e., between the resonance peaks on the loading.

Measurements of the cavity Qs were carried out using the ceramic-insulated loop antenna to excite the waves. The excitation frequency was 12 MHz, and the toroidal magnetic field on axis was varied from 3.25 kG to 5.50 kG in increments of 0.25 kG. The antenna input impedance was simultaneously monitored, as described in Chapter 6. For each of the first five modes occurring during the density rise after the gas puff, the loaded Q was calculated as described above; the impedance measurements were then used to convert this value to the unloaded Q.

The results are shown in Figure 7-12, where the unloaded Q is plotted on a logarithmic scale. The curves for each mode are labeled in order of their appearance during the density rise. The Qs of the modes increase dramatically for successive modes; they range, at a toroidal field of 4 kG, from ~25 for the first mode to ~900 for the fifth mode, with the largest increase

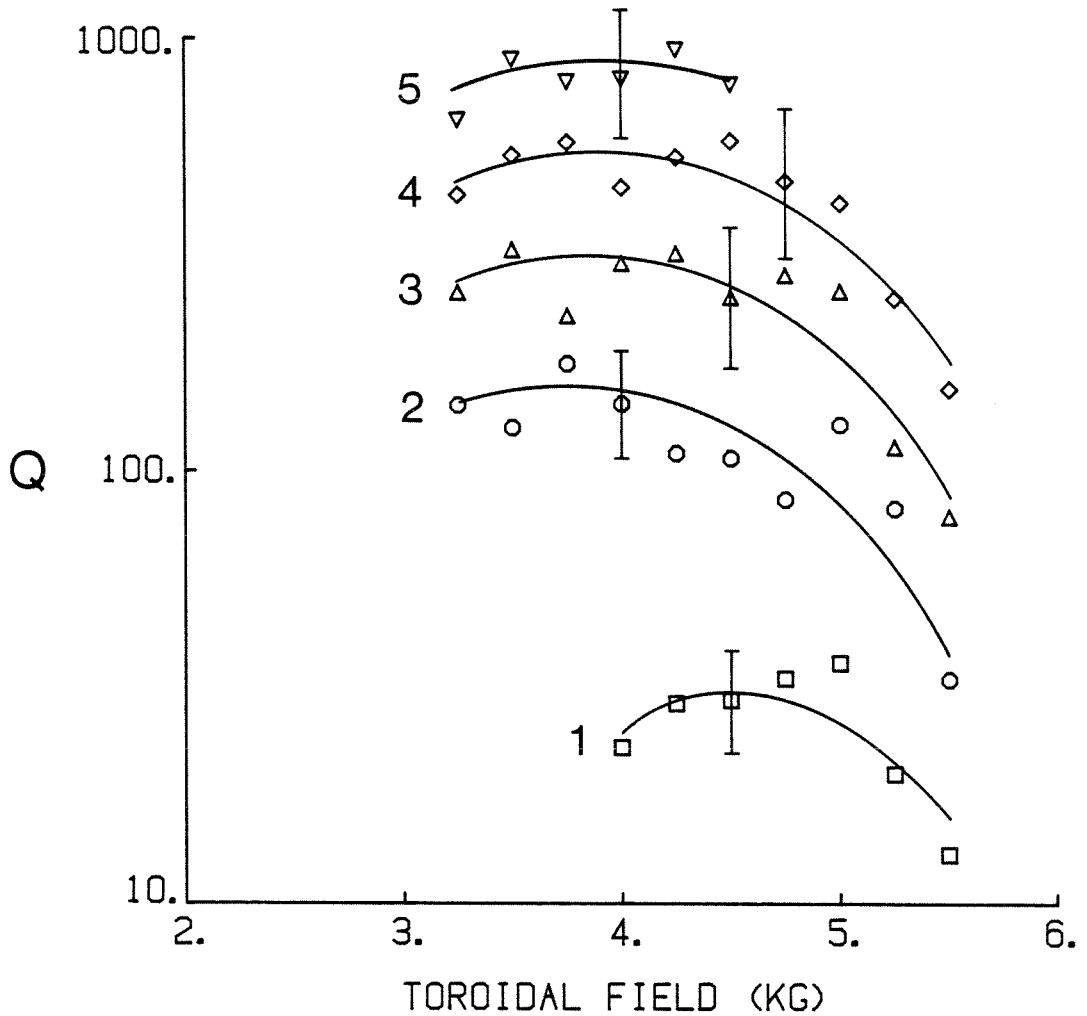

FIG. 7-12. The unloaded Qs for the first five eigenmodes to appear during the density rise after the gas puff, as functions of the toroidal magnetic field. The ceramic-insulated loop antenna was used to excite the waves at a frequency of 12 MHz. The measured (loaded) Qs were converted to the unloaded Qs using the simultaneous impedance measurements. Note that the second-harmonic ($2\omega_{ci}$) layer enters the tokamak when $B_0 \simeq 2.5$ kG and exits when $B_0 \simeq 5.3$ kG; the fundamental (ω_{ci}) layer enters the tokamak when $B_0 \simeq 5.1$ kG.

occurring between the first and second modes. Each experimental point on the plot represents the average of data from a number of tokamak shots; note that the indicated scatter in the data is substantial. The first four modes exhibit a substantial decrease in Q as the toroidal magnetic field is raised above $\sim$5 kG (the density is not sufficient to reach the fifth mode at these high fields). Noting that the fundamental ion cyclotron layer enters the tokamak when $B_0 \simeq 5.1$ kG, the decrease in Q at this point suggests fundamental cyclotron damping as the mechanism.

The observed Q values are not in agreement with any of the theoretical Q calculations described in section 2.3. Referring to Figures 2-12 through 2-17, the only damping mechanism which predicts eigenmode Qs which increase with the toroidal mode number is second harmonic cyclotron damping. Although the second harmonic cyclotron layer is within the plasma over most of the range of toroidal field used in the experiment (it enters the tokamak when $B_0 \sim 2.5$ kG and exits when $B_0 \sim 5.3$ kG), the results are not in quantitative agreement. For an ion temperature of 100 eV, the most heavily damped mode (the cutoff or $N=0$ mode) has a predicted Q due to second harmonic damping of $\sim$1000. The actual first observed mode in these experiments is likely an $N=1$ or $N=3$ mode; the predicted Qs for these modes are $\sim$1200 and $\sim$3200, respectively, much higher than the observed Q of $\sim$25. Adding the effects of the various theoretical damping mechanisms, assuming independence, lowers the predicted Q as shown in Tables 2-1 and 2-2. The total Q, however, still decreases dramatically as the toroidal mode number increases, in contrast to the opposite experimental result. Thus it appears that some physical damping mechanism other than those considered in Chapter 2 must be responsible for the wave damping observed in the Caltech tokamak. One possibility [Thompson, 1982] involves mode conversion of the fast wave, near the second-harmonic resonant layer, to an electrostatic

Bernstein wave (which appears only when thermal effects are considered).

Damping Length Measurements

Another view of wave damping in the tokamak is to consider the attenuation that a wave suffers in traveling around the torus. If the wave were propagating in an infinite cylinder rather than in a torus, the damping could be measured by simply observing the difference in wave amplitudes with two probes spaced along the cylinder axis. In the tokamak geometry, however, where the wave attenuation length is long compared to the toroidal circumference and interference effects are important, the situation is more complicated.

A simple model can yield a relation between wave magnetic field quantities and the wave damping per unit length. Assume a periodic cylinder model of the tokamak, where z is the axial length along the cylinder corresponding to the toroidal coordinate in the tokamak. The RF antenna is located at $z=0$ and the ends of the cylinder (at which the periodic boundary conditions apply) are at $z=\pm\pi R_0$, where R_0 corresponds to the major radius of the tokamak. If the effect of the poloidal field is ignored, the antenna launches waves symmetrically in both the $+z$ and $-z$ directions. A wave, upon reaching one of the boundaries, is assumed to appear with the same phase at the other boundary. For a given antenna excitation current, the field at a point in the cylinder can be found by summing the contributions from each pass of the wave. Constant wave absorption per unit axial length is assumed, and the wave propagates in the z–direction as $e^{ik_{\|}z-\alpha|z|}$, where $k_{\|}$ is the parallel wavenumber, $\alpha\equiv 1/L_D$ is the inverse wave damping length, and a harmonic time dependence is assumed. Limiting the discussion to positions $0<z\leq\pi R_0$, the contribution to a field component from waves traveling in the $+z$ direction is

$$B_+ = \sum_{j=0}^{\infty} A_+ e^{(ik_{\|}-\alpha)(2\pi jR_0+z)} = A_+ \frac{e^{(ik_{\|}-\alpha)(2\pi R_0+z)}}{1-e^{2\pi R_0(ik_{\|}-\alpha)}}, \qquad (7.2)$$

and the contribution from the waves traveling in the $-z$ direction is

$$B_- = \sum_{j=0}^{\infty} A_- e^{(i k_\parallel - \alpha)[2\pi(j+1)R_0 - z]} = A_- \frac{e^{(i k_\parallel - \alpha)(2\pi R_0 - z)}}{1 - e^{2\pi R_0 (i k_\parallel - \alpha)}}, \tag{7.3}$$

where A_+ and A_- are constants related to the coupling efficiency of the antenna to the waves and proportional to the antenna current. Assuming equal coupling coefficients, the total field at location z is just

$$B \equiv B_+ + B_- = A \frac{\cosh\left[(z - \pi R_0)(i k_\parallel - \alpha)\right]}{\sinh\left[\pi R_0 (i k_\parallel - \alpha)\right]}. \tag{7.4}$$

The parallel wavenumber, $k_\parallel$, is a function of the plasma density. In an actual experiment, the excitation frequency is fixed, and $k_\parallel$ increases as the density rises. Eigenmodes, or peaks in the wave amplitude, occur when $k_\parallel = N/R_0$, where N, an integer, is the toroidal mode number. Anti-resonances, or points where the wave amplitude is a minimum, occur when $k_\parallel = (N + \frac{1}{2})/R_0$. A particularly useful relation can be found by considering the fields at location $z = \pi R_0$, corresponding, in the tokamak geometry, to a position 180° toroidally away from the RF antenna. At that location, the magnitude of the ratio of the field at a resonance ($k_\parallel = N/R_0$) to that at an adjacent anti-resonance ($k_\parallel = (N + \frac{1}{2})/R_0$) can be easily shown to be

$$\gamma \equiv \left| \frac{B_{res}}{B_{anti}} \right| = \frac{1 + e^{-2\pi R_0 \alpha}}{1 - e^{-2\pi R_0 \alpha}}, \tag{7.5}$$

where B_{res} is the field component at the resonance, B_{anti} is the component at the anti-resonance, and the antenna coupling efficiency is assumed to not change significantly over the plasma density range between the resonance and anti-resonance. The above equation can be solved for the damping length:

$$L_D \equiv \frac{1}{\alpha} = 2\pi R_0 \left[\ln\left(\frac{\gamma + 1}{\gamma - 1} \right) \right]^{-1}, \tag{7.6}$$

a result first derived by Takahashi [1977]. Thus the wave attenuation length in

an infinite cylindrical plasma, L_D, can be estimated by measurements in the tokamak of the eigenmode wave field amplitude at a resonance and an adjacent anti-resonance.

The set of tokamak shots which provided the eigenmode Q data was analyzed in the above fashion for the damping length of each mode; the results are plotted in Figure 7-13 as functions of the toroidal magnetic field. The curves for each of the five eigenmodes are labeled in the order of their appearance during the density rise after the gas puff. The damping length increases for each successive mode, and for the higher three modes, the damping length is considerably longer than tokamak major circumference ($2\pi R_0 = 2.9$ m). Note also that the damping length decreases for all of the modes as the toroidal field increases. These results show the same features as were suggested by the Q measurements: the plasma wave damping decreases for successive toroidal modes and increases as the fundamental cyclotron layer enters the plasma.

The eigenmode Q measurements and the wave damping length measurements are different views of the same physical absorption process. Takahashi [1977] shows that the two are related by the wave group velocity:

$$L_D = \frac{2 Q v_g}{\omega}, \tag{7.7}$$

where v_g is the group velocity of the wave in the toroidal direction. Thus the independent measurements of L_D and Q can be used to estimate the group velocity. Table 7-1 shows the calculated group velocity for the five modes at a toroidal magnetic field of 4.0 kG. The modes occur at successively higher densities; thus the table gives information about the variation of the group velocity with density. Note the data predict that the group velocity decreases as the density increases.

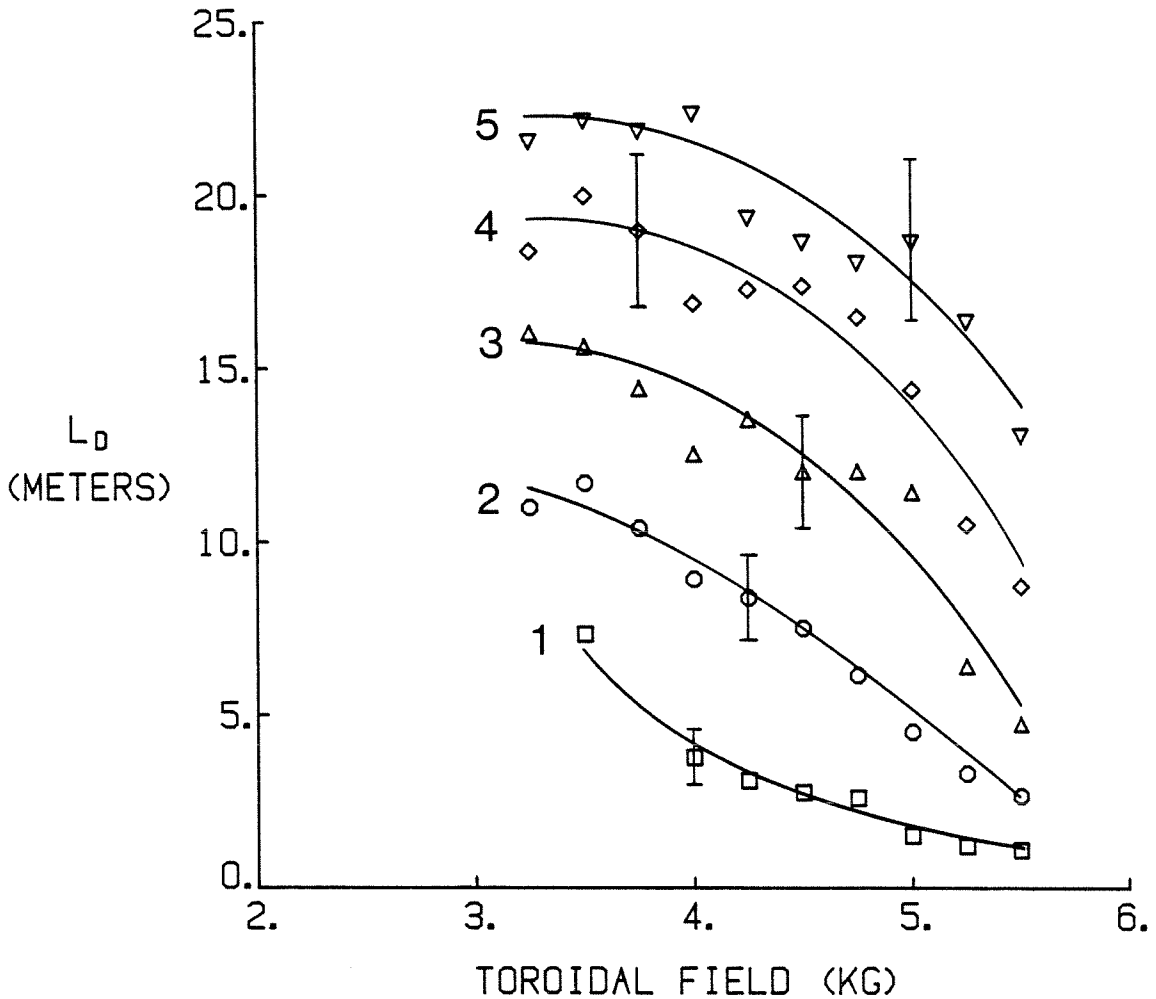

FIG. 7-13. The axial damping length, L_D, for the first five modes to appear during the density rise after the gas puff, as functions of the toroidal magnetic field. The ceramic-insulated loop antenna was used to excite the waves at a frequency of 12 MHz. The data set analyzed was the same as for Figure 7-12. Note that the second-harmonic ($2\omega_{ci}$) layer enters the tokamak when $B_0 \simeq 2.5$ kG and exits when $B_0 \simeq 5.3$ kG; the fundamental (ω_{ci}) layer enters the tokamak when $B_0 \simeq 5.1$ kG.

Mode Order	Density (cm^{-3})	Q	L_D (m)	v_g (cm/sec)
1	2.7×10^{12}	25	4.2	6.36×10^{8}
2	4.1×10^{12}	152	9.5	2.39×10^{8}
3	5.5×10^{12}	308	14.5	1.77×10^{8}
4	6.8×10^{12}	541	18.5	1.29×10^{8}
5	7.9×10^{12}	884	21.5	0.92×10^{8}

TABLE 7-1. Calculation of the parallel group velocity, v_g, from measurements of the wave Q and the damping length L_D, using equation 7.7. The excitation frequency was 12 MHz and the toroidal magnetic field on axis was 4.0 kG.

7.2 Wave-Packet Experiments

7.2.1 Introduction

The wave response in the tokamak plasma is dominated by interference leading to toroidal eigenmodes at specific plasma densities. The large amplitude peaks at the resonances complicate wave measurements, and some are only feasible at the discrete eigendensities. For instance, the wave damping and cavity Q measurements (and consequently, the group velocity calculation), described in section 7.1.5 yield information only at the discrete set of densities corresponding to modes. It would be useful, from the point of view of understanding the physics of the wave propagation and damping, to be able to observe the waves without interference effects, as would be the case if the waves were propagating in an infinite cylinder geometry. Since the waves travel with finite group velocity, one approach is to examine the waves on a time scale short compared with the characteristic time for eigenmode formation, i.e., short compared with the transit time of the wave around the torus. Launching wave-packets from the antenna with very short bursts of RF current was found to be a useful approach to study wave propagation without interference. The time-of-flight of the wave disturbance around the tokamak gives direct information about the parallel (toroidal) group velocity.

Wave-packet techniques have been used previously in plasma physics, primarily to investigate the propagation of electron plasma surface waves in cylindrical geometry [Demokan et al., 1971; Anicin et al., 1972; Landt et al., 1974]. A good review of this work is given by Moisan [1982]. In tokamaks, the only previous use of the technique appears to be an experiment which launched lower hybrid waves in the Doublet IIa tokamak [Luxon et al., 1980]. The antenna in that case was excited with 100 nsec bursts of RF current at 800 MHz. Use of the technique in the ion cyclotron range of frequencies is difficult in the Caltech Research Tokamak because the tokamak dimensions

are small and the group velocity is relatively high: the wave can propagate a substantial fraction of the toroidal circumference in one wave period. In order to localize the excited wave-packet in frequency space, long RF pulses consisting of many oscillations are desirable. This must compete, however, with the need to make the spatial extent of the wave-packet small compared to the toroidal circumference of the tokamak in order to maximize the sensitivity of the time-delay measurement.

7.2.2 Experimental Method

The RF system required some modification to permit excitation of the antenna with very short wavetrains. A typical antenna current waveform in these experiments consisted of about 4−5 periods of a sine wave; at a typical frequency of 12 MHz, the duration of this RF burst was then ~300 nsec. The apparatus used to generate such a pulse is shown in Figure 7-14. A double-balanced mixer (Minicircuits model ZAY-3-1) was used as a very fast RF switch (switching time ~1 nsec), gating a continuous signal generator. The output of the mixer was amplified by a 10 watt broadband amplifier (ENI 411LA); for lower frequencies a specially modified Marko solid state 100 watt amplifier (originally designed for amateur radio use) could be used as well.

The high-Q impedance-matching network which was used in all of the previously described experiments to match the antenna impedance to that of the generator was removed for these experiments; this was necessary in order to prevent the network from ringing for a long period of time when excited with the short RF burst. The output of the broadband amplifier led, through a long 50 Ω coaxial cable, directly to the ceramic insulator on the end of the antenna feeder tube (a coaxial connector was constructed for this arrangement). Since the impedance mismatch between the cable from the generator and the antenna was now very large, the RF pulse incident on the antenna gave rise to

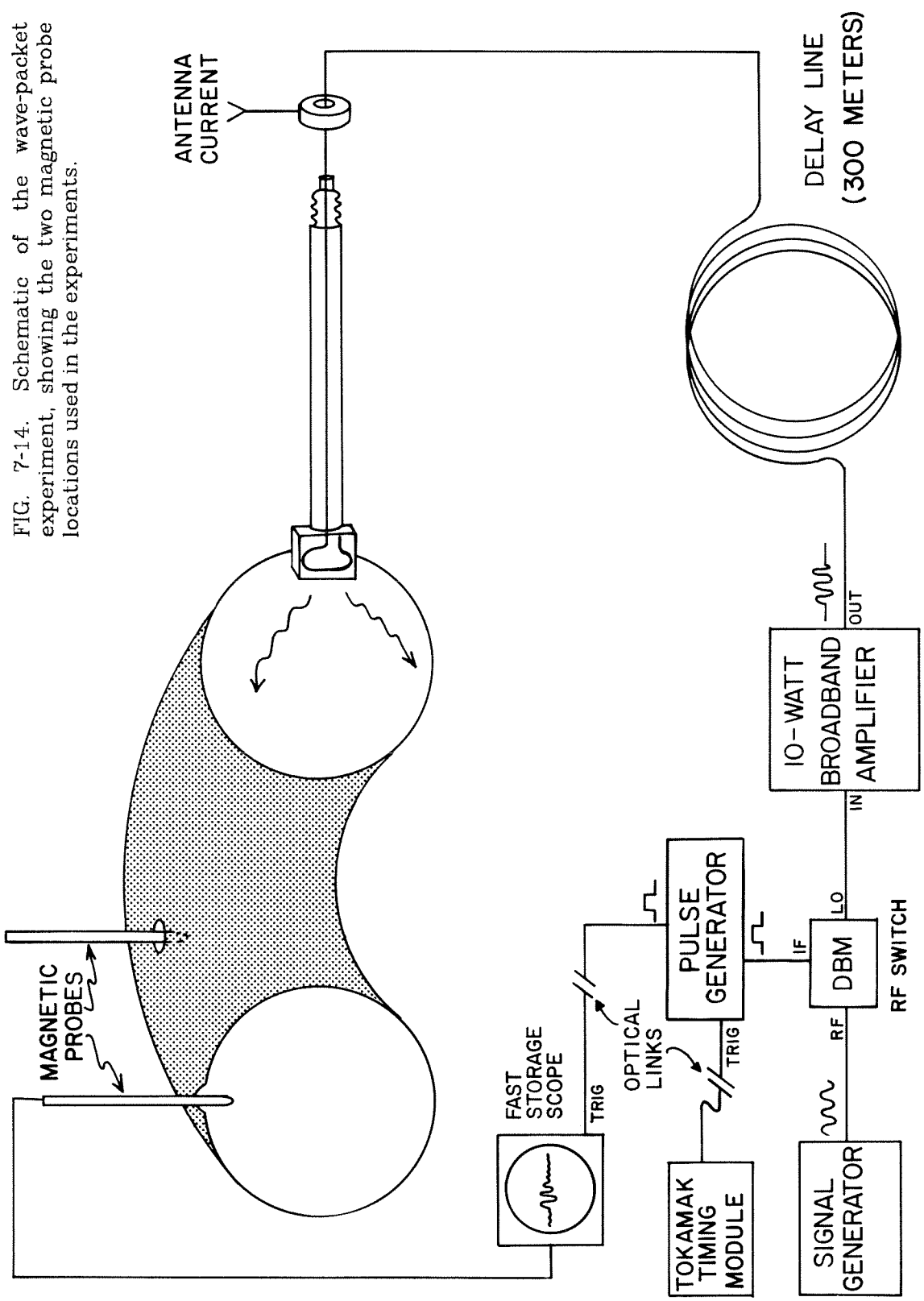

FIG. 7-14. Schematic of the wave-packet experiment, showing the two magnetic probe locations used in the experiments.

a substantial reflected pulse. This reflected pulse traversed the cable back to the generator at which point another reflected pulse was generated, traveling again toward the antenna. The object of this experiment was to excite the RF antenna with a short, isolated burst of RF current. Therefore, the cable between the generator and the antenna was made sufficiently long (300 m) that the round-trip propagation time for the reflected wave (~3 μsec) was long compared to the time scales of interest. In order to prevent excessive power loss in the incident pulse, the delay line was made from a large-diameter cable (RG-17 A/U).

The antenna current waveform for the ceramic-insulated loop antenna was observed with an RF current monitor (Ion Physics Co. model CM-100-L) mounted at the end of the antenna feeder tube. The "T" antenna was also used to excite wave-packets, and it was more convenient in this case to use a broad-band directional coupler, mounted at the end of the antenna feeder tube, to monitor the incident waveform. The wave fields in the tokamak were detected with the magnetic probes described previously; the signal from the probe was sometimes amplified with a broadband (1 – 520 MHz) +30 db gain amplifier (TRW model CA2820). The only available data recording system capable of handling the sub-microsecond time scales of these experiments was a Tektronix model 466 storage oscilloscope with a bandwidth of 100 MHz. The scope trace was recorded with a standard Polaroid camera. In order to avoid the need for corrections, the cables leading from the magnetic probe and from the antenna current monitor (or directional coupler) to the RF electronics cabinet were matched in length. Also, the time delays associated with the antenna current monitor and the directional coupler were investigated and found to be negligible.

A timing module in the tokamak control rack provided the initial signal to start the experiment. The module provided a pulse which could be delayed to

any portion of the tokamak shot. The signal triggered a pulse generator (Systron-Donner model 101) with two outputs. One of the outputs gated the RF switch; the other triggered the fast oscilloscope. High-speed optical links (H.P. model HBFR-0500) with very low triggering jitter were used for isolation between the tokamak timing module and the pulse generator, and between the pulse generator and the oscilloscope. These electrical breaks eliminated all ground loops from the system. A schematic of the entire experiment is shown in Figure 7-14.

Since only one high-speed storage channel was available, it had to be switched between the exciting signal (the RF antenna current) and the received signal (from the magnetic probe). In order to ascertain the propagation time between the launched wave and the received signal, it was crucial that the oscilloscope trigger at precisely the same time from shot to shot. This was investigated at some length during actual tokamak shots; the triggering was found to be completely independent of interference from the tokamak stray magnetic fields and the triggering jitter was negligible.

7.2.3 Experimental Data

Some typical raw probe signals are shown in Figure 7-15. The diagram at the top of the figure depicts the experimental geometry; in this case the magnetic probe was located in tokamak port #1, 180° toroidally and 90° poloidally away from the RF antenna. The antenna was the ceramic-insulated loop, the fundamental frequency of excitation was 12 MHz, the toroidal magnetic field on axis was 4.0 kG, and the magnetic probe was 3.0 cm past the tokamak wall, oriented to measure the toroidal component of the wave field. The RF pulse was triggered at a time during the plasma shot when the density was $\sim 8 \times 10^{12}$ cm^{-3}. In each plot of raw signals, the top trace is the RF current (or incident voltage) which excites the antenna and the bottom trace is the

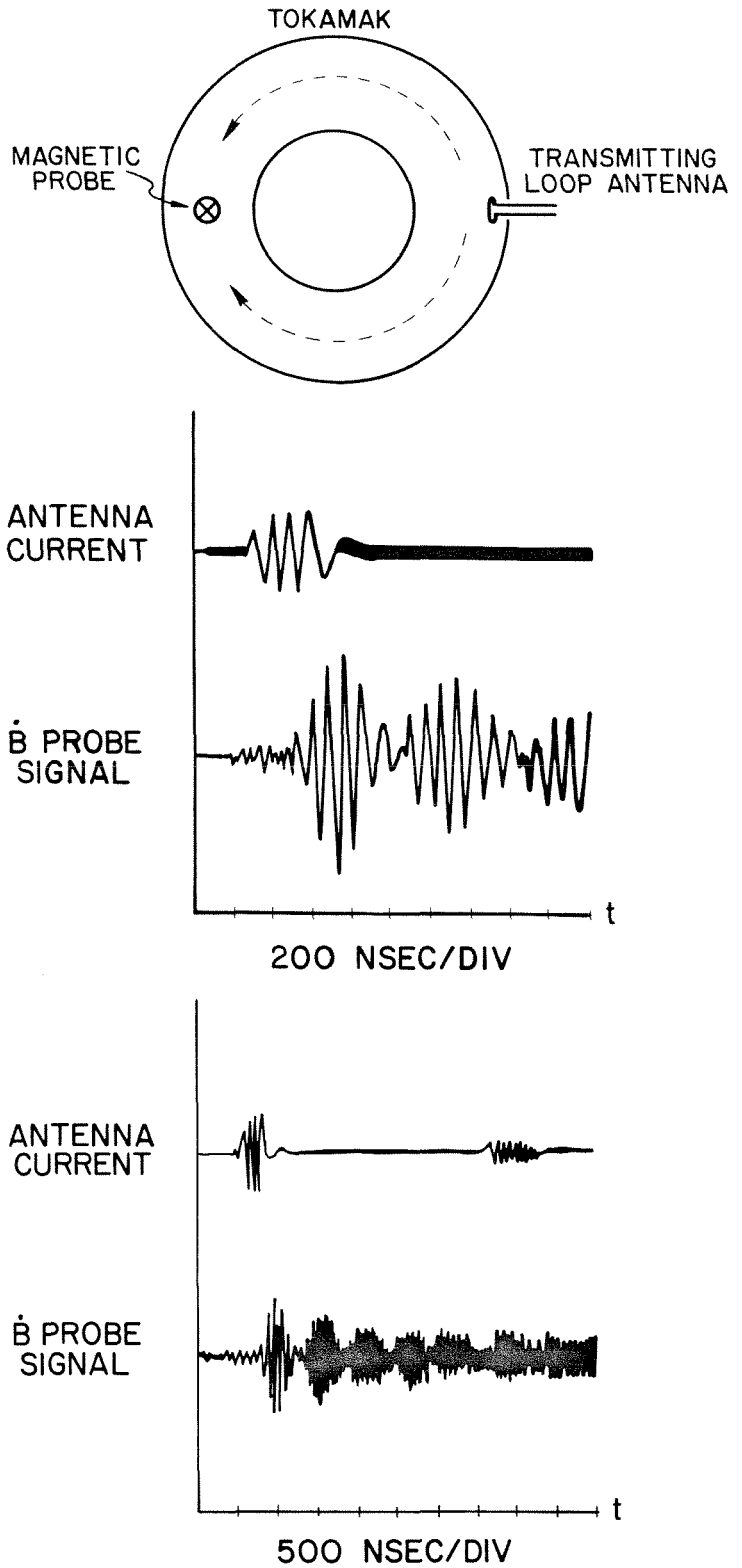

FIG. 7-15. Typical magnetic probe and antenna current signals for two different time scales, using the ceramic-insulated loop antenna. The probe was located in tokamak port #1.

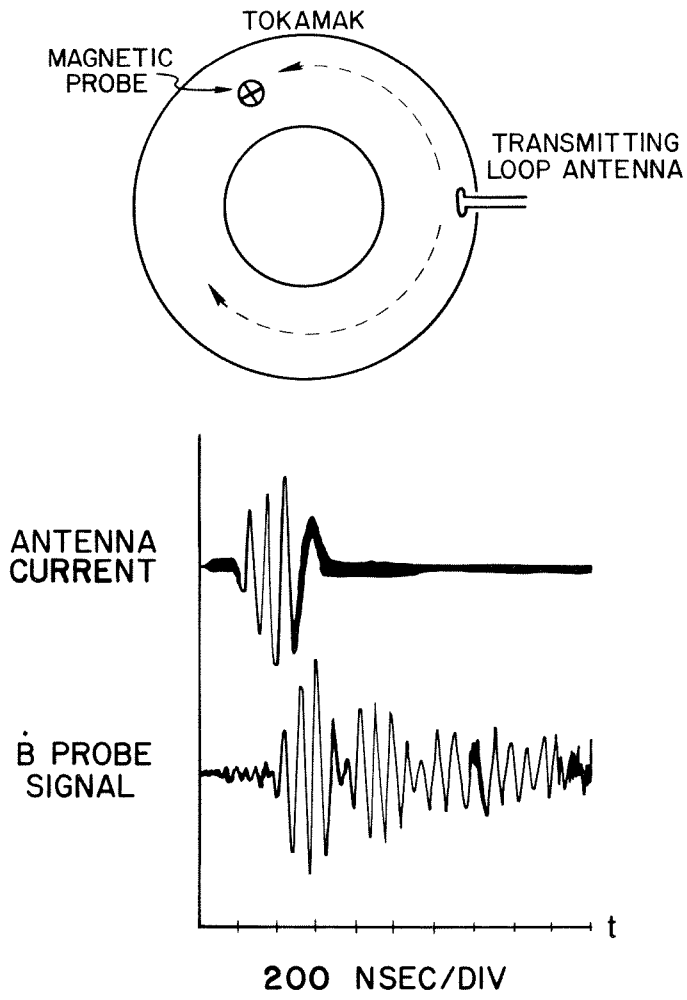

FIG. 7-16. Typical magnetic probe and antenna current signals for the ceramic-insulated loop antenna; the probe was located in tokamak port #3.

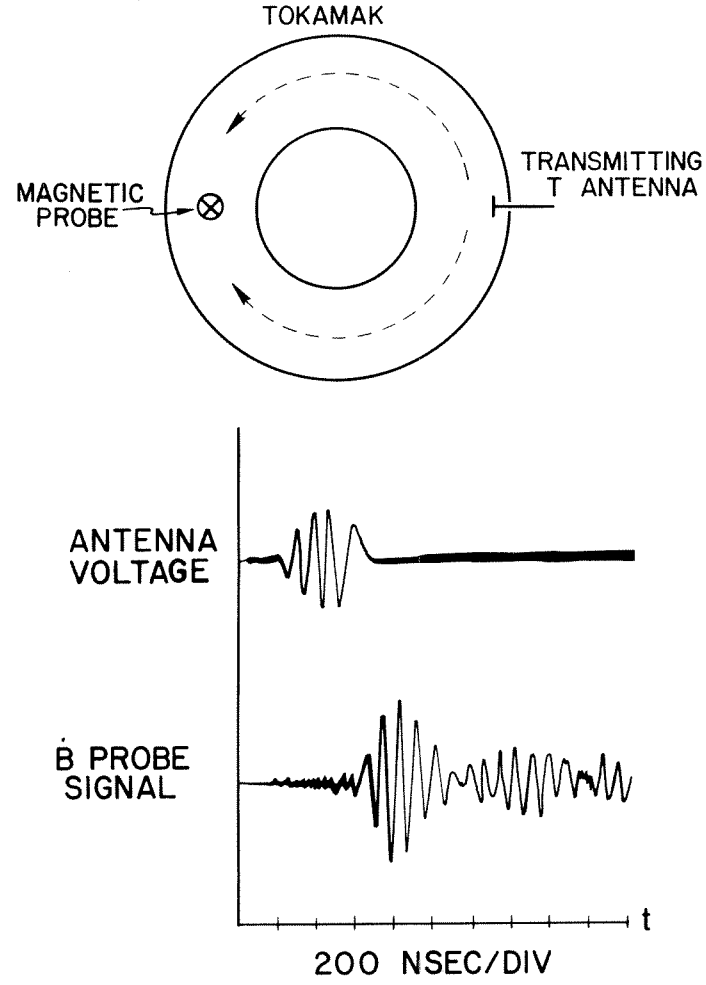

FIG. 7-17. Typical magnetic probe and antenna forward voltage signals for the "T" antenna; the probe was located in tokamak port #1.

received signal from the magnetic probe; the time axis is the same for both. Note that the antenna current and magnetic probe signals were taken from successive tokamak shots (because only one data channel was available). The antenna excitation current signal varied negligibly from shot to shot and was, in fact, unaffected by the tokamak firing (i.e., the same trace was obtained by triggering the RF system alone).

The antenna current pulse shown in the center plot of Figure 7-15 is about four periods long. The received signal has a distinct structure. It consists of a series of envelopes of diminishing amplitude, with the first envelope somewhat delayed with respect to the antenna current pulse. As depicted in the diagram at the top, these signals apparently result from wave-packets traveling symmetrically in opposite directions around the tokamak. The first envelope results when the packets have traveled half way around the torus; the second envelope results from the packets traveling another full circuit around the torus. Note that the time delay between the centers of the antenna current envelope and the first received signal envelope is roughly half of the time delay between the centers of the first and second received signal envelopes; this is consistent with the idea that the disturbance travels toroidally with constant velocity.

The lower plot in Figure 7-15 shows the signals from another tokamak shot on a longer time scale; all other parameters were approximately the same. The small signal appearing at $t \sim 3.5$ μsec on the antenna current trace is the first reflection from the incident pulse, having traveled through the delay line and back to the antenna again. Note that the received probe signal displays at least four distinct envelopes of diminishing amplitude. The successive envelopes appear to become broader and eventually the signal loses its coherent structure. The envelopes which are clear are approximately equally spaced in time, supporting the hypothesis that they result from wave-packets

making multiple transits around the tokamak.

Figure 7-16 shows typical raw signals when the magnetic probe was located in tokamak port #3, 105° toroidally and 90° poloidally away from the RF antenna. Other experimental parameters were the same as for the previous figure. Now only the first two received signals envelopes are distinct. The peak of the second envelope occurs about 300 nsec after the peak of the first envelope, whereas in Figure 7-15 the peaks of the first two envelopes are separated by ~600 nsec. This is not unreasonable, if we postulate that two wave-packets are indeed propagating in opposite directions around the tokamak at constant velocity v_g. From Figure 7-15, the packet velocity is approximately 5×10^8 cm/sec. Then for the geometry of Figure 7-16, the expected time delay between the arrivals of the clockwise-going and counterclockwise-going wave-packets at the magnetic probe is $\frac{2\pi R_0}{v_g}\left\{\frac{2\times(180^\circ - 105^\circ)}{360^\circ}\right\} \simeq 240$ nsec, in reasonable agreement with the observation.

The wave-packets propagating around the tokamak have a finite spatial extent, and this limits the precision of the time-of-flight measurement. The toroidal length of the wave-packet could be shortened by reducing the length of the current excitation pulse. This does not in general help to increase the clarity of the received signal envelopes, however, because the shorter the pulse is in time, the broader it is in frequency-space. Due to non-linear dispersion ($\frac{\partial^2 \omega}{\partial k_\parallel^2} \neq 0$), the wave-packet envelope broadens as it travels; the shorter the excitation pulse, the greater the broadening. Experimentally, the optimum antenna current pulse typically consisted of 4−5 cycles. Locating the magnetic probe 180° away from the RF antenna in the toroidal direction also optimized the received signal envelope separation, as that position allowed the greatest time between passes of the wave-packet.

The "T" antenna was also used to excite wave-packets. An example of the raw signals using this antenna is shown in Figure 7-17. The excitation frequency was 12 MHz, and the toroidal magnetic field on axis was 5.5 kG. The magnetic probe was positioned, as shown in the diagram, 180° toroidally away from the RF antenna. The probe coil was 2.0 cm past the tokamak wall and was oriented to measure the toroidal component of the wave magnetic field. The first received signal envelope is clearly visible, although the second is less distinct. The amplitude of the second envelope was typically less with the "T" antenna than the corresponding amplitude using the loop antenna. Note that the time delay of the received signal with respect to the excitation current is longer than for the previously displayed shots. The reason for this, as will be seen in more detail later, is that the group velocity decreases as the toroidal magnetic field increases; this shot used a substantially higher toroidal field.

Wave-Packet Parameter Scans

Approximately 500 tokamak shots were recorded (using the digital data system for the standard tokamak diagnostics and Polaroid film for the wave-packet signals) while changing various tokamak and RF parameters. The magnetic probe used for these investigations was located in tokamak port #1 and was oriented to respond to the toroidal component of the wave magnetic field. The resulting data set was analyzed to yield the packet velocity as a function of the RF frequency, the toroidal magnetic field, the plasma density, and the probe insertion past the wall; in addition, the amplitude of the packet signal was investigated as a function of the probe insertion. The packet velocity was defined as the major toroidal circumference (2.92 m) divided by the time delay between the centers of the first and second received signal envelopes. In cases where the second signal envelope was not clear (as with some of the data taken with the "T" antenna), half of the major circumference was divided by the time

delay between the centers of the antenna current envelope and the first received signal envelope. Because the signal records were photographic in nature, the digital data analysis techniques used for all of the other experiments were unavailable. Tracings were (laborously) made of the signal on each photograph, and the envelopes were sketched in; measurements were then made on the tracing using a scale subdivided to 0.25 mm. This procedure was, of course, subject to some arbitrary judgements. Nevertheless, although the precision of the experiment was not great, useful trends in the wave-packet velocity were clearly established.

The variation of the wave-packet velocity with the RF excitation frequency is shown in Figure 7-18 for both the ceramic-insulated loop antenna and the "T" antenna. The toroidal magnetic field on axis was 4.0 kG, and the RF pulse was triggered at a point during the density rise after the gas puff when the density was approximately 8×10^{12} cm^{-3}. The results for the two antennas were similar, with the packet velocity increasing almost linearly with frequency.

The variation of the wave-packet velocity with the toroidal magnetic field is shown in Figure 7-19 for the loop and "T" antennas. The excitation frequency was 12 MHz and the density at the time at which the RF pulse was triggered was again $\sim8\times10^{12}$ cm^{-3}. The packet velocities for the two antennas were similar in amplitude and decreased as the toroidal field was raised.

The dependence of the packet velocity on the plasma density is shown in Figure 7-20 for the loop antenna; for this experiment the excitation frequency was 12 MHz and the toroidal field on axis was 4.0 kG. The density was increased at the time of the RF pulse by keeping the gas puff constant and varying the time during the discharge density rise at which the RF pulse was triggered. The results show that the packet velocity decreased somewhat as the density increased.

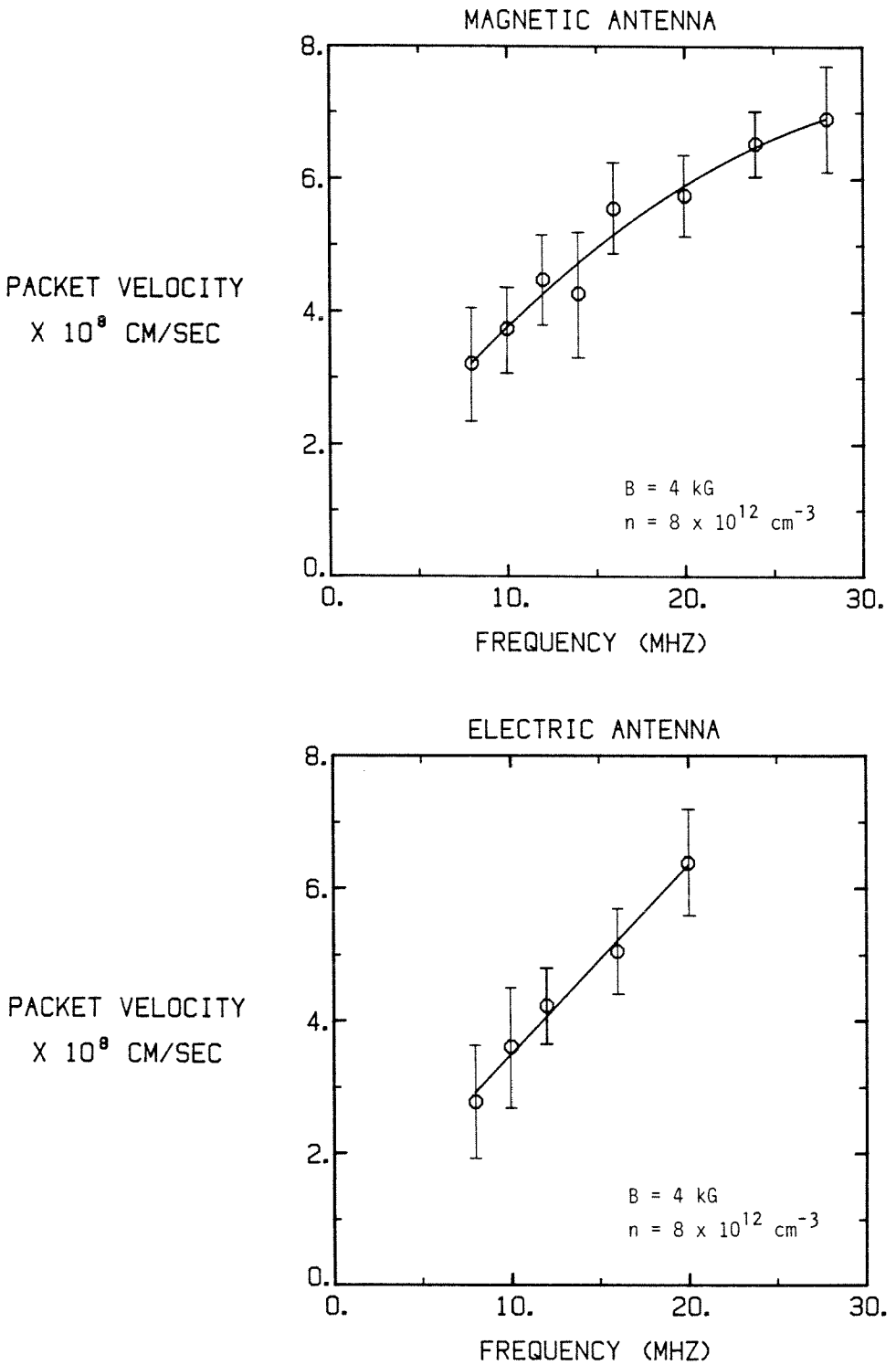

FIG. 7-18. Variation of the wave-packet velocity with excitation frequency, for the ceramic-insulated loop antenna (top) and the "T" antenna (bottom).

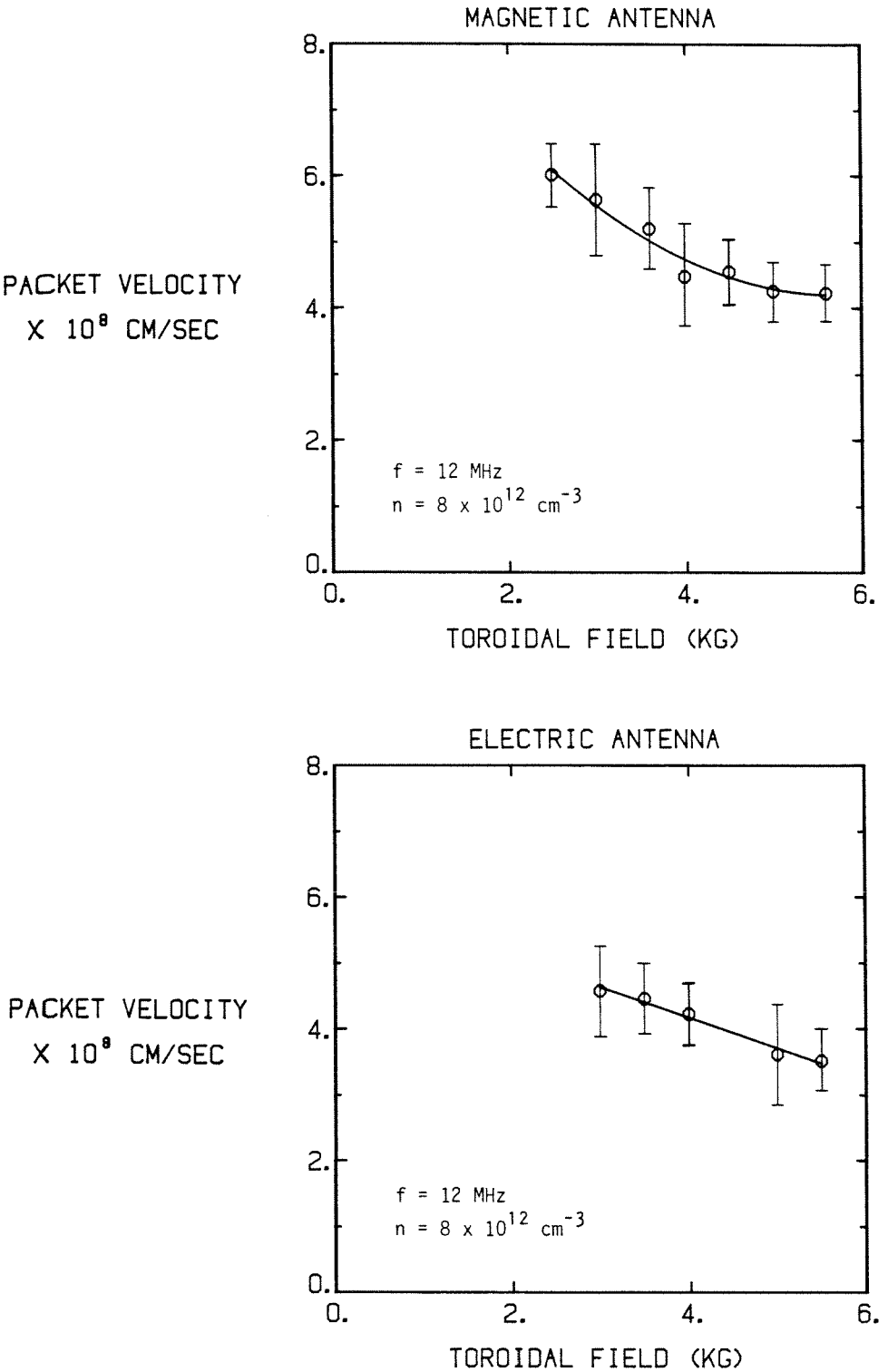

FIG. 7-19. Variation of the wave-packet velocity with toroidal magnetic field, for the ceramic-insulated loop antenna (top) and the "T" antenna (bottom).

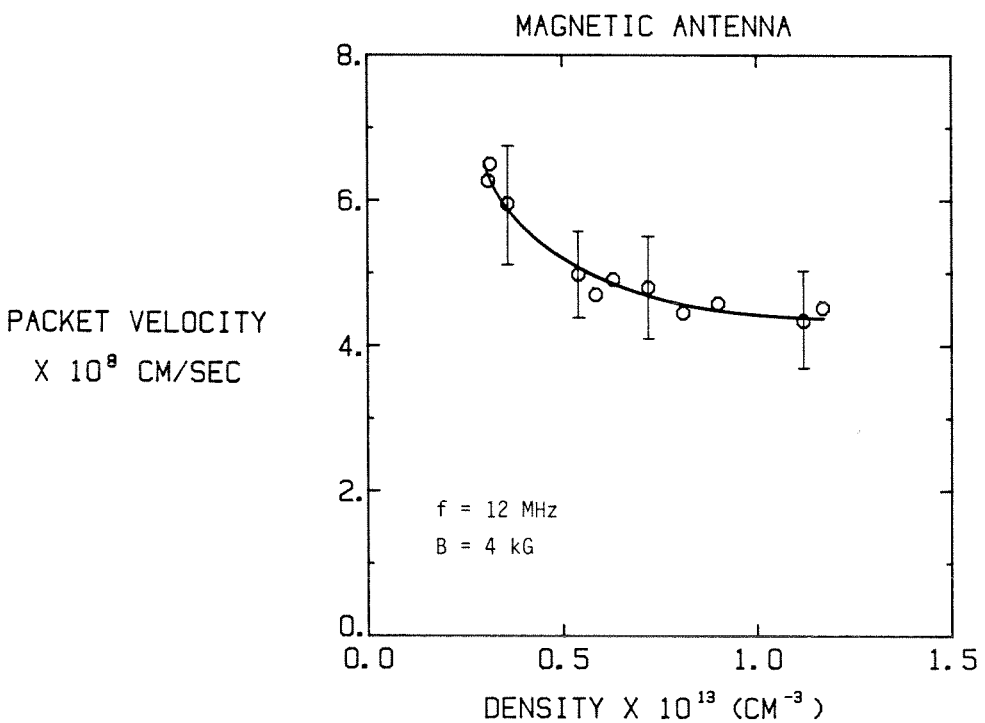

FIG. 7-20. Variation of the wave-packet velocity with plasma density, for the ceramic-insulated loop antenna.

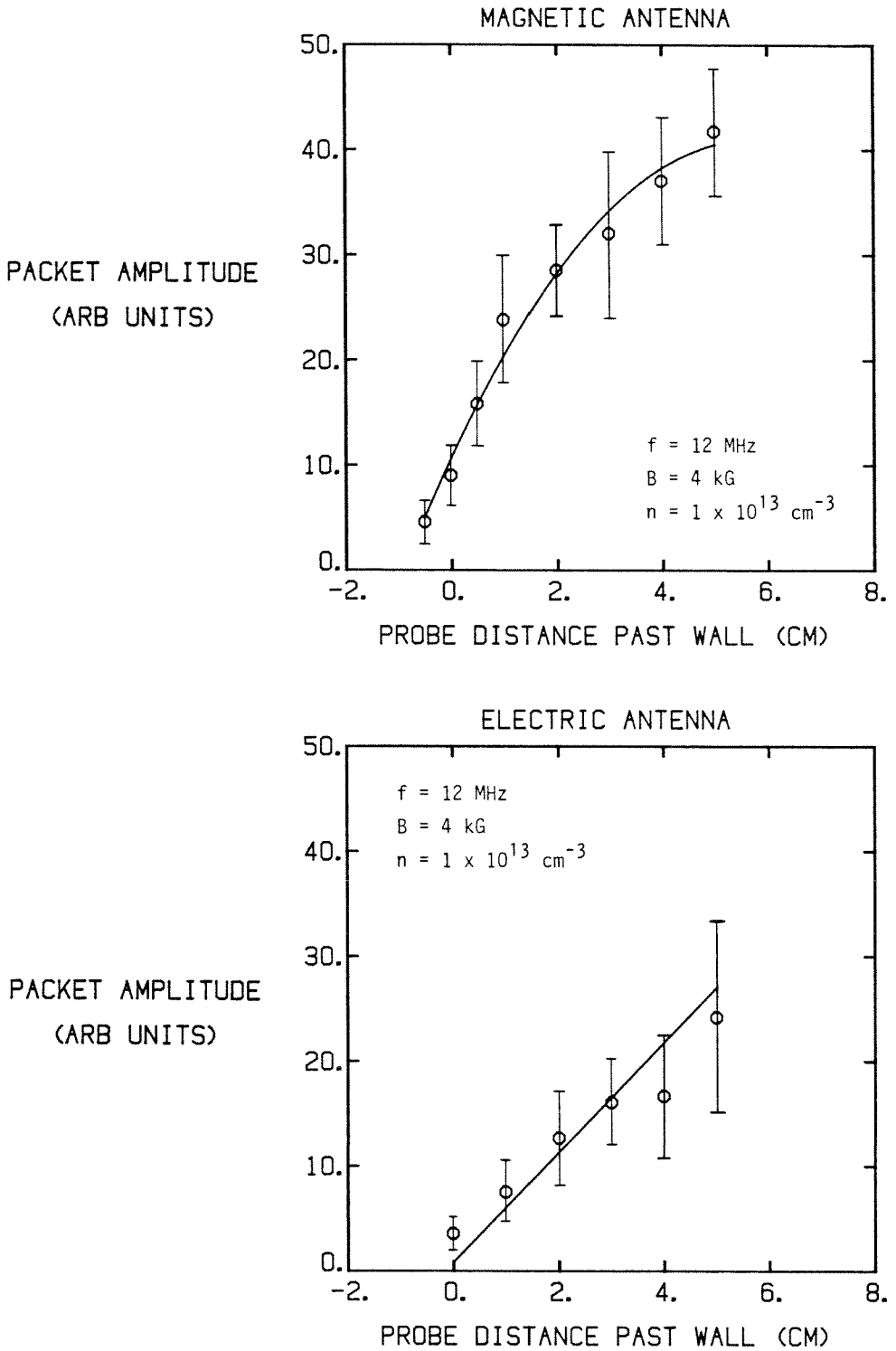

FIG. 7-21. Variation of the wave-packet peak magnetic probe signal with probe insertion past the wall, for the ceramic-insulated loop antenna (top) and the "T" antenna (bottom).

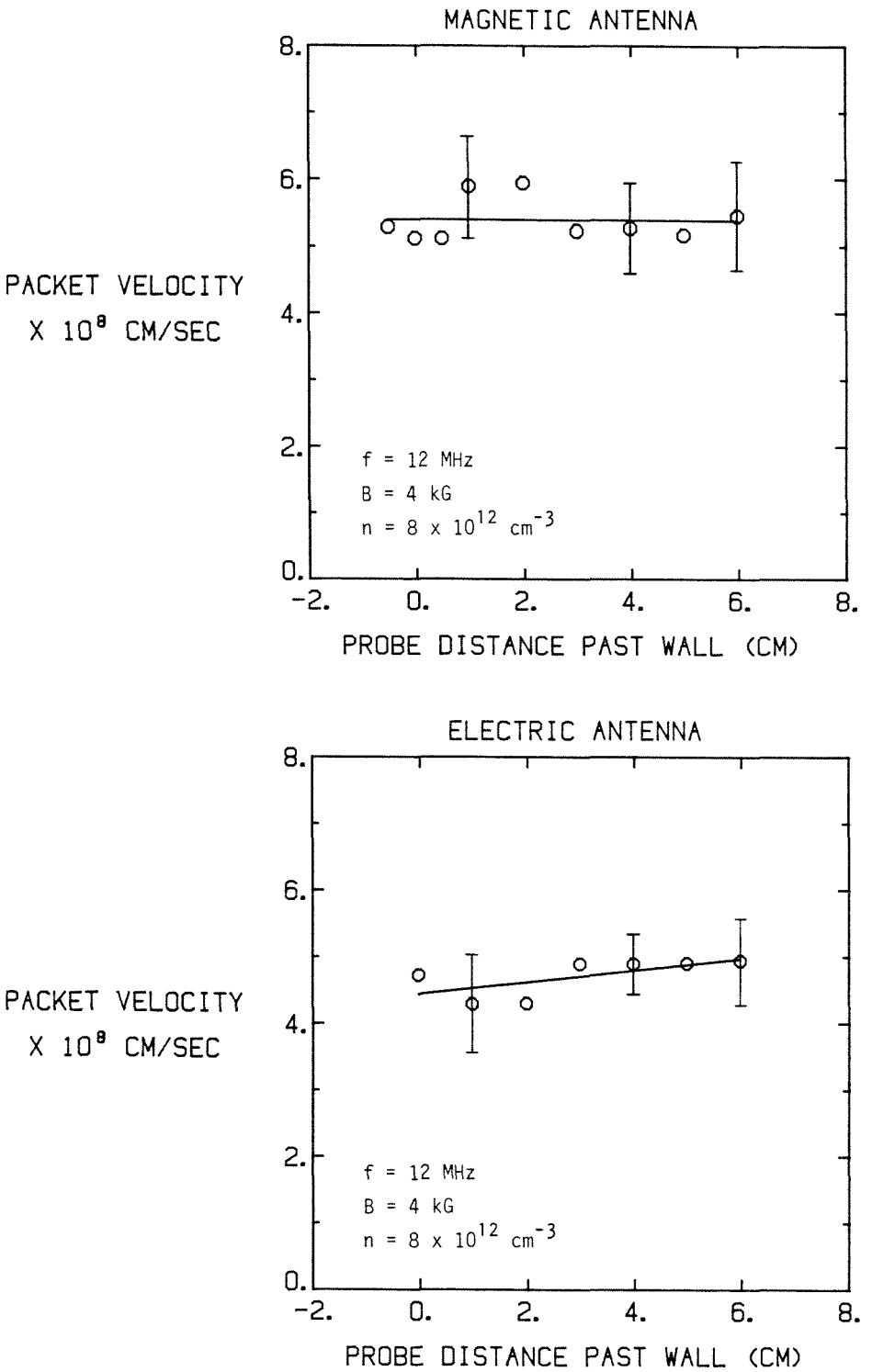

FIG. 7-22. Variation of the wave-packet velocity with insertion of the probe past the wall, for the ceramic-insulated loop antenna (top) and the "T" antenna (bottom).

The wave-packet peak magnetic field amplitude is plotted as a function of the probe insertion in Figure 7-21 for both the loop and "T" antennas. The excitation frequency was 12 MHz, the toroidal magnetic field on axis was 4.0 kG, and the plasma density at the time of the RF pulse was $\sim 1\times10^{13}$ cm^{-3}. The packet amplitude increases substantially as the probe moves into the plasma. This result shows that the observed wave-packet was not simply a surface-wave phenomena; the fields propagated throughout the plasma.

Finally, the variation of the wave-packet velocity as the magnetic field probe was inserted into the plasma is shown in Figure 7-22 for both the loop and "T" antennas. Again, the excitation frequency was 12 MHz, the toroidal magnetic field on axis was 4.0 kG, and the plasma density at the time of the RF pulse was $\sim 8\times10^{12}$ cm^{-3}. There was no significant change in the velocity as the probe moved up to 6 cm into the plasma. Thus, the wave-packet propagated toroidally with a constant velocity, independent of radius.

7.2.4 Theoretical Model

A disturbance localized in space can be represented as

$$B(\mathbf{x}, t) = \int A(\mathbf{k}) e^{i(\mathbf{k}\cdot\mathbf{x} - \omega t)}\, d^3\mathbf{k}, \tag{7.8}$$

where B is some field component and $\mathbf{k}$ is the wavevector and is related to ω through the dispersion relation. For a localized wave-packet, the coefficient $A(\mathbf{k})$ is peaked around some specific wavenumber $\mathbf{k}_c$. If the dispersion is not too great, then $\omega(\mathbf{k})$ can be expanded:

$$\omega(\mathbf{k}) = \omega_c + \left.\frac{\partial\omega}{\partial\mathbf{k}}\right|_{\mathbf{k}_c} (\mathbf{k} - \mathbf{k}_c) + \cdots \tag{7.9}$$

where $\omega_c = \omega(\mathbf{k}_c)$. Using this expansion in expression (7.8) yields [Jackson, 1960]:

$$B(\mathbf{x}, t) \simeq B\left[\mathbf{x} - \frac{\partial \omega}{\partial \mathbf{k}} t,\ 0\right] \cdot e^{i\left[\mathbf{k}_c \cdot \frac{\partial \omega}{\partial \mathbf{k}}\Big|_{\mathbf{k}_c} - \omega_c t\right]}, \tag{7.10}$$

so the initial spatial disturbance propagates without change in form (apart from an overall phase factor) at the group velocity $\mathbf{v}_g \equiv \frac{\partial \omega}{\partial \mathbf{k}}$. Including higher-order terms in the expansion 7.9 shows that the initial spatial form of the packet spreads out or broadens as it propagates.

The theoretical models discussed in Chapter 2 describe the propagation of waves in a cylindrical model of the tokamak. The fields away from the excitation source can be written as a sum over all of the normal modes:

$$B(\rho, \theta, z; t) = \int dk_{\|} \sum_{m,l} f_{m,l}(\rho)\, e^{i(k_{\|} z + m\theta - \omega t)}. \tag{7.11}$$

where m and l are the poloidal and radial mode numbers, and the cylinder is assumed to be of infinite extent so that $k_{\|}$ is not discretized. For each mode, $k_{\|}$ is related to ω through the dispersion relation, which, for the cold plasma, zero-electron mass model, is given by equation 2.66. The observed modes were propagating in the z-direction and were not evanescent in either the radial or poloidal directions; hence $k_{\|}$, m, and l must all be real. From Figure 2-9d, it is expected that over most of the density and frequency parameter range of the experiments, the only toroidally-propagating ($k_{\|} > 0$) mode is the $m = 1$, $l = 1$ mode. This presumption is also supported by the results of section 7.1.3 which show that the first $4-5$ eigenmodes all have $m = 1$ poloidal character. If only a single mode is propagating, the velocity at which a disturbance travels can be easily calculated.

The group velocity in the toroidal direction for the $m = 1$ modes can be found by calculating $\frac{\partial \omega}{\partial k_{\|}}$. Making use of the dispersion relation for the zero-electron mass model (equation 2.66), the group velocity is predicted to decrease sharply as the density decreases and approaches the cutoff density;

this can be seen intuitively from Figure 2-9a. The eigenmode curves can be viewed as curves of constant and equally-spaced $k_{\|}$ in density-frequency space; these curves are more closely spaced near the cutoff ($N=0$) curve. Thus, for a given $\Delta\omega$, the resulting change in $k_{\|}$ is greater for densities near the cutoff curve than it is for higher densities, and $\frac{\Delta\omega}{\Delta k_{\|}}$ is correspondingly smaller. The fact that this dependence of group velocity on density was contradictory to the experimental result (Figure 7-20) led to the consideration of further models.

The effect of a radial plasma density profile on the dispersion relation was considered in section 2.4. Using the numerically computed dispersion relation to calculate the group velocity did not change the form of the group velocity dependence on density near the cutoff; the group velocity was still found to decrease as the density decreased. The radial density profiles considered in section 2.4 were restricted in that the density had to be sufficiently large that $k_{\|}^2 - \varepsilon_{\perp} k_0^2 > 0$ everywhere, where $\varepsilon_{\perp}$ is the component of the cold-plasma dielectric tensor and $k_0 \equiv \frac{\omega}{c}$. For the cutoff mode, this requires the density to be large enough that the lower hybrid frequency (ω_{lh}) is everywhere greater than the excitation frequency (ω). The effect of a region of density low enough that $\omega_{lh} < \omega$ can be modeled with a vacuum layer at the plasma edge. The most dramatic effect of a vacuum layer, first discovered by Paoloni [1975b], is that the waves then have no cutoff, i.e., at a given frequency they can propagate down to very low densities.

Consider a radial plasma density profile given by

$$\begin{array}{lll} \text{Region I:} & n(\rho) = n_0 & (0 \le \rho < \rho_v) \\ \text{RegionII} & n(\rho) = 0 & (\rho_v \le \rho \le \rho_0) \end{array} \qquad (7.12)$$

Assuming that the fields vary as $e^{i(k_{\|} z + m\theta - \omega t)}$, and neglecting the electron mass so that $E_z = 0$, the solution for the z–component of the magnetic field in

region I is, from the discussion of section 2.2.6,

$$B_{I_z}(\rho) = J_m(p\rho) \tag{7.13}$$

where p is the radial wavenumber given by equation 2.63 and the field has been normalized so that $B_{I_z}(\rho_0) = 1$. In region II, the wave equations (2.36) become uncoupled:

$$\nabla_\perp^2 B_{II_z} - T^2 B_{II_z} = 0 \tag{7.14a}$$

$$\nabla_\perp^2 E_{II_z} - T^2 E_{II_z} = 0\,, \tag{7.14b}$$

where $T^2 \equiv k_\parallel^2 - \frac{\omega^2}{c^2}$. The solutions for B_z and E_z in region II are then given by

$$B_{II_z}(\rho) = \alpha I_m(T\rho) + \beta K_m(T\rho) \tag{7.15a}$$

$$E_{II_z}(\rho) = \gamma I_m(T\rho) + \delta K_m(T\rho)\,, \tag{7.15b}$$

where I_m and K_m are the modified Bessel functions and α, β, γ, and δ are arbitrary constants. The boundary at $\rho = \rho_0$ is assumed to be perfectly conducting, hence E_{II_z} and E_{II_θ} vanish there. Continuity of the tangential component of the electric field at the interface between the two regions requires $E_{II_z}(\rho_V) = 0$, hence it follows that $\gamma = \delta = 0$ and E_z vanishes everywhere.

Using the relation between field components given by equation 2.52, the remaining components can be written as:

$$\text{Region I:} \quad \begin{cases} B_{I_\theta}(\rho) = -\dfrac{m}{\rho} G_1 B_{I_z} + G_3 \dfrac{\partial B_{I_z}}{\partial \rho} \\ B_{I_\rho}(\rho) = -\dfrac{im}{\rho} G_3 B_{I_z} + iG_1 \dfrac{\partial B_{I_z}}{\partial \rho} \\ E_{I_\theta}(\rho) = \dfrac{im}{\rho} G_2 B_{I_z} + iG_4 \dfrac{\partial B_{I_z}}{\partial \rho} \\ E_{I_\rho}(\rho) = \dfrac{m}{\rho} G_4 B_{I_z} + G_2 \dfrac{\partial B_{I_z}}{\partial \rho} \end{cases} \tag{7.16}$$

in region I, where the factors G_1, G_2, G_3, and G_4 are defined in equation 2.51. In region II, the fields are given simply by

$$\text{Region II:} \quad \begin{cases} B_{II_\theta}(\rho) = \dfrac{m}{\rho} \dfrac{k_\parallel}{T^2} B_{II_z} \\ B_{II_\rho}(\rho) = -i \dfrac{k_\parallel}{T^2} \dfrac{\partial B_{II_z}}{\partial \rho} \\ E_{II_\theta}(\rho) = i \dfrac{k_0}{T^2} \dfrac{\partial B_{II_z}}{\partial \rho} \\ E_{II_\rho}(\rho) = \dfrac{m}{\rho} \dfrac{k_0}{T^2} B_{II_z} \end{cases} \tag{7.17}$$

Since the boundary is perfectly conducting, it follows that the normal component of the magnetic field must vanish there: $B_{II_\rho}(\rho_0) = 0$. Using the above relations, this boundary condition yields a relation between α and β:

$$\frac{\alpha}{\beta} = (-1)^{m+1} \frac{\left(T K_{m+1}(T\rho_0) + \dfrac{m}{\rho_0} K_m(T\rho_0) \right)}{\left(T I_{m+1}(T\rho_0) + \dfrac{m}{\rho_0} I_m(T\rho_0) \right)}. \tag{7.18}$$

Continuity of the z–component of the magnetic field at the plasma-vacuum interface, $B_{I_z}(\rho_v) = B_{II_z}(\rho_v)$ gives another relation between α and β:

$$\beta = \frac{J_m(p\rho_v) - \alpha I_m(T\rho_v)}{K_m(T\rho_v)}. \tag{7.19}$$

which, together with equation 7.18, allows solution for α and β in terms of the plasma parameters. Note that the θ–component of the magnetic field will, in general, not be continuous across the vacuum-plasma interface, because the infinite plasma conductivity in the z–direction arising from neglect of the electron mass allows a surface current to flow in the z–direction.

The θ–component of the electric field must also be continuous at the plasma-vacuum interface, i.e., $E_{I_\theta}(\rho_v) = E_{II_\theta}(\rho_v)$, which yields the following relation:

$$\frac{k_0}{T^2}\left[\alpha\left[T\,I_{m+1}(T\rho_v) + \frac{m}{\rho_v}I_m(T\rho_v)\right]\right] + (-1)^m\beta\left[T\,K_{m+1}(T\rho_v) + \frac{m}{\rho_v}K_m(T\rho_v)\right]$$

$$= \frac{m}{\rho_v}G_2\,J_m(p\,\rho_v) + G_4\left[\frac{m}{\rho_v}J_m(p\,\rho_v) - J_{m+1}(p\,\rho_v)\right] \quad . \tag{7.20}$$

Since α and β are determined from the other boundary conditions, the above equation represents the dispersion relation, relating ω to $k_\parallel$, the plasma parameters, and the geometry.

Numerical evaluation of the dispersion relation for parameters appropriate to the Caltech tokamak demonstrates the lack of a cutoff when the vacuum layer is present. Figure 7-23 shows a plot of $k_\parallel$ as a function of the plasma density, for fixed frequency (12 MHz) and toroidal magnetic field (4.0 kG). Evaluations for the $m = 1$, first radial mode, are shown for vacuum layers 0.1 cm and 1.0 cm thick, as well as the result for a constant density profile without a vacuum layer. The density plotted is the line-averaged density for each curve, i.e., $n_0\frac{\rho_v}{\rho_0}$. Note that the curve evaluated without a vacuum layer shows a cutoff at a density of $\sim 3.6\times10^{12}$ cm^{-3}, while the curves for the cases with vacuum layers do not display cutoffs. For a given (line-averaged) density, the parallel wavenumber increases as the vacuum layer thickness increases.

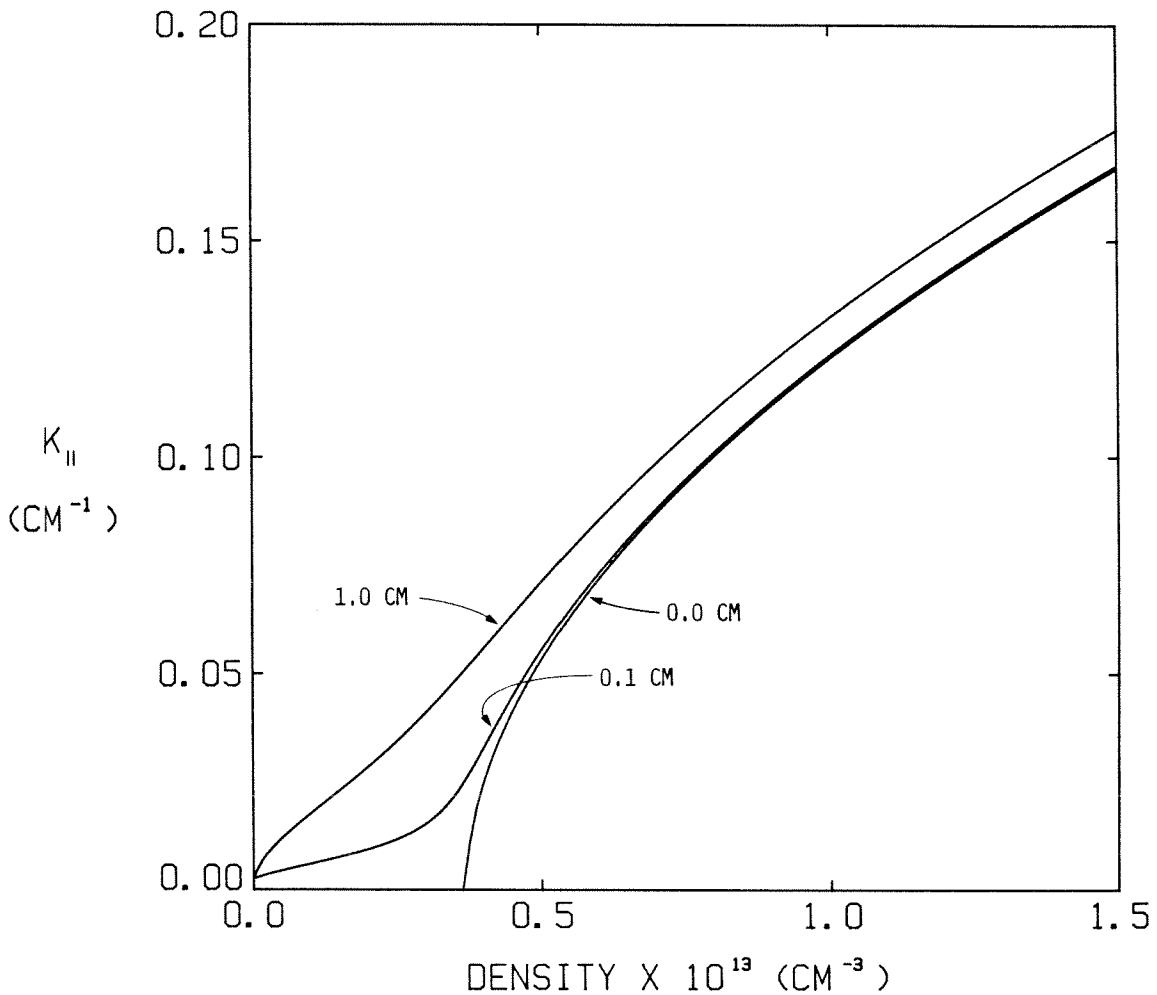

FIG. 7-23. Theoretical evaluation of $k_{\parallel}$ as a function of the line-averaged plasma density, for vacuum layers 0.1 cm and 1.0 cm thick; the result without a vacuum layer is also shown. Here $\omega/\omega_{ci} = 12$ MHz, $B_0 = 4.0$ kG, $p_0 = 16.2$ cm, and the calculations are for the $m = 1$, $l = 1$ mode. Note the absence of a cutoff when the vacuum layer is present.

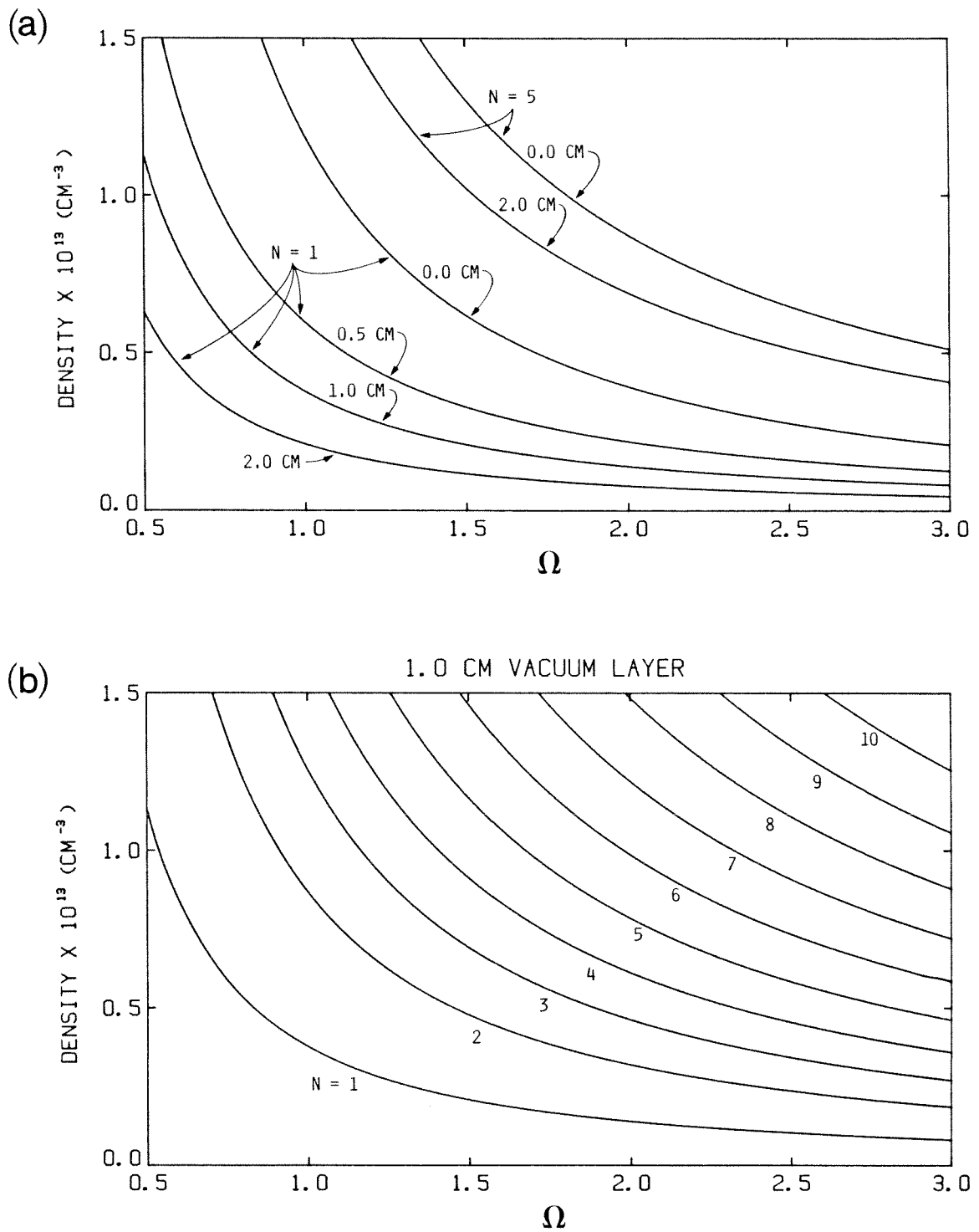

FIG. 7-24. a) Effect of various vacuum layers on the eigenmode dispersion curves for the $N=1, 5$, $m=1$, $l=1$ modes. Here $B_0=4.0$ kG and $\rho_0=16.2$ cm; also $\Omega \equiv \omega/\omega_{ci}$. b) Eigenmode curves for the $N=1-10$, $m=1$, $l=1$ modes, with a 1.0 cm vacuum layer. Again $B_0=4.0$ kG and $\rho_0=16.2$ cm. These curves should be compared with those of Figure 2-9a, calculated for the same parameters but without a vacuum layer.

Having obtained this result, it is easy to examine the effect of a vacuum layer on the eigenmode curves in density-frequency space. Referring to Figure 7-23, the eigenmodes occur at the densities for which $k_{\|} = \frac{N}{R_0} \simeq (0.022)\, N\ \mathrm{cm}^{-1}$, where R_0 is the the major toroidal radius and N is the toroidal mode number. Figure 7-24a shows the effect of various vacuum layers on the eigenmode curves for the $m = 1$, $l = 1$, $N = 1, 5$ modes. For a given excitation frequency, the larger the vacuum layer, the lower the corresponding density at which the eigenmode occurs. For a given vacuum layer thickness, the relative displacement of the eigenmode curve decreases for higher toroidal mode numbers (larger $k_{\|}$); this is also evident from Figure 7-23. For a 1.0 cm thick vacuum layer, the first ten toroidal eigenmode curves are shown in Figure 7-24b. Note that these results show the same qualitative effect as was observed with the quadratic density profile considered in section 2.4.2. In that case, however, the waves still suffered a cutoff at sufficiently low densities.

Returning to the discussion of the group velocity for wave packets, the dispersion relation in an infinite cylinder including a vacuum layer (equation 7.20) can be used to calculate the group velocity, $v_g = \frac{\partial \omega}{\partial k_{\|}}$, for the desired poloidal and radial mode. In keeping with the previous discussion, we consider only the $m = 1$, $l = 1$ mode; all other modes are assumed to be evanescent in the toroidal direction. Numerical evaluations of the group velocity as functions of the density, frequency, and toroidal field, for various vacuum layers, are displayed in Figures 7-25, 7-26, and 7-27; also plotted are the data from the wave-packet experiments.

Figure 7-25 shows the group, or wave-packet, velocity as a function of the plasma line-averaged density; the experimental points shown are for the ceramic-insulated loop antenna, taken from Figure 7-20. For these experi-

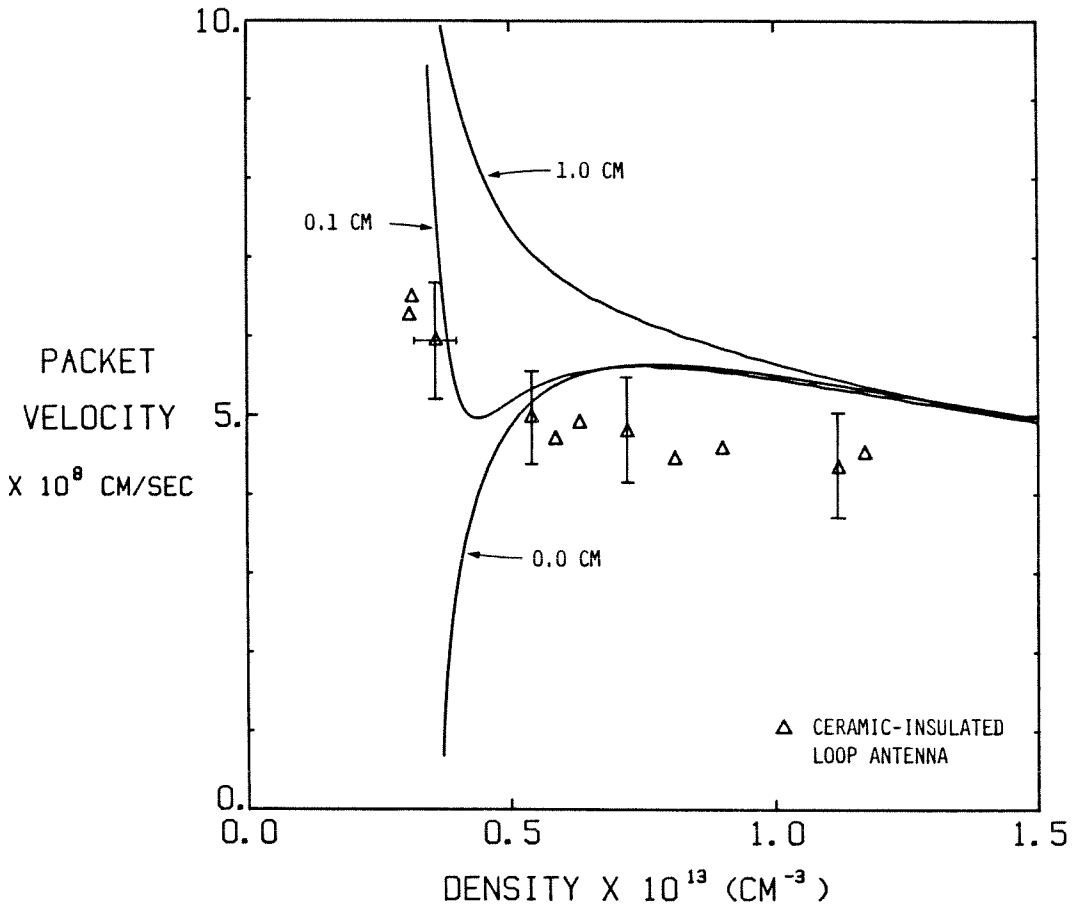

FIG. 7-25. Wave-packet velocity as a function of the line-averaged plasma density. The theoretical results (solid lines) are plotted for vacuum layers of 0.0, 0.1 and 1.0 cm; the experimental points are from Figure 7-20. Also $\omega/(2\pi) = 12$ MHz and $B_0 = 4.0$ kG.

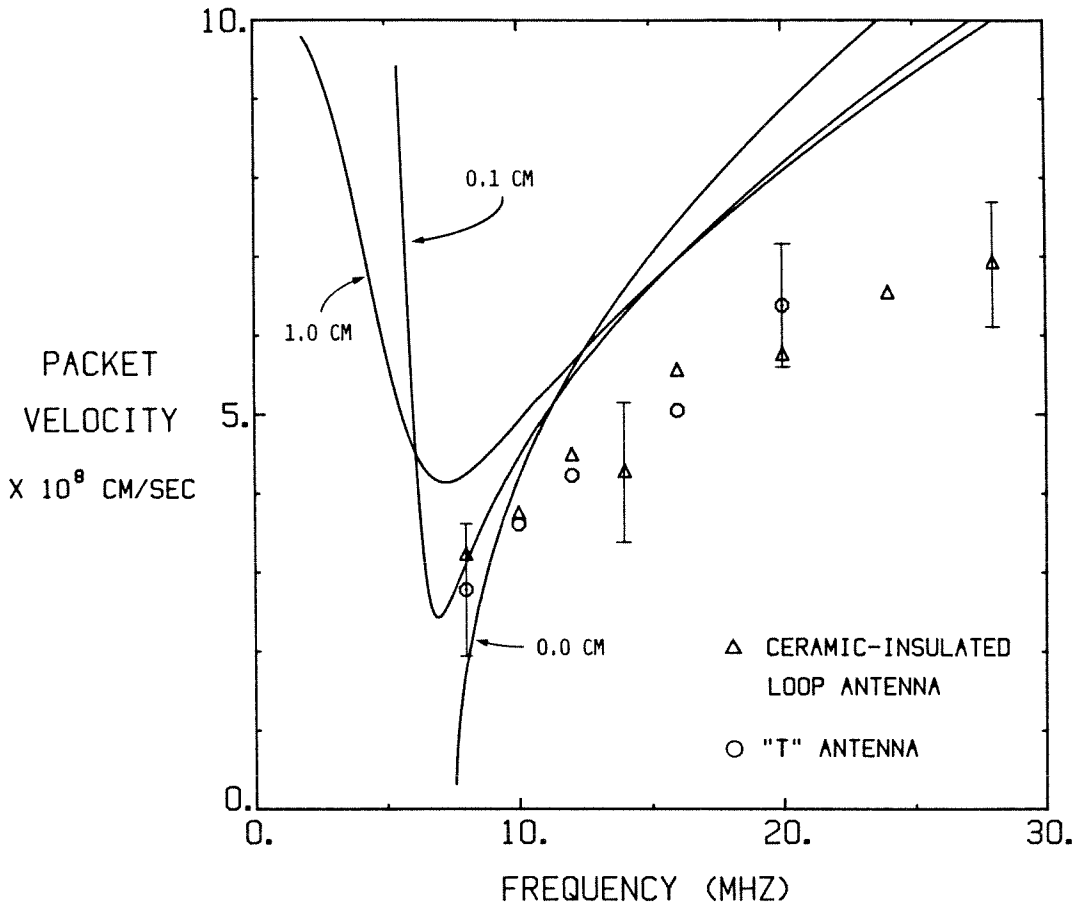

FIG. 7-26. Wave-packet velocity as a function of the excitation frequency. The theoretical results (solid lines) are plotted for vacuum layers of 0.0, 0.1, and 1.0 cm; the experimental points are from Figure 7-18. Also $n \simeq 8 \times 10^{12}$ cm^{-3} and $B_0 = 4.0$ kG.

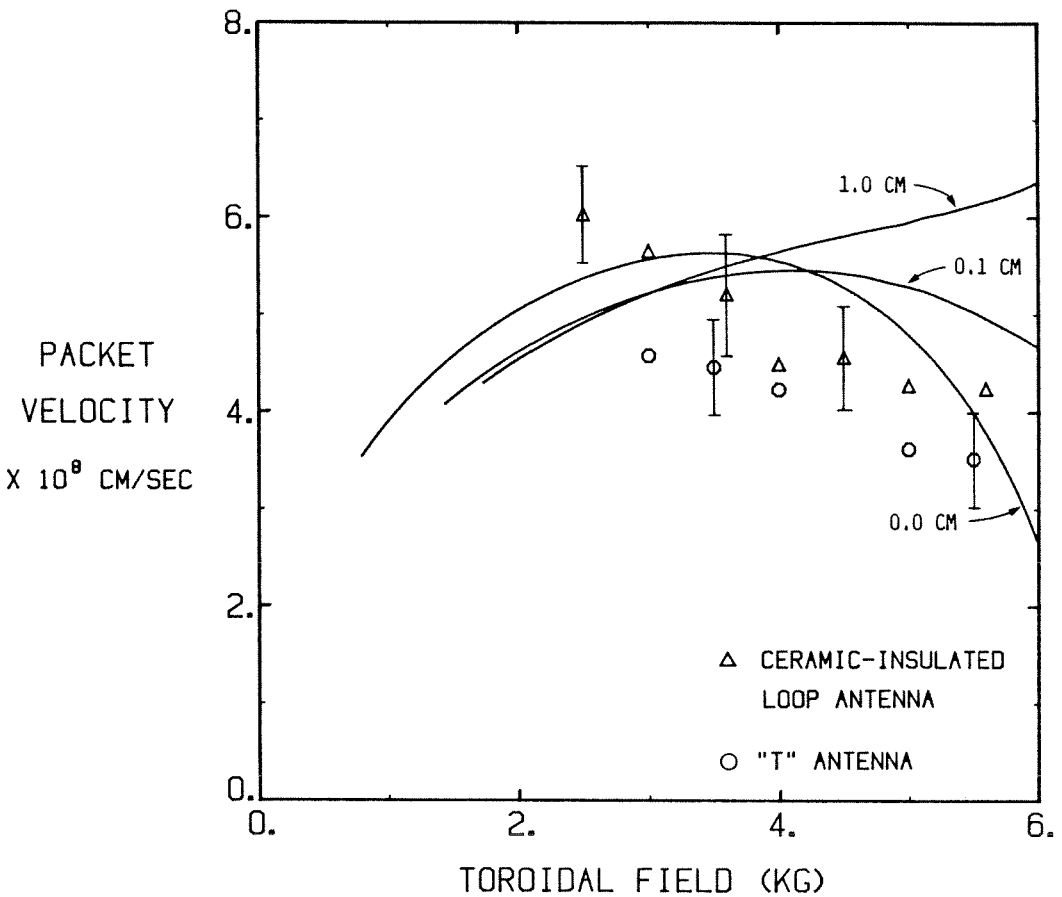

FIG. 7-27. Wave-packet velocity as a function of the toroidal magnetic field. The theoretical results (solid lines) are plotted for vacuum layers of 0.0, 0.1, and 1.0 cm; the experimental points are from Figure 7-19. Also $\omega/(2\pi) = 12$ MHz and $n \simeq 8 \times 10^{12}$ cm^{-3}.

ments and calculations, $\omega = 12$ MHz and $B_0 = 4.0$ kG. The most striking feature of the results is that the inclusion of a vacuum layer in the theoretical model yields a group velocity which increases as the density decreases, at low densities. This is in contrast to the result shown for the case without a vacuum layer which predicts the opposite dependence. Note that the curve for the 0.1 cm thick vacuum layer shows reasonable agreement with the experimental points; the other two curves show significant disagreement with each other and with the experimental data at low densities.

The theoretical and experimental variation of the group velocity with excitation frequency is shown in Figure 7-26. Here the density was 8×10^{12} cm^{-3} and the toroidal magnetic field was 4.0 kG; the experimental points are from Figure 7-18. The theoretical curves for the various vacuum layers do not differ greatly above a frequency of $\simeq$8 MHz. Below this frequency, the curves for the models with vacuum layers show increasing group velocity as the frequency decreases, while the curve for the case without a vacuum layer continues to decrease. The lowest frequency investigated experimentally, however, was 8.5 MHz, so the experiment cannot resolve the difference between the vacuum layer and constant density models at low frequencies. The agreement between the experimental points and the theoretical curves is reasonable, although at higher frequencies the experimental points occur at somewhat lower velocities than the theoretical curves. Part of the discrepancy at higher frequencies may be due to the excitation of other poloidal modes (most likely the $m = 0$ mode).

Variation of the group velocity with toroidal magnetic field is shown in Figure 7-27. Here the frequency was 12 MHz, the density was 8×10^{12} cm^{-3}, and the experimental points are from Figure 7-19. The agreement between the theoretical curves and the experimental points is again reasonable, except for the curve associated with the 1.0 cm vacuum layer; at high fields that curve predicts increasing group velocity with toroidal field, in contrast to the

experimental observation.

In summary, the agreement between the experimentally observed wave packet velocities and the theoretically calculated group velocity is surprisingly good. Inclusion of a vacuum layer at the plasma edge in the theoretical model yields the experimentally observed increase in group velocity as the density decreases, in contrast to the opposite result obtained without a vacuum layer. The best agreement is found for a vacuum layer $\sim$0.1 cm thick. The dependence of group velocity on frequency is similar for all of the theoretical models over the frequency range pertinent to the experimental results; substantial differences are predicted, however, at points below the lowest experimental frequency. The experimental data and the theoretical curves show a similar increase as the frequency is raised, but the agreement becomes worse at high frequencies; this may be the result of excitation of other poloidal modes. Finally, reasonable agreement between the experiment and the theory is observed for the variation of group velocity with toroidal magnetic field, except for part of the curve calculated with the 1.0 cm thick vacuum layer.

The results of this study are not intended to suggest that a vacuum layer such as described actually exists, but rather that the very low density plasma region near the tokamak wall can significantly affect the wave propagation. It should be noted that the discontinuous plasma density function assumed in the vacuum layer model neglects the lower hybrid resonance which occurs when $k_{\parallel}^2 - \varepsilon_{\perp} k_0^2 = 0$; the singularities which appear in the wave equations at this point may be important. Proper treatment of this effect requires consideration of warm-plasma effects and is beyond the scope of this thesis.

7.3 RF Current Probe Experiment

A surprising result of the impedance invesigations reported in Chapter 6 was that the exposed electric field antennas (the bare plate and "T" antennas) exhibited a large density-dependent loading which was independent of wave excitation. Nevertheless, the eigenmode excitation efficiency, defined as the wave amplitude divided by the antenna current, was comparable for both the electric field antennas and the more conventional loop antennas. The mechanism of coupling of the bare plate and "T" antennas to the fast wave eigenmodes, however, is not clear. One possibility is that the electric fields associated with the antennas couple directly to the wave electric fields; another is that the antennas drive currents in the plasma which then interact with the magnetic component of the wave fields. Because of the large continuous antenna loading, these antennas drive substantial RF currents throughout the tokamak shot.

The RF current leaving an electric field antenna must return via some path to the tokamak wall. The current within the plasma is carried largely by the charged particles; displacement current is usually negligible. This section presents the first direct observation of RF particle current in a tokamak plasma. Using a plasma-compatable Rogowski current monitor with a small, rotatable electric field antenna, the spatial distribution of this RF plasma current was studied.

7.3.1 Experimental Method

The design and construction of the RF plasma current monitor was described in detail in section 5.5, as was the antenna fixture with which it was used. The orientation of the antenna fixture in the tokamak chamber is shown in Figure 7-28. As mentioned in section 5.5, in order to minimize perturbation of the plasma by the Rogowski monitor, it was necessary to keep the major axis

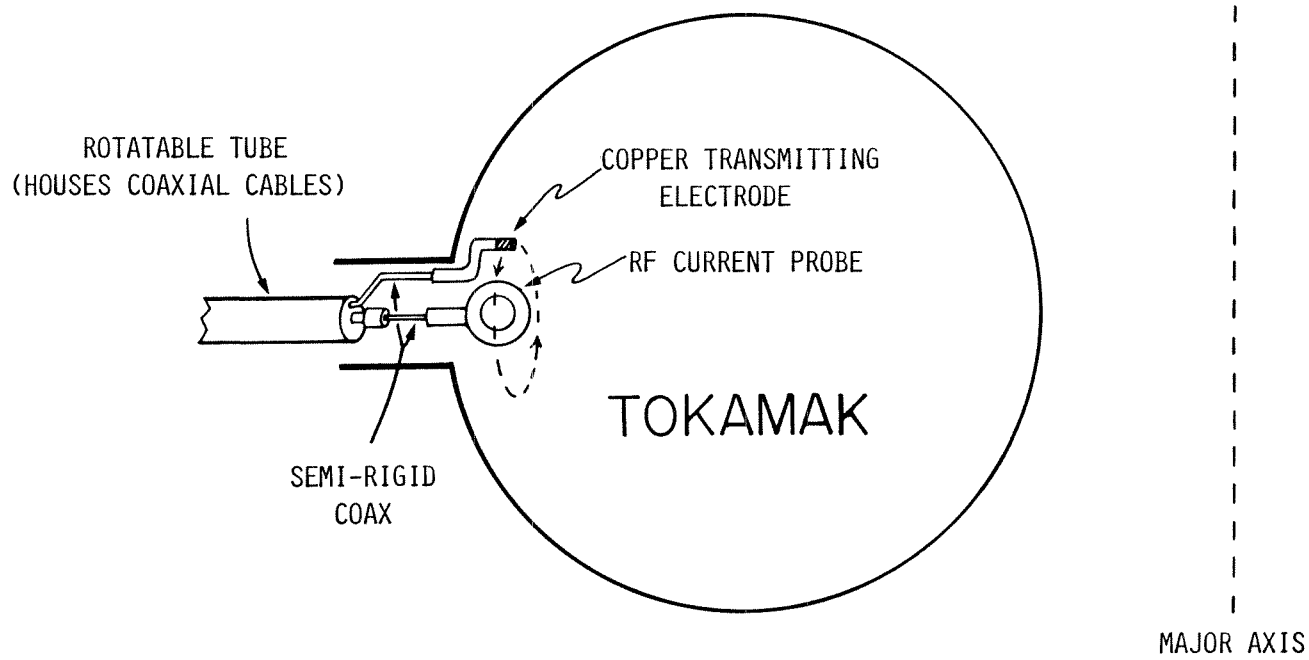

FIG. 7-28. Orientation of the rotatable antenna fixture with the RF plasma current monitor in the tokamak port. Both the transmitting antenna electrode and the current probe can be translated and rotated independently.

of the monitor parallel to the static toroidal magnetic field. Therefore, in order to investigate the distribution of current leaving the small electric field antenna, the antenna element was moved rather than the current monitor.

Although the ability to move the electric field antenna in orthogonal directions with respect to the monitor would have been useful, the mechanical difficulties associated with such a design, considering the rather limited access within the tokamak, were prohibitive. The simplest degrees of freedom were utilized, that is, rotation and translation of the antenna probe with respect to the current monitor. As seen in the diagram and described in section 5.5, the output semi-rigid coaxial cable of the current monitor passed through a vacuum O-ring seal which allowed translation and rotation of the monitor; this section of coax was colinear with the axis of the stainless steel tube into which it passed. The semi-rigid coax leading to the transmitting probe also made a vacuum seal at the end of the stainless steel tube but was rigidly fixed to the tube. The stainless steel tube itself passed through a differentially-pumped double O-ring seal which allowed it to translate and rotate. Thus, during an experiment, the current monitor could be held fixed in position while the transmitting antenna rotated around it. Similarly, the rotatable antenna could be fixed in a position and the current monitor could be independently translated into or out of the plasma. Thus, even with the limited access to the tokamak, several degrees of freedom were available for the investigations.

The transmitting antenna was fed from the impedance-matching box, as were all of the other RF antennas. The only difference in operation was a special coaxial fitting which connected the output of the matching box to the BNC connector on the end of the semi-rigid coaxial cable section. The one-meter length of coaxial cable had a characteristic impedance of 50 Ω, and there was no difficulty in tuning the matching network to the antenna, even though the antenna impedance was rather high due to the small antenna area. The

output of the Rogowski monitor led, via a 50 Ω coaxial cable, to the RF electronics cabinet where it was amplified or attenuated as needed.

During an experiment, the usual standard tokamak diagnostics were recorded, along with the RF forward and reflected voltages, the antenna RF current, voltage, and phase, the output amplitude from the Rogowski monitor, and the signal from at least one magnetic probe. The desired result from the experiments was the RF current passing through current monitor, normalized to the total RF current leaving the transmitting probe. Since the antenna current was measured at the output of the matching box, approximately 1.2 m from the antenna element itself, it was necessary to transform the measured current using the following result from transmission-line theory:

$$I_a = I_m \left[\cos(\beta L) - i \frac{Z_m}{Z_0} \sin(\beta L) \right] \tag{7.21}$$

where I_a is the desired current at the antenna element, I_m is the measured current at the input to the transmission line section, Z_m is the measured input impedance, Z_0 is the characteristic impedance of the section ($50\,\Omega$), L is the length of the section, and β is the wavenumber in the section. Therefore, the antenna input impedance was monitored, as described in Chapter 6, during these experiments. The actual ratio of the observed current to the current transformed to the transmitting antenna element turned out in practice to be within ~20% of unity.

7.3.2 Experimental Results

A typical tokamak shot, showing the raw signals for the plasma current, the plasma density, the output from the Rogowski monitor, and the output from the antenna current monitor, is displayed in Figure 7-29. Note that the antenna current and the Rogowski monitor signals have similar forms. The absolute level of the antenna current depends on a number of factors,

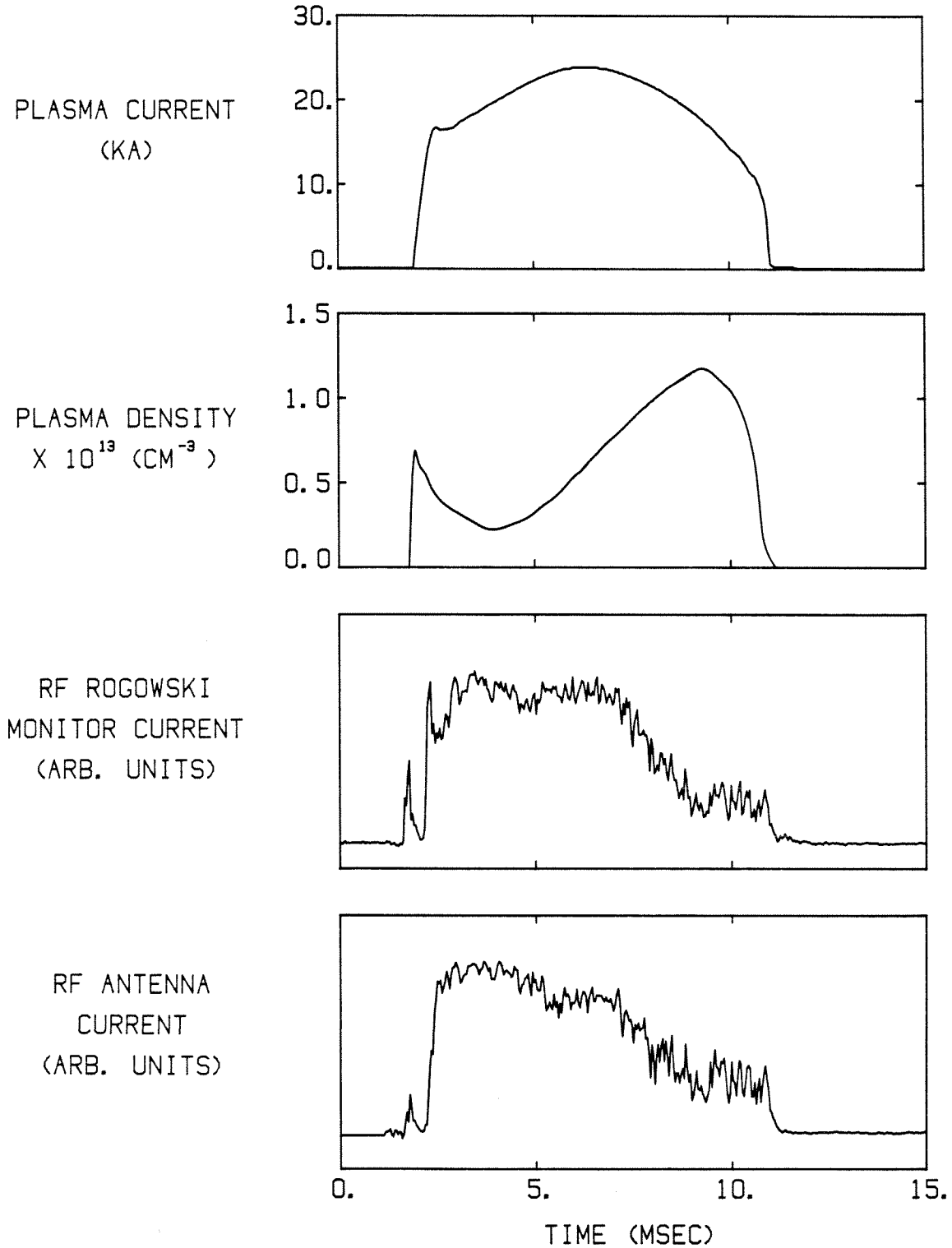

FIG. 7-29. Raw data from a typical tokamak shot, showing the plasma current, the line-averaged plasma density, the amplitude of the RF signal from the plasma current Rogowski monitor, and the amplitude of the RF signal from the antenna current monitor. For this shot, $\omega/(2\pi) = 12$ MHz and $B_0 = 4.0$ kG.

including the setting of the impedance-matching network and the type of RF exciter used. What is important in this study is the *ratio* of current passing through the aperture of the Rogowski monitor to the current leaving the RF antenna, as this gives information about the spatial distribution of the RF current density.

Several checks were performed to insure that the observed signal from the Rogowski monitor was in fact due to RF plasma current. Rotating the current monitor by 90°, so that its major axis was in the poloidal direction, reduced the output from the monitor during a tokamak shot by more than 40 db. This is consistent with the idea that the major axis of the monitor must be oriented in the toroidal direction so that plasma may stream through it. Exciting the antenna with all tokamak fields firing, but with no gas in the machine (and hence no plasma), yielded no detectable output from the Rogowski monitor; hence direct pickup by the monitor was negligible.

Two experiments were performed in order to investigate the spatial variation of the current driven by the RF antenna. For both of the experiments, the antenna excitation frequency was 12 MHz, the toroidal magnetic field on axis was 4.0 kG, and the data points were taken following the gas puff when the plasma density reached a value of $\sim 8 \times 10^{12}$ cm^{-3}.

In the first experiment, the Rogowski monitor was fixed in location, with its major axis oriented in the toroidal direction and its leading edge fixed 4.0 cm past the tokamak wall; this corresponded to the entire body of the monitor being just past the wall. The transmitting antenna element was positioned so that its leading face was 2.7 cm past the wall. A series of tokamak shots were recorded while the transmitting antenna was rotated a full 360° around the Rogowski monitor; typically 4 – 6 shots were recorded at each angular orientation. The records were then analyzed as described above. A polar plot of the magnitude of the ratio of the current passing through the

Rogowski monitor to the current leaving the RF antenna is shown in Figure 7-30. In this plot, $\theta=0$ corresponds to the orientation with the transmitting probe directly above the current monitor, and the dashed circle corresponds to a current ratio of 0.50. The plot shows a dramatic increase in the normalized Rogowski monitor current over a very small range of θ, corresponding approximately to the range over which the toroidal projection of the antenna on the current monitor intersects the aperture of the monitor. Note that the peak signal occurs for $\theta\simeq\pm 90°$, where the transmitting antenna is aligned toroidally with the center of the aperture of the current monitor; the magnitude of this peak is $\sim$0.43. Thus, even though the transmitting antenna was some 5 cm away in the toroidal direction from the current monitor (at $\theta=90°$), greater than 40% of the current leaving the antenna passed through the aperture of the monitor. The plot is nearly symmetrical about $\theta=0°$, which shows that the current flows equally in both directions and is highly localized along the toroidal direction. Thus, nearly all the current leaving the antenna is accounted for.

The second experiment consisted of a radial current scan. The transmitting antenna was fixed in position, 2.7 cm past the wall and at an angle of $\theta=90°$, and the current monitor was inserted, starting at a position withdrawn from the plasma. Again, some 4–6 tokamak shots were recorded at each position of the current monitor, and the data records were analyzed as before. The results are shown in Figure 7-31; here ξ is the distance from the outer face of the transmitting antenna copper plug (i.e., the face at larger minor radius) to the inner face of the current monitor. Thus, $\xi=0$ corresponds to the position where the toroidal projection of the antenna on the current monitor just begins to intersect the aperture of the monitor. The results show that the normalized current increases substantially at just this point, consistent with the idea that the current does indeed flow largely in the toroidal direction.

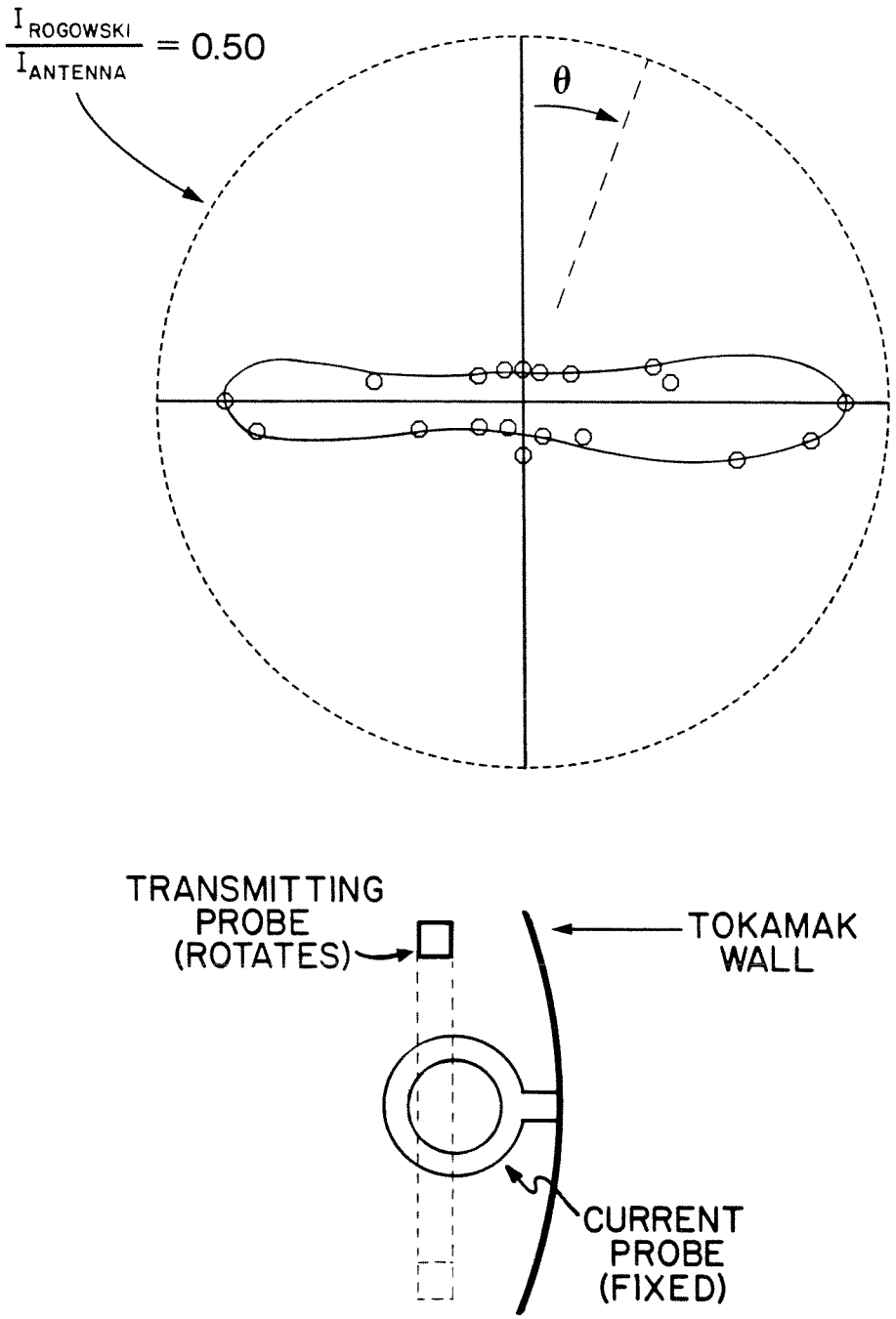

FIG. 7-30. Polar plot of the magnitude of the ratio of the RF current passing through the plasma current monitor aperture ($I_{ROGOWSKI}$) to the RF current at the transmitting probe ($I_{ANTENNA}$), as a function of the angle of rotation of the transmitting probe about the current monitor. The dashed circle corresponds to a ratio of 0.50. The geometry of the experiment is shown beneath the plot; the Rogowski current monitor is fixed in position while the transmitting probe rotates around it. The position $\theta = 0°$ corresponds to the transmitting probe being vertically above the Rogowski monitor.

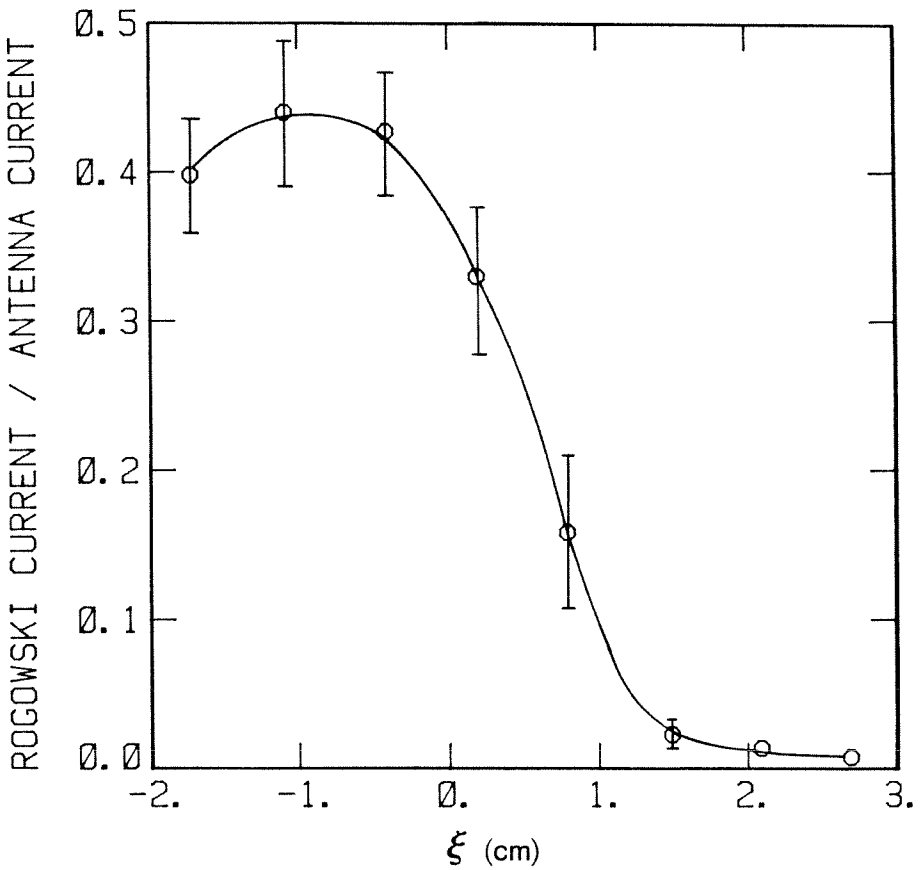

FIG. 7-31. Plot of the magnitude of the normalized RF current passing through the aperture of the plasma current monitor, as a function of the coordinate ξ. The geometry of the experiment is shown beneath the plot; the transmitting probe is fixed at $\theta = 0°$ while the current monitor translates radially into the plasma. ξ is the distance between the outer face of the transmitting probe (the face at larger minor radius) and the inner face of the current probe, as shown in the diagram. For $\xi < 0$, the toroidal projection of the transmitting probe intersects the aperture of the current monitor.

Note that at the maximum insertion of the current monitor, when the toroidal projection of the antenna element is completely within the aperture of the current monitor, greater than 40% of the current leaving the antenna passes through the monitor.

These experiments offer convincing evidence that the current being driven by the electric field antennas flows largely along the toroidal direction and maintains this structure some distance away from the antenna. Although a theoretical explanation for this phenomenon is not yet at hand, the results do suggest a mechanism for the good coupling to toroidal eigenmodes observed with these antennas. The highly localized current density flowing from the RF antenna results in a poloidal magnetic field compoent, and it is likely that this component is responsible for the coupling. Note from Figures 2-10 (theory) and 7-11 (experiment) that, although traditional loop antennas couple to the toroidal (z) component of the eigenmode magnetic field because it is the largest component in the outer plasma, the poloidal (θ) component is also significant at the plasma edge and coupling to the wave fields through it should be possible.

CHAPTER VIII

Summary and Conclusions

This thesis has discussed a diverse array of topics pertaining the coupling, propagation, and damping of ICRF waves in a tokamak plasma. As in many research endeavors, the original questions gave rise to many more. This chapter briefly reviews some of the more important conclusions of this work.

Theoretical models were pursued largely to explain experimental results. The model discussed in Chapter 2, however, of the effect of radial density perturbations was of interest in its own right. It was found that even a very small coherent radial density perturbation could greatly enhance the left-hand circularly polarized component of the wave electric field; i.e., the component responsible for second-harmonic cyclotron damping. The model used a uniform magnetic field, however, and in the tokamak the magnetic field gradient causes cyclotron damping to occur near a resonant surface consisting of a cylindrical shell. Thus, more work needs to be done to assess the potential effect of density perturbations on wave absorption in an actual tokamak.

The experimental work was divided into two major areas: antenna impedance measurements, and wave propagation investigations. The two were not entirely unrelated; for instance, the antenna impedance due to eigenmode generation could be explained qualitatively and quantitatively in terms of wave measurements of the cavity Qs.

An extensive study of the impedance characteristics of five different RF antennas was performed by directly measuring the RF antenna voltage and

current and the phase between the two. The very small phase changes observed during the plasma shot necessitated the design of an extremely sensitive phase detector with wide dynamic range.

The impedance observations separated into two regimes - those antennas whose conducting elements were insulated from contact with the plasma, and those which were not. The loading resistances of the insulated antennas (the ceramic-covered and Faraday-shielded loop antennas) displayed peaks coincident with the generation of eigenmodes; this was expected and was modeled reasonably well by a simple theory. Those antennas which were uninsulated (the bare plate, bare loop, and "T" antennas) did not show this eigenmode-related impedance form. Rather, their loading resistance was dominated by a much larger continuous background resistance which depended primarily on the plasma density at the antenna location; this was, in fact, the "anomalous" or parasitic ICRF antenna loading. An initially surprising result was that the bare loop antenna exhibited a loading resistance which increased with density, while the bare plate and "T" antennas displayed loading resistances with the opposite density dependence. A simple model was developed which explained this behavior. The model does not include wave propagation and treats the bare plate and "T" antennas as RF-driven Langmuir probes. The plasma sheath presents a non-linear impedance which can be modeled with the classical probe $I-V$ curve. Using experimentally obtained probe curves, the RF impedance of the driven antenna was calculated. Since the current drawn by a probe is directly proportional to the plasma density at the probe location, it follows that the shunt resistance seen by the probe or antenna depends inversely on plasma density; this result was confirmed experimentally. A more severe test of the model involved the dependence of the loading resistance of the bare plate or "T" antennas on the excitation level; good agreement with the model was obtained here as well. Finally, the density dependence of the

bare loop antenna impedance was explained in a consistent fashion by considering a model with the plasma shunting the loop at its midpoint.

Thus, the so-called anomalous density-dependent antenna loading was adequately explained in terms of a very simple model based on particle collection through the plasma sheath. The above results suggest that particle collection by the antenna is an important effect which should be considered in the design of ICRF systems. These effects have thus far not been included in any of the sophisticated coupling codes used to study the design of high power ICRF wave launchers [Bhatnagar et al., 1982; Elet and Chiu, 1982; Ram and Bers, 1982].

The wave experiments described in Chapter 7 began with studies of the eigenmode dispersion characteristics. The simple cold-plasma, periodic-cylinder theory was seen to qualitatively explain many of the results. For instance, the observation, based on phase measurements of the wave magnetic fields, that the first $4-5$ eigenmodes to appear after the initiation of a gas puff were all $m=1$ poloidal modes of low and successively increasing toroidal mode number is exactly what the theory predicts. The toroidal mode number could not be identified absolutely, but the first observed mode was likely an $N=1$ or $N=3$ mode. Similar results have been previously seen in other laboratories [Takahashi, 1979; Coleman, 1983].

A new and surprising feature of the study, however, was the discovery that the very simple electric-field antennas (the bare plate and "T" antennas) could excite the ICRF eigenmodes with comparable efficiency to the traditional loop couplers, in terms of wave amplitude normalized to antenna current. The eigenmodes generated with these antennas were shown to have approximately the same form and dispersion characteristics as those generated with the magnetic antennas; it is likely that they were in fact the same modes. This result is believed to represent the first report of ICRF fast wave excitation with an

electric-field structure; other laboratories employ loop couplers exclusively. Although the electric field antennas exhibited good coupling to the eigenmodes, it is not suggested that they are candidates for wave launchers for heating experiments. The coupling efficiency was defined in terms of the antenna current; since the electric field antennas also exhibited a large background loading resistance, much more input power was required to excite a mode to a given amplitude than was needed with the loop antennas. Nevertheless, these coupling structures may prove useful for exciting ICRF waves for diagnostic purposes; their extreme compactness is an advantage in a tokamak environment where port space is at a premium.

Wave damping measurements showed the anomalously high dissipation seen in other laboratories, i.e., the eigenmode Qs predicted from theory were much higher than those observed in the experiments. The damping was investigated both from the point of view of the cavity resonances (by measuring the cavity Qs) and from the point of view of the waves being attenuated as they travel axially around the torus (by measuring the wave damping length). The two damping measurements are related by the group velocity, which was calculated from the two independent observations. One distinct feature of the damping measurements was that the cavity Qs increased as the toroidal mode number increased; this this is in contrast to the dependence predicted by theory, but the effect has also been observed in other tokamaks [Bhatnagar et al., 1978a]. Also, the wave damping was observed to increase as the fundamental ion cyclotron resonant layer entered the plasma, an unexpected result since fundamental damping in a one-component plasma is usually neglected.

It is clear from the wave measurements that, although the wave propagation is described reasonably well by the theoretical models, the simple damping mechanisms discussed in Chapter 2 do not adequately explain the observed damping. The disposition of the energy lost in the antenna-plasma system is

thus obscured. One possible explanation recently considered by Thompson [1982] involves mode conversion of the fast wave near the second-harmonic resonance layer. This damping mechanism does not, however, appear to explain the large increase in wave damping observed when the fundamental cyclotron resonance layer enters the tokamak. More work is certainly needed in this area in order to identify the wave damping processes and to clarify the eventual destination of the RF power.

In a different approach to the investigation of ICRF waves in a tokamak, a wave-packet technique was used to study the propagation of waves in the torus on very short time scales, unencumbered by the eigenmode resonances. Exciting the antennas with short bursts of RF current (4–5 cycles) launched identifiable wave-packets which could be observed to travel many times around the torus; the time delay between passes gave a direct indication of the toroidal group velocity. These experiments represent the first observations of ICRF wave-packets in a tokamak.

The group velocity was investigated as a function of a variety of plasma parameters. The results were compared with theoretical models and, in general, reasonable agreement was noted. The observed increase in group velocity as the density decreased could be explained with a model which included a vacuum layer at the plasma edge to simulate the very low-density layer that probably exists at the plasma-wall interface.

Finally, the RF Rogowski current monitor experiments demonstrated for the first time direct measurement of RF particle current in a plasma. The study showed that the current driven by the electric field antennas in the outer tokamak plasma is spatially localized along the toroidal field lines. Thus, it is proposed that the electric field antennas couple to the toroidal eigenmodes through the poloidal (θ) component of the magnetic field generated by the current flowing along the localized toroidal path. It would be of interest to

pursue these studies further to see, for example, how far away from the antenna the localized current path extends and how it eventually returns to the wall.

APPENDIX A

Coupling Efficiency to ICRF Toroidal Eigenmodes and Transmission between Two Identical Antennas†

Measurements by Hwang [1979] indicate that with careful design of the antenna and matching network so as to minimize losses in both, at least 75% to 85% of the available input power can be deposited in the antenna-plasma system at an eigenmode resonance. The disposition of this power, however, is not clear: is it carried globally throughout the plasma by the fast wave fields, or is the power perhaps being deposited locally near the antenna or in the antenna-plasma sheath? Knowledge of the wave fields everywhere within the plasma volume would permit calculation of the energy carried by the wave; this measurement, however, is not practical experimentally. Magnetic probes are routinely used to investigate the magnetic fields associated with the waves, but they are restricted to the outer few centimeters of the plasma and to a few specific locations around the tokamak.

If the energy being deposited in the plasma at an eigenmode resonance is, in fact, being transported globally by the fields, then the question arises as to whether that energy can again be extracted with high efficiency by another antenna. The transport of power from one antenna to another across the tokamak would provide a convincing demonstration.

† This paper was presented at the 21st Annual Meeting of the Division of Plasma Physics, Boston, Mass. [Greene and Gould, 1979]. The equivalent circuit model was originally derived by R. W. Gould.

The expected transmission efficiency between the two antennas will not simply be the square of the wave-launching efficiency since energy is also dissipated in the plasma. In the following derivation, the addition of a tightly-coupled receiving antenna into the plasma is found to reduce somewhat the coupling efficiency.

Consider the simple circuit model of the system[1] shown in Figure A-1a. Here R_0 is the internal resistance of the generator (50 Ω), R_a is the intrinsic resistance of the antenna, and L_a is the antenna inductance. C_1 and C_2 are the variable capacitors which provide the necessary impedance transformation. Each cavity eigenmode is represented by a resonant circuit with parameters selected for the proper resonant frequency and quality factor Q; the coupling between the i^{th} mode and each antenna is represented by mutual inductances M_i. The transmitting and receiving antennas are assumed to be identical and to be located 180 degrees apart azimuthally along the torus.

When one high Q toroidal eigenmode is resonant, the non-resonant modes have little effect and will be ignored. In this case, the circuit can be redrawn using Thevenin's theorem as shown in Figure A-1b. The form of the quantities V', R_0', and C' as functions of the circuit parameters need not be displayed explicitly for the present discussion. The loop equations for this circuit can be solved and simplify considerably if we assume that both antenna circuits and the toroidal eigenmode are simultaneously resonant, i.e., that $L_a C' = L_p C_p = \frac{1}{\omega^2}$. Then the circuit model can be further simplified as shown in Figure A-1c.

In the absence of a receiving antenna, the input impedance is just $R_a + \frac{\omega^2 M^2}{R_p}$. The latter term represents the resistance reflected back into the

1. For justification of this equivalent circuit approach, see Collin [1966].

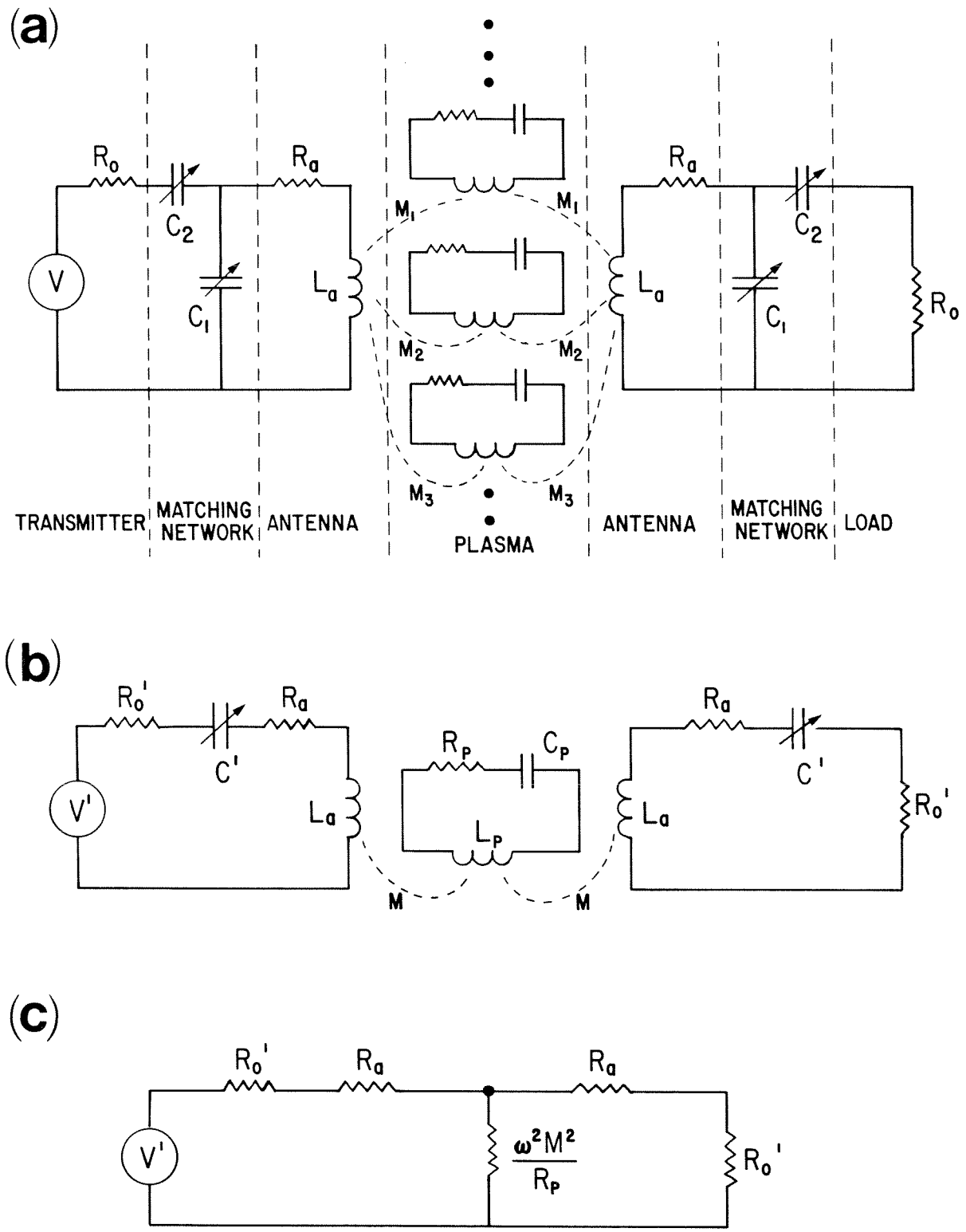

FIG. A-1. a) Equivalent circuit model for the system. Each toroidal eigenmode is represented by an $R-L-C$ resonant circuit. b). Equivalent circuit when one toroidal eigenmode is resonant. c). Equivalent circuit when both antenna circuits and the toroidal eigenmode are simultaneously resonant.

antenna due to the toroidal eigenmode while R_a is the ohmic resistance of the antenna. To maximize power transfer from the generator to the eigenmode, C_1 and C_2 are adjusted so that $R_0' = R_a + \frac{\omega^2 M^2}{R_p}$, and the ratio of power delivered to the eigenmode to power available from the generator is then

$$\eta_{coup} = \frac{P_{eigen}}{P_{avail}} = \frac{1}{\left(1 + \frac{1}{\gamma}\right)}, \tag{A.1}$$

where $\gamma = \frac{\omega^2 M^2}{R_a R_p}$.

With the addition of the second antenna, it can be shown from Figure A-1c that the ratio of the power delivered to the receiving antenna load to that available from generator is

$$\frac{P_{load}}{P_{avail}} = \frac{4\gamma^2(\chi-1)^2}{\chi^2(\chi+2\gamma)^2}, \tag{A.2}$$

where $\chi = 1 + \frac{R_0'}{R_a}$. For a given mode and antenna design, γ is fixed, but χ can be adjusted (by tuning the variable capacitors C_1 and C_2) so as to maximize the above ratio. This maximum occurs when $\chi = 1 + (1+2\gamma)^{\frac{1}{2}}$; note that this condition is *not* the same as that which leads to optimum power transfer to the eigenmode in the absence of the receiving antenna. The optimum transmission efficiency is found to be

$$\eta_{trans} = \frac{4\gamma^2(1+2\gamma)}{\left[1+(1+2\gamma)^{\frac{1}{2}}\right]^2\left[1+2\gamma+(1+2\gamma)^{\frac{1}{2}}\right]^2}. \tag{A.3}$$

A comparison between the optimum efficiency of power transfer between the two antennas, η_{trans}, and the efficiency of power coupling to the eigenmode, η_{coup}, as functions of the parameter γ is shown in Figure A-2. Note that η_{trans} is substantially smaller than η_{coup} for all values of γ. It is of interest, under these circumstances, to give an accounting of the disposition of

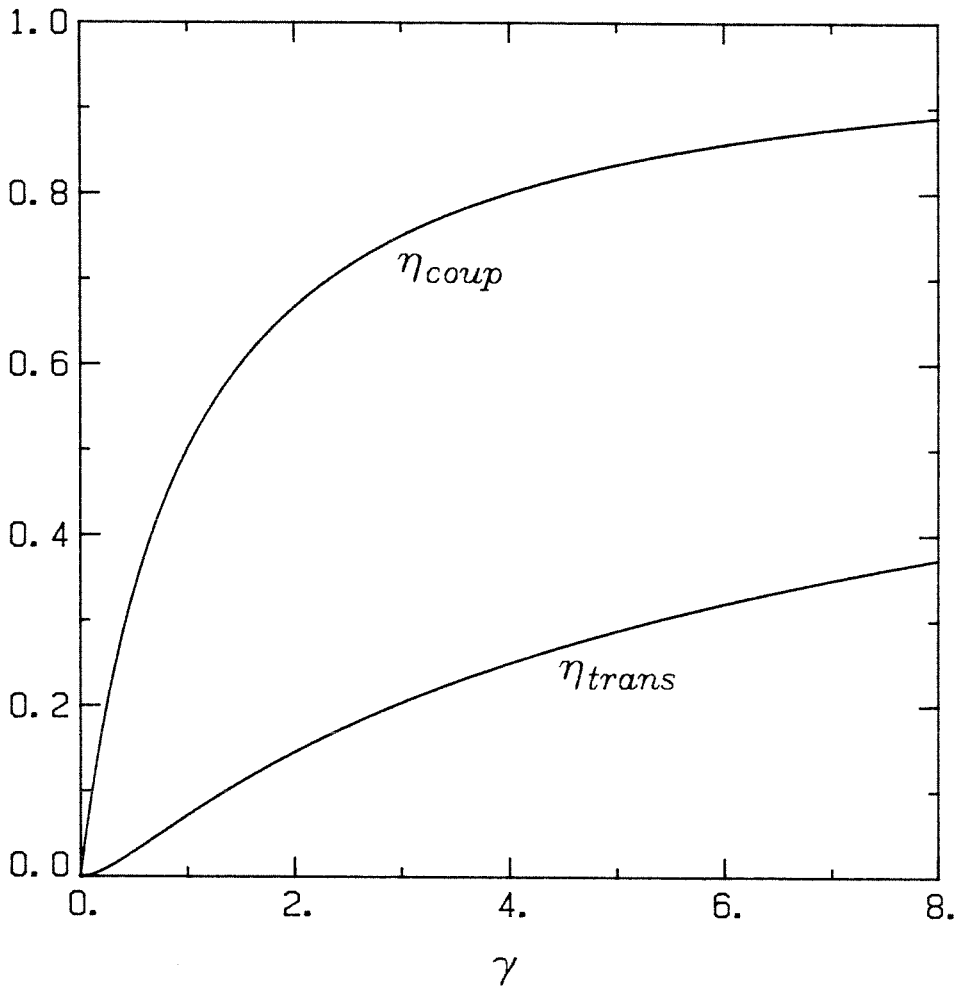

FIG. A-2. Plots of the optimum efficiency of power transfer between the two antennas, η_{trans}, and the efficiency of power coupling to a single eigenmode in the absence of a second antenna, η_{coup}, as functions of the parameter γ.

the available power for, say, $\gamma = 4$, corresponding to the case where, in the absence of the receiving antenna, 80% of the available power would be transferred to the eigenmode. Of the available power, 33% is dissipated in the transmitting antenna, 33% is dissipated in the plasma, 8% is dissipated in the receiving antenna, and 25% of the power is delivered to the receiving antenna load.

The experiment performed on the Caltech tokamak is shown schematically in Figure A-3. The glass-covered two-turn loop antennas which were used were described previously by Hwang [1979]. Two identical antennas were positioned in two tokamak ports separated by 180° toroidally. Two identical L-network impedance-matching boxes were constructed using high-Q vacuum capacitors. One of the antennas was connected, through a matching network, to a 300 W broadband amplifier which was driven at a frequency of 16 MHz with a signal generator; the other antenna was connected, through the other matching network, to a 50 Ω load. Directional couplers monitored the power being delivered to the antenna and to the load. Crystal detectors were used to monitor the RF signal amplitudes; each detector was calibrated over a wide range of input voltages and these calibrations were used during the data analysis to properly unfold the signals.

The experiments were carried out in the first few milliseconds of the tokamak discharge during the initial plasma density rise and fall; no gas puffing was used. The impedance-matching networks were tuned, from shot to shot, to maximize the fraction of input power which was delivered to the load for a particular eigenmode. A shot showing the highest power coupling which was achieved is shown in Figure A-4. The maximum value of the power coupling efficiency for one eigenmode is about 23% which agrees well with the prediction of Figure A-2 for $\gamma \simeq 4$.

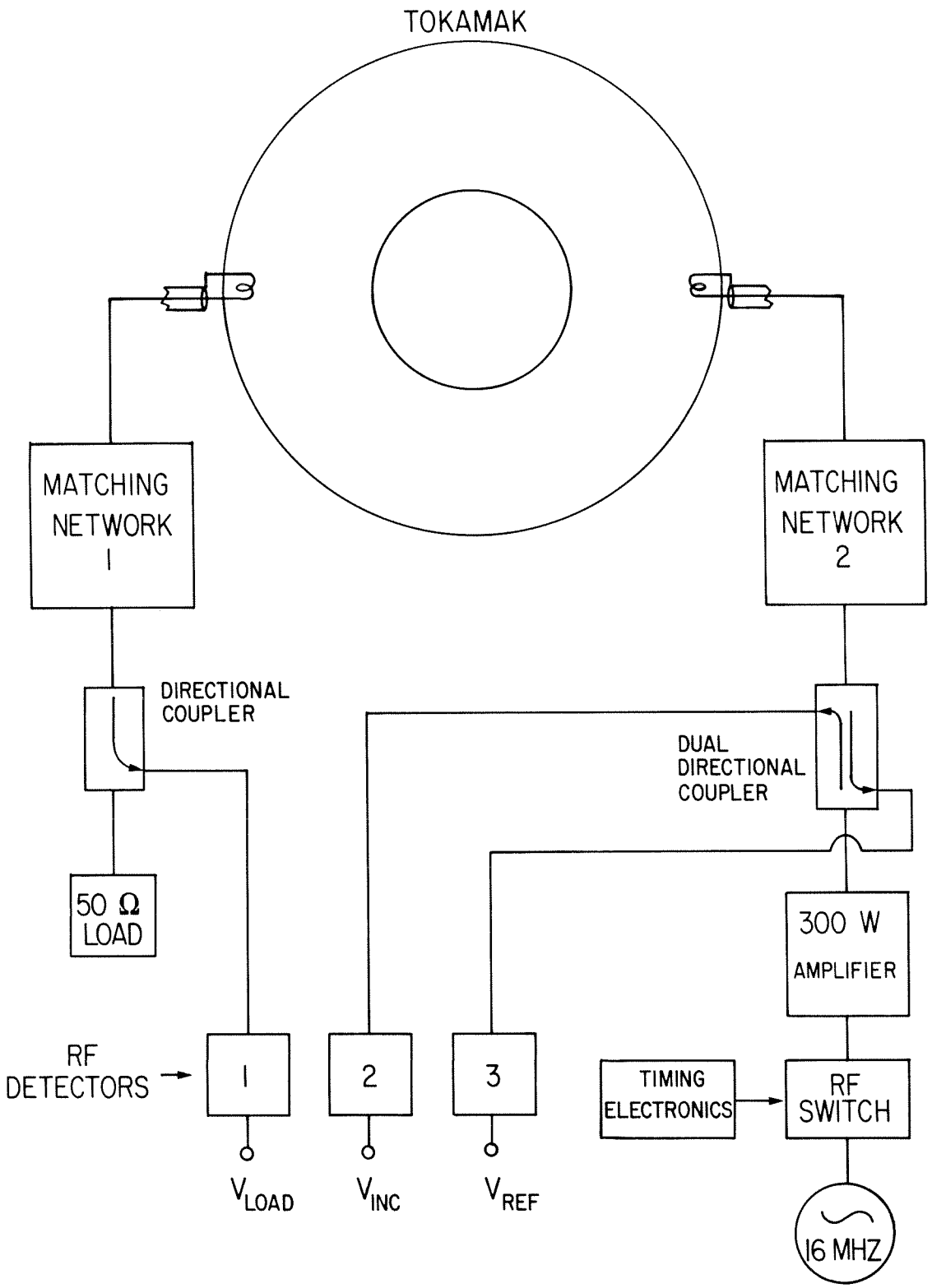

FIG. A-3. Schematic diagram of the power transfer experiment.

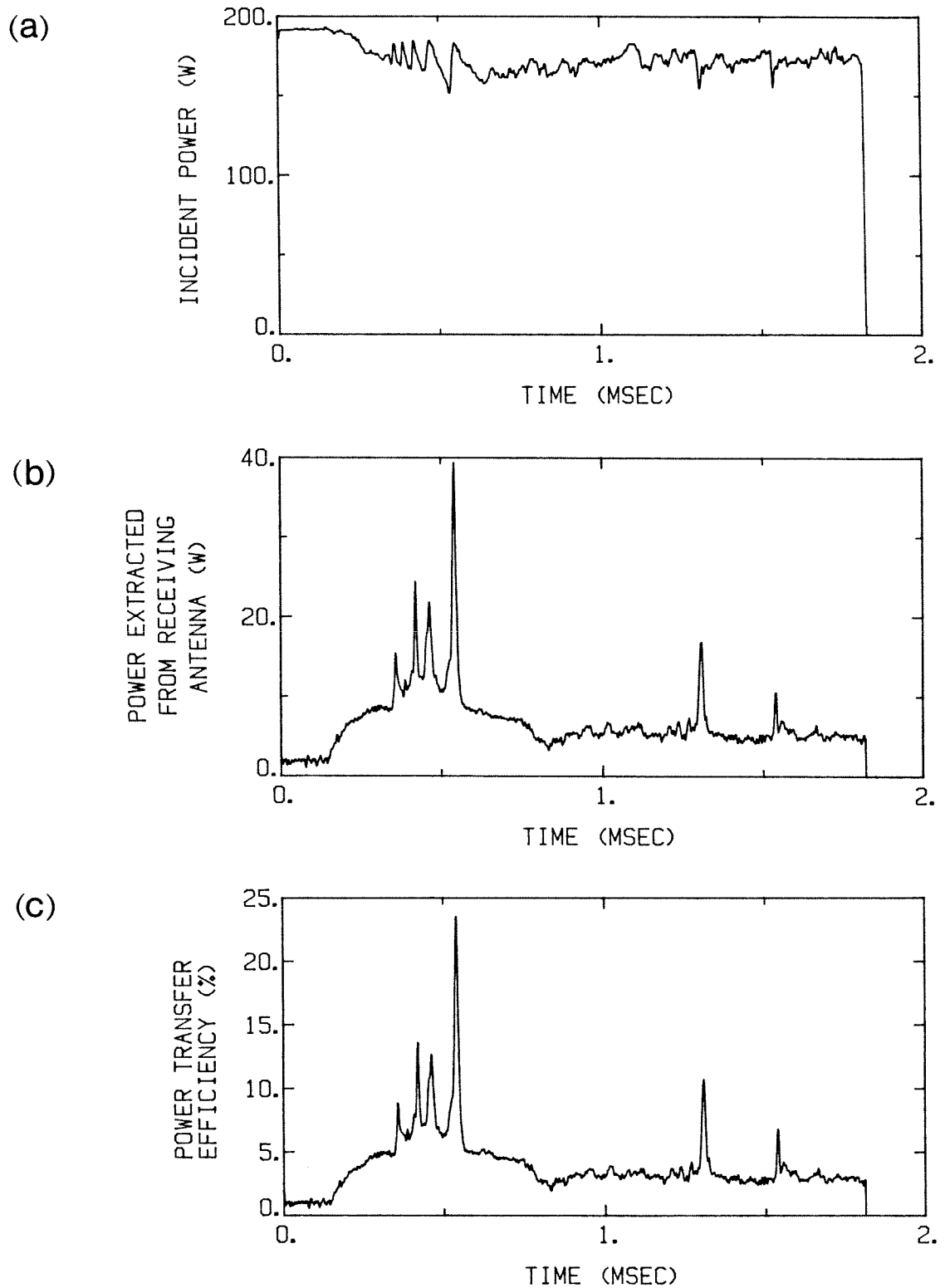

FIG. A-4. Records of a tokamak shot showing the highest power transfer acheived. Tokamak fires at $t \simeq 0.1$ msec; RF pulse ends at $t \simeq 1.9$ msec. a) Power incident on transmitting antenna. b) Power extracted from receiving antenna. c) Ratio of extracted to incident power.

In summary, a simple equivalent circuit model has been developed to predict the power transmission efficiency between two identical antennas, given the coupling efficiency from a single antenna to an eigenmode. The experimental results agree reasonably with this estimate and demonstrate convincingly the global transport of power by the eigenmode.

APPENDIX B

Transient RF Heating of a Conducting Cylinder

When an RF current flows along a conducting wire or rod, joule heating occurs due to the finite resistivity of the metal. At low frequency, the current is uniformly distributed throughout the cross-section of the cylinder, and the temperature profile is also uniform. At sufficiently high frequencies, the current distribution is peaked at the surface of the rod because of the skin effect, and the temperature of the surface rises more rapidly than that of the interior. It may therefore be important to include the skin effect in the thermal design of high power RF antennas and systems.

This appendix presents a calculation of the transient RF heating of a uniform conducting cylinder of infinite length, assuming that ohmic losses are the only heat source and that there is no conductive or radiative cooling. The geometry of the problem is shown in Figure B-1. The heat equation with the appropriate source term is Laplace-transformed, and a Green's function for the equation is found. The solution of the problem is then obtained by inverse Laplace-transformation and integration of the Green's function.

B.2 RF Current Profile

The current density ($\mathbf{j}$) in an isotropic conductor is given by Ohm's law: $\mathbf{j} = \sigma \mathbf{E}$, where σ is the conductivity and $\mathbf{E}$ is the electric field. Assuming that all fields vary as $e^{-i\omega t}$, the Maxwell equation for the magnetic induction $\mathbf{B}$ becomes

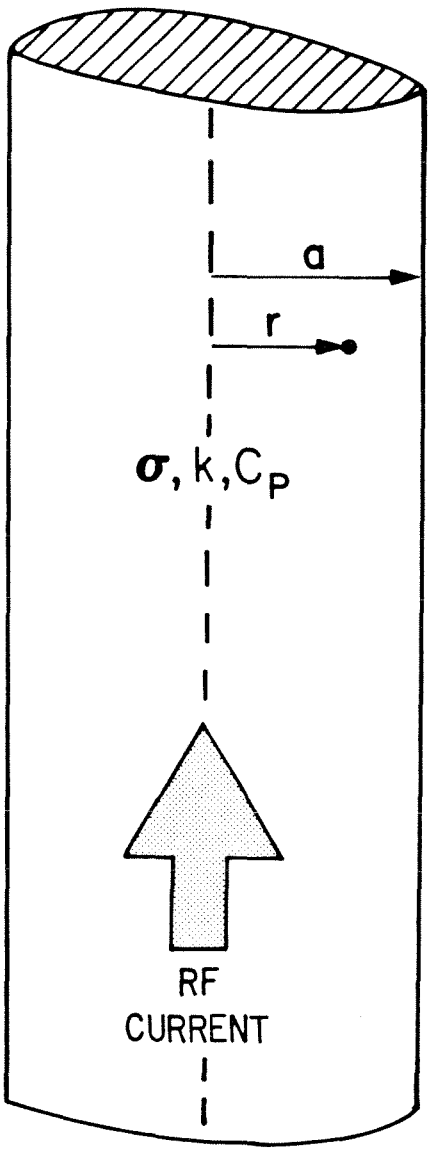

FIG. B-1. Geometry of the problem. RF current flows axially through a cylinder of radius a, conductivity σ, diffusivity k, and heat capacity C_p.

$$\nabla \times \mathbf{B} = \frac{\mu}{c}(4\pi\sigma - i\omega\varepsilon)\mathbf{E}\,, \tag{B.1}$$

where μ and ε are the permeability and dielectric constant of the conductor, respectively, and c is the velocity of light. For all reasonable conductors at RF frequencies, the inequality $\sigma \gg \omega\varepsilon$ is satisfied, so the displacement current may be neglected. Using Faraday's law then yields an equation for $\mathbf{j}$:

$$\nabla^2\mathbf{j} = -i\sigma\mu\omega\mathbf{j}\,. \tag{B.2}$$

The solution in cylindrical geometry which is finite as $r \to 0$ is

$$j(r) \equiv |\mathbf{j}(\mathbf{r})| \propto J_0\left\{r\sqrt{\sigma\mu\omega}\; e^{i\frac{\pi}{4}}\right\}, \tag{B.3}$$

which can also be written in terms of ber_0 and bei_0 functions [Ramo and Whinnery, 1944].

The quantity $\delta \equiv \frac{1}{\sqrt{\sigma\mu\omega}}$ is called the skin depth and is a measure of how far the RF fields penetrate into the conductor. For the frequencies and materials considered here, $\delta \ll a$, and the current distribution becomes simply

$$j(r) = A\, e^{-\left[\frac{a-r}{\delta}\right](1-i)}\,. \tag{B.4}$$

Integrating equation B.4 over the cross-section of the cylinder yields the relation between the constant A and the total current I_0 flowing in the cylinder:

$$I_0 = \sqrt{2}\,\pi A\,\delta^2(\gamma - \tfrac{1}{2})\,, \tag{B.5}$$

where $\gamma = \frac{a}{\delta}$ and terms of order $(1/\gamma)^2$ and higher have been neglected. The joule heating energy input to the conductor, per unit volume and unit time, is then given by

$$h(r) = \frac{\eta I_0^2}{2\pi^2\delta^4(\gamma - \frac{1}{2})^2}\, e^{-2\gamma\left[1-\frac{r}{a}\right]} \tag{B.6}$$

where η is the resistivity of the conductor.

B.3 The Heat Equation

The heat equation is given by

$$\frac{\partial u(r,t)}{\partial t} = k\nabla^2 u(r,t) + q(r,t)\,, \tag{B.7}$$

where $u(r,t)$ is the temperature, k is the thermal diffusivity and

$$q(r,t) = \frac{h(r)}{C_p} g(t) \tag{B.8}$$

is the heat source term. Here C_p is the heat capacity per unit volume at constant pressure, and $g(t)$ is a function of time. The RF current will be assumed to be turned on at time $t = 0$ for a period t_0, so that

$$g(t) = \begin{cases} 0 & \text{if} \quad t < 0 \\ 1 & \text{if} \quad 0 \le t \le t_0 \\ 0 & \text{if} \quad t > t_0 \end{cases} \tag{B.9}$$

and the temperature at time $t = 0$ will be assumed to be zero. The boundary condition at $r = a$ is the vanishing of outward heat flux:

$$\nabla u \cdot \mathbf{r}\Big|_{r=a} = \frac{\partial u}{\partial r}\Big|_{r=a} = 0\,, \tag{B.10}$$

and the other necessary boundary condition is that the solution be finite as $r \to 0$.

B.4 Laplace Transformation

The Laplace transform of $u(r,t)$ is defined by

$$L\{u(r,t)\} \equiv \hat{u}(r,s) = \int_0^\infty e^{-st}\, u(r,t)\, dt \tag{B.11}$$

where s is restricted to the half-plane $\mathrm{Re}(s) > 0$. For convenience, we

introduce a new function $f(r) \equiv \frac{h(r)}{C_p}$ such that $q(r,t) = f(r)\,g(t)$. Taking the Laplace transform of the heat equation then yields

$$s\,\hat{u}(r,s) = k\left[\frac{\partial^2 \hat{u}}{\partial r^2} + \frac{1}{r}\frac{\partial \hat{u}}{\partial r}\right] + f(r)\hat{g}(s)\,, \tag{B.12}$$

where $\hat{g}(s) = \frac{1-e^{-s\,t_0}}{s}$, and the boundary condition at $r = a$ becomes

$$\left.\frac{\partial \hat{u}}{\partial r}\right|_{r=a} = 0\,. \tag{B.13}$$

Defining new variables $\lambda^2 = \frac{s}{k}$ and $F(r) = -\frac{r}{k} f(r)$, equation B.12 may be cast into the form of an inhomogeneous modified Bessel equation:

$$\frac{\partial}{\partial r}\left[r\,\frac{\partial \hat{u}}{\partial r}\right] - r\lambda^2 \hat{u} = F(r)\,\hat{g}(s)\,. \tag{B.14}$$

B.5 Green's Function

A solution $\hat{\Gamma}(r,r';s)$ to the equation

$$\frac{\partial}{\partial r}\left[r\,\frac{\partial \hat{\Gamma}}{\partial r}\right] - r\lambda^2 \hat{\Gamma} = \hat{g}(s)\,F(r')\delta(r-r')\,, \tag{B.15}$$

where δ is the Dirac delta function, is a Green's function for the inhomogeneous equation. Let the solution of equation B.15 in the region $0 < r < r'$ be called $\hat{\Gamma}_1$, and in the region $r' < r < a$, $\hat{\Gamma}_2$. Then, using the boundary conditions, it follows that

$$\hat{\Gamma}_1(r) = B\left[I_0(\lambda r) + \frac{I_1(\lambda a)}{K_1(\lambda a)} K_0(\lambda r)\right] \quad \text{for } r' < r < a \tag{B.16a}$$

and

$$\hat{\Gamma}_2(r) = D\,I_0(\lambda r) \quad \text{for } 0 < r < r'\,, \tag{B.16b}$$

where B and D are constants, and I and K are the modified Bessel functions.

The solutions $\hat{\Gamma}_1$ and $\hat{\Gamma}_2$ in the two regions must be joined at $r = r'$. Integrating the differential equation B.15 from $r = r' - \varepsilon$ to $r = r' + \varepsilon$, and taking the limit $\varepsilon \to 0$, shows that the slope of the solution is discontinuous at $r = r'$:

$$\left.\frac{\partial \hat{\Gamma}_2}{\partial r}\right|_{r=r'+\varepsilon} - \left.\frac{\partial \hat{\Gamma}_1}{\partial r}\right|_{r=r'-\varepsilon} = \frac{\hat{g}(s)\,F(r')}{r'} \tag{B.17}$$

A trial solution of equation B.15 valid throughout the range $0 < r < a$ is

$$\hat{\Gamma}(r, r'; s) = G\,\hat{\Gamma}_1(r_<)\,\hat{\Gamma}_2(r_>)\,, \tag{B.18a}$$

where G is a constant, and $r_<$ and $r_>$ are defined by

$$r_< = \begin{cases} r & \text{if } r < r' \\ r' & \text{if } r' < r \end{cases} \tag{B.18b}$$

and

$$r_> = \begin{cases} r & \text{if } r > r' \\ r' & \text{if } r' > r \end{cases} \tag{B.18c}$$

Substituting equation B.18a into equation B.17 then yields

$$G = \frac{\hat{g}(s)F(r')}{r'\,W[\hat{\Gamma}_1(r'), \hat{\Gamma}_2(r')]}\,, \tag{B.19}$$

where $W[\hat{\Gamma}_1, \hat{\Gamma}_2] = \hat{\Gamma}_1 \dfrac{d\hat{\Gamma}_2}{dr'} - \dfrac{d\hat{\Gamma}_1}{dr'}\hat{\Gamma}_2$ is the Wronskian. Noting that $W[K_0(\xi), I_0(\xi)] = \dfrac{1}{\xi}$ [Abramowitz and Stegun, 1972], it follows that $W[\hat{\Gamma}_1(r'), \hat{\Gamma}_2(r')] = -\dfrac{DB}{r'}$. The Green's function solution can then be written as

$$\hat{\Gamma}(r, r'; s) = \hat{g}(s)[\hat{y}_1(s) + \hat{y}_2(s)]\,, \tag{B.20a}$$

where

$$\hat{y}_1(s) = -F(r')\,I_0\left(\left[\frac{s}{k}\right]^{\frac{1}{2}} r_<\right) K_0\left(\left[\frac{s}{k}\right]^{\frac{1}{2}} r_>\right) \tag{B.20b}$$

and

$$\hat{y}_2(s) = -F(r')\, I_0\left(\left[\frac{s}{k}\right]^{\frac{1}{2}} r_<\right) I_0\left(\left[\frac{s}{k}\right]^{\frac{1}{2}} r_>\right) \frac{K_1\left(\left[\frac{s}{k}\right]^{\frac{1}{2}} a\right)}{I_1\left(\left[\frac{s}{k}\right]^{\frac{1}{2}} a\right)} \qquad \text{(B.20c)}$$

B.6 Inversion

The Green's function solution is now inverse Laplace-transformed, using the complex inversion integral [Mathews and Walker, 1970],

$$\Gamma(r, r'; t) = L^{-1}[\hat{\Gamma}(r, r'; s)] = \frac{1}{2\pi i} \int_{\eta - i\infty}^{\eta + i\infty} e^{st}\, \hat{\Gamma}(r, r'; s)\, ds \qquad \text{(B.21)}$$

where $t > 0$ and η is real and chosen so that all the poles of the integrand lie to the left of the contour in the complex s-plane.

Since $I_0(z)$ is an entire function of z, and $K_0(z)$ is regular in the z-plane with a branch cut along the negative real axis, an appropriate contour for the evaluation of $y_1(t) = L^{-1}\{\hat{y}_1(s)\}$ is shown in Figure B-2a. The integrals along contours B and F can be shown to vanish as $R \to \infty$, while the integral around contour D vanishes as $\zeta \to 0$. Furthermore, the integrals along paths C and D cancel. Since

$$\int_{\eta - i\infty}^{\eta + i\infty} = -\lim_{R \to \infty,\, \zeta \to 0} \left[\int_B + \int_C + \int_D + \int_E + \int_F \right], \qquad \text{(B.22)}$$

it follows that $y_1(t) = 0$.

The inversion of $\hat{y}_2(s)$ is more complicated because of the poles from the modified Bessel function I_1 in the denominator of the integrand. These poles are simple, and occur at $s = s_n \equiv -\lambda_n^2 \frac{k}{a^2}$, where λ_n is the n^{th} zero of the Bessel function J_1. Since λ_n must be real [Abramowitz and Stegun, 1972], all the poles lie on the negative real axis in the complex s-plane.

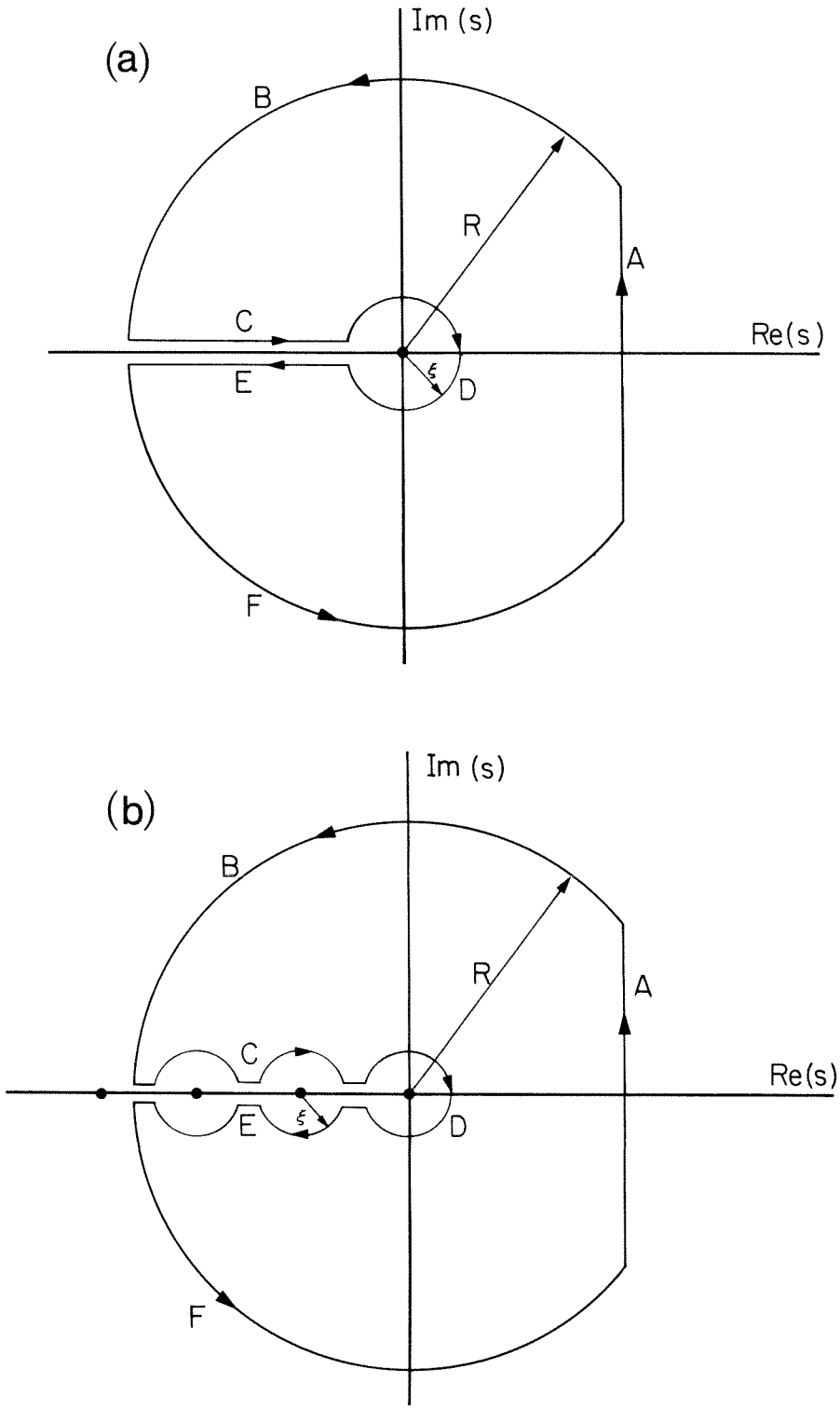

FIG. B-2. a) Contour for the evaluation of $L^{-1}\{\hat{y}_1(s)\}$. b) Contour for the evaluation of $L^{-1}\{\hat{y}_2(s)\}$. The poles occur at $s = -\lambda_n^2 k / a^2$.

The contour for evaluation of $L^{-1}\{\hat{y}_2(s)\}$ is shown in Figure B-2b. Again, the contribution from the paths B and F vanish as $R \to \infty$. The contribution from the integral around path D, in the limit $\zeta \to 0$, is

$$\frac{1}{2\pi i}\int_D \hat{y}_2(s)\,ds \to -\frac{2r'}{a^2}f(r)\,. \tag{B.23}$$

The integrals along paths C and D contribute

$$\frac{1}{2\pi i}\int_{C,D} \hat{y}_2(s)\,ds = \sum_{n=1}^{\infty} R_n\,, \tag{B.24}$$

where R_n is the residue of the integrand at the pole s_n. Evaluation of the residue yields

$$R_n = -\frac{\pi r'\lambda_n}{a^2}f(r)\,e^{-\frac{k}{a^2}\lambda_n^2 t}\,J_0\left(\lambda_n\frac{r_<}{a}\right)J_0\left(\lambda_n\frac{r_>}{a}\right)\frac{Y_1(\lambda_n)}{J_0(\lambda_n)}\,, \tag{B.25}$$

and the inverse transform is then

$$y_2(t) = -\frac{2r'}{a^2}f(r) - \sum_{n=1}^{\infty} R_n\,. \tag{B.26}$$

The inverse transform of equation B.20a is then given by the convolution theorem:

$$L^{-1}\left\{\hat{\Gamma}(r,r';s)\right\} = \int_0^t g(\xi)\,y_2(r-\xi)\,d\xi\,. \tag{B.27}$$

Using equations B.26 and B.9, the above reduces, after some algebra, to

$$\Gamma(r,r';t) = \frac{2r'}{a^2}f(r)\,t_< - \frac{\pi r'}{k}f(r)\sum_{n=0}^{\infty}\left[e^{-\frac{k}{a^2}\lambda_n^2(t_>-t_0)} - e^{-\frac{k}{a^2}\lambda_n^2 t}\right]$$

$$\cdot\,\frac{J_0\left(\lambda_n\frac{r_<}{a}\right)J_0\left(\lambda_n\frac{r_>}{a}\right)Y_1(\lambda_n)}{\lambda_n J_0(\lambda_n)}\,, \tag{B.28}$$

where $t_<$ is the lesser of $\{t_0, t\}$, and $t_>$ is the greater of $\{t_0, t\}$.

The desired solution of the original heat equation, $u(r,t)$, may now be obtained by integrating the Green's function:

$$u(r,t) = \int_0^a \Gamma(r,r';t)\,dr'$$

$$= \frac{t_< H}{\gamma^2}\left(\gamma - \frac{1}{2}\right) - \pi \frac{a^2}{k} H \sum_{n=1}^{\infty} \left[e^{-\frac{k}{a^2}\lambda_n^2 (t_> - t_0)} - e^{-\frac{k}{a^2}\lambda_n^2 t} \right]$$

$$\cdot \frac{J_0\left[\lambda_n \frac{r}{a}\right] Y_1\left[\lambda_n\right]}{\lambda_n J_0\left[\lambda_n\right]} W_n(\gamma)\,, \tag{B.29a}$$

where

$$H = \frac{\eta I_0^2}{2\pi^2 \delta^4 \left(\gamma - \frac{1}{2}\right)^2} \tag{B.29b}$$

and we have defined a new function,

$$W_n(\gamma) = \int_0^1 \xi J_0(\lambda_n \xi) e^{-2\gamma(1-\xi)}\,d\xi\,. \tag{B.29c}$$

B.7 Convergence

The convergence of the summation in equation B.29a can be investigated by examining the behavior of S_n, the n^{th} term in series, as $n \to \infty$. We note that for n large, $\lambda_n \sim \left(n + \frac{1}{4}\right)\pi$, and for z large (where z is a dummy variable),

$$Y_1(z) \sim J_0(z) \sim \left[\frac{2}{\pi z}\right]^{\frac{1}{2}} \cos\left[z - \frac{\pi}{4}\right]. \tag{B.30}$$

Then a upper bound on the magnitude of S_n is

$$\left|S_n\right| < \frac{|K|\,|W_n(\gamma)|}{n^{\frac{3}{2}}} \qquad (n \to \infty)\,, \tag{B.31}$$

where K is a constant independent of n.

Using a integral representation for J_0, the function $W_n(\gamma)$ can be written as

$$W_n(\gamma) = \frac{2}{\pi}\int_0^{\infty} \frac{2\gamma\sin(\lambda_n \cosh t) - \lambda_n \cosh t \cos(\lambda_n \cosh t)}{4\gamma^2 + \lambda_n^2 \cosh^2 t}\,dt\,. \tag{B.32}$$

Expressing the sine and cosine terms in complex exponential form, the integral can be evaluated asymptotically for large n using the method of stationary phase [Copson, 1965]. The result is

$$W_n(\gamma) \sim (-1)^n \frac{2\sqrt{2}}{\pi} \frac{\gamma}{\sqrt{n}\left(4\gamma^2 + n^2\pi^2\right)}\,. \tag{B.33}$$

The magnitude of the n^{th} term in the series then decreases as $n^{-\frac{5}{2}}$, for $n \to \infty$, and hence the series does converge.

B.8 Discussion

The term involving the summation in equation B.29a can be neglected for large times ($\gg t_0$), so that

$$u(r\,,\, t \to \infty) = u_\infty(t_0) \equiv \frac{t_0 H}{\gamma^2}\left(\gamma - \frac{1}{2}\right)\,. \tag{B.34}$$

It is easy to show that the energy per unit volume absorbed by the rod at any time t is just

$$E(t) = \frac{\eta A^2}{\gamma^2} t_< \left(\gamma - \frac{1}{2}\right) = u_\infty(t_<)\, C_p\,. \tag{B.35}$$

Hence $u_\infty(t_<)$ corresponds to the temperature that would be obtained if the same energy that was deposited in the cylinder by the RF current at time t

had been deposited uniformly over the cross-section.

The function $u(r, t)$ has been evaluated numerically for a variety of parameters. An example which shows some prominent features of the solution is shown in Figure B-3. The peak in the temperature profile always occurs at the surface of the rod. As expected, the surface temperature rises more quickly than the interior temperature. After the RF pulse ends at time t_0, the temperature profile begins to flatten out; the temperature in the outer part of the rod decreases while that of the inner part continues to rise. The profile will eventually become uniform with a temperature $u = u_\infty(t_0)$.

To investigate the solution over a wide range of parameters, it is desirable to recast equation B.29 in terms of dimensionless variables. The scale lengths appearing in the problem are a, the cylinder radius, and δ, the skin depth. The ratio of the two, γ, has already been defined. A characteristic time for heat flow is $t_c = \frac{a^2}{k}$. We introduce new dimensionless variables: $\tau = \frac{t}{t_c}$, $\tau_> = \frac{t_>}{t_c}$, $\tau_< = \frac{t_<}{t_c}$, $\tau_0 = \frac{t_0}{t_c}$, $\rho = \frac{r}{a}$, and $\Theta(\rho, \tau) = \frac{u(r, t)}{u_\infty(t_<)}$. The quantity Θ represents the ratio between the physical temperature and the temperature that would result if the same amount of energy were deposited uniformly; it is a measure of the importance of the skin effect on the temperature profile.

Making the above substitutions, equation B.29 becomes

$$\Theta(\rho, \tau) = 1 - \frac{\pi\gamma^2}{\tau_<(\gamma - \frac{1}{2})} \sum_{n=1}^{\infty} \left(e^{-\lambda_n^2(\tau_> - \tau_0)} - e^{-\lambda_n^2 \tau} \right) \frac{J_0(\lambda_n \rho)\, Y_1(\lambda_n)}{\lambda_n J_0(\lambda_n)} W_n(\gamma) \,. \qquad \text{(B.36)}$$

Since we are mostly interested in peak temperatures, we shall limit our further discussion to the case $\tau \leq \tau_0$, so that $\tau_< = \tau$.

A numerical evaluation of Θ is plotted as a function of ρ, for various times τ, in Figures B-4a (for $\gamma = 10$) and B-4b (for $\gamma = 100$). The temperature distribution is sharply peaked at the surface ($\rho = 1$) for times $\tau \ll 1$, and it

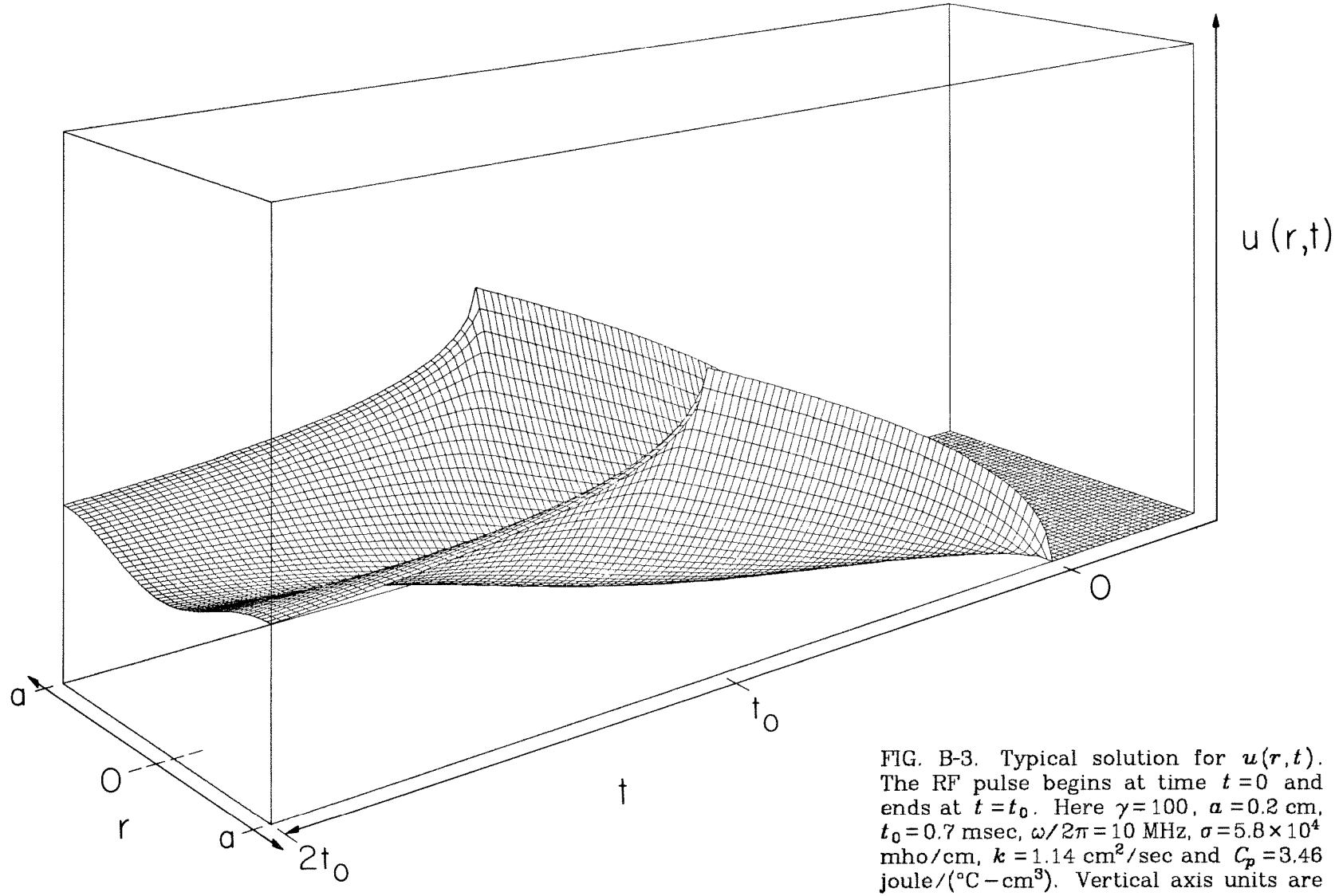

FIG. B-3. Typical solution for $u(r,t)$. The RF pulse begins at time $t=0$ and ends at $t=t_0$. Here $\gamma=100$, $a=0.2$ cm, $t_0=0.7$ msec, $\omega/2\pi=10$ MHz, $\sigma=5.8\times10^4$ mho/cm, $k=1.14$ cm^2/sec and $C_p=3.46$ joule/(°C$-$cm^3). Vertical axis units are arbitrary.

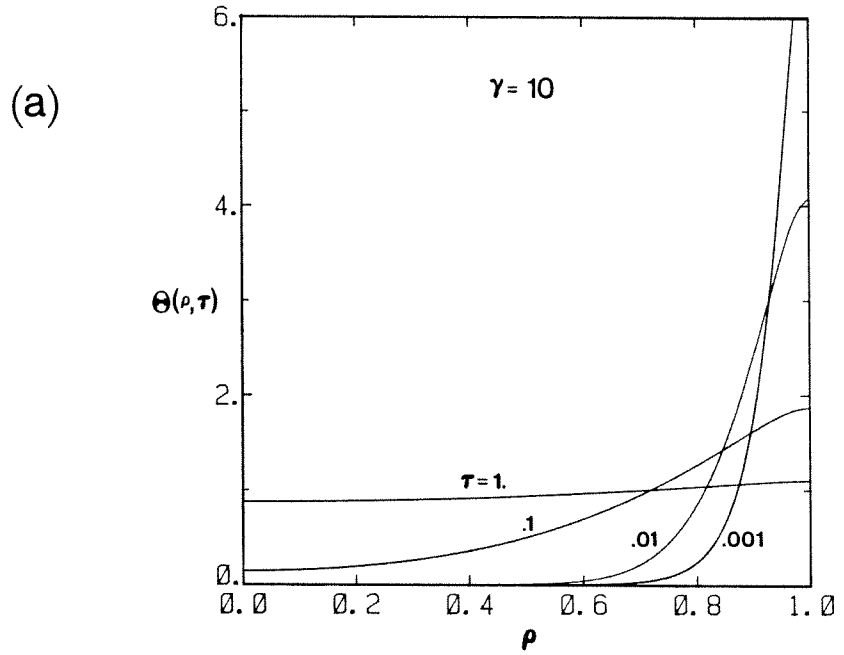

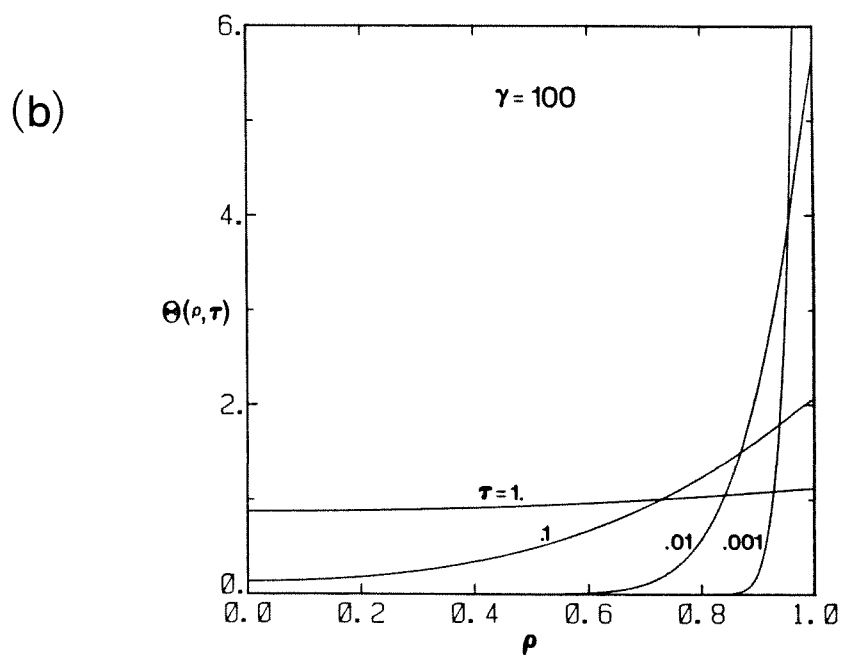

FIG. B-4. Plot of $\Theta(\rho,\tau)$ as a function of ρ, for various τ. a) Evaluation for $\gamma = 10$. b) Evaluation for $\gamma = 100$.

gradually flattens out to a nearly uniform profile for $\tau \gtrsim 1$. At a given time τ, the distribution is more sharply peaked for larger γ since the corresponding skin depth is smaller and the energy is being deposited in a narrower region at the surface.

A quantity of some importance for the design of RF systems is the peak surface temperature, $\Theta(1, \tau)$. It is important to limit the peak temperature, both to prevent excessive impurity evolution from adsorbed gases on the antenna surface and to prevent possible vaporization of the surface.

A plot of $\Theta(1, \tau)$ as a function of τ is shown in Figure B-5 for a wide range of γ. The skin effect causes greatly enhanced surface temperatures for $\tau \ll 1$, i.e., when the energy is deposited on a time scale short compared to the characteristic heat diffusion time. $\Theta(1, \tau)$ is again seen to increase as γ increases.

As an example, consider a copper rod, 0.63 cm in radius, carrying an RF current at a frequency of 10 Mhz. Then $\gamma \simeq 300.$, and since $k \simeq 1.14\ \mathrm{cm}^2/\mathrm{sec}$ for copper, it follows that $t_c = 0.35$ sec. For a 1.0 msec long RF pulse, $\tau_0 = 2.9 \times 10^{-3}$, and, from the numerical evaluation, $\Theta(1, \tau_0) = 10.5$. Then $u(a, t_0) = 10.5\, u_\infty(t_0) = 1.8 \times 10^{-7} I_0^2$ $(^\circ C)$, where u_∞ has been evaluated using $\eta = 1.72 \times 10^{-6}\ \Omega$–cm and $C_p = 3.46$ joule/$(^\circ C\,\mathrm{cm}^3)$. So, for example, an RF current of 50 kA (rms) would yield a peak surface temperature rise of about $900^\circ C$.

For parameters characteristic of the experiments described in this thesis (a = 2 cm, $\omega/2\pi$ = 12 Mhz, $t_0 = 5$ msec, $I_0 = 350$ A (rms)), the results are $u_\infty(t_0) = 0.51^\circ C$ and $\Theta(1, \tau_0) = 2.65$, hence $u(a, t_0) = 1.35^\circ C$. Therefore heating of the antenna structure from ohmic currents will be negligible.

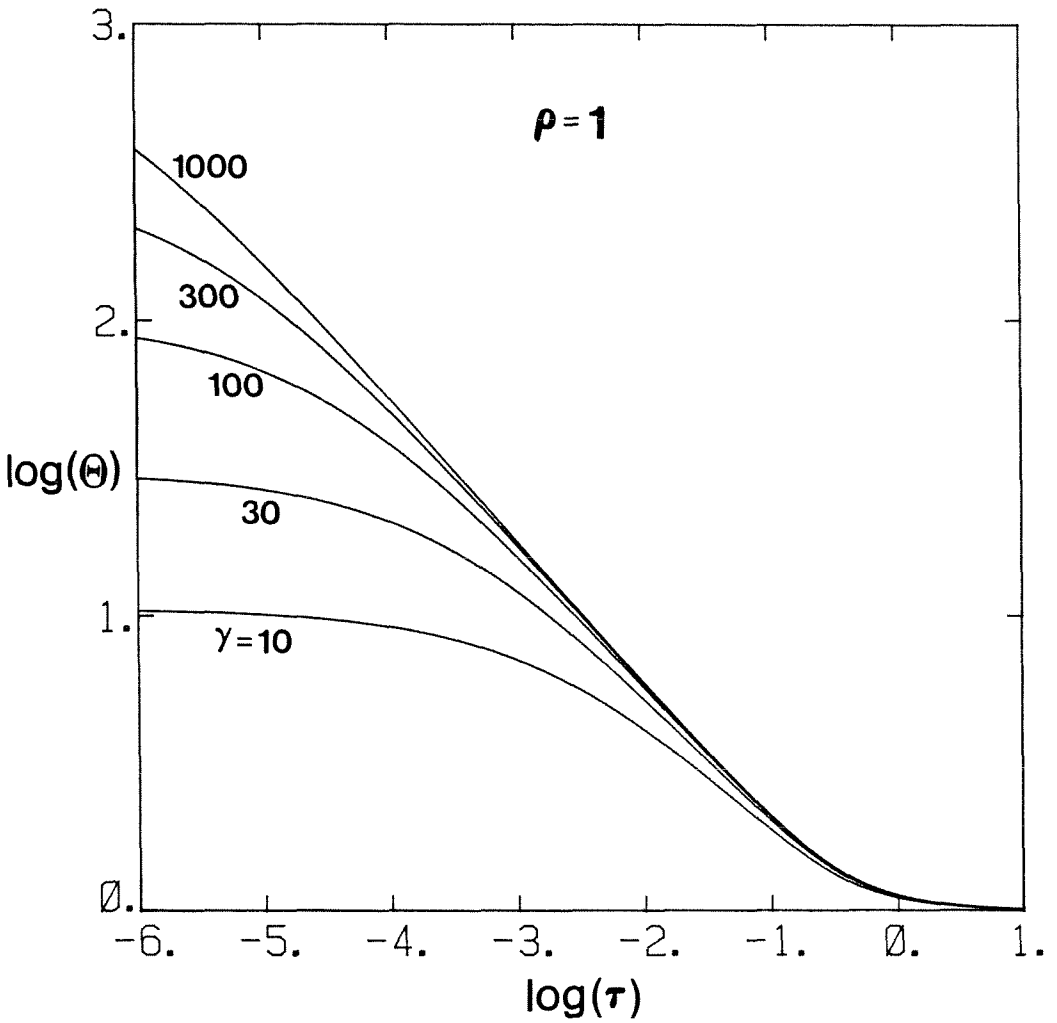

FIG. B-5. Plot of normalized surface temperature $\Theta(1,\tau)$ as a function of τ, for various γ.

B.8 Conclusion

A solution has been presented for the transient temperature distribution of a conducting cylinder heated by an RF current and has been solved numerically for a wide range of parameters. Significantly enhanced peak surface temperatures are found for short times ($\tau \ll 1$). The effect is very small for parameters appropriate to the experiments performed on the Caltech tokamak but may be important for systems operating in other regimes with very high currents or higher frequencies.

REFERENCES

Abramowitz, M. and Stegun, I. (eds.), *Handbook of Mathematical Functions* (National Bureau of Standards, Washington, D.C., 1972), passim.

Adam, J., et al., "Wave Generation and Heating in the ST-Tokamak at the Fundamental and Harmonic Ion Cyclotron Frequencies," in *Plasma Physics and Controlled Nuclear Fusion Research 1974* (Proc. 5th Int. Conf., Tokyo, 1974), vol. **I**, IAEA, Vienna (1975) 65-73.

Adam, J., and Jacquinot, J., "Eigenmode Field Structure of the Fast Magnetosonic Wave in a Tokamak and Loading Impedance of Coupling Structures," Report EUR-CEA-FC-886, Association Euratom-CEA, Fountenay-aux-Roses, France (1977).

Afrosimov, V. V., et al., "Method of Investigation of the Flux of Atoms Emitted by a Plasma," *Sov. Phys.-Tech. Phys.* **5**, 1378-1388 (1961).

Aksornkitti, S., et al., "Dispersion of an Electromagnetic Pulse," *Am. J. Phys.* **37**, 783-784 (1969).

Allis, W., Buchsbaum, S., and Bers, A., *Waves in Anisotropic Plasmas* (M.I.T. Press, Cambridge, Mass., 1963), passim.

Anderson, J. M., "Wide Frequency Range Current Transformers," *Rev. Sci. Instrum.* **42**, 915-926 (1971).

Anicin, B. A., et al., "Excitation of Nanosecond Waves on Positive Columns," *J. Plasma Phys.* **7**, 403-416 (1972).

Artsimovich, L. A., "Tokamak Devices," *Nucl. Fusion* **12**, 215-252 (1972).

Artsimovich, L. A., et al., "Investigation of Plasma Neutron Radiation from the Tokamak T-3A," *Sov. Phys. JETP* **34**, 306-309 (1972).

Ashby, D. E., et al., "A Multi-Coil Magnetic Probe," *J. Sci. Instrum.* **40**, 364-367 (1963).

Barnett, C. V. and Ray, J. A., "A Calibrated Neutral Atom Spectrometer for Measuring Plasma Ion Temperatures in the 0.165- to 10-keV Energy Region," *Nucl. Fusion* **12**, 65-72 (1972).

Belinski, V. N., et al., "Characteristics of the Use of a Rogowski Loop for Measuring Steady currents in a Plasma (trans.)," *Teplofizika Vysokikh Temperatur* **11**, 39-45 (1973), trans. in *High Temp. (USSR)* **11**, 34-38 (1973).

Bhatnagar, V. P., et al., "Magnetosonic Resonance Heating in the Erasmus Tokamak," Internal Report, Laboratoire de Physique des Plasmas, Ecole Royale Militaire, Brussels, Belgium (1978a).

Bhatnagar, V. P., et al., "Experimental Results on the Erasmus Tokamak," Laboratory Report No. 66, Laboratoire de Physique des Plasmas, Ecole Royale Militaire, Brussels, Belgium (1978b).

Bhatnagar, V. P., et al., "A 3-D Analysis of the Coupling Characteristics of Ion Cyclotron Resonance Heating Antennae," *Nucl. Fusion* **22**, 280-288 (1982).

Biddle, A. P., "Ion Heating in the Ion Cyclotron Range of Frequencies in the Wisconsin Tokapole II," Ph.D. Thesis, University of Wisconsin, Madison, Wis. (1980).

Boff, A. F., "Power Meter and Mismatch Indicator," *Wireless Engineer* **28**, 278-281 (1951).

Boyd, T. J. M. and Sanderson, J. J., *Plasma Dynamics* (Barnes & Noble, Inc., New York, N.Y., 1969), passim.

Brillouin, L., *Wave Propagation and Group Velocity* (Academic Press, New York, N.Y., 1960), chapter 4.

Budny, R., "Results from Langmuir probe measurements in PDX and PLT," *J. Vac. Sci. Technol.* **20**, 1238-1241 (1982).

Burrous, C. N., et al., "Detection Efficiency of a Continuous Channel Electron Multiplier for Positive Ions," *Rev. Sci. Instrum.* **38**, 1477-1481 (1967).

Butler, H. S. and Kino, G. S., "Plasma Sheath Formation by Radio-Frequency Fields," *Phys. Fluids* **6**, 1346-1355 (1963).

Buzankin, V. V., et al., "Experiments in Magnetoacoustic Heating of Plasma in Tokamak T-4," in *Plasma Physics and Controlled Nuclear Fusion Research 1976* (Proc. 6^{th} Int. Conf., Berchtesgaden, 1976), vol. **III**, IAEA, Vienna (1977) 61-74.

Carlin, H. J. and Amstutz, P., "On Optimum Broad-band Matching," *IEEE Trans. on Circuits and Systems* **CAS-28**, 401-405 (1981).

Chen, F. F., "Electric Probes," in *Plasma Diagnostic Techniques*, Huddlestone, R. H. and Leonard, S. L., eds., (Academic Press, New York, N.Y., 1965), chapter 4.

Chen, F. F., *Introduction to Plasma Physics* (Plenum Press, New York, N.Y., 1974), p. 132.

Chipman, R. A., *Theory and Problems of Transmission Lines* (McGraw-Hill, New York, N.Y., 1968), chapter 7.

Coleman, P. D., "Propagation and Damping of the Fast Alfvén Wave in the Texas Tech Tokamak," Ph.D. Thesis, Texas Tech University, Lubbock, Tx. (1983).

Colestock, P. L. and Kashuba, R. J., "The Theory of Mode Conversion and Wave Damping near the Ion Cyclotron Frequency," Report PPPL-1930, Plasma Physics Laboratory, Princeton University, Princeton, N.J. (1982).

Colestock, P. L., "Review of ICRF Experiments," lecture notes distributed at IEEE 1983 Mini-course on RF Heating and Current Drive in Magnetic Fusion Plasmas (May 25-27, San Diego, 1983).

Collin, R. W., *Foundations for Microwave Engineering* (McGraw-Hill Book Co., Inc., New York, N.Y., 1966), passim.

Cooper, J., "On the High-Frequency Response of a Rogowski Coil," *Plasma Phys.* **5**, 285-289 (1963).

Copson, E. T., *Asymptotic Expansions* (Cambridge University Press, Cambridge, Great Britain, 1965), chapter 4.

Cross, R. C., "Construction of Diagnostic Equipment for the Texas Tech Tokamak," Technical Report No. 2, Plasma Laboratory, Texas Tech University, Lubbock, Tex. (1977).

Decker, G. and Honea, D. L., "Magnetic Probes with Nanosecond Response Time for Plasma Experiments," *J. Phys. E.* **5**, 481-484 (1972).

DeMaw, D., *ARRL Electronics Data Book* (American Radio Relay League, Inc., Newington, Ct., 1976), passim.

DeMaw, D., *Practical RF Communications Data* (Howard Sams, Inc., Indianapolis, Ind., 1978), p. 48.

DeMaw, D. (ed.), *The Radio Amateur's Handbook* (ARRL, Inc., Newington, Ct., 1979), chapter 6.

DeMichelis (ed.) and the T.F.R. Group, "Tokamak Plasma Diagnostics," *Nucl. Fusion* **18**, 652 (1978).

Demokan, Q., et al., "A Time-of-Flight Study of Waves Guided by a Plasma Column," *Plasma Phys.* **13**, 29-32 (1971).

Dimock, D. L., et al., "The Ontogeny of a Tokamak Discharge," *Nucl. Fusion* **13**, 271-280 (1973).

Ecker, V. G., et al., "Fehlerabschatzung fur Messungen mit Magnetischen Sonden," *Ann. Physik.* **10**, 220-228 (1962).

Elet, R. S. and Chiu, S. C., "ICRF Antenna Coupling Studies," Report GA-A16848, General Atomic Company, La Jolla, Ca. (1982).

Eubank, H. P., "Determination of Plasma Ion Temperatures by Analysis of Charge-Exchange Neutrals," in *Diagnostics for Fusion Experiments*, Sindoni, E. and Wharton, C. (eds.) (Pergamon Press, New York, N.Y., 1979).

Fano, R. M., ""Theoretical Limitations on the Broadband Matching of Arbitrary Impedances," *J. Franklin Inst.* **249**, 57-83 and 139-155 (1960).

Faulconer, D. W., "Adverse Magnetic Shielding of Electrostatically Shielded Strip Line Antennas; Application to ICRF Heating," *Bull. Am. Phys. Soc.* **26**, 896 (1981).

Fleischmann, H. H. and Tuckfield, R. G., "Sensitivity of a Stripping Analyzer for Neutral Hydrogen Atoms in the Energy Range from 50 to 300 eV," *Nucl. Fusion* **8**, 81-88 (1968).

Fonck, R. J., "High Confinement Regime in PDX," *Bull. Am. Phys. Soc.* **28**, 1052 (1983).

Frank-Kamenetskii, D. A., "Magnetic Sound in Three-Component Plasma," *Zh. Tekh. Fiz.* **30**, 893-898 (1960).

Furth, H., "Magnetic Confinement Experiments," *Nucl. Fusion* **23**, 97-120 (1983).

Gaudreau, M. P. J., "Comparative Study of Fundamental and Second Harmonic ICRF Wave Propagation and Damping at High Density in the Alcator Tokamak," Sc.D. Thesis, Massachusetts Institute of Technology, Cambridge, MA (1981).

Golovin, D., et al., "Stable Plasma Column in a Longitudinal Magnetic Field," in *Proc. 2nd U.N. Conf. Peaceful Uses At. Energy, Geneva* **32**, 72-81 (I.D.S. Columbia Univ. Press, New York, N.Y., 1959).

Goldston, R. J., "Diagnostic Techniques for Magnetically Confined High Temperature Plasmas II," Report PPPL-1924, Plasma Physics Laboratory, Princeton University, Princeton, N.J. (1982).

Goodrich, G. W. and Wiley, W. C., "Continuous Channel Electron Multiplier," *Rev. Sci. Instrum.* **33**, 761-762 (1962). Also see "Electron Multiplier," U.S. Patent No. 3,128,408.

Gould, R. W., "Magnetohydrodynamic Waves in Cylindrical Geometry For Finite ω/ω_{ci}," Internal Laboratory Report, California Institute of Technology, Pasadena, Ca. (January, 1960).

Gould, R. W., "Ion Cyclotron Resonance in a Toroidal Magnetic Field," Internal Laboratory Report, California Institute of Technology, Pasadena, Ca.

(January, 1975).

Greene, G. J. and Hedemann, M. A., "Some Aspects of the Design and Construction of the Caltech Research Tokamak," in *Proceedings of the Small Toroidal Plasma Devices Users Meeting*, Kristiansen, M. and Hagler, M. (eds.) (D.O.E. report no. DOE-ET-78-G-05-5918, 1978).

Greene, G. J. and Gould, R. W., "Coupling Efficiency to ICRF Toroidal Eigenmodes and Transmission Between Two Identical Antennas," *Bull. Am. Phys. Soc.* **24**, 1062 (1979).

Greene, G. J. and Gould, R. W., "ICRF Experiments on the Caltech Tokamak," *Bull. Am. Phys. Soc.* **25**, 931 (1981).

Greene, G. J. and Gould, R. W., "Electric and Magnetic Excitation of ICRF Waves: Eigenmodes and Wave Packets," in *1983 IEEE Intl. Conf. on Plasma Sci.* (IEEE cat. no. 83CH1847-3), p. 18.

Hamming, R. W., *Digital Filters* (Prentice-Hall, Inc., Englewood Cliffs, N.J., 1977), passim.

Harrower, B. A., "Measurement of Electron Energies by Deflection in a Uniform Electric Field," *Rev. Sci. Instrum.* **26**, 850-854 (1955).

Hawryluk, R. J., "Perpendicular Neutral Beam Injection in PDX," *Bull. Am. Phys. Soc.* **26**, 918 (1981).

Hedemann, M. A., "Measurements of Magnetic Field Fluctuations in the Caltech Research Tokamak," Ph.D Thesis, California Institute of Technology, Pasadena, Ca. (1982).

Hosea, J., et al., "Fast-Wave Heating of Two-Ion Plasmas in the Princeton Large Torus through Minority-Cyclotron-Resonance Damping," *Phys. Rev. Lett.*

43, 1802 (1979).

Hwang, D. Q., et al., "Complex Antenna Impedance Measurements for Magnetosonic Eigenmodes of a Tokamak," *Bull. Am. Phys. Soc.* **23**, 820 (1978a).

Hwang, D., et al., "Fast Magnetosonic Wave Mode-Tracking in PLT," *Bull. Am. Phys. Soc.* **23**, 836 (1978b).

Hwang, D. Q., "Propagation of the Fast Magnetosonic Wave in a Tokamak Plasma," Ph.D. Thesis, California Institute of Technology, Pasadena, Ca. (1979).

Hwang, D. Q. and Gould, R. W., "Measurements of the Complex Plasma Loading Impedance of the Magnetosonic Cavity Mode," *Phys. Fluids* **23**, 614-623 (1980).

Hwang, D. Q., et al., "Heating of Plasma Ions in a Tokamak by the Second-Harmonic Ion-Cyclotron Resonance Interaction with Radio-Frequency Waves," *Phys. Rev. Lett.* **51**, 1865-1868 (1983).

Ichimaru, S., *Basic Principles of Plasma Physics* (W. A. Benjamin, Inc., Reading, Mass., 1973), p. 52.

Iglesias, G. E. and McGarity, J. O., "Channel Electron Multiplier Efficiency for Protons of 0.2 - 10 keV," *Rev. Sci. Instrum.* **42**, 1728-1729 (1971).

Ivanov, N. V., et al., "Generation of Magnetosonic Oscillation in the Tokamak TO-1," *JETP Lett.* **14**, 138-140 (1971).

Ivanov, N. V., et al., "Excitation of the Spectrum of Natural Oscillations of the Plasma Pinch in the Tokamak TO-1," *Sov. J. At. En.* **32**, 389-393 (1972).

Jackson, J. D., *Classical Electrodynamics* (John Wiley and Sons, Inc., New York,

N.Y., 1962), passim.

Jahns, G. L., et al., "Internal Disruptions in Tokamaks," *Nucl. Fusion* **18**, 609-628 (1978).

Josea, J., et al., "Fast-Wave Heating of Two-Ion Plasmas in the Princeton Large Torus through Minority-Cyclotron-Resonance Damping," *Phys. Rev. Lett.* **43**, 1802-1806 (1979).

Klima, R., et al., "High-Frequency Heating of Plasma with Two Ion Species," *Nucl. Fusion* **15**, 1157-1171 (1975).

Klein, A. G., "Demonstration of Ampere's Circuital Law using a Rogowski Coil," *Am. J. Phys.* **43**, 368-370 (1975).

Kubena, R., "Fluctuations in a Tokamak Plasma," Ph.D. Thesis, California Institute of Technology, Pasadena, Ca. (1978).

Krall, N. A. and Trivelpiece, A. W., *Principles of Plasma Physics* (McGraw-Hill Book Co., Inc., New York, N.Y., 1973), passim.

Landt, D. L., et al., "Properties of Waves Guided by a Plasma Column as Determined by Time-of-Flight Measurements," *Plasma Phys.* **16**, 407-412 (1974).

Langmuir, I. and Mott-Smith, H. Jr., "Studies of Electric Discharges in Gases at Low Pressures," *General Electric Review* **27**, 449-455, 538-548, 616-623, 762-771, 810-820 (1924).

Lecioni, D. E., et al., "Influence of a Toroidal Field on Plasma Confined in a Toroidal Octupole," *Phys. Fluids* **11**, 1115 (1968).

Levine, B. S., "Particle Confinement and Magnetic Fluctuations in Tokamak

Discharges with Gas Puffing," Ph.D. Thesis, California Institute of Technology, Pasadena, Ca. (1980).

Lovberg, R., "Magnetic Probes," in *Plasma Diagnostic Techniques*, Huddlestone, R. H. and Leonard, S. L., eds. (Academic Press, New York, N.Y., 1965), chapter 3.

Luxon, J. L., et al., "RF Heating in Doublet IIA," Report GA-A15820, General Atomic Company, La Jolla, Ca. (1980).

Malmberg, J. H., "Magnetic Probe Resolution," *Rev. Sci. Instrum.* **35**, 1622-1623 (1964).

Martin, T., *Electronic Circuits* (Prentice-Hall Inc., Englewood Cliffs, N.J., 1955), p. 452.

Mathews, J. and Walker, R. L., *Mathematical Methods of Physics* (W. A. Benjamin, Inc., Menlo Park, Ca., 1970), passim.

Mazzucato, E., "Spectrum of Small-Scale Density Fluctuations in Tokamaks," *Phys. Rev. Lett.* **48**, 1828-1830 (1982).

Messiaen, A. M., et al., "Coupling of RF Energy in Toroidal Devices by Means of Magneto-Acoustic Resonances," Internal Report, Laboratoire de Physique des Plasmas, Ecole Royale Militaire, Brussels, Belgium (1978).

Messiaen, A. M. and Weynants, R., "Design of ICRH Launching Structures," in *Proceedings of the Third Joint Varenna-Grenoble International Symposium on Heating in Toroidal Plasmas*, Grenoble, France (1982).

Minicircuits Laboratory, *Mixer Application Handbook* (Minicircuits Laboratory, Brooklyn, N.Y., 1980), passim.

Moisan, M., et al., "Experimental Investigations of the Propagation of Surface Waves Along a Plasma Column," *Plasma Phys.* **24**, 1331-1400 (1982).

Nassisi, V. and Luches, A., "Rogowski Coils: Theory and Experimental Results," *Rev. Sci. Instrum.* **50**, 900-902 (1979).

Oren, L. and Taylor, R. J., "Trapping and Removal of Oxygen in Tokamaks," *Nucl. Fusion* **17**, 1143-1151 (1977).

Paoloni, F. J., "Coupling to Fast MHD Eigenmodes in a Toroidal Cavity," Report MATT-1119, Plasma Physics Laboratory, Princeton University, Princeton, N.J. (1975a).

Paoloni, F. J., "Boundary Effects on M = 0, ±1 Alfvén Waves in a Cylindrical, Collisionless Plasma," *Phys. Fluids* **18**, 640-644 (1975b).

Paoloni, F. J., "Coupling to Fast Eigenmodes in a Non-Uniform Plasma," *Nucl. Fusion* **18**, 359-366 (1978).

Parsons, C. R. and Medley, S. S., "On the Interpretation of Charge-Exchange Ion Temperature Measurements in Tokamaks," *Plasma Phys.* **16**, 267-273 (1974).

Parzen, B. and Yarlow, A., "Theory and Design of the Reflectometer," *Proc. I.R.E.* **24**, 94 (1947).

Parzen, B., "Impedance Measurements with Directional Couplers and Supplementary Voltage Probe," *Proc. I.R.E.* **37**, 1208-1211 (1949).

Pellinen, D., et al., "Rogowski Coil for Measuring Fast, High-level Pulsed Currents," *Rev. Sci. Instrum.* **51**, 1535-1540 (1980).

Perkins, F. W., "Hydromagnetic Wave Heating of Tokamak Plasmas," *Symposium*

on Plasma Heating and Injection, International School of Plasma Physics, Varenna, Italy (September 1972).

Piperno, F. and Solaini, G., "On Rogowski Coil as a Quantitative Probe for Current Density Measurements in a Linear Pinch," *Il Nuovo Cimento* **29**, 239-251 (1975).

Pistolkors, A. and Neuman, M., "Device for Direct Measurement of the Coefficient of a Travelling Wave in Feeder (trans.)," *Elecktrosvyas* **9**, 9-15 (1941).

Pridmore-Brown, D. C., "Alfvén Waves in a Stratified Incompressible Fluid," *Phys. Fluids* **9**, 1290-1292 (1966).

Ram, A. and Bers, A., "Antenna-Plasma Coupling Theory for ICRF Heating of Large Tokamaks," Plasma Fusion Center Report PFC/CP-82-2, Massachusetts Institute of Technology, Cambridge, Mass. (1982).

Ramo, S. and Whinnery, J. R., *Fields and Waves in Modern Radio* (John Wiley and Sons, Inc., New York, N.Y., 1944), chapter 5.

Rogowski, W. and Steinhaus, W., "Die Messung der Magnetischen Spannung," *Arch. Electrotech.* **1**, 141 (1912).

Ruthroff, C.L., "Some Broad-Band Transformers," *Proc. I.R.E.* **47**, 1337-1342 (1959).

Sato, M., "Ion-Probe Current in a Magnetized Plasma," *Phys. Fluids* **15**, 2427-2433 (1972).

Schmidt, J. A., "High Impedance Langmuir Probes," *Rev. Sci. Instrum.* **39**, 1297-1299 (1968).

Schneidermann, A. M. and Patrick, R. M., "Axial Current Distribution in the Exhaust of the Magnetic Annular Arc," *AIAA J.* **5**, 249-253 (1967).

Schwartz, R., "Bibliography on Directional Couplers," *Trans. IRE* **MTT-2**, 58-63 (1954).

Segre, S. E. and Allen, J. E., "Magnetic Probes of High Frequency Response," *J. Sci. Instrum.* **37**, 369-371 (1960).

Sevick, J., "Simple Broadband Matching Networks," *QST* **LX**, 20-23 (1976).

Spitzer, L., *Physics of Fully Ionized Gases* (Interscience Publishers, New York, N.Y., 1962), passim.

Stix, T. H. and Palladino, R. W., "Observation of Ion Cyclotron Waves," *Phys. Fluids* **3**, 641-647 (1960).

Stix, T. H., *The Theory of Plasma Waves* (McGraw-Hill Book Co., Inc., New York, N.Y., 1962), passim.

Stix, T. H., "Fast Wave Heating of a Two Component Plasma," *Nucl. Fusion* **15**, 737-754 (1975).

Stix, T. H., "Radiofrequency Heating of Plasmas using Alfvén Waves," lecture notes distributed at IEEE 1983 Mini-course on RF Heating and Current Drive in Magnetic Fusion Plasmas (May 25-27, San Diego, 1983).

Stygar, W. and Gerdin, G., "High Frequency Rogowski Coil Response Charateristics," *IEEE Trans. on Plasma Science* **PS-10**, 40-44 (1982).

Surko, C. M. and Slusher, R. E., "Study of Plasma Density Fluctuations by the Correlation of Crossed CO_2 Laser Beams," *Phys. Fluids* **23**, 2425-2439 (1980).

Nuclear Fusion Research 1976 (Proc. 6th Int. Conf., Berchtesgaden, 1976), vol. **III**, IAEA, Vienna (1977) 39-59.

Thompson, H. R., "Fast Magnetosonic Wave Propagation and Damping near the Second Ion Cyclotron Harmonic in PLT," *Bull. Am. Phys. Soc.* **27**, 1044 (1982).

Vdovin, V. L., et al., "Excitation of Magnetosonic Resonance in the Tokamak Plasma," *JETP Lett.* **14**, 149 (1971).

Von Goeler, S., et al., "Studies of Internal Disruptions and m=1 Oscillations in Tokamak Discharges with Soft-X-Ray Techniques," *Phys. Rev. Lett.* **33**, 1201-1203 (1974).

Vignone, E., "RF Current Standard for the Calibration of Current Probes," in *Proceedings of the 5th Annual ISA Test Measurement Symposium* (Instrum. Soc. Am., Pittsburgh, Pa., 1968), pp. 28-31.

Weyants, R. R., "Ion Heating at Twice the Ion-Cyclotron Frequency in Reactor-Oriented Machines," *Phys. Rev. Lett.* **33**, 78-82 (1974).

Youla, D. C., "A New Theory of Broadband Matching," *IEEE Trans. on Circuit Theory* **CT-11**, 30-50 (1964).

Zweben, S. J., et al., "Vacuum Photodiode Detector Array for Broadband UV Detection in a Tokamak Plasma," *Rev. Sci. Instrum.* **50**, 50-56 (1979).

Zweben, S. J. and Gould, R. W., "Scaling of Edge-Plasma Turbulence in the Caltech Tokamak," *Nucl. Fusion* **23**, 1625-1641 (1983).